Research Topics

The response of microalgae and plankton to climate change and human activities

Edited by
Zhaohe Luo, Yanpei Zhuang and Kieng Soon Hii

Coordinated by
Hala F. Mohamed

Published in
Frontiers in Marine Science

ISSN 1664-8714
ISBN 978-2-8325-4442-6
DOI 10.3389/978-2-8325-4442-6

About Frontiers

Frontiers is more than just an open access publisher of scholarly articles: it is a pioneering approach to the world of academia, radically improving the way scholarly research is managed. The grand vision of Frontiers is a world where all people have an equal opportunity to seek, share and generate knowledge. Frontiers provides immediate and permanent online open access to all its publications, but this alone is not enough to realize our grand goals.

Frontiers journal series

The Frontiers journal series is a multi-tier and interdisciplinary set of open-access, online journals, promising a paradigm shift from the current review, selection and dissemination processes in academic publishing. All Frontiers journals are driven by researchers for researchers; therefore, they constitute a service to the scholarly community. At the same time, the *Frontiers journal series* operates on a revolutionary invention, the tiered publishing system, initially addressing specific communities of scholars, and gradually climbing up to broader public understanding, thus serving the interests of the lay society, too.

Dedication to quality

Each Frontiers article is a landmark of the highest quality, thanks to genuinely collaborative interactions between authors and review editors, who include some of the world's best academicians. Research must be certified by peers before entering a stream of knowledge that may eventually reach the public - and shape society; therefore, Frontiers only applies the most rigorous and unbiased reviews. Frontiers revolutionizes research publishing by freely delivering the most outstanding research, evaluated with no bias from both the academic and social point of view. By applying the most advanced information technologies, Frontiers is catapulting scholarly publishing into a new generation.

What are Frontiers Research Topics?

Frontiers Research Topics are very popular trademarks of the *Frontiers journals series*: they are collections of at least ten articles, all centered on a particular subject. With their unique mix of varied contributions from Original Research to Review Articles, Frontiers Research Topics unify the most influential researchers, the latest key findings and historical advances in a hot research area.

Find out more on how to host your own Frontiers Research Topic or contribute to one as an author by contacting the Frontiers editorial office: frontiersin.org/about/contact

February 2024

The response of microalgae and plankton to climate change and human activities

Topic editors
Zhaohe Luo — Third Institute of Oceanography, Ministry of Natural Resources, China
Yanpei Zhuang — Jimei University, China
Kieng Soon Hii — University of Malaya, Malaysia

Topic Coordinator
Hala F. Mohamed — Al-Azhar University, Egypt

Citation
Luo, Z., Zhuang, Y., Hii, K. S., Mohamed, H. F., eds. (2024). *The response of microalgae and plankton to climate change and human activities*.
Lausanne: Frontiers Media SA. doi: 10.3389/978-2-8325-4442-6

Table of contents

frontiers | Frontiers in Marine Science

TYPE Editorial
PUBLISHED 29 January 2024
DOI 10.3389/fmars.2024.1366749

Check for updates

OPEN ACCESS

EDITED AND REVIEWED BY
Stelios Katsanevakis,
University of the Aegean, Greece

*CORRESPONDENCE
Zhaohe Luo
luozhaohe@tio.org.cn

RECEIVED 07 January 2024
ACCEPTED 17 January 2024
PUBLISHED 29 January 2024

CITATION
Luo Z, Hii KS, Zhuang Y and Mohamed HF (2024) Editorial: The response of microalgae and plankton to climate change and human activities.
Front. Mar. Sci. 11:1366749.
doi: 10.3389/fmars.2024.1366749

Editorial: The response of microalgae and plankton to climate change and human activities

Zhaohe Luo[1]*, Kieng Soon Hii[2], Yanpei Zhuang[3] and Hala F. Mohamed[4]

[1]Key Laboratory of Marine Ecological Conservation and Restoration, Third Institute of Oceanography, Ministry of Natural Resources, Xiamen, China, [2]Bachok Marine Research Station, Institute of Ocean and Earth Sciences, University of Malaya, Bachok, Kelantan, Malaysia, [3]Polar and Marine Research Institute, College of Harbor and Coastal Engineering, Jimei University, Xiamen, China, [4]Botany & Microbiology Department, Faculty of Science, Al-Azhar University (Girls Branch), Cairo, Egypt

KEYWORDS

climate change, human activities, microalgae, plankton, harmful algal bloom

Editorial on the Research Topic
The response of microalgae and plankton to climate change and human activities

This special Research Topic is dedicated to exploring the responses of microalgae and plankton to climate change and human-induced environmental alterations. Encompassing disciplines such as ecology, environmental science, marine biology, and biogeochemistry, this Research Topic reflects the intricate and pressing nature of this interdisciplinary field.

Microalgae and plankton are integral to the stability and health of global marine ecosystems. They form the foundation of aquatic food webs, contribute to climate regulation through carbon dioxide absorption, and support biodiversity. Yet, these organisms face unprecedented challenges due to climate change and anthropogenic factors including ocean acidification, rising temperatures, hypoxia, and coastal eutrophication, which profoundly affect their community dynamics and ecological functions (Di Pane et al., 2022). Current knowledge on the mechanisms of microalgae and plankton community response to these changing environmental conditions remains limited. Ocean acidification, a direct consequence of increased CO2 emissions, is altering the carbonate chemistry of marine waters, affecting calcifying organisms and disrupting marine food webs (Doney et al., 2020). Rising ocean temperatures are causing shifts in the distribution of microalgae and plankton species, with poleward movements observed in various regions, indicating changes in oceanic ecosystems (Benedetti et al., 2021). Eutrophication, primarily driven by agricultural runoff and urban wastewater, triggers harmful algal blooms (Glibert, 2020; Kang et al., 2022). These blooms, upon decomposition, disrupt the food chain, leading to the demise of higher trophic level marine animals, and can even pose risks to human health (Liu et al., 2020). Furthermore, hypoxia, resulting from eutrophication and increased stratification of water bodies, leads to the formation of dead zones where marine life struggles to survive, posing a significant threat, especially in coastal and estuarine areas (Wallace and Gobler, 2021). These alterations affect not only the biodiversity and functioning of marine ecosystems but also have socio-economic implications, particularly for fisheries and aquaculturethat rely heavily on the health of planktonic communities (Doney et al., 2020). Recent research has shed light on the adaptive responses of microalgae and plankton to environmental stressors. Some species demonstrate resilience by adapting their life cycles and physiological processes (Kholssi et al., 2023). However, the long-term implications of these adaptations are still not fully understood. The complexity of interactions between various stressors, such as the combined effects of acidification, warming, and deoxygenation, presents a challenge in predicting the future of these crucial organisms (Doney et al., 2020). In light of these challenges, this Research Topic aims to provide current knowledge on the impact of climate change and human activities on microalgae and plankton. By bringing together studies from diverse geographical regions and ecological contexts, we aim to develop a comprehensive understanding of how these organisms are responding to global environmental changes. This understanding is crucial for developing effective conservation and management strategies to protect and sustain marine ecosystems in a rapidly changing world.

In this Research Topic, 11 papers collaboratively address the multifaceted effects of environmental changes on microalgae and plankton. Key themes include the historical context, ecological sensitivity, and adaptive responses of these organisms.

Several papers focus on historical and regional studies: The first article explores the diatom distribution in Holocene sediments in the West Caroline Basin, offering paleoceanographic insights (Chen et al.). The third paper is related to nanophytoplankton and microphytoplankton in the Western Tropical Pacific Ocean and enhances our understanding of phytoplankton community structures and carbon biomass (Yan et al.). The eighth paper, focusing on planktonic protist Communities in the Jeju Strait, uncovers the complex dynamics and species interactions within these communities (Min and Kim). The tenth paper and analyzes the phytoplankton spring succession patterns in the Yellow Sea, and links these patterns to environmental factors (Hyun et al.).

The vulnerability and adaptive responses of marine organisms to current environmental stressors are central to other papers. The second article investigated the Southern Ocean pteropods' life cycles and discusses the sensitivity of Southern Ocean pteropods to ocean acidification and climate change (Gardner et al.), while the fifth paper examines the warming adaptation of the coccolithophore *Emiliania huxleyi*, highlighting its limited adaptation over 800 generations (Zhou et al.). The seventh paper focuses on the shift in the photophysiology of sea ice algae in response to salinity changes, pertinent to Arctic freshening (Forgereau et al.).

The impact of human activities is also a significant theme. The fourth paper investigates the effects of shellfish aquaculture on phytoplankton, revealing complex interactions between human practices and marine ecosystems (Mo et al.). The ninth article delves into the harmful algal species *Heterosigma akashiwo*, providing insights into the mechanisms of harmful algal blooms (Giesler et al.).

Furthermore, two papers emphasize monitoring and detection techniques as vital tools in marine ecology. The sixth paper stresses the importance of monitoring chlorophyll *a* concentration in the China Sea as an indicator of marine ecological health and its implications for fisheries (Zhang et al.). The eleventh and final article introduces a novel approach for detecting anomalies in phytoplankton populations, a crucial step in understanding the impacts of environmental changes (Ciranni et al.).

These contributions not only deepen our understanding of microalgae and plankton responses to environmental changes but also offer critical insights for future research directions and management strategies. This compilation underscores the vital role of interdisciplinary efforts in advancing our knowledge and addressing challenges within global marine ecosystems. We trust that this Research Topic will spark further dialogue, investigation, and innovation in the pursuit of sustainable solutions for marine environmental issues.

Author contributions

ZL: Writing – original draft, Writing – review & editing. KH: Writing – review & editing. YZ: Writing – review & editing. HM: Writing – review & editing.

Funding

The author(s) declare financial support was received for the research, authorship, and/or publication of this article. ZL was funded by the National Key Research and Development Program of China (2019YFE0124700).

Acknowledgments

We extend our gratitude to all contributors and reviewers of this Research Topic for their invaluable insights and expertise.

Conflict of interest

The authors declare that the research was conducted in the absence of any commercial or financial relationships that could be construed as a potential conflict of interest.

Publisher's note

References

Benedetti, F., Vogt, M., Elizondo, U. H., Righetti, D., Zimmermann, N. E., and Gruber, N. (2021). Major restructuring of marine plankton assemblages under global warming. *Nat. Commun.* 12 (1), 5226. doi: 10.1038/s41467-021-25385-x

Di Pane, J., Wiltshire, K. H., McLean, M., Boersma, M., and Meunier, C. L. (2022). Environmentally induced functional shifts in phytoplankton and their potential consequences for ecosystem functioning. *Global Change Biol.* 28 (8), 2804–2819. doi: 10.1111/gcb.16098

Doney, S. C., Busch, D. S., Cooley, S. R., and Kroeker, K. J. (2020). The impacts of ocean acidification on marine ecosystems and reliant human communities. *Annu. Rev. Environ. Resour.* 45 (1), 83–112. doi: 10.1146/annurev-environ-012320-083019

Glibert, P. M. (2020). Harmful algae at the complex nexus of eutrophication and climate change. *Harmful Algae* 91, 101583. doi: 10.1016/j.hal.2019.03.001

Kang, J., Mohamed, H. F., Liu, X., Pei, L., Huang, S., Lin, X., et al. (2022). Combined culture and DNA metabarcoding analysis of cyanobacterial community structure in response to coral reef health status in the South China Sea. *J. Mar. Sci. Eng.* 10 (12), 1984. doi: 10.3390/jmse10121984

Kholssi, R., Lougraimzi, H., and Moreno-Garrido, I. (2023). Effects of global environmental change on microalgal photosynthesis, growth and their distribution. *Mar. Environ. Res.* 184, 105877. doi: 10.1016/j.marenvres.2023.105877

Liu, M., Gu, H., Krock, B., Luo, Z., and Zhang, Y. (2020). Toxic dinoflagellate blooms of *Gymnodinium catenatum* and their cysts in Taiwan Strait and their relationship to global populations. *Harmful Algae* 97, 101868. doi: 10.1016/j.hal.2020.101868

Wallace, R. B., and Gobler, C. J. (2021). The role of algal blooms and community respiration in controlling the temporal and spatial dynamics of hypoxia and acidification in eutrophic estuaries. *Mar. pollut. Bull.* 172, 112908. doi: 10.1016/j.marpolbul.2021.112908

Frontiers in Marine Science

TYPE Original Research
PUBLISHED 09 February 2023
DOI 10.3389/fmars.2023.1110621

OPEN ACCESS

EDITED BY
Yanpei Zhuang,
Jimei University, China

REVIEWED BY
Jinpeng Zhang,
Guangzhou Marine Geological Survey,
China
Chun Chen,
Island Research Center of the Ministry of
Natural Resources, China
Alexander Matul,
P.P. Shirshov Institute of Oceanology (RAS),
Russia

*CORRESPONDENCE
Min Chen
✉ chenmin@tio.org.cn
Jishang Xu
✉ jishangxu@ouc.edu.cn

SPECIALTY SECTION
This article was submitted to
Marine Ecosystem Ecology,
a section of the journal
Frontiers in Marine Science

RECEIVED 29 November 2022
ACCEPTED 20 January 2023
PUBLISHED 09 February 2023

CITATION
Chen M, Huang G, Xu J, Wang C, Xu J,
Qi H and Zhang A (2023) Diatom
distribution in Holocene sediments from
the northern West Caroline Basin
(western equatorial Pacific) and their
environmental significance.
Front. Mar. Sci. 10:1110621.
doi: 10.3389/fmars.2023.1110621

Diatom distribution in Holocene sediments from the northern West Caroline Basin (western equatorial Pacific) and their environmental significance

Min Chen[1,2,3]*, Guobiao Huang[1,2], Jishang Xu[4]*, Chengtao Wang[1], Jizheng Xu[5], Hongshuai Qi[1] and Aimei Zhang[1]

[1]Third Institute of Oceanography, Ministry of Natural Resources, Xiamen, China, [2]School of Advanced Manufacturing, Fuzhou University, Jinjiang, China, [3]Fujian Provincial Key Laboratory of Marine Physical and Geological Processes, Xiamen, China, [4]Key Laboratory of Submarine Geosciences and Prospecting Techniques (Ministry of Education), Ocean University of China, Qingdao, China, [5]Engineering Research Center of Marine Petroleum Development and Security Safeguard (Ministry of Education), Ocean University of China, Qingdao, China

Diatoms are an important component of submarine biogenic sediments and often used for carrying out palaeoceanographical reconstructions. To understand the relationship between diatoms and environment in the western equatorial Pacific, diatoms from the Holocene sediments in the northern West Caroline Basin were selected for analysis. We made quantitative statistics on diatoms and divided diatom assemblages through cluster analysis. A total of 53 species or varieties of diatoms belonging to 22 genera were identified. The range of diatom abundance was 0-88,373 valves/g. The diatoms found were mainly oceanic warm-water species. Overall, *Azpeitia nodulifera* was the species with the highest contribution, followed by *Hemidiscus cuneiformis* and *Thalassiosira pacifica* with these three species together accounting for approximately 80% in this area. We identified four diatom groupings and divided the study area into three regions. Diatom assemblage I in the West Caroline Basin was mainly affected by the North Equatorial Counter Current (NECC), Antarctic Intermediate Water (AAIW) and upwelling, and the supply of nutrients was relatively high. Assemblage II in the West Caroline Ridge was less influenced by currents, and thus had lower abundance and species diversity than assemblage I. The complex diatom assemblages in the Yap Trench were probably controlled by Upper Circumpolar Deep Water (UCPW) and Lower Circumpolar Deep Water (LCPW).

KEYWORDS

diatom, western equatorial Pacific, environmental significance, West Caroline Basin, Holocene sediment

1 Introduction

The West Caroline Basin is located in the core of the Western Pacific Warm Pool, where the annual average sea-surface temperature is a minimum of 28°C (Wang et al., 2009; Qi et al., 2020; Chen et al., 2021). Sea temperature anomalies in the region influence climate change in the Asia-Pacific region and even the world by heating seawater and transporting radiant heat to the atmosphere (Long et al., 2021). Understanding the generation and burial of biological sediments in the region is crucial to understanding the global carbon cycle and changes in marine conditions (Lyle and Baldauf, 2015).

As one of the general primary producers, diatoms are an important component of submarine biogenic sediments. In sea areas where the water depth is greater than the carbonate compensation depth, fossil diatom frustules are relatively well preserved (Zhang et al., 2015). The distribution of diatoms in sediment deposits, and the factors that control their distributions, are often discussed by researchers when reconstructing both contemporary environments and paleoenvironments (Chen et al., 2019). Diatoms from upper sediments have been studied extensively in various regions (Esper and Gersonde, 2014; Ren et al., 2014), allowing for reliable paleoceanographic reconstructions. (Tsoy and Moiseenko, 2014; Shen et al., 2017b). However, only a few investigations were published in the western Pacific. In the West Philippine Basin, the relative abundance of seven tropical pelagic diatoms was greater than 20%, and their distribution pattern was influenced by the flow of the Kuroshio Current (Zhai et al., 2010; Chen et al., 2014; Shen et al., 2017a). In the southern Mariana Trench, Cai (2019) found a large number of *Ethmodiscus rex* (Rattray) Hendey and other small diatoms, dominated by warm-water and eurythermal species.

The purpose of this study was to investigate the species composition and abundance of diatoms in Holocene sediments of the northern West Caroline Basin. We analyzed the environmental factors that control the distribution of diatoms by considering a series of processes, including their production, sedimentation and burial, and explored the differences of diatom assemblages in different environments and their causes. This study enriched diatom research in the western Pacific and contributed to the establishment of a comprehensive diatom–based data set, which was necessary for carrying out future paleoceanographic reconstructions in the region.

2 Study area

The study area is located in the northern West Caroline Basin (136°0′E-142°0′E, 4°0′-9°0′N; Figure 1). The bathymetric range of the study area is highly variable (2395-7837 m), with an average water depth of 4,015 m, including the Yap Trench (> 6500 m), the West Caroline Ridge (< 3000 m), and a flat topographic basin in the southern part (Qi et al., 2020; Chen et al., 2020a). In general, the water depth gradually decreases from southwest to northeast. Because the study area is located in the deep sea, it is influenced little by continental runoff and the seawater possesses a high transparency of 20-40 m throughout the year (Yue et al., 2018; Zhang, 2020).

The West Caroline Basin experiences a typical tropical marine climate with high temperature and rainfall all year round (Qi et al., 2020). The thermocline depth in the study area is 100-150 m. The surface seawater possesses high temperature, low salinity and low nutrient content, and is characterized by a two-layer system. A barrier layer separates the nutrient-rich deep water from the surface water (Vinogradov, 1981; Kobayashi and Takahashi, 2002; Chen et al., 2021).

The many currents in the western Pacific (Zhang, 2008) comprise water masses of different characteristics that have an important impact on phytoplankton including diatoms. Formed from the eastward diversion of Mindanao Current (MC), the North

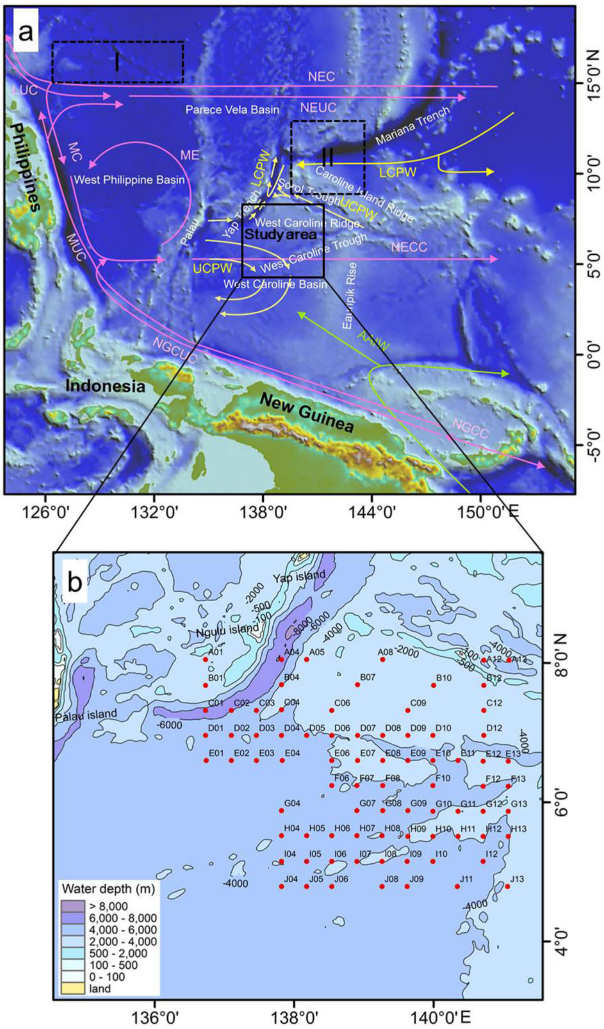

FIGURE 1
(A) Study area (dashed boxes I and II indicate the study areas of Shen et al. 2017a and Cai (2019), respectively) and **(B)** Sampling stations. The red arrows represent surface and subsurface currents (Hu et al., 2015; Pujari et al., 2021), the yellow arrows represent deep currents (Kawano et al., 2006; Kender et al., 2018; Chen et al., 2020a; Liu et al., 2022), and the green arrows represent the Antarctic Intermediate Water (Bingham and Lukas, 1995). Abbreviations: NEC, North Equatorial Current; NECC, North Equatorial Counter Current; NEUC, North Equatorial Undercurrent; NGCC, New Guinea Coastal Current; NGCUC, New Guinea Coastal Undercurrent; LUC, Luzon Undercurrent; MC: Mindanao Current; ME, Mindanao Eddy; MUC, Mindanao Undercurrent; AAIW, Antarctic Intermediate Water; LCPW, Lower Circumpolar Deep Water; UCPW, Upper Circumpolar Deep Water.

Equatorial Counter Current (NECC;1-8°N) crosses the West Caroline Basin from west to east and influences the study area (Christian et al., 2004). The Antarctic Intermediate Water (AAIW; 500-1200 m water depth) enters the equatorial western Pacific Ocean through the Vitiaz Channel and its northwestward branch flows to and affects the study area (Bingham and Lukas, 1995). The deep Upper Circumpolar Deep Water (UCPW) and Lower Circumpolar Deep Water (LCPW) currents do not directly affect diatoms in the euphotic zone, but, may play a role in the sedimentation and burial of diatom frustules.

3 Methods

3.1 Sample information

The studied samples were obtained from the Global Change and Air-Sea Interaction Special-West Pacific Block PAC-CJ15 Submarine Sediment and Benthic Organisms Investigation Project. The samples were collected using a box corer from April to June 2017 (Zhang et al., 2021; Zhou et al., 2021). We selected 80 upper sediment samples (0-10 cm) for analysis, and the samples contained sediments since the Holocene referring to the sedimentation rate near the study area (Cai, 2019). The distribution of sampling stations is shown in Figure 1B.

3.2 Diatom sample processing and identification

All samples were processed in the diatom analysis laboratory of the Third Institute of Oceanography, Ministry of Natural Resources, Xiamen, China. We prepared samples following a modified version of the method of Hakansson (1984). Briefly, samples weighing ca. 5 g were dried in an oven at 60°C and weighed before processing. Samples were treated with 10% HCL and 30% H_2O_2 to remove carbonates and organic material, respectively, and washed in distilled water to remove these chemicals from the solution. Samples were then soaked in distilled water for 24 h and scattered using an ultrasonic dispersion instrument (120 Hz) for 2 min. Diatoms (>15 μm) were the main components, which indicates their relationship to the environment would be reliable. Small diatoms (<15 μm) have been shown to little effect on the results of this type of study, so were not considered (Chen et al., 2019). Therefore, samples were filtered through a 15-μm sieve to remove microdiatoms and other material finer than 15 μm, after which the suspension containing diatoms was concentrated to 2 ml. When completely homogeneous, the sub-sample of the suspension was transferred to a cover slip and air-dried. Finally, three permanent slides were made for each sample using Canadian balsam as a fixative (Chen et al., 2020b). The prepared slides were observed and identified under an optical microscope (Olympus BX51, objective lens 40×, ocular lens 20×), and at least 300 diatom valves were counted for each sample. For incomplete individuals, valves were counted if they were more than half complete. Diatom classification and identification mainly followed illustrations from published studies (Jin et al., 1982; Round et al., 1990; Jin et al., 1991; Cheng et al., 1996; Guo and Qian, 2003; Qi and Li, 2004; Smol and Stoermer, 2010; Cheng and Gao, 2012). Because *Ethmodiscus rex* specimens in the samples were fragmentary, we performed only area-based qualitative statistics.

3.3 Data processing and statistical methods

The total abundance of diatoms is the total number of valves per gram of air-dried sediment (valves/g). Species diversity was calculated using the Shannon-Weaver index (Shannon and Weaver, 1949). The diatom assemblages were statistically analyzed using the R software environment and correlated with various environmental factors. Prior to statistical analysis, data were first standardized for all species. In the analysis, species with >2% relative abundance in at least one sample were included (Imbrie and Kipp, 1971), and rare species (those occurring at fewer than five stations) and data for station E13 (where no diatoms were found) were excluded. Diatom assemblages were differentiated using cluster analysis. Since detrended correspondence analysis showed a maximum gradient of 1.68 < 2, redundancy analysis (RDA) was used to determine whether differences in the assemblage vectors of each sample were statistically significant.

3.4 Environmental variables

The environmental data obtained in this study included sea-surface temperature (SST), salinity (SSS), dissolved oxygen (DO), nutrients (silicate, phosphate and nitrate), chlorophyll a, net primary production (NPP), particulate organic carbon (POC) and water depth (WD). Data such as SST and SSS were obtained *in situ* using the SBE 911Plus Conductivity-Temperature-Depth system; nutrient and oxygen levels were derived from the CARS2009 dataset for 1930 to 2009 with 1/2°-resolution (Qu et al., 2022); chlorophyll a and POC concentrations for 1997 to 2009 at 9-km resolution were downloaded from https://oceancolor.gsfc.nasa.gov/l3/; NPP data for 1997 to 2009 with 1/6°-resolution were downloaded from http://www.science.oregonstate.edu/ocean.productivity/custom.php; and WD data in those figures from the GEBCO-2020 Grid at 15 arc-second intervals were downloaded from https://data.noaa.gov/onestop.

4 Results

4.1 Environmental characteristics

According to the data obtained from *in situ* measurements and websites (Figure 2), SST at each station varied relatively little, with a range of 28.90 to 29.27°C (average 29.12°C). The SSS variation was also small, from 33.94 to 34.07 (average 33.99) whereas the DO content varied from 4.52 to 4.56 ml/l (average 4.54 ml/l). Nitrate and phosphate contents varied little, ranging from 0.03 to 0.06 μmol/l and 0.04 to 0.11 μmol/l, respectively, whereas silicate content varied widely (1.11-2.97 μmol/l) and showed a trend of gradual increase from the northeast to the southwest. This increase occurs because the study area is located in the main pathway for the invasion of the silica-rich AAIW into the Northwest Pacific Ocean (Reid, 1973; Zhang, 2008; Zhang et al., 2016). In addition, NPP, POC and chlorophyll a

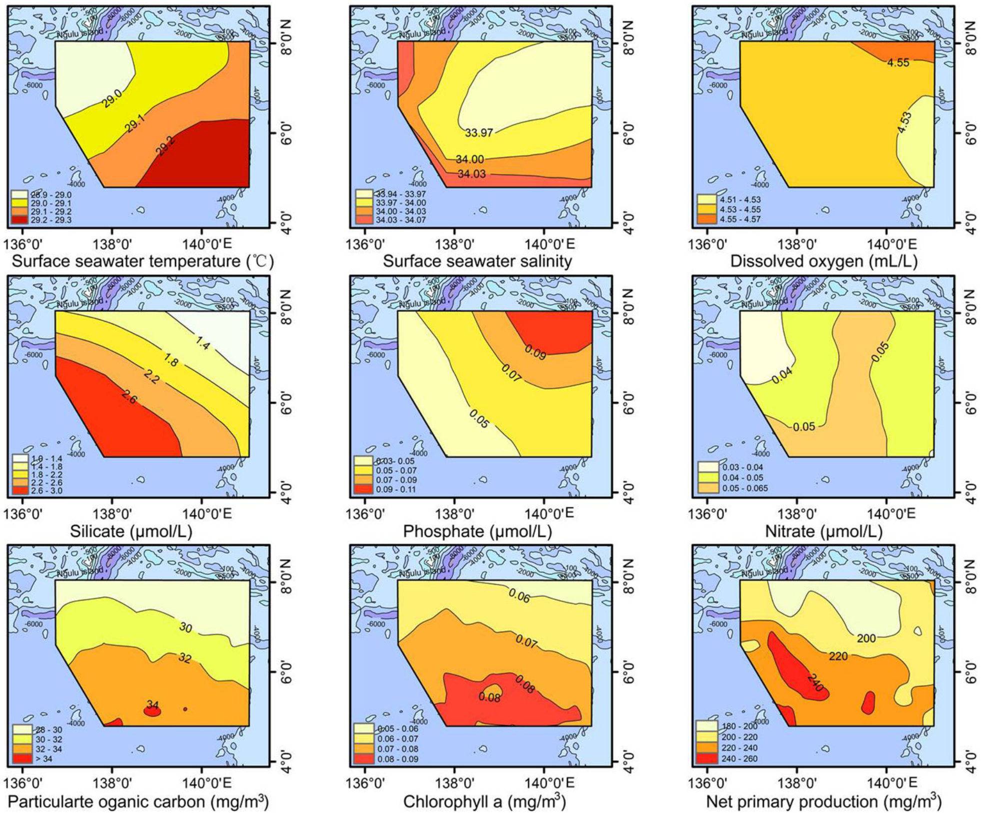

FIGURE 2
Environmental characteristics of the study area.

content all showed a gradual increase from north to south, indicating higher phytoplankton biomass and primary production in the southern part of the study area.

4.2 Diatom distributions

A total of 53 species or varieties of diatoms belonging to 22 genera were identified at 80 stations. The relative percentages of each taxa were listed in the table of supplementary material. Diatom abundance varied from 0 to 88,373 valves/g, with an average of 14,319 valves/g. Some individual stations (E13, C03, B04, A01) yielded few diatoms, although diatom abundance was generally high, especially in the southern part of the study area where the abundance was generally greater than 20,000 valves/g (Figure 3). The diatom abundance and species diversity in the southern deep-sea basin of the study area were higher than those in the West Caroline Ridge and Yap Trench in the north. Correlation analysis showed a strong positive correlation

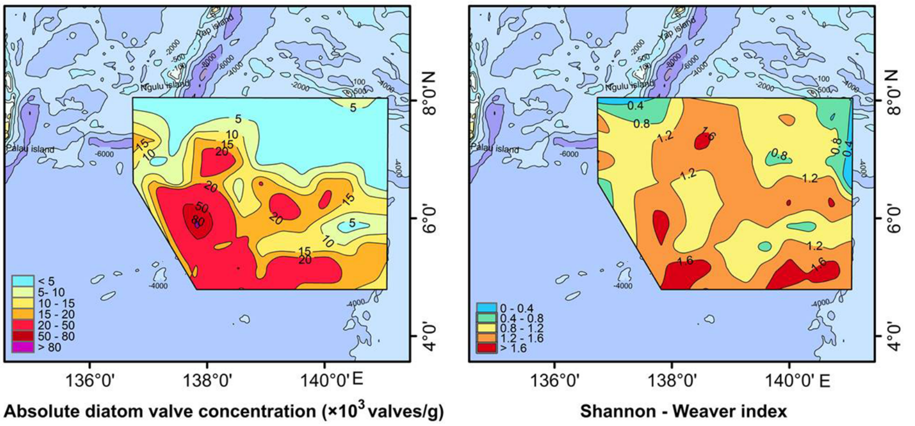

FIGURE 3
Total diatom abundance and Shannon-Weaver index.

between diatom abundance and the content of chlorophyll a and POC (Table 1). Silicate was the most significant environmental factor affecting the distribution of diatom abundance, and there was a negative correlation between phosphate and diatom abundance.

In this study, diatoms with relative percentages more than 10% were designated as dominant species, and those with percentages greater than 5% but less than 10% were designated as sub–dominant species (Pokras and Molfino, 1986). Therefore, the dominant species were *Azpeitia africanus*, *Azpeitia nodulifera*, *Coscinodiscus* sp., *Hemidiscus cuneiformis*, *Synedra* sp., *Synedra tabulata*, *Thalassiosira pacifica* and *Thalassiosira leptopus*, with the sub-dominant species being *Coscinodiscus argus*, *Coscinodiscus decrescens*, *Roperia tesselata*, *Thalassionema nitzschioides* and *Thalassiosira excentrica* (Table 2 and Figure 4). *Azpeitia nodulifera* (an oceanic warm-water species; Shen et al., 2017a) had the highest mean percentage content, followed by *H. cuneiformis* (an oceanic warm-water species; Shen et al., 2017a) and *T. pacifica* (a cosmopolitan species; Halse and Syvertsen, 1996). Overall, these three species together accounted for approximately 80% in this area.

All stations in the study area were dominated by warm-water diatoms (Figure 5), which constituted on average 79.81% of the diatom abundance. The most abundant species were *A. nodulifera*, *H. cuneiformis* and *A. africanus*, which made up 78.62% of the total. Other warm-water species included *Asteromphalus heptactis*, *Asterolampra marylandica*, *Asterolampra* sp., *Coscinodiscus radiatus*, *Mastogloia cocconeiformis*, *Rhizosolenia bergonii*, *Roperia tesselata* and *Triceratium pentacrinus*. This diversity of warm-water species was consistent with the environmental conditions of the Western Pacific Warm Pool, where the study area was located. In addition, because of the location in the deep sea, the diatoms were mainly planktonic taxa (average 99.67%) and benthic diatoms occurred only sporadically in the study area (Figure 5).

Ethmodiscus rex fragments were widely distributed in the West Caroline Basin (Figure 6). The valves of *E. rex* are huge and readily broken, so most of the individuals recorded were present as fragments. High concentrations of *E. rex* fragments were mainly recorded at stations in the deeper basins and troughs in the southern part of the study area, whereas the number of fragments in the shallow West Caroline Ridge was generally low. The correlation analysis showed that *E. rex* abundance had a weak positive correlation with WD. The study of *E. rex* in the southern Mariana Trench by Cai (2019) also found that this species was more abundant in deeper waters and less abundant in shallower waters, and that there was a positive correlation between *E. rex* abundance and WD, consistent with our findings.

4.3 Statistical analysis

For the statistical analysis of species data, species with relative percentages > 2% were selected and rare species (those occurring at fewer than five stations) were excluded. The environmental data

TABLE 1 Results of the correlation analysis between diatom abundance and environmental factors.

PCCs	WD	SST	SSS	DO	Si	N	P	NPP	Chlor	POC
DA	0.339**	0.227*	0.233*	0.224*	0.562**	0.329**	-0.367**	0.529**	0.548**	0.581**

*indicates significant correlation ($p < 0.05$), ** indicates significant correlation ($p < 0.01$); WD, water depth; SST, sea-surface temperature; SSS, sea-surface salinity; DO, dissolved oxygen; Si, silicate; N, nitrate; P, phosphate; NPP, net primary production; Chlor, chlorophyll a; POC, particulate organic carbon; DA, diatom abundance.

TABLE 2 Species represented in Holocene sediments in the study area.

Dominant species (Relative abundance >10%)			Sub-dominant species (Relative abundance 5-10%)		
Name	Abundance range (%)	Average abundance(%)	Name	Abundance range (%)	Average abundance(%)
Azpeitia africanus Janisch	0-15.00	2.57	*Coscinodiscus argus* Ehrenberg	0-6.25	0.84
Azpeitia nodulifera A. Schmidt	34.19-100	69.86	*Coscinodiscus decrescens* Grunow	0-6.52	0.32
Coscinodiscus sp.	0-25.00	3.65	*Roperia tesselata* (Rop.) Grunow	0-5.71	0.43
Hemidiscus cuneiformis Wallich	0-19.05	6.19	*Thalassionema nitzschioides* Grunow	0-8.55	0.40
Synedra sp.	0-18.43	2.47	*Thalassiosira excentrica* (Ehr.) Cleve	0-7.51	0.82
Synedra tabulata (Ag.) Kuetzing	0-29.06	2.31			
Thalassiosira leptopus (Grun) Hasle et G. Fryxell	0-25.00	1.58			
Thalassiosira pacifica Gran et Angst	0-11.36	3.69			

Station E13 (where no diatoms were found) was excluded from the calculation of the relative percentage content of diatoms in this study.

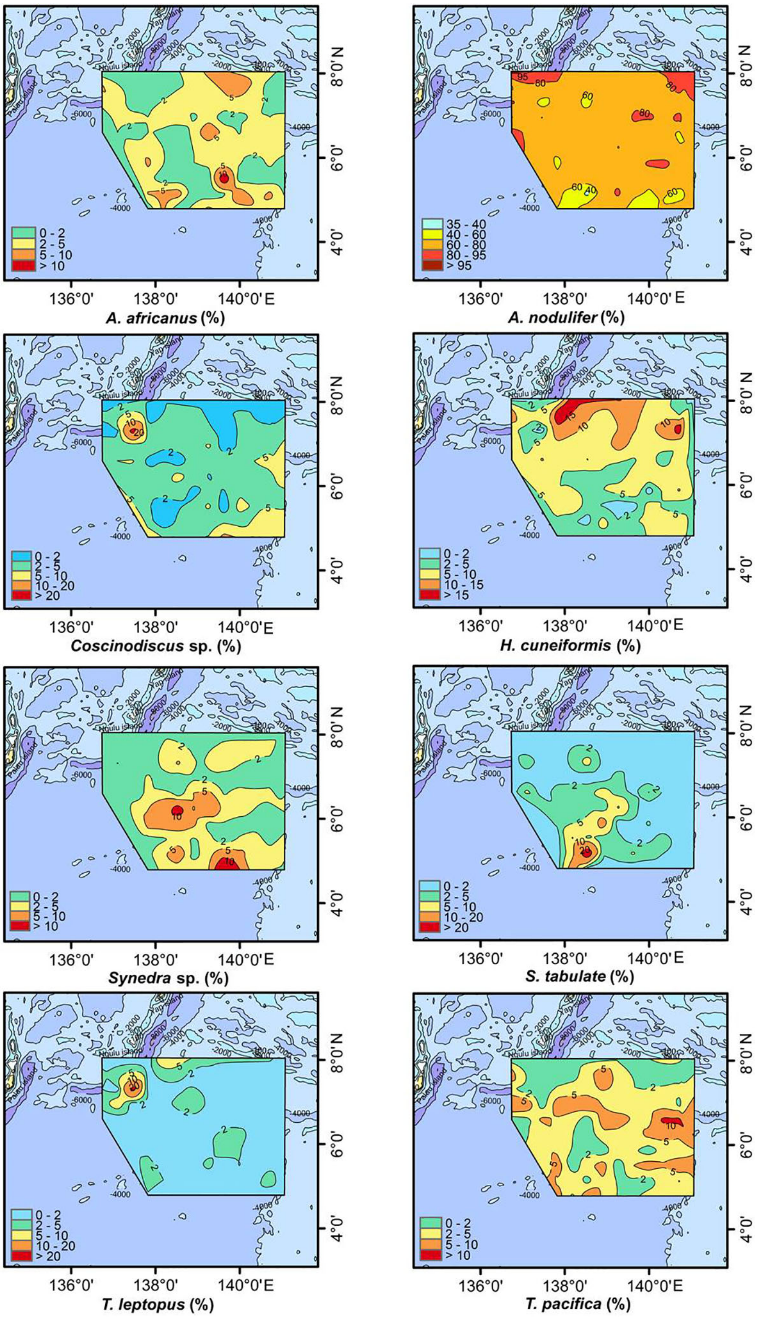

FIGURE 4
Distributions of dominant diatom species in Holocene sediments.

included WD, SST, SSS, silicate, nitrate, phosphate, DO, POC, NPP and chlorophyll a. The RDA results for environmental variables and samples, and for environmental variables and diatom species, are provided in Table 3 and Figures 7, 8. The first two RDA axes explained 35.8% and 23.2% of the total variation, respectively. Correlation between environmental variables and RDA axes are shown by both length and angle of arrows. Using cluster analysis, the 80 samples could be divided into four groupings based on the composition of the diatom species and diatom abundance (Figures 7, 9).

4.3.1 Diatom assemblage I: *A. nodulifera-H. cuneiformis-S. tabulata-A. undulatus*

Assemblage I occurred at most stations, particularly in the deep-sea basins in the central and southern part of the study area. The diatoms were mainly oceanic warm-water species *A. nodulifera* and *H. cuneiformis*, with some coastal species (e.g., *S. tabulata*, *C. argus*, and *Coscinodiscus divisus*) and a few benthic species, such as *A. undulatus*. The percentage abundances of the species in the assemblage were as follows: *A. nodulifera* 34.19% to 90.70% (average 68.16%); *H. cuneiformis* 0% to 15.16% (average 5.70%); *S.*

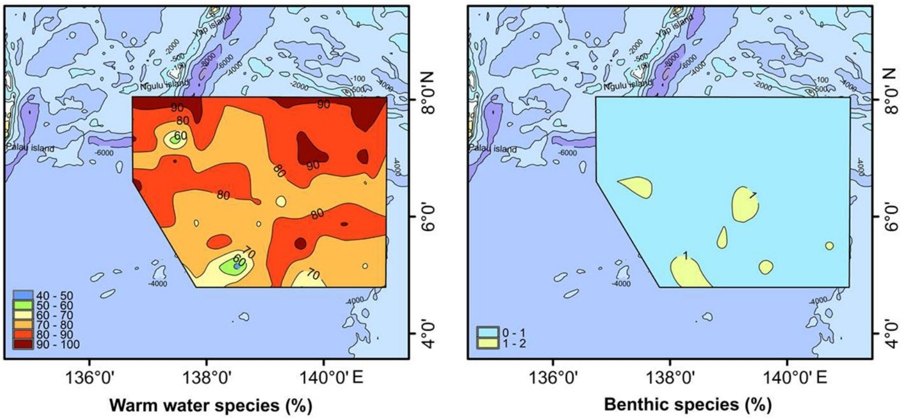

FIGURE 5
Distribution of warm-water and benthic diatom species.

tabulata 0% to 29.06% (average 2.87%); and *A. undulatus* 0% to 2.04% (average 0.32%). The total diatom abundance in this assemblage was generally high (3,696-88,373 valves/g), with an average of 17,826 valves/g. In addition, warm-water species only accounted for 78.37% of the assemblage, because of the relatively high number of eurythermal species. Assemblage I was positively correlated with SST and silicate and negatively correlated with phosphate and represents a tropical oceanic environment.

4.3.2 Diatom assemblage II: *A. nodulifer-H. cuneiformis-T. pacifica-C. argus*

Assemblage II was mainly detected in the northern part of the study area at the West Caroline Ridge. This assemblage has a species composition similar to Assemblage I, dominated by *A. nodulifera*, *H. cuneiformis* and *T. pacifica*. The relative percentages were: *A. nodulifera* 63.16% to 91.3% (average 76.89%); *H. cuneiformis* 0% to 19.05% (average 8.52%); *T. pacifica* 0% to 8.11% (average 2.41%); and the coastal species *C. argus* 0% to 5.41% (average 1.53%). Compared to Assemblage I, the total diatom abundance of this assemblage was markedly lower (640-2483 valves/g), with an average of 1,705 valves/g, and warm-water species accounted for 88.04% of the assemblage. Assemblage II was positively correlated with phosphate and negatively correlated with SST and silicate. The water depth of its tropical oceanic environment is shallower than Assemblage I.

4.3.3 Diatom assemblage III: *A. nodulifera-H. cuneiformis-C. argus*

Assemblage III was detected at two stations, A01 and B04, located in the waters near the Yap Trench. This assemblage exhibited both a low total diatom abundance (average 132 valves/g) and a relatively

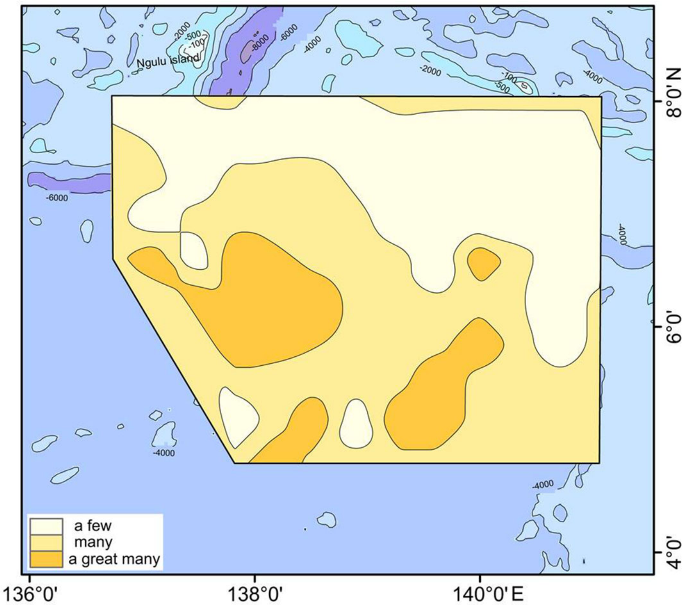

FIGURE 6
Distribution of *Ethmodiscus rex* fragments in the study area. There are definitions for 'a few' (< 10,000 per g), 'many' (10,000–1,000,000 per g) and 'a great many' (> 1,000,000 per g).

TABLE 3 Summary of RDA analyses.

Axes	1	2	3	4	5	6	7	8	9	10
Eigenvalues	0.01033	0.00669	0.00384	0.00274	0.00169	0.00104	0.00092	0.00088	0.00051	0.00020
Proportion explained	0.35827	0.23220	0.13328	0.09490	0.05856	0.03594	0.03185	0.03065	0.01754	0.00679
Cumulative proportion	0.35827	0.59047	0.72375	0.81865	0.87721	0.91316	0.94501	0.97566	0.99321	1.00000

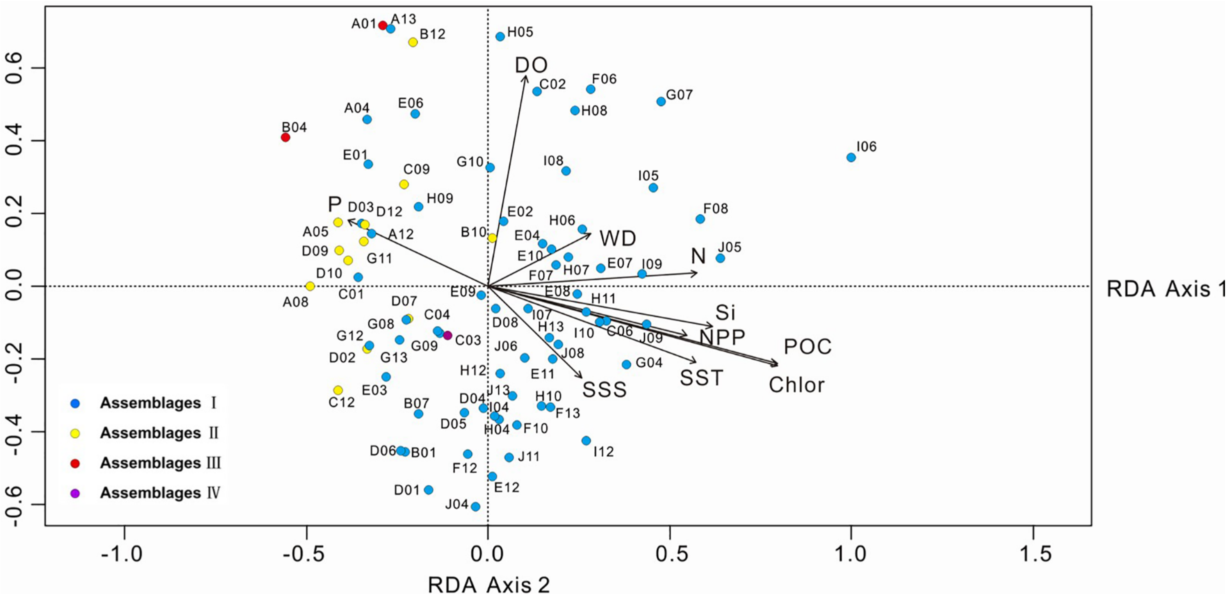

FIGURE 7
RDA biplot of environmental variables and samples. The eigenvalues for RDA axis 1 and 2 are 0.010 and 0.007, respectively. SST, sea-surface temperature; SSS, sea-surface salinity; DO, dissolved oxygen; Si, silicate; P, phosphate; N, nitrate; POC, particulate organic carbon; Chlor, chlorophyll a; NPP, net primary production; WD, water depth.

homogeneous species composition, with only three diatom species identified. The average abundances of *A. nodulifera*, *H. cuneiformis* and *C. argus* were 87.5%, 9.375% and 3.125%, respectively. Warm-water species represented a maximum of 96.875% of the total. Assemblage III was positively correlated with phosphate and DO.

4.3.4 Diatom assemblage IV (station C03): *A. nodulifera*-*T. leptopus*

The fourth assemblage only included station C03, located in the southern Yap Trench. The total abundance of diatoms at this station was only 76 valves/g, of which *A. nodulifera* constituted 50%, *T. leptopus* made up 25%, and the remainder were *Coscinodiscus* sp. The proportion of warm-water species was 50%. Assemblage IV was negatively correlated with DO and WD.

5 Discussion

5.1 Indication of diatoms in Holocene sediments to environment

In the study area, warm-water diatoms possessed an absolute advantage, with the lowest percentage abundance of these diatoms being 44.44% at station I06, indicating a tropical oceanic environment. The tropical pelagic species *A. nodulifera* was the most abundant diatom at each station, consistent with the view that *A. nodulifera* is the main component of diatom assemblages in the surface sediments of the tropical Pacific (Jousé et al., 1971). *E. rex* fragments are also widely distributed in this area, corresponding with the nutrient-poor environment in the Western Pacific Warm Pool (Abrantes et al., 2007). Compared with study area I in the West Philippine Basin (Figure 1), there are the same four dominant species, *A. africanus*, *A. nodulifera*, *H. cuneiformis* and *T. leptopus*, indicating that the two areas possess similar growth conditions for diatoms. However, the proportion of warm-water diatoms, especially *A. nodulifera*, in the West Caroline Basin was obviously greater than in the West Philippine Basin as a result of latitudinal differences and a more typical pelagic environment.

T. nitzschioides is widely distributed at low latitudes, and is often used as an indicator of upwelling and increased production in coastal areas; however, the species is as abundant in nutrient-poor open oceans as in coastal areas, and is described as a cosmopolitan species (Kobayashi and Takahashi, 2002; Ren et al., 2014; Lyle and Baldauf, 2015). In this study, *T. nitzschioides* was mainly detected in the high-productivity area in the southern West Caroline Basin (Figure 10). Considerable upwelling (3-10°N, strongest at 6-7°N) is observed in this area (Long et al., 2021), suggesting that *T. nitzschioides* is also good

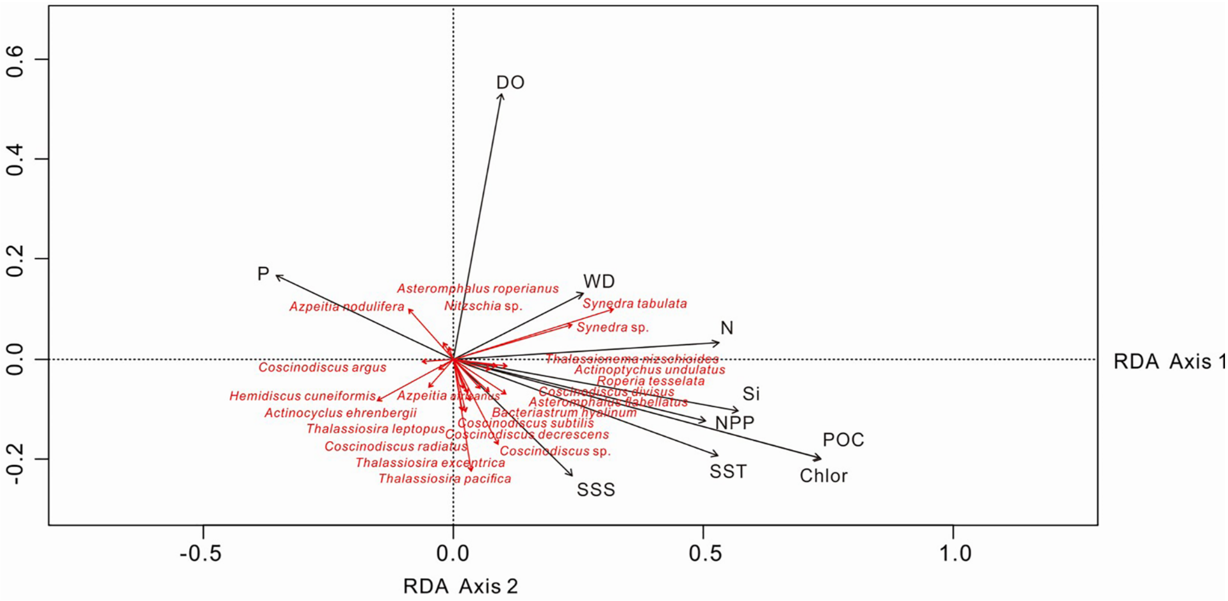

FIGURE 8

RDA biplot of diatom taxa and environmental factors. The eigenvalues for RDA axis 1 and 2 are 0.010 and 0.007, respectively. SST, sea-surface temperature; SSS, sea-surface salinity; DO, dissolved oxygen; Si, silicate; P, phosphate; N, nitrate; POC, particulate organic carbon; Chlor, chlorophyll a; NPP, net primary production; WD, water depth.

proxy for upwelling and increased production in the open ocean. Similarly, Kobayashi and Takahashi (2002) found *T. nitzschioides* may reflect weak upwelling in the equatorial western Pacific.

5.2 Diatom assemblages and their environmental significance

The distribution of diatoms in sediments is directly related to the different temperature and salinity conditions in the euphotic zone; however, diatom frustules experience dissolution in the water column, current transport and various geological processes during sinking and after deposition on the seafloor. As a result, there are many factors affecting the distribution of diatoms in sediments (Zhang et al., 2013; Astakhov et al., 2015). Using the diatom assemblage distribution (Figure 9), the study area was divided into three regions: West Caroline Basin, West Caroline Ridge and Yap Trench. The West Caroline Basin mainly contains diatom assemblage I, the West Caroline Ridge is dominated by diatom assemblage II, and the Yap Trench has a mixed assemblage and more complex diatom distribution.

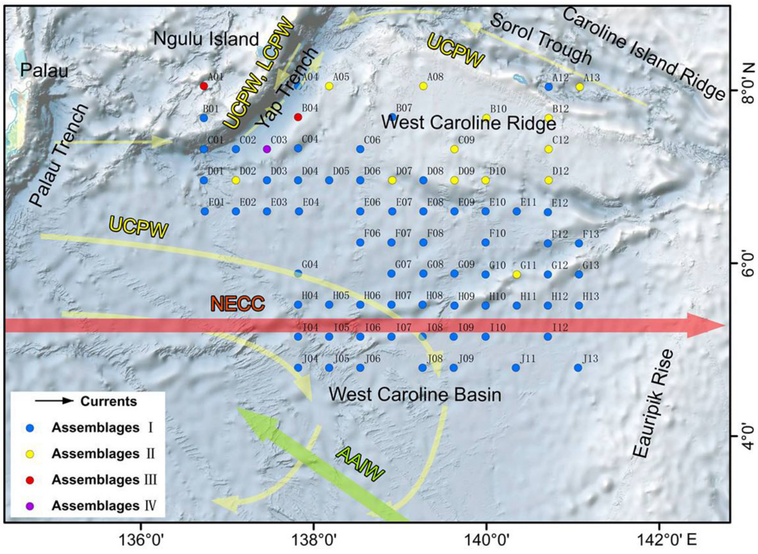

FIGURE 9

Distribution of diatom assemblages in the study area. The red arrow represents the NECC, the green arrow represents the AAIW and the yellow arrows represent deep currents.

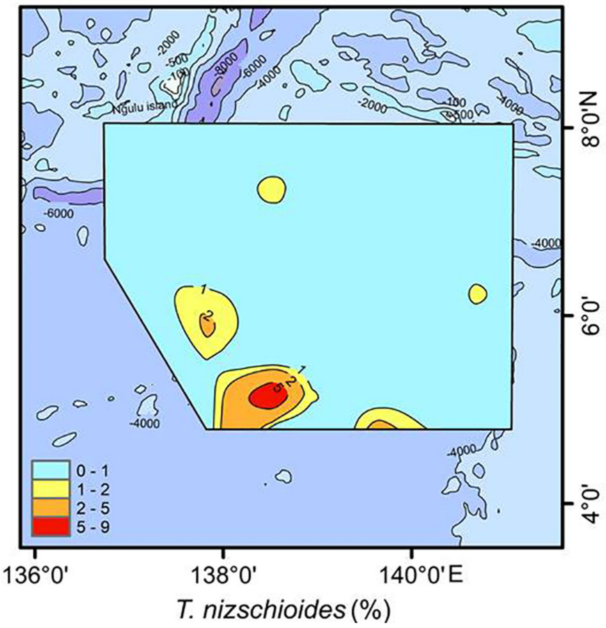

FIGURE 10
Distribution of *T. nitzschioides* in the study area.

5.2.1 West Caroline Basin

Compared with the northern part of the study area, the deep-sea basin has higher primary production. Correspondingly, the total abundance of assemblage I is obviously higher than other assemblages. Sufficient nutrients are needed for diatoms to flourish in this area, and the supply of nutrients is likely from horizontal and vertical current transport.

Previous studies have shown that the NECC is the main cause of high chlorophyll a in the surface water of the Western Pacific Warm Pool and the New Guinea Coastal Current transports nutrients that fertilize the southern waters of the NECC region (Christian et al., 2004; Chen et al., 2017). In general, the west-to-east NECC delivers warm, nutrient-rich water, which is conducive to the growth and reproduction of diatoms in the study area. In addition, the AAIW exhibits low temperatures and high silicon and low phosphorus contents (Bostock et al., 2004; Zhang, 2008; Zhang, 2016; Kashino et al., 2020). The current brings silicon-rich water and increases the silicate content of surface water in the West Caroline Basin through upwelling, which also weakens the dissolution of siliceous fossils. Because of the strong influence of NECC, AAIW and upwelling in the West Caroline Basin, diatom assemblage I has higher abundance and species diversity than other assemblages.

Different diatom species have different nutrient requirements and the ratio of nutrients in water has a significant effect on diatom species diversity and abundance (Owen and Crossley, 1992). RDA analysis shows that *A. nodulifera* and *H. cuneiformis* are positively correlated with phosphate, *S. tabulate* is positively correlated with nitrate, whereas *T. leptopus* and *T. pacifica* are not sensitive to nutrient changes (Figure 8). Therefore, lower phosphate concentrations in the West Caroline Basin are responsible for the lower content of *A. nodulifera* and *H. cuneiformis* in assemblage I. There are also some coastal species such as *S. tabulata*, *C. argus* and *C. divisus*, and even the benthic species *A. undulatus* in assemblage I. We assume that the presence of these species is the result of NECC transport from the shallow coastal waters of the Palau Islands.

5.2.2 West Caroline Ridge

The low total abundance of assemblage II (640-2,483 valves/g) in the West Caroline Ridge is caused by the weak influence of NECC and AAIW in this region, resulting in limited supply of nutrients. The absence of *T. nitzschioides* in assemblage II also suggests that this region is hardly influenced by upwelling. Meanwhile, sediments on the ridge are easily scoured by currents (Sun et al., 2013; Shen et al., 2017a). The lack of nutrients (especially silicate) and upwelling, combined with an unfavorable topography for sediment accumulation, gives rise to the low abundance and species diversity of this assemblage.

As can be seen in Figure 2, the phosphate levels were relatively high in the West Caroline Ridge, and assemblage II was positively correlated with phosphate. Accordingly, the relative abundance of *A. nodulifera* and *H. cuneiformis* was very high (85.42%). The presence of coastal species such as *C. argus*, *Actinocyclus ehrenbergii* and *Bacteriastrum hyalinum* in assemblage II indicates an input of terrestrial material from the northern islands.

5.2.3 Yap Trench

Similar to the West Caroline Ridge, the Yap Trench is located at the margin of the NECC and is less affected by this current, causing diatom abundance to be generally low. In addition, the diatom species composition varied greatly among stations in this area, and the distribution of diatom assemblages was complex. Previous studies have shown that UCPW and LCPW (deeper than UCPW) are the main deep water masses in the Yap Trench and form a counterclockwise circulation in the south of the trench (Liu et al., 2022). The mixing of diatom assemblages in the region is assumed to be caused by the large topographic variations and migration of diatom frustules via abyssal flow.

6 Conclusions

A total of 53 diatom species or varieties belonging to 22 genera were identified in Holocene sediments of the northern West Caroline Basin. Diatom abundance varied from 0 to 88,373 valves/g, with an average of 14,319 valves/g. The dominant diatom species were *A. africanus*, *A. nodulifera*, *Coscinodiscus* sp., *H. cuneiformis*, *Synedra* sp., *S. tabulata*, *T. leptopus* and *T. pacifica*. Warm-water diatom species were overwhelmingly dominant, with the tropical oceanic species *A. nodulifera* being the dominant component in the diatom assemblages. *T. nitzschioides* reflected the upwelling and increased production in the West Caroline Basin.

Four groupings of diatoms were identified by cluster analysis and the study area could be divided into three regions. Diatom assemblage I in the West Caroline Basin was mainly affected by NECC, AAIW and upwelling, and the supply of nutrients was sufficient to maintain relatively high productivity. Assemblage II in the West Caroline Ridge was less influenced by currents, and the diatom species were dominated by *A. nodulifera* and *H. cuneiformis*, with less species diversity. The complex diatom assemblages in the Yap Trench were probably controlled by the deep UCPW and LCPW currents.

This study is the first to investigate Holocene diatom assemblage distributions and reveal their reflection on the environment in the West Caroline Basin, providing fundamental new information for paleoceanographic reconstruction in the western Pacific based on fossil diatom records.

Data availability statement

The raw data supporting the conclusions of this article will be made available by the authors, without undue reservation.

Author contributions

MC: conceptualization, methodology, writing - review and editing, supervision. GH: data curation, drawing, writing - original draft. JisX: resources, investigation, background information collection. CW: data curation. JizX: resources, investigation. HQ: supervision, writing - references editing. AZ: Chinese to English. All authors contributed to the article and approved the submitted version.

Funding

We acknowledge financial support from the National Key Research and Development Program of China (Grant No. 2019YFE0124700), the Global Change and Air-Sea Interaction Project granted by the Ministry of Natural Resources of China (Grant No. GASI-02-PACCJ15), and the National Natural Science Foundation of China (41976198, 91858203).

Acknowledgments

We are grateful to the crew and scientists on the GASI-02-PAC-CJ15 cruise, who collected the samples analyzed in this study. We thank Sev Kender, from Liwen Bianji (Edanz) (www.liwenbianji.cn) for editing the English text of a draft of this manuscript.

Conflict of interest

The authors declare that the research was conducted in the absence of any commercial or financial relationships that could be construed as a potential conflict of interest.

Publisher's note

Supplementary material

The Supplementary Material for this article can be found online at: https://www.frontiersin.org/articles/10.3389/fmars.2023.1110621/full#supplementary-material

References

Abrantes, F., Lopes, C., Mix, A., and Pisias, N. (2007). Diatoms in southeast pacific surface sediments reflect environmental properties. *Quat. Sci. Rev.* 26 (1-2), 155–169. doi: 10.1016/j.quascirev.2006.02.022

Astakhov, A. S., Bosin, A. A., Kolesnik, A. N., and Obrezkova, M. S. (2015). Sediment geochemistry and diatom distribution in the chukchi Sea: application for bioproductivity and paleoceanography. *Oceanography* 28 (3), 190–201. doi: 10.5670/oceanog.2015.65

Bingham, F. M., and Lukas, R. (1995). The distribution of intermediate water in the western equatorial pacific during January-February 1986. *Deep-Sea Res. Part I* 42 (9), 1545–1573. doi: 10.1016/0967-0637(95)00064-D

Bostock, H. C., Opdyke, B. N., Gagan, M. K., and Fifield, L. K. (2004). Carbon isotope evidence for changes in Antarctic intermediate water circulation and ocean ventilation in the southwest pacific during the last deglaciation. *Paleoceanography* 19 (4), 4013. doi: 10.1029/2004PA001047

Cai, Y. (2019). *Sedimentary diatoms records and their paleoenvironmental indications in the southern Mariana trench and its adjacent areas* (Xiamen, China: Xiamen University).

Cheng, Z., and Gao, Y. (2012). *Marine bacillariophyta pennatae (I) flora of China seas* (Beijing: Science Press).

Cheng, Z., Gao, Y., and Mike, D. (1996). *Color atlas of diatoms* (Beijing: Ocean Press).

Chen, M., Lan, B. B., Shen, L. N., Lan, D. Z., Fang, Q., and Qi, H. S. (2014). Characteristics of diatom distribution in the surface sediments of the Western Philippine basin. *Acta Micropalaeontol. Sin.* 31 (4), 321–334.

Chen, M., Li, Y. H., Qi, H. S., Wang, L., Zhang, A. M., Shen, L. N., et al. (2019). The influence of season and typhoon morakot on the distribution of diatoms in surface sediments on the inner shelf of the East China Sea. *Mar. Micropaleontol.* 146 (2019), 59–74. doi: 10.1016/j.marmicro.2019.01.003

Chen, M., Qi, H. S., Intasen, W., Kanchanapant, A., Wang, C. T., and Zhang, A. M. (2020b). Distributions of diatoms in surface sediments from the chanthaburi coast, gulf of Thailand, and correlations with environmental factors. *Reg. Stud. Mar. Sci.* 34, 100991. doi: 10.1016/j.rsma.2019.100991

Chen, Z., Sun, J., Chen, D. W., Wang, S. H., Yu, H., Chen, H. T., et al. (2021). Effects of ocean currents in the Western pacific ocean on net-phytoplankton community compositions. *Diversity-Basel* 13 (9), 428. doi: 10.3390/d13090428

Chen, Y. Y., Sun, X. X., Zhu, M. L., Zheng, S., Yuan, Y. Q., and Denis, M. (2017). Spatial variability of phytoplankton in the pacific western boundary currents during summer 2014. *Mar. Freshw. Res.* 68 (10), 1887–1900. doi: 10.1071/MF16297

Chen, K., Xu, J. S., Li, G. X., Tian, J., Yang, J. C., Zhou, S., et al. (2020a). Grain-size characteristics of the surface clastic sediments on the southern margin of the yap trench and their provenance implications. *Mar. Geol. Quat. Geol.* 40 (5), 46–57. doi: 10.16562/j.cnki.0256-1492.2019110601

Christian, J. R., Murtugudde, R., Ballabrera-Poy, J., and Mcclain, C. R. (2004). A ribbon of dark water: phytoplankton blooms in the meanders of the pacific north equatorial countercurrent. *Topical Stud. Oceanogr.* 51 (1-3), 209–228. doi: 10.1016/j.dsr2.2003.06.002

Esper, O., and Gersonde, R. (2014). New tools for the reconstruction of pleistocene Antarctic sea ice. *Palaeogeogr. Palaeoclimatol. Palaeoecol.* 399, 260–283. doi: 10.1016/j.palaeo.2014.01.019

Guo, Y., and Qian, S. (2003). *Marine bacillariophyta centricae flora of China seas* (Beijing: Science Press).

Håkansson, H. (1984). The recent diatom succession of Lake HavgårdssjÖn, south Sweden. In: D. G. Mann Ed. *Proceedings of the Seventh International Diatom Symposium* (Otto Koeltz: Philadelphia), 411–429.

Halse, G. R., and Syvertsen, E. E. (1996). “Marine diatoms,” in *Identifying marine diatoms and dinoflagellates*, 5–385. Academic Press, The United States. doi: 10.1016/B978-012693015-3/50005-X

Hu, D. X., Wu, L. X., Cai, W. J., Gupta, A. S., Ganachaud, A., Qiu, B., et al. (2015). Pacific western boundary currents and their roles in climate. *Nature* 522 (7556), 299. doi: 10.1038/nature14504

Imbrie, J., and Kipp, N. G. (1971). “A new micropaleontological method for quantitative paleoclimatology: Application to a late pleistocene Caribbean core,” in *The late Cenozoic glacial ages*. Ed. K. Turekian (New Haven, Conn: Yale Univ. Press), 71–181.

Jin, D., Cheng, Z., Lin, J., and Liu, S. (1982). *Benthic diatoms of China seas* (Beijing: China Ocean Press).

Jin, D., Cheng, Z., Liu, S., and Ma, J. (1991). *Benthic diatoms of China seas* (Beijing: China Ocean Press).

Jousé, A. P., Kozlova, O. G., and Muhina, V. V. (1971). Distribution of diatoms in the surface layer of sediment from the pacific ocean. *Micropaleontol. Oceans*, 263–269.

Kashino, Y., Hasegawa, T., Syamsudin, F., and Ueki, I. (2020). Temperature and salinity variability at intermediate depths in the western equatorial pacific revealed by TRITON buoy data. *J. Oceanogr.* 76 (2), 121–139. doi: 10.1007/s10872-019-00530-9

Kawano, T., Fukasawa, M., Kouketsu, S., Uchida, H., Doi, T., Kaneko, I., et al. (2006). Bottom water warming along the pathway of lower circumpolar deep water in the pacific ocean. *Geophys. Res. Lett.* 33 (23), 23613–1-236. doi: 10.1029/2006GL027933

Kender, S., Bogus, K. A., Cobb, T. D., and Thomas, D. J. (2018). Neodymium evidence for increased circumpolar deep water flow to the north pacific during the middle Miocene climate transition. *Paleoceanogr. Paleoclimatol.* 33 (7), 672–682. doi: 10.1029/2017PA003309

Kobayashi, F., and Takahashi, K. (2002). Distribution of diatoms along the equatorial transect in the western and central pacific during the 1999 la niña conditions. *Deep Sea Res. Part II: Topical Stud. Oceanogr.* 49 (13-14), 2801–2821. doi: 10.1016/S0967-0645(02)00059-0

Liu, X. H., Liu, Y. Z., Cao, W., and Li, D. (2022). Flow pathways of abyssal water in the yap trench and adjacent channels and basins. *Front. Mar. Sci.* 9. doi: 10.3389/fmars.2022.910941

Long, Y., Noman, M. A., Chen, D. W., Wang, S. H., Yu, H., Chen, H. T., et al. (2021). Western Pacific zooplankton community along latitudinal and equatorial transects in autumn 2017 (northern hemisphere). *Diversity* 13 (2), 58. doi: 10.3390/d13020058

Lyle, M., and Baldauf, J. (2015). Biogenic sediment regimes in the neogene equatorial pacific, IODP site U1338: Burial, production, and diatom community. *Palaeogeogr. Palaeocl.* 433, 106–128. doi: 10.1016/j.palaeo.2015.04.001

Owen, R. B., and Crossley, R. (1992). Spatial and temporal distribution of diatoms in sediments of lake Malawi, central Africa, and ecological implications. *J. Paleolimnol.* 7 (1), 55–71. doi: 10.1007/BF00197031

Pokras, E., and Molfino, B. (1986). Oceanographic control of diatom abundances and species distributions in surface sediments of the tropical and southeast Atlantic. *Mar. Micropaleontol.* 10 (1-3), 165–188. doi: 10.1016/0377-8398(86)90028-9

Pujari, L., Narale, D., Kan, J. J., Wu, C., Zhang, G. C., Ding, C. L., et al. (2021). Distribution of chromophytic phytoplankton in the eddy-induced upwelling region of the West pacific ocean revealed using rbcL genes. *Front. Microbiol.* 12. doi: 10.3389/fmicb.2021.596015

Qi, Y., and Li, J. (2004). *Flora algarum sinicarum aquae dulcis (Tomus X)* (Beijing: Science Press).

Qi, Z., Xu, J., Li, G., Zhao, M., Zhai, K., Long, H., et al. (2020). The variation of carbonate lysocline depth in the western tropical pacific ocean. *Acta Geol. Sin.* 94 (12), 3852–3863. doi: 10.19762/j.cnki.dizhixuebao.2020048

Qu, H. X., Wang, J. B., Xu, Y., Xu, J. S., and Li, X. Z. (2022). Radiolarian assemblages controlled by ocean production in the western equatorial pacific. *Deep-Sea Res. Part I* 182, 103721. doi: 10.1016/j.dsr.2022.103721

Reid, J. L. (1973). The shallow salinity minima of the pacific ocean. *Deep Sea Res. Oceanogr. Abstr.* 20 (1), 51–68. doi: 10.1016/0011-7471(73)90042-9

Ren, J., Gersonde, R., Esper, O., and Sancetta, C. (2014). Diatom distributions in northern north pacific surface sediments and their relationship to modern environmental variables. *Palaeogeogr. Palaeocl.* 402, 81–103. doi: 10.1016/j.palaeo.2014.03.008

Round, F. E., Crawford, R. M., and Mann, D. G. (1990). *Diatoms: biology and morphology of the genera* (Cambridge, UK.: Cambridge university press).

Shannon, C. E., and Weaver, W. (1949). *The mathematical theory of communication (Urbana, IL)* (Illinois, USA: University of illinois Press IL).

Shen, L. N., Chen, M., Lan, B. B., Qi, H. S., Zhang, A. M., Lan, D. Z., et al. (2017a). Diatom distribution as an environmental indicator in surface sediments of the West Philippine basin. *Chin. J. Oceanol. Limn.* 35 (2), 431–443. doi: 10.1007/s00343-016-5306-8

Shen, L. N., Gao, A. G., Li, C., and Chen, M. (2017b). Diatom distribution and its relationship to sediment property in the minjiang estuary, southeast China. *Acta Oceanol. Sin.* 36 (10), 20–30. doi: 10.1007/s13131-017-1070-7

Smol, J. P., and Stoermer, E. F. (2010). *The diatoms: applications for the environmental and earth sciences* (Cambridge, UK: Cambridge University Press).

Sun, M. Q., Lan, D. Z., Fu, P., Chen, M., and Ye, Y. Q. (2013). Diatom distribution in surface sediment and its relation with environment factors in the south China Sea. *J. Appl. Oceanogr.* 32 (1), 46–51. doi: 10.3969/J.ISSN.2095-4972.2013.01.006

Tsoy, I. B., and Moiseenko, I. A. (2014). Diatoms from surface sediments of amurskiy bay, Sea of Japan. *Russ. J. Mar. Biol.* 40 (1), 10–23. doi: 10.1134/S106307401401009X

Vinogradov, M. (1981). “Ecosystems of equatorial upwellings,” in *Analysis of marine ecosystems*. Ed. A. Longhurst (London: Academic Press), 69–93.

Wang, H. N., Chen, J. N., and Lv, X. Y. (2009). Spatial and temporal variability in ocean temperature in West pacific warm pool and its effect in ENSO cycle. *Oceanol. Et Limnol. Sin.* 40 (1), 1–7. doi: 10.11693/hyhz200901001001

Yue, X. A., Yan, Y. X., Ding, H. B., Sun, C. J., and Yang, J. P. (2018). Biological geochemical characteristics of the sediments in the yap trench and its oceanographic significance. *Periodical Ocean Univ. China* 48 (3), 88–96. doi: 10.16441/j.cnki.hdxb.20170145

Zhai, B., Li, T. G., Chang, F. M., and Cao, Q. Y. (2010). Vast laminated diatom mat deposits from the west low-latitude pacific ocean in the last glacial period. *Chin. Sci. Bull.* 55 (2), 171–175. doi: 10.1007/s11434-009-0447-1

Zhang, Y. H. (2008). *The analyses of the subsurface water masses and intermediate water masses of the tropical Western pacific and their decadal variation* (Shandong Province, China: Institute of Oceanology, Chinese Academy of Sciences).

Zhang, S. (2016). *The upper water body structure evolution in the core region of the Western pacific warm pool and its correlation to the ENSO-like process and ITCZ shift since MIS10* (Shandong Province, China: Institute of Oceanology, Chinese Academy of Sciences), 172.

Zhang, Z. Y. (2020). *Geomorphological characteristics and its influence to surface sedimentation in the junction of yap trench and Mariana trench, Western pacific ocean* (Shandong Province, China: Shandong University of Science and Technology).

Zhang, J. P., Deng, X. G., Yang, S. X., He, G. W., and Zhu, B. D. (2015). Diatom ooze found in 7000 m submarine area of challenger depth in Mariana trench. *Geol. Bull. Of China* 34 (12), 2352–2354.

Zhang, J. P., Deng, X. G., Zhu, B. D., Yang, S. X., Guo, L. H., Chen, C. X., et al. (2016). Diatom ooze from the surface sediments in the challenger deep of the Western pacific ocean. *Acta Micropalaeontol. Sin.* 33 (1), 1–8. doi: 10.16087/j.cnki.1000-0674.2016.01.001

Zhang, Y., Xu, J. S., Li, G. X., and Liu, Y. (2021). ENSO-like patterns and its driving mechanism in Western pacific warm pool during the glacial cycles. *Earth Sci. Front.* 29 (4), 168–178. doi: 10.13745/j.esf.sf.2022.1.5

Zhang, J. P., Zhu, B. D., Chen, C. X., and Zhang, J. Y. (2013). Distribution pattern of diatom in surface sediments of the northwestern south China Sea and its environmental implications. *Mar. Geol. Front.* 29 (11), 8–13. doi: 10.16028/j.1009-2722.2013.11.003

Zhou, S., Xu, J. S., Liu, Y., Li, G. X., Li, A. L., Cao, L. H., et al. (2021). Effects of biological components on geotechnical properties of seafloor surface sediments in the Western pacific warm pool. *Earth Sci. Front.* 29 (5), 119–132. doi: 10.13745/j.esf.sf.2021.5.2

frontiers | Frontiers in Marine Science

TYPE Original Research
PUBLISHED 25 April 2023
DOI 10.3389/fmars.2023.1147271

Check for updates

OPEN ACCESS

EDITED BY
Zhaohe Luo,
Ministry of Natural Resources, China

REVIEWED BY
Wanchun Guan,
Wenzhou Medical University, China
Wee Cheah,
University of Malaya, Malaysia
Yu Wang,
Ministry of Natural Resources, China

*CORRESPONDENCE
Jun Sun
✉ phytoplankton@163.com

SPECIALTY SECTION
This article was submitted to Marine Ecosystem Ecology, a section of the journal Frontiers in Marine Science

RECEIVED 18 January 2023
ACCEPTED 04 April 2023
PUBLISHED 25 April 2023

CITATION
Yan W, Chen Z, Zhang L, Wang F, Zhang G and Sun J (2023) Nanophytoplankton and microphytoplankton in the western tropical Pacific Ocean: its community structure, cell size and carbon biomass. *Front. Mar. Sci.* 10:1147271. doi: 10.3389/fmars.2023.1147271

Nanophytoplankton and microphytoplankton in the western tropical Pacific Ocean: its community structure, cell size and carbon biomass

Wenzhuo Yan[1,2], Zhuo Chen[2,3,4], Linlin Zhang[5,6], Feng Wang[2,5,6], Guicheng Zhang[1,2] and Jun Sun[1,2,3,4]*

[1]Research Centre for Indian Ocean Ecosystem, Tianjin University of Science and Technology, Tianjin, China, [2]Institute for Advanced Marine Research, China University of Geosciences, Guangzhou, China, [3]State Key Laboratory of Biogeology and Environmental Geology, China University of Geosciences (Wuhan), Wuhan, China, [4]College of Marine Science and Technology, China University of Geosciences (Wuhan), Wuhan, China, [5]Key Laboratory of Ocean Circulation and Waves, Institute of Oceanology, Chinese Academy of Sciences, Qingdao, China, [6]Laboratory for Marine Ecology and Environmental Science, Pilot National Laboratory for Marine Science and Technology, Qingdao, China

Phytoplankton, as a crucial component of the marine ecosystem, plays a fundamental role in global biogeochemical cycles. This study investigated the composition and distribution of phytoplankton in the western Tropical Pacific Ocean using the Utermöhl method and carbon volume conversion. We identified four primary groups of phytoplankton: dinoflagellates (181 species), diatoms (73 species), cyanobacteria (4 species), and chrysophyceae (2 species). The clustering analysis classified phytoplankton into four groups based on their composition, which were found to be closely related to ocean currents. Diatoms were highly abundant in areas influenced by current-seamount interaction. In contrast, areas with little influence from ocean currents were dominated by *Trichodesmium*. The majority of phytoplankton had an equivalent spherical diameter (ESD) of 2-12 μm, with a few exceeding 25 μm. Although nanophytoplankton (ESD = 2-20 μm) dominated cell abundance, microphytoplankton (ESD = 20-200 μm) contributed significantly to carbon biomass (792.295 mg m^{-3}). This study yielded valuable insights into the distribution and composition of phytoplankton in the western tropical Pacific Ocean, shedding light on the relationship between species distribution and ocean currents. In addition, it provided fundamental information regarding cell size and carbon biomass within the region.

KEYWORDS

phytoplankton, species composition, carbon biomass, cell size, environmental factors, quantile regression

1 Introduction

Phytoplankton are single-celled algae that drift with ocean currents and are widely distributed in the upper layers of the ocean. They play a crucial role as primary producers in the ocean, converting CO_2 into organic matter for other marine organisms to survive (Sun, 2011). Moreover, they fix carbon and regulate atmospheric CO_2 concentrations, making them important contributors to global climate regulation (Zhang et al., 2022). However, their community structure is highly sensitive to environmental changes, especially in extensive oligotrophic oceans where changes in physical factors can have profound effects on phytoplankton clusters. As changes in phytoplankton community structure and biomass can affect global climate in terms of productivity and carbon fluxes, studying their changes in relation to global climate is a key issue in marine ecology (Street and Paytan, 2005). Previous studies have shown that changes in phytoplankton community structure are influenced by environmental factors, such as changes in currents, topography, and nutrient availability (Wang et al., 2015; Wei et al., 2017; Mena et al., 2019). Therefore, understanding the responses of phytoplankton to environmental changes is essential for predicting and mitigating the effects of climate change on marine ecosystems (Morán et al., 2010; Winder and Sommer, 2012).

Accurately determining the carbon biomass of phytoplankton is crucial in assessing their ability to convert inorganic carbon to organic carbon and to store carbon (Gosselain et al., 2000). Although chlorophyll-based estimates of phytoplankton carbon biomass are widely used, they are vulnerable to environmental variations (Thomalla et al., 2017). Chemical methods like the Redfield ratio are rapid but can be inaccurate (Teng et al., 2014). Hillebrand's geometric model, which calculates phytoplankton volume from microscopic measurements and converts it to carbon biomass using equations, overcomes these limitations by being independent of environmental factors and providing accurate results (Hillebrand et al., 1999). Furthermore, this method allows for the investigation of the relationship between cell volume and carbon biomass. Sun further refined the model proposed by Hillebrand to improve its applicability (Sun and Liu, 2003).

The size structure of phytoplankton has significant implications for both the biology of individual organisms and the ecology of the entire community (Finkel et al., 2010; Weithoff and Beisner, 2019). As a primary functional trait, cell size affects the way phytoplankton interact with their environment (Finkel, 2001; Sciascia et al., 2013; Pérez-Hidalgo and Moreno, 2016; Charalampous et al., 2021). Phytoplankton can be classified according to their equivalent spherical diameter (ESD) into picophytoplankton (<2 µm), nanophytoplankton (2-20 µm), and microphytoplankton (20-200 µm).Larger-sized cells experience greater self-shading due to the packing effect of pigment molecules, resulting in less light absorbed per unit of chlorophyll (Finkel et al., 2004; Wang et al., 2015). Additionally, cell size affects the uptake of nutrients. Under oligotrophic conditions, the growth of phytoplankton is limited when nutrient concentrations fall below a certain threshold that increases exponentially with increasing cell size (Marañón et al., 2013). Small-sized phytoplankton also play a vital role in the carbon pool. While larger-sized phytoplankton are often assumed to be the primary contributors to carbon export, recent studies have highlighted the importance of small-sized phytoplankton in this process (Stukel and Landry, 2010; Shiozaki et al., 2019; Irion et al., 2021; Wei and Sun, 2022). Overall, understanding the implications of phytoplankton size structure is critical for predicting the response of marine ecosystems to environmental change.

The western Tropical Pacific Ocean (WTP) plays a crucial role in global climate regulation due to its unique geographical position, influenced by various currents that bring together water masses from different seas (McCreary and Lu, 1994; Li et al., 2013; Hu et al., 2020). The WTP's surface water receives strong solar radiation throughout the year, resulting in a temperature exceeding 28°C (Zhao et al., 2003). However, severe stratification of seawater causes difficulties in vertical water exchange, leading to the WTP being classified as a typical oligotrophic sea (Zhang D. et al., 2012). This unique marine environment profoundly affects the phytoplankton community and size structure of the WTP (Wang et al., 2015). Despite the increasing number of studies on the phytoplankton community structure of the WTP (Mackey et al., 2002; Chen et al., 2017; Chen et al., 2018; Chen et al., 2021), few reports exist on cell size and carbon biomass in this region. Therefore, this study aims to investigate the phytoplankton community structure of the WTP, revealing the response of phytoplankton to environmental factors, filling the gap in the study of phytoplankton cell size, and providing fundamental information on carbon storage in this region.

2 Sampling and analysis methods

2.1 Study area and sampling

This study relies on the shared voyage of the WTP commissioned by the National Natural Science Foundation of China. Physical, biological, chemical, and geological surveys were carried out on the R/V "Kexue" from October to December 2019. The survey included 45 stations, divided into four sections (Figure 1).

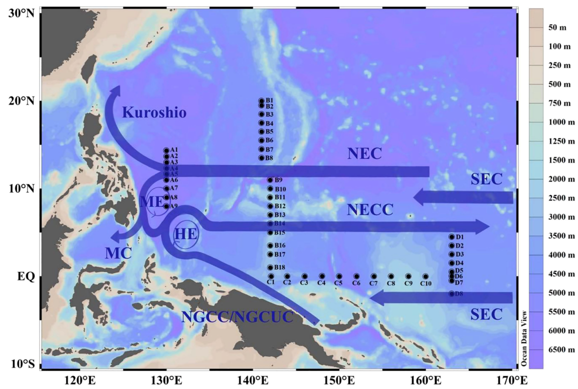

FIGURE 1
Station locations and currents in the study area in the WTP. NEC, North Equatorial Current, MC, Mindanao Current, NECC, North Equatorial Counter Current, SEC, South Equatorial Current, NGCC, New Guinea Coastal Current, NGCUC, New Guinea Coastal Undercurrent Current, ME, Mindanao Eddy, HE, Halmahera Eddy.

Section A comprised stations A1-A9 (8°-14°N, 129°E), section B included stations B1-B18 (1°-20°N, 141°E), section C consisted of stations C1-C10 (0°, 142°-160°E), and section D comprised stations D1-D8 (2°S-4°N, 163°E). Samples were collected at depths of 5, 25, 50, 75, 100, 150, and 200m, with a total of 315 bottles collected.

2.2 Identification of phytoplankton

CTD collected samples of the phytoplankton community structure. Samples from different water layers were placed in 1 L PE bottles, fixed with formaldehyde solution (3%), and stored in a cool place. The phytoplankton samples were shaken gently and settled in a 100 ml sedimentation column for 48 hours in the laboratory. The structure of the phytoplankton community was identified qualitatively and quantitatively under an inverted microscope (Motic AE 2000) based on Utermöhl method (Sun et al., 2002). The phytoplankton species were identified according to Jin, Isamu Y (Isamu, 1991), and Sun (Sun et al., 2002).

2.3 Analysis of the nutrient

Dissolved inorganic nitrogen (DIN), dissolved inorganic phosphorus (DIP) and dissolved silicon (DSi) were measured by colorimetric method using Technicon AA3 Auto-Analyzer (Bran Luebbe, Germany). The DIN measured included Nitrate (NO_3-N), Nitrite (NO_2-N), and Ammonium (NH_4-N). Using the cadmium-copper column reduction method to determine NO_3-N, the limit of detection (LOD) was 0.01 µmol L^{-1} (Wood et al., 1967).The naphthalene ethylenediamine method was used to determine NO_2-N with a LOD of 0.01 µmol L^{-1} (Wang et al., 2022). Using the sodium salicylate method to determine NH_4-N with a LOD of 0.03 µmol L^{-1} (Verdouw et al., 1978). DIP was determined as PO_4-P with a LOD of 0.02 µmol L^{-1} using the phosphomolybdenum blue method (Taguchi et al., 1985). DSi was determined as SiO_3-Si. The LOD was 0.02 µmol L^{-1} using the silicon-molybdenum blue method (Isshiki et al., 1991).

2.4 Measurement of cell size and carbon biomass

The carbon biomass of the cells was estimated based on the cell volume with conversion factors. A fluorescence microscope (RX50) was used to measure phytoplankton-related volume parameters at a magnification of 200× (or 400×). Each phytoplankton cell was measured 25-30 times, and the volume parameters were averaged to find the cell volume (Sun et al., 1999). Calculate the cell volume regarding Sun's model and formula (Sun and Liu, 2003). Biomass calculation was based on Eppley (Eppley et al., 1970):

$$\text{Diatoms}: log_{10}C = 0.76log_{10}V - 0.352$$

$$\text{Other microalgae}: log_{10}C = 0.94log_{10}V - 0.60$$

represents the single-cell volume (μm^3); Crepresents the single-cell carbon biomass (pg).

The phytoplankton importance was calculated using the method of Sun (Sun, 2004):

$$K = \frac{B_i}{B} \cdot f_i$$

where K is the importance of keystone species in the survey; B_i is the total carbon biomass of species i (µg L^{-1}); B is the total carbon biomass of all phytoplankton (nanophytoplankton and microphytoplankton) in one survey (µg L^{-1}); f_i is the frequency of occurrence of species i in the survey.

In this study, phytoplankton carbon biomass in the water column calculated using trapezoidal integration (Uitz et al., 2006):

$$C = \left[\sum_{i=1}^{n-1} \frac{C_{i+1} + C_i}{2} \cdot (D_{i+1} - D_i)\right] / (D_{max} - D_{min})$$

where C is the average value of phytoplankton carbon biomass in water column (mg m^{-3}); n is the total number of layers sampled; C_i is the carbon biomass of layer i (mg m^{-3}); D_i is the sampling depth of layer i (m); D_{max} represents the maximum sampling depth and D_{min} represents the minimum sampling depth (m).

2.5 Data analysis

Calculation of the dominance of phytoplankton:

$$Y = (\frac{n_i}{N}) \times f_i$$

N is the total number of individuals; n_i is the number of individuals of species i; f_i is the frequency of occurrence of species i.

The Shannon index was calculated using the "Vegan" package (Oksanen et al., 2022) in R version 4.2.1, and significance was tested using the Wilcoxon rank-sum test. To account for the heterogeneous cell size distribution in the studied sea area, quantile regression was used to analyze cell size trends, as it provides a clearer understanding of cell volume. Quantile regressions of cell size were calculated using the "quantreg" package (Maniaci et al., 2022) in R version 4.2.1, and significance was determined using the P-test. Pearson's correlation coefficient was used to assess the relationship between phytoplankton abundance, diversity of phytoplankton and environmental factors. Canonical Correspondence Analysis (CCA) was performed using Canoco 5.0 on the cell abundance of species and environmental factors, with both data sets being log10(x+1) transformed. The species data consisted of the abundance of the top 60 dominant species. Hierarchical Clustering was used for cluster analysis of phytoplankton, and the dissimilarity between different groups of phytoplankton was calculated using Primer 6 (6.1.12.0).

3 Results

3.1 Hydrology and nutrients analyses

In 2019, the surface temperature distribution in the western Tropical Pacific Ocean (WTP) was characterized by high values, with a mean surface temperature of about 28°C, which is a typical feature of the western Pacific warm pool (Figures 2A-D). The water temperature decreased unevenly with increasing depth, and a sharp thermocline was observed at around 100 m at all sections. Salinity also increased unevenly with depth, due to the presence of North Pacific Tropical Water and South Pacific Tropical Water at the thermocline (Figures 2E–H). In section B (2°-15°N), both isothermals and isohalines were elevated. The subsurface water temperature and salinity were higher in sections C and D near the equator, owing to the warm pool and saline South Pacific Tropical Water (Figures 2C, D, G, H). Surface nutrients were deficient and only gradually increased at depths of 100 m (Figure 3). Similar to the vertical distribution of temperature and salinity, nutrients had a bump in the 2°-15°N section of section B (Figures 3B, F, J)

3.2 Species composition and community structure of phytoplankton

This investigation identified a total of 260 species from 4 phyla: Bacillariophyta, Dinophyta, Cyanophyta, and Chrysophyta, across 64 genera (Table S1). Diatoms were represented by 33 genera and 73 species, dinoflagellates by 28 genera and 181 species, cyanobacteria by 2 genera and 4 species, and chrysophyceae by 1 genus and 2 species. Dinoflagellates had the largest number of species, accounting for 69.92% of the total species with a cell abundance of 9698 cells L^{-1}. Diatoms made up 28.08% of the species with a cell abundance of 9026 cells L^{-1}. Cyanobacteria had the highest cell abundance of 121,398 cells L^{-1}, but their species accounted for only 1.54% of the total. The smallest proportion of both species and cell abundance was from chrysophyceae, at 0.77% and 896 cells L^{-1}, respectively. The top ten dominant species identified in the investigation included four dinoflagellates, three cyanobacteria, and three diatoms (Table 1).

Overall, the distribution of phytoplankton varied significantly among the four sections (Figure 4A). Dinoflagellates were found to be evenly distributed across all four sections. Section B had the highest proportion of cyanobacteria, while the proportion of diatoms sharply increased in sections B9-B15. Sections C and D had a similar phytoplankton composition, with higher levels of diatoms near land in section C. The dominant species of phytoplankton also differed across the sections (Figure 4B). *Trichodesmium thiebautii* was the dominant species in stations A1, A2, A8, and A9, while *Scrippsiella trochoidea*, *Nitzschia* sp., and *Thalassiothrix longissima* were the dominant species in other stations. Section B was mainly dominated by *Trichodesmium thiebautii*, *Trichodesmium hildebrandtii*, and *Trichodesmium erythraeum*, except for stations B9-B12 and B14, which had

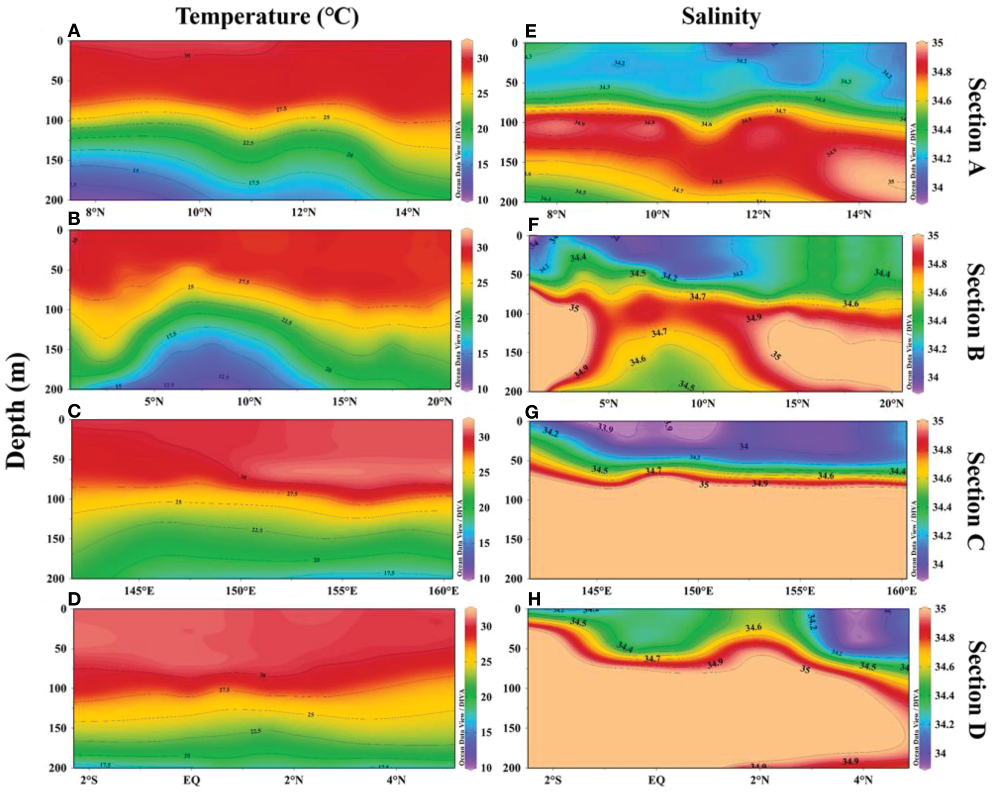

FIGURE 2
Vertical distribution of temperature **(A–D)** and salinity **(E–H)** in the WTP in 2019.

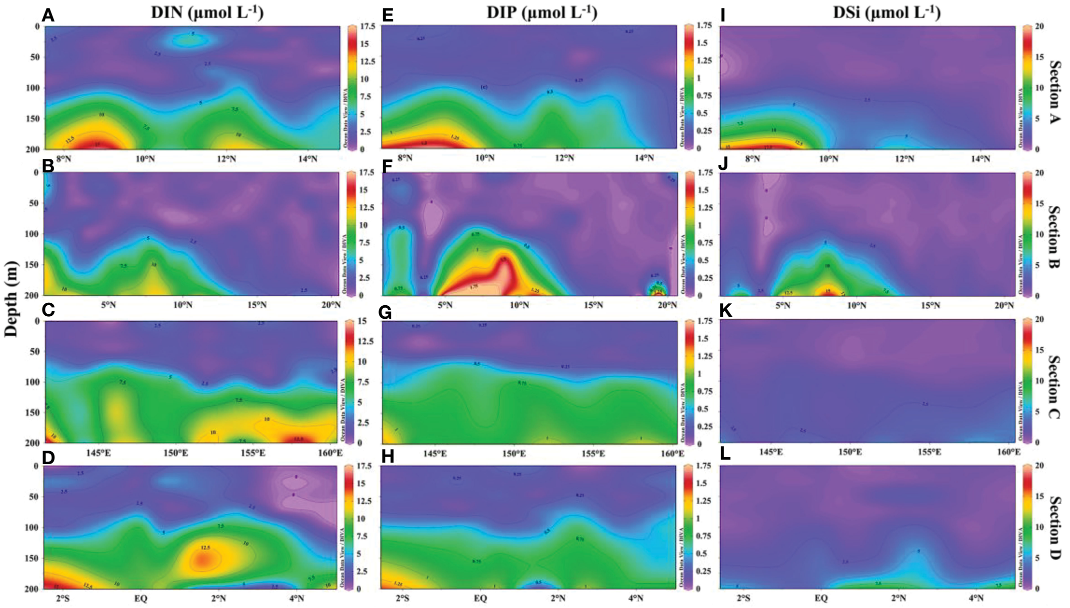

FIGURE 3
Vertical distribution of nutrients (μmol L^{-1}) in the WTP in 2019. **(A-D)** vertical distribution of DIN; **(E-H)** vertical distribution of DIP; **(I-L)** vertical distribution of DSi.

high levels of diatoms such as *Nitzschia* sp. and *Synedra* sp. Sections C and D had a similar phytoplankton composition, with dominant species including *Synedra* sp., *Scrippsiella trochoidea*, *Nitzschia* sp., *Thalassiothrix longissima*, *Dictyocha fibula* and *Coscinodiscus granii*.

For the diversity of phytoplankton, the Shannon diversity index of sites B1-B8 is lower, while sections C and D near the equator have higher diversity (Figure 5). Therefore, the difference in planktonic plant diversity between section B and sections C and D is very significant, while the difference relative to section A is relatively small.

3.3 Cell size of phytoplankton

When cell abundance was regressed against equivalent sphere diameter (ESD) using all data, a high degree of significance was found (p-value< 0.01), with 38.1% of the change in abundance being explained by ESD. The slope of the fitted straight line of cell abundance versus ESD increased with increasing cell volume, indicating that the decrease in cell abundance rate is faster when the cells are larger (Figure 6A). However, the slope hardly changes when the quantile is 0.01-0.3 (Figure 6C), suggesting that cell abundance is high and does not vary much in this ESD range of approximately 2 to 12 μm. At a quantile

TABLE 1 Dominant phytoplankton species in the WTP.

Species	Percentage of the ratio to total phytoplankton (%)	Frequency (*fi*)	Dominance (*Y*)
Trichodesmium thiebautii	63.24	0.143	0.0903
Nitzschia sp.	1.39	0.750	0.0104
Scrippsiella trochoidea	1.26	0.661	0.0083
Trichodesmium hildebrandtii	16.19	0.045	0.0072
Synedra sp.	1.11	0.479	0.0053
Trichodesmium erythraeum	6.16	0.036	0.0022
Oxytoxum variabile	0.47	0.446	0.0021
Thalassiothrix longissima	0.68	0.298	0.0020
Gymnodinium lohmanni	0.46	0.354	0.0016
Oxytoxum pacbyderme	0.43	0.360	0.0016

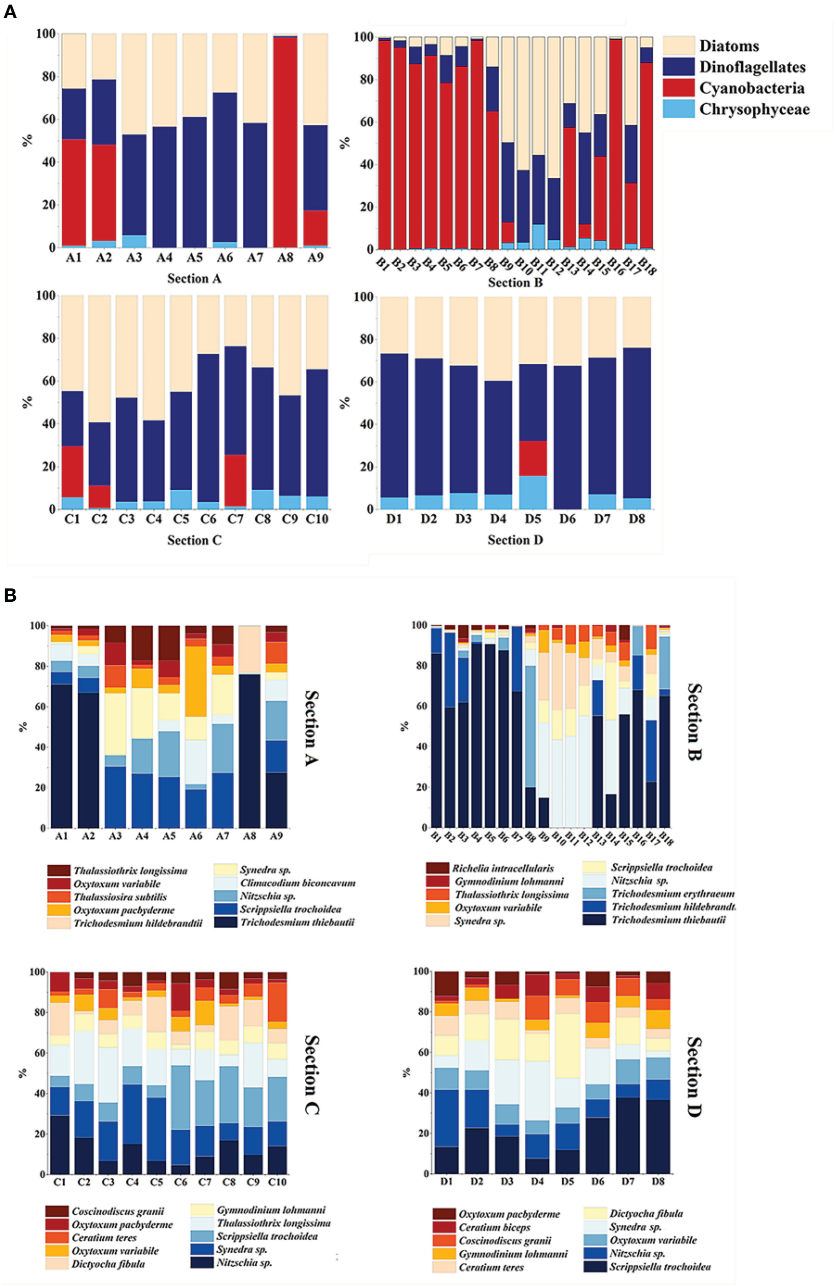

FIGURE 4
Composition of phytoplankton **(A)** and dominant species **(B)** in four sections in the WTP.

of approximately 0.3, the slope decreases, indicating that the abundance of cells with ESD greater than 12 µm begins to decrease. At quantile 0.8, the slope decreases again, and the ESD is about 25 µm, indicating that the abundance of cells with ESD greater than 25 µm is small, and the abundance of cells becomes smaller as the cell volume increases.

3.4 Distribution of phytoplankton cell abundance and carbon biomass

Along sections A and B, cell abundance was dominated by cyanobacteria, which were present only in the surface layer (Figures 7C, O). In section A, cell abundance distribution was similar for diatoms and dinoflagellates, but diatoms distributed in deeper layers (Figures 7A, B). The cell abundance of chrysophyceae was small and mainly distributed in the subsurface layer (Figure 7D). Compared to microphytoplankton, nanophytoplankton had a giant cell abundance and was mainly distributed in the upper layers, while microphytoplankton was mainly distributed in the lower layers (Figures 7E, F). Notably, cyanobacteria were more widespread in section B (Figure 7O) and phytoplankton were distributed in deeper layers compared to section A (Figures 7Q, R).

The cell abundance and carbon biomass of sections C and D are shown in Figure 8. In sections C and D, the phytoplankton

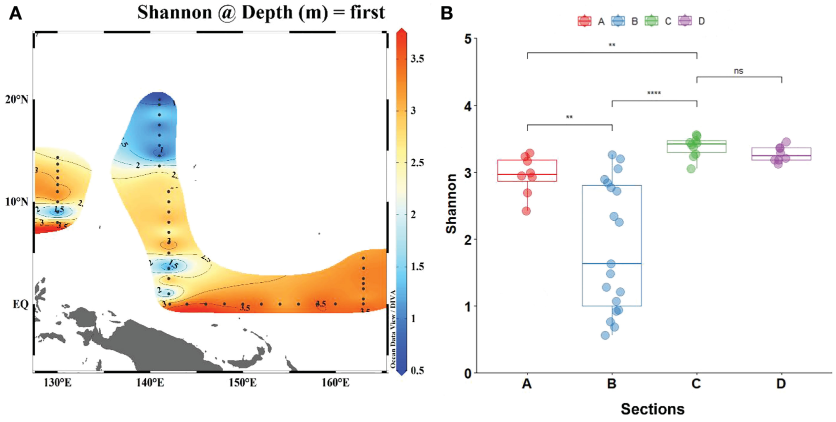

FIGURE 5
Comparison of Shannon diversity index between all stations **(A)** and four sections **(B)**. (The significance results of section D between sections A and B were the same as those of section C). “*” represents significance, *: $p < 0.05$, **: $p < 0.005$, ***: $p < 0.001$. “ns” means no significance.

abundance was dominated by dinoflagellates and diatoms, with little presence of cyanobacteria (Figures 8A–C, M–O). Dinoflagellates were primarily concentrated in the surface layer (Figure 8B), while the abundance of diatoms and chrysophyceae increased in section C, especially near land (Figures 8A, D). The cell abundance of microphytoplankton was greatest in section C, mainly distributed around 75m, and the cell abundance in section D was the smallest among all sections (Figures 8Q, R). The cell abundance of diatoms in section D decreased and was almost exclusively distributed in the subsurface layer (Figure 8A).

The carbon biomass in the survey area ranged from 6.597 mg m^{-3} to 155.627 mg m^{-3}, with a mean value of 25.969 ± 24.752 mg m^{-3} (Table S1). The carbon biomass of different species and cell sizes of phytoplankton were examined separately (Figures 9A, B). In terms of phytoplankton species, the carbon biomass of dinoflagellates, diatoms, cyanobacteria, and chrysophyceae was 674.266 mg m^{-3}, 338.329 mg m^{-3}, 125.266 mg m^{-3}, and 30.758 mg m^{-3}, respectively, accounting for 57.698%, 28.951%, 10.719%, and 2.632%, respectively (Figure 9A). Dinoflagellates contributed more than 50% of the carbon in each section. The carbon contribution of diatoms increased in sections C and D, with an abrupt increase at stations B9 to B17. The carbon contributed by cyanobacteria was mainly concentrated in stations A8, B1-B7, and B16. In terms of phytoplankton size, the total carbon biomass of nanophytoplankton and microphytoplankton was 376.324 mg m^{-3} and 792.295 mg m^{-3}, respectively, accounting for 32.202% and 67.798% of the total carbon biomass (Figure 9B). The carbon contribution of microphytoplankton exceeded 60% in each section.

Analysis of the vertical distribution of carbon biomass revealed that diatoms contributed the most to the carbon biomass in sections B and C, and were primarily distributed in the subsurface layer (Figures 7S, 8G). In contrast, dinoflagellates and cyanobacteria showed higher carbon biomass in the upper layer (Figures 7H, T, I, U, 8H, T, I, U). Nanophytoplankton contributed more carbon biomass in sections A and B, and were primarily found in the surface layer (Figures 7K, W). The carbon biomass of

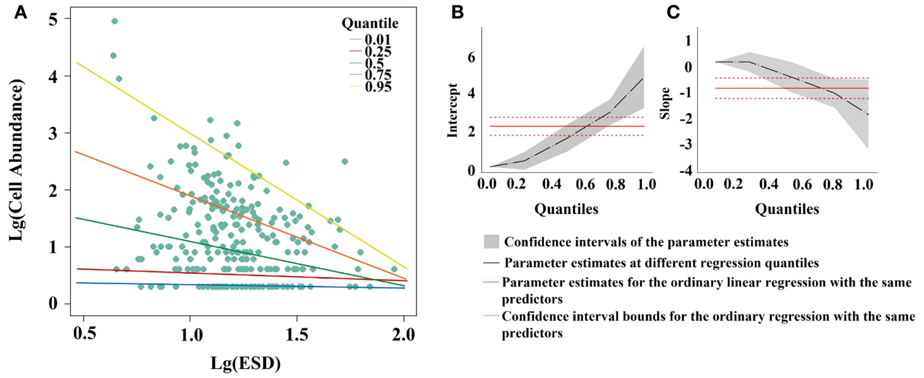

FIGURE 6
Quantile regression analysis of equivalent sphere diameter (ESD) versus cell abundance in the WTP. Least squares fit to log 10 transformed data. **(A)** Results of fitting ESD to cell abundance at different percentile; **(B)** intercepts of different interquartile fits; **(C)** slopes of different interquartile fits.

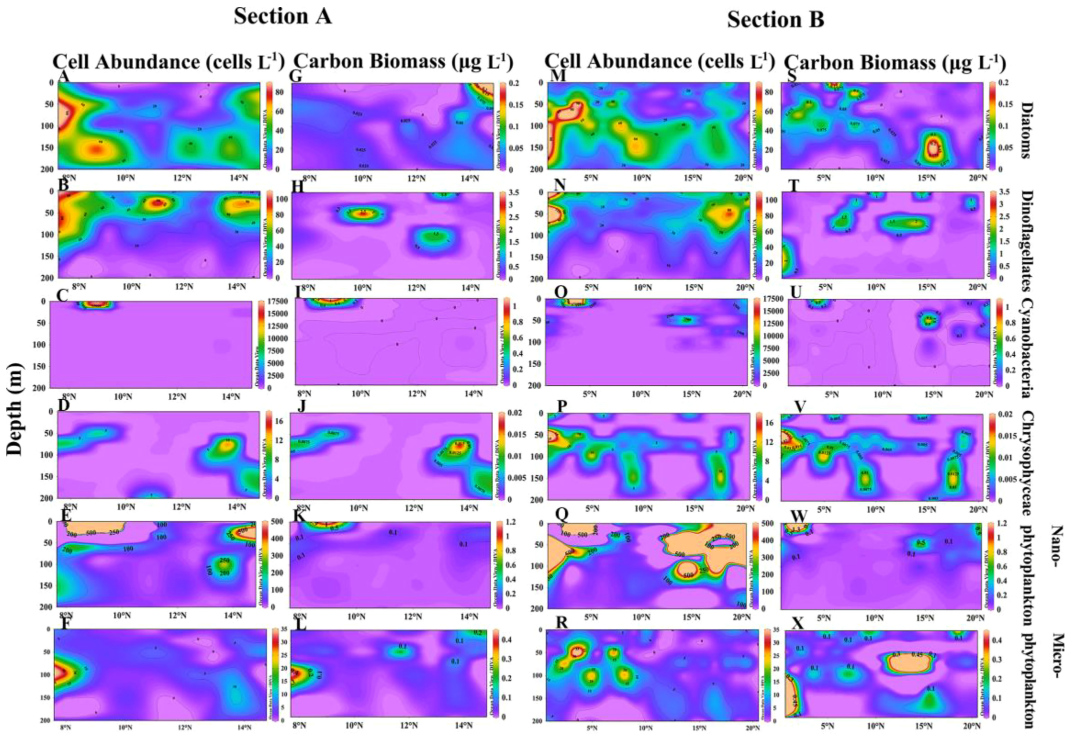

FIGURE 7
Vertical distribution of cell abundance and carbon biomass of phytoplankton in sections A and B. Cell abundance and carbon biomass of diatoms **(A, G)**, dinoflagellates **(B, H)**, cyanobacteria **(C, I)**, chrysophyceae **(D, J)**, nanophytoplankton **(E, K)** and microphytoplankton **(F, L)** in section A; Cell abundance and carbon biomass of diatoms **(M, S)**, dinoflagellates **(N, T)**, cyanobacteria **(O, U)**, chrysophyceae **(P, V)**, nanophytoplankton **(Q, W)** and microphytoplankton **(R, X)** in section B.

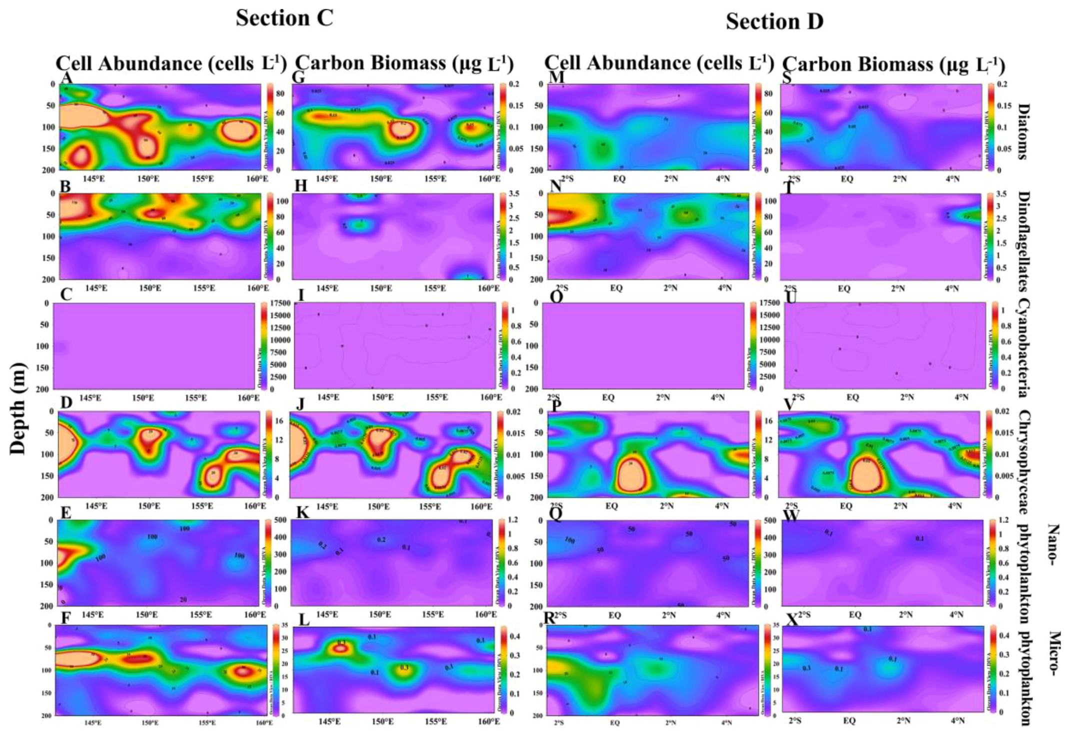

FIGURE 8
Vertical distribution of cell abundance and carbon biomass of phytoplankton in sections C and D. Cell abundance and carbon biomass of diatoms **(A, G)**, dinoflagellates **(B, H)**, cyanobacteria **(C, I)**, chrysophyceae **(D, J)**, nanophytoplankton **(E, K)** and microphytoplankton **(F, L)** in section C; Cell abundance and carbon biomass of diatoms **(M, S)**, dinoflagellates **(N, T)**, cyanobacteria **(O, U)**, chrysophyceae **(P, V)**, nanophytoplankton **(Q, W)** and microphytoplankton **(R, X)** in section D.

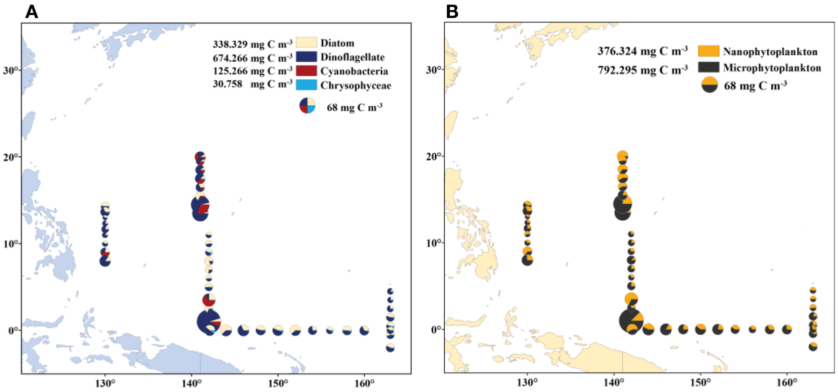

FIGURE 9
Spatial distribution of carbon biomass of phytoplankton. **(A)** Carbon biomass distribution of diatoms, dinoflagellates, cyanobacteria and chrysophyceae; **(B)** carbon biomass of nanophytoplankton and microphytoplankton.

microphytoplankton was highest in section B, and mainly concentrated in the subsurface layer (Figures 7X).

3.5 Keystone species for carbon biomass

To better understand the role of low abundance and high volume cells in the ecosystem, this study utilized a combination of phytoplankton carbon biomass and dominance calculations to identify key species in the WTP phytoplankton community (Table 2). The importance of each species to carbon biomass was used to determine the keystone species, with dinoflagellates (3 species) and diatoms (2 species) being the primary contributors, followed by cyanobacteria (1 species). *Scrippsiella trochoidea* was frequently observed and had the highest importance among the identified keystone species, while *Coscinodiscus granii* had the highest single-cell carbon biomass (Table 2). *Trichodesmium thiebautii* was also considered a keystone species due to its high abundance despite its minimal single-cell carbon amount.

The carbon biomass of dinoflagellates and cyanobacteria peaked at depths of 5-50 m, with *Trichodesmium thiebauti* and *Ceratium pulchellum* having the highest mean carbon biomass at 5 m, at 0.430 μg L^{-1} and 0.583 μg L^{-1}, respectively (Figures S2D, F). The peak carbon biomass of *Gymnodinium lohmanni* was observed at 50 m, with 0.395 μg L^{-1} (Figure S2C). In contrast, diatoms had a deeper distribution, with the peak carbon biomass of *Coscinodiscus granii* at 100 m (0.280 μg L^{-1}) (Figure S2B), and *Synedra* sp. at 150 m (0.359 μg L^{-1}) (Figure S2E).

3.6 Community structure and hydrological characteristics of four groups of phytoplankton

Cluster analysis was employed to classify phytoplankton into four groups. The results showed that group 1 and group 2 were highly similar, while group 3 and group 4 were also highly similar (Figure 10). Compared to group 2, group 1 had a higher diatom abundance, with *Nitzschia* sp. and *Thalassiothrix longissima* having the highest abundance among the four groups (Table 3). In group 2, the abundance of *Trichodesmium thiebautii* was the highest among the four groups, but *Trichodesmium hildebrandtii* and *Trichodesmium erythraeum* were not observed. Group 3 exhibited distinct characteristics of low temperature and low salinity, with the highest diatom abundance. *Synedra* sp. and *Thalassiothrix longissima* also had higher abundance in group 3.

TABLE 2 Keystone species and their carbon biomass in the WTP.

Species	Single-cell carbon biomass (pg L^{-1})	Percentage in conversion carbon (%)	Frequency in samples (%)	Importance
Scrippsiella trochoidea	1188.800	4.416	66.1	0.0292
Coscinodiscus granii	11299.507	4.669	26.8	0.0125
Gymnodinium lohmanni	2767.565	2.575	35.4	0.0091
Trichodesmium thiebautii	64.450	5.036	14.3	0.0072
Synedra sp.	801.635	1.070	47.9	0.0051
Ceratium pulchellum	4482.851	2.142	18.5	0.0040

TABLE 3 Mean values of temperature (℃), salinity, nutrients (μmol L^{-1}) and species cell abundance (cells L^{-1}) of four groups of phytoplankton obtained by clustering analysis.

	Group 1	Group 2	Group 3	Group 4
Temperature	26.151 ± 0.999	25.601 ± 1.254	25.065 ± 1.678	26.975 ± 0.505
Salinity	34.629 ± 0.150	34.627 ± 0.152	34.512 ± 0.158	34.751 ± 0.069
NO_3-N	2.333 ± 1.260	1.796 ± 1.417	2.657 ± 0.431	3.217 ± 0.404
NO_2-N	0.132 ± 0.082	0.107 ± 0.081	0.082 ± 0.068	0.030 ± 0.023
NH_4-N	1.134 ± 0.473	0.742 ± 0.492	0.907 ± 0.671	1.293 ± 0.328
PO_4-P	0.348 ± 0.168	0.277 ± 0.215	0.416 ± 0.097	0.458 ± 0.031
SiO_3-Si	1.798 ± 1.218	1.738 ± 1.239	2.587 ± 0.890	1.820 ± 0.489
Diatoms	157 ± 245	109 ± 86	401 ± 44	182 ± 71
Dinoflagellates	212 ± 73	131 ± 115	308 ± 47	210 ± 66
Cyanobacteria	17 ± 519	3 ± 11355	515 ± 8	8315 ± 40
Chrysophyceae	24 ± 29	12 ± 13	24 ± 9	15 ± 16
Trichodesmium thiebautii	12801 ± 9510	99935 ± 107363	118 ± 322	224 ± 478
Nitzschia sp.	2196 ± 1112	1297 ± 672	1221 ± 782	732 ± 275
Scrippsiella trochoidea	1026 ± 294	703 ± 299	645 ± 265	818 ± 361
Trichodesmium hildebrandtii	0 ± 0	27675 ± 37731	0 ± 0	0 ± 0
Synedra sp.	1373 ± 1312	1383 ± 633	1039 ± 476	1598 ± 1171
Trichodesmium erythraeum	0 ± 0	8507 ± 18035	0 ± 0	0 ± 0
Oxytoxum variabile	534 ± 258	346 ± 277	229 ± 147	266 ± 223
Thalassiothrix longissima	1078 ± 1459	528 ± 582	284 ± 136	1006 ± 774
Gymnodinium lohmanni	626 ± 279	501 ± 622	86 ± 78	292 ± 187
Oxytoxum pacbyderme	491 ± 217	279 ± 284	145 ± 135	179 ± 141

3.7 Environmental effects on phytoplankton community, cell size and carbon biomass

The Pearson correlation reflects the relationship between phytoplankton and environmental factors (Figure S3). Cyanobacteria were highly significantly and positively correlated with temperature, suggesting that temperature may affect their distribution. Dinoflagellate abundance was highly significantly and positively correlated with temperature and negatively correlated with nutrition, reflecting that the growth of dinoflagellates is susceptible to temperature. At the same time, dinoflagellates may can survive better under nutrient-deficient conditions. Diatom abundance was positively correlated with DIN and DIP, indicating that nutrients can influence the distribution of diatoms. Microphytoplankton was extremely significantly and positively correlated with diatoms reflecting that it is mainly composed of diatoms. Several diatom species, such as *Thalassiothrix longissimi* and *Synedra* sp., were positively correlated with nitrate and negatively correlated with temperature (Figure 11). In contrast, the majority of cyanobacteria and dinoflagellate species showed a negative correlation with nitrate and a positive correlation with temperature, such as *Trichodesmium thiebautii* and *Scrippsiella trochoidea*.

4 Discussion

4.1 Classification of phytoplankton and their corresponding hydrological environments

We used cluster analysis to divide phytoplankton into four groups, and the differences in phytoplankton composition between stations reflected changes in ocean currents, which profoundly affected the diversity and distribution of phytoplankton. Although the changes in phytoplankton composition cannot be strictly distinguished by ocean currents, the variation in phytoplankton at different sections still showed certain patterns. For instance, in section A, the phytoplankton composition underwent a transition from Group 1 to Group 3 and then back to Group 1, respectively, which confirms that this section was impacted by the influence of distinct water masses. Kuroshio, known for its high temperature and low nutrient levels, provides suitable conditions for the growth of cyanobacteria, resulting in an increase in cyanobacteria abundance at stations A1 and A2 (Figures 4A, S3). Although station A9 is also classified under Group 1, it may be affected by the Mindanao Eddy, which brings up nutrient-rich cold water to the surface within the eddy. This causes the thermocline depth to

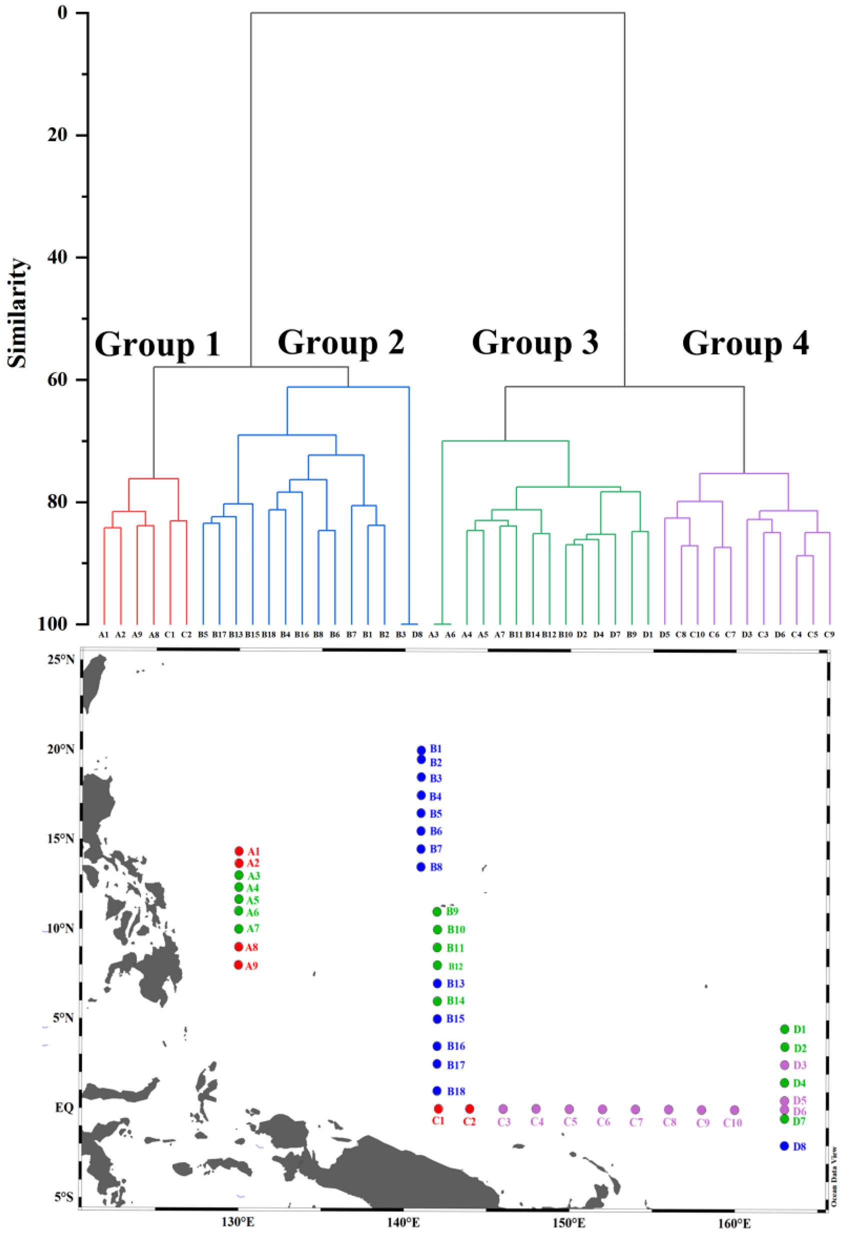

FIGURE 10
Results and location of cluster analysis of phytoplankton composition in the WTP.

become shallower, promoting the growth of diatoms, according to Zhang's study (Zhang Q. et al., 2012). Unlike Group 1, Group 3 had the lowest temperature and salinity and higher nitrate concentration (Table 3). This may be due to the current-seamount interaction generated by the North Equatorial Current encountering seamounts at stations B9-B12 (Figures 1–3), consistent with the research by Ma (Ma et al., 2019). This effect creates a unique phytoplankton community structure in Group 3, which is dominated by diatoms that prefer low temperature and high nutrients (Figures 4B, 11). Except for the stations affected by current-seamount interaction, the phytoplankton in section B was dominated by cyanobacteria, with low species diversity, possibly due to minimal ocean current influence and distance from the land (Figure 1). In contrast to section B, the species diversity in sections C and D was high (Figure 5). On the one hand, the thermocline in the eastern equatorial Pacific is much lower than that in the western Tropical Pacific Ocean, and nutrient-rich seawater is transported by the South Equatorial Current to the Gulf of Papua, and nutrient levels are increasing due to the influence of the New Guinea continent (Gordon and Fine, 1996; Mackey et al., 2002). On the other hand, the New Guinea coastal upwelling, which flows southeast to northwest year-round, also carries high salinity and nutrient-rich South Pacific water northward along the coast (Christian et al., 2004). Therefore, the waters outside the New

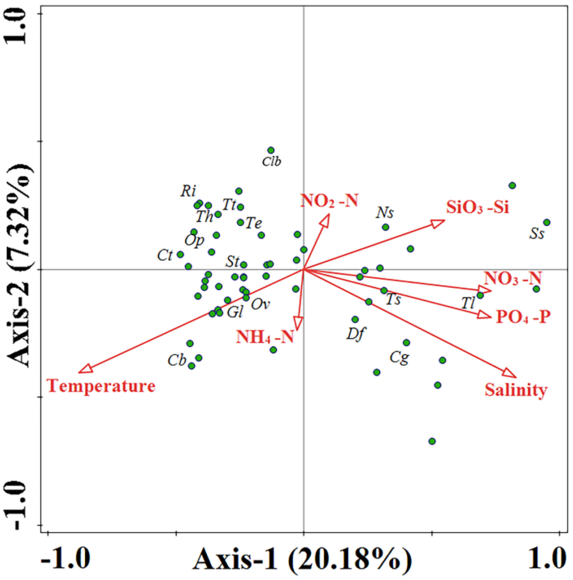

FIGURE 11
Canonical Correspondence Analysis (CCA) of phytoplankton species and environmental factors in the WTP. *Clb, Climacodium biconcavum*; *Ri, Richelia intracellularis*; *Tt, Trichodesmium thiebautii*; *Th, Trichodesmium hildebrandtii*; *Te, Trichodesmium erythraeum*; *Ct, Ceratium teres*; *St, Scrippsiella trochoidea*; *Gl, Gymnodinium lohmanni*; *Ov, Oxytoxum variabile*; *Op, Oxytoxum pacbyderme*; *Cb, Ceratium biceps*; *Ns., Nitzschia* sp.; *Ss., Synedra* sp.; *Tl, Thalassiothrix longissimi*; *Ts, Thalassiosira subtilis*; *Df, Dictyocha fibula*; *Cg, Coscinodiscus granii*.

Guinea Islands have higher species diversity and diatom biomass (Figure 5, 9A), consistent with the research by Dong (Dong et al., 2012).

4.2 Environmental preferences of dominant species

Different dominant species exhibit specific environmental preferences and can significantly influence the characteristics of entire ecological communities. Our study employs both cluster analysis and CCA analysis to identify two distinct types of phytoplankton: the high-temperature low-nitrate type, represented by *Trichodesmium* and *Scrippsiella trochoidea*, and the low-temperature high-nitrate type, represented by *Thalassiothrix longissima* and *Synedra* sp. (Figures 10, 11). *Trichodesmium*, a crucial nitrogen-fixing alga in the ocean, contributes substantially to primary production and biomass in our study area. However, factors such as wind, phosphorus, and unique metal characteristics can significantly impact the abundance of *Trichodesmium* (Chang et al., 2000; Nuester et al., 2012). Our survey has indicated that *Trichodesmium erythraeum* and *Trichodesmium hildebrandtii* solely appeared in Group 2, suggesting their affinity for living in undisturbed oligotrophic water bodies. Chen's research also supports our findings, demonstrating that *Trichodesmium thiebautii* primarily dominates areas outside the New Guinea Islands with large ocean currents. Conversely, *Trichodesmium erythraeum* and *Trichodesmium hildebrandtii* have a greater abundance in sections unaffected by ocean currents (5°-35°N, 145° E). *Scrippsiella trochoidea*, a dominant and key species in the western Tropical Pacific Ocean, exhibits widespread distribution and high abundance across four sections, ranging from northern to tropical waters. This species has been reported to bloom in various regions, such as Japan, the Mediterranean, and the US coast (Montresor et al., 1998; Zinssmeister et al., 2011; Morozova et al., 2016). Our survey has also revealed that *Scrippsiella trochoidea* can maintain high density even in low-nutrient conditions, corroborating existing literature (Yin et al., 2008).

The dominant diatom species identified in this survey mostly belong to nanophytoplankton. The small cell size of these diatoms enables them to remain suspended and to rapidly absorb nutrients. Some diatom species have become elongated or flattened to increase their surface area-to-volume ratio for better nutrient absorption (Reynolds, 2006), such as *Thalassiothrix longissima* and *Synedra* sp. (Figure S1). *Ceratium biceps* is an important species that distinguishes Group 3 from Group 4 (Table S4). It prefers high-salinity conditions of Group 4 (Table 3), which is consistent with the results of CCA analysis (Figure 11). In the continental shelf area close to land, the abundance of *Ceratium biceps* is higher, which is consistent with the findings (Hallegraeff and Jeffrey, 1984).

5 Conclusion

We investigated the community structure, cell size, and carbon biomass of phytoplankton in the western Tropical Pacific Ocean in 2019. The phytoplankton community was mainly composed of dinoflagellates (181 species), diatoms (73 species), cyanobacteria (4 species), and chrysophyceae (2 species), with most species having equivalent spherical diameters of 2-12 μm and dominated by nanophytoplankton. Despite their lower abundance, microphytoplankton contributed 792.295 mg m^{-3} of carbon, while nanophytoplankton contributed 376.324 mg m^{-3}. In this study, we found that the composition and distribution of phytoplankton were closely related to ocean currents. For example, the abundance of diatoms increased under the influence of the South Equatorial Current and the coastal currents of the New Guinea Coastal Undercurrent Current, while the abundance of *Trichodesmium* was very high in areas with little disturbance from ocean currents. Overall, this survey provided valuable insights into the distribution and composition of phytoplankton in the western tropical Pacific Ocean. It highlighted the relationship between species distribution and ocean currents and provided basic information on cell size and carbon biomass in the region.

Data availability statement

The original contributions presented in the study are included in the article/Supplementary Material. Further inquiries can be directed to the corresponding author.

Author contributions

JS: Conceptualization, Methodology, Project administration, Resources, Supervision, Visualization, Review & editing. WY: Sample measurement, Data analysis, Writing the manuscript. ZC: Sample identification, Data analysis. FW and GZ: Sample collection, Environmental factor determination. LZ: CTD data interpretation and review. All authors contributed to the article and approved the submitted version.

Funding

This research was supported by the National Natural Science Foundation of China (41876134), and the Changjiang Scholar Program of the Chinese Ministry of Education (T2014253) through grants to Jun Sun. The research was also partially supported by the State Key Laboratory of Biogeology and Environmental Geology, China University of Geosciences (GKZ22Y656).

Acknowledgments

CTD data and water samples were collected on board of R/V KeXue implementing open research cruises NORC2019-09 and NORC2021-09 supported by NSFC Shiptime Sharing Projects (Nos. 41849909 and 42049909) and Laoshan Science and Technology Innovation project (No. LSKJ202201700).

Conflict of interest

The authors declare that the research was conducted in the absence of any commercial or financial relationships that could be construed as a potential conflict of interest.

Publisher's note

Supplementary material

The Supplementary Material for this article can be found online at: https://www.frontiersin.org/articles/10.3389/fmars.2023.1147271/full#supplementary-material

References

Chang, J., Chiang, K.-P., and Gong, G.-C. (2000). Seasonal variation and cross-shelf distribution of the nitrogen-fixing cyanobacterium, trichodesmium, in southern East China Sea. *Cont Shelf Res.* 20 (4), 479–492. doi: 10.1016/S0278-4343(99)00082-5

Charalampous, E., Matthiessen, B., and Sommer, U. (2021). Grazing induced shifts in phytoplankton cell size explain the community response to nutrient supply. *Microorganisms* 9 (12), 2440. doi: 10.3390/microorganisms9122440

Chen, Z., Sun, J., Gu, T., Zhang, G., and Wei, Y. (2021). Nutrient ratios driven by vertical stratification regulate phytoplankton community structure in the oligotrophic western pacific ocean. *Ocean Sci.* 17 (6), 1775–1789. doi: 10.5194/os-17-1775-2021

Chen, Z., Sun, J., and Zhang, G. (2018). Netz-phytoplankton community structure of the tropical Western pacific ocean in summer 2016. *Mar. Sci.* 42 (7), 114–130. doi: 10.11759//hykx20180331002

Chen, Y., Sun, X., Zhu, M., Zheng, S., Yuan, Y., and Denis, M. (2017). Spatial variability of phytoplankton in the pacific western boundary currents during summer 2014. *Mar. Freshw. Res.* 68 (10), 1887–1900. doi: 10.1071/MF16297

Christian, J., Murtugudde, R., Ballabrera, J., and McClain, C. (2004). A ribbon of dark water: phytoplankton blooms in the meanders of the pacific north equatorial countercurrent. *Deep Sea Res. Part II: Topical Stud. Oceanography* 51, 209–228. doi: 10.1016/j.dsr2.2003.06.002

Dong, L., Li, L., Wang, H., He, J., and Wei, Y. (2012). PHYTOPLANKTON DISTRIBUTION IN SURFACE WATER OF WESTERN PACIFIC DURING WINTER 2008: a STUDY OF MOLECULAR ORGANIC GEOCHEMISTRY. *Mar. Geology Quaternary Geology* 32, 51–60. doi: 10.3724/SP.J.1140.2012.01051

Eppley, R. W., Reid, F. M. H., and Strickland, J. D. H. (1970). Estimates of phytoplankton crop size, growth rate, and primary production. *Bull. Scripps Inst Oceanogr* 17, 33–42.

Finkel, Z. V. (2001). Light absorption and size scaling of light-limited metabolism in marine diatoms. *Limnol Oceanogr* 46 (1), 86–94. doi: 10.4319/lo.2001.46.1.10086

Finkel, Z. V., Beardall, J., Flynn, K. J., Quigg, A., Rees, T. A. V., and Raven, J. A. (2010). Phytoplankton in a changing world: cell size and elemental stoichiometry. *J. Plankton Res.* 32, 119–137. doi: 10.1093/PLANKT/FBP098

Finkel, Z. V., Irwin, A., and Schofield, O. (2004). Resource limitation alters the 3/4 size scaling of metabolic rates in phytoplankton. *Mar. Ecol-Prog Ser.* 273, 269–279. doi: 10.3354/meps273269

Gordon, A. L., and Fine, R. A. (1996). Pathways of water between the pacific and Indian oceans in the Indonesian seas. *Nature* 379 (6561), 146–149. doi: 10.1038/379146a0

Gosselain, V., Hamilton, P., and Descy, J.-P. (2000). Estimating phytoplankton carbon from microscopic counts: an application for riverine systems. *Hydrobiologia* 438, 75–90. doi: 10.1023/A:1004161928957

Hallegraeff, G., and Jeffrey, S. W. (1984). Tropical phytoplankton species and pigments of continental shelf waters of north and north-West Australia. *Mar. Ecol-Prog Ser.* 20, 59–74. doi: 10.3354/meps020059

Hillebrand, H., Dürselen, C.-D., Kirschtel, D., Pollingher, U., and Zohary, T. (1999). Biovolume calculation for pelagic and benthic microalgae. *J. Phycol* 35, 403–424. doi: 10.1046/j.1529-8817.1999.3520403.x

Hu, D., Wang, F., Sprintall, J., Wu, L., Riser, S., Cravatte, S., et al. (2020). Review on observational studies of western tropical pacific ocean circulation and climate. *J. Oceanology Limnology* 38 (4), 906–929. doi: 10.1007/s00343-020-0240-1

Irion, S., Christaki, U., Berthelot, H., L'Helguen, S., and Jardillier, L. (2021). Small phytoplankton contribute greatly to CO2-fixation after the diatom bloom in the southern ocean. *ISME J.* 15 (9), 2509–2522. doi: 10.1038/s41396-021-00915-z

Isamu, Y. (1991). *Illustrations of the marine plankton of Japan* (Hoikusha Press: Tokyo, Japan).

Isshiki, K., Sohrin, Y., and Nakayama, E. (1991). Form of dissolved silicon in seawater. *Mar. Chem.* 32 (1), 1–8. doi: 10.1016/0304-4203(91)90021-N

Li, Y., Wang, F., and Tang, X. (2013). Spatial-temporal variability of thermohaline intrusions in the northwestern tropical pacific ocean. *Chin. Sci. Bull.* 58 (9), 1038–1043. doi: 10.1007/s11434-012-5359-9

Ma, J., Song, J., Li, X., Yuan, H., Li, N., Duan, L., et al. (2019). Environmental characteristics in three seamount areas of the tropical Western pacific ocean: focusing on nutrients. *Mar. pollut. Bull.* 143, 163–174. doi: 10.1016/j.marpolbul.2019.04.045

Mackey, D. J., Blanchot, J., Higgins, H. W., and Neveux, J. (2002). Phytoplankton abundances and community structure in the equatorial pacific. *Deep Sea Res. Part II: Topical Stud. Oceanography* 49 (13), 2561–2582. doi: 10.1016/S0967-0645(02)00048-6

Maniaci, G., Brewin, R. J. W., and Sathyendranath, S. (2022). Concentration and distribution of phytoplankton nitrogen and carbon in the Northwest Atlantic and

Indian ocean: a simple model with applications in satellite remote sensing. *Front. Mar. Sci.* 9. doi: 10.3389/fmars.2022.1035399

Marañón, E., Cermeño, P., Lopez-Sandoval, D., Rodríguez-Ramos, T., Sobrino, C., Huete-Ortega, M., et al. (2013). Unimodal size scaling of phytoplankton growth and the size dependence of nutrient uptake and use. *Ecol. Lett.* 16, 371–379. doi: 10.1111/ele.12052

McCreary, J. P., and Lu, P. (1994). Interaction between the subtropical and equatorial ocean circulations: the subtropical cell. *J. Phys. Oceanogr* 24 (2), 466–497. doi: 10.1175/1520-0485(1994)024<0466:Ibtsae>2.0.Co;2

Mena, C., Reglero, P., Hidalgo, M., Sintes, E., Santiago, R., Martín, M., et al. (2019). Phytoplankton community structure is driven by stratification in the oligotrophic Mediterranean Sea. *Front. Microbiol.* 10. doi: 10.3389/fmicb.2019.01698

Montresor, M., Zingone, A., and Sarno, D. (1998). Dinoflagellate cyst production at a coastal Mediterranean site. *J. Plankton Res.* 20 (12), 2291–2312. doi: 10.1093/plankt/20.12.2291

Morán, X. A. G., López-Urrutia, Á., Calvo-Díaz, A., and Li, W. K. W. (2010). Increasing importance of small phytoplankton in a warmer ocean. *Glob Change Biol.* 16 (3), 1137–1144. doi: 10.1111/j.1365-2486.2009.01960.x

Morozova, T. V., Orlova, T. Y., Efimova, K. V., Lazaryuk, A. Y., and Burov, B. A. (2016). Scrippsiella trochoidea cysts in recent sediments from amur bay, Sea of Japan: distribution and phylogeny. *Botanica Marina* 59 (2-3), 159–172. doi: 10.1515/bot-2015-0057

Nuester, J., Vogt, S., Newville, M., Kustka, A., and Twining, B. (2012). The unique biogeochemical signature of the marine diazotroph trichodesmium. *Front. Microbiol.* 3. doi: 10.3389/fmicb.2012.00150

Oksanen, J., Kindt, R., and O'Hara, B. (2005). *Community Ecology Package*. The vegan Package: 21–26.

Pérez-Hidalgo, L., and Moreno, S. (2016). Nutrients control cell size. *Cell Cycle* 15 (13), 1655–1656. doi: 10.1080/15384101.2016.1172471

Reynolds, C. S. (2006). *The ecology of phytoplankton* (Cambridge: Cambridge University Press).

Sciascia, R., De Monte, S., and Provenzale, A. (2013). Physics of sinking and selection of plankton cell size. *Phys. Lett. A* 377 (6), 467–472. doi: 10.1016/j.physleta.2012.12.020

Shiozaki, T., Hirose, Y., Hamasaki, K., Kaneko, R., Ishikawa, K., and Harada, N. (2019). Eukaryotic phytoplankton contributing to a seasonal bloom and carbon export revealed by tracking sequence variants in the Western north pacific. *Front. Microbiol.* 10. doi: 10.3389/fmicb.2019.02722

Street, J. H., and Paytan, A. (2005). Iron, phytoplankton growth, and the carbon cycle. *Met Ions Biol. Syst.* 43, 153–193. doi: 10.1201/9780824751999.ch7

Stukel, M. R., and Landry, M. R. (2010). Contribution of picophytoplankton to carbon export in the equatorial pacific: a reassessment of food web flux inferences from inverse models. *Limnol. Oceanogr.* 55, 2669–2685. doi: 10.4319/lo.2010.55.6.2669

Sun, J. (2004). *Geometric models for calculating cell biovolume and surface area for marine phytoplankton and its relative conversion biomass. (Master).* Ed. P. R. Qingdao (China: Ocean University of China).

Sun, J. (2011). Marine phytoplankton and biological carbon sink. *Acta Ecol. Sin.* 31 (18), 5372–5378. doi: CNKI:SUN:STXB.0.2011-18-031

Sun, J., and Liu, D. (2003). Geometric models for calculating cell biovolume and surface area for phytoplankton. *J. Plankton Res.* 25 (11), 1331–1346. doi: 10.1093/plankt/fbg096

Sun, J., Liu, D., and Qian, S. (1999). Study on phytoplankton biomass i. phytoplankton measurement biomass from cell volume or plasma volume. *Acta Oceanol Sin.* , 21 (2), 75–85.

Sun, J., Liu, D., and Qian, S. (2002). A quantative research and analysis method for marine phytonplankton: an introduction to utermohl method and its modification (in Chinese with English abstract). *J. Oceanography Huanghai Bohai Seas (黄渤海海洋)* 20, 105–112. doi: 10.3969/j.issn.1671-6647.2002.02.016

Taguchi, S., Ito-Oka, E., Masuyama, K., Kasahara, I., and Goto, K. (1985). Application of organic solvent-soluble membrane filters in the preconcentration and determination of trace elements: spectrophotometric determination of phosphorus as phosphomolybdenum blue. *Talanta* 32 (5), 391–394. doi: 10.1016/0039-9140(85)80104-1

Teng, Y.-C., Primeau, F. W., Moore, J. K., Lomas, M. W., and Martiny, A. C. (2014). Global-scale variations of the ratios of carbon to phosphorus in exported marine organic matter. *Nat. Geosci* 7 (12), 895–898. doi: 10.1038/ngeo2303

Thomalla, S. J., Ogunkoya, A. G., Vichi, M., and Swart, S. (2017). Using optical sensors on gliders to estimate phytoplankton carbon concentrations and chlorophyll-to-Carbon ratios in the southern ocean. *Front. Mar. Sci.* 4. doi: 10.3389/fmars.2017.00034

Uitz, J., Claustre, H., Morel, A., and Hooker, S. B. (2006). Vertical distribution of phytoplankton communities in open ocean: an assessment based on surface chlorophyll. *J. Geophys Res. Oceans* 111 (C8), 1–23. doi: 10.1029/2005JC003207

Verdouw, H., Van Echteld, C. J. A., and Dekkers, E. M. J. (1978). Ammonia determination based on indophenol formation with sodium salicylate. *Water Res.* 12 (6), 399–402. doi: 10.1016/0043-1354(78)90107-0

Wang, S., Ishizaka, J., Hirawake, T., Watanabe, Y., Zhu, Y., Hayashi, M., et al. (2015). Remote estimation of phytoplankton size fractions using the spectral shape of light absorption. *Opt Express* 23 (8), 10301–10318. doi: 10.1364/OE.23.010301

Wang, F., Wei, Y., Zhang, G., Zhang, L., and Sun, J. (2022). Picophytoplankton in the West pacific ocean: a snapshot. *Front. Microbiol.* 13. doi: 10.3389/fmicb.2022.811227

Wei, Y., Liu, H., Zhang, X., Xue, B., Munir, S., and Sun, J. (2017). Physicochemical conditions in affecting the distribution of spring phytoplankton community. *Chin. J. Ocean Limnol* 35 (6), 1342–1361. doi: 10.1007/s00343-017-6190-6

Wei, Y., and Sun, J. (2022). A Large silicon pool in small picophytoplankton. *Front. Microbiol.* 13. doi: 10.3389/fmicb.2022.918120

Weithoff, G., and Beisner, B. E. (2019). Measures and approaches in trait-based phytoplankton community ecology – from freshwater to marine ecosystems. *Front. Mar. Sci.* 6. doi: 10.3389/fmars.2019.00040

Winder, M., and Sommer, U. (2012). Phytoplankton response to a changing climate. *Hydrobiologia* 698, 5–16. doi: 10.1007/s10750-012-1149-2

Wood, E. D., Armstrong, F. A. J., and Richards, F. A. (1967). Determination of nitrate in sea water by cadmium-copper reduction to nitrite. *J. Mar. Biol. Assoc. UK* 47 (1), 23–31. doi: 10.1017/S002531540003352X

Yin, K., Song, X.-X., Liu, S., Kan, J., and Qian, P.-Y. (2008). Is inorganic nutrient enrichment a driving force for the formation of red tides?: a case study of the dinoflagellate scrippsiella trochoidea in an embayment. *Harmful Algae* 8 (1), 54–59. doi: 10.1016/j.hal.2008.08.004

Zhang, M., Cheng, Y., Bao, Y., Zhao, C., Wang, G., Zhang, Y., et al. (2022). Seasonal to decadal spatiotemporal variations of the global ocean carbon sink. *Glob Change Biol.* 28 (5), 1786–1797. doi: 10.1111/gcb.16031

Zhang, D., Wang, C., Liu, Z., Xu, X., Wang, X., and Zhou, Y. (2012). Spatial and temporal variability and size fractionation of chlorophyll a in the tropical and subtropical pacific ocean. *Acta Oceanol Sin.* 31 (3), 120–131. doi: 10.1007/s13131-012-0212-1

Zhang, Q., Zhou, H., and Liu, H. (2012). Interannual variability in the Mindanao eddy and its impact on thermohaline structure pattern. *Acta Oceanol Sin.* 31 (6), 56–65. doi: 10.1007/s13131-012-0247-3

Zhao, Y., Wu, A., Chen, Y., and Hu, D. (2003). The climatic jump of the Western pacific warm pool and its climatic effects. *J. Trop. Meteorol* 9 (1), 9–18. doi: 10.3969/j.issn.1006-8775.2003.01.002

Zinssmeister, C., Soehner, S., Facher, E., Kirsch, M., Meier, K. J. S., and Gottschling, M. (2011). Catch me if you can: the taxonomic identity of scrippsiella trochoidea (F.Stein) A.R.Loebl. (Thoracosphaeraceae, dinophyceae). *Syst. Biodivers.* 9 (2), 145–157. doi: 10.1080/14772000.2011.586071

frontiers | Frontiers in Marine Science

TYPE Original Research
PUBLISHED 11 May 2023
DOI 10.3389/fmars.2023.1118570

EDITED BY
Kieng Soon Hii,
University of Malaya, Malaysia

REVIEWED BY
Teruaki Yoshida,
University Malaysia Sabah, Malaysia
Fatimah Atirah Mohamad,
Universiti Malaysia Sarawak, Malaysia

*CORRESPONDENCE
Clara Manno
clanno@bas.ac.uk

SPECIALTY SECTION
This article was submitted to
Marine Biology,
a section of the journal
Frontiers in Marine Science

RECEIVED 07 December 2022
ACCEPTED 28 March 2023
PUBLISHED 11 May 2023

CITATION
Gardner J, Peck VL, Bakker DCE,
Tarling GA and Manno C (2023)
Contrasting life cycles of Southern Ocean
pteropods alter their vulnerability to
climate change.
Front. Mar. Sci. 10:1118570.
doi: 10.3389/fmars.2023.1118570

Contrasting life cycles of Southern Ocean pteropods alter their vulnerability to climate change

Jessie Gardner[1,2], Victoria L. Peck[1], Dorothee C. E. Bakker[3], Geraint A. Tarling[1] and Clara Manno[1*]

[1]Ecosystems, British Antarctic Survey, Cambridge, United Kingdom, [2]Department of Arctic and Marine Biology, UiT – The Arctic University of Norway, Tromsø, Norway, [3]Centre for Ocean and Atmospheric Sciences, School of Environmental Sciences, University of East Anglia, Norwich, United Kingdom

Pteropods are a key part of biogeochemical cycling and epipelagic food webs in the Southern Ocean. However, shelled pteropods are vulnerable to climate change, due to their aragonite shells being particularly sensitive to ocean acidification. Currently our understanding of pteropod responses to environmental change is hindered by uncertainties surrounding their life cycles and population dynamics. In this study, we describe polar shelled pteropod diversity in the north-eastern Scotia Sea, inferring life history and population structures of the dominant pteropod species, *Limacina rangii* (formerly *Limacina helicina antarctica*) and *Limacina retroversa*. An annual timeseries of *Limacina* shell morphometrics was derived from individuals collected in a moored sediment trap at 400 m depth. We found that *L. rangii* and *L. retroversa* have contrasting life history strategies. *L. rangii* has a continuous spawning and recruitment period from November to March and can overwinter as juveniles and adults. *L. retroversa* has discrete spawning events from November to May, producing non–overlapping cohorts of juveniles and adults. Their development to the adult stage takes between two and five months, upon which they overwinter as adults. Our findings suggest different vulnerabilities of *L. rangii* and *L. retroversa* to a changing ocean. For example, since all life stages of *L. rangii* co-exist, vulnerability of one cohort is not detrimental to the stability of the overall population whereas, if one *L. retroversa* cohort fails to recruit, the entire population is threatened. Changes in pteropod populations could have cascading ramifications to Antarctic ecosystems and carbon cycling.

KEYWORDS

pteropod life history, sediment trap, Scotia Sea, *Limacina helicina antarctica*, marine ecology, Antarctic, population dynamics, zooplankton

1 Introduction

Thecosome (shelled) pteropods are holoplanktonic gastropods with a cosmopolitan distribution throughout the world's oceans. In the Southern Ocean, pteropods can occur in high densities (Bednaršek et al., 2017; Burridge et al., 2017), especially in regions characterized by high phytoplankton concentrations (Hunt et al., 2008; Ward et al., 2008) where they play a key role in the marine ecosystem. Pteropods are efficient omnivorous grazers (Hopkins and Torres, 1989; Bernard and Froneman, 2009), are prey for higher trophic levels (Hunt et al., 2008) and form an important contribution to organic and inorganic carbon cycling (Bednaršek et al., 2012c; Manno et al., 2018).

Despite extensive research into pteropods there remains considerable uncertainty in estimates of their growth rate, longevity, spawning season(s), and seasonal population structures within and between species (i.e. Kobayashi, 1974; Fabry, 1990; Gannefors et al., 2005; Hunt et al., 2008; Bednaršek et al., 2012a; Thibodeau et al., 2020). Such uncertainties arise from differences in sampling protocols (McGowan John and Fraundorf Vernie, 1966; Cermeño et al., 2014) and geographical ranges and scales (Wiens, 1989) between studies. For example, sampling net mesh sizes may select or exclude certain cohorts, biasing the size distribution of sampled populations (Hunt et al., 2008). Furthermore, each pteropod species inhabits specific geographical ecoregions, such that life cycles tend to be species-specific in response to local environmental conditions. Certain life stages, such as the high growth veliger phase (the immature pteropod stages that have yet to develop wings), which demand high energy budgets, often coincide with local phytoplankton blooms (Maas et al., 2011). Acclimation and adaptation of pteropods to localized conditions therefore leads to inter- and intra-species differences in environmental tolerances (Bednaršek et al., 2017). Variation in life history may also occur within taxonomic sub-units, for example, *Limacina helicina* comprises of several morphotypes (not classed as separate species) in the Arctic Ocean (*acuta*, *helicina*, and *pacifica*). Similarly, several *L. retroversa* formae are found in the Arctic (*balea and retroversa*) and the Southern Ocean (*australis*) (Hunt et al., 2010; Jennings et al., 2010).

Shell morphometric analyses are an effective tool to assess age structure and spawning events of pteropods (Wang et al., 2017) based on the assumption that the rate of shell extension is linear throughout Limacinidae life cycles (Hsiao, 1939; Lalli and Wells, 1978; Lalli and Gilmer, 1989). Thibodeau et al. (2020) and Weldrick et al. (2021) estimated *L. rangii* phenology using shell morphometrics of specimens collected from sediment traps deployed along the Western Antarctic Peninsula and the Indian sector of the Southern Ocean, respectively. While sediment traps primarily record the vertical flux of passive particulate matter from the upper ocean (Turner, 2015), Makabe et al. (2016) showed that the abundance of live pteropods entering the sediment trap (active "swimmers", likely in search of prey) correlates well with their relative abundance in corresponding net samples. Identifying swimmers within sediment trap samples can therefore be considered representative of the seasonal population structure. Moored sediment traps allow year-round sampling at a fixed geographical location at user-defined temporal intervals. Sediment trap sampling is particularly valuable in remote and difficult to access areas, such as in the Southern Ocean. Furthermore, sediment traps do not select for specific size cohorts, making sediment traps an effective tool to estimate pteropod life history and population dynamics (Makabe et al., 2016).

In this study, we estimate the abundance and seasonal variability of thecosome pteropod species collected within a sediment trap moored for one year downstream of South Georgia in the northeast region of the Scotia Sea. We investigate life history and population structures (i.e., spawning, growth rates, cohort and life stage dynamics and longevity) by assessing the shell morphometrics of the two dominant pteropod species *L. rangii* and *L. retroversa australis* (hereafter *L. retroversa*) through December 2014 to November 2015. Characterizing local life history and population structures of pteropods is critical to forecast potential cascading impacts on biogeochemical cycling and epipelagic food webs in the face of anthropogenic climate change. The Scotia Sea is undergoing some of the fastest rates of climatic change in the Southern Ocean (Henson et al., 2017). Due to their aragonite shells being particularly sensitive to ocean acidification (Manno et al., 2017), and the rapidity of change in this region, there is an urgency to better understanding and monitoring the ecology of this sentinel species.

2 Materials and methods

2.1 Sample collection

A McLane PARFLUX sediment trap (0.5 m^2 capture area, McLane Labs, Falmouth, MA, USA) was deployed at 400 m water depth (sea floor depth of 3787 m) on a bottom-tethered mooring line for 350 days (12 December 2014-28 November 2015) at the sustained observation location P3 in the north eastern Scotia Sea (52°48.7" S, 40°06.7" W) (Figure 1). The site P3 is bounded by the Polar Front to the north and the Southern Antarctic Circumpolar Current Front to the south and east and is situated in an area of high biological productivity, with extensive and prolonged phytoplankton blooms (Borrione and Schlitzer, 2013). In December 2014 the chlorophyll-*a* max was 2.7 $\mu g\ l^{-1}$ at ~30 m (Liszka et al., 2019).

The sediment trap was equipped with 21 x 500 ml collection cups filled with 4% formaldehyde buffered with excess sodium tetraborate (borax). These preservatives poison swimmers swiftly, minimising physical damage to the sample caused by opportunistic scavengers, arresting biological degradation and stopping pteropod shell dissolution (Goto et al., 2016). Cups rotated on a 14-17 (spring and summer) and 30-31 (autumn and winter) day schedule with 15 cups being utilised within the sampling period (Supplementary Material 1).

Sensors attached to the mooring line measured temperature (°C, SAMI) and pH (total scale, SAMI) were measured at 200 m depth and oxygen (µM, optode within the Aquadopp current meter) at

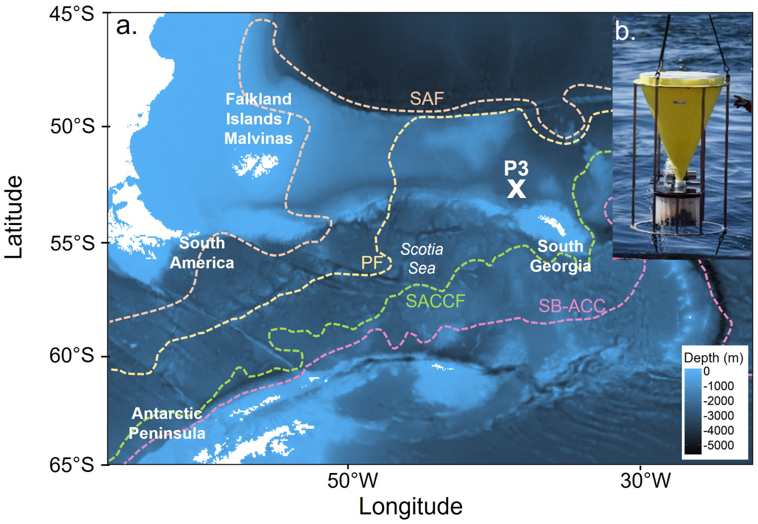

FIGURE 1
(A). The location of the sediment trap mooring (P3: 52°48.7" S, 40°06.7" W) sampling site and **(B)**. An image of the sediment trap as it was recovered in November 2015. The blue shading indicates the seafloor depth, while the white represents the land. Dashed lines indicate the position of the Sub-Antarctic Front (SAF), Polar Front (PF), Southern Antarctic Circumpolar Current Front (SACCF) and the Southern Boundary of the Antarctic Circumpolar Current (SB-ACC). Positions of the SAF, PF and SB-ACC were taken from Orsi et al. (1995), while the position of the SACCF was from Thorpe et al. (2002).

400 m depth. Chlorophyll-*a* data (mg m^{-3}) from Aqua MODIS with a 4 km resolution, (NASA Ocean Biology) from a 12 x 12 km box centered on P3. A current meter 1 m underneath the sediment trap recorded mean current speeds of 0.05 (range: 0-0.22) cm/s (SeaGuard TD262a). Current speed measurements were taken adjacent to the sediment trap every 15 minutes and averaged over a 1 minute intervals. Hydrodynamic bias was negligible since current speeds over the sampling period were below the level where trapping efficiency is considered to decrease (Supplementary Material 2), and where considerable lateral advection might occur (10-12 cm/s) (Baker et al., 1988; Whitehouse et al., 2012).

2.2 Pteropod identification

The sediment trap samples were analysed in their entirety to avoid splitting biases and to maximize morphometric information (Gerhardt et al., 2000; Chiarini et al., 2013). Specimens were identified, counted and photographed dorsoventrally for shell morphometric characteristics under a dissection microscope (Olympus SZX16 fitted with a Canon EOS 60D DSLR camera).

Identification of unbroken specimens was to species and formae level as described by Van der Spoel and Dadon (1999) and Hunt et al. (2008). Pteropods generally had shells fully intact, however, some shell fragments were found. Shell fragments were only counted as an individual if a protoconch was present. Damaged shells were excluded from morphometric analyses. Unbroken pteropod shells were classed into three categories (Figures 2E–H) to reflect their condition, being 1. Well preserved, retracted soft body with a transparent shell, 2. Signs of degradation of the relaxed soft body with the shell being uniformly frosted or 3. The soft body missing but the shell intact and completely transparent. All pteropods fitting category 1 were assumed to have been alive upon entering the trap (swimmers) and representative of the living cohort present within the area at that time. Those in category 2 were most likely dead when entering the trap (passive sinkers) since uniform shell dissolution is an indicator of post-mortem decay (Oakes et al., 2019). Pteropods in category 3 are most likely to have been predated, i.e. the shells entered the trap empty after the soft body was removed and there was no internal dissolution by decaying tissue. Gymnosomes are specialized predators on thecosome pteropods, grasping the shell and inserting their modified mouth parts inside the aperture to extract the soft body within (Lalli and Gilmer, 1989). Damaged apertures on many of the category 3 shells is consistent with gymnosomes discarding the shell after predation.

2.3 Assessment of shell morphometrics

Shell diameter, shell width (otherwise called the line of aperture or aperture length), spire height and the number of whorls of *L. rangii, L. retroversa* and *Limacina* spp were measured using ImageJ software (Schindelin et al., 2012) (Figure 2). A Principal Component Analysis (PCA; run in R using prcomp{base}) determined that any of the shell morphometrics are adequate for representing pteropod shell size throughout the sampling period. Hereafter, shell width for *L. rangii* and *Limacina* veligers and spire height for *L. retroversa* will be used since these are common measures in the literature. Full details of the shell morphometric assessment are given in Supplementary Material 3.

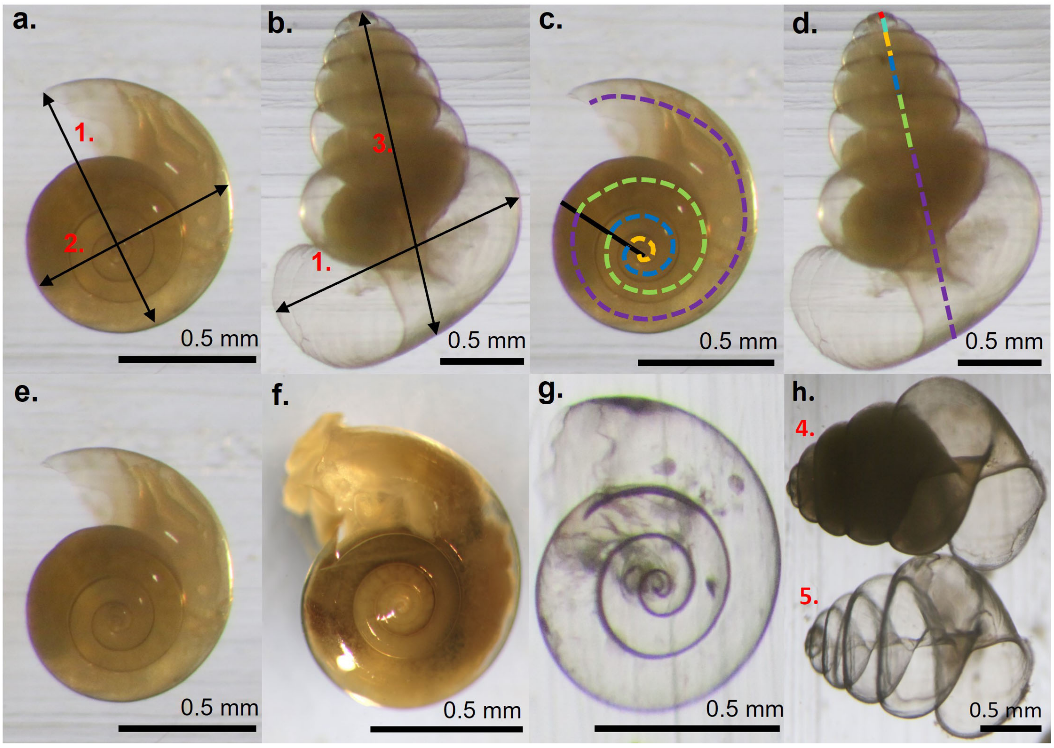

FIGURE 2
Shell morphometrics used to define pteropod cohorts of **(A)** *L. rangii* and **(B)**, *L. retroversa* where 1. is the shell width (otherwise known as the line of aperture), 2. the shell diameter and 3. the spire height (for *L. retroversa*). Insets **(C, D)**. indicate how the number of whorls was measured on *L. rangii* and *L. retroversa*, respectively, where each colour corresponds to one whorl. **(E–H)** indicate pteropod shell conditions being category 1/swimmers **(E)**: *L. rangii*, **(H)**4: *L. retroversa*), category 2/passive sinkers **(F)**: *L. rangii*) or category 3/predated **(G)**: *L. rangii*, **(H)**5: *L. retroversa*).

2.4 Cohort and group identification

L. rangii with a shell width of <0.3 mm were classed as veligers, 0.3 - 4 mm as juveniles and >4 mm as adults. Similarly, *L. retroversa* individuals with a spire height of <0.3 mm, 0.3 - 1 mm and >1 mm were classified as veligers, juveniles and adults, respectively (Lalli and Wells, 1978; Lalli and Gilmer, 1989). Veligers have only a single shell whorl and cannot be distinguished to species level and are therefore classed as *Limacina* spp.

Mixture models of shell morphometrics were fitted using normal, lognormal, gamma and Weibull distributions to one, two and three components extracted based on peaks observed on the size-frequency histograms using the R package 'mixdist' (MacDonald and Juan, 2012). The best-fitting distribution type and number of components were selected based on a combination of chi-square goodness of fit and visual inspection of histograms.

2.5 Shell growth, spawning behaviour and longevity

Groups of similarly sized specimens with the sample population were identified by the mixture analysis and tracked throughout the year, from the time of recruitment to when they no longer appear within the population (due to die-off or migration out of the sample area). It was assumed these subgroups represented cohorts. Tracking cohorts across sediment trap samples enables estimation of the mean increase in shell width per day (the growth rate) for each cohort. The difference in mean shell width between the two dates of observation was divided by the intervening time. This cohort definition assumes sampling was representative of a static population and that growth was continuous and linear between each sample interval.

We assumed modal peaks in the mixdist analysis below <0.3 mm signify a hatching event of *Limacina* individuals. Continuous spawning can be detected by the persistent presence of this smaller size class. Previous studies on *Limacina* species have indicated that hatching occurs between 1- 10 days after spawning (Paranjape, 1968; Kobayashi, 1974; Lalli and Wells, 1978; Gannefors et al., 2005; Howes et al., 2014; Akiha et al., 2017) with rapid growth and development of parapodia (wings) within 30 days (Van der Spoel and Dadon, 1999). Therefore, spawning events can be assumed to have occurred within 10 days of the capture of veligers in the samples.

Longevity was estimated from the date of a cohort's recruitment until its disappearance from size-frequency histograms assuming a static population that did not migrate in or out of the sampling region. Since some life stages were not observed with the sediment trap (e.g. adult *L. rangii*) our study has limitations. To anticipate longevity of this species we extrapolated the growth rates determined in younger life stages of the cohort to estimate the amount of time it would take to reach the maximum adult sizes recorded within the literature.

3 Results

3.1 Pteropod abundance and seasonal trends

Six species of thecosome pteropod were identified within the sediment trap: *Limacina rangii*, formerly *L. helicina antarctica* (LH), *Limacina retroversa* f. *australis* (LR), *Clio pyramidata* f. *sulcata*, and *Clio pyramidata* f. *excise*. Over the entire sampling period, four *Clio piatkowski* and three *Peraclis* cf. *valdiviae* were also collected (Supplementary Material 4).

3.1.1 *Limacina rangii*

The total abundance of *L. rangii* per month peaked in austral summer, January (6696 ind.), February (5258 ind.) and March (5466 ind.) and did not exceed 201 individuals (November) in the remaining months. No adult *L. rangii* were collected during the sampling period. The majority of *L. rangii* collected each month were swimmers, with the highest proportion of swimmers in February (94% of February LH abundance, 4921 ind.) and the lowest in April (56% of April LH abundance, 98 ind.) (Figures 3A; 4A). Passively sinking *L. rangii* were most abundant in January (718 ind.), and proportionally most abundant in April (37% of April LH abundance, 64 ind.) (Figures 3B; Supplementary Material 5). The highest abundance of predated *L. rangii* was collected in January (1%, 64 ind.) while the highest proportion of predated individuals was collected in September (8% of September LH abundance, 4 ind.) and April (7% April LH abundance, 12 ind.) (Figure 3C).

3.1.2 *Limacina retroversa*

L. rangii were more abundant than *L. retroversa* between September and April (Total monthly abundance range for LH: 50-6,696 ind. and LR: 32-44 ind.), however, *L. retroversa* were more abundant than *L. rangii* between May and August (Total monthly abundance range for LR: 80-188 ind. and LH: 63-90 ind.). Both adult and juvenile *L. retroversa* were identified, with adults making up the majority of specimens collected from June to October (52-90% of monthly LR abundance, 16-166 ind.), and juveniles from November to May (56-100% of monthly LR abundance, 26-196 ind.). Most *L. retroversa* collected each month were swimmers, with the highest proportion in June (92% of June LR abundance, 153 ind.) and the lowest in December (54% of December LR abundance, 14 ind.) (Figures 3D, 4B; Supplementary Material 5). The greatest proportion of passively sinking *L. retroversa* was collected in

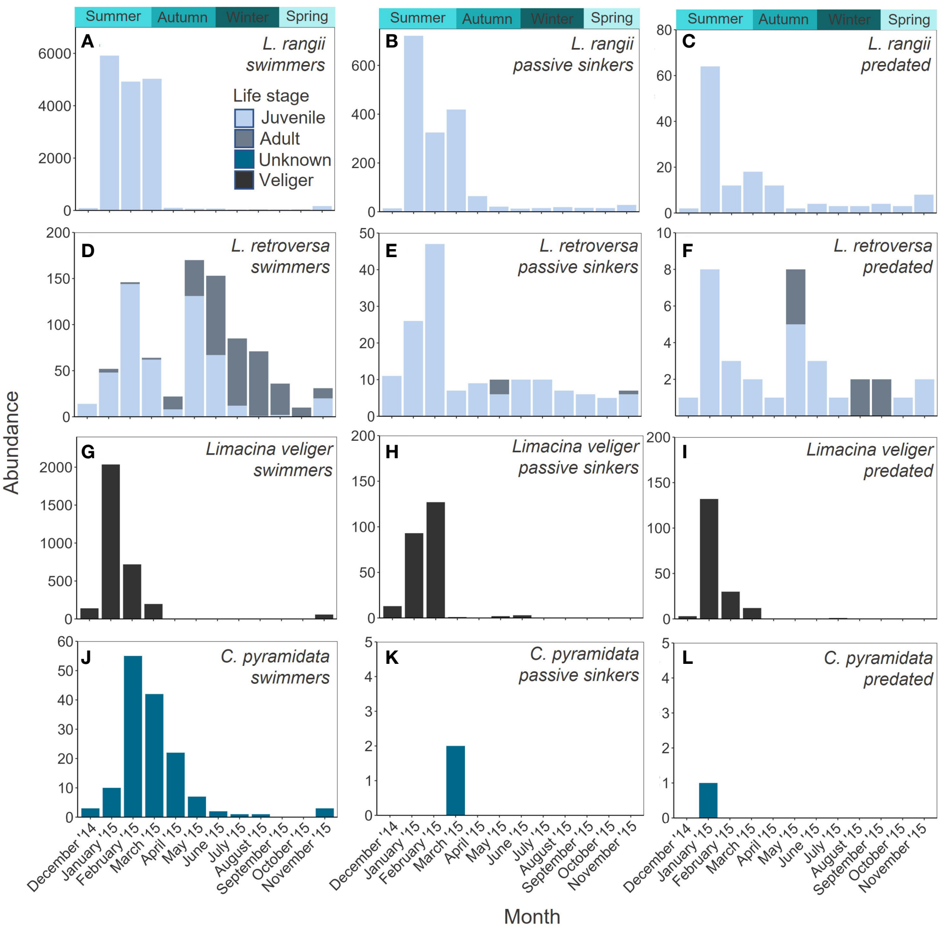

FIGURE 3
Monthly abundance of *L. rangii* **(A–C)**, *L. retroversa* **(D–F)**, *Limacina* spp **(G–I)** and *C. pyramidata* **(J–L)** collected in a sediment trap at site P3 (Scotia Sea, Southern Ocean) at 400 m depth between December 2014 and November 2015.

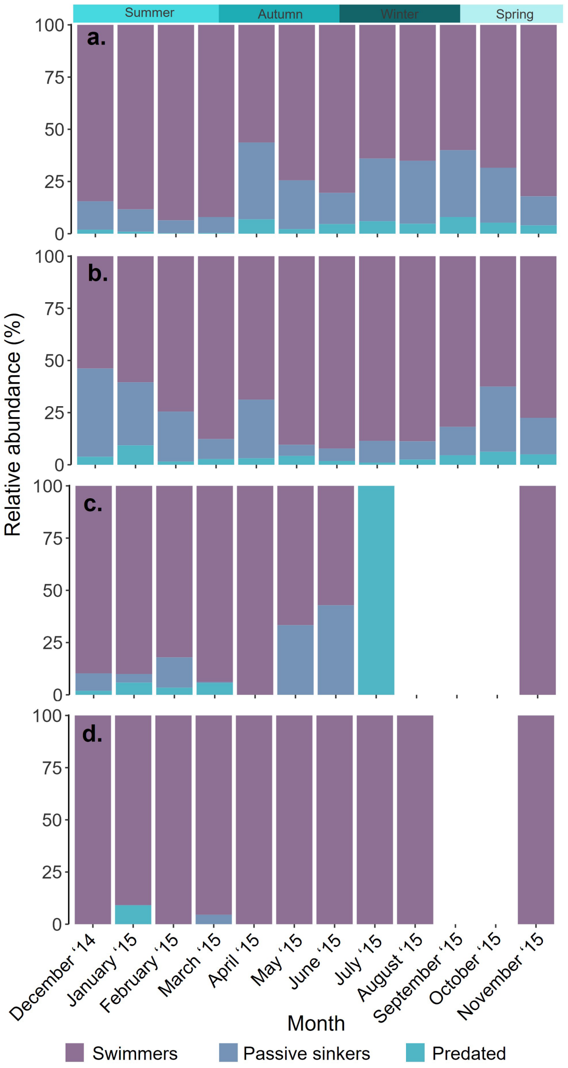

FIGURE 4
Proportional abundance (%) of the number of swimming, passively sinking and predated **(A)**. *Limacina rangii*, **(B)**. *Limacina retroversa*, **(C)**. *Limacina* veliger and **(D)**. *Clio pyramidata* each month between December 2014 and November 2015 in a sediment trap deployed at 400 m depth at site P3 (Scotia Sea, Southern Ocean).

December (42% of December LR abundance, 11 ind.) and the lowest proportion in May (5% of May LR abundance, 10 ind.) (Figure 3E). The highest abundance of predated *L. retroversa* was collected in January (9% of January LR abundance, 8 ind.) and lowest in July (1% of July LR abundance, 1 ind.) (Figure 3F).

3.1.3 *Limacina* veligers

Limacina veligers were only collected between November and July, with total abundance peaking in January (2260 ind.), February (877 ind.) and March (210 ind.) (Figure 3C). The majority of *Limacina* veligers collected were swimmers between November and June (57- 100% of veliger monthly abundance) (Figures 3G, 4C; Supplementary Material 5). Passively sinking *Limacina* veligers were most abundant in February (14% of veliger February abundance, 127 ind.) and proportionally most abundant in June (43% of veliger June abundance, 3 ind.) (Figure 3H). No passively sinking *Limacina* veligers were collected in April or July-November. The highest abundance of predated *Limacina* veligers was collected in January (132 ind.) accounting for 6% of total abundance in January (Figure 3I).

3.1.4 *Clio pyramidata*

The total abundance of *C. pyramidata* peaked in February (55 ind.), March (46 ind.) and April (22 ind.). Almost all *C. pyramidata* collected were swimmers (Figures 3J, 4D; Supplementary Material 5), with two passively sinking individuals being collected in March and one predated individual being collected in January (Figures 3K, L).

3.2 *Limacina rangii* population structure and growth rates

The recruitment of *L. rangii* veligers into the juvenile life stage and the similarly-sized subgroups LH1 - 5 can be deduced from the mean shell sizes identified by the Mixture analysis (Figures 5.1, 6A; Supplementary Materials 6-7). However, the entire life cycle of *L. rangii* was not captured by the Mixture analysis since no *L. rangii* adults were collected. We do not consider LH1 - LH5 to represent discrete cohorts given their wide and overlapping distributions (Figures 5.1, 6A). LH1 represents young, newly recruited juveniles with a mean shell width range of 0.34-0.37 mm and were collected between December and March 2014. LH2 is comprised of larger, older juveniles than LH1 (mean shell width range 0.47-1.01 mm) and was collected between December and April. LH3 (mean shell width 0.5 mm) and LH4 (mean shell width 0.38 mm) were collected in May and June, respectively. Finally, LH5 was collected between June and November (monthly mean shell width 0.52-1.79 mm) and represents overwintering juveniles.

The prolonged presence of LH1 and LH4, which contain small juveniles (mean shell width 0.34 and 0.38 mm), as well as the presence of veligers between December and March, indicates protracted spawning by *L. rangii*. Growth rates can only be estimated for LH3 and LH4, as they were present after the last spawning event in March. Since it is unclear when LH1, LH2 or LH5 were spawned, growth rates could not be calculated for these subgroups. If LH3 individuals were spawned in February or March, the shell growth rate of LH3 would be 0.005-0.008 mm d^{-1} to reach a shell width 0.50 mm by May (Figure 6B). The growth rate of LH4 would be 0.003-0.004 mm d^{-1} to reach a shell width of 0.38 mm by June. These growth rate calculations assume that *L. rangii* veligers emerged from the egg-sac 10 days after spawning with a shell size of 0.07 mm.

3.3 *Limacina retroversa* population structure and growth rates

Four non-overlapping cohorts of *L. retroversa* juveniles and adults were identified, spawning in December (cohort LR1), February (cohort LR2), May (cohort LR3) and November (cohort LR4) (Figures 5.2, 6C). Each cohort can be observed to increase in size to achieve adulthood (>1 mm) over two to five months with rates of

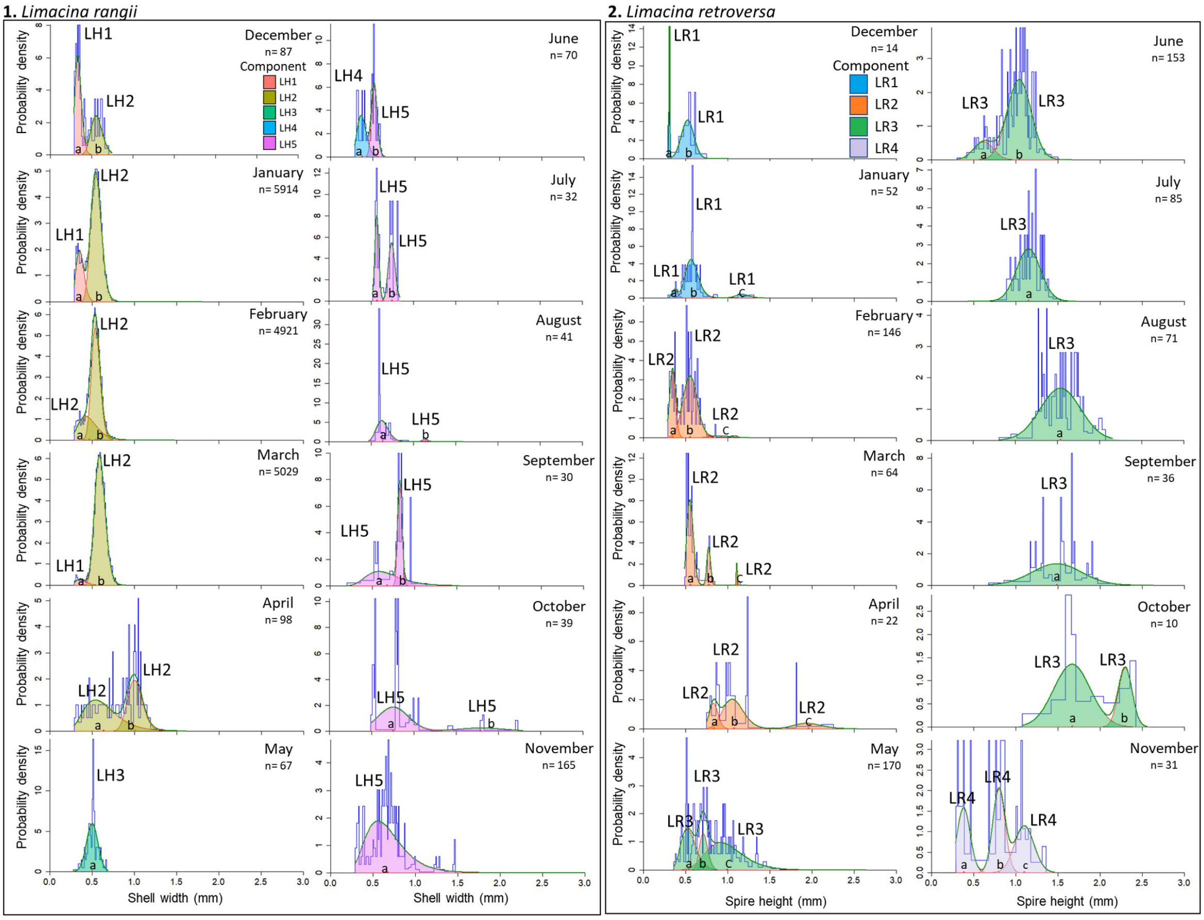

FIGURE 5
Components identified by the mixture analysis on shell width data of 1. *L. rangii* (L.H.) swimmers and 2. *L. retroversa* (L.R.) swimmers for each month of a year-long sampling period. Mixture analysis was performed by the R package *Mixdist*. Tracking components through the course of the year provides an estimate of growth rate. Blue lines represent the original length-frequency distribution representing the shell heights/widths, red lines are the individual fitted distributions (a-c) and green lines are the sum of fitted distributions.

shell spire height increase averaging LR1: 0.014 mm d^{-1}, LR2: 0.018 mm d^{-1}, LR3: 0.010 mm d^{-1} and LR4: 0.24 mm d^{-1} (Figure 6D). Adult individuals were not collected in samples containing veligers of the subsequent cohort, suggesting *L. retroversa* have a longevity of one to seven months.

The veligers recruited into cohort LR1 in December (mean spire height 0.31 mm) likely hatched in November, making the growth rate 0.006 mm d^{-1}. Veligers recruited into LR2 in February (mean spire height 0.35 mm) hatched in January and grew 0.007 mm d^{-1}. Because juvenile LR3 were first recorded in May (mean spire height of 0.54 mm), the growth rate of LR3 veligers was 0.005 mm d^{-1} or 0.006 mm d^{-1} assuming they hatched in February or March, respectively. LR4 individuals hatched in November, with veligers growing at 0.016 mm d^{-1} and becoming juveniles in the same month (mean shell size 0.39 mm).

3.3.1 Environmental data

Mean temperature ranged from 0.73°C (± 0.03 S.E.) in October to 1.15°C (± 0.01 S.E.) in May with the greatest intra-month variability occurring in November (1.03°C) (± 0.03 S.E.) (Figure 7). pH reached a maximum of 8.13 (± 0.00 S.E.) in November and a minimum of 7.95 in December (± 0.01 S.E.) with the greatest variation in December (7.95 ± 0.01 S.E.). The highest oxygen concentration occurred in November and 200.1 µM (± 0.02 S.E.) while the lowest mean values occurred in December and January (191.3 µM (± 0.02 S.E.) and 192.6 µM (± 0.01 S.E.), respectively). The greatest mean chlorophyll-*a* concentrations were in December 2014 (2.07 mg m^{-3} ± 0.02 S.E.), November 2015 (2.03 mg m^{-3} ± 0.03 S.E.) and February 2015 (2.32 mg m^{-3} ± 0.05 S.E.). Cloud cover was too dense from May to July to allow satellite chlorophyll-*a* measurements. An initial bloom started to form in October (1.32 mg m^{-3} ± 0.02 S.E.), which expanded and intensified around P3 through November and December (Supplementary Material 8). The minimum chlorophyll-*a* concentration was recorded in August (0.01 mg m^{-3} ± 0.00 S.E.).

4 Discussion

4.1 Pteropod diversity

True polar species *L. rangii* was the most abundant pteropod collected at P3, consistent with similar observations made south of

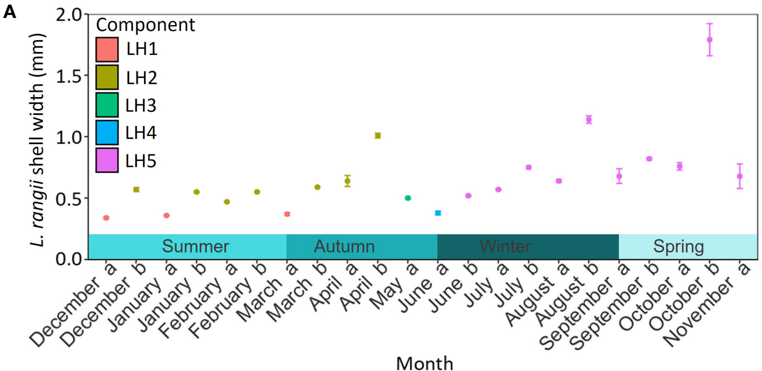

B

Group	Month Spawned	Number of days growth	Mean shell width (mm)	Shell width minus embryonic shell growth (mm)	Growth rate (mm/day)
LH3	March	52	0.50	0.43	0.008
LH3	February	80	0.50	0.43	0.005
LH4	March	83	0.38	0.31	0.004
LH4	February	111	0.38	0.31	0.003

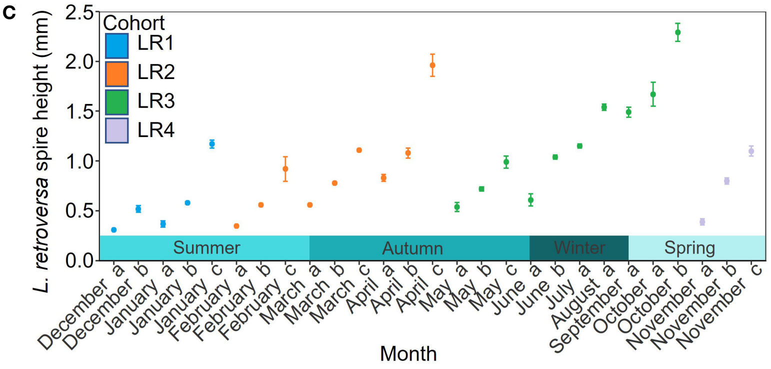

D

Cohort	Month recruited	Number of days growth	Minimum cohort spire height (mm)	Maximum cohort spire height (mm)	Overall spire growth (mm)	Growth rate (mm/day)
LR1	December	62	0.31	1.17	0.86	0.014
LR2	February	89	0.35	1.96	1.61	0.018
LR3	May	184	0.54	2.29	1.75	0.010
LR4	November	30	0.39	1.1	0.71	0.024

FIGURE 6

The temporal sequence of mean shell width from the mixture analysis of **(A)** *Limacina rangii* (LH) with standard error of each component. **(B)** Growth rates of *L. rangii* for LH3 and LH4. Two calculations were made for each component to capture uncertainty on whether spawning was in February or March. **(C)** The temporal sequence of mean spire height of L. retroversa australis (LR) with standard error of each component computed by the mixture analysis (a-c). **(D)**. Growth rates of LR are based on tracking each of the four components over time. Individuals were collected in a sediment trap deployed at P3 (Scotia Sea, Southern Ocean) at 400 m depth between December 2014 and November 2015.

the Polar Front (Dadon, 1990; Ward et al., 2004; Hunt et al., 2008; Bernard and Froneman, 2009; Akiha et al., 2017). Subpolar species *L. retroversa* was the second most abundant species, as it is typically most abundant north of the Polar Front (Chen and Bé, 1964; Van der Spoel, 1967; Van der Spoel, 1976).

C. pyramidata forma *sulcata* is commonly captured in small numbers alongside *Limacina* species throughout the Southern Ocean (Hunt et al., 2008). No records could be found of the thecosome pteropods *Clio piatkowskii*, *Peraclis* cf. *valdiviae* and *C. pyramidata* f. *excise* in the Scotia Sea. *C. piatkowskii* have been documented in the Weddell Sea (Van der Spoel et al., 1992; Van der Spoel and Dadon, 1999), Lazarev Sea (Flores et al., 2011) and near Bouvetøya (Hunt et al., 2008) at 300-1000 m water depth. *Peraclis* cf. *valdiviae* has previously been recorded south of Tasmania, within the Sub-Antarctic Zone down to 150 m water depth (Van der Spoel and Dadon, 1999; Howard et al., 2011; Roberts et al., 2011). *C. pyramidata* f. *excise* has been recorded in the Lazarev Sea (MSIP, 2017). The high diversity and abundance of pteropods collected in this study highlights that *s*ediment traps are effective at long-term, remote sampling of pteropods in regions that are difficult to access.

4.2 Environmental conditions

The chlorophyll-*a* observations indicate that high primary productivity persisted north of South Georgia from October until February, peaking in November, as is typical for this region (Korb

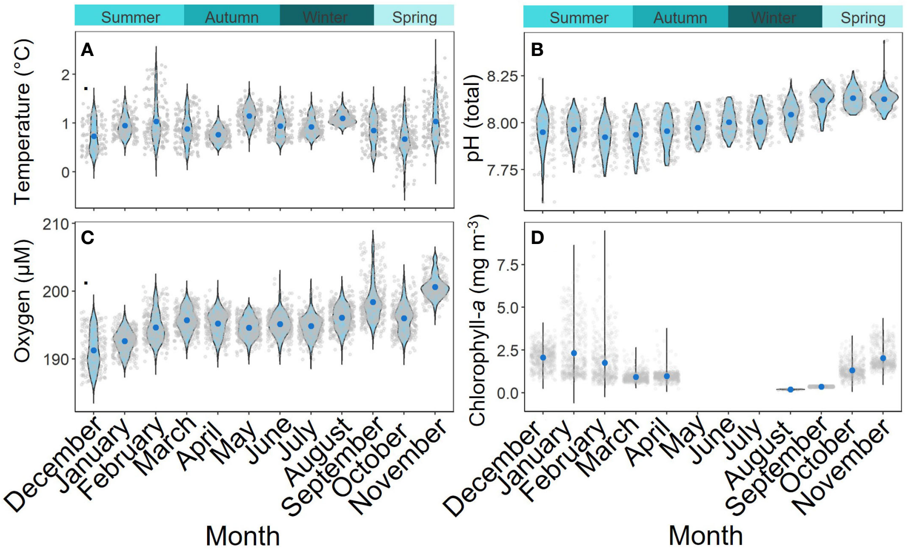

FIGURE 7
Monthly environmental conditions associated with the sediment trap deployed at P3 (Scotia Sea; Southern Ocean) between December 2014-November 2015. Temperature **(A)** and pH **(B)** were measured *in-situ* at 200 m. Oxygen **(C)** (µM) was measured *in-situ* at 400 m. Chlorophyll-*a* **(D)** measurements were taken from Aqua MODIS at 4 km resolution satellite data (NASA; Ocean Biology). Grey dots are individual data points, Blue dots are the means and the thickness of the violin plot represents data probability density.

and Whitehouse, 2004; Korb et al., 2005; Atkinson et al., 2012). The high oxygen concentrations observed from September to November likely reflects deep wind-driven mixing entraining surface water down to 200 m depth. The lowest mean oxygen concentrations between December and January likely reflect a reduction in surface mixing, and increased respiration and remineralisation following the bloom.

4.3 The life cycle of *Limacina rangii* in the Scotia Sea

Five similarly-sized subgroups of juvenile *L. rangii* were identified (LH1 - 5) as being recruited into the population between November 2014 and December 2015. *L. rangii* is inferred to have continuously spawned between November and March and with concurrent recruitment of juveniles into LH1 - 2. The spawning and early growth period of LH1 - 2 was coincident with the warmest temperatures and peak of the of the South Georgia bloom, providing sufficient food for these energetically expensive life stages (Seibel et al., 2012; Bednaršek et al., 2016; Manno et al., 2017).

The absolute abundance of *L. rangii* juveniles collected in the sediment trap dropped by 97% at the end of the productive period (April). This dramatic decline in abundance is a phenomenon observed by numerous studies (Gilmer and Harbison, 1986; Seibel and Dierssen, 2003; Maas et al., 2011) and has been attributed to: 1. a fatal environmental perturbation, 2. a die-off event, 3. a change in current speed or direction transporting the population away or 4. active migration (Gilmer and Harbison, 1986; Collier et al., 2000; Accornero et al., 2003; Seibel and Dierssen, 2003; Maas et al., 2011). Current activity did not change, suggesting that the population was not physically transported away, ruling out scenario 3. Swimmers remained the dominant classification of specimens collected in the trap, suggesting that this was not a mass mortality event affecting the entire population. However, the relative abundance of type 2 (passive, dead) specimens of *L. rangii* did increase somewhat in April, as did the number of predated shells. There are no notable anomalies within the environmental parameters beyond the natural, seasonal decline in chlorophyll-*a* at the end of the bloom. It would seem that the decline in the population is related closely to the cessation of the phytoplankton bloom. As food resources became scarce the incidence of natural and predated deaths increased. It may be possible that the population migrated laterally, possibly following food availability elsewhere, however we have no evidence to support or dispute this. Another possibility is that once juveniles had matured enough to perform their diurnal migrations, the end of the bloom meant that there was no longer any incentive to migrate into the shallow waters. That is, once the phytoplankton bloom had ceased and the remaining organic matter sank through the water column, there was no reason for *L. rangii* to migrate vertically above the depth of the sediment trap. *L. helicina* are known to enter a diapause at depth during the winter in the Arctic when food is scarce (Gannefors et al., 2005). Our findings here suggest that *L. rangii* may well do the same outside of the bloom season in the Scotia Sea (Figures 3, 7; Supplementary Material 2, respectively). The specimens of *L. rangii* collected during the winter months (LH5) were all juveniles. This overwintering population appears to have adopted two different growth patterns, with some entering diapause (a state of suspended growth) and others continuing to grow. Such contrasting growth patterns likely reflect the patchiness of food sources during the winter, meaning not all juveniles had the available resources to invest into growth (Meyer et al., 2017). As Akiha et al. (2017), we collected no adult *L. rangii* in the sediment trap. The absence of adults may reflect the tendency of more mature specimens to dwell below the depth of the sediment trap by day, reducing the potential incidence of adult *L. rangii* entering the trap passively (dead). The absence of adult *L. rangii* entering the trap as swimmers may reflect a survival instinct and ability to swim out of danger (Adhikari et al., 2016; Gilmer and Harbinson, 1986).

The current study found that *L. rangii* has a protracted spawning period, ending at the end of the productive period in March. After March individuals continued growing and some overwintered as juveniles. Hunt et al. (2008) and Van der Spoel (1967) postulated that *L. rangii* could spawn twice in a year, with the first occurring during the summer, and the second in the autumn, where these late comers enter a diapause and overwinter without growth. The autumnal spawning theory was based on observations of *L. helicina helicina* in the Arctic (Kobayashi, 1974; Gannefors et al., 2005) and limited winter net samples in the Southern Ocean (Hunt et al., 2008). Bednaršek et al. (2012b) inferred from net samples in the Scotia Sea that the spawning of *L. rangii* was a discrete event, occurring predominantly during the summer. While the timing of the discrete spawning event identified by Bednaršek et al. (2012b) corresponds to the peak of spawning at P3 in the current study, the continuous recruitment of small *L. rangii* juveniles evidence in the sediment trap at P3 indicates that spawning occurred over a much longer period (summer to early autumn). It is likely that the difference in spawning period estimates arises from differences in the scale of the respective studies. Bednaršek et al. (2012b) considered spawning across the entire Scotia Seaand did not have the time series of data afforded by the sediment trap.

The rate of growth for veligers to reach the small juvenile size-bins (LH3 and LH4) was calculated as between 0.005 and 0.008 mm d^{-1} (LH3) or 0.003 and 0.004 mm d^{-1} (LH4) in the current study, depending on whether spawning occurred in February or March. Bednaršek et al. (2012b) also calculated the growth rate of *L. rangii* using a cohort analysis from plankton net samples in the Scotia Sea between October and March (1996-2005). *L. rangii* in the current study are mainly comparable to their group “G2”, which had a growth rate of 0.007 mm d^{-1} (after conversion of shell diameter to shell width (Supplementary Material 3). The growth rates estimated for LH3 (0.005- 0.008 mm d^{-1}) largely in agreement Bednaršek et al. (2012b), however, LH4 growth rates are about half (0.003 - 0.004 mm d^{-1}) those estimated by Bednaršek et al. (2012b). The lower growth rates for LH4 may reflect the scarcity of food towards the end of the bloom for this subgroup that spawned later (Figure 7; Supplementary Material 8). Since we have established that growth rates are not continuous or linear, rather dependent on life stage and environmental conditions we were unable to calculate the amount of time to reach maturity or longevity for *L. rangii.*

4.4 The life cycle of *Limacina retroversa* in the Scotia Sea

Four generations of *L. retroversa* were collected that included all life stages and no overlapping of cohorts. These distinct cohorts were identified as juveniles and adults between December and January (LR1), February and April (LR2), May and October (LR3) and in November (LR4). Individuals that reach adulthood in late summer/autumn appear to stay in the upper 400 m of the water column and overwinter as adults until the spring, when they spawn. The veligers then hatch and undergo a rapid period of growth to reach adulthood in the summer and then spawn themselves. Veligers that hatch in late summer reach adulthood in the autumn and overwinter before spawning in the spring.

L. retroversa adults in autumn (LR2) and winter (LR3) were larger (mean spire height: 2.19 - 2.42 mm) in comparison to the spring (LR4) and summer (LR1) cohorts (mean spire height: 1.15 - 1.19 mm). This growth strategy was also observed in *L. retroversa* of the Argentine Sea, where the mean spire height of wintertime cohorts measured 1.99 - 3.20 mm while the summer mean spire heights measured 1.25 - 1.80 mm (Dadon and de Cidre, 1992). In many gastropods, fecundity is directly related to gonad volume, which increases with shell size (Ghiselin, 1969; Dillon, 2000). Therefore, investing in shell growth and delaying spawning until conditions are favourable for early life stages increases reproductive output and veliger survival rate (Lalli and Wells, 1978; Lalli and Gilmer, 1989).

The greatest rate of shell growth in *L. retroversa* (LR4: 0.024 mm d^{-1}) occurred during the spring when juveniles, fueled by the parallel phytoplankton bloom, reached maturity. This same cohort spawned during the summer, when food supply remained sufficient to support another generation of veligers (LR1). Dadon and de Cidre (1992) also observed that growth rates were highest during springtime in the Argentine Sea, although, growth rates were lower than in the Scotia Sea, at 0.008 - 0.012 mm d^{-1} (Dadon and de Cidre, 1992). However, the autumn to winter *L. retroversa* growth rates in the Scotia Sea were similar (LR3: 0.010 mm d^{-1}) to those in the Argentine Sea (0.009 - 0.015 mm d^{-1}). Higher growth rates in the Scotia Sea are likely due to the abundant food supplied by the phytoplankton bloom north of South Georgia being more prolonged and stable between spring and autumn in comparison to the small, discrete blooms of the Argentine Sea (Dadon, 1990; Dadon and de Cidre, 1992; Lutz et al., 2009) (Figure 7; Supplementary Material 8). The longer productive season in the Scotia Sea means spawning and veliger growth of *L. retroversa* occur between November and March, supporting a four-generation per year life cycle. In comparison, *L. retroversa* in the Argentine Sea have discrete spawning events in February and September, in parallel to discrete phytoplankton bloom events, supporting a two-generation a year life cycle (Dadon, 1990; Dadon and de Cidre, 1992). During the winter, *L. retroversa* in both the Scotia Sea and Argentine Sea continue to grow, but at much lower rates than in the rest of the year due to reduced and poorer quality food supplies and/or reliance on lipid reserves (Dadon and de Cidre, 1992; Lischka and Riebesell, 2012; Lischka and Riebesell, 2016)

At the end of each growth period, adult individuals ‘disappeared’ from the sediment trap. This ‘disappearance’ was also observed in samples from the Argentine Sea, which Dadon and de Cidre (1992) concluded was due to a die-off based upon observations of *L. retroversa retroversa* in the Arctic. However, in the Scotia Sea there is no evidence for adult L. retroversa dying-off as no passive sinking or predated adults were found in any month except May. Therefore, it is most probable that adult *L. retroversa*, like many other *Limacina* species worldwide (Van der Spoel and Heyman, 2013; Almogi-Labin et al., 1988), undergo an ontogenic migration to deeper water after spawning. Based on the cohort identification, it took between one (LR4) and seven (LR3) months for *L. retroversa australis* to transition from the small juvenile stage to adult stage. However, since there was no clear die-off of adults, it is unclear what their longevity was. Dadon and de Cidre (1992) concluded that *L. retroversa* in the Argentine Sea lived for a year, while in the northern hemisphere, *L. retroversa retroversa* has a longevity of between 0.5 years (Thabet et al., 2015) and 1 year (Lebour, 1932; Hsiao, 1939), which is similar to longevity estimates in the current study.

4.5 The implications of contrasting life cycle strategies in a changing Southern Ocean

Thecosome pteropods are functionally important components in the Scotia Sea ecosystem, being central to food webs, organic carbon fluxes and calcium carbonate exports (Collier et al., 2000; Hunt et al., 2008; Manno et al., 2018). However, warming and ocean acidification are environmental perturbations affecting this region that are potentially deleterious to their viability. *Limacina* populations in the northern Scotia Sea (e.g. at P3) are especially sensitive to climatic changes since *L. rangii* are at the northern limit of their polar distribution, and *L. retroversa* are at the southern limit of their boreal distribution (Hunt et al., 2008). The capacity of pteropods to maintain a viable population in the Southern Ocean depends on their capability to recruit successfully. Shallow undersaturation with respect to aragonite in the Scotia Sea is expected to occur episodically from 2030 onwards, first during the winter before becoming more prolonged and intense with time (McNeil and Matear, 2008; Hauri et al., 2016; Landschützer et al., 2018). If exposed to undersaturation events, thecosome pteropod populations in the Scotia Sea may experience higher mortality, shell dissolution and more energetic demands to maintain their shell (Manno et al., 2017; Peck et al., 2018). Pteropods that overwinter are most vulnerable to undersaturation, since undersaturation with respect to aragonite is expected to commence in the winter months before extending to other seasons (McNeil and Matear, 2008; Hauri et al., 2016; Landschützer et al., 2018). We have shown that *L. retroversa* and *L. rangii* at P3 overwinter as juveniles and adults, meaning that these life stages are most likely to be the first to be exposed to undersaturated conditions. These later life stages are potentially more capable of tolerating exposure to undersaturated waters than early developmental stages. Their higher tolerance is not just due to their established life stage, but also the likelihood that during the winter months they tend to dwell deeper in the water column, likely below the shallow saturation horizon. Overwintering pteropods appear to enter a diapause stage during the food scarcity of the winter months, where their metabolism and calcification rates drop allowing them to focus energy on egg production in the spring (Ghiselin, 1969; Dillon, 2000). This ‘hibernation’ strategy likely reduces their exposure to environmental perturbations in the surface waters, however as the intensity and duration of these stressors increase in the future of these factors will likely begin to impact Limacina. Laboratory incubations suggest that veligers of *L. rangii* are susceptible to shell malformation, dissolution, and high mortality when exposed to increased temperature and aragonite undersaturation (Comeau et al., 2010; Thabet et al., 2015; Gardner et al., 2018). When, as predicted, the duration of winter undersaturation events begin to overlap with the onset of the South Georgia bloom and spawning time of Limacina, vulnerable veligers restricted to surface waters will become exposed.

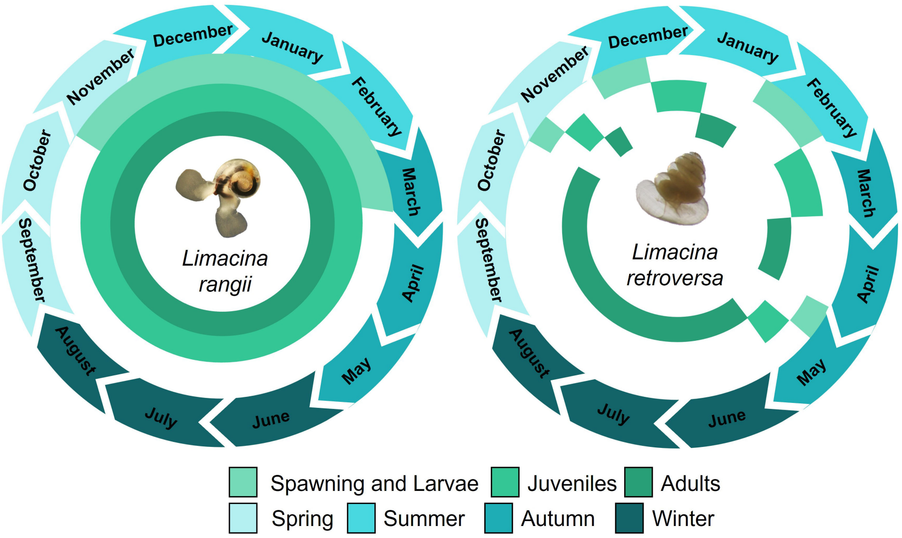

FIGURE 8
A conceptual schematic illustrating the seasonal and monthly presence of veliger, juvenile and adult *Limacina rangii* and *Limacina retroversa*, as well as their spawning period. The schematic is based on shell morphometrics of individuals collected in a sediment trap deployed at P3 (Scotia Sea, Southern Ocean) at 400 m depth between December 2014 and November 2015.

This study shows the population of *L. rangii* at P3 comprises several overlapping cohorts with a life cycle of over a year. Therefore, since all life stages of *L. rangii* co-exist, vulnerability of one cohort is not detrimental to the stability of the overall population. Conversely, there is no overlap in juvenile and adult stages in the life cycle of *L. retroversa* meaning that, if one cohort is removed, the entire population may be vulnerable. If deleterious conditions impacted a cohort of *L. retroversa* prior to sexual maturity, a population bottleneck or local extinction may result. Therefore, based on the assumption of a static population which is not advected into or out of the sampling area, *L. retroversa* populations are more likely to be impacted than *L. rangii* on exposure to episodes of undersaturation. Regardless of cohort structure, repeated or prolonged exposure to unfavourable conditions is likely to impact all cohorts across both species if rates of spawning and survival to sexual maturity decline. Such a progressive population decline was observed in the Ross Sea, where long-term food shortages due to reduced primary productivity eventually led to the short-term localized extinction of *L. rangii* (Seibel and Dierssen, 2003; Maas et al., 2011).

In conclusion, we indicate contrasting life history strategies of the dominant Southern Ocean pteropod species, *L. rangii* and *L. retroversa* (Figure 8), suggesting that *L. retroversa* populations in the Scotia Sea may be particularly vulnerable to exposure to deleterious conditions. Declines in pteropod populations in the Southern Ocean will have cascading implications on regional biogeochemical cycling and epipelagic food webs.

Data availability statement

The datasets analyzed for this study can be found in the Supplementary Material and in the UK Polar Data Centre.

Author contributions

JG, CM, VP and GT carried out the fieldwork and sample collection with support from other scientists on board cruise JR304 and JR15002. JG carried out the sample and statistical analysis with support from CM and GT. JG wrote the manuscript with support from CM, GT, VP and DB. All authors contributed to the article and approved the submitted version.

Funding

This work was funded by a NERC studentship granted through the EnvEast Doctoral Training Partnership (Grant No. NE/L002582/1) at the University of East Anglia. This work was carried out as part of the Ecosystems programme at the British Antarctic Survey and the Scotia Sea Open Ocean Laboratories (SCOOBIES) sustained observation programme during the Western Core Box survey cruises on board the *RRS James Clark Ross*.

Acknowledgments

We would like to acknowledge the captain, officers, crew, and scientists aboard the *RRS James Clark Ross* during cruises JR304 and JR15002 for their support in all the logistical operations on board. We also thank Peter Enderlein, Scott Polfrey, Sophie Fielding and Gabriele Stowasser for their support during deployment and recovery of the sediment trap mooring.

Conflict of interest

The authors declare that the research was conducted in the absence of any commercial or financial relationships that could be construed as a potential conflict of interest.

Publisher's note

Supplementary material

The Supplementary Material for this article can be found online at: https://www.frontiersin.org/articles/10.3389/fmars.2023.1118570/full#supplementary-material

References

Accornero, A., Manno, C., Esposito, F. G. M. C., and Gambi, M. C. (2003). The vertical flux of particulate matter in the polynya of Terra Nova bay. part II. *Biol. components. Antarctic Sci.* 15 (2), 175–188. doi: 10.1017/S0954102003001214

Adhikari, D., Webster, D. R., and Yen, J. (2016). Portable tomographic PIV measurements of swimming shelled Antarctic pteropods. *Experiments Fluids* 57 (12), 180–189. doi: 10.1007/s00348-016-2269-7

Akiha, F., Hashida, G., Makabe, R., Hattorid, H., and Sasaki, H. (2017). Distribution in the abundance and biomass of shelled pteropods in surface waters of the Indian sector of the Antarctic ocean in mid-summer. *Polar Sci.* 12, 12–18. doi: 10.1016/j.polar.2017.02.003

Almogi-Labin, A., Hemleben, C., and Deuser, W. G. (1988). Seasonal variation in the flux of euthecosomatous pteropods collected in a deep sediment trap in the Sargasso Sea. *Deep Sea Res. Part A. Oceanographic Res. Papers* 35 (3), 441–464. doi: 10.1016/0198-0149(88)90020-9

Atkinson, A., Ward, P., Hunt, B. P. V., Pakhomov, E. A., and Hosie, G. W. (2012). An overview of southern ocean zooplankton data: abundance, biomass, feeding and functional relationships. *CCAMLR Sci.* 19, 171–218.

Baker, E. T., Milburn, H. B., and Tennant, D. A. (1988). Field assessment of sediment trap efficiency under varying flow conditions. *J. Mar. Res.* 46 (3), 573–592.

Bednaršek, N., Harvey, C. J., Kaplan, I. C., Feely, R. A., and Moz, J. (2016). Pteropods on the edge: Cumulative effects of ocean acidification, warming and deoxygenation. *Prog. Oceanogr.* 145, 1–24. doi: 10.1016/j.pocean.2016.04.002

Bednaršek, N., Klinger, T., Harvey, C. J., Weisberg, S., McCabe, R. M., Feely, R. A., et al. (2017). New ocean, new needs: Application of pteropod shell dissolution as a biological indicator for marine resource management. *Ecol. Indic.* 76, 240–244. doi: 10.1016/j.ecolind.2017.01.025

Bednaršek, N., Mozina, J., Vuckovic, M., Vogt, M., O'Brien, C., and Tarling, G. A. (2012c). Global distribution of pteropods representing carbonate functional type biomass. *Earth System Sci. Data Discussions* 5, 317–350.

Bednaršek, N., Tarling, G. A., Bakker, D. C. E., Fielding, S., Cohen, A., Kuzirian, A., et al. (2012a). Description and quantification of pteropod shell dissolution: A sensitive bioindicator of ocean acidification. *Global Change Biol.* 18 (7), 2378–2388. doi: 10.1111/j.1365-2486.2012.02668.x

Bednaršek, N., Tarling, G. A., Bakker, D. C. E., Fielding, S., Jones, E. M., Venables, H. J., et al. (2012b). Extensive dissolution of live pteropods in the southern ocean. *Nat. Geosci.* 5 (12), 881–885. doi: 10.1038/NGEO1635

Bernard, K. S., and Froneman, P. W. (2009). The sub-Antarctic euthecosome pteropod, limacina retroversa: Distribution patterns and trophic role. *Deep Sea Res. Part I: Oceanographic Res. Papers* 56 (4), 582–598. doi: 10.1016/j.dsr.2008.11.007

Borrione, I., and Schlitzer, R. (2013). Distribution and recurrence of phytoplankton blooms around south Georgia, southern ocean. *Biogeosciences* 10 (1), 217–231. doi: 10.5194/bg-10-217-2013

Burridge, A. K., Hörnlein, C., Janssen, A. W., Hughes, M., Bush, S. L., Marlétaz, F., et al. (2017). Time-calibrated molecular phylogeny of pteropods. *PloS One* 12 (6), e0177325. doi: 10.1371/journal.pone.0177325

Cermeño, P., Teixeira, I. G., Branco, M., Figueiras, F. G., and Marañón, E. (2014). Sampling the limits of species richness in marine phytoplankton communities. *J. Plankton Res.* 36 (4), 1135–1139. doi: 10.1093/plankt/fbu033

Chen, C., and Bé, A. W. (1964). Seasonal distributions of euthecosomatous pteropods in the surface waters of five stations in the Western north Atlantic. *Bull. Mar. Sci.* 14 (2), 185–220.

Chiarini, F., Capotondi, L., Dunbar, R. B., Giglio, F., Mammì, I., Mucciarone, D. A., et al. (2013). A revised sediment trap splitting procedure for samples collected in the Antarctic sea. *Methods Oceanography* 8, 13–22. doi: 10.1016/j.mio.2014.05.003

Collier, R., Dymond, J., Honjo, S., Manganini, S., Francois, R., and Dunbar, R. (2000). The vertical flux of biogenic and lithogenic material in the Ross Sea: moored sediment trap observations 1996–1998. *Deep Sea Res. Part II: Topical Stud. Oceanography* 47 (15), 3491–3520. doi: 10.1016/S0967-0645(00)00076-X

Comeau, S., Jeffree, R., Teyssié, J. L., and Gattuso, J. P. (2010). Response of the Arctic pteropod *Limacina helicina* to projected future environmental conditions. *PloS One* 5 (6), e11362. doi: 10.1371/journal.pone.0011362

Dadon, J. R. (1990). Annual cycle of *Limacina retroversa* in Patagonian waters. *Am. Malacological Bull.* 8 (1), 77–84. doi: 10.1007/BF00350035

Dadon, J. R., and de Cidre, L. L. (1992). The reproductive cycle of the thecosomatous pteropod limacina retroversa in the western south Atlantic. *Mar. Biol.* 114 (3), 439–442. doi: 10.1007/BF00350035

Dillon, R. T. (2000). *The ecology of freshwater molluscs* (Cambridge: Cambridge University Press).

Fabry, V. J. (1990). Shell growth rates of pteropod and heteropod molluscs and aragonite production in the open ocean: implications for the marine carbonate system. *J. Mar. Res.* 48 (1), 209–222. doi: 10.1357/002224090784984614

Flores, H., van Franeker, J. A., Cisewski, B., Leach, H., Van de Putte, A. P., Meesters, E. H., et al. (2011). Macrofauna under sea ice and in the open surface layer of the lazarev Sea, southern ocean. *Deep Sea Res. Part II: Topical Stud. Oceanography* 58 (19-20), 1948–1961. doi: 10.1016/j.dsr2.2011.01.010

Gannefors, C., Böer, M., Kattner, G., Graeve, M., Eiane, K., Gulliksen, B., et al. (2005). The Arctic sea butterfly *Limacina helicina*: lipids and life strategy. *Mar. Biol.* 147 (1), 169–177. doi: 10.1007/s00227-004-1544-y

Gardner, J., Manno, C., Bakker, D. C., Peck, V. L., and Tarling, G. A. (2018). Southern ocean pteropods at risk from ocean warming and acidification. *Mar. Biol.* 165 (1), 8–18. doi: 10.1007/s00227-017-3261-3

Gerhardt, S., Groth, H., Rühlemann, C., and Henrich, R. (2000). Aragonite preservation in late quaternary sediment cores on the Brazilian continental slope: implications for intermediate water circulation. *Int. J. Earth Sci.* 88 (4), 607–618. doi: 10.1007/s005310050291

Ghiselin, M. T. (1969). The evolution of hermaphroditism among animals. *Q. Rev. Biol.* 44, 189–208. doi: 10.1086/406066

Gilmer, R. W., and Harbison, G. R. (1986). Morphology and field behaviour of pteropod molluscs: feeding methods in the families cavoliniidae, limacinidae and peraclididae (Gastropoda: Thecosomata). *Mar. Biol.* 91 (1), 47–57. doi: 10.1007/BF00397570

Goto, N., Hisamatsu, K., Yoshimizu, C., and Ban, S. (2016). Effectiveness of preservatives and poisons on sediment trap material in freshwater environments. *Limnology* 17 (1), 87–94. doi: 10.1007/s10201-015-0467-2

Harbison, G. R., and Gilmer, R. W. (1986). Effects of animal behavior on sediment trap collections: implications for the calculation of aragonite fluxes. *Deep Sea Res. Part A. Oceanographic Res. Papers* 33 (8), 1017–1024. doi: 10.1016/0198-0149(86)90027-0

Hauri, C., Friedrich, T., and Timmermann, A. (2016). Abrupt onset and prolongation of aragonite undersaturation events in the southern ocean. *Nat. Climate Change.* 6, 172–176. doi: 10.1038/nclimate2844

Henson, S. A., Beaulieu, C., Ilyina, T., John, J. G., Long, M., Séférian, R., et al. (2017). Rapid emergence of climate change in environmental drivers of marine ecosystems. *Nat. Commun.* 8, 14682. doi: 10.1038/ncomms14682

Hopkins, T. L., and Torres, J. J. (1989). Midwater food web in the vicinity of a marginal ice zone in the western weddell Sea. *Deep Sea Res. Part A. Oceanographic Res. Papers* 36 (4), 543–560. doi: 10.1016/0198-0149(89)90005-8

Howard, W. R., Roberts, D., Moy, A. D., Lindsay, M. C. M., Hopcroft, R. R., Trull, T. W., et al. (2011). Distribution, abundance and seasonal flux of pteropods in the Sub-Antarctic zone. *Deep Sea Res. Part II: Topical Stud. Oceanography* 58 (21-22), 2293–2300. doi: 10.1016/j.dsr2.2011.05.031

Howes, E. L., Bednaršek, N., Büdenbender, J., Comeau, S., Doubleday, A., Gallager, S. M., et al. (2014). Sink and swim: a status review of thecosome pteropod culture techniques. *J. Plankton Res.* 36 (2), 299–315. doi: 10.1093/plankt/fbu002

Hsiao, S. C. (1939). The reproductive system and spermatogenesis of *Limacina* (Spiratella) *retroversa* (Flem.). *Biol. Bull.* 76 (1), 7–25. doi: 10.2307/1537632

Hunt, B. P. V., Pakhomov, E. A., Hosie, G. W., Siegel, V., Ward, P., and Bernard, K. (2008). Pteropods in southern ocean ecosystems. *Prog. Oceanography* 78 (3), 193–221. doi: 10.1016/j.pocean.2008.06.001

Hunt, B., Strugnell, J., Bednaršek, N., Linse, K., Nelson, R. J., Pakhomov, E., et al. (2010). Poles apart: the "bipolar" pteropod species *Limacina helicina* is genetically distinct between the Arctic and Antarctic oceans. *PloS One* 5 (3), e9835. doi: 10.1371/journal.pone.0009835

Jennings, R. M., Bucklin, A., Ossenbrügger, H., and Hopcroft, R. R. (2010). Species diversity of planktonic gastropods (Pteropoda and heteropoda) from six ocean regions based on DNA barcode analysis. *Deep Sea Res. Part II: Topical Stud. Oceanogr.* 57 (24), 2199–2210. doi: 10.1016/j.dsr2.2010.09.022

Kobayashi, H. A. (1974). Growth cycle and related vertical distribution of the thecosomatous pteropod *Spiratella* ("*Limacina*") *helicina* in the central Arctic ocean. *Mar. Biol.* 26 (4), 295–301. doi: 10.1007/BF00391513

Korb, R. E., and Whitehouse, M. (2004). Contrasting primary production regimes around south Georgia, southern ocean: large blooms versus high nutrient, low chlorophyll waters. *Deep Sea Res. Part I: Oceanographic Res. Papers* 51 (5), 721–738. doi: 10.1016/j.dsr.2004.02.006

Korb, R. E., Whitehouse, M. J., Thorpe, S. E., and Gordon, M. (2005). Primary production across the Scotia Sea in relation to the physico-chemical environment. *J. Mar. Syst.* 57 (3), 231–249. doi: 10.1016/j.jmarsys.2005.04.009

Lalli, C. M., and Gilmer, R. W. (1989). *Pelagic snails: the biology of holoplanktonic gastropod mollusks.* (California: Stanford University Press).

Lalli, C. M., and Wells, F. E. (1978). Reproduction in the genus *Limacina* (Opisthobranchia: Thecosomata). *J. Zoology* 186, 95–108. doi: 10.1111/j.1469-7998.1978.tb03359.x

Landschützer, P., Gruber, N., Bakker, D. C., Stemmler, I., and Six, K. D. (2018). Strengthening seasonal marine CO_2 variations due to increasing atmospheric CO_2. *Nat. Climate Change* 8, 146–150. doi: 10.1038/s41558-017-0057-x

Lebour, M. V. (1932). *Limacina retroversa* in Plymouth waters. *J. Mar. Biol. Assoc. United Kingdom* 18 (1), 123–126. doi: 10.1017/S0025315400051341

Lischka, S., and Riebesell, U. (2012). Synergistic effects of ocean acidification and warming on overwintering pteropods in the Arctic. *Global Change Biol.* 18 (12), 3517–3528. doi: 10.1111/gcb.12020

Lischka, S., and Riebesell, U. (2016). Metabolic response of Arctic pteropods to ocean acidification and warming during the polar night/twilight phase in kongsfjord (Spitsbergen). *Polar Biol.* 40 (6), 1211–1227. doi: 10.1007/s00300-016-2044-5

Liszka, C. M., Manno, C., Stowasser, G., Robinson, C., and Tarling, G. A. (2019). Mesozooplankton community composition controls fecal pellet flux and remineralization depth in the southern ocean. *Front. Mar. Sci.* 6, 230. doi: 10.3389/fmars.2019.00230

Lutz, V. A., Segura, V., Dogliotti, A. I., Gagliardini, D. A., Bianchi, A. A., and Balestrini, C. F. (2009). Primary production in the Argentine Sea during spring estimated by field and satellite models. *J. Plankton Res.* 32 (2), 181–195. doi: 10.1093/plankt/fbp117

Maas, A. E., Elder, L. E., Dierssen, H. M., and Seibel, B. A. (2011). Metabolic response of Antarctic pteropods (Mollusca: Gastropoda) to food deprivation and regional productivity. *Mar. Ecol. Prog. Ser.* 441, 129–139. doi: 10.3354/meps09358

Macdonald, P., and Juan, D. (2012) *Mixdist: Finite mixture distribution models.* Available at: https://CRAN.R-project.org/package=mixdist (Accessed 03/05/16).

Makabe, R., Hattori, H., Sampei, M., Darnis, G., Fortier, L., and Sasaki, H. (2016). Can sediment trap-collected zooplankton be used for ecological studies? *Polar Biol.* 39 (12), 2335–2346. doi: :10.1007/s00300-016-1900-7

Manno, C., Bednaršek, N., Tarling, G., Peck, V., Comeau, S., Adhikari, D., et al. (2017). Shelled pteropods in peril: Assessing vulnerability in a high CO_2 ocean. *Earth-Science Rev.* 169, 132–145. doi: 10.1016/j.earscirev.2017.04.005

Manno, C., Giglio, F., Stowasser, G., Fielding, S., Enderlein, P., and Tarling, G. A. (2018). Threatened species drive the strength of the carbonate pump in the northern Scotia Sea. *Nat. Commun.* 9 (1), 1–7. doi: 10.1038/s41467-018-07088-y

McGowan John, A., and Fraundorf Vernie, J. (1966). The relationship between size of net used and estimates of zooplankton diversity. *Limnology Oceanography* 11 (4), 456–469. doi: 10.4319/lo.1966.11.4.0456

McNeil, B. I., and Matear, R. J. (2008). Southern ocean acidification: a tipping point at 450 ppm atmospheric CO_2. *Proc. Natl. Acad. Sci. United States America* 105 (48), 18860–18864. doi: 10.1073/pnas.0806318105

Meyer, B., Freier, U., Grimm, V., Groeneveld, J., Hunt, B. P., Kerwath, S., et al. (2017). The winter pack-ice zone provides a sheltered but food-poor habitat for larval Antarctic krill. *Nat. Ecol. Evol.* 1 (12), 1853–1861. doi: 10.1038/s41559-017-0368-3

MSIP (2017) *Marine species identification portal*. Available at: http://species-identification.org/index.php (Accessed 08/07/2017).

Oakes, R. L., Peck, V. L., Manno, C., and Bralower, T. J. (2019). Degradation of internal organic matter is the main control on pteropod shell dissolution after death. *Global Biogeochemical Cycles* 33 (6), 749–760. doi: 10.1029/2019GB006223

Orsi, A. H., Whitworth, III, T., and Nowlin, Jr, W. D. (1995). On the meridional extent and fronts of the Antarctic Circumpolar Current. *Deep Sea Res. Part I: Oceanograph. Res. Papers* 42 (5), 641–673. doi: 10.1016/0967-0637(95)00021-W

Paranjape, M. (1968). The egg mass and veligers of limacina helicina phipps. *Veliger* 10, 322–326.

Peck, V. L., Oakes, R. L., Harper, E. M., Manno, C., and Tarling, G. A. (2018). Pteropods counter mechanical damage and dissolution through extensive shell repair. *Nat. Commun.* 9 (1), 264.

Roberts, D., Howard, W. R., Moy, A. D., Roberts, J. L., Trull, T. W., Bray, S. G., et al. (2011). Inter-annual pteropod variability in sediment traps deployed above and below the aragonite saturation horizon in the Sub-Antarctic southern ocean. *Polar Biol.* 34 (11), 1739–1750. doi: 10.1007/s00300-011-1024-z

Schindelin, J., Arganda-Carreras, I., Frise, E., Kaynig, V., Longair, M., Pietzsch, T., et al. (2012). Fiji: An open-source platform for biological-image analysis. *Nat. Methods* 9 (7), 676–682. doi: 10.1038/nmeth.2019

Seibel, B. A., and Dierssen, H. M. (2003). Cascading trophic impacts of reduced biomass in the Ross Sea, Antarctica: Just the tip of the iceberg? *Biol. Bull.* 205 (2), 93–97. doi: 10.2307/1543229

Seibel, B. A., Maas, A. E., and Dierssen, H. M. (2012). Energetic plasticity underlies a variable response to ocean acidification in the pteropod, *Limacina helicina* antarctica. *PloS One* 7 (4), e30464. doi: 10.1371/journal.pone.0030464

Thabet, A. A., Maas, A. E., Lawson, G. L., and Tarrant, A. M. (2015). Life cycle and early development of the thecosomatous pteropod *Limacina retroversa* in the gulf of Maine, including the effect of elevated CO_2 levels. *Mar. Biol.* 162 (11), 2235–2249. doi: 10.1007/s00227-015-2754-1

Thibodeau, P. S., Steinberg, D. K., McBride, C. E., Conroy, J. A., Keul, N., and Ducklow, H. W. (2020). Long-term observations of pteropod phenology along the Western Antarctic peninsula. *Deep Sea Res. Part I: Oceanographic Res. Papers* 166, 103363. doi: 10.1016/j.dsr.2020.103363

Thorpe, S. E., Heywood, K. J., Brandon, M. A., and Stevens, D. P. (2002). Variability of the southern Antarctic Circumpolar Current front north of South Georgia. *J. Mar. Syst.* 37 (1-3), 87–105. doi: 10.1016/S0924-7963(02)00197-5

Turner, J. T. (2015). Zooplankton fecal pellets, marine snow, phytodetritus and the ocean's biological pump. *Prog. Oceanography* 130, 205–248. doi: 10.1016/j.pocean.2014.08.005

Van der Spoel, S. (1967). *Euthecosomata: A group with remarkable developmental Stages. (Gastropoda, pteropoda)*. Ed. J Noorduijn. PhD thesis. University of Amsterdam.

Van der Spoel, S. (1976). Finer sculptures in euthecosomatous shells, and their value for taxonomy (Mollusca, pteropoda). *Beaufortia* 24 (314), 105–121.

Van der Spoel,, and Dadon, S. (1999). "Pteropoda," in *South Atlantic zooplankton*. Ed. D. Boltovskoy (Leiden: Backhuys Publishers, Leiden), 649–706.

Van der Spoel, S., and Heyman, R. P. (2013). *A comparative atlas of zooplankton: biological patterns in the oceans.* (Berlin: Springer Science & Business Media), 161p.

Van der Spoel, S., Schalk, P. H., and Bleeker, J. (1992). *Clio piatkowskii*, a mesopelagic pteropod new to science (Gastropoda, opisthobranchia). *Beaufortia* 43 (1), 1–6.

Wang, K., Hunt, B. P., Liang, C., Pauly, D., and Pakhomov, E. A. (2017). Reassessment of the life cycle of the pteropod limacina helicina from a high resolution interannual time series in the temperate north pacific. *ICES J. Mar. Sci.* 74 (7), 1906–1902. doi: 10.1093/icesjms/fsx014

Ward, P., Grant, S., Brandon, M., Siegel, V., Sushin, V., Loeb, V., et al. (2004). Mesozooplankton community structure in the Scotia Sea during the CCAMLR 2000 survey: January–February 2000. *Deep Sea Res. Part II: Topical Stud. Oceanography* 51 (12-13), 1351–1367. doi: 10.1016/j.dsr2.2004.06.016

Ward, P., Meredith, M. P., Whitehouse, M. J., and Rothery, P. (2008). The summertime plankton community at south Georgia (Southern ocean): Comparing the historica/1927) and modern (post 1995) records. *Prog. Oceanography* 78 (3), 241–256. doi: 10.1016/j.pocean.2008.05.003

Weldrick, C. K., Makabe, R., Mizobata, K., Moteki, M., Odate, T., Takao, S., et al. (2021). The use of swimmers from sediment traps to measure summer community structure of southern ocean pteropods. *Polar Biol.* 44 (3), 457–472. doi: 10.1007/s00300-021-02809-4

Wiens, J. A. (1989). Spatial scaling in ecology. *Funct. Ecol.* 3 (4), 385–397. doi: 10.2307/2389612

Whitehouse, M. J., Atkinson, A., Korb, R. E., Venables, H. J., Pond, D. W., and Gordon, M. (2012). Substantial primary production in the land-remote region of the central and northern Scotia Sea. *Deep Sea Res II: Top Stud Oceanogr.* 59 (4), 47–56.

frontiers | Frontiers in Marine Science

TYPE Original Research
PUBLISHED 26 June 2023
DOI 10.3389/fmars.2023.1211804

EDITED BY
Zhaohe Luo,
Ministry of Natural Resources, China

REVIEWED BY
Jianrong Xia,
Guangzhou University, China
Gustaaf Marinus Hallegraeff,
University of Tasmania, Australia

*CORRESPONDENCE
Kunshan Gao
ksgao@xmu.edu.cn

†These authors have contributed equally to this work and share first authorship

RECEIVED 25 April 2023
ACCEPTED 08 June 2023
PUBLISHED 26 June 2023

CITATION
Zhou C, Zhang D, Yi X, Beardall J and Gao K (2023) No adaptation to warming after selection for 800 generations in the coccolithophore *Emiliania huxleyi* BOF 92. *Front. Mar. Sci.* 10:1211804.
doi: 10.3389/fmars.2023.1211804

No adaptation to warming after selection for 800 generations in the coccolithophore *Emiliania huxleyi* BOF 92

Cong Zhou[1†], Di Zhang[2†], Xiangqi Yi[1†], John Beardall[1,3] and Kunshan Gao[1,4*]

[1]State Key Laboratory of Marine Environmental Science & College of Environment and Ecology, Xiamen University, Xiamen, China, [2]School of Ocean, Yantai University, Yantai, China, [3]School of Biological Sciences, Monash University, Clayton, VIC, Australia, [4]Co-Innovation Center of Jiangsu Marine Bio-industry Technology, Jiangsu Ocean University, Lianyungang, China

Ocean warming is suggested to exert profound effects on phytoplankton physiology and growth. Here, we investigated how the coccolithophore *Emiliania huxleyi* (BOF 92, a non-calcifying strain) responded to changes in temperature in short- and long-term thermal treatments. The specific growth rate after 10 days of acclimation increased gradually with increasing temperatures (14, 17, 21, 24, 28°C) and peaked at ~23°C, followed by a significant decrease to 28°C. Chlorophyll *a* content, cell size, photosynthetic rate, and respiratory rate increased significantly from 14°C to 24°C, but the cellular particulate organic carbon (POC) and nitrogen (PON) showed the lowest values at the optimal temperature. In contrast, during long-term thermal treatments at 17°C and 21°C for 656 days (~790 generations for 17°C treatment; ~830 generations for 21°C treatment), the warming significantly stimulated the growth in the first 34 days and the last 162 days, but there was no significant difference in specific growth rate from Day 35 to Day 493. Chlorophyll *a* content, cell size, cellular POC/PON, and the ratio of POC to PON, showed no significant difference between the warming and control for most of the duration of the long-term exposure. The warming-selected population did not acquire persistent traits in terms of growth and cell quotas of POC and PON, which resumed to the levels in the control temperature treatment after about 9 generations in the shift test. In summary, our results indicate that warming by 4°C (17°C and 21°C) enhanced the growth, but did not result in adaptative changes in *E. huxleyi* (BOF 92) over a growth period of about 800 generations, reflecting that mild or non-stressful warming treatment to *E. huxleyi* isolated from cold seas does not alter its phenotypic plasticity.

KEYWORDS

***Emiliania huxleyi*, seawater warming, growth, photosynthesis, phytoplankton**

1 Introduction

The anthropogenic emissions of greenhouse gases are responsible for global and ocean warming. Under a business-as-usual emissions scenario (Shared Socioeconomic Pathway 5-8.5, SSP5-8.5), global warming will increase the global mean temperature by up to 4.3°C (Masson-Delmotte et al., 2021), with the ocean surface temperature being predicted to rise by 2.34-2.82°C by the end of this century (Pörtner et al., 2019). Warming could alter phytoplankton physiological functions by regulating cell metabolism *via* controlling the activities of various enzyme-related reactions (Raven and Geider, 1988; Gillooly et al., 2001).

As a major group of marine phytoplankton, coccolithophores can not only perform photosynthesis to convert inorganic carbon to organic carbon thereby driving the biological carbon pump but also release CO_2 through calcification in what has been described as a carbonate reverse pump (Rost and Riebesell, 2004). Photosynthetic carbon fixation by coccolithophores has been reported to account for about 10% of marine primary production (Poulton et al., 2007), and their calcification has been reported to account for about 50% of the global pelagic calcium carbonate production, with an average output of about 0.8 Pg y^{-1} (Geisen et al., 2002; Balch et al., 2007). *Emiliania huxleyi* is the most widely distributed species of coccolithophorid (Bach et al., 2013) and its physiological responses to environmental fluctuations have been intensively investigated. For example, in *E. huxleyi* CCMP371, both the photosynthesis and growth rate were significantly improved by elevated temperature (4°C), even under low light conditions (Feng et al., 2008). Under elevated temperatures, both calcification and photosynthesis rates in *E. huxleyi* CS369 were found to be positively correlated (Xu et al., 2011). In *E. huxleyi* CCMP373, warming (from 17°C to 21°C) increased the specific growth rate by 2.9% but decreased its cell size from 5.2 µm to 4.0 µm (Arnold et al., 2013). However, our understanding of the warming effects on coccolithophores is mainly based on short-term studies, and little has been documented on the effects of long-term warming (Schlüter et al., 2014; Listmann et al., 2016). While these two studies observed adaptative responses to warming in *E. huxleyi* after having been grown for 400-500 generations, evolutionary changes may depend on the thermal ranges to which the microalgae were exposed. Rapid adaptation to warming within hundreds of generations has also been reported in other phytoplankton species (Padfield et al., 2015; Schaum et al., 2018; Cheng et al., 2022; Jin et al., 2022). In particular, Schaum et al. (2018) reported that specific adaptations to moderate warming (26°C, which was lower than the optimal growth temperature) were more rapid than those to severe warming (32°C, which was higher than the optimal growth temperature) in *Thalassiosira pseudonana* CCMP 1335. *E. huxleyi* is a cosmopolitan species with a worldwide distribution (Holligan et al., 1983), and intraspecific differences in response to environmental changes have been widely reported (Leonardos and Geider, 2005; McKew et al., 2015; Zhang et al., 2023). Therefore, evaluating the adaptative potential of *E. huxleyi* strains isolated from different sites is essential for predicting the responses and feedbacks of this globally important phytoplankton species to ocean warming. In the present study, we have carried out both a short-term and a long-term experiment, to investigate the effects of seawater warming on *E. huxleyi* BOF 92 as well as a shift experiment in which cells grown at elevated temperature were shifted back to the original conditions. We did not observe adaptative changes to warming after cultures had been grown over 800 generations.

2 Materials and methods

2.1 Experimental setup of the short- and long-term cultures

Emiliania huxleyi BOF 92 was established in 1993 from strain 5/90/25j, which was originally isolated in 1990 from the North Atlantic by John C. Green (Paasche et al., 1996; Paasche, 1999). In the present study, this strain was obtained from Jimei University (Xiamen, China). The *E. huxleyi* strain was initially able to calcify but lost the capacity for calcification after having been cultured in the laboratory (Nanninga and Tyrrell, 1996), and did not resume the capability to calcify as shown in a recent study (Fu and Gao, 2022). A modified IMR medium (Eppley et al., 1967), with NO_3^- = 24.7 µM and PO_4^{3-}= 2.5 µM, was used to culture the *E. huxleyi* cells. The photon flux was set at 100 µmol photons m^{-2} s^{-1} (measured by a US-SQS/WB spherical micro quantum sensor, Walz, Germany) with a 12:12 light:dark period. For the short-term experiment, the culture temperature was set at five different levels, 14°C, 17°C, 21°C, 24°C, and 28°C. During the short-term experiment, sterilized seawater with the addition of IMR nutrients was renewed every 3 days to achieve stable carbonate chemistry (Gao, 2021), and the cell concentrations were 1.5-2.0×10^4 cells $ml^{-1}$and and 8.0-15.0×10^4 cells ml^{-1} after and before the medium renewal, respectively. All vessels were sterilized by autoclave to avoid contaminations. Periodic microscopic examination verified that the cultures remained mono-algal, but we cannot guarantee the axenic nature of the cultures. Three independent replicates for each treatment were grown for about ten generations (≥10), and various physiological parameters were collected at the end of this period.

The stock culture of *Emiliania huxleyi* BOF 92 has been maintained for many years at 17°C, which represents the annual mean temperature of its isolation site. For the long-term warming experiments, 17°C and 21°C were selected as control and seawater warming treatments, respectively. Three independent replicate cultures were used for each treatment. The long-term semi-continuous culture lasted for 656 days from March 6, 2019 to December 21, 2020. The light conditions and nutrients used in the long-term culture were the same as those in the short-term experiment. The sterilized seawater with the addition of IMR nutrients was renewed every 5-10 days, and the cell concentration before dilution ranged 5.0-10×10^4 cell ml^{-1} and was set at ~500 cells ml^{-1} after each dilution. The growth was recorded and cells were regularly collected before dilution throughout the experiment except from Day 348 (February 17, 2020) to Day 437 (May 16, 2020). In this period, the cultures were diluted regularly but not sampled for measurements of physiological parameters due to the COVID-19 pandemic.

2.2 Measurements of specific growth rate, cell diameter, and Chl *a* content

The specific growth rate and cell size (diameter) were measured using a Z-2^{TM} Coulter particle Count and Size Analyzer (Beckman Coulter, USA), and the particle size range was set as 3-8 μm. The specific growth rate (μ) was calculated as: $\mu = (1nC_2 - 1nC_1)/(T_2 - T_1)$, where C_2 and C_1 were the cell concentrations at time T_2 and T_1, respectively. The number of generations (G) was estimated as: $G = (1nC_2 - 1nC_1)/1n_2$

To determine the cellular contents of chlorophyll *a* (Chl *a*), cells were collected on the GF/F membrane (Whatman, 25mm, USA) by suction filtration within a pressure of 0.01MPa to prevent cell damage from excessive pressure. The collected samples were extracted overnight in 10 ml of absolute methanol at 4°C in darkness. After centrifugation (5000*g* for 10 minutes), the absorption values of the supernatant were measured with a UV-VIS spectrophotometer (DU800, Beckman Coulter, USA) across the wavelength range 400-800nm. The concentrations of Chl *a* were calculated according to Porra (2002),

$$\text{Chl } a \text{ (pg cell}^{-1}\text{)} = \frac{[16.29 \times (A_{665}\text{-}A_{750})\text{-}8.54 \times (A_{652}\text{-}A_{750})] \times V_E}{C \times V_c} \times 10^6$$

where A_x is the absorbance under the x-wavelength, V_E is the volume of the methanol extraction, V_C is the volume of the algae solution, and C is the concentration of algae cells (cells ml^{-1}).

2.3 Short-term thermal response curve for growth

In short-term experiments, the measured specific growth rate of *E. huxleyi* cultured at 14°C, 17°C, 21°C, 24°C, and 28°C was fitted to temperature according to Schoolfield et al. (1981) and Padfield et al. (2016):

$$\ln(\mu(T)) = E_a\left(\frac{1}{kT_c} - \frac{1}{kT}\right) + \ln(\mu(T_c)) - \ln\left(1 + e^{E_h\left(\frac{1}{kT_h} - \frac{1}{kT}\right)}\right)$$

where μ(T) represents the specific growth rate at temperature T (kelvin - K), E_a is the activation energy (eV) for growth, E_h is the deactivation energy (eV) characterizing high-temperature-induced inactivation above the deactivation temperature T_h (K), k is Boltzmann's constant with a value of 8.62×10^{-5} eV K^{-1}, and T_c represents the reference temperature (17°C, 290.15K). The optimum growth temperature (T_{opt}) was calculated from T_c, T_h, E_a, and E_h as (Yi et al., 2020):

$$T_{opt} = \frac{E_h T_h}{E_h + kT_h \ln\left(\frac{E_h}{E_a}\right)}$$

2.4 Photosynthetic oxygen evolution and dark respiration rates

In the short-term experiment, net photosynthesis and dark respiration rates of *E.huxleyi* cells were determined using a Clark-type oxygen electrode (Hansatech, Norfolk, UK) under the growth temperatures and irradiance (100 μmol photons m^{-2} s^{-1}). Cells were gently collected on polycarbonate membranes (1.2 μm, Millipore, Ireland) and resuspended with sterilized seawater. The resuspended cells were placed in an oxygen electrode chamber equipped with a magnetic stirrer. Both net photosynthesis rate and dark respiration rate were measured for 10 minutes and calculated from the slope of oxygen concentration vs time. After measurement, the resuspended cells were counted by the Z-2^{TM} Coulter particle Count and Size Analyzer, and the calculated photosynthesis and respiration rates are presented as oxygen concentration change per cell per hour (fmol O_2 cell^{-1} h^{-1}).

2.5 POC and PON analysis

Cells were collected onto pre-combusted (450°C for 6h) Whatman GF/F membranes (25 mm) and frozen at -20°C. Before the measurement, the filter membranes were placed in a closed container filled with HCl for 24 hours to completely remove any inorganic carbon and then dried in an oven at 80°C for 24 hours. Subsequently, all the filters were analyzed by a Perkin Elmer Series II CHNS/O Analyzer 2400 (Perkin Elmer Waltham, MA). Production rates (P) of particulate organic nitrogen (PON) and particulate organic carbon (POC) were calculated as P (pg cell^{-1} d^{-1}) = specific growth rate (d^{-1}) × cellular PON or POC content (pg cell^{-1}), respectively.

2.6 Measurements of chlorophyll fluorescence

A Multi-color PAM fluorescence monitoring system (Walz, Effeltrich, Germany) was employed to measure the photosynthetic performance of *E. huxleyi* cells in the short-term experiment. The minimal fluorescence (F_o) for 15 minutes dark-adapted cells was induced by a modulated red measuring light of low irradiance (~5 μmol photons m^{-2} s^{-1}), maximum fluorescence (F_m) was measured during a 0.8 s saturating flash (~10,000 μmol photons m^{-2} s^{-1}), steady-state fluorescence (F) was monitored periodically under a ~100 μmol photons m^{-2} s^{-1} actinic light, and the 0.8 s saturating flash was applied to induce the maximum fluorescence under actinic light (F_m'). The maximum quantum yield of photosystem II (PSII) (F_v/F_m), the effective quantum yield of PSII (YII), and the non-photochemical quenching (NPQ) were calculated as (F_m-F_o)/F_m, (F_m'-F)/F_m', and (F_m – F_m')/F_m', respectively. For the measurements of rapid light curves, cells were illuminated for 20 s with 10 incremental steps of increasing actinic irradiance (PAR). A saturation flash was applied following each irradiance to generate corresponding F and F_m' values. Relative electron transport rates (rETR) were calculated as (F_m'-F)/F_m' × PAR. Photosynthetic parameters α (photosynthetic light harvesting efficiency), β (a photoinhibition constant), and $rETR_s$ (potential rETR maximum without photoinhibition) were obtained by fitting the rETR data to the function (Platt et al., 1980): $rETR = rETRs \times [1 - e^{-\alpha\times PAR/rETRs}] \times e^{-\beta\times PAR/rETRs}$. The minimum saturating light intensity, I_k, was calculated as $rETR_{max}/\alpha$, and the maximal rETR, $rETR_{max}$, was calculated as $rETR_s \times (\frac{\alpha}{\alpha+\beta}) \times (\frac{\beta}{\alpha+\beta})^{\beta/\alpha}$.

2.7 Shift experiment

After having been grown in their respective temperature conditions for 656 days, corresponding to ~790 generations for 17°C and ~830 generations for 21°C, cells were transferred to the reciprocal temperature to acclimate for another 7 days (~9 generations). Such shift experiments were used to evaluate whether evolutionary changes stemming from the selection environment occurred (Tong et al., 2017 and references therein). The specific growth rates, the cellular POC, PON contents, as well as the ratio of POC/PON were measured in the shift experiment.

2.8 Data analysis

Data analyses were performed with SPSS19.0 (SPSS Inc., Chicago, USA) or R language (version 4.1.1). One-way ANOVA with *post-hoc* Tukey HSD test was used to test the differences among treatments in the short-term experiment. The homogeneity of variance was examined using Levene's test. Differences were considered to be significant at $p< 0.05$. For data collected in the long-term experiment, generalized additive models (GAMs) were built (R language and package "mgcv") to test the effects of warming on the time series of specific growth rate, diameter, Chl *a* content, and cellular contents of POC and PON (van Rij et al., 2019). The GAMs for the time series of Chl *a*, POC, and PON contents indicated that these parameters changed linearly with time, so linear mixed effects modes (LMMs) were used instead (R language and package "nlme"; Pinheiro and Bates, 2006). The pairwise comparisons between control and warming treatments on each day were achieved using the R packages "itsadug" and "emmeans" for GAMs and LMMs, respectively. The building, selection, and validation of the statistical models followed the principles and guidelines provided in Pinheiro and Bates (2006); Zuur et al. (2009) and Wood (2017). The tested statistical models and the corresponding values of the Akaike information criterion (AIC) are presented in the Supplementary Material (Table S1-8), and AIC values were calculated using the R language function "AIC".

3 Results

3.1 Short-term warming effects

As shown in Figure 1A, the specific growth rate (SGR) of *E. huxleyi* in short-term cultures displayed a significant difference among the five temperature treatments (One-way ANOVA, $p< 0.05$), with an increase from 14°C to 23°C and a sharp decrease from 23°C to 28°C (*post-hoc* Tukey HSD test, $p<0.05$ for all pairwise comparisons). The cells survived at 28°C but cannot replicate, so the calculated SGR was about 0. Diameters measured by the Z-2^{TM} Coulter (Figure 1B) indicated that the size of cultured cells was significantly larger under the highest temperature conditions (One-way ANOVA, $p<0.05$). Compared with 14°C, the average cell diameter increased by 29.1% at 28°C (*post-hoc* Tukey HSD test, $p<0.05$). Since cells cultured at 28°C could not be harvested in sufficient numbers, only 4 temperature treatments, i.e. 14°C, 17°C, 21°C, and 24°C, were analyzed for photosynthetic and respiratory performance. As with SGR, both photosynthetic O_2 evolution and respiratory rates increased gradually with temperature and peaked at 24°C (Figure 1C). In these four various temperature treatments (at 14°C, 17°C, 21°C and 24°C), the O_2 evolution rates were 5.1, 8.3, 12.7, and 26.8 fmol O_2 cell^{-1} h^{-1}, and the respiratory rates were 6.3, 7.4, 10.1 and 15.1 fmol O_2 cell^{-1} h^{-1}, respectively. Due to the low-density of *E. huxleyi* cells cultured in our long-term experiment, insufficient cells were available to measure both photosynthetic O_2 evolution and respiratory rates. Results from the short-term thermal response curve for growth (Figure 1A) showed that the activation energy E_a, the deactivation energy E_h, and the deactivation temperature T_h were 0.34 eV, 17.80 eV, and 24.62°C (297.77 K), respectively. The calculated optimal growth temperature for *E. huxleyi* BOF 92 was around 22.9°C (296.1 K).

With the increasing temperature, cellular Chl *a* content increased gradually, displaying the maximum value of ~0.25 pg cell^{-1} and a significant difference at 24°C (One-way ANOVA, $p<0.05$, Figure 2A), while the cellular contents of POC and PON showed no significant change between 17°C and 21°C (*post-hoc* Tukey HSD test, $p=0.372$ and 0.418, respectively, Figure 2B). Compared with 17°C or 21°C, the POC and PON contents of cells grown at 14°C or 24°C were significantly higher by ~ 5% (*post-hoc* Tukey HSD test, $p<0.05$, Figure 2B). The ratios of POC to PON of cells grown under different temperatures remained within the range of 7.5 to 8.2. In terms of POC and PON production rate, values mainly depended on SGR and were positively correlated with increasing temperature (Figure 2C).

The chlorophyll fluorescence parameters determined using the Multi-color PAM are shown in Table 1. The maximum photochemical efficiency (F_v/F_m) and effective photochemical efficiency (Y(II)) of coccolithophores photosystem II showed no significant difference among the five different culture temperature conditions (One-way ANOVA, $p = 0.75$ for F_v/F_m, $p = 0.66$ for Y (II)), with an average value of F_v/F_m from 0.64 to 0.66 and an average value of Y(II) from 0.53 to 0.59. The value of $rETR_{max}$ at 17°C was significantly higher than that of cells grown under the other temperature treatments, which were 20.6% (*post-hoc* Tukey HSD test, $p<0.05$), 25.3% (*post-hoc* Tukey HSD test, $p<0.05$), and 59.8% (*post-hoc* Tukey HSD test, $p<0.01$) higher than at 14°C, 21°C, and 24°C, respectively. The light utilization efficiency, i.e. values of α, exhibited the highest value under 24°C, which was significantly higher than that of cultures grown at 14°C, 17°C and 21°C (*post-hoc* Tukey HSD test, $p<0.05$ for 14°C and 17°C, $p<0.01$ for 21°C). In terms of β, the degree of photoinhibition, no significant difference was observed between cells grown at 14°C and 17°C (*post-hoc* Tukey

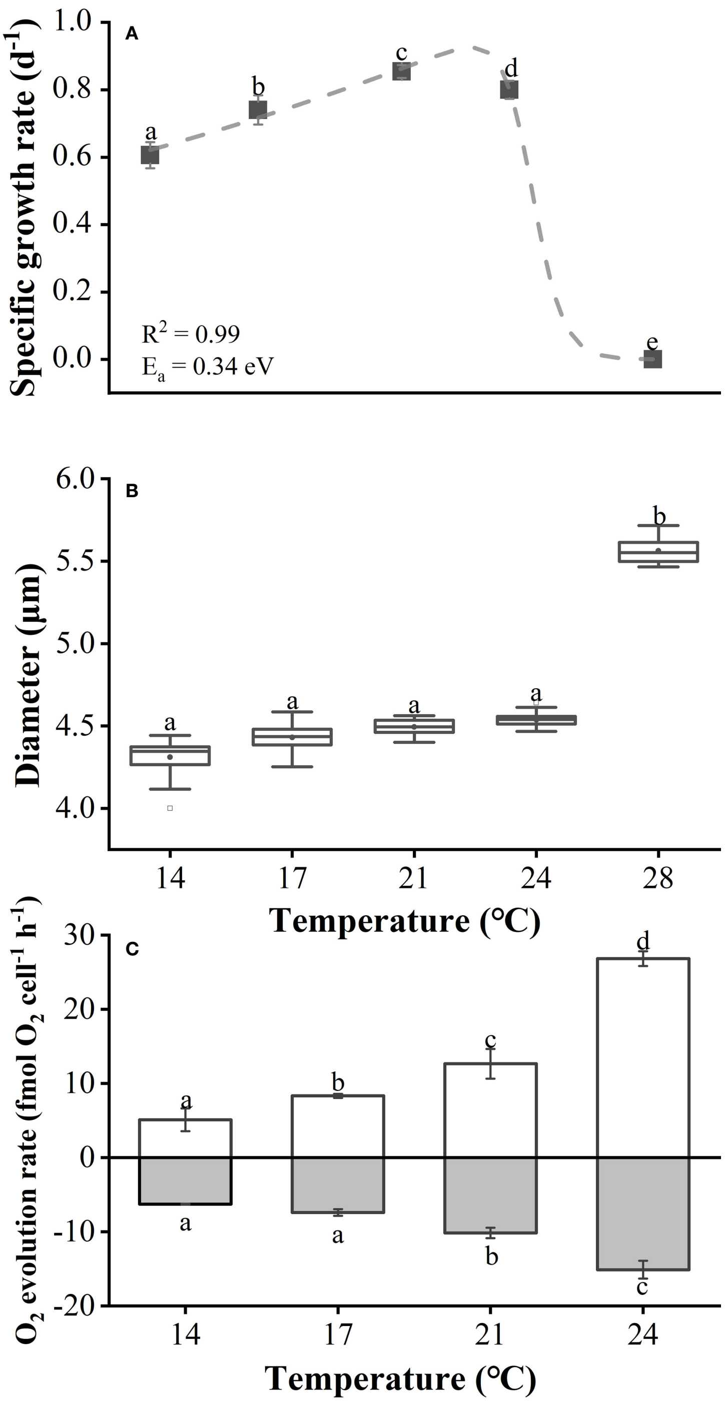

FIGURE 1
Specific growth rate **(A)**, cell diameter **(B)** and the net photosynthesis rates and dark respiration rates **(C)** of *Emiliania huxleyi* BOF92 as a function of growth temperatures. The data was obtained after the cells had acclimated to the growth temperatures for 7-10 days (about 10 generations). Data are mean ± SD (n=3), the different letters above the bars indicate a significant difference between the treatments (p< 0.05, One-way ANOVA).

HSD test, p=0.797), but its value was significantly higher than that of cells from the two elevated temperatures (*post-hoc* Tukey HSD test, p<0.05 for both 21°C and 24°C). Similarly, variation of the minimum saturation light intensity (I_k) also showed the highest value at 17°C, which was significantly higher than those of two elevated temperatures (*post-hoc* Tukey HSD test, p<0.05 for both 21°C and 24°C).

3.2 Long-term warming effects

During the long-term culture (656 days) at 17°C and 21°C, cells had been growing for ~790 and ~830 generations, respectively. The average SGRs under 17°C was 0.84 d^{-1} which was slightly lower than that (0.88 d^{-1}) at 21°C; the elevated seawater temperature thus increased the growth of *E. huxleyi* by 5.28% (Figure 3A,

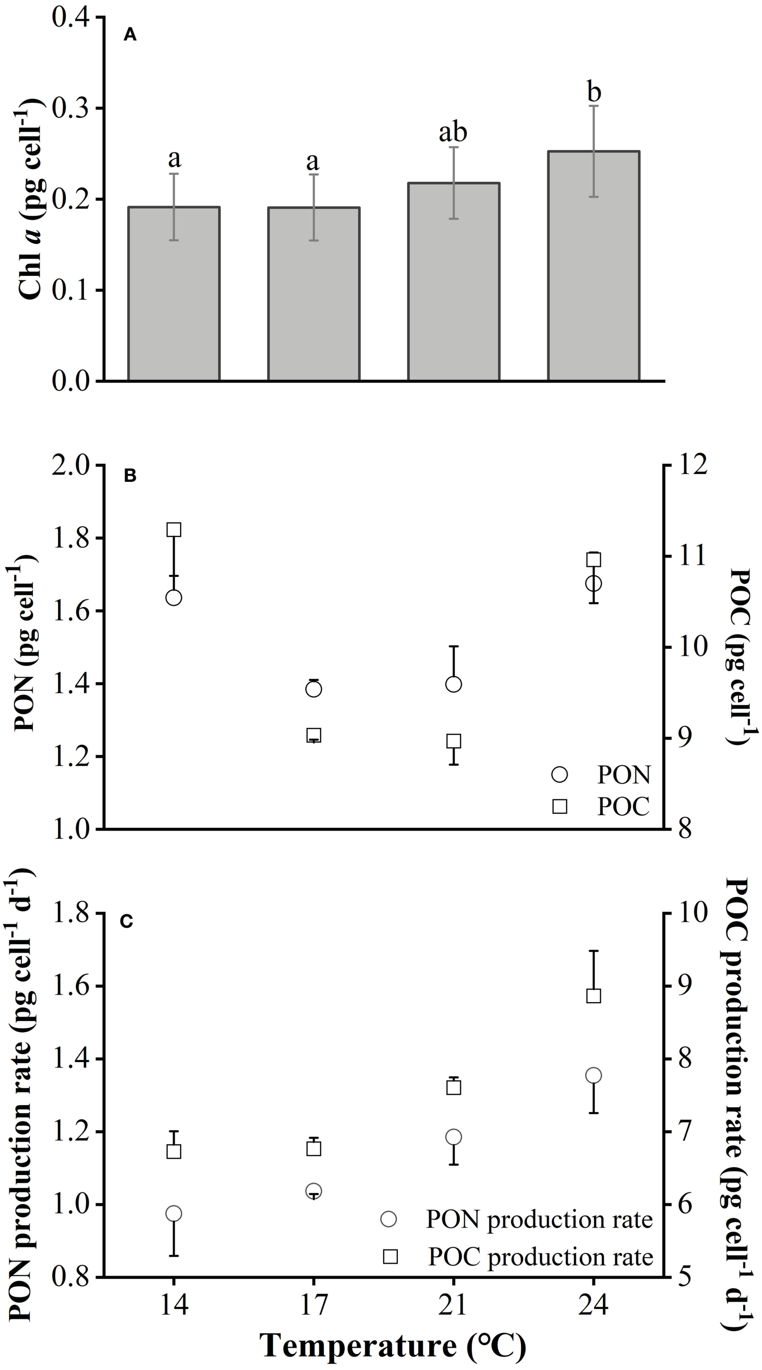

FIGURE 2
Cellular chlorophyll *a* content (Chl *a*) **(A)**, POC and PON contents **(B)** and their production rate **(C)** of *Emiliania huxleyi* BOF92 cultured under short-term exposure to a range of temperatures. Data are mean ± SD (n=3).

Supplementary Table S2). The GAM analysis demonstrated that throughout the whole process, the elevated seawater temperature significantly improved SGR in the first 34 days and last 162 days, and no significant difference in SGR was detected between the control and warming treatments from Day 35 to Day 493 (Figure 3B). The average cell diameter in control and warming treatments were 4.59 µm and 4.64 µm, respectively (Figure 3C; Supplementary Table S4). Although the GAM analysis found that the elevated temperature did enlarge the cell size (Wald tests, p<0.001, Table S4), the pairwise comparisons between control and warming treatments at each day showed no significant difference on most days (Figure 3D). Similar results were also observed in the cellular Chl *a* content (Wald tests, p=0.0205 for temperature, Figure 4, Table S6).

During the long-term culture at 17°C and 21°C, no significant differences (Supplementary Table S8) were observed in both cellular contents of POC (Figure 5A) and PON (Figure 5B), as well as in the ratio of POC to PON (Figure 5C). However, there was a trend that

TABLE 1 The maximum relative electron transfer rate ($rETR_{max}$), the apparent photosynthetic efficiency (α), the degree of photoinhibition(β) and the initial light saturation point (I_k, µmol photons m^{-2} s^{-1}) fitted from rapid light curves as well as the maximum photochemical quantum yields (F_v/F_m), effective photochemical quantum yields (Y(II)) and non-photochemical quenching values (NPQ) for *Emiliania huxleyi* BOF92 cultured under short-term exposure to a range of temperatures.

T (°C)	$rETR_{max}$	α	β	I_k	Y(II)	Fv/Fm	NPQ
14	175.312 ± 9.881^a	0.289 ± 0.006^a	0.045 ± 0.007^{ab}	613.970 ± 24.313^{ab}	0.572 ± 0.004^a	0.639 ± 0.003^a	0.040 ± 0.014^a
17	211.400 ± 15.498^b	0.302 ± 0.006^b	0.052 ± 0.010^b	709.972 ± 79.127^a	0.538 ± 0.086^a	0.638 ± 0.025^a	0.025 ± 0.024^a
21	168.674 ± 9.991^a	0.317 ± 0.009^c	0.033 ± 0.006^a	537.393 ± 70.456^b	0.528 ± 0.072^a	0.651 ± 0.010^a	0.015 ± 0.051^a
24	132.319 ± 5.345^c	0.332 ± 0.009^d	0.028 ± 0.004^a	399.156 ± 27.130^c	0.585 ± 0.015^a	0.658 ± 0.006^a	0.014 ± 0.014^a

Data are means ± SD (n=3), the different letters indicate a significant difference between the treatments ($p < 0.05$, One-way ANOVA).

the cellular contents of POC and PON increased gradually with the time. This was supported by the analysis based on the linear mixed-effects model, which indicated that both the cellular contents of POC and PON were significantly affected by the time (Wald tests, $p<0.001$, Supplementary Table S8).

3.3 Shift experiments

After the 17°C-selection cells were acclimated to 21°C for 7 days, their SGR significantly increased by 22% compared to the cells continuously grown at 17°C (post-hoc Tukey HSD test, $p<0.05$). In contrast, SGR was observed to decrease by 14%, as cells were transferred from 21°C to 17°C (*post-hoc* Tukey HSD test, $p<0.05$, Figure 6A). Changes of temperatures showed no significant effects on cellular POC contents, PON contents, as well as the ratio of POC to PON (Figure 6B for POC contents, 6C for PON contents, 6D for POC : PON). These results suggested that no adaptative changes occurred during the long-term seawater warming treatments.

4 Discussion

In the present study, warming (21°C vs. 17°C) resulted in a steady increase of the specific growth rate after ~600 generations until about 800 generations, showing similar warming-induced

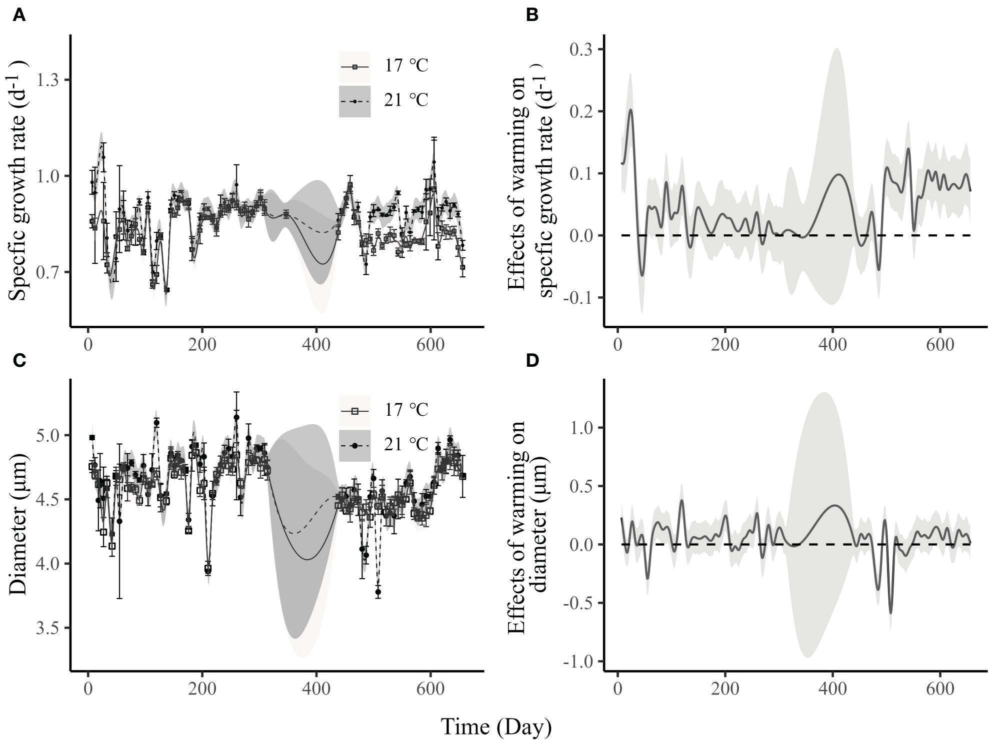

FIGURE 3
The specific growth rate **(A)** and cell diameter **(C)** of *Emiliania huxleyi* BOF92 cultured under 17°C (~790 generations) and 21°C (~830 generations) over the course of the long-term warming experiment; differences in specific growth rate **(B)** and cell diameter **(D)** between 21°C and 17°C treatments. Data are mean ± SD (n=3). Lines with shadow represents the mean with 95% confidential intervals estimated by the generalized additive model. The large uncertainty around Day 400 is due to lack of sampling during the COVID-19 epidemic. In panel B and D, significant differences between the control and warming treatments at certain days are justified by the lack of intersection of the 95% confidence intervals and the x axis.

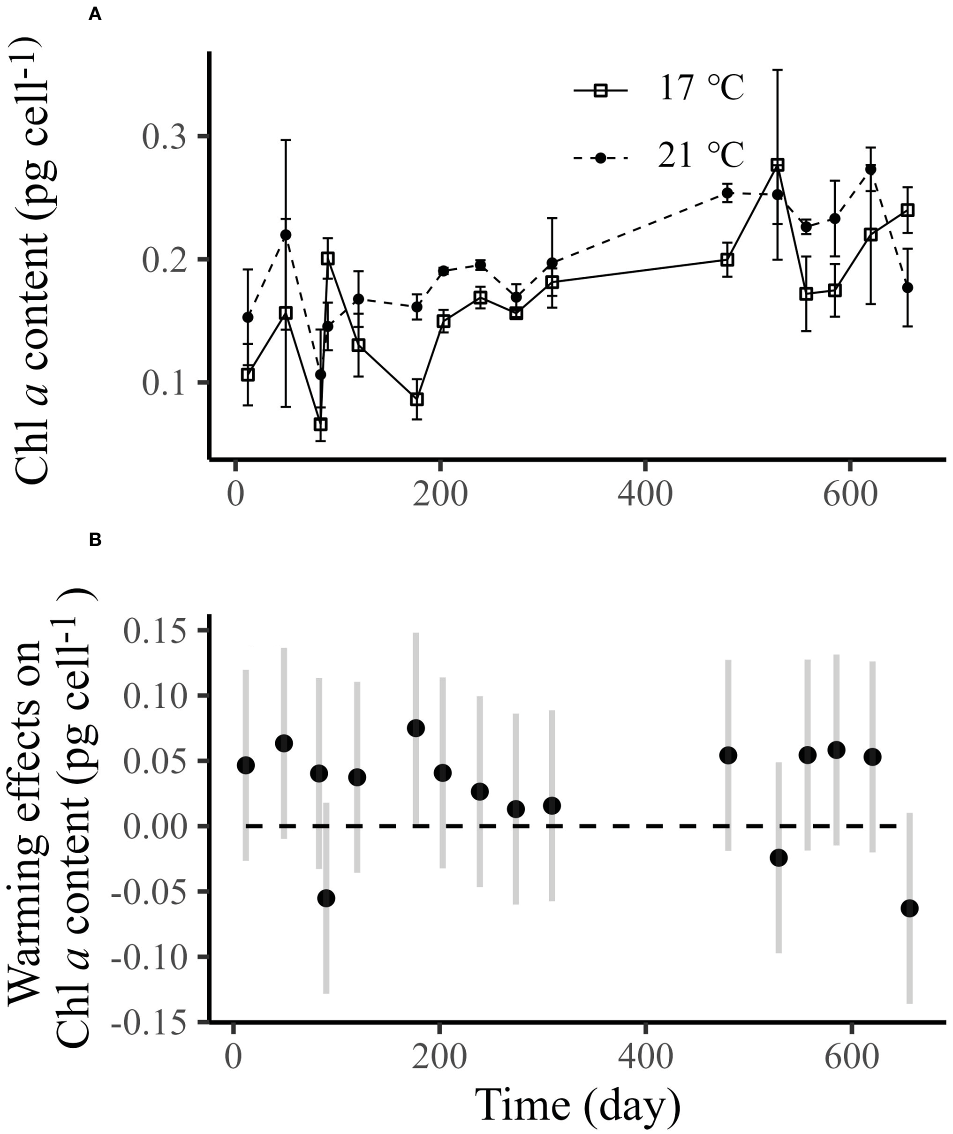

FIGURE 4
Panel **(A)** is the cellular chlorophyll *a* content of *Emiliania huxleyi* BOF92 cultured under 17°C (~790 generations) and 21°C (~830 generations) over the course of long-term seawater warming experiment, and data are mean ± SD (n=3). Panel B shows the differences of cell diameter between 21°C and 17°C, and data are means with 95% confidential intervals estimated by the linear mixed-effect model. In panel **(B)**, significant differences between the control and warming treatments at certain days are justified by the lack of intersection of the 95% confidence intervals and the x axis.

enhancement as in the short acclimation. However, there were no evolutionary traits observed. This finding indicates that non-stressful warming may not bring about any adaptation over the generations span employed here.

4.1 Physiological responses to temperature change

Acceleration of metabolic activity at elevated temperatures is a common response among phytoplankton, which could further prompt their growth (Lund, 1949; Feng et al., 2008; Schaum et al., 2017). However, the temperature rising from 21°C to 24°C further increased photosynthesis and respiration but reduced specific growth rate in the present work. The temperature elevation from 21°C to 24°C stimulated the ability to obtain carbon but also increased the cellular demand for carbon due to increased respiration, leading to reduced rate of growth. Since cellular POC production rates play an important role in global carbon cycles (Poulton et al., 2007), warming from 17°C to 21°C over 800 generations promoted the role of *E. huxleyi* BOF 92 in primary productivity.

While the annual mean temperature of its isolation site was about 17°C, the optimal growth temperature and the upper thermal limit of *E. huxleyi* BOF 92 were found in this work to be ~23°C and ~28°C, respectively. This supports the general understanding that

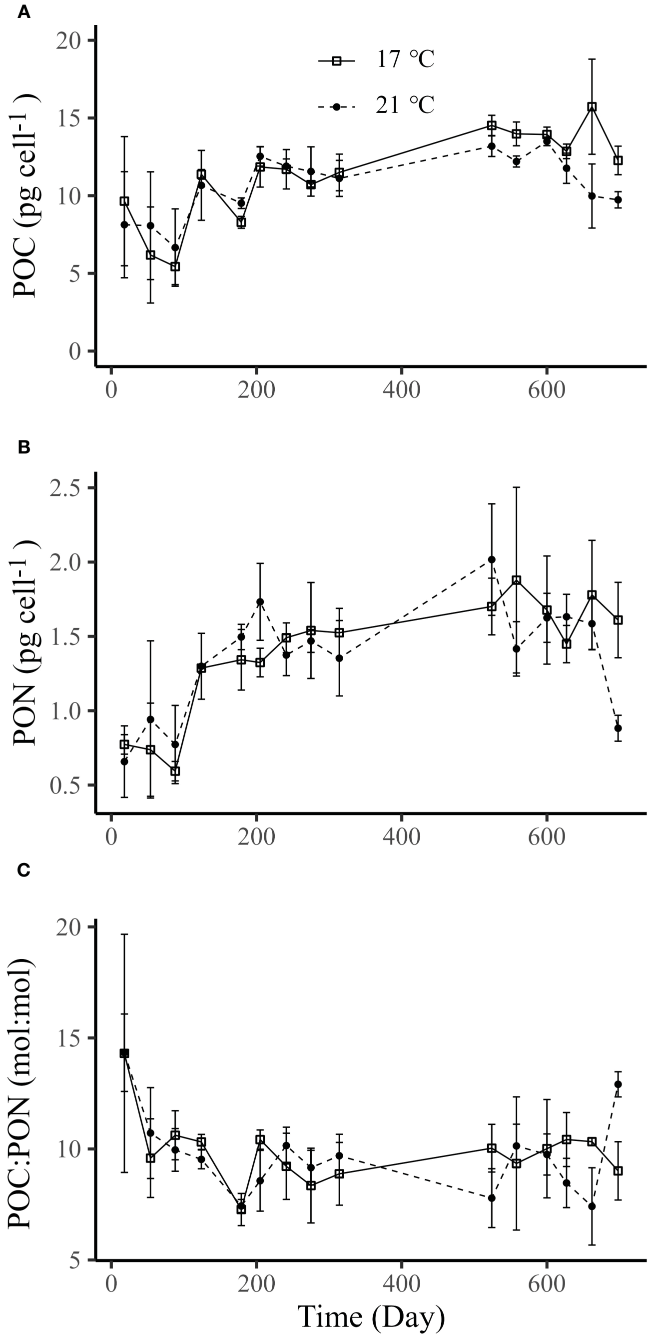

FIGURE 5
Cellular POC **(A)**, PON contents **(B)** and POC/PON ratio **(C)** of *Emiliania huxleyi* BOF92 cultured under 17°C (~790 generations) and 21°C (~830 generations) over the course of the long-term seawater warming experiment. Data are mean ± SD (n=3).

the optimal temperatures of phytoplankton strains from high latitude oceans are considerably higher than their mean annual temperatures (Thomas et al., 2012; Brandenburg et al., 2019). Therefore, *Emiliania huxleyi* living in high latitude oceans might benefit from ocean warming irrespective of other environmental changes that would synchronously occur with it. That the cell size increased at thermal stress (28°C) in this study can be attributed to retardation of nutrient utilization by the cells, leading to reduced cell division (Smith and Kalff, 1982; Savage et al., 2004; Litchman et al., 2007; Marañón, 2015).

4.2 Inconsistent warming effects on growth in the long-term experiment

In the long-term selection experiment, varied response of phytoplankton to warming has been recognized to be related to evolutionary adaptation. For example, in a green alga *Chlorella vulgaris*, population growth was initially (~10 generations) limited at a high temperature because its respiration was more sensitive to temperature than photosynthesis, leading to less carbon utilization for growth (Padfield et al., 2016). However, after acclimating for 100

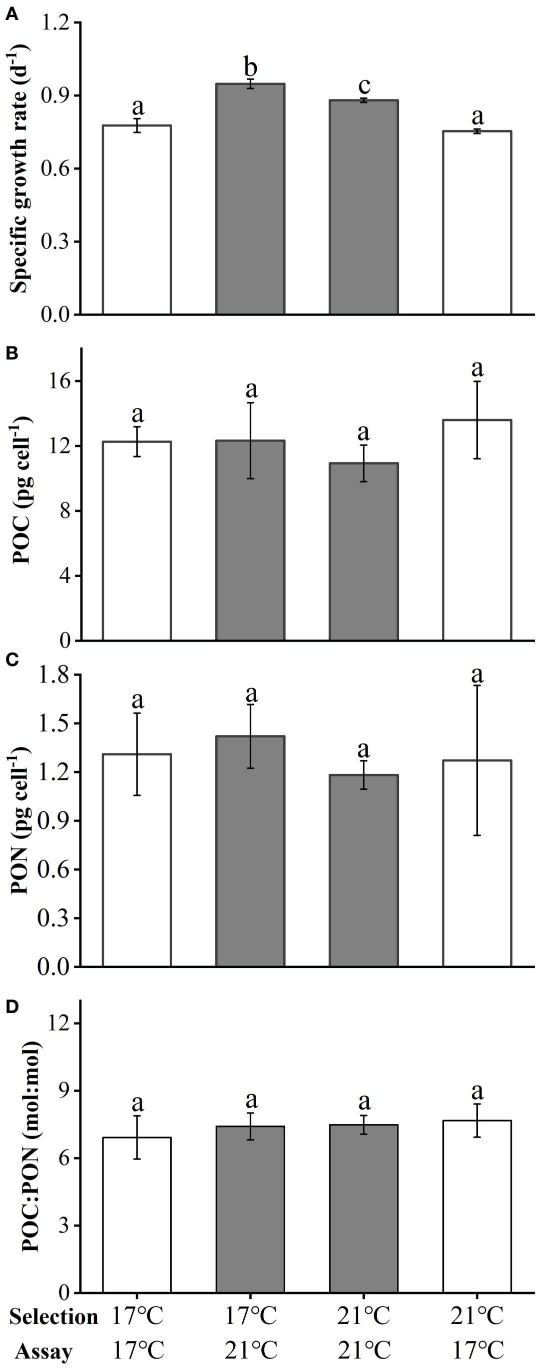

FIGURE 6
The specific growth rate **(A)**, cellular POC **(B)**, PON contents **(C)** and POC/PON ratio **(D)** of *Emiliania huxleyi* BOF92 during the shift experiment. Data are mean ± SD (n=3), the different letters indicate a significant difference between the treatments ($p < 0.05$, One-way ANOVA).

generations under the elevated temperature, the down-regulation of respiration would drive phytoplankton to overcome the metabolic constraint and allocate more fixed carbon to growth (Padfield et al., 2016). In *Chlamydomonas reinhardtii*, the increase in photosynthetic rate, but not a trade-off between respiration and growth, was suggested to be the main adaptive response to warming (Schaum et al., 2017). For *E. huxleyi* BOF 92 examined in this work, warming at 21°C increased its cellular photosynthesis and respiration increased by 53% and 37%, respectively, compared to 17°C (Figure 1C). Such stimulations to both photosynthesis and respiration may be the main reason for the enhancement of growth observed in the early stage of the culture period, but was inconsistent with the lack of effect in the middle stage of the culture period. On the other hand, the growth enhancement after ~600 generations and the shift experiment indicated that selection cultures at 21°C did not bring about any adaptation due to the warming, though both cell quotas of POC and PON gradually increased with duration time (Figure 5). This implies that the non-stressful warming only resulted in plastic acclimatory changes over about 800 generations. In a recently published work on the diatom *Skeletonema dohrnii* (Cheng et al., 2022), warming (24°C vs. 20°C; 28°C vs. 20°C) significantly decreased the cellular POC and PON contents after 300 generations of selection, but the changes were completely recovered after 700 generations of selection. This variation of POC and PON contents was accompanied by significant proteome plasticity (Cheng et al., 2022). The mechanism behind the inconsistent warming effects on growth in our long-term experiment is unclear. Since we did not obtain proteomic or transcriptomic data, future work is needed to link the phenotypic responses to the molecular responses, which may help interpret similar phenomena (Schaum et al., 2018; Jin et al., 2022).

The result that warming-selected cells over about 800 generations shifted back to their ancestral traits (Figure 6) suggest that *E. huxleyi* cells maintained their phenotypic plasticity. While warming could increase the fitness of phytoplankton (Schlüter et al., 2014; Listmann et al., 2016), evolutionary changes can be dependent on thermal stress levels or latitudes. In warm seas, some diatoms adapted to warming with trade-offs in photosynthetic efficiency and growth rate (Jin and Agustí, 2018). By contrast, the warming treatment (21 °C) for *E. huxleyi* BOF 92 from high latitude in our study was below its optimal growth temperature (~23°C), resulting in no adaptation over 800 generations. This implies that mild warming treatment that exerts no selective pressure can hardly give rise to evolutionary change (Xu et al., 2023).

In terms of the long-term adaptation of phytoplankton to environmental changes, its evolutionary process seems to be strain-specific (Supplementary material, Table S9). In coccolithophorids, the existence of coccoliths, i.e. the calcification process, could affect its adaptability to environmental changes. For example, in non-calcified *Gephyrocapsa oceanica* NIES-1318, elevated pCO_2 initially prompted its growth and carbon, nitrogen assimilation rates from generations ~670 to ~1550 (Jin et al., 2013). However, in the same strain with coccoliths, high CO_2-selected populations exhibited reduced growth and calcification rates and enhanced POC and PON production (Tong et al., 2018). *E. huxleyi* BOF 92 cultured in the present study used to be a calcified strain (Paasche, 1999), but lost its calcification capability during the laboratory cultures which lasted for about 30 years. Low light, high nutrients and absence of solar ultraviolet radiations might be responsible for the loss of ability to calcify (Paasche, 2002 and references therein; Guan and Gao, 2010). Nevertheless, the naked cells exhibit the same other morphological features as those of calcified cells (Paasche, 2002), and the measured growth rate and cell size were also comparable with previous reports (Paasche, 1999). Our data in the present study may partially imply the physiological responses of *E. huxleyi* BOF 92 to future warming, but may not be representative of all *E. huxleyi* generally, bearing in mind that this strain might differ genetically from its ancestral form.

Increasing temperature is a key factor that directly determines phytoplankton distribution, production, and metabolic function (Morán et al., 2010; Thomas et al., 2012; Toseland et al., 2013). Its interaction with other environmental drivers, e.g., light irradiance, has also been reported to affect the acclimation of phytoplankton to temperature change (Feng et al., 2008; Edwards et al., 2016). The growth irradiance used in this study (100 µmol photons m^{-2} s^{-1}) is lower than the saturating irradiancies for both growth and photosynthesis (> 200 µmol photons m^{-2} s^{-1}) of *E. huxleyi* BOF 92 (Nanninga and Tyrrell, 1996; Paasche, 2002). Higher irradiance can stimulate the growth and reproduction of *E. huxleyi* BOF 92, resulting in shorter generation times. Theory predicts that populations with shorter generation times evolve faster because of the accumulation of more DNA replication errors per unit time (Weller and Wu, 2015). Therefore, growing *E. huxleyi* BOF 92 population under higher and more favorable irradiance might promote its adaptation to warming. In addition, the increasing seawater temperature induced by additional atmospheric CO_2 accumulation is accompanied by other environmental changes, such as ocean acidification. Studies exploring the adaptative responses of phytoplankton to the combination of ocean warming and acidification suggest that ocean warming might exert a greater impact than ocean acidification and the latter might serve as a modulating factor (Schlüter et al., 2014; Zhong et al., 2021; Jin et al., 2022; Xu et al., 2023; Supplementary Material Table S9). For phytoplankton living in the natural dynamic environment, either an acclimation or an adaptation strategy is essential in determining “winners” and “losers” under the influences of climate changes (Somero, 2010). Different timescales of exposure to a perturbation can result in similar or different physiological responses of phytoplankton species from different regions; when mild warming treatment is applied to phytoplankton strains isolated from cold seas, as in the present work, phenotypic plasticity prevails.

Data availability statement

The original contributions presented in the study are included in the article/Supplementary Material. Further inquiries can be directed to the corresponding author.

Author contributions

KG designed the experiments, CZ, DZ performed the experiments, DZ, XY wrote the original draft, JB, KG reviewed and edited the manuscript. All authors contributed to the article and approved the submitted version.

Funding

This study was supported by the national key R&D program (2022YFC3105303) and National Natural Science Foundation of China (41721005, 41890803).

Acknowledgments

The authors are grateful to the laboratory engineers Xianglan Zeng and Wenyan Zhao for their logistical and technical support and to Dr. Liming Qu for helping maintaining the algal cultures during COVID-19 pandemic.

Conflict of interest

The authors declare that the research was conducted in the absence of any commercial or financial relationships that could be construed as a potential conflict of interest.

Publisher’s note

Supplementary material

The Supplementary Material for this article can be found online at: https://www.frontiersin.org/articles/10.3389/fmars.2023.1211804/full#supplementary-material

References

Arnold, H. E., Kerrison, P., and Steinke, M. (2013). Interacting effects of ocean acidification and warming on growth and DMS-production in the haptophyte coccolithophore *Emiliania huxleyi*. *Global Change Biol.* 19 (4), 1007–1016. doi: 10.1111/gcb.12105

Bach, L. T., Mackinder, L. C., Schulz, K. G., Wheeler, G., Schroeder, D. C., Brownlee, C., et al. (2013). Dissecting the impact of CO_2 and pH on the mechanisms of photosynthesis and calcification in the coccolithophore *Emiliania huxleyi*. *New Phytol.* 199 (1), 121–134. doi: 10.1111/nph.12225

Balch, W., Drapeau, D., Bowler, B., and Booth, E. (2007). Prediction of pelagic calcification rates using satellite measurements. *Deep Sea Res. Part II: Topical Stud. Oceanography* 54 (5-7), 478–495. doi: 10.1016/j.dsr2.2006.12.006

Brandenburg, K. M., Velthuis, M., and Van de Waal, D. B. (2019). Meta-analysis reveals enhanced growth of marine harmful algae from temperate regions with warming and elevated CO_2 levels. *Global Change Biol.* 25 (8), 2607–2618. doi: 10.1111/gcb.14678

Cheng, L.-M., Zhang, S.-F., Xie, Z.-X., Li, D.-X., Lin, L., Wang, M.-H., et al. (2022). Metabolic adaptation of a globally important diatom following 700 generations of selection under a warmer temperature. *Environ. Sci. Technol.* 56 (8), 5247–5255. doi: 10.1021/acs.est.1c08584

Edwards, K. F., Thomas, M. K., Klausmeier, C. A., and Litchman, E. (2016). Phytoplankton growth and the interaction of light and temperature: a synthesis at the species and community level. *Limnology Oceanography* 61 (4), 1232–1244. doi: 10.1002/lno.10282

Eppley, R. W., Holmes, R. W., and Strickland, J. D. (1967). Sinking rates of marine phytoplankton measured with a fluorometer. *J. Exp. Mar. Biol. Ecol.* 1 (2), 191–208. doi: 10.1016/0022-0981(67)90014-7

Feng, Y., Warner, M. E., Zhang, Y., Sun, J., Fu, F. X., Rose, J. M., et al. (2008). Interactive effects of increased pCO_2, temperature and irradiance on the marine coccolithophore *Emiliania huxleyi* (Prymnesiophyceae). *Eur. J. Phycology* 43 (1), 87–98. doi: 10.1080/09670260701664674

Fu, Q., and Gao, K. (2022). Reduced salinity exacerbates the viral infection on the coccolithophorid *Emiliania huxleyi* at elevated pCO_2. *Front. Mar. Sci.* 9. doi: 10.3389/fmars.2022.1091476

Gao, K. (2021). Approaches and involved principles to control pH/pCO_2 stability in algal cultures. *J. Appl. Phycology* 33 (6), 3497–3505. doi: 10.1007/s10811-021-02585-y

Geisen, M., Billard, C., Broerse, A. T., Cros, L., Probert, I., and Young, J. R. (2002). Life-cycle associations involving pairs of holococcolithophorid species: intraspecific variation or cryptic speciation? *Eur. J. Phycology* 37 (4), 531–550. doi: 10.1017/S0967026202003852

Gillooly, J. F., Brown, J. H., West, G. B., Savage, V. M., and Charnov, E. L. (2001). Effects of size and temperature on metabolic rate. *Science* 293 (5538), 2248–2251. doi: 10.1126/science.1061967

Guan, W., and Gao, K. (2010). Impacts of UV radiation on photosynthesis and growth of the coccolithophore *Emiliania huxleyi* (Haptophyceae). *Environ. Exp. Bot.* 67 (3), 502–508. doi: 10.1016/j.envexpbot.2009.08.003

Holligan, P. M., Viollier, M., Harbour, D. S., Camus, P., and Champagne-Philippe, M. (1983). Satellite and ship studies of coccolithophore production along a continental shelf edge. *Nature* 304 (5924), 339–342. doi: 10.1038/304339a0

Jin, P., and Agustí, S. (2018). Fast adaptation of tropical diatoms to increased warming with trade-offs. *Sci. Rep.* 8 (1), 17771. doi: 10.1038/s41598-018-36091-y

Jin, P., Gao, K., and Beardall, J. (2013). Evolutionary responses of a coccolithophorid gephyrocapsa oceanica to ocean acidification. *Evolution* 67 (7), 1869–1878. doi: 10.1111/evo.12112

Jin, P., Wan, J., Zhou, Y., Gao, K., Beardall, J., Lin, J., et al. (2022). Increased genetic diversity loss and genetic differentiation in a model marine diatom adapted to ocean warming compared to high CO_2. *ISME J.* 16 (11), 2587–2598. doi: 10.1038/s41396-022-01302-y

Leonardos, K., and Geider, R. J. (2005). Elevated atmospheric carbon dioxide increases organic carbon fixation by *Emiliania huxleyi* (haptophyta), under nutrient-limited high-light conditions. *J. Phycology* 41, 1196–1203. doi: 10.1111/j.1529-8817.2005.00152.x

Listmann, L., LeRoch, M., Schlüter, L., Thomas, M. K., and Reusch, T. B. H. (2016). Swift thermal reaction norm evolution in a key marine phytoplankton species. *Evolutionary Appl.* 9 (9), 1156–1164. doi: 10.1111/eva.12362

Litchman, E., Klausmeier, C. A., Schofield, O. M., and Falkowski, P. G. (2007). The role of functional traits and trade-offs in structuring phytoplankton communities: scaling from cellular to ecosystem level. *Ecol. Lett.* 10 (12), 1170–1181. doi: 10.1111/j.1461-0248.2007.01117.x

Lund, J. W. G. (1949). Studies on asterionella: i. the origin and nature of the cells producing seasonal maxima. *J. Ecol.* 37, 389–419. doi: 10.2307/2256614

Marañón, E. (2015). Cell size as a key determinant of phytoplankton metabolism and community structure. *Annu. Rev. Mar. Sci.* 7, 241–264. doi: 10.1146/annurev-marine-010814-015955

Masson-Delmotte, V., Zhai, P., Pirani, A., Connors, S. L., Péan, C., Chen, Y., et al. (2021). *IPCC 2021: climate change 2021: the physical science basis. contribution of working group I to the sixth assessment report of the intergovernmental panel on climate change* (Cambridge: Cambridge University Press).

McKew, B. A., Metodieva, G., Raines, C. A., Metodiev, M. V., and Geider, R. J. (2015). Acclimation of *Emiliania huxley*) to nutrient limitation involves precise modification of the proteome to scavenge alternative sources of n and p. *Environ. Microbiol.* 17 (10), 4050–4062. doi: 10.1111/1462-2920.12957

Morán, X. A. G., López-Urrutia, Ángel., Calvo-Díaz, A., and Li, W. K. (2010). Increasing importance of small phytoplankton in a warmer ocean. *Global Change Biol.* 16 (3), 1137–1144. doi: 10.1111/j.1365-2486.2009.01960.x

Nanninga, H. J., and Tyrrell, T. (1996). Importance of light for the formation of algal blooms by *Emiliania huxleyi*. *Mar. Ecol. Prog. Ser.* 136, 195–203. doi: 10.3354/meps136195

Paasche, E. (1999). Reduced coccolith calcite production under light-limited growth: a comparative study of three clones of *Emiliania huxleyi* (Prymnesiophyceae). *Phycologia* 38 (6), 508–516. doi: 10.2216/i0031-8884-38-6-508.1

Paasche, E. (2002). A review of the coccolithophorid *Emiliania huxleyi* (Prymnesiophyceae), with particular reference to growth, coccolith formation, and calcification-photosynthesis interactions. *Phycologia* 40 (6), 503–529. doi: 10.2216/i0031-8884-40-6-503.1

Paasche, E., Brubak, S., Skattebøl, S., Young, J. R., and Green, J. C. (1996). Growth and calcification in the coccolithophorid *Emiliania huxleyi* (Haptophyceae) at low salinities. *Phycologia* 35 (5), 394–403. doi: 10.2216/i0031-8884-35-5-394.1

Padfield, D., Yvon-Durocher, G., Buckling, A., Jennings, S., and Yvon-Durocher, G. (2016). Rapid evolution of metabolic traits explains thermal adaptation in phytoplankton. *Ecol. Lett.* 19 (2), 133–142. doi: 10.1111/ele.12545

Pinheiro, J. C., and Bates, D. M. (2006). *Mixed-effects models in S and S-PLUS* (New York, NY: Springer).

Platt, T. G. C. L., Gallegos, C. L., and Harrison, W. G. (1980). Photoinhibition of photosynthesis in natural assemblages of marine phytoplankton. *J. Mar. Res.* 38, 687–701.

Porra, R. J. (2002). The chequered history of the development and use of simultaneous equations for the accurate determination of chlorophylls *a* and *b*. *Photosynthesis Res.* 73, 149–156. doi: 10.1023/A:1020470224740

Pörtner, H.-O., Roberts, D. C., Masson-Delmotte, V., Zhai, P., Tignor, M., Poloczanska, E., et al. (2019). "IPCC special report on the ocean and cryosphere in a changing climate," in *IPCC intergovernmental panel on climate change*, vol. 1. (Cambridge, UK and New York, NY, USA: Cambridge University Press).

Poulton, A. J., Adey, T. R., Balch, W. M., and Holligan, P. M. (2007). Relating coccolithophore calcification rates to phytoplankton community dynamics: regional differences and implications for carbon export. *Deep Sea Res. Part II: Topical Stud. Oceanography* 54 (5-7), 538–557. doi: 10.1016/j.dsr2.2006.12.003

Raven, J. A., and Geider, R. J. (1988). Temperature and algal growth. *New Phytol.* 110 (4), 441–461. doi: 10.1111/j.1469-8137.1988.tb00282.x

Rost, B., and Riebesell, U. (2004). *Coccolithophores and the biological pump: responses to environmental changes* (Berlin, Heidelberg: Coccolithophores, Springer), 99–125.

Savage, V. M., Gillooly, J. F., Brown, J. H., West, G. B., and Charnov, E. L. (2004). Effects of body size and temperature on population growth. *Am. Nat.* 163 (3), 429–441. doi: 10.1086/381872

Schaum, C. E., Barton, S., Bestion, E., Buckling, A., Garcia-Carreras, B., Lopez, P., et al. (2017). Adaptation of phytoplankton to a decade of experimental warming linked to increased photosynthesis. *Nat. Ecol. Evol.* 1 (4), 0094. doi: 10.1038/s41559-017-0094

Schaum, C. E., Buckling, A., Smirnoff, N., Studholme, D. J., and Yvon-Durocher, G. (2018). Environmental fluctuations accelerate molecular evolution of thermal tolerance in a marine diatom. *Nat. Commun.* 9 (1), 1719. doi: 10.1038/s41467-018-03906-5

Schlüter, L., Lohbeck, K. T., Gutowska, M. A., Gröger, J. P., Riebesell, U., and Reusch, T. B. H. (2014). Adaptation of a globally important coccolithophore to ocean warming and acidification. *Nat. Climate Change* 4 (11), 1024–1030. doi: 10.1038/nclimate2379

Schoolfield, R. M., Sharpe, P. J. H., and Magnuson, C. E. (1981). Non-linear regression of biological temperature-dependent rate models based on absolute reaction-rate theory. *J. Theor. Biol.* 88 (4), 719–731. doi: 10.1016/0022-5193(81)90246-0

Smith, R. E., and Kalff, J. (1982). Size-dependent phosphorus uptake kinetics and cell quota in phytoplankton. *J. Phycology* 18 (2), 275–284. doi: 10.1111/j.1529-8817.1982.tb03184.x

Somero, G. N. (2010). The physiology of climate change: how potentials for acclimatization and genetic adaptation will determine 'winners' and 'losers'. *J. Exp. Biol.* 213 (6), 912–920. doi: 10.1242/jeb.037473

Thomas, M. K., Kremer, C. T., Klausmeier, C. A., and Litchman, E. (2012). A global pattern of thermal adaptation in marine phytoplankton. *Science* 338 (6110), 1085–1088. doi: 10.1126/science.1224836

Tong, S., Gao, K., and Hutchins, D. A. (2018). Adaptive evolution in the coccolithophore *Gephyrocapsa oceanica* following 1,000 generations of selection under elevated CO_2. *Global Change Biol.* 24 (7), 3055–3064. doi: 10.1111/gcb.14065

Toseland, A., Daines, S. J., Clark, J. R., Kirkham, A., Strauss, J., Uhlig, C., et al. (2013). The impact of temperature on marine phytoplankton resource allocation and metabolism. *Nat. Climate Change* 3 (11), 979–984. doi: 10.1038/nclimate1989

van Rij, J., Hendriks, P., van Rijn, H., Baayen, R. H., and Wood, S. N. (2019). Analyzing the time course of pupillometric data. *Trends Hearing* 23, 2331216519832483. doi: 10.1177/2331216519832483

Weller, C., and Wu, M. (2015). A generation-time effect on the rate of molecular evolution in bacteria. *Evolution* 69 (3), 643–652. doi: 10.1111/evo.12597

Wood, S. N. (2017). *Generalized additive models: an introduction with r* (Chapman and Hall/CRC).

Xu, K., Gao, K., Villafañe, V. E., and Helbling, E. W. (2011). Photosynthetic responses of *Emiliania huxleyi* to UV radiation and elevated temperature: roles of calcified coccoliths. *Biogeosciences* 8 (6), 1441–1452. doi: 10.5194/bg-8-1441-2011

Xu, D., Zheng, G., Brennan, G., Wang, Z., Jiang, T., Sun, K., et al. (2023). Plastic responses lead to increased neurotoxin production in the diatom *Pseudo-nitzschia* under ocean warming and acidification. *ISME J.* 17, 525–536. doi: 10.1038/s41396-023-01370-8

Yi, X., Fu, F. X., Hutchins, D. A., and Gao, K. (2020). Light availability modulates the effects of warming in a marine N_2 fixer. *Biogeosciences* 17 (4), 1169–1180. doi: 10.5194/bg-17-1169-2020

Zhang, Y., Zhang, Y., Ma, S., Chen, H., Li, J., Li, Z., et al. (2023). Reallocation of elemental content and macromolecules in the coccolithophore *Emiliania huxleyi* to acclimate to climate change. *Biogeosciences* 20 (7), 1299–1312. doi: 10.5194/bg-20-1299-2023

Zhong, J., Guo, Y., Liang, Z., Huang, Q., Lu, H., Pan, J., et al. (2021). Adaptation of a marine diatom to ocean acidification and warming reveals constraints and trade-offs. *Sci. Total Environ.* 771, 145167. doi: 10.1016/j.scitotenv.2021.145167

Zuur, A. F., Ieno, E. N., Walker, N. J., Saveliev, A. A., and Smith, G. M. (2009). *Mixed effects models and extensions in ecology with r* (New York, NY: Springer).

frontiers | Frontiers in Marine Science

TYPE Original Research
PUBLISHED 21 July 2023
DOI 10.3389/fmars.2023.1204508

Inapparent decrease in phytoplankton biomass accompanied by significant size composition succession in the shellfish aquaculture farm in the western Taiwan strait

Yu Mo[1,2,3], Aifeng Li[2,4], Zhaohe Luo[1], Cun Jia[1], Rimei Ou[1], Jinli Qiu[1], Xinyu Chang[1,5], Hao Huang[1] and Lei Wang[1]*

[1]Fujian Provincial Key Laboratory of Marine Ecological Conservation and Restoration, Third Institute of Oceanography, Ministry of Natural Resources, Xiamen, China, [2]College of Environmental Science and Engineering, Ocean University of China, Qingdao, China, [3]Guangxi Key Laboratory of Polysaccharide Materials and Modification, School of Marine Sciences and Biotechnology, Guangxi Minzu University, Nanning, China, [4]Key Laboratory of Marine Environment and Ecology, Ocean University of China, Ministry of Education, Qingdao, China, [5]College of Fisheries and Life Science, Dalian Ocean University, Dalian, China

We conducted an annual monthly sampling in the aquaculture areas of Lianjiang and Zhangpu, Fujian province, in the west coast of the Taiwan Strait, to gain insight into the effects of shellfish aquaculture on total phytoplankton biomass and its distribution in phytoplankton size fractions. We observed that the total chlorophyll-a (TChl-a) concentration was higher in Zhangpu (annual mean 2.690 ± 2.375 µg/L) than in Lianjiang (annual mean 1.700 ± 1.500 µg/L) and that Lianjiang had a high N/P ratio during the study, which may have been the main reason for the differences in phytoplankton biomass between the two shellfish aquaculture areas. The response of phytoplankton to shellfish aquaculture was different in the northern versus southern areas. During the aquaculture period of Lianjiang, the TChl-a concentration of surface water was approximately 14% lower than that of bottom water, and such a decreasing trend of Chl-a concentration was consistently present in micro-, nano-, and pico-size fractions. Phytoplankton depletion was not observed during investigation in Zhangpu, which showed highly variable in environmental factors. The contribution of pico-sized Chl-a to TChl-a is evaluated by shellfish aquaculture to some extent in Lianjiang. The shift from the dominance of nano-phytoplankton to the dominance of micro- phytoplankton and pico-phytoplankton was caused mainly by seasonal variation in environmental conditions. In complex marine environments, the distribution of phytoplankton biomass in phytoplankton size fractions showed no significant response to shellfish aquaculture.

KEYWORDS

phytoplankton, size structure, aquaculture, hydrodynamic, Taiwan strait

Check for updates

OPEN ACCESS

EDITED BY
Susana Carvalho,
King Abdullah University of Science and Technology, Saudi Arabia

REVIEWED BY
Solomon Dan,
Beibu Gulf University, China
Jiaxing Liu,
Chinese Academy of Sciences (CAS), China

*CORRESPONDENCE
Lei Wang
wanglei@tio.org.cn

RECEIVED 12 April 2023
ACCEPTED 05 July 2023
PUBLISHED 21 July 2023

CITATION
Mo Y, Li A, Luo Z, Jia C, Ou R, Qiu J, Chang X, Huang H and Wang L (2023) Inapparent decrease in phytoplankton biomass accompanied by significant size composition succession in the shellfish aquaculture farm in the western Taiwan strait. *Front. Mar. Sci.* 10:1204508. doi: 10.3389/fmars.2023.1204508

1 Introduction

Coastal ecosystems, as transitional zones for material and energy exchange at land-sea interface, are facing frequent anthropogenic disturbances that affect aquatic biota (Srichandan et al., 2019). As the environment deteriorates and pressure on natural fisheries, aquaculture is experiencing rapid development, with shellfish as the world's largest aquaculture species in terms of production (FAO, 2020). Shellfish is capable of filtering plankton and particulate organic matters from the water for growth (Dame, 2011). The filtration of plankton by shellfish may exert a top-down control on the plankton community (Ward & Shumway, 2004). Meanwhile, the metabolism and excretion of shellfish affect the turnover rates and stoichiometry of nutrients (Souchu et al., 2001), thereby exerting bottom-up control on phytoplankton. Intensive coastal aquaculture may amplify these two processes, thereby exacerbating anthropogenic disturbances to offshore ecosystems.

Phytoplankton are sensitive indicators of changes in coastal ecosystems due to their high growth rate to a short-term anthropogenic disturbances or natural environmental variation (Paerl et al., 2006). For shellfish aquaculture system, a decrease in phytoplankton abundance and changes in phytoplankton community composition has been observed in poorly flushed waters as a result of high filtration rates of shellfish feeding (Ogilvie et al., 2000; Strohmeier et al., 2008; Jiang et al., 2016). Active feeding by shellfish affects production of the dominant phytoplankton species (Newell, 2004), meanwhile the feeding preferences can efficiently remove some certain type or class of phytoplankton (Rosa et al., 2017). Phytoplankton depletion was commonly found in micro- and nano-sized fraction, resulting in high abundance of picoplankton (Trottet et al., 2008; Smaal et al., 2013; Jiang et al., 2016). Moreover, the efficient recycle of nitrogen and phosphorus relative to silica through shellfish metabolism, may favors the growth of non-diatom microalgae (Newell, 2004; Lucas et al., 2016). These interaction between shellfish and phytoplankton are affected by system flushing rate (Newell et al, 2005). Short residence time precludes the accumulation of phytoplankton biomass, which affect food availability for shellfish, and plays a key role in the advection of nutrients and/or phytoplankton (Filgueira et al., 2016; Campbell & Hall, 2019). Hydrodynamics may complicate the impact of aquaculture on phytoplankton.

The Taiwan Strait (TWS) is a typical strait ecosystem, and is an important channel between the East China Sea (ECS) and the South China Sea (SCS). Circulations in the TWS are strongly influenced by the East Asian monsoon. The SCS Warm Current and Kuroshio Current intrude into the TWS in both monsoon seasons, with stronger invasion along the middle and eastern TWS during the northeast (NE) monsoon (September-March) (Zhong et al., 2020). Wind-driven with topographic forcing upwellings (e.g. Dongshan upwelling, Pingtan upwelling) occur during southwest (SW) monsoon (June-August) (Tang et al., 2002). Meanwhile, low-salinity water from the Min River, the Jiulong River, the Han River and even the Pearl River also extends into the TWS (Hong et al., 2011). Significantly different water masses produced great heterogeneity in the physics, chemistry and biology of the TWS (Hong et al., 2011; Zhong et al., 2020). Moreover, the human forces along the west coast of the TWS is rising up along with the development of socioeconomics (Dai et al., 2023). The eutrophication coupled with the recurrent of harmful algal blooms (HABs) are threatening the ecosystem stability, with increasing HABs occurring in the northern TWS (Peng et al., 2021).

Accumulating human impacts could pose a threat to coastal ecosystem, and an understanding of dynamic aquaculture-environment interactions is important for effective coastal management (Filgueira et al., 2016; Dai et al., 2023). The impact of aquaculture on coastal water provides essential information for a balance between production and protection. Control of phytoplankton by shellfish farming in the western TWS is not well studied. We hypothesized that the impact of shellfish aquaculture on phytoplankton differs from different hydrodynamics conditions. Annual surveys were conducted in two typical aquaculture areas in the northern and southern regions of the TWS to a) quantify the contribution of different phytoplankton size classes to the total biomass, and b) evaluate the impact of aquaculture on phytoplankton size class patterns and the surrounding ecosystem.

2 Materials and methods

2.1 Description of the study sites

The shellfish aquaculture farming of Lianjiang and Zhangpu are located in the north and south coastal areas of the western TWS, respectively, with water depth less than 10 m (Figure 1). The Zhangpu site is located in the seasonal upwelling-influenced area of Dongshan (Figure 1A), and the Lianjiang site is near the Min River estuary (Figure 1B) (Hong et al., 2011; Zhong et al., 2020). These sites are subjected to the SW monsoon from June to August and the NE monsoon from September to March, with April and May being the monsoon transition period (Jan et al., 2006). Except for its southern region, the TWS is dominated by regular semi-diurnal tides (Hong et al., 2011), with an average tidal current amplitude of 0.46 m/s and a maximum amplitude of 0.80 m/s at in the northeast and southeast of the strait entrance (Wang et al., 2003).

Fujian Province, which is on the west coast of the TWS, is the second-largest seawater aquaculture province in China, with oyster and abalone as the main shellfish aquaculture species, and the numbers of shellfish aquaculture farming increasing gradually from north to south (Peng et al., 2021; Liu et al., 2022; Ma et al., 2022). The combined investigation of oyster and abalone aquaculture can provide an overall understanding of phytoplankton biomass and size composition affected by shellfish aquaculture in the western TWS. The oyster aquaculture period in Lianjiang was February-August, while abalone aquaculture occurs only in December and from February to April. During the warm season, the abalone was transferred to the north of China. The aquaculture season in Zhangpu is longer. It takes place almost all year round, except July-August for oyster, and January-February for abalone. Both

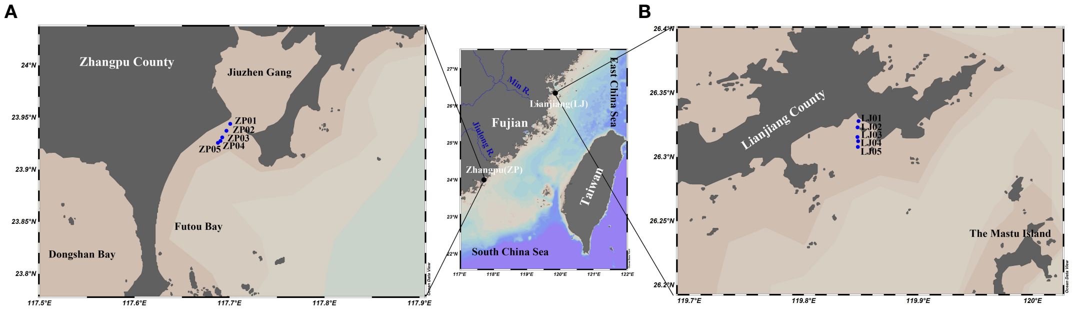

FIGURE 1
Sampling sites in Taiwan strait. Zhangpu site **(A)**, Lianjiang site **(B)**.

types of shellfish are cultured with rafts, with culture rope/cages placed at a depth of about 1 m underwater.

2.2 Sampling

Monthly surveys were conducted from October 2021 to September 2022. Three groups of sampling sites, including one reference station, two oyster aquaculture stations, and two abalone aquaculture stations, were set up in each of the Lianjiang and Zhangpu shellfish aquaculture farming. To assess the effects of seawater shellfish aquaculture on the total phytoplankton biomass and its distribution in phytoplankton size fractions, we delineated culture and non-culture periods for each of the two shellfish species according to its aquaculture periods.

Surface water and bottom water sampling was conducted using a Plexiglas water collector during the field investigation (the absent of bottom water in Lianjiang during March–April and June, and the absent of bottom water in Zhangpu in March). Temperature, salinity, dissolved oxygen (DO), and turbidity were *in situ* measured using YSI multiparameter EXO-3 (Yellow Springs Instrument, Yellow Springs, OH, USA). Nutrient concentrations were determined by colorimetry using a nutrient analyzer (QuaTro, Seal Analytical, Mequon, WI, USA) (Strickland and Parsons, 1972), and the limit of detection for NH_4-N, NO_3-N, NO_2-N, soluble reactive phosphorus (SRP), and dissolved silicate (DSi) was 0.02, 0.01, 0.02, 0.004, and 0.005 µmol/L, respectively. Dissolved inorganic nitrogen (DIN) was determined as the sum of NO_3-N, NO_2-N, and NH_4-N.

2.3 Chlorophyll-a

At each station, 0.1–2.0 L of water samples were vacuum filtered (vacuum pressure<0.02 MPa) using 25 mm diameter membranes with a pore size of 20 µm (Nylon membrane filters, Millipore, Burlington, MA, USA), 2.7 µm (GF/D, Whatman, Maidstone, UK), or 0.3 µm (GF-75, Advantec, Toyo Roshi Kaisha, Japan). The full-size chlorophyll-a (Chl-a) was acquired according to the GF-75 filter, and we modified the size-fractional Chl-a concentration for >20 µm, 2.7–20 µm, and 0.3–2.7 µm to represent micro-, nano-, and pico-phytoplankton, respectively (Sieburth et al., 1978). The collected filters were placed in 5 mL plastic centrifuge tubes and 90% acetone was added, followed by extraction in dark at −20°C for 24 h. Fluorometric analysis of Chl-a was performed using a Turner Designs Model fluorometer (Model No. Trilogy 040, San Jose, CA, USA) (Strickland and Parsons, 1972).

2.4 Definition of phytoplankton depletion index

A phytoplankton depletion index (PDI, %) was modified from Filgueira et al. (2014):

Phytoplankton depletion index. (PDL, %) $= \frac{[\mathrm{Chl-a}]_{surf.}}{[\mathrm{Chl-a}]_{bot.}} \times 100 - 100$, where $[\mathrm{Chl\text{-}a}]_{\mathrm{surf.}}$ and $[\mathrm{Chl\text{-}a}]_{\mathrm{bot.}}$ are the concentrations of a certain type of Chl-a at surface water and bottom water, respectively. Values of this ratio below 0% indicate depletion, whereas values above 0% indicate enrichment of a certain Chl-a in the surface water compared with that in the bottom water.

2.5 Statistic analysis

Data analyses were performed using Origin 2023. The nonparametric Wilcoxon test and Kruskal-wallis ANOVA were performed to evaluate the differences in surface and bottom water, culture period and non-culture period, respectively. The differences with $p<0.05$ were considered to be significant. Multiple correlations of Redundancy analysis (RDA) were used to understand the ecological linkage between physicochemical and biological variables of different seasons (Clarke and Warwick, 2001).

3 Results

3.1 Hydrological parameters

Seasonal changes in water temperature, salinity, DO, and turbidity are shown in Figures 2A–D. Surface water temperature varied from 10.3°C to 31.9°C in Lianjiang. Compared with other months in Lianjiang, salinity was significantly lower in June to

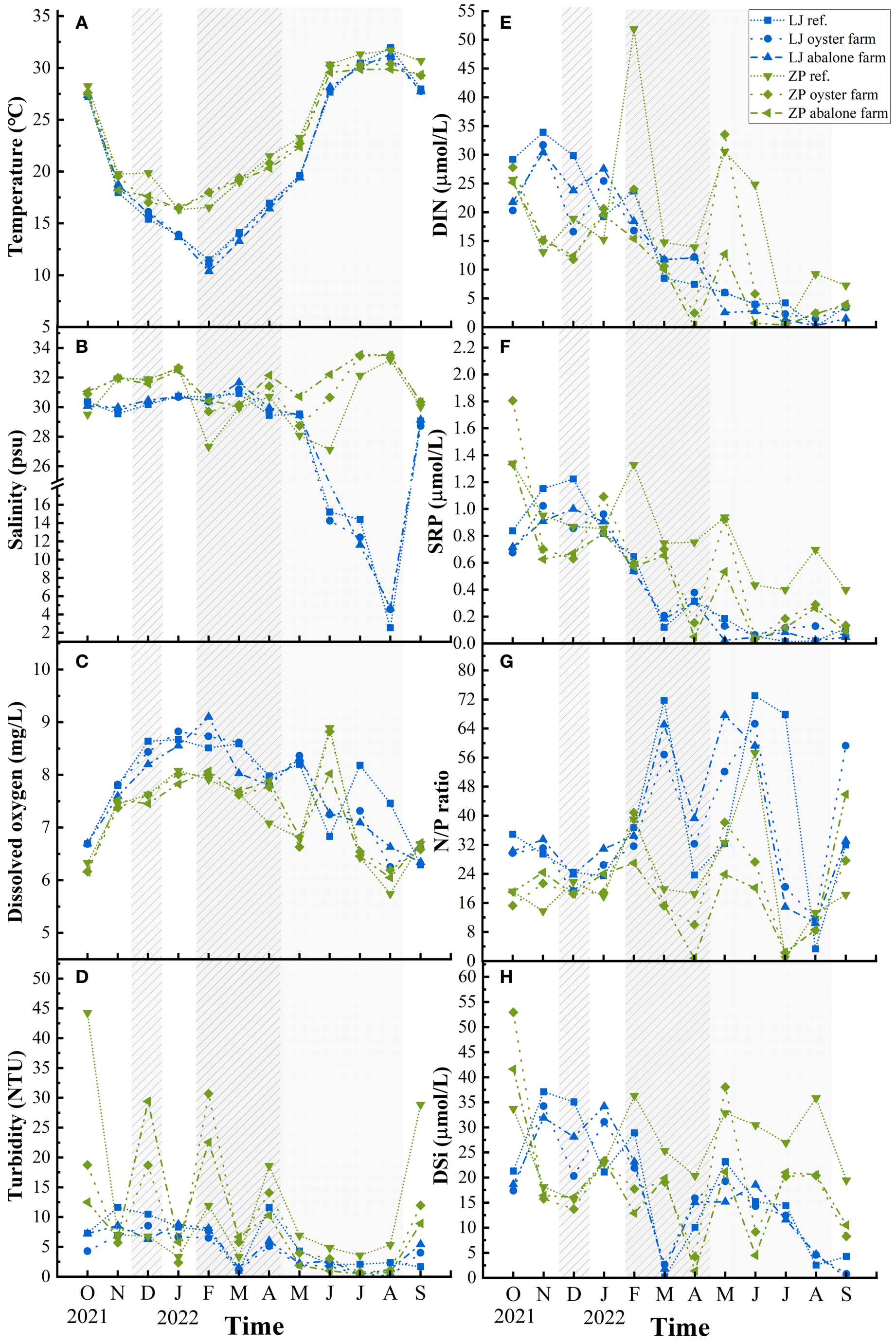

FIGURE 2
Temporal and spatial variations of surface environmental parameters in Lianjiang site and Zhangpu site. Grey and shaded areas represent oyster and abalone culture period in Lianjiang. Culture periods in Zhangpu cover a whole year, except Jul. and Aug. for oyster and Jan. and Feb. for abalone. **(A)** temperature; **(B)** salinity; **(C)** dissolved oxygen; **(D)** Turbidity; **(E)** dissolved inorganic nitrogen; **(F)** soluble reactive phosphate; **(G)** N/P ratio; **(H)** dissolved inorganic silicate.

August ($p < 0.01$) and varied from 2.5 to 19.6. Except for March, the salinity in all months was lower than 30. DO and turbidity distributed in a similar pattern, being high in the cold season and low in warm season.

Surface water temperature in Zhangpu varied from 16.3°C to 31.7°C. Salinity of the aquaculture stations increased to 33.6 in July and August. Compared with the aquaculture stations, salinity of the reference station varied to a smaller extent, being lower than 30 in February–May. DO peaked sharply in June, and turbidity showed great fluctuations in the cold season. Differences in water temperature, DO, and turbidity between surface and bottom waters was observed at both aquaculture areas (Table 1).

TABLE 1 Averages of environmental parameters and size-fractioned concentration of Chl-a in surface and bottom water of Lianjiang and Zhangpu sites during culture and nonculture period.

	LJ culture period		LJ nonculture period		ZP culture period		ZP nonculture period	
Parameters	Surface	Bottom	Surface	Bottom	Surface	Bottom	Surface	Bottom
T	19.7 ± 8.3**	18.2 ± 7.0**	21.8 ± 7.7	21.1 ± 6.1	23.7 ± 5.2**	23.4 ± 4.8**	24.2 ± 6.2**	23.7 ± 6.2**
S	22.9 ± 10.5	23.6 ± 9.6	26.8 ± 7.8	26.6 ± 8.2	31.4 ± 1.2	31.5 ± 1.2	31.3 ± 2.0	31.4 ± 1.9
DO	7.99 ± 0.98	7.38 ± 1.98	7.64 ± 0.86	7.33 ± 1.20	7.22 ± 0.80*	7.09 ± 0.90*	7.17 ± 0.84*	7.10 ± 0.88*
Turb.	3.91 ± 3.23**	10.78 ± 5.23**	5.73 ± 3.06	9.28 ± 4.98	10.0 ± 10.6**	21.3 ± 23.5**	10.6 ± 11.9**	17.1 ± 17.2**
DIN	11.46 ± 8.69	9.65 ± 7.66	16.10 ± 12.00	16.00 ± 11.09	12.09 ± 10.48	11.42 ± 10.25	15.07 ± 12.46	12.74 ± 9.75
SRP	0.409 ± 0.327	0.408 ± 0.295	0.550 ± 0.421	0.524 ± 0.412	0.543 ± 0.496	0.500 ± 0.457	0.668 ± 0.336	0.632 ± 0.334
DSi	18.29 ± 7.99	17.25 ± 7.24	19.52 ± 11.85	19.79 ± 11.61	18.69 ± 13.45	17.77 ± 12.53	23.49 ± 7.39	21.16 ± 7.48
N/P ratio	29.0 ± 13.7*	20.4 ± 7.9*	42.8 ± 53.4	50.7 ± 56.1	35.8 ± 64.0	30.1 ± 32.5	19.8 ± 13.6	18.2 ± 10.3
Micro	0.093 ± 0.081*	0.468 ± 0.687*	0.090 ± 0.063	0.193 ± 0.313	0.591 ± 1.109*	0.664 ± 1.287*	0.417 ± 0.671*	0.567 ± 0.982*
Nano	0.647 ± 0.556	1.112 ± 1.075	0.313 ± 0.879	0.983 ± 1.158	1.160 ± 1.076	1.129 ± 1.027	1.608 ± 1.524	1.467 ± 1.200
Pico	0.435 ± 0.442	0.756 ± 1.008	0.368 ± 0.423	0.417 ± 0.743	0.728 ± 0.706	0.786 ± 0.871	1.283 ± 1.250	1.191 ± 1.235
TChl-a	1.178 ± 0.829	2.336 ± 2.536	1.318 ± 1.253	1.593 ± 2.074	2.476 ± 2.157	2.579 ± 2.327	3.308 ± 2.890	3.224 ± 2.801

T, temperature (°C); S, salinity; DO, Dissolved oxygen (mg/L); Turb., Turbidity (NTU); DIN, dissolved inorganic nitrogen (μmol/L); SRP, soluble reactive phosphate (μmol/L); DSi: dissolved inorganic silicate (μmol/L); Chl-a, Chlorophyll-a (μg/L); ∗ $p<0.05$ and ∗∗ $p<0.01$ indicate Wilcoxon test result between surface and bottom waters.

3.2 Nutrients

Surface DIN, SRP, and N/P ratio exhibited clear seasonality at both aquaculture areas (Figures 2E, F). Concentrations of DIN and SRP presented an annual cycle characterized by high concentrations from October to February. In Lianjiang, SRP was generally below 0.1 μmol/L since July. The N/P ratio increased dramatically from 32 during cold season to 75 during warm season, with an annual mean of 36.1 (Figure 2G). DSi in Lianjiang declined sharply in March, August, and September (Figure 2H). Concentrations of DIN, SRP and DSi at the Zhangpu reference station were generally higher than that at the aquaculture stations, with DIN depleted only in July and SRP remaining above 0.4 μmol/L. Except for May, DIN and SRP decreased significantly at the aquaculture stations in April–September. The annual mean of N/P ratio in Zhangpu was 20.7, and was constantly low in July–August. DSi at the Zhangpu aquaculture stations depleted in April and June. Significant difference in nutrient concentrations were not observed between the culture and non-culture periods ($p > 0.05$), nor between the surface and bottom waters ($p > 0.05$) (Table 1). Redfield ratio (N:P:Si ratio) was calculated and plotted (Figure 3) (Brzezinski, 1985). N/P ratio was above 16 except for July and August at both areas. Average of N/Si ratio in Lianjiang during March was 12.9, and was below 1.5 in the other months.

3.3 Spatial and temporal changes of size fractioned Chl-a concentration

Total chlorophyll-a (TChl-a) of Lianjiang and Zhangpu exhibited multi-peaks during March-August (Figure 4). Decrease of TChl-a, by 23% on average, was observed in Lianjiang aquaculture stations compared to the reference station during the culture period, with the maximum decline occurring in March-April. Micro-sized Chl-a at the aquaculture stations peaked in June (1.051–1.389 μg/L), which accounted for 36.7% of the TChl-a. Nano-sized Chl-a was dominant in October–May at the aquaculture stations, accounting for 69% of the TChl-a. Proportion of pico-sized Chl-a to TChl-a increased since May at the aquaculture stations, and accounted for more than 60% in September (Figures 4B, C). In Lianjiang, the nano-sized Chl-a comprised 73% of TChl-a on average at reference station in October-August.

The TChl-a at the Zhangpu aquaculture stations decreased compared to the reference station during investigation (Figures 4D–F), even decreasing by 32% on average during the non-culture period. The temporal changes of size composition were similar between aquaculture and reference station, with micro-sized Chl-a comprising 57% of TChl-a on average in March and April, and pico-sized Chl-a comprising 58% of TChl-a on average in July–September. Nano-sized Chl-a was dominant in other months.

During the culture period, concentrations of micro-sized Chl-a in Lianjiang was significantly lower in the surface water than in the bottom water ($p < 0.05$), and the difference was not observed during non-culture period (Table 1). Micro-sized Chl-a was significantly lower in the surface water than in the bottom water in Zhangpu during both culture and non-culture periods ($p < 0.05$, $p < 0.05$). Surface Chl-a concentration of each sized-fraction in Lianjiang decreased compared to that in the bottom water during the culture period (Figure 5A). The phytoplankton depletion index (PDI) of micro- and pico-phytoplankton in Lianjiang was significantly lower during the culture period than during the non-culture period ($p < 0.05$, $p < 0.01$), with a mean value of −38% and −44%, respectively. The PDI of total Chl-a and nanophytoplankton

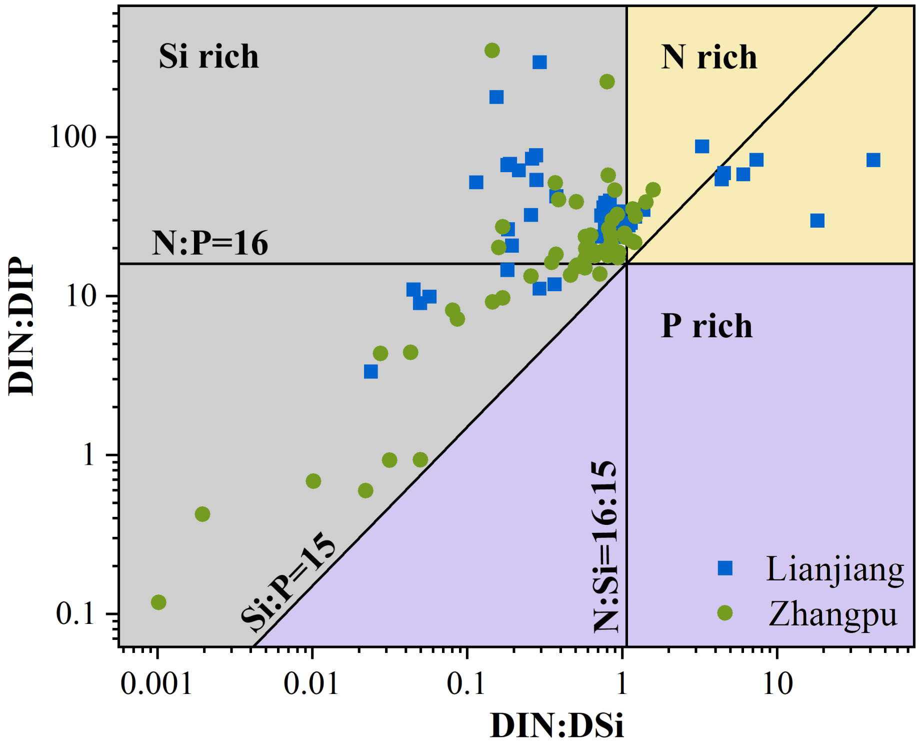

FIGURE 3
Plot of DIN : DSi vs. DIN : DIP ratio in Lianjiang site and Zhangpu site.

dropped to –14% and –16%, respectively. In Zhangpu, however, the PDI of each sized-fraction Chl-a in the culture period was generally consistent with that in the non-culture period (Figure 5B).

3.4 Size fractioned Chl-a concentration and environmental variables

The effects of environmental factors on the distribution of size-fractional Chl-a were explored using redundancy analysis (RDA). Base on the seasonal variability of environmental variables, we grouped water samples by season. It is evident that samples taken during spring and summer fell on the right side of RDA axis 1, while autumn and winter clustered on the left side (Figure 6). In Lianjiang, environmental factors accounted for 91.5% of the variance of size-fractional Chl-a. The dominant size-fraction was nano-phytoplankton during spring and converted to micro-, pico-phytoplankton during summer. The Chl-a concentrations of different size classes were negatively correlated with nutrient concentrations and positively correlated with the N/P ratio. In Zhangpu, environmental factors accounted for 86.9% of the variance of size-fractional Chl-a, with the micro- and picophytoplankton being the dominant fraction in spring and summer, respectively. The nano-sizedd Chl-a was the main contributor to the TChl-a. The pico-sized Chl-a was positively correlated with temperature and salinity, whereas the TChl-a concentration was negatively correlated with the N/P ratio.

4 Discussion

4.1 The response of phytoplankton biomass to aquaculture in the western TWS

Shellfish are opportunistic filter feeders, relying on aquatic particulate matter, especially phytoplankton as their food source (Hulot et al., 2020). When the intensity of filter-feeding of phytoplankton by shellfish exceeds the recovery rate of phytoplankton, phytoplankton exhibit negative growth (Prins et al., 1997). The decrease in phytoplankton biomass as a result of filter-feeding in shellfish aquaculture areas has been widely reported (Ogilvie et al., 2000; Strohmeier et al., 2008; Lin et al., 2016; Jiang et al., 2016), with the Chl-a concentration of surface water during culture periods being 40–80% lower in aquaculture areas than in non-culture areas. However, phytoplankton biomass decreased in a small extent in both aquaculture areas of western TWS. The impact of shellfish aquaculture on phytoplankton community and biomass depends on culture density as well as phytoplankton biomass and hydrodynamic characteristics (Trottet et al., 2008). Aquaculture areas where phytoplankton biomass was known to decrease significantly are often located in poorly flushed bay with tidal current velocities of <10 cm/s (Ogilvie et al., 2000; Jiang et al., 2016). A weak water exchange rate is conducive to the accumulation of phytoplankton biomass, and an extension of water residence time increases the probability of filter-feeding by shellfish (Strohmeier

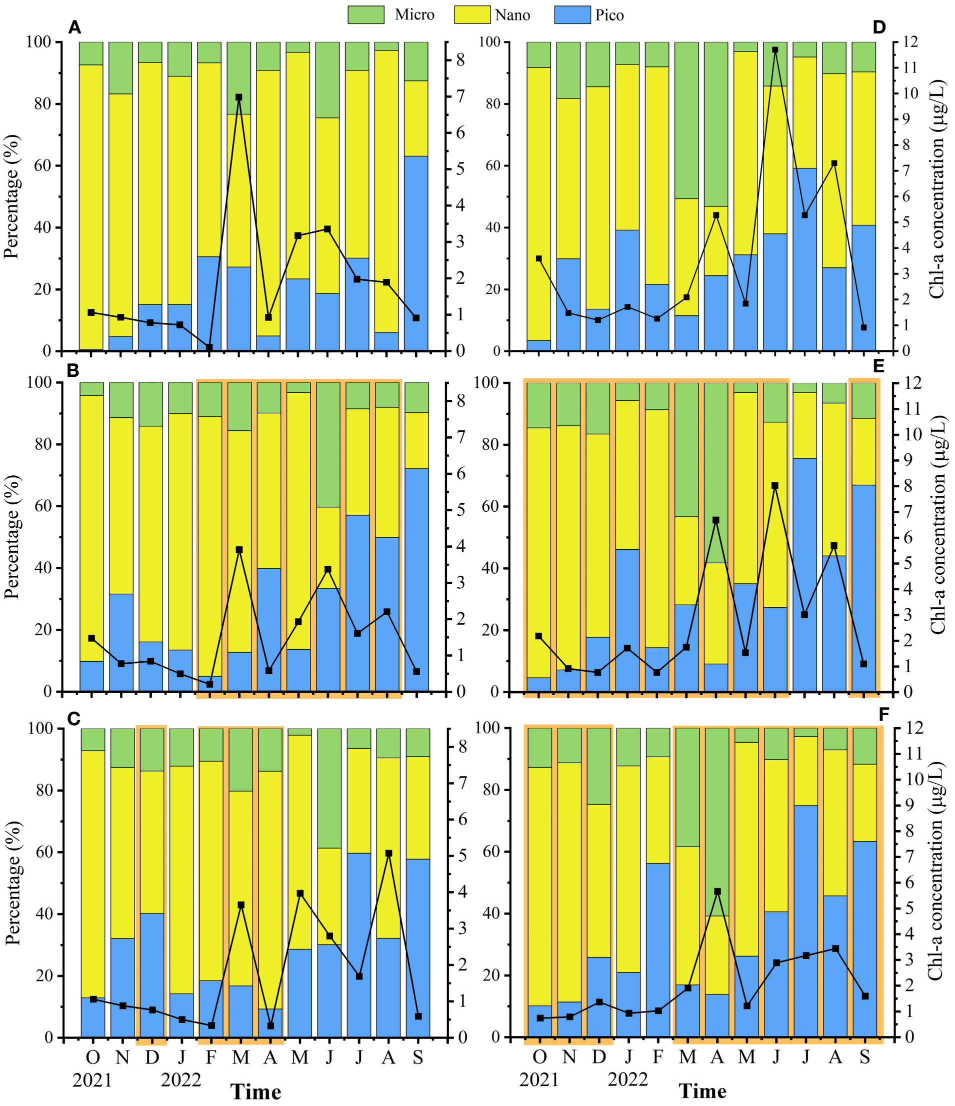

FIGURE 4
Temporal and spatial variations of surface total Chl-a concentration and percentage of size-fractioned Chl-a to Total Chl-a in Lianjiang site **(A)** reference station, **(B)** Oyster farm, **(C)** Abalone farm) and Zhangpu site **(D)** reference station, **(E)** Oyster farm, **(F)** Abalone farm). Orange areas indicate culture period.

et al., 2005; Sun et al., 2021). Decline of phytoplankton biomass in shellfish aquaculture areas decrease with increasing water flow velocity (Cerco & Noel, 2010). The TWS, as a key channel connecting the ECS and the SCS, has complex hydrodynamic conditions, with tidal current velocity about 40 cm/s on average (Wang et al., 2003; Hong et al., 2011). Tidal current propagating from ECS has been the dominant force in driving the hydrodynamics in the TWS, and it is amplified due to the shoaling topography, which strengthens on the west coast of TWS (Jan et al., 2004; Yu et al., 2015). In this study, the investigated stations were located in the west coast of TWS, with highly variable in environmental parameters, especially in Zhangpu area. The active water exchange between coastal water and open sea water may responsible for the slight decline of phytoplankton biomass in the aquaculture areas of western TWS.

Phytoplankton biomass showed no depletion in April at the Zhangpu aquaculture stations compared with the reference station, and exhibited a peak along with the massive consumption of nutrients. Notably, in April, the TChl-a concentration was slightly higher at the Zhangpu aquaculture stations than at the reference station, and the reference station had high levels of nutrients, especially phosphorous, while maintaining high biomass. These phenomena, when combined with the salinity changes at the reference station, suggest that the reference station received additional nutrient inputs. In a poor flushing bay, environmental parameters varied in a similar way for both reference stations and aquaculture stations (Jiang et al., 2016). In this study, the reference station was close to the aquaculture stations, but it still showed significant variation. Therefore, it was not a suitable reference station in open waters with complex hydrological changes to investigate changes in the grazing pressure on phytoplankton. During the survey period, the surface water and the bottom water at any sampling stations did not differ from each other in nutrient variation, although they differed from each other in temperature

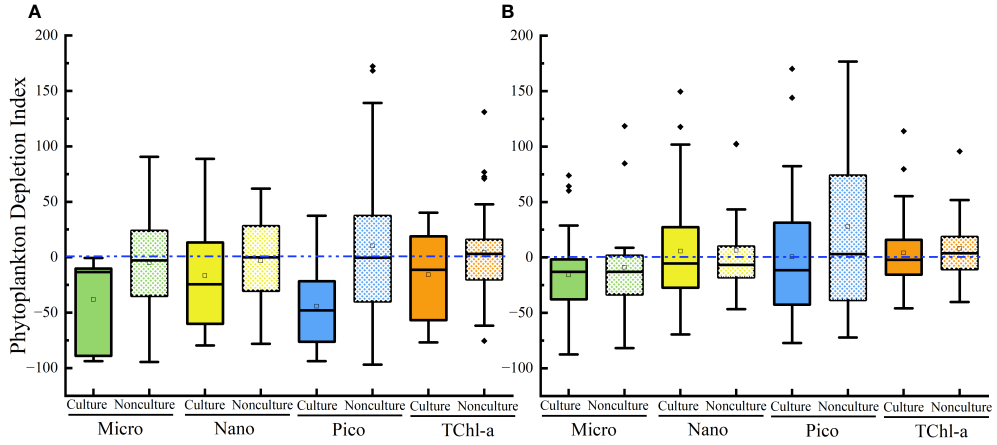

FIGURE 5
Phytoplankton depletion index of size-fractioned Chl-a and TChl-a in Lianjiang site **(A)** and Zhangpu site **(B)**. Blue dash lines show depletion index of zero.

and turbidity. Therefore, we selected the Chl-a of bottom water as a reference to evaluate phytoplankton depletion.

4.2 The difference of phytoplankton depletion in north and south of the western TWS

Particles removal rate in turbid water is faster than that in clean waters, and residence time was shorter when the concentration of suspend particle matters was higher (Yang et al., 2006; Zhong et al., 2019). The southern shellfish aquaculture area, characterizing by high temperature, high salinity and high turbidity, showed faster particle removal rate than that in northern area with low temperature, low salinity and low turbidity (Wei et al., 2010). In Lianjiang, consumption of the TChl-a was observed as well as the different size-fractional Chl-a during the culture period. In contrast, no difference of depletion index in Zhangpu was observed between the culture and non-culture periods. Decline in phytoplankton biomass was supposed increase with increasing culture density (Jiang et al., 2016), however phytoplankton biomass in Zhangpu showed negligible reduction, despite a higher culture density in the Zhangpu compared with in Lianjiang (Ma et al., 2022). The obvious fluctuations in environmental parameters in the Zhangpu shellfish aquaculture farms may responsible for the complex interaction between aquaculture and surrounding water (Campbell & Hall, 2019). The growth of shellfish in aquaculture areas is achieved through feed input and filter-feeding on phytoplankton, which leads to increased release of nutrients and excreta debris (Bouwman et al., 2013). The released nutrients can promote the growth of phytoplankton, which offsets, to some extent, the reduction in phytoplankton biomass caused by filter-feeding. In some shellfish

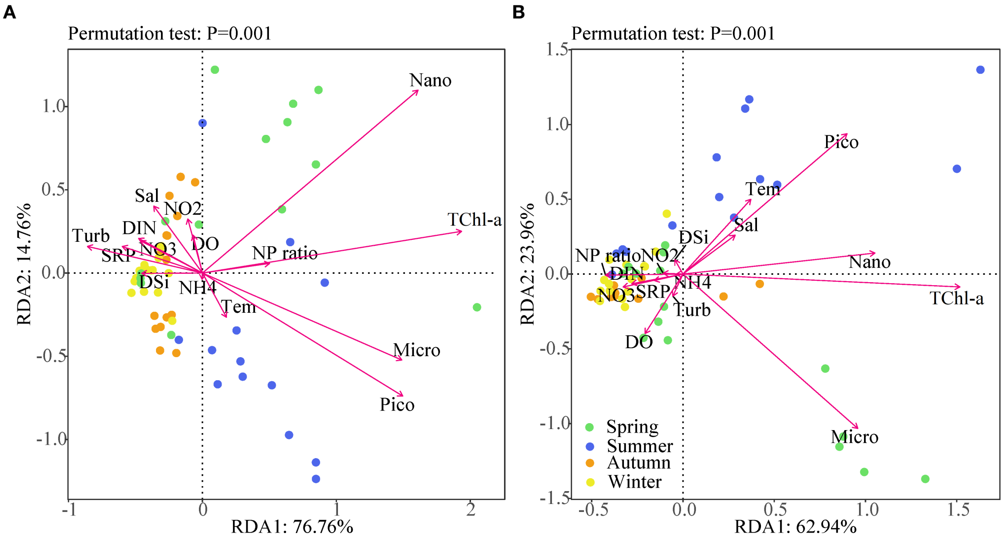

FIGURE 6
RDA t showing the interrelationship between physicochemical and biological variables in Lianjiang site **(A)** and Zhangpu site **(B)**. Dots represent the different seasons. The arrow lengths are proportional to the influence of the individual variables in the ordination.

aquaculture areas, such as the Grande-Entrée Lagoon, phytoplankton depletion had not been observed (Trottet et al., 2008), and sometimes Chl-a in the aquaculture area was even higher than that in reference areas (Sonier et al., 2016). The filter-feeding efficiency of shellfish varied with its growth period, with oysters showing the highest growth rates in April and October, and lower growth rates in summer (Campbell & Hall, 2019). In the aquaculture area of Lianjiang, TChl-a decreased by 48% in March and April, but significant decreases did not occur in other months. Seasonal differences have also been observed in the mussel aquaculture area of Beatrix Bay (Ogilvie et al., 2000).

Dinoflagellates are reported to be more nutritious than diatoms (Menden-Deuer & Lessard, 2000), and a preference for dinoflagellate by shellfish was observed in filed studies (Ward & Shumway, 2004; Jiang et al., 2016). Diatom was the first major group in Dongshan-Zhangpu area, while dominant species shifted from dinoflagellate to diatom in Lianjiang during late spring (Wang et al., 2016; Zhang et al., 2023). The phosphorus deficient water in Lianjiang also favors the growth of dinoflagellate comparing with diatom (Ou et al., 2006). The relative lack of favorable food source in Zhangpu aquaculture area, which has a longer culture period than Lianjiang, may also explain the negligible phytoplankton depletion in Zhangpu. However, the contribution of diatoms to shellfish diet still requires further study in the western TWS. Overall, the difference of phytoplankton depletion in the northern and southern TWS suggests a more resilient system to shellfish aquaculture in Zhangpu than that in Lianjiang.

4.3 Phytoplankton size class dynamics in aquaculture areas of the western TWS

The filter-feeding process of shellfish exhibits selectivity toward particle size, and the filtration efficiency increases non-linearly with particle size (Ward & Shumway, 2004). Oysters can remove 50% of the 1.7-µm particles, and the filtration efficiency for particles >7 µm reaches 100% (Riisgård, 1988; Ward & Shumway, 2004). Remarkable decrease of micro-phytoplankton was observed during culture period in a high-density oyster aquaculture farm (Jiang et al., 2016). The filter-feeding of shellfish can also reduce the abundance of small plankton, such as ciliates and flagellates, which lowers the grazing pressure on small phytoplankton and leads to a shift in the phytoplankton community toward dominance of pico-size plankton (Tomaru et al., 2002). The dominance of pico-phytoplankton is considered to be an indicator of phytoplankton depletion in shellfish aquaculture areas (Safi & Gibbs, 2003; Jiang et al., 2016). In Lianjiang, the contribution of pico-phytoplankton to the total Chl-a concentration generally varied with season, but it occasionally increased during the culture period. The preferential filtration for micro-phytoplankton by shellfish aquaculture may enhance the dominance of smaller size-fractional phytoplankton. Nano- and pico-phytoplankton account for 60–80% of the total phytoplankton biomass in the TWS, with nano-phytoplankton accounting for up to 59% in the northern region and pico-phytoplankton accounting for 71% in the southern region (Wang et al., 1997). Although the impact of shellfish aquaculture on phytoplankton biomass is not obvious, the size composition of phytoplankton is affected by shellfish aquaculture to some extent.

A distinction of biomass and size composition of phytoplankton between two shellfish aquaculture areas was showed in the conceptual graph (Figure 7). Studies have shown that the composition of phytoplankton size fractions is more influenced by season and geographic location than by the aquaculture process (Pitta et al., 1998; Jiang et al., 2016). The general pattern of biomass was low during NE monsoon and high during SW monsoon, with phytoplankton community shifting from nano-phytoplankton during NE monsoon to micro- and pico-phytoplankton during SW monsoon in this study. Phytoplankton bloom was basically coincident with an apparent decline of silica in both Lianjiang and Zhangpu. Small diatoms with fast growth rate benefit from nutrient absorption and are dominant in temperate sea waters (Terseleer et al., 2014; Leblanc et al., 2018). It is suggested that nanoplankton diatoms thrive and lead to N/Si ratio exceeding 2 in March in Lianjiang.

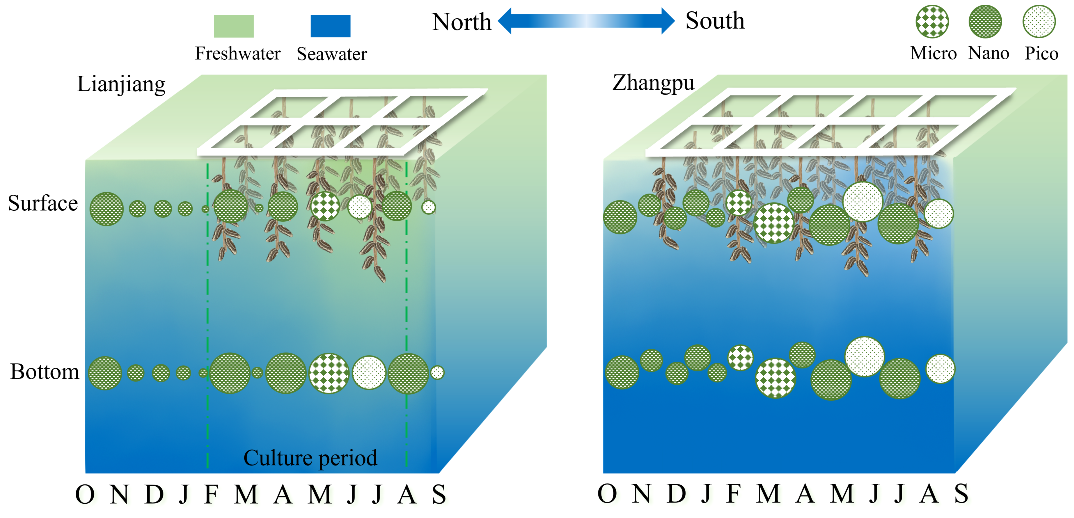

FIGURE 7
Schematic representation of the temporal variations of dominant fraction Chl-a in Lianjiang and Zhangpu aquaculture areas.

Different from Lianjiang, microplankton diatoms prevailed during spring in Zhangpu, where nutrients and temperature were suitable for the growth of centric and chain-forming diatoms (Wang et al., 2016; Rajaneesh et al., 2018). As nutrient decreasing during summer, picoplankton (e.g., *Prochlorococcus*, *Synechococcus*) with high-temperature and high-salinity and low-nutrient niches takes advantage to growth (Zhong et al., 2020). Considering the relatively broad niche breadths for each environmental variable of *Synechococcus*, together with the N-deficient waters during summer in this study, it could conclude that *Synechococcus* constitutes most part of picoplankton in Zhangpu and Lianjiang (Wen et al., 2017; Zhong et al., 2020).

4.4 Nutrient inputs in the aquaculture areas of the western TWS

Fundamentally, nutrient availability or assimilate deviations from N:Si:P ratio of 16:15:1 suggest the possibility of nutrient-limited (Brzezinski, 1985). The nutrient ratios considered in the present study show that phosphorus is the main limited nutrient in the western TWS, especially in Lianjiang. Phytoplankton growth is usually limited by phosphorus in the TWS (Ou et al., 2006; Wang et al., 2016; Wen et al., 2017). Nutrient input from vertical mixing and upwelling is primary supply for phytoplankton in the southern TWS, and phosphorus limitation can be abated during upwelling events (Ou et al., 2006; Hong et al., 2011). Although we are lack of direct evidence to demonstrate vertical mixing in Zhangpu area, the fluctuations of high turbidity and high silica concentration indicate a turbulent water to some extent (Wen et al., 2017; Rajaneesh et al., 2018). Upwelling occurs in the Taiwan Bank in the summer, which was characterized by low temperature and high salinity ($T< 25°C$, $S > 33.9$) (Hu et al., 2015). Accordingly, in this study, we observed that the aquaculture station with a salinity of 33.6 in Zhangpu in July and August. It is supposed that the continuous nutrient supply maintains the high phytoplankton biomass in Zhangpu. In contract, nutrient concentrations in Lianjiang are constantly low during warm season. Nutrient inputs from submarine groundwater discharge (SGD) are supposed to be the predominant regulator in Lianjiang aquaculture area, with DIN and SRP fluxes contributing by SGD over total nutrient inputs approximately 58% and 73%, respectively in July (Peng et al., 2021). An obvious elevation in nitrogen concentration was not observed despite the dramatic decrease of salinity occurred in this study. Due to the changing environment such as tides, precipitation and assimilation of phytoplankton, it is not adequate for illustrating the low nutrient concentration with data presented in this study (Jiang et al., 2016; Zhang et al., 2023).

5 Conclusion

In this study, we assessed the phytoplankton community structure variation under the influence of marine shellfish aquaculture in the west coast of the TWS in terms of the Chl-a concentration and the size fractions. A weak change of phytoplankton biomass and size structure in response to shellfish aquaculture was observed. Phytoplankton depletion was different between the northern and southern shellfish aquaculture areas. During the culture period in the northern aquaculture area (Lianjiang), the TChl-a concentration of surface water at aquaculture stations was approximately 14% lower than that of bottom water, and this decreasing trend was consistently present in micro-, nano-, and pico-size fractions. Phytoplankton biomass showed negligible depletion during culture period in the southern aquaculture area (Zhangpu), where environmental parameters varied greatly during the survey period. The shift from a dominance of nano-phytoplankton to the dominance of micro- and pico-phytoplankton was caused mainly by seasonal changes in environmental conditions. In aquaculture areas with complex hydrological conditions, the Chl-a of bottom water may serve as an appropriate reference for evaluating phytoplankton depletion.

Data availability statement

The raw data supporting the conclusions of this article will be made available by the authors, without undue reservation.

Author contributions

Conceptualization, LW and ZL; methodology, LW; software, YM; validation, YM; formal analysis, YM, CJ and XC; investigation, RO and JQ; writing—original draft preparation, YM; writing—review and editing, LW; visualization, YM; supervision, AL and HH; funding acquisition, LW. All authors have read and agreed to the published version of the manuscript.

Funding

This study was funded by the National Key Research and Development Program of China No. 2022YFF0802204, the Scientific Research Foundation of Third Institute of Oceanography, M.N.R., No. 2018017, 2019017 & 2019018.

Acknowledgments

We are grateful to the measurements and analyses of samples by Ms. Lulu Pei and Dr. Jianhua Kang. We also thank the graphic processing software of Ocean Data View (version 4.5.7) contributed by Schlitzer, R., http://odv.awi.de, and OriginPro 8.5 (OriginLab Corporation©, Northampton, MA 01060 USA). We do appreciate the comments and suggestions on the manuscript from reviewers.

Conflict of interest

The authors declare that the research was conducted in the absence of any commercial or financial relationships that could be construed as a potential conflict of interest.

Publisher's note

References

Bouwman, L., Beusen, A., Glibert, P. M., Overbeek, C., Pawlowski, M., Herrera, J., et al. (2013). Mariculture: significant and expanding cause of coastal nutrient enrichment. *Environ. Res. Lett.* 8 (4), 44026. doi: 10.1088/1748-9326/8/4/044026

Brzezinski, M. A. (1985). The Si:C:N ratio of marine diatoms: interspecific variability and the effecct of some environmental variables. *J. Phycol.* 21 (3), 347–357. doi: 10.1111/j.0022-3646.1985.00347.x

Campbell, M. D., and Hall, S. G. (2019). Hydrodynamic effects on oyster aquaculture systems: a review. *Rev. Aquac.* 11 (3), 896–906. doi: 10.1111/raq.12271

Cerco, C. F., and Noel, M. R. (2010). Monitoring, modeling, and management impacts of bivalve filter feeders in the oligohaline and tidal fresh regions of the Chesapeake Bay system. *Eco. Modell.* 221 (7), 1054–1064. doi: 10.1016/j.ecolmodel.2009.07.024

Clarke, K. R., and Warwick, R. M. (2001). A further biodiversity index applicable to species lists: variation in taxonomic distinctness. *Mar. Ecol. Prog. Ser.* 216, 265–278. doi: 10.3354/MEPS216265

Dai, M. H., Zhao, Y. Y., Chai, F., Chen, M. R., Chen, N. ,. W., Chen, Y. ,. M., et al. (2023). Persistent eutrophication and hypoxia in the coastal ocean. *Cambridge Prisms: Coast. Futur.* 1, 1–28, e19. doi: 10.1017/cft.2023.7

Dame, R. F. (2011). *Ecology of Marine Bivalves: An Ecosystem Approach. 2nd edn* (Boca Raton, USA: CRC Press). doi: 10.1201/b11220

FAO (2020). *The state of world fisheries and aquaculture* (Rome: Food and Aquaculture Organization of the United Nations), 29–31. Available at: https://www.fao.org/publications/sofia/2022/en/.

Filgueira, R., Guyondet, T., Comeau, L. A., and Grant, J. (2014). Physiological indices as indicators of ecosystem status in shellfish aquaculture sites. *Ecol. Indic.* 39, 134–143. doi: 10.1016/j.ecolind.2013.12.006

Filgueira, R., Guyondet, T., Comeau, L. A., and Tremblay, R. (2016). Bivalve aquaculture-environment interactions in the context of climate change. *Glob. Change Biol.* 22, 3901–3913. doi: 10.1111/gcb.13346

Hong, H., Chai, F., Zhang, C., Huang, B., Jiang, Y., and Hu, J. (2011). An overview of physical and biogeochemical processes and ecosystem dynamics in the Taiwan Strait. *Cont. Shelf Res.* 31 (6), S3–S12. doi: 10.1016/j.csr.2011.02.002

Hu, J., Lan, W., Huang, B., Chiang, K.-P., and Hong, H. (2015). Low nutrient and high chlorophyll a coastal upwelling system – A case study in the southern Taiwan Strait. *Estuarine Coast. Shelf Sci.* 166, 170–177. doi: 10.1016/j.ecss.2015.05.020

Hulot, V., Saulnier, D., Lafabrie, C., and Gaertner-Mazouni, N. (2020). Shellfish culture: a complex driver of planktonic communities. *Rev. Aquac.* 12 (1), 33–46. doi: 10.1111/raq.12303

Jan, S., Chern, C. S., Wang, J., and Chao, S. Y. (2004). The anomalous amplification of M_2 tide in the Taiwan Strait. *Geophy. Res. Lett.* 31, L07308. doi: 10.1029/2003GL019373

Jan, S., Sheu, D. D., and Kuo, H. M. (2006). Water mass and throughflow transport variability in the Taiwan Strait. *J. Geophys. Res.* 111, (C12). doi: 10.1029/2006jc003656

Jiang, T., Chen, F., Yu, Z., Lu, L., and Wang, Z. (2016). Size-dependent depletion and community disturbance of phytoplankton under intensive oyster mariculture based on HPLC pigment analysis in Daya Bay, South China Sea. *Environ. pollut.* 219, 804–814. doi: 10.1016/j.envpol.2016.07.058

Leblanc, K., Qu´eguiner, B., Diaz, F., Cornet, V., Michel-Rodriguez, M., Durrieu de Madron, X., et al. (2018). Nanoplanktonic diatoms are globally overlooked but play a role in spring blooms and carbon export. *Nat. Commun.* 9, 953. doi: 10.1038/s41467-018-03376-9

Lin, J., Li, C., and Zhang, S. (2016). Hydrodynamic effect of a large offshore mussel suspended aquaculture farm. *Aquaculture* 451, 147–155. doi: 10.1016/j.aquaculture.2015.08.039

Liu, X., Wang, Z., Yang, X., Liu, Y., Liu, B., Zhang, J., et al. (2022). Mapping China's offshore mariculture based on dense time-series optical and radar data. *Int. J. Digit. Earth* 15 (1), 1326–1349. doi: 10.1080/17538947.2022.2108923

Lucas, L. V., Thompson, J. K., Stacey, M. T., and Koseff, J. R. (2016). Bivalve grazing can shape phytoplankton communities. *Front. Mar. Sci.* 3. doi: 10.3389/fmars.2016.00014

Ma, Y., Qu, X., Feng, D., Zhang, P., Huang, H., Zhang, Z., et al. (2022). Recognition and statistical analysis of coastal marine aquacultural cages based on R^3Det single-stage detector: A case study of Fujian Province, China. *Ocean Coast. Manage.* 225, 106244. doi: 10.1016/j.ocecoaman.2022.106244

Menden-Deuer, S., and Lessard, E. J. (2000). Carbon to volume relationships for dinoflagellates, diatoms, and other protist plankton. *Limnol. Oceanogr.* 45, 569–579. doi: 10.4319/lo.2000.45.3.0569

Newell, R. I. E. (2004). Ecosystem influences of natural and cultivated populations of suspension-feeding bivalve molluscs: a review. *J. Shellfish Res.* 23 (1), 51–62. Available at: https://link.gale.com/apps/doc/A118543914/AONE?u=anon~1220bc4e&sid=bookmark-AONE&xid=63f7edd4.

Newell, R. I. E., Fisher, T. R., Holyoke, R. R., and Cornwell, J. C. (2005). "Influence of eastern oysters on nitrogen and phosphorus regeneration in Chesapeake Bay, USA," in *The Comparative Roles of Suspension - Feeders in Ecosystems*. Eds. R. F. Dame and S. Olenin (Dordrecht, The Netherlands: Springer), 93–120. doi: 10.1007/1-4020-3030-4_6

Ogilvie, S. C., Ross, A. H., and Schiel, D. R. (2000). Phytoplankton biomass associated with mussel farms in Beatrix Bay, New Zealand. *Aquaculture* 181 (1), 71–80. doi: 10.1016/S0044-8486(99)00219-7

Ou, L. J., Huang, B. Q., Lin, L. Z., and Hong, H. S. (2006). Phosphorus stress of phytoplankton in the Taiwan Strait determined by bulk and single-cell alkaline phosphatase activity assays. *Mar. Ecol. Prog. Ser.* 327, 95–106. doi: 10.3354/meps327095

Paerl, H. W., Valdes, L. M., Peierls, B. L., Adolf, J. E., and Harding, L. (2006). Anthropogenic and climatic influences on the eutrophication of large estuarine ecosystems. *Limnol. Oceanogr.* 51, 448–462. doi: 10.4319/lo.2006.51.1_part_2.0448

Peng, T., Zhu, Z. Y., Du, J. Z., and Liu, J. N. (2021). Effects of nutrient-rich submarine groundwater discharge on marine aquaculture: A case in Lianjiang, East China Sea. *Sci. Total Environ.* 786, 147388. doi: 10.1016/j.scitotenv.2021.147388

Pitta, P., Karakassis, I., Tsapakis, M., and Zivanovic, S. (1998). Natural vs. mariculture induced variability in nutrients and plankton in the eastern Mediterranean. *Hydrobiologia* 391 (1), 179–192. doi: 10.1023/A:1003501832069

Prins, T. C., Smaal, A. C., and Dame, R. F. (1997). A review of the feedbacks between bivalve grazing and ecosystem processes. *Aquat. Ecol.* 31 (4), 349–359. doi: 10.1023/A:1009924624259

Rajaneesh, K. M., Mitbavkar, S., and Anil, A. C. (2018). Dynamics of size-fractionated phytoplankton biomass in a monsoonal estuary: Patterns and drivers for seasonal and spatial variability. *Estuar. Coast. Shelf Sci.* 207, 325–337. doi: 10.1016/j.ecss.2018.04.026

Riisgård, H. U. (1988). Efficiency of particle retention and filtration rate in 6 species of Northeast American bivalves. *Mar. Ecol. Prog. Ser.* 45, 217–223. doi: 10.3354/MEPS045217

Rosa, M., Ward, J. E., Holohan, B. A., Shumway, S. E., and Wikfors, G. H. (2017). Physicochemical surface properties of microalgae and their combined effects on particle selection by suspension-feeding bivalve molluscs. *J. Exper. Mar. Bio. Eco.* 486, 59–68. doi: 10.1016/j.jembe.2016.09.007

Safi, K. A., and Gibbs, M. M. (2003). Importance of different size classes of phytoplankton in Beatrix Bay, Marlborough Sounds, New Zealand, and the potential implications for the aquaculture of the mussel, Perna canaliculus. *N. Z. J. Mar. Freshw. Res.* 37 (2), 267–272. doi: 10.1080/00288330.2003.9517164

Sieburth, J. M., Smetacek, V., and Lenz, J. (1978). Pelagic ecosystem structure: Heterotrophic compartments of the plankton and their relationship to plankton size fractions 1. *Limnol. Oceanogr.* 23 (6), 1256–1263. doi: 10.4319/lo.1978.23.6.1256

Smaal, A. C., Schellekens, T., van Stralen, M. R., and Kromkamp, J. C. (2013). Decrease of the carrying capacity of the Oosterschelde estuary (SW Delta, NL) for bivalve filter feeders due to overgrazing? *Aquaculture* 404–405, 28–34. doi: 10.1016/j.aquaculture.2013.04.008

Sonier, R., Filgueira, R., Guyondet, T., Tremblay, R., Olivier, F., Meziane, T., et al. (2016). Picophytoplankton contribution to Mytilus edulis growth in an intensive culture environment. *Mar. Biol.* 163 (4), 73. doi: 10.1007/s00227-016-2845-7

Souchu, P., Vaquer, A., Collos, Y., Landrein, S., Deslous-Paoli, J.-M., and Bibent, B. (2001). Influence of shellfish farming activities on the biogeochemical composition of the water column in Thau lagoon. *Mar. Ecol. Prog. Ser.* 218, 141–152. doi: 10.3354/meps218141

Srichandan, S., Baliarsingh, S. A.-O. X., Prakash, S., Lotliker, A. A., Parida, C., and Sahu, K. C. (2019). Seasonal dynamics of phytoplankton in response to environmental variables in contrasting coastal ecosystems. *Environ. Sci. pollut. Res.* 26, 12025–12041. doi: 10.1007/s11356-019-04569-5

Strickland, J. D. H., and Parsons, T. R. (1972). *A Practical Handbook of Seawater Analysis. 2nd ed* Vol. 167 (Ottawa, Canada: Fisheries Research Board of Canada Press).

Strohmeier, T., Aure, J., Duinker, A., Castberg, T., Svardal, A., and Strand, Ø. (2005). Flow reduction, seston depletion, meat content and distribution of diarrhetic shellfish toxins in a long-line blue mussel *(Mytilus edulis)* farm. *J. Shellfish Res.* 24 (1), 15–23. doi: 10.2983/0730-8000(2005)24[15:FRSDMC]2.0.CO;2

Strohmeier, T., Duinker, A., Strand, Ø., and Aure, J. (2008). Temporal and spatial variation in food availability and meat ratio in a longline mussel farm (*Mytilus edulis*). *Aquaculture* 276 (1-4), 83–90. doi: 10.1016/j.aquaculture.2008.01.043

Sun, K., Zhang, J., Lin, F., Ren, J. S., Zhao, Y., Wu, W., et al. (2021). Evaluating the growth potential of a typical bivalve-seaweed integrated mariculture system - a numerical study of Sungo Bay, China. *Aquaculture* 532, 736037. doi: 10.1016/j.aquaculture.2020.736037

Tang, D., Kester, D. R., Ni, I. H., Kawamura, H., and Hong, H. (2002). Upwelling in the Taiwan Strait during the summer monsoon detected by satellite and shipboard measurements. *Remote Sens. Environ.* 83 (3), 457–471. doi: 10.1016/S0034-4257(02)00062-7

Terseleer, N., Bruggeman, J., Lancelot, C., and Gypens, N. (2014). Trait-based representation of diatom functional diversity in a plankton functional type model of the eutrophied southern North Sea. *Limnol. Oceanogr.* 59, 1958–1972. doi: 10.4319/lo.2014.59.6.1958

Tomaru, Y., Udaka, N., Kawabata, Z., and Nakano, S.i. (2002). Seasonal change of seston size distribution and phytoplankton composition in bivalve pearl oyster Pinctada fucata martensii culture farm. *Hydrobiologia* 481 (1), 181–185. doi: 10.1023/A:1021232832390

Trottet, A., Roy, S., Tamigneaux, E., Lovejoy, C., and Tremblay, R. (2008). Impact of suspended mussels (*Mytilus edulis* L.) on plankton communities in a Magdalen Islands lagoon (Québec, Canada): A mesocosm approach. *J. Exp. Mar. Biol. Ecol.* 365 (2), 103–115. doi: 10.1016/j.jembe.2008.08.001

Wang, H., Huang, B., and Hong, H. (1997). Size-fractionated productivity and nutrient dynamics of phytoplankton in subtropical coastal environments. *Hydrobiologia* 352 (1), 97–106. doi: 10.1023/A:1003017726533

Wang, Y. H., Jan, S., and Wang, D. P. (2003). Transports and tidal current estimates in the Taiwan Strait from shipboard ADCP observations, (1999–2001). *Estuar. Coast. Shelf Sci.* 57 (1), 193–199. doi: 10.1016/S0272-7714(02)00344-X

Wang, Y., Kang, J. H., Ye, Y. Y., Lin, G. M., Yang, Q. L., and Lin, M. (2016). Phytoplankton community and environmental correlates in a coastal upwelling zone along western Taiwan Strait. *J. Mar. Syst.* 154, 252–263. doi: 10.1016/j.jmarsys.2015.10.015

Ward, E. J., and Shumway, S. E. (2004). Separating the grain from the chaff: particle selection in suspension- and deposit-feeding bivalves. *J. Exp. Mar. Biol. Ecol.* 300 (1), 83–130. doi: 10.1016/j.jembe.2004.03.002

Wei, C. L., Tsai, J. R., Hou, Y. R., Wen, L. S., Sheu, D. D., and Chou, W. C. (2010). Scavenging phenomenon elucidated from ^{234}Th/^{238}U disequilibrium in surface water of the Taiwan Strait. *Terr. Atmos. Ocean. Sci.* 21 (4), 713–726. doi: 10.3319/TAO.2009.08.26.01(Oc

Wen, Z. Z., Lin, W. F., Shen, R., Hong, H. Z., Kao, S. J., and Shi, D. L. (2017). Nitrogen fixation in two coastal upwelling regions of the Taiwan Strait. *Sci. Rep.* 7, 17601. doi: 10.1038/s41598-017-18006-5

Yang, W. F., Huang, Y. P., Chen, M., Zhang, L., Liu, H. B., Liu, G. S., et al. (2006). Disequilibria between ^{210}Po and ^{210}Pb in surface waters of the southern South China Sea and their implications. *Sci. China Earth Sci.* 49, 103–112. doi: 10.1007/s11430-004-5233-y

Yu, H. Q., Yu, H. M., Ding, Y., Wang, L., and Kuang, L. (2015). On M_2 tidal amplitude enhancement in the Taiwan Strait and its asymmetry in the cross-strait direcction. *Continent. Shelf Res.* 109 (15), 198–209. doi: 10.1016/j.csr.2015.09.005

Zhang, X. S., Zhen, G. M., Cui, X. R., Zeng, Y. L., Gao, W. M., Yu, K. L., et al. (2023). Effect of dissolved organic nutrients on the bloom of *Prorocentrum donghaiense* in the East China Sea coastal waters. *Mar. Environ. Res.* 183, 105841. doi: 10.1016/j.marenvres.2022.105841

Zhong, Y. P., Liu, X., Xiao, W. P., Laws, E. A., Chen, J. X., Wang, L., et al. (2020). Phytoplankton community patterns in the Taiwan Strait match the characteristics of their realized niches. *Progr. Oceanogr.* 186, 102366. doi: 10.1016/j.pocean.2020.102366

Zhong, Q. Q., Wang, J. L., Du, J. Z., Bi, Q. Q., and Zhao, F. (2019). The ^{210}Po/^{210}Pb disequilibrium in a spring-blooming marginal sea, the Southern Yellow Sea. *J. Environ. Radioact.* 207, 15–26. doi: 10.1016/j.jenvrad.2019.05.017

frontiers | Frontiers in Marine Science

TYPE Original Research
PUBLISHED 09 August 2023
DOI 10.3389/fmars.2023.1212992

OPEN ACCESS

EDITED BY
Zhaohe Luo,
Ministry of Natural Resources, China

REVIEWED BY
Zuhao Zhu,
Ministry of Natural Resources, China
Wei Qian,
Fujian Normal University, China

*CORRESPONDENCE
Yingfeng Chen
✉ chenyingfeng@jmu.edu.cn

RECEIVED 27 April 2023
ACCEPTED 20 July 2023
PUBLISHED 09 August 2023

CITATION
Zhang K, Zhao X, Xue J, Mo D, Zhang D, Xiao Z, Yang W, Wu Y and Chen Y (2023) The temporal and spatial variation of chlorophyll a concentration in the China Seas and its impact on marine fisheries. *Front. Mar. Sci.* 10:1212992.
doi: 10.3389/fmars.2023.1212992

The temporal and spatial variation of chlorophyll a concentration in the China Seas and its impact on marine fisheries

Kunlong Zhang[1,2,3], Xunbo Zhao[1,2,3], Jing Xue[1,2,3], Danqi Mo[1,2,3], Dongyu Zhang[1,2,3], Zhongyong Xiao[1,3], Wei Yang[1,2], Yingxu Wu[1,2] and Yingfeng Chen[1,2,3]*

[1]College of Harbour and Coastal Engineering, Jimei University, Xiamen, China, [2]Polar and Marine Research Institute, College of Harbor and Coastal Engineering, Jimei University, Xiamen, China, [3]National Geographic Conditions Monitoring Research Center, College of Harbor and Coastal Engineering, Jimei University, Xiamen, China

Marine chlorophyll a is a key molecule for photosynthesis of marine plants and some plankton, which is important in marine ecosystems. This study utilized the chlorophyll a concentration data product observed by the MODIS sensor (MODerate resolution Imaging Spectroradiometer) to construct a long-term sequence of chlorophyll a concentration dataset by processing the raw data. Based on this, the multi-time-scale chlorophyll a concentration data was synthesized, and it was used to analyze the spatial and temporal variation characteristics of chlorophyll a concentration in China Seas. In addition, several oceanographic variables, including sea surface temperature, nutrients (phosphate, nitrate, silicate), partial pressure of seawater carbon dioxide, net primary productivity of the ocean, physical dynamics of seawater processes (mixed layer), were analyzed to ascertain their potential influence on chlorophyll a concentration. Finally, we analyzed the effects of changes in chlorophyll a concentration on marine fisheries. The result showed that: The average value of chlorophyll a concentration in China Seas from 2002 to 2022 was 0.874 mg/m^3, with the highest concentration observed in the Bohai Sea area (4.547 mg/m^3) and the lowest in the South China Sea area (0.288 mg/m^3). The spatial variation of chlorophyll a concentration revealed an overall decrease of 0.0095 mg/m^3 in China Seas from 2002 to 2022. From the perspective of time changes, the concentration of chlorophyll a in China's Bohai Sea area showed a downward trend from 2002 to 2022, while the Yellow Sea area showed an upward trend. The concentration remained relatively stable in the East China Sea area, whereas a significant declining trend was observed in the South China Sea area. The relationship between temperature and chlorophyll a concentration was non-linear, and chlorophyll a concentration showed some fluctuation or threshold effect with the change of seawater temperature. The three nutrient salts studied have a promoting effect on chlorophyll a, among which phosphate has the most obvious promoting effect on chlorophyll a. Chlorophyll a was negatively correlated with pCO_2 and positively correlated with ocean net primary productivity. Seasonal changes in the mixed layer had a significant effect on changes in the upper marine nutrients, which in turn affected changes in chlorophyll a concentration. Six of the eight types of algae studied show a trend toward deeper sea depths, which may have implications for the food availability of marine fish at different levels and pose new challenges for marine fisheries development.

KEYWORDS

chlorophyll a, spatial and temporal variation, physical and chemical properties of seawater, marine algae, marine fisheries

Highlights

1. Spatial and temporal variation of chlorophyll a concentration in China Seas over long time series and characteristics of chlorophyll a concentration at different time scales.
2. Autocorrelation test of chlorophyll a concentration in China Seas and temporal decomposition to study the periodicity of temporal variation of chlorophyll a concentration.
3. Analysis of the effects of multiple factors such as ocean surface temperature, seawater nutrients (phosphate, nitrate, silicate), partial pressure of CO_2, and physical movement of seawater on chlorophyll a concentration in China Seas, as well as a summative analysis considering the above factors.
4. To study the change of algal habitat and analyze the impact on the development of marine fishery, taking Zhoushan fishing grounds as an example, to draw the society's attention to the sustainable development of marine fishery.

1 Introduction

Chlorophyll a is an important group of pigments associated with photosynthesis. Phytoplankton fix carbon dioxide through photosynthesis and absorb atmospheric carbon dioxide through a biochemical "biological pump" function and remit it to the ocean carbon pool (Falkowski et al., 2000). Therefore, chlorophyll a plays a very important role in the global ecosystem carbon cycle. In addition, chlorophyll a, as an important biological indicator of marine primary productivity (Dang et al., 2022), phytoplankton extant and some fishing grounds, can provide necessary basic support for the development of marine fisheries and also provide a restoration countermeasure for the increasingly depleted fishery resources (Cury et al., 2000). Therefore, it is very important to study the spatial and temporal characteristics of chlorophyll in the China Seas to explore the influence mechanism of marine pollution (e.g., red tide), early warning and exploitation of marine resources (Wang et al., 2022). In addition, chlorophyll a concentration reflects the environmental quality of water ecology and is an important parameter for evaluating the eutrophication status of seawater (Firdhouse et al, 2019), and the study of the influencing factors of chlorophyll a can effectively analyze the changes of marine chlorophyll concentration. Therefore, the spatial and temporal distribution of chlorophyll concentration and its correlation with environmental factors can reflect the regional marine ecological and environmental quality status, which has important research value.

With the rapid development of the application of remote sensing technology in the marine field, the use of satellite data to establish regression and inversion models of chlorophyll concentration to achieve the determination of chlorophyll concentration provides a possibility for real-time monitoring of a wide range of sea areas (Blondeau-Patissier et al., 2014). International research on the study of chlorophyll a is mainly focused on the following aspects. The establishment and validation of chlorophyll concentration inversion models based on remote sensing technology methods, such as the establishment of remote sensing methods for chlorophyll-a concentration inversion in semi-arid turbid waters (Lin et al., 2011), and the algorithm for chlorophyll-a concentration inversion in seawater with different nutrient status (Hu et al., 2012). It is concerned with the temporal and spatial characteristics of chlorophyll-a, the seasonal variation of chlorophyll-a (Gregg et al., 2003) and the response to climate change (Behrenfeld et al., 2005). The relationship between chlorophyll-a and marine ecosystems and the interaction of environmental factors have been studied, such as investigating the chlorophyll-a concentration and species composition of different phytoplankton communities (Fragoso et al., 2018) and exploring the effects of water temperature, nutrient concentration and light intensity on the spatial and temporal variation of chlorophyll-a (Demarcq et al., 2003). Chlorophyll-a monitoring and management: Using chlorophyll-a data for monitoring and management of marine ecosystems, such as detecting seawater eutrophication and mitigating marine pollution (Paerl, 2009).

Research in China has focused on the establishment and validation of chlorophyll concentration inversion models (Yue et al., 1999), the inversion of chlorophyll concentration models for different China Seas using the Gaofen 4 satellite (Yang et al., 2017), and the validation of simultaneous field sampling data for chlorophyll a concentration (Zheng et al., 2017). Some progress has also been made in the study of the spatial and temporal variation of chlorophyll in China Seas. Lian et al. (2020) studied the characteristics and causes of seasonal variation of surface chlorophyll a in the South China Sea and analyzed the effects of surface ocean temperature and dynamic processes on marine chlorophyll. Cong et al. (2006) studied the changes of chlorophyll a concentration in the Chinese continental shelf seas from 1998 to 2003 based on satellite inversion, and Hao (2010) studied the spatial and temporal distribution characteristics and environmental regulation mechanisms of chlorophyll a and primary productivity in Chinese coastal seas. In China, there are few analyses of the spatial and temporal variability of marine chlorophyll a concentration over long time series. And there is a lack of comparative variation analysis of the overall China Seas area and each constituent sea area. Moreover, the spatial and temporal variability of chlorophyll a concentration has not been explored regularly.

In this paper, we constructed a long time series of chlorophyll a concentration data in China Seas using the marine chlorophyll a concentration products of satellite remote sensing (MODIS/Aqua) inversions from 2002-2022. The temporal and spatial variation characteristics of chlorophyll a concentration were analyzed on the basis of long time-series of chlorophyll a concentration data, and the temporal coefficient of variation and spatial coefficient of variation were used to characterize the temporal fluctuations and spatial heterogeneity. Secondly, the accumulation difference was used to represent the cumulative multi-year variation of chlorophyll a concentration in China Seas. In addition, the correlation between chlorophyll a concentration and ocean surface temperature, ocean net primary productivity and seawater carbon dioxide partial pressure were analyzed to explore the influencing factors of chlorophyll a concentration in Chinese marine waters. Finally, the influence of the change of ocean chlorophyll a concentration on marine fishing grounds was analyzed using Zhoushan fishing grounds as an example. It is expected to provide some data support and research reference for China's marine research and provide an important scientific basis for marine pollution management, marine ecological protection and rational marine use and development in China.

2 Study area, data and methods

2.1 Study area

Since this study requires the determination of specific chlorophyll a study values for specific sea areas, boundary delimitation has an impact on the study results. The boundary ranges of the four Chinese seas for this study are described (the specific boundary ranges may be subject to international law and controversy among related countries, and there are no strict sea boundary restrictions in this paper):

Boundary range of the Bohai Sea: East: bordered by the Yellow Sea. South: bordered by Shandong Peninsula. West: bordered by Hebei, Liaoning and other Chinese mainland provinces. North: Connected to the Gulf of Korea.

Boundary range of the Yellow Sea: East: bordering with North Korea, including Yeonpyeong Island, the Jinju Peninsula and other areas. South: bordered by the Bohai Sea. West: bordered by the Shandong Peninsula of China. North: Connected to the Democratic People's Republic of Korea *via* Yalu River and East Korea Bay.

Boundary range of the East China Sea: East: bordered by Ryukyu Islands of Japan in the east. South: bordered by the Taiwan Strait. West: bordered by the Korea Strait. North: bordered by the Yellow Sea.

Boundary range of the South China Sea: East: bordered by Luzon Island of the Philippines. South: South to the Strait of Malacca. Southwest: bordering the Indonesian province of Papua, including the South China Sea Islands. West: bordered by Vietnam. North: Connected to the East China Sea.

2.2 Data source

2.2.1 Chlorophyll a concentration data

Chlorophyll a (Chl-a) concentration data were obtained from the NASA Oceancolor website (https://oceancolor.gsfc.nasa.gov/) Chlor_a L3B Chl-a data product obtained by the MODIS (MODerate resolution Imaging) sensor on board the Aqua satellite. The temporal resolution of the products used in this study is months, and the spatial resolution is 4 km, and the data used in this paper span the period from August 2002 to November 2022. The data product is based on the algorithm of Hu et al. (2012), which combines the empirical band-difference method at low Chl-a concentrations and the ratio-transformation method at higher Chl-a concentrations. Cui et al. (2014) verified the accuracy and applicability of Chl-a concentration inversion using this method for MODIS data in China Seas by comparing the MODIS satellite Oceancolor products with the measured values in the Yellow Sea and East China Sea. And the data error showed that the error was 32% in the Chinese near-shore waters, which was better than that of similar products such as SeaWiFS (error 40%) and MERIS (error 54%). The accuracy and applicability of the data inversion using the combination of the empirical band difference method and the ratio transformation method are higher in the Chinese offshore data. The sampling points of Chl-a concentration used for analysis with other seawater physicochemical properties are shown in Figure 1A.

2.2.2 Physical and chemical characteristics data of seawater

The sea surface temperature (SST) data is the SST L3 data product from the NASA Oceancolor website, which was also acquired by the MODIS sensor on board the Aqua satellite. And the product used for the study is a composite of the entire mission from July 2002 to August 2020, with a spatial resolution of 4 km. The data product is based on an improved version of the nonlinear SST algorithm (NLSST) of Walton et al. (1998) and uses empirical coefficients derived from regression of *in situ* and satellite measurements. The sampling points of the SST used for analysis with Chl-a concentration are shown in Figure 1B.

The nutrient (Garcia et al., 2018) and the mixed layer depth (Garcia et al., 2019) data were obtained from the NOAA world ocean atlas website (WOA, https://www.ncei.noaa.gov/access/world-ocean-atlas-2018f/). WOA is the data result after analysis and quality control based on the World Ocean Data Database (WOD) (Takahashi et al., 2020) The nutrient salt data used in this study were respectively the annual data of phosphate, nitrate and

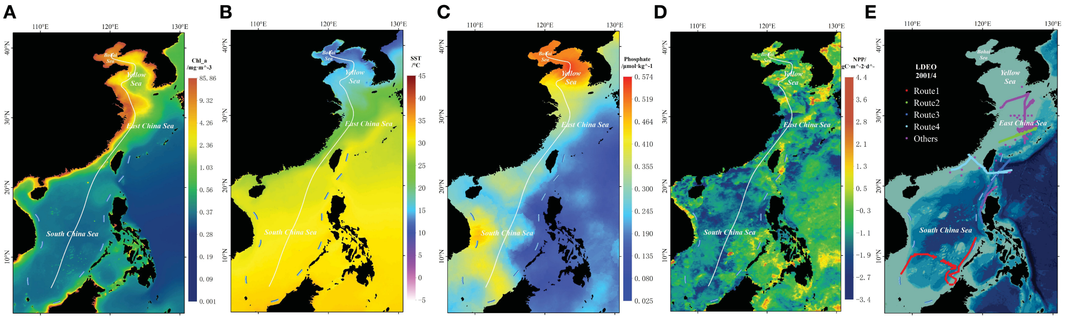

FIGURE 1
Sampling area of chlorophyll a concentration **(A)** versus sea surface temperature **(B)**, nutrient salinity **(C)**, net primary productivity of the ocean **(D)**, and pCO_2 data **(E)**. The solid white line in the figure represents the sampling path. Among the nutrients, phosphate is used as a representative for the argument **(C)**, and all three nutrients were actually collected.

silicate in WOA 2009, 2013 and 2018, with a spatial resolution of 1°. These three years were chosen mainly because there were missing data due to different spatial locations in different years of the data, while the data for these three years were completer and more suitable for analytical processing. This study focused on the nutrient salt concentration on the ocean surface. The mixed layer depth data was obtained using January and July 2018 WOA data with a spatial resolution of 0.25°. The sampling points of nutrient salts used for analysis with Chl-a concentration are shown in Figure 1C.

Ocean net primary productivity (NPP) data was obtained from the Marine Science Data Center of the Chinese Academy of Sciences (http://msdc.qdio.ac.cn). The NPP data are the global 9 km ocean primary productivity distance level dataset from 1998 to 2018 (Xue, 2019), and the data used for analysis in this study is December 2018 data with a spatial resolution of 9 km. The data format is GeoTIFF, using the WGS-84 projection coordinate system. The sampling points of NPP used for analysis with Chl-a concentration are shown in Figure 1D.

Surface seawater partial pressure of carbon dioxide (pCO_2) data were obtained from the NOAA Marine Carbon and Acidification Data System (Takahashi et al., 2020) (OCADS, https://www.ncei.noaa.gov/products/ocean-carbon-acidification-data-system) global surface pCO_2 (LDEO) 2019 version of the data set. The dataset is based on direct seawater p_{CO2} measurements using the balancer-CO_2 analyzer system from continuous navigation system observations and major national and international oceanographic programs. The spatial and temporal distribution of the LDEO V2019 data is uneven. A large number of measurements are concentrated in the coastal areas of Europe, eastern Japan and North America, while the number of measurements in the waters of China is relatively small. After data screening and comparing the spatio-temporal coincidence degree with other data, the study selected the measured data of LDEO V2019 data set in April 2001. The sampling points of pCO2 used for analysis with Chl-a concentration are shown in Figure 1E.

2.2.3 Marine algae data

Data on marine algae were obtained from the Ocean Biogeographic Information System (OBIS, 2023), and data on the distribution of algae in the eastern coastal region of China were selected. Species selection was based on the top eight species of marine algae observed in greatest numbers.

2.3 Research methodology

2.3.1 Spatial analysis

In terms of spatial change, this study combines monthly data at different time scales to analyze spatial change. Due to the influence of cloud cover and sensor performance, the monthly data is empty for the unscanned data, that is, no data is given. Due to the relatively loose "hollowing" range of empty values, small voids and different positions, a part of error can be offset after operation. Therefore, sampling and interpolation are carried out to eliminate voids, and then raster operation is performed on the image after interpolation, annual Chl-a concentration data were generated.

Based on the synthetic annual data, the cumulative difference method was used to investigate the specific spatial variation. The cumulative difference formula is expressed as:

$$\Delta = (2022-2021) + (2021-2020) + \ldots + (2005-2004) + (2004-2003) \quad (1)$$

Numbers indicate year.

At the same time, we used the coefficient of variation to examine spatial heterogeneity. The coefficient of variation (CV) is the ratio of the standard deviation (σ) to mean (μ) (Getis and Ord, 1992). The calculation formula is as follows:

$$CV = \sigma/\mu \quad (2)$$

where "σ" and "μ" are calculated from the data of regional spatial distribution data, respectively (Getis and Ord, 1992).

2.3.2 Time analysis

Using satellite remote sensing data analysis software SeaDAS data to extract monthly NC file data. Taking Bohai Sea, Yellow Sea, East China Sea and South China Sea as mask areas, we used SeaDAS statistical function to extract data including mean value, maximum value, minimum value and concentration threshold percentage of Chl-a concentration from the four major sea areas of China and reconstruct the Chl-a concentration time data of the long time series from 2002 to 2022, which provided the data basis for the subsequent time distribution analysis. The coefficient of variation was used to study the fluctuations over time and was calculated as in equation (2), where "σ" and "μ" are calculated using the extracted statistics, respectively.

2.3.3 Trend analysis

The slope function is used to calculate the slope (i.e. trend) of a linear regression model. It is based on the least squares method of fitting a linear equation to find the line of best fit. The slope function is commonly used to analyze long-term trends in time series data. (Montgomery et al., 2012). We used slope analysis to trend the mean Chl-a concentration for long time series. Slope>0 indicates that Chl-a concentration presents an increasing trend over time, while slope<0 indicates that Chl-a concentration presents a decreasing trend. Formula for calculating the slope coefficient (Groebner et al, 2018):

$$slope = \frac{\sum[(x_i - \bar{x})(y_i - \bar{y})]}{\sum(\bar{x} - x_i)} \tag{3}$$

x_i is for each month from 2002 to 2022; y_i is the average concentration of Chl-a in each ocean region for each month; $\bar{x}$ is the monthly average, $\bar{y}$ is the monthly mean Chl-a concentration in all months from 2002 to 2022.

2.3.4 Time series decomposition

Time series decomposition is a method of breaking down time series data into its component parts, including trends, seasonality, and residuals. This decomposition can help us better understand the characteristics and structure of time series (Hamilton, 1994). Seasonality indicates the recurrence of fluctuations in time series data over a fixed time interval (e.g., annually, quarterly, monthly). Commonly used seasonality models include additive and multiplicative models. In this study, the additive model is chosen. Additive Model: time series = trend + seasonality + residuals.

The equation for time series decomposition can be expressed as

$$Y(t) = T(t) + S(t) + R(t) \tag{4}$$

where Y(t) denotes the time series observations at moment t, T (t) denotes the trend component at moment t, S(t) denotes the seasonal component at moment t, and R(t) denotes the residual component at moment t (Chatfield, 2004).

In this study for the four seas Chl-a concentration time series were decomposed by time series in steps of one month to twelve months, and the step with the most appropriate length was selected for analysis.

2.3.5 Autocorrelation function

The autocorrelation function (ACF) provides insight into the presence of periodicities and repetitive patterns in a time series by calculating the autocorrelation coefficients of the time series at different lagged moments. If the time series is periodic, then its ACF will show the presence of significant peaks or periodic patterns at certain lagged values. These peaks correspond to periodic repetitions in the time series.

The formula for the Autocorrelation Function (ACF) is shown below:

$$ACF(k)=(Cov(X(t), X(t-k)))/(Var(X(t))) \tag{5}$$

where ACF(k) denotes the autocorrelation coefficient with lag k. Cov(X(t), X(t-k)) denotes the covariance of X(t) with X(t-k). Var(X (t)) denotes the variance of X(t) (Hamilton, 1994).

3 Results and discussion

3.1 Spatial distribution characteristics of Chl-a concentration

Figure 2 and Table 1 show the multi-year average Chl-a concentration, cumulative concentration changes and average temporal coefficients of variation in China Seas from 2002 to 2022. Figure 2A shows the spatial distribution characteristics of Chl-a concentration in China, the average multi-year Chl-a concentration from 2002 to 2022 is 0.8741 mg/m^3, 80% of the sea area Chl-a concentration is below 1.331 mg/m^3, 95% of the sea area Chl-a concentration is below 4.159 mg/m^3. It can be seen from the Figure 2A that the spatial distribution of Chl-a concentration in China Seas varies significantly over the years, with the Chl-a concentration reaching an extreme value of 48.022 mg/m^3 in some nearshore waters and a minimum value of 0.084 mg/m^3 in the vast offshore waters, with the high value areas mainly concentrated in the Bohai Sea waters and along the narrow range of the nearshore, while the Chl-a concentration is also high in the Yellow Sea and the eastern part of the East China Sea; The low value area is mainly concentrated in the vast sea area of the South China Sea; as shown in Table 1, the average Chl-a concentration in the Bohai Sea from 2002 to 2022 is 4.547 mg/m^3, the average Chl-a concentration in the Yellow Sea is 2.511 mg/m^3, the average Chl-a concentration in the East China Sea is 1.488 mg/m^3, and the average concentration of Chl-a in the South China Sea is 0.288 mg/m^3. The multi-year average Chl-a concentration in each sea area is from high to low in the order of Bohai Sea, Yellow Sea, East China Sea and South China Sea. The average Chl-a concentration in the coastal sea is higher than that in the outer sea, and the Chl-a concentration decreases from the coastal sea to the outer sea, and the Chl-a concentration gradually increases from south to north in each sea.

Figure 2B shows the cumulative difference of Chl-a concentration from 2003 to 2022, and the red areas are the areas with decreasing Chl-a concentration. In addition, the Chl-a concentration in the northern part of the Bohai Sea, the Yellow Sea and the discontinuous coastal waters in the western part of the East China Sea also decreases significantly. Overall, as shown in Table 1, the Chl-a concentration in China Seas showed a decrease from 2002 to 2022. Specifically, the concentration decreased by 0.0095 mg/m^3 overall. In the Bohai Sea, the Chl-a concentration

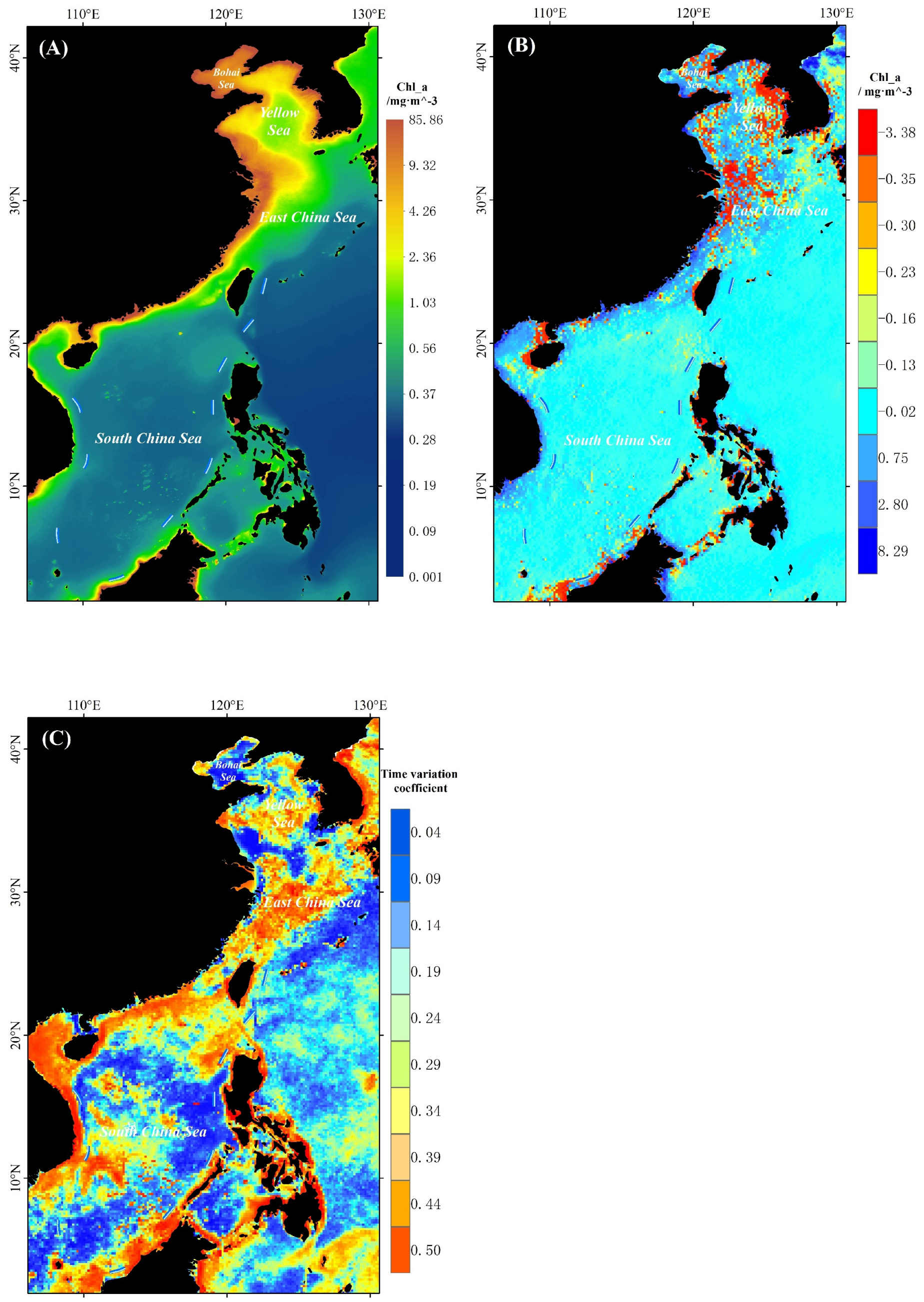

FIGURE 2

Multi-year average chlorophyll a concentration distribution **(A)**, Cumulative change of multi-year chlorophyll a concentration **(B)** and time variation coefficient of multi-year chlorophyll a concentration **(C)** in China seas from 2002 to 2022. Both cumulative concentration changes and temporal coefficients of variation were calculated using equations (1) and (2) for the year-by-year average chlorophyll a concentration values from 2002 to 2022 on the basis of the spatial distribution of the synthesized annual chlorophyll a concentration.

decreased by 0.270 mg/m^3, while in the Yellow Sea, it decreased by 0.086 mg/m^3. Similarly, the East China Sea experienced a decrease of 0.079 mg/m^3 in Chl-a concentration, and the South China Sea observed a decrease of 0.020 mg/m^3. The overall decrease in Chl-a concentration in China Seas has a negative impact on the marine and global ecological environment. The decrease in Chl-a concentration affects the photosynthesis of marine phytoplankton and algae, leading to a decrease in marine productivity and a negative impact on marine energy flow, which in turn has a negative effect on the marine biological ecological chain. In addition, marine Chl-also profoundly affects the global ecological carbon cycle. Chl-a is the main pigment for photosynthesis of marine phytoplankton, and the decrease in Chl-a concentration reduces the photosynthesis of phytoplankton, which in turn leads to a decrease in the ocean's carbon sequestration capacity.

In terms of spatial variation, as shown in Figure 2C, the closer the color is to red, the larger the temporal coefficient of variation is, and the greater the fluctuation variation of Chl-a concentration in

TABLE 1 Multi-year average chlorophyll a concentration, Cumulative change of chlorophyll a concentration and time variation coefficient of chlorophyll a concentration in China seas from 2002 to 2022.

Sea Areas	Average concentration/mg·m^{-3}	Accumulated change in concentration/mg·m^{-3}	Average coefficient of variation
The Bohai Sea	4.547	0.270	0.109
The Yellow Sea	2.511	0.086	0.149
The East China Sea	1.488	-0.079	0.206
The South China Sea	0.288	-0.020	0.156
Overall	0.874	-0.0095	0.163

this space. The average temporal coefficient of variation in the Bohai Sea is 0.1092, which is the least spatially variable among the four major seas in China, and the distribution of Chl-a concentration is the most stable. From the Figure 2C, we can see that the temporal coefficient of variation in the East China Sea is larger, with an average coefficient of variation of 0.2063, and the spatial distribution of Chl-a concentration is the most unstable. Besides, the spatial distribution of Chl-a concentration in the South China Sea is unstable, and the temporal coefficient of variation is also larger in the central-western and northern coasts of the South China Sea and the offshore areas.

3.2 Seasonal variation of Chl-a concentration

Figures 3, 4 show the seasonal variation of the multi-year average Chl-a concentration in China Seas. It is clear from the Figures 3, 4 that the Chl-a concentration in the Yellow Sea and East China Sea reaches its highest values in winter throughout the year, and the concentrations in the Bohai Sea is generally very high throughout the year. The seasonal differences are most pronounced in the vast intersection of the central Yellow Sea waters and the estuary of the Yangtze River. The seasonal differences in Chl-a concentration were most significant in the Bohai Sea and the Yellow Sea, and the seasonal changes in Chl-a concentration were smaller in the East China Sea and the South China Sea.

As shown in Table 2, the total Chl-a concentration in China Seas reached the maximum value of 0.914 mg/m^3 in winter and the lowest Chl-a concentration of 0.832 mg/m^3 in summer, with a seasonal distribution of Chl-a concentration throughout the year of winter > spring > autumn > summer. The seasonal distribution of Chl-a concentration varies among the seas. By region, the Chl-a concentration in the Bohai Sea was summer > winter > spring > autumn, in the Yellow Sea was winter > spring > autumn > summer, in the East China Sea was spring > winter > summer > autumn, and in the South China Sea was winter > autumn > summer > spring.

We noticed significant differences in the status of Chl-a concentration in different seasons in different China Seas. This is mainly related to the seasonal dominance of Chl-a in different seas. We have discussed this significant difference in more detail in Section 3.5 below.

3.3 Interannual variation of Chl-a concentration

Figure 5 shows the monthly variation characteristics of Chl-a concentration in four major China Seas from August 2002 to December 2022.It is clear from the Figure that Chl-a concentration shows a clear seasonal cycle, indicating that Chl-a concentration is most influenced by seasonal temperature factors. The graph clearly shows that there are significant differences in Chl-a concentration between the seas, with the highest Chl-a concentration in the Bohai Sea, followed by the Yellow Sea, and the lowest in the South China Sea, showing clear latitudinal differences. The graph shows that the monthly mean Chl-a concentration in the four major China Seas shows a clear periodic variation with the month, while the month corresponding to the high and low variation of Chl-a concentration varies from one sea to another. As shown in Table 3, according to the slope analysis, the slope values of the Bohai Sea and the South China Sea are less than zero and show a trend of decreasing concentration, while the slope values of the Yellow Sea and the East China Sea are greater than zero and show a trend of increasing concentration, and the trend of decreasing Chl-a concentration in the South China Sea is the most obvious. Due to the lack of the latest long-term changes in Chl-a concentration, we compared it with previous studies. Zhao et al. (2019); Zhu et al. (2010); Jun and Liu (2015) investigated the temporal and spatial variations of Chl-a concentration in China Seas at different time scales, and the results showed that Chl-a concentration in Bohai and Yellow Sea waters showed an increasing trend for a long time (Jun and Liu (2015): slope=0.0063 and slope=0.0013 from 1997 to 2012), which are consistent with our research results (Bohai Sea slope=0.0567 and Yellow Sea slope=0.0266 from 2002 to 2013). He et al. (2013) also found that the bloom intensity in the Bohai Sea and the Yellow Sea doubled from 1998 to 2011, which also reflected the high rise of Chl-a concentration in the Bohai Sea and the Yellow Sea during this period, which was confirmed by our study (Chl-a concentration slope=0.0752 in the Bohai Sea from 2002 to 2011, Yellow Sea Chl-a concentration slope=0.0146).

In order to investigate whether Chl-a concentration changes are cyclical, an autocorrelation analysis was first performed. Observe the autocorrelation function image Figure 6, the autocorrelation function graph of the Yellow Sea chl_a concentration time series has an obvious trend of periodic changes, the graph shows a

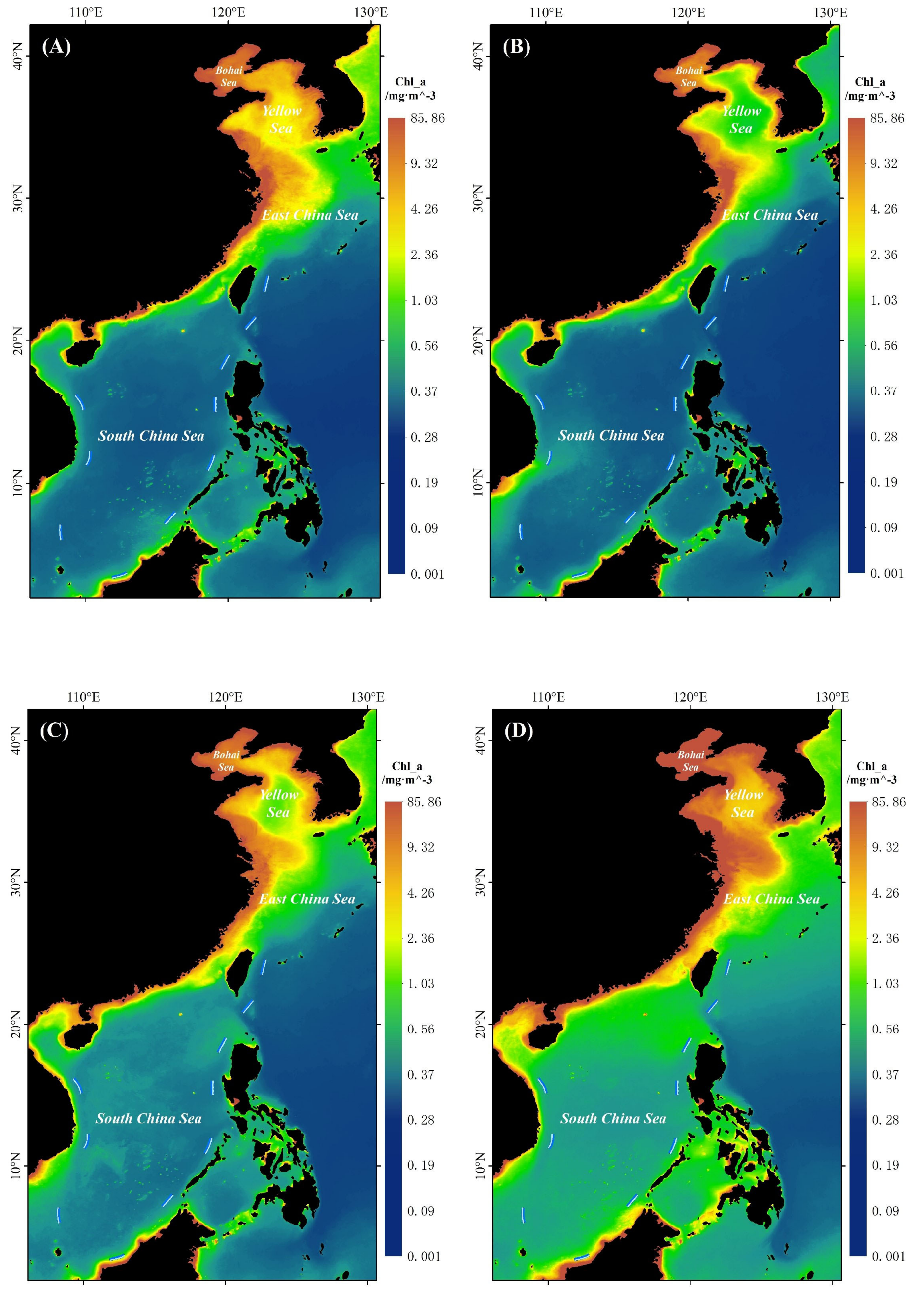

FIGURE 3
Distribution of multi-year average chlorophyll a concentration by season in China seas from 2002 to 2022. **(A)**Spring, **(B)**Summer, **(C)**Autumn, **(D)**Winter.

symmetrical distribution about the lag order of the horizontal axis, and there are significant peaks at a specific lag order. The autocorrelation coefficients in the autocorrelation function image of Yellow Sea chl_a concentration time series decreases slowly and regularly with the increase of the lag order, not abruptly truncating the tail. The above analysis of the autocorrelation function graphs of the Yellow Sea chl_a concentration time series can be concluded that the Yellow Sea chl_a concentration time series has a more obvious periodicity. It should be pointed out here that the other three seas are not free from the phenomenon of periodicity, but the phenomenon of periodicity of chl_a concentration in the Yellow Sea is more significant. In addition, observing the graph of autocorrelation function, by looking for the peak and decay rate, with the principle that higher peak and slower decay rate indicate stronger periodicity, we can also see that the periodicity of South China Sea chl_a concentration is also more obvious.

By decomposing the time series in steps of one month to twelve months, the most appropriate step size is four months. The time decomposition of the original time series is carried out, and the decomposition time length is 4, i.e. the time step is four months. As shown in Figure 7, the numbers 1, 2, 3 and 4 in each column represent the Bohai Sea, Yellow Sea, East Sea and South China Sea respectively, and the graphs in each column from the first column on the left represent the original time series of chl_a concentration,

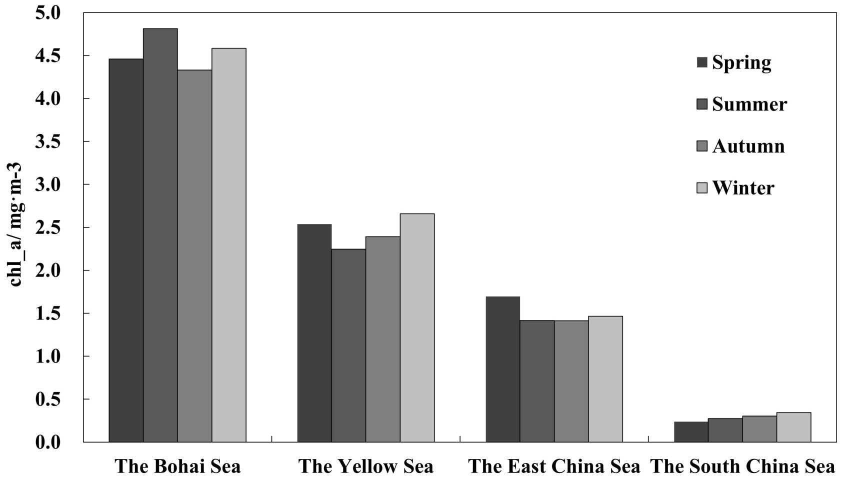

FIGURE 4
Comparison of the average chlorophyll a concentration in four major seas of China: Bohai Sea, Yellow Sea, East China Sea and South China Sea from 2002 to 2022 and the differences in seasonal chlorophyll a concentration in the four major seas.

TABLE 2 Average chlorophyll a concentration(mg/m^3) in four major China seas at different periods.

Sea Areas	Spring	Summer	Autumn	Winter
The Bohai Sea	4.458	4.814	4.330	4.584
The Yellow Sea	2.539	2.246	2.391	2.660
The East China Sea	1.695	1.415	1.412	1.466
The South China Sea	0.239	0.274	0.304	0.345
Overall	0.868	0.832	0.851	0.914

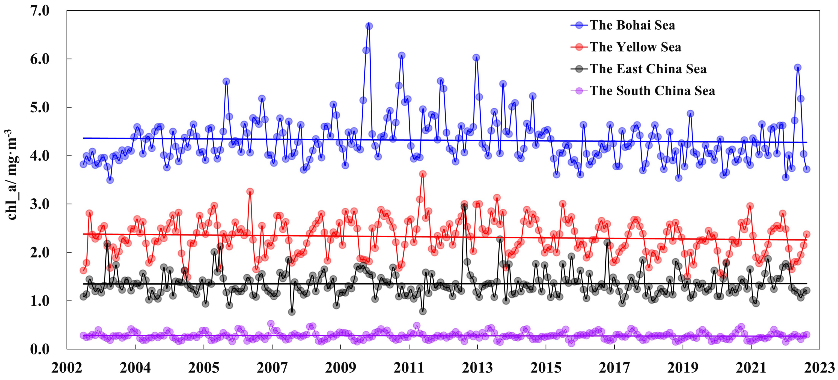

FIGURE 5
Monthly average chlorophyll a concentration in four major China Seas for a long time series from 2002 to 2022.

the trend series of chl_a concentration, the seasonal series of chl_a concentration and the residual series of chl_a concentration respectively. The second column of trend series can be regarded as the simulation of the graphical form of the first column of the original time series or the rounded performance of the curve. Comparing the data in the first two columns, it can be seen that the Yellow Sea and the South China Sea have a more obvious cyclical phenomenon compared with the Bohai Sea and the East China Sea, which is due to the differences caused by the closed sea area of the Bohai Sea, the large influence of human activities, and the large exchange of energy of land-based materials in the East China Sea. By observing the seasonal series, we can find out whether there is a fixed cyclical pattern in the data. The seasonal series of the four seas show a repeating pattern of fluctuations, indicating the existence of seasonal influences, the most obvious being temperature. Analysis of the residual series can reveal the part of

TABLE 3 Multi-year chlorophyll a concentration variance and slope values in four major China Seas from 2002 to 2022.

Sea Areas	Variance	Slope
The Bohai Sea	0.48	-0.0004
The Yellow Sea	0.36	0.0136
The East China Sea	0.26	0.0000
The South China Sea	0.07	-0.0763

the original series that is not explained by the trend and seasonality, i.e., the residual term. It can be seen that there is no obvious pattern in the residual series of the four seas, indicating that the trend and seasonality have been well explained in the model. (Note that here the seasonal series in columns three and four as well as the residual series are shown only for the graphical images of 2016-2020 due to the high density of the graph.)

Figure 8 and Table 3 show the average Chl-a concentration values, the temporal coefficient of variation and the variance for each year in each sea area. The variance of the monthly Chl-a concentration in the Bohai Sea during this period was 0.48, while the interannual variation of the temporal coefficient of variation was large, indicating that the interannual variation of the Chl-a concentration in the Bohai Sea was highly variable and the temporal distribution of the Chl-a concentration was unstable. There are obvious anomalies in the variation of the long time series, as shown in Figures 5 , 6. Within 2010 to 2013, the monthly mean Chl-a concentration fluctuated the most, and the coefficient of temporal variation was generally large. The data collection revealed that sudden and rare ice conditions occurred in Liaodong Bay, Bohai Bay, Laizhou Bay and the northern Yellow Sea and Jiaozhou Bay in the Bohai Sea in 2010 (Sun et al., 2011), and the CNOOC oil spill in Bohai Bay in 2011 (Chen, 2013), indicating that the influence of environmental or human factors may cause fluctuating changes in Chl-a concentration. The interannual variation of the coefficient of temporal variation in the South China Sea is not too high and the variance of Chl-a concentration in each month during this period is 0.07. The interannual distribution of Chl-a concentration is stable, which is largely related to the latitude distribution, sea area and sea distribution. The high latitude of the Bohai Sea results in greater temperature fluctuations. And the sea area is smaller and more occluded, and the human population density is higher. The change of human discharge of various types of production and living materials into the Bohai Sea leads to a greater interannual variation of Chl-a concentration in the Bohai Sea. In addition, there are significant interannual differences in the flow of rivers entering the Bohai Sea. The decrease in inlet water flow during dry periods and the increase in inlet river flow during rainy periods in turn have an impact on the interannual variation of Chl-a concentration. The South China Sea, on the other hand, is an open and large area, which has a stronger regulating effect on Chl-a. Moreover, the South China Sea is located at low latitudes, where seasonal fluctuations in temperature are small, which in turn causes small seasonal variations in Chl-a concentration. In addition, based on the temporal coefficient of variation, it can be concluded that the

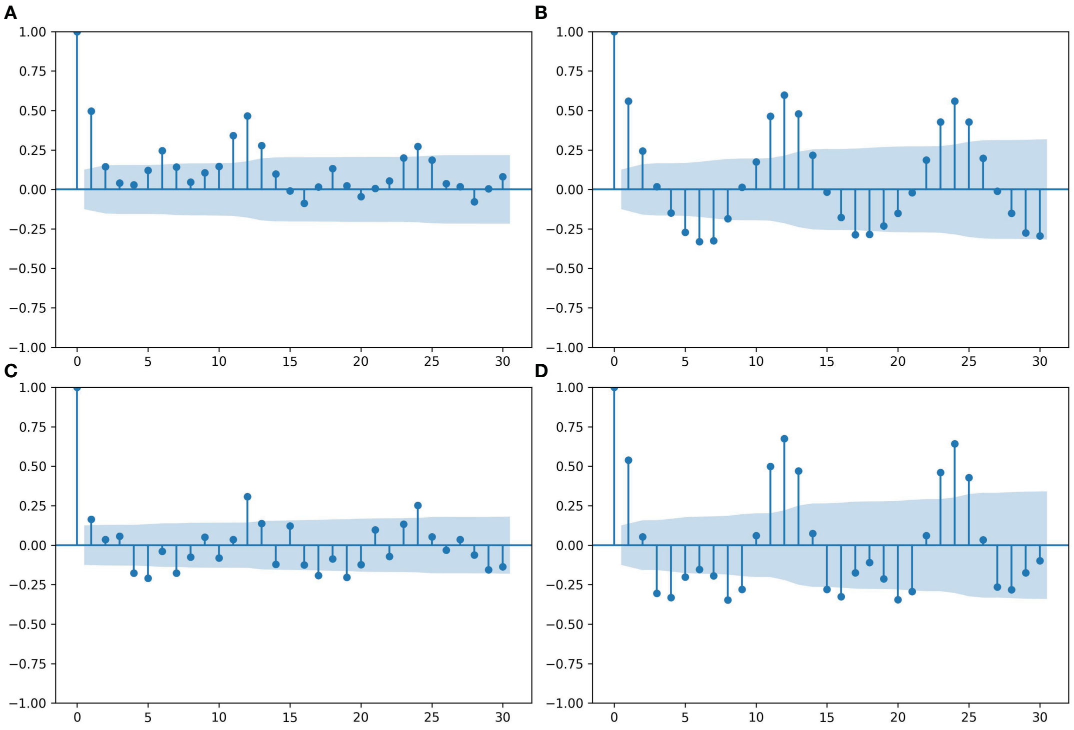

FIGURE 6
The autocorrelation function images of four sea areas. **(A)** Bohai Sea, **(B)** the Yellow Sea, **(C)** the East China Sea, and **(D)** the South China Sea. The blue solid points are the autocorrelation function values, and the blue shaded area is the confidence interval.

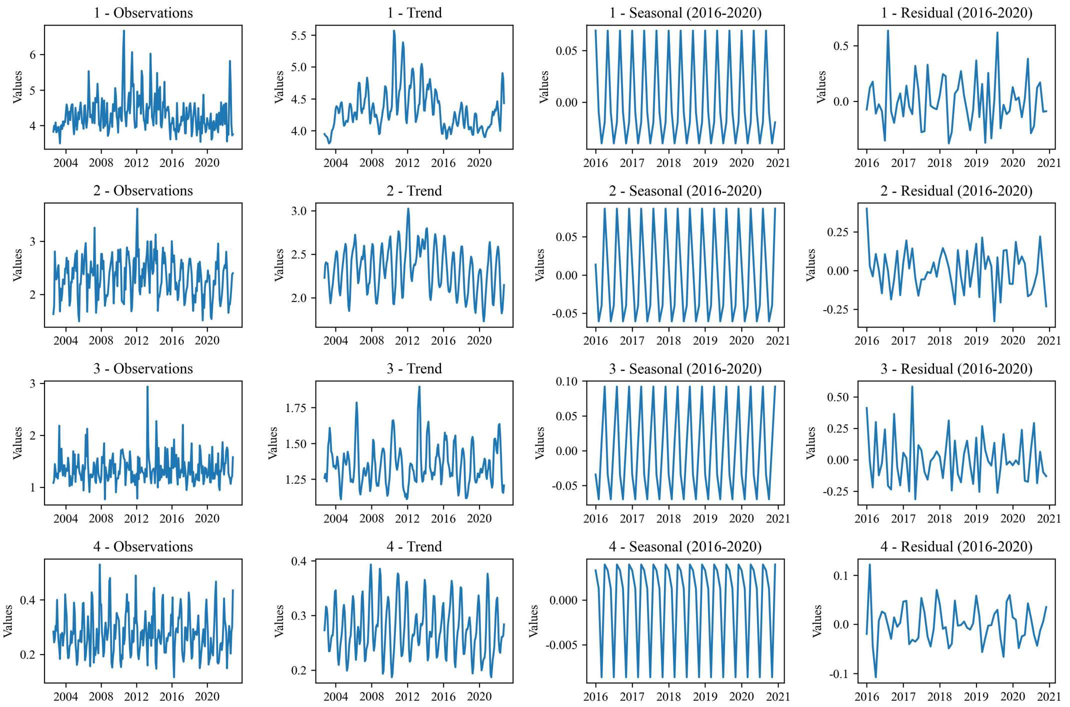

FIGURE 7
Time decomposition analysis plots of chlorophyll a concentration time series for the four sea areas. Serial number one represents the Bohai Sea, serial number two represents the Yellow Sea, serial number three represents the East China Sea, and serial number four represents the South China Sea. The first column of images represents the original time series plot, the second column represents the trend plot after time decomposition, the third column represents the seasonal component plot after time decomposition, and the fourth column represents the residual plot after time decomposition.

interannual fluctuations of Chl-a concentration in the Bohai Sea and the East China Sea show an increasing trend, while the interannual fluctuations of Chl-a concentration in the Yellow Sea and the South China Sea do not vary significantly.

3.4 Correlation analysis of Chl-a concentration and physicochemical characteristics of seawater

3.4.1 Chl-a and seawater physical and chemical characteristics

Since some data are missing at some locations on the sampling line, the ARIMA model (Box et al, 2015) was firstly used to fit at the maximum extent, on the basis of which the analysis was carried out in the observation.

As shown in Figure 9A, analysis of the relationship between temperature and Chl-a concentration shows a non-linear relationship, with Chl-a concentration showing some fluctuation or threshold effect with the change of seawater temperature. The positive correlation on a certain interval is due to the fact that higher temperature can provide a more favorable growth environment and promote the growth and reproduction of phytoplankton, which leads to an increase in Chl-a concentration. And a negative correlation on a certain interval, this is because high temperature may lead to the acceleration of metabolic processes in phytoplankton, which increases their demand for nutrients and also accelerates the consumption of photosynthesis products, thus decreasing Chl-a concentration.

Because Chl-a concentration directly affects the intensity of biological photosynthesis, it is also an important characteristic quantity to characterize biological productivity. On the one hand, the increase of Chl-a concentration promotes the photosynthesis of marine phytoplankton, and under the condition of certain energy consumption by itself, the accumulated organic matter increases and the net primary productivity increases; on the other hand, when the net primary productivity of marine phytoplankton is increased by other factors, the phytoplankton On the other hand, when the net primary productivity of marine phytoplankton increases due to other factors, the photosynthetic efficiency will also increase, promoting itself to produce more Chl-a to meet the photosynthetic load. So there is an overall synergistic change between the two in the Figure 9B.

Observing the Figure 9C, it can be roughly seen that the three nutrients and Chl-a concentration also show a trend of synergistic change, but not very obvious. So phosphate, nitrate, and silicate were extracted from the ocean surface on the sampling route in 2009, 2013, and 2018, respectively, and regressed with Chl-a. The results are shown in Figures 9E–G, respectively. All three nutrient salts have different degrees of contribution to Chl-a. Phosphate had the most significant promotion effect on Chl-a concentration, followed by nitrate, and silicate had the weakest promotion effect on Chl-a concentration. The concentration of phosphate in seawater is the lowest among the three nutrients, but small changes in its concentration have the greatest effect on Chl-a.

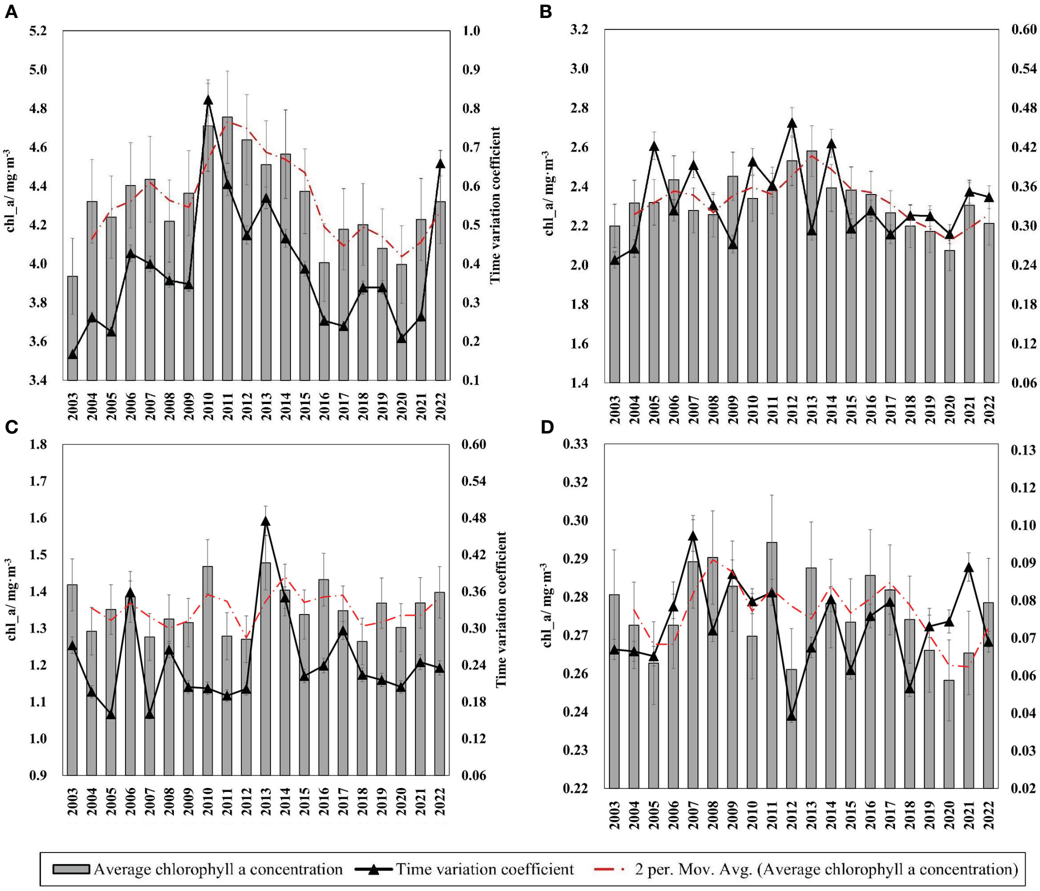

FIGURE 8
Multi-year annual average chlorophyll a concentration and time variation coefficient of the four major China seas from 2002 to 2022. **(A)** Bohai Sea, **(B)**Yellow Sea, **(C)**East China Sea, **(D)**South China Sea. The coefficient of temporal variation for each year was calculated from the monthly chlorophyll a concentration values for that year. The red dotted line in the figures is a moving average simulation of the annual change in chlorophyll a concentration for each sea area.

Poornima et al. (2014) analyzed the relationship between Chl-and phosphate in an experiment using *in situ* nutrient enrichment experiments and showed significant uptake and utilization of phosphate by phytoplankton. Numerous studies on HABs have also shown that phosphorus deficiency greatly inhibits the growth of HABs (Adolf et al., 2009; Au et al., 2010; Guan and Ping, 2017; Lema et al., 2017), which in turn can affect Chl-a concentrations. In addition, the annual average concentrations of phosphate, nitrate, and silicate in China Seas in 2009, 2013, and 2018 (Table 4) showed a decreasing trend in all three nutrient concentrations in China Seas to varying degrees. 2018 phosphate concentrations decreased by 11.51%, nitrate by 2.87%, and silicate by 2.46% compared to 2009, which also corroborates the overall decrease of Chl-a concentration in China Seas by -0.0095 mg/m^3 over 20 years.

Phytoplankton in the ocean (e.g., algae and phytoplankton) absorb light energy through photosynthesis and use carbon dioxide and water to synthesize organic matter, while releasing oxygen. This process regulates pCO$_2$ in seawater, so Chl-a concentration is strongly related to the partial pressure of carbon dioxide in seawater. As the Figure 9D shows, the relationship between pCO$_2$ and Chl-a concentration is not obvious. Therefore, the regression analysis was performed on the pCO$_2$ data collected from cruise lines 1, 2, 3, and 4 and the Chl-a concentration data at the same point in that month, respectively, and the analysis results are shown in Figure 9H. Here again, the logarithm operation was performed on Chl-a. Since the relationship between the two is complex, the direct regression analysis does not portray the relationship well, so after the logarithm processing of Chl-a The two showed a more regular correlation. Bai et al. (2015) proposed a "MeSAA" algorithm to evaluate pCO$_2$ using temperature, salinity, and Chl-a concentration, and their process analysis also showed a negative correlation. The expression for photosynthesis is as follows (Yuan et al., 2013):

$$136CO_2+16NO_3^-+HPO_4^{2-}+0.5SO_4^{2-}+85H_2O+19H^+ = C_{136}H_{190}O_{37}N_{16}P_1S_{0.5}+188O_2 \quad (6)$$

Marine phytoplankton convert dissolved inorganic carbon dissolved in the ocean into organic carbon form through photosynthesis, which directly affects the partial pressure of carbon dioxide in seawater and reduces pCO$_2$.

3.4.2 Chl-a and seawater dynamics processes

Figures 10A, B show the mixed layer depths in January as well as July 2018.It is clear from the figure that the mixed layer depth in

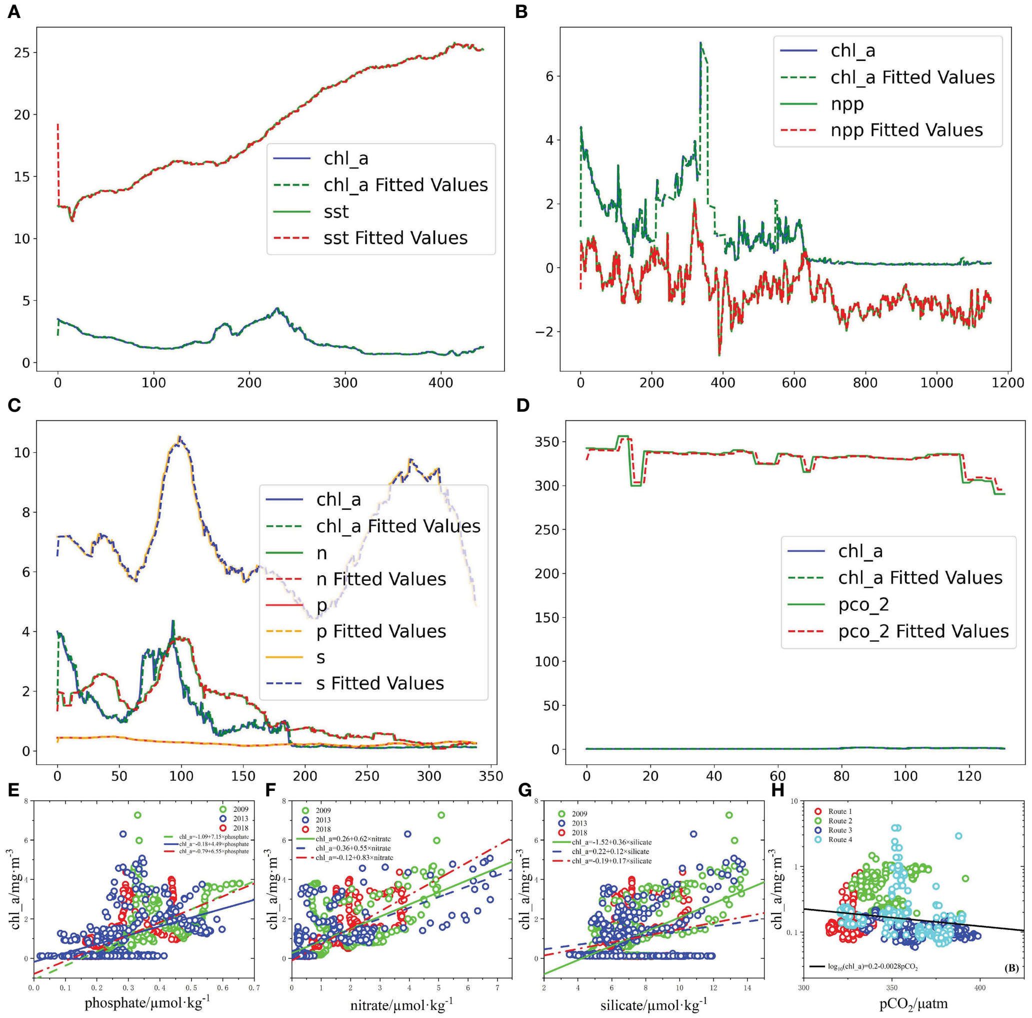

FIGURE 9
(A) Correlation between chlorophyll a concentration and seawater surface temperature as shown, **(B)** correlation between chlorophyll a concentration and net primary productivity of the ocean, **(C)** correlation between chlorophyll a concentration and nitrate, phosphate, and silicate, and **(D)** correlation between chlorophyll a concentration and partial pressure of carbon dioxide in seawater. The dotted lines in the above plots are the curves after each data has been fitted by ARIMA time model. Note that for simplicity of study, **(A–D)** are dimensionless. **(E–G)** are the regression plots of phosphate, nitrate, and silicate with chlorophyll a concentration, respectively, and **(H)** is the regression plot of seawater carbon dioxide partial pressure with chlorophyll a concentration on the four sampling lines.

January is generally greater than that in July in China Seas. The seasonal variation of Chl-a concentration in the South China Sea and the East China Sea, for example, the Chl-a concentration in the South China Sea reaches its peak in winter, while the East China Sea reaches its peak in spring, as shown in Figure 10A. Compared with the East China Sea, the northeast monsoon prevails in the South China Sea in winter, and the strong winter wind acts on the sea-air interface, causing the ocean dynamics process, the vertical movement of seawater is significant, and the mixed layer of the water body deepens during the vertical flow of seawater, and the rich nutrients are brought to the surface layer of the ocean under the action of the surge current (Boyd and Trull, 2007), which provides rich material supply for marine phytoplankton, so the Chl-a concentration in the South China Sea is high in winter. Figures 10C, D show the cumulative differences in phosphate concentrations at three different ocean depths in the South China

TABLE 4 Annual average values of three nutrients (μmol/kg) and percentage decrease in 2009, 2013 and 2018.

Nutritional salts	2009	2013	2018	Decrease in percentage
Silicate	7.320	7.216	7.140	2.46
Nitrate	0.890	0.740	0.864	2.87
Phosphate	0.262	0.222	0.232	11.51

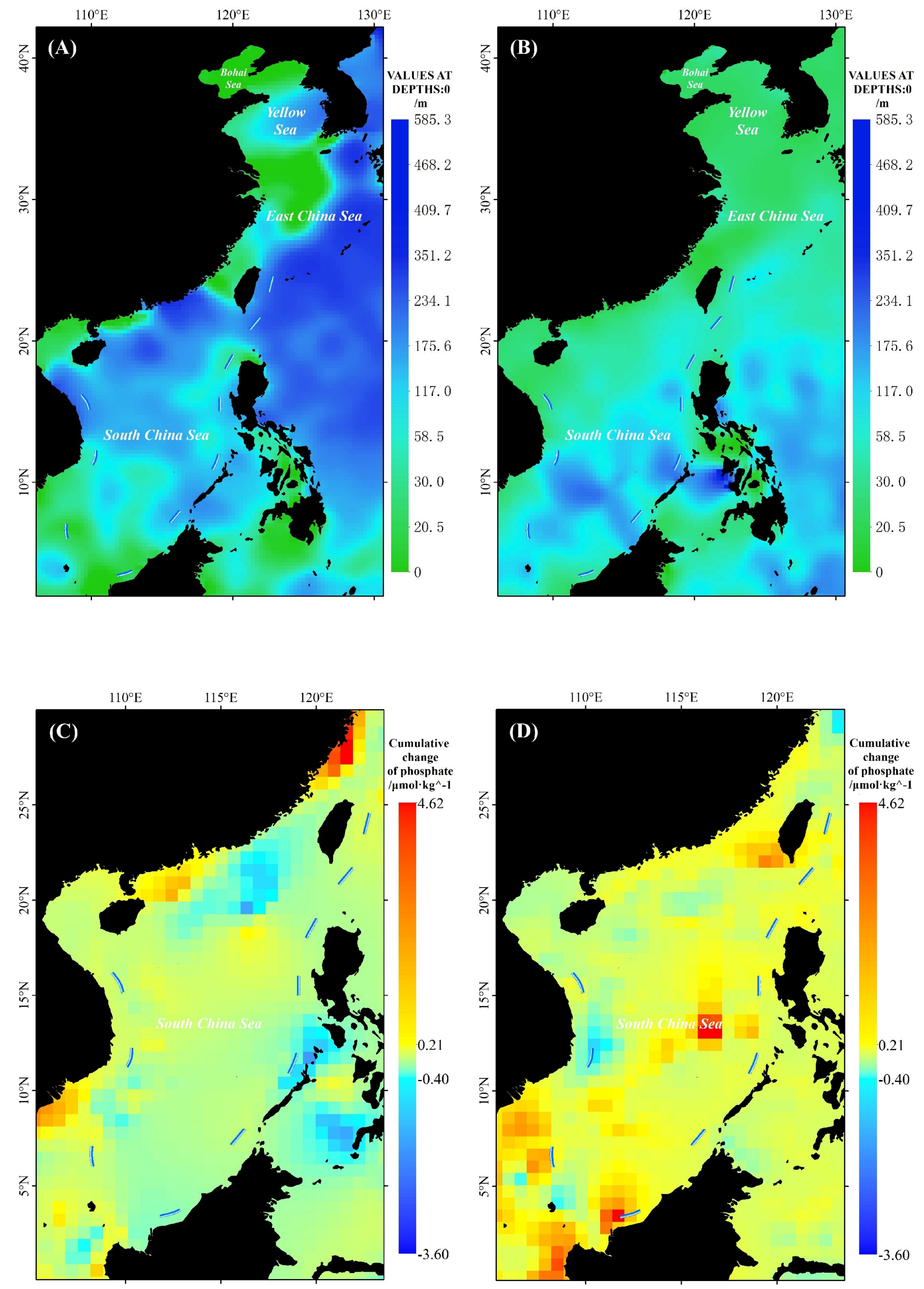

FIGURE 10
Depth of mixed layer in winter **(A)** and summer **(B)** in China Seas in 2018 and cumulative difference between winter **(C)** and summer **(D)** concentrations of phosphate at sea level, 25m below sea level, and 50m below sea level in the South China Sea in 2018.

Sea: the ocean surface, 25 m below the sea surface, and 50 m below the sea surface in winter and summer (corresponding to January and July at mixed layer depths, respectively) (phosphate was selected for analysis because it has the greatest effect on Chl-a concentration as analyzed above), and Table 5 shows the phosphate concentrations at different ocean depths in 2018. From the cumulative difference in phosphate concentration across ocean depths, the difference in nutrient concentration with ocean depth in the photosynthetic zone (surface layer of the ocean) becomes smaller compared to summer due to the influence of mixed layer deepening in winter, which allows phosphate in seawater to be transported from deeper ocean areas to shallower layers of seawater, facilitating nutrient supply to phytoplankton in the photosynthetic zone and thus promoting more Chl-a production, which explains

TABLE 5 Concentration of phosphate at different sea depths in 2018.

Depth(m)	Summer(μmol/kg)	Winter(μmol/kg)
0 (Sea Level)	0.3905	0.2244
25	0.4596	0.2694
50	0.6068	0.2766

the specific influence mechanism of how mixed layer deepening promotes higher Chl-a concentration.

3.5 A comprehensive explanation of the spatial and temporal variation of Chl-a concentration in China Seas by multiple influencing factors of Chl-a

In the context of global warming, the China Seas produces El Niño-like ocean surface temperature anomalies (Dai et al., 2011), and the overall seawater temperature shows an increasing trend, and with the above analysis of the negative correlation between Chl-a and SST, the increase of seawater temperature makes the decrease of Chl-a concentration; in addition, the nutrient salts in the China Seas have decreased to different degrees during 2009-2018, and different nutrient salts play a role in the Therefore, the decrease of nutrient salt concentration is not conducive to the growth of marine phytoplankton, resulting in the decrease of Chl-a concentration. The above analysis explains the overall decrease of 0.0095 mg/m^3 in Chl-a concentration in China Seas from 2002 to 2022.

From north to south, the sea surface temperature of the Bohai Sea, Yellow Sea, East Sea and South China Sea shows a decreasing trend, and the negative correlation effect of the temperature factor makes the Chl-a concentration show a decreasing trend; human production activities discharge a large amount of wastewater waste into the ocean, and a large proportion of these substances will cause eutrophication of near-shore seawater, which makes a phenomenon similar to algal bloom, and Chl-a concentration rises, while the near-shore of the Bohai Sea, Yellow Sea, East Sea and South China Sea The population density and number gradually decline, the impact of human activities is different, and the impact on Chl-a concentration is different; in addition, the Bohai Sea is closed, seawater mobility is poor, nutrients are more easily enriched, so the Chl-a concentration is large, while the South China Sea is open, seawater flow phase is strong, seawater exchange capacity is strong, nutrient dispersion mobility is strong, also will have an impact on Chl-a concentration. The above analysis explains the reason why the Chl-a concentration gradually decreases from north to south in four different seas in China.

In section 3.2, we can clearly observe a very clear seasonal difference in Chl-a concentration in different sea areas. The concentration of Chl-a in the Bohai Sea reaches its highest in summer, when the main controlling factor is no longer temperature, but the material and energy output from the land system to the marine system. In summer, the rainfall in northern China and the Loess Plateau area increases significantly, especially the Loess Plateau area has more heavy rainfall, and because of the loose loess soil, a large amount of sediment is carried by rainwater under the erosion of heavy rain pouring through the land runoff process and finally from the Yellow River inlet into the sea, a large amount of sediment in the sea contains a large amount of nutrients, providing rich growth energy for the growth of phytoplankton in the Bohai Sea, so the high concentration of Chl-a in the Bohai Sea in summer Therefore, the concentration of Chl-a in the Bohai Sea is high in summer. The Chl-a concentration in the Yellow Sea is winter>spring>autumn>summer, and its Chl-a concentration is consistent with the seasonal change of temperature and is most regulated by the temperature factor. The Chl-a concentration in the East China Sea reaches its maximum in spring, when the temperature of the East China Sea rises in spring and reaches the temperature required for phytoplankton growth, temperature is no longer a limiting factor, but plays a role in promoting the growth and development of marine phytoplankton, when phytoplankton multiply and marine productivity is improved. The Chl-a concentration in the South China Sea is winter > autumn > summer > spring, and the main influencing factor is the temporal change of nutrient salts regulated by the physical process of seawater (as in section 3.4.2: surge flow, mixed layer changes).

Attempts to establish quantitative relationships between Chl-a and its various influencing factors are very difficult. Not only various influencing factors have an effect on Chl-a, but also various influencing factors interact, influence and change synergistically with each other. As shown in equation (6), marine phytoplankton not only convert dissolved inorganic carbon to organic carbon in the process of photosynthesis, which directly affects seawater pCO_2, but the process is also accompanied by changes in the utilization of various nutrient salts in the reservoir and changes in seawater pH, which further affect pCO_2. Furthermore, changes in nutrient salts in seawater can cause changes in seawater pH, which not only directly affects phytoplankton, but also changes in pH have an effect on the ionization of chemicals in seawater, which further affects the growth and development of phytoplankton. In addition, in different seas and at different times, as analyzed above, the main controlling factors of Chl-a are different, and a generalized summary of the law cannot well describe the complex situation of floating changes of multiple influencing factors.

3.6 Marine fisheries under the influence of spatial and temporal variation of Chl-a concentration in China Seas - Zhoushan fishing grounds as an example

Since the concentration of marine Chl-a can be used as one of the indicators of the abundance of marine phytoplankton and algal organisms, the changes in the concentration of marine chl_a in China essentially reflect the changes in marine plants. Therefore, the following study is conducted from the perspective of marine algal plants to analyze the effects on marine fish.

We analyzed the plant distributions of Thalassia hemprichii, Halophila ovalis, Cymodocea rotundata, Enhalus acoroides, Halodule pinifolia, Zostera subg. Zostera marina, Favites pentagona, Halodule uninervis recorded in the eastern coast of China since 2008-2018 based on OBIS. Zostera subg. Zostera marina, Favites pentagona, Halodule uninervis, and other marine algae were statistically analyzed at the depth of the observed plant distribution according to sea level each year. These eight species of marine plants are found in shallow offshore waters and are usually attached to rocks or other substrates, allowing some fish to use the zooplankton or benthos attached to the algae as an additional food source (Shoji et al., 2010). Some specific fishes, such as Perciformes and Stonefish, are classified as algal-feeding fishes, which feed mainly on algae. These fishes have adapted their digestive systems and oral structures to efficiently digest and ingest algae as their main food source (Payne et al., 2008). Therefore, the growth and distribution of these algae can greatly affect the survival of marine fishes that feed on or depend on algae for their environment.

In our study, as shown in Figure 11, we found that two groups of algae, Thalassia hemprichii and Halophila ovalis, showed an increasing trend of growing sea depth over the years, while the remaining six species, Cymodocea rotundata, Enhalus acoroides, Halodule pinifolia, Zostera subg. Zostera marina, Favites pentagona, and Halodule uninervis plants showed a deepening trend in growing sea depth. We speculate that this is related to global warming. On the one hand, global warming makes the temperature of shallow seawater rise, and since the optimal growth temperature of algal plants is specific, the rise in seawater temperature makes marine plants tend to go to a deeper layer of seawater to meet their optimal habitat. On the other hand, the increase in seawater temperature will have an impact on the dissolved oxygen content in seawater. In general, when seawater temperature increases, the dissolved oxygen content in seawater decreases. (Breitburg et al., 2018) As seawater deepens, dissolved oxygen levels are usually higher due to increased water pressure, so algal plants seek a more suitable supply of oxygen and carbon dioxide in deeper water to promote their own growth.

The above changing status of marine algal plant habitats corresponds to Figure 2B. Figure 2B concentrates on the long-term evolution of Chl-a concentration in Chinese waters. The tendency of marine algal plant habitats to deeper seawater corresponds to the decrease in cumulative Chl-a concentration in eastern Chinese waters, which corroborate each other. Therefore, the long-term evolution of Chl-a concentration in Chinese waters is a response to the long-term evolution of marine algae. Correspondingly, the impact of Chl-a concentration changes in Chinese waters is essentially the impact of the evolution of marine algae on Chinese waters. Algal plants are the basis of the marine food chain. They produce organic matter through photosynthesis, which serves as bait and a source of nutrients for other organisms. If algal plants grow deeper, this may result in more algal plants growing in deeper waters, which in turn changes the structure and abundance of the food chain. This may have implications for food availability for marine fishes in different strata. (Smale et al., 2019) Because marine ecosystems are an interconnected whole, small changes in the environment in which marine plants grow can also have a large impact on marine fishes.

Located in the northeastern part of Zhejiang Province, east of Hangzhou Bay and southeast of the estuary of the Yangtze River, Zhoushan Fishery is the largest fishery in China, with the four major economic fishes, big yellowtail, small yellowtail, striped bass and squid, as the main aquatic products. The fishery resources have suffered serious damage due to the long-term indiscriminate fishing and marine pollution (Zhu and Qian, 2022).

Marine Chl-a is mainly derived from marine algae, which form the energy base of the aquatic food chain and play a vital role in the aquatic ecosystem. Chl-a concentration is an important basis for judging the growth and production level of marine algae, so the level of Chl-a concentration indirectly reflects the food abundance and habitat quality of fish.

The main purpose of the fishing moratorium is to avoid the peak period of fish growth and reproduction and to prevent the

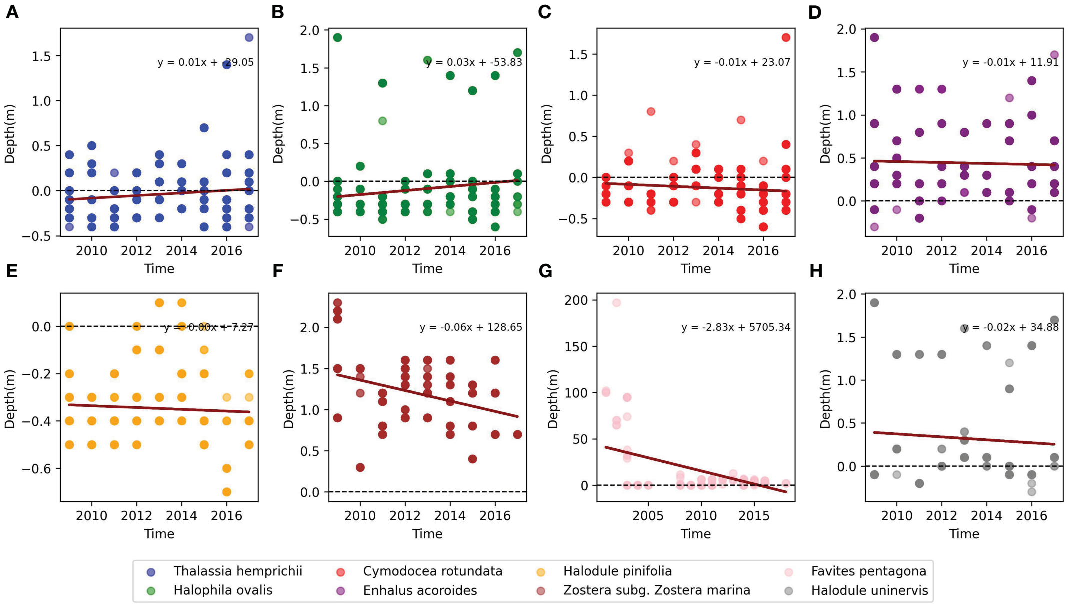

FIGURE 11
Each graph represents the observed growing water depth of eight marine plants during 2008-2020, with negative values below the sea surface and positive values above the sea surface. **(A–H)** represent, in order, Thalassia hemprichii, Halophila ovalis, Cymodocea rotundata, Enhalus acoroides, Halodule pinifolia, Zostera subg. Zostera marina. Solid dots represent bathymetric values, black dashed lines represent sea level, and red realizations represent trend changes over years.

decline of biological populations due to overfishing. As shown in Figure 12, the Chl-a concentration in Zhoushan fishing grounds during the fishing moratorium showed a fluctuating downward trend, reflecting that the growth environment and nutrient synthesis of phytoplankton in the fishing grounds were in a decreasing trend. The food abundance of marine fish had decreased, which was not conducive to the growth and reproduction of marine fish during the golden recovery period of the fishing moratorium, nor was it conducive to the recovery of marine fish resources and the sustainable development of marine fisheries, which were potential challenges for modern fisheries. In order to maintain the sustainable development of marine fisheries, both a reasonable rest-fishing balance and attention to environmental protection are needed to maintain a good growing environment for marine fish and the food sources on which they depend. Meanwhile, according to statistics, the marine fish catch in Zhoushan fishing grounds increased from 1,155,480,000 tons to 1,541,289,000 tons between 2002 and 2021, an increase of 33.4% in 20 years (Zhoushan Bureau of Statistics, 2022). The decline in fish habitat quality caused by the decrease in Chl-a concentration is contrasted with the increasing fishing capacity of Zhoushan fishing ground over the years. The unreasonable fishing activities of contrasted with aggravate the deterioration of the marine ecological environment and lead to the decrease of Chl-a concentration in the fishing ground. Simultaneously, in the face of the decreasing trend of Chl-a concentration, if the human continues to maintain high growth of fishing volume will certainly lead to the depletion of fish resources.

4 Concluding remarks

In this study, spatial distribution characteristics data of long time series were constructed to delineate the spatial and temporal variation characteristics of Chl-a concentration in China Seas. In addition, the potential effects of several oceanographic variables on Chl-a concentrations were analyzed. Finally, the potential impacts on marine fisheries and the urgency of sustainable development of marine fisheries were investigated from the essence of changes in Chl-a concentrations and changes in marine algal plants The results of the study showed that:

1. The multi-year average Chl-a concentration in China Seas from 2002 to 2022 was 0.874 mg/m^3. the average Chl-a concentration in Bohai Sea waters over the years was the highest, at 4.547 mg/m^3, and in South China Sea waters was the lowest, at 0.288 mg/m^3. in terms of spatial variation, the overall Chl-a concentration in China Seas from 2002 to 2022 decreased cumulatively by 0.0095 mg/m^3, with the largest cumulative increase of 0.270 mg/m^3 in the Bohai Sea and the largest cumulative decrease of 0.079 mg/m^3 in the East China Sea. the largest multi-year spatial variation of 0.2063 in the East China Sea indicates that the spatial distribution pattern of Chl-a concentrations has evolved significantly.
2. In terms of temporal variation, Chl-a concentration in the Bohai Sea in China from 2002 to 2022 showed a decreasing trend, the Yellow Sea showed an increasing trend, the East China Sea remained basically unchanged, and the South China Sea showed a decreasing trend In terms of temporal variation, Chl-a concentration in the Bohai Sea fluctuated significantly from year to year, and there were obvious differences in Chl-a concentration in each year.
3. The time series of Chl-a concentration changes in the four seas were analyzed by autocorrelation as well as time decomposition analysis, and the changes of Chl-a concentration over a long period of time had obvious periodic phenomena, among which the time decomposition periodicity was most obvious in four-

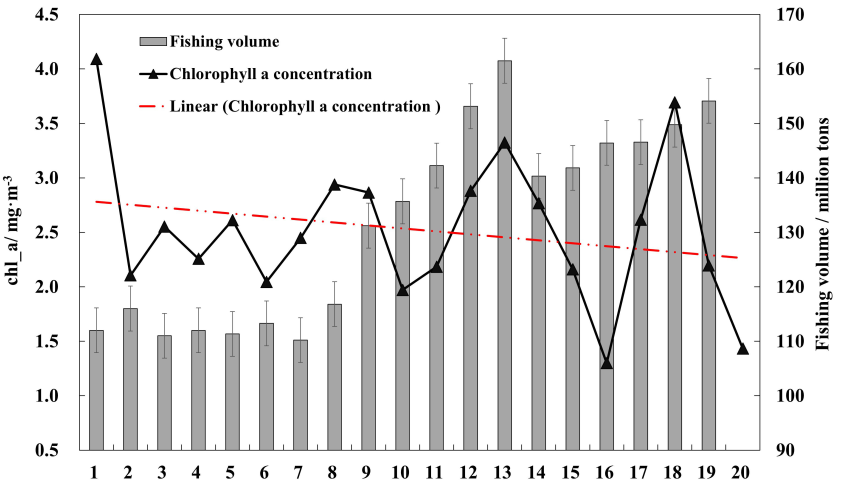

FIGURE 12
Changes in chlorophyll a concentration during the fishing moratorium in Zhoushan fishery from 2003 to 2022 and changes in fish catch from 2003 to 2021. The red dotted line in the figure is a linear simulation of the annual variation of chlorophyll a concentration during the fishing moratorium in Zhoushan fishery.

month steps, which was obviously related to seasonal temperature changes. Among them, the cyclical phenomenon was most obvious in the Yellow Sea.

(4) There was an overall negative correlation between Chl-a and sea surface temperature, but the correlation varied between different temperature bands. All three nutrient salts studied promoted Chl-a, with phosphate having the most pronounced promotion effect on Chl-a. Chl-a was negatively correlated with pCO_2. Seasonal changes in the mixed layer had a strong influence on the variation of nutrients in the upper ocean.

(5) There is a trend of increasing water depth for the growth of the studied algae plants, and this change can greatly affect the survival of marine fish that feed on or depend on algae for their environment. The Chl-a concentration in Zhoushan fishing grounds during the fishing moratorium showed a decreasing trend, while the catch of Zhoushan fishing grounds showed an increasing trend year by year. The decrease of Chl-a concentration limits the food source of fish during the fishing moratorium, which is not conducive to the sustainable development of marine fisheries.

Data availability statement

The datasets presented in this study can be found in online repositories. The names of the repository/repositories and accession number(s) can be found below: https://www.ncei.noaa.gov/access/ocean-carbon-acidification-data-system/oceans/LDEO_Underway_Database/ and https://oceancolor.gsfc.nasa.gov/.

Author contributions

XZ contributed to the synthesis of chlorophyll a data. DM and JX contributed to the data visualization. DZ examined and verifiedthe results of the research process data. KZ and YC analyzed the data and drafted the manuscript. All authors participated in the discussion of the data, interpretations, and manuscript revision.

Funding

This work was funded by the National Science Foundation of Fujian Province, China (Grant No. 2022J01818), National Fund Cultivation Program Project of Jimei University (Grant No. ZP2022016), the Fund of Fujian Ocean Synergy Alliance (FOCAL) (Grant No. FOCAL2023-0101), and Independent Research Projects of the Southern Marine Science and Engineering Guangdong Laboratory (Zhuhai) (Grant No. SML2021SP306).

Acknowledgments

The authors express our sincere gratitude to Prof. DQ for his helpful supports as well as the data service provided by the Oceanographic Data Center (Chinese Academy of Sciences, CASODC), National Centers for Environmental Information (NOAA) and NASA EarthData OceanColor Web.

Conflict of interest

The authors declare that the research was conducted in the absence of any commercial or financial relationships that could be construed as a potential conflict of interest.

Publisher's note

References

Adolf, J. E., Bachvaroff, T. R., and Place, A. R. (2009). Environmental modulation of karlotoxin levels in strains of the cosmopolitan dinoflagellate Karlodinium veneficum (Dinophyceae). *J. Phycol.* 45, 176–192. doi: 10.1111/j.1529-8817.2008.00641.x

Au, F. X., Place, A. R., Garcia, N. S., et al. (2010). CO_2 and phosphate availability control the toxicity of the harmful bloom dinoflagellate Karlodinium veneficum. *Aquat. Microbial Ecol.* 59, 55–65. doi: 10.3354/ame01396

Bai, Y., Cai, W. J., He, X., Zhai, W. D., Pan, D. L., Dai, M. H., et al. (2015). A mechanistic semi-analytical method for remotely sensing sea surface pCO2 in river-dominated coastal oceans: A case study from the East China Sea. *J. Geophys. Res. Oceans.* 120, 2331–2349. doi: 10.1002/2014JC010632

Behrenfeld, M. J., Boss, E., Siegel, D. A., et al. (2005). Carbon-based ocean productivity and phytoplankton physiology from space. *Global Biogeochem. Cycles.* 19 (1). doi: 10.1029/2004GB002299

Blondeau-Patissier, D., Gower, J. F., Dekker, A. G., et al. (2014). A review of ocean color remote sensing methods and statistical techniques for the detection, mapping and analysis of phytoplankton blooms in coastal and open oceans. *Prog. Oceanography.* 123, 123–144. doi: 10.1016/j.pocean.2013.12.008

Box, G. E., Jenkins, G. M., Reinsel, G. C., and Ljung, G. M. (2015). *Time series analysis: forecasting and control.* Hoboken, NY: John Wiley Sons.

Boyd, P. W., and Trull, T. W. (2007). Understanding the export of biogenic particles in oceanic waters: Is there consensus? *Prog. Oceanography* 72 (4), 276–312. doi: 10.1016/j.pocean.2006.10.007

Breitburg, D., Levin, L. A., Oschlies, A., Grégoire, M., Chavez, F. P., Conley, D. J., et al. (2018). Declining oxygen in the global ocean and coastal waters. *Science.* 359 (6371), eaam7240. doi: 10.1126/science.aam7240

Chatfield, C. (2004). *The analysis of time series: an introduction. 6th edition.* (New York, NY: Chapman & Hall/CRC).

Chen, K. Q. (2013). On citizens' Right to safety in the marine environment - reflections arising from the bohai bay oil spill. *Legal Sci.* 31, 63–71. doi: 10.16290/j.cnki.1674-5205.2013.02.001

Cong, P. F., Niu, Z., Meng, J. H., et al. (2006). Variability of chlorophyll a retrieved from satellite in Chinese shelf sea from1998 to 2003. *Mar. Environ. Sci.* 1, 30–33. doi: 10.1016/S1872-2040(06)60041-8

Cui, T., Zhang, J., Tang, J., Sathyendranath, S., Groom, S., Ma, Y., et al. (2014). Assessment of satellite ocean color products of MERIS, MODIS and SeaWiFS along the East China Coast (in the Yellow Sea and East China Sea). *J. Photogrammetry Remote Sensing.* 87, 137–151. doi: 10.1016/j.isprsjprs.2013.10.013

Cury, P., Bakun, A., Crawford, R. J. M., Jarre, A., Quiñones, R. A., Shannon., L. J., et al. (2000). Small pelagics in upwelling systems: patterns of interaction and structural changes in "wasp-waist" ecosystems. *ICES J. Mar. Sci.* 57 (3), 603–618. doi: 10.1006/jmsc.2000.0712

Dai, A. (2011). Drought under global warming: a review. *Wiley Interdiscip. Reviews: Climate Change.* 2 (1), 45–65. doi: 10.1002/wcc.81

Dang, E., Li, Z., Kangli, G., et al. (2022). The spatial distribution of chlorophyll a and its environment regulation in coastal area of Zhuhai. *Acta Scientiae Circumstantiae.* 42, 240–247. doi: 10.13671/j.hjkxxb.2021.0028

Demarcq, H., Barlow, R. G., and Shillington, F. A. (2003). Climatology and variability of sea surface temperature and surface chlorophyll in the benguela and agulhas ecosystems as observed by satellite imagery. *South African J. Mar. Sci.* 25 (1), 363–372. doi: 10.2989/18142320309504022

Falkowski, P. G., Barber, R. T., and Smetacek, V. (2000). The global carbon cycle: a test of our knowledge of earth as a system. *Science.* 290 (5490), 291–296. doi: 10.1126/science.290.5490.291

Firdhouse, M., Smith, J., Johnson, A., et al. (2019). Assessment of water quality using chlorophyll-a: A review. *Environ. Dev. Sustainability.* 34 (5), 1754–1760.

Fragoso, G. M., Brotas, V., Mendes, C. R., et al. (2018). Chlorophyll-a concentration as a proxy for phytoplankton primary production in different marine environments. *Estuarine Coast. Shelf Sci.* 209.

Garcia, H. E., Boyer, T. P., Baranova, O. K., Locarnini, R. A., Mishonov, A. V., Grodsky, A., et al. (2019). *World ocean atlas 2018: product documentation (A. Mishonov, Technical Editor).* (Silver Spring, MD: Ocean Climate Laboratory).

Garcia, H. E., Weathers, K., Paver, C. R., Smolyar, I., Boyer, T. P., Locarnini, R. A., et al. (2018). *World Ocean Atlas 2018, Volume 4: Dissolved Inorganic Nutrients (phosphate, nitrate and nitrate+nitrite, silicate) (Mishonov Technical Ed.; NOAA Atlas NESDIS)* (Silver Spring, MD: National Centers for Environmental Information), 35.

Getis, A., and Ord, J. K. (1992). The analysis of spatial association by use of distance statistics. *Geogr. Anal.* 24 (3), 189–206. doi: 10.1111/j.1538-4632.1992.tb00261.x

Gregg, W. W., Conkright, M. E., Ginoux, P., et al. (2003). Ocean primary production and climate: Global decadal changes. *Geophys. Res. Letters.* 30 (15). doi: 10.1029/2003GL016889

Groebner, D. F., Shannon, P. W., and Fry, P. C. (2018). *Business statistics: A decision-making approach*. Boston, MA: Pearson.

Guan, W., and Ping, (2017). Dependency of UVR-induced photoinhibition on atomic ratio of N to P in the dinoflagellate Karenia mikimotoi. *Mar. Biology: Int. J. Life Oceans Coast. Waters.* 164, 31. doi: 10.1007/s00227-016-3065-x

Hamilton, J. D. (1994). *Time series analysis* (Princeton, NJ: Princeton University Press).

Hao, Q. (2010). *Spatial and temporal distribution characteristics and environmental regulation mechanisms of chlorophyll and primary productivity in the Chinese offshore* (Qingdao, CN: Ocean University of China).

He, X., Bai, Y., Pan, D., Chen, C.-T. A., Cheng, Q., Wang, D., et al. (2013). Satellite views of the seasonal and interannual variability of phytoplankton blooms in the eastern China seas over the past 14 yr, (1998–2011). *Biogeosciences* 10, 4721–4739. doi: 10.5194/bg-10-4721-2013

Hu, C., Lee, Z., and Franz, B. (2012). Chlorophyll a algorithms for oligotrophic oceans: A novel approach based on three-band reflectance difference. *J. Geophys. Res.* 117, C01011. doi: 10.1029/2011JC007395

Jun, C., and Liu, J. (2015). The spatial and temporal changes of chlorophyll-a and suspended matter in the eastern coastal zones of China during 1997–2013. *Continental Shelf Res.* 95, 89–98. doi: 10.1016/j.csr.2015.01.004

Lema, K. A., Latimier, M., NÉZAN, É., et al. (2017). Inter and intra-specific growth and domoic acid production in relation to nutrient ratios and concentrations in Pseudo-nitzschia: phosphate an important factor. *Harmful Algae.* 64, 11–19. doi: 10.1016/j.hal.2017.03.001

Lian, Z., Wang, X. Y., and Wei, Z. X. (2020). Features and driving mechanisms of the intra-seasonal variations of sea surface chlorophyll a in the South China Sea. *Adv. Mar. Science.* 38, 649–661. doi: 10.3969/j.issn.1671-6647.2020.04.009

Lin, Z., Rong-Hua, M., Hong-Tao, D., et al. (2011). Remote sensing retrieval for chlorophyll-a concentration in turbid case ii waters(i): the optimal model. *J Infrared Millim Terahertz Waves* 30 (6), 531–536. doi: 10.1140/epjd/e2011-20005-8

Montgomery, D. C., Peck, E. A., and Vining, G. G. (2012). *Introduction to linear regression analysis. 5th ed*. (Hoboken, NY: Wiley).

OBIS (2023). bis. *Retrieved https://obis.org/ June* 28, 2023.

Paerl, H. W. (2009). Controlling eutrophication along the freshwater–marine continuum: dual nutrient (N and P) reductions are essential. *Estuaries Coasts.* 32 (4), 593–601. doi: 10.1007/s12237-009-9158-8

Payne, A., Cotter, J., and Potter, T. (2008). *Advances in fishery science: 50 years on from beverton and holt* (Oxford, UK: Blackwell Publishing Ltd).

Poornima, T. K., Ranith, R., et al. (2014). Nutrient enrichment experiment to establish relationship between chlorophyll and phosphate. *Int. J. Comput. Sci. Eng.* 3, 211–224.

Shoji, J., Nakamura, Y., and Nakano, S. (2010). Seaweed beds as habitats for fish and mobile epifauna: an experimental approach to the evaluation of habitat complexity. *J. Exp. Mar. Biol. Ecol.* 386 (1-2), 12–19.

Smale, D. A., Wernberg, T., and Connell, S. D. (2019). Ocean warming and seagrass loss modify fish communities. *Global Change Biol.* 25 (1), 411–422.

Sun, S., Su, J., and Shi, P. J. (2011). Features of sea ice disaster in the Bohai Sea in 2010. *J. Nat. Disasters.* 20, 87–93. doi: 10.13577/j.jnd.2011.0615

Takahashi, T., Sutherland, S. C., and Kozyr, A. (2020). *Global ocean surface water partial pressure of CO2 database: measurements performed during 1957-2019 (LDEO database version 2019) (NCEI accession 0160492). Version 9.9.* (Silver Spring, MD: National Centers for Environmental Information). doi: 10.3334/CDIAC/OTG.NDP088(V2015

Walton, C. C., Pichel, W. G., Sapper, J. F., et al. (1998). The development and operational application of nonlinear algorithms for the measurement of sea surface temperatures with the NOAA polar-orbiting environmental satellites. *J. Geophys. Res.* 103, 27999–28012. doi: 10.1029/98JC02370

Wang, Q. Y., Du, Y. M., and Liu, L. (2022). Distribution of hlorophyll a and its relationship With environmental factors in summer 2013. *Mar. Lakes Marshes Bull.* 44 (02), 121–127. doi: 10.13984/j.cnki.cn37-1141.2022.02.016

Xue, C. J. (2019). A dataset of global 9km marine net primary productivity anomalies from 1998 to 2018. [Data set]. Available at: https://data.worldbank.org/indicator.

Yang, C. Y., Tang, D. L., and Ye, H. B. (2017). A study on retrieving chlorophyll concentration by using GF-4 data. *J. Trop. Oceanography.* 36, 33–39. doi: 10.11978/2017008

Yuan, X. G., Huang, W. M., Bi, Y. H., et al. (2013). Relationship between pCO2 and algal biomass in xiangxi bay in spring. *Environ. Sci.* 34, 1754–1760. doi: 10.13227/j.hjkx.2013.05.031

Yue, H. F., Zhao, T. C., Chen, L. D., et al. (1999). Test of the ocean color radiant models in SeaWiFS data. *Mar. Environ. Sci.* 4, 57–61.

Zhao, N., Zhang, G., Zhang, S., et al. (2019). Temporal-spatial distribution of chlorophyll-a and impacts of environmental factors in the bohai sea and yellow sea. *IEEE Access.* 7, 160947–160960. doi: 10.1109/ACCESS.2019.2950833

Zheng, X. S., Zhang, X., and Jia, C. (2017). Inversion and verification of chlorophyll a concentration in the Bohai Bay. *Mar. Sci. Bull.* 19, 51–61.

Zhoushan Bureau of Statistics (2022) *Total fish production over the years*. Available at: http://zstj.zhoushan.gov.cn/art/2022/12/5/art_1229705814_58865872.html (Accessed April 15, 2023).

Zhu, Q., He, X., Pan, D., et al. (2010). Climatology and long-time change of the sea surface temperature and chlorophyll concentration in East China Seas. *Remote Sens. Coast. ocean land atmosphere environment.* 310012, 2010. doi: 10.1117/12.869400

Zhu, M. H., and Qian, W. G. (2022). Reasons for the decline of fishery resources in Zhoushan fishing grounds and countermeasures for their restoration. *Rural Economy Technol.* 33, 79–82.

frontiers | Frontiers in Marine Science

TYPE Original Research
PUBLISHED 17 August 2023
DOI 10.3389/fmars.2023.1225640

Diversity and assembly of planktonic protist communities in the Jeju Strait, Korea

Juhee Min and Kwang Young Kim*

Department of Oceanography, College of Natural Sciences, Chonnam National University, Gwangju, Republic of Korea

OPEN ACCESS

EDITED BY
Zhaohe Luo,
Third Institute of Oceanography, Ministry of Natural Resources, China

REVIEWED BY
Abdullah Al Mamun,
Chinese Academy of Sciences (CAS), China
Zhangxi Hu,
Guangdong Ocean University, China

*CORRESPONDENCE
Kwang Young Kim
✉ kykim@chonnam.ac.kr

RECEIVED 19 May 2023
ACCEPTED 18 July 2023
PUBLISHED 17 August 2023

CITATION
Min J and Kim KY (2023) Diversity and assembly of planktonic protist communities in the Jeju Strait, Korea. *Front. Mar. Sci.* 10:1225640. doi: 10.3389/fmars.2023.1225640

This study examined planktonic protists—microbial eukaryotes with cell sizes between 2 and 200 μm—to understand their diversity, assembly processes, and co-existence patterns in surface waters of the Jeju Strait (JS), Korea. Using small organelle-enriched metagenomics, the study identified 252 operational taxonomic units (OTUs) across three distinct oceanographic regions of the JS during multiple seasons. Interestingly, there were no significant variations in the diversity or phylogenetic structures of these planktonic protist communities (PPCs), indicating a uniform distribution of PPCs across the strait. However, a higher clustering of their phylogenetic structure was observed in November, implying that seasonal environmental factors influenced their assembly. The study also discovered that seasonal shifts had a major impact on the composition of these communities. For example, Myzozoa was more prevalent in March, while Ochrophyta dominated in November. Protist size also varied seasonally, with larger protists increasing from June to November and then decreasing by March. Neutral community model analysis provided insights into the role of stochastic processes in shaping community assembly. The majority of OTUs fell into the neutral category, while a smaller proportion displayed non-neutral patterns. For instance, certain species like *Pseudo-nitzschia* and *Chaetoceros* were frequently found but had lower abundance, while other species like *Alexandrium* and *Protoceratium* were less frequent but more abundant. The feeding patterns, or trophic modes, of these protists also showed variations. Additionally, the study unveiled a complex network of species interactions within the strait, including positive mutualistic relationships and negative competitive interactions. The intricate interaction network consisted of 61 distinct modules, suggesting the presence of specialized subgroups within the PPCs that fulfill unique ecological roles. These subgroups contribute significantly to the overall stability and resilience of the ecosystem.

KEYWORDS

assembly processes, co-existence patterns, diversity, modules, neutral community model (NCM), operational taxonomic units (OTUs), planktonic protist community (PPC), small organelle-enriched metagenomics (SoEM)

Introduction

The Jeju Strait (JS) is a 90 km long stretch of water located between the Korean mainland and Jeju Island. The Kuroshio Current System influences this strait, which is divides into the Western Kuroshio Branch and the Eastern Kuroshio Branch. These branches further divided into various currents, including the Tsushima Warm Current (TWC), and the Jeju Warm Current (JWC) (Lie and Cho, 1997). The JS links the Yellow Sea and the East China Sea, forming part of the Korea Strait (also known as the South Sea of Korea). Within the JS, water masses with different temperatures and salinities flow and interact, creating a complex hydrodynamic environment (Chang et al., 2004). The temperature and salinity in the JS can be greatly affected by seasonal changes. During winter, lower current shear and a mixed layer are induced, while in summer, warmer and less saline surface water leads to stratification and higher surface current velocities (Shin et al., 2022). The unique current system of the JS also facilitates the development of thermohaline fronts (Kim et al., 2022).

The JS is useful for studying ecological phenomena, such as the annual red tides caused by both phytoplankton and seasonal environmental fluctuations. The JS also experiences human-induced disturbances and hosts blooms of various planktonic species (Lee et al., 2020; Won et al., 2021; Min and Kim, 2023). Despite being in a temperate region, the JS is a transition area between temperate and subtropical zones, based on water temperature and the presence of tropical/subtropical species (Kim et al., 2020a; Lee et al., 2023). Understanding the processes shaping the JS's plankton communities is crucial because of its role as a biological corridor for migrating species, as well as its oceanographic dynamics, making it an ideal model for studying biogeochemical processes (Kim and Lee, 2022).

Marine protists, which are diverse organisms that significantly contribute to marine primary production and biogeochemical cycles, support food webs and influence local ecosystems through various behaviors and interactions, playing a vital role in regulating the marine carbon cycle (Caron et al., 2012; Lima-Mendez et al., 2015; Seeleuthner et al., 2018; Glibert and Mitra, 2022; Lim and Jeong, 2022). Pico- and nano-plankton, play a significant role in the global carbon cycle. However, studying these tiny protists is challenging due to their small size and non-distinctive morphology (Eom et al., 2021). The emergence of high-throughput DNA sequencing has enhanced our understanding of marine protist diversity and species abundance (Lee et al., 2021a; Ok et al., 2021; Gutiérrez-Rodríguez et al., 2022; Min and Kim, 2022; Jin et al., 2023). In this study, small organelle-enriched metagenomics (SoEM) was used to investigate the composition and distribution of planktonic protist communities (PPCs) in the JS, a largely unexplored region in the eastern part of the Korea Strait bordering the northeastern East China Sea. As climate change increasingly impacts the physical and chemical status of the oceans, gaining insights into the biogeography and distribution of such communities is becoming increasingly important (de Vargas et al., 2015; Lee et al., 2021b; Ok et al., 2022).

Ecological community assembly is influenced by niche theory, which suggests that species co-occurrence via interactions with each other and their environment (Hutchinson, 1957), and neutral theory, which posits that community composition is determined by random processes (Chase and Myers, 2011). The four main processes shaping community assembly are selection, dispersal, speciation, and ecological drift (Vellend and Agrawal, 2010; Stegen et al., 2012; Zhou and Ning, 2017). Recent studies have explored the relative importance of these processes in different ecosystems, including soil, freshwater, and marine environments (Stegen et al., 2012; Aguilar and Sommaruga, 2020; Skouroliakou et al., 2022). In PPCs, both deterministic (selection) and stochastic (neutral theory) processes influence assembly (Ramond et al., 2021; Skouroliakou et al., 2022). Diverse microbial assemblies can create spatial patterns, and varying dispersal levels can disrupt selection, thereby shaping the complex nature of PPCs (Leibold et al., 2004; Heino et al., 2015).

This study explores the diversity, distribution, and assembly processes of planktonic protists in the JS by leveraging high-resolution metagenomic sequencing data and environmental parameters. The aim is to scrutinize PPCs across different water masses and seasons to pinpoint the factors impacting protist diversity and co-occurrence. Specifically, the study will focus on the alpha diversity (phylogenetic structure) and beta diversity (phylogenetic turnover) of the smallest eukaryotic members of the JS surface ocean. The expected outcomes will shed light on the role of environmental filtering in shaping protist communities, as well as the diverse factors that influence their diversity and co-occurrence. Moreover, it is hoped that the results from the null model and neutral community model analysis will enhance comprehension of planktonic protist assembly mechanisms. This research is significant as relatively few studies have been carried out to investigate microbial eukaryotic diversity and community assembly processes in the JS, particularly in the northeastern East China Sea.

Materials and methods

Study stations and surface plankton sampling

Environmental variables in the JS were measured at eight stations during four sampling periods: June, September, and November 2017, and March 2018. In addition, surface seawater samples were collected specifically for the analysis of planktonic protists, with three of the eight stations chosen for this purpose (Figure 1A). These stations were located in three distinct regions: the shallow-water (S) region adjacent to the Korean peninsula, the middle region of the strait where a seasonal thermohaline front (F) is present, and the deep-water (D) region near Jeju Island. However, due to adverse weather conditions, we were unable to operate the research vessel (R/V) between December and February as originally planned.

At each site, approximately one ton of surface seawater was collected using a submerged pump with a flow rate of 70 liters per minute. The collected seawater was subjected to a filtration process for the harvesting of the planktonic protists. Initially, the seawater was pre-filtered through a 200 μm mesh to eliminate large

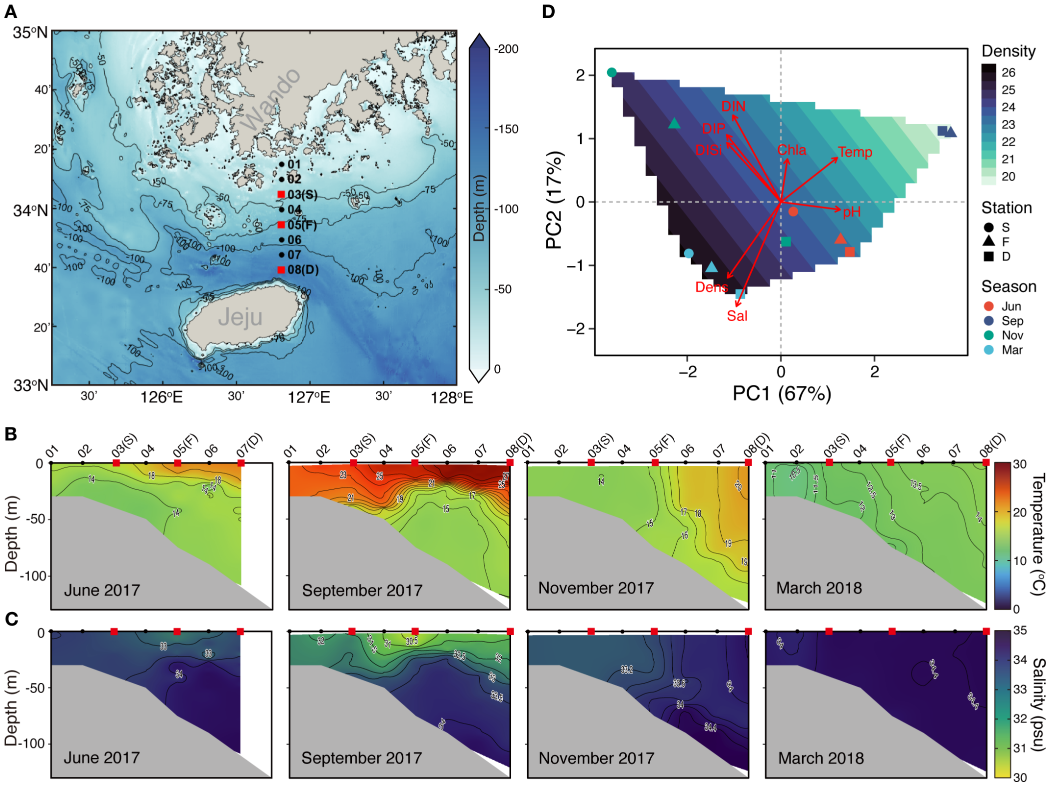

FIGURE 1
Overview of the Jeju Strait (JS) environmental conditions and sampling stations. **(A)** Map of sampling stations and depths sourced from the GEBCO gridded bathymetry data (accessed April, 5, 2023 from https://www.gebco.net/data_and_products/gridded_bathymetry_data/): The red squares represent surface water sampling stations, including shallow-water (S, average depth 44 m), thermohaline front (T, 78 m), and deep-water (D, 125 m) stations for planktonic protist community and environmental variable analysis. The black dots indicate stations solely for environmental variable measurement. **(B)** Vertical distribution of temperature along a transect across the JS from June 2017 to March 2018. **(C)** Vertical distribution of salinity along the same transect across the JS from June 2017 to March 2018. **(D)** Principal component analysis (PCA) plot of spatiotemporal changes: The symbols represent planktonic protist communities at JS stations across four seasons. The background contours depict water density. The red arrows indicate the contribution of environmental variables (e.g., temperature (Temp), salinity (Sal), water density (Den), dissolved inorganic nitrogen (DIN), dissolved inorganic phosphate (DIP), dissolved inorganic silicate (DISi), chlorophyll *a* (Chla), and pH to the first two principal components.

organisms and debris. Then, it was further filtered through a 1 µm Nylon conical-shaped net, which retain the planktonic protists while allowing excess water to pass through. The filtrate fractions were transferred to 50 mL conical tubes and centrifuged at 2,500×g for 30 min. This centrifugation step effectively removes any residual seawater and resulted in a pellet of concentrated plankton. The pellet was immediately frozen and stored in liquid nitrogen until genomic DNA (gDNA) extraction, in order to preserve the DNA quality as much as possible.

Measurement of environmental variables

Temperature and salinity profiles were recorded using a CTD probe (Sea-Bird Electronics, WA, USA). Seawater samples from various depths were collected using Niskin bottles attached to a CTD-Rosset sampler. Nutrients analysis, including dissolved inorganic nitrogen (DIN), dissolved inorganic phosphorus (DIP), and dissolved inorganic silicate (DISi), was conducted using water samples obtained from multiple stations at depths ranging from 0 to 125 m. To assess pH levels, water samples were taken from the surface, middle, and bottom. Total chlorophyll *a* (TChl *a*) concentrations were specifically determined from water samples collected at depths of 0, 10, and 30 m. To assess the nutrient levels in seawater, a 100 mL sample was filtered through a 0.45 µm PTFE syringe filter (Advantec, Japan) and stored at -20°C. The sample was later measured using an auto-analyzer (Quattro, Seal Analytical, Norderstedt, Germany). The pH of the seawater samples was measured at 25°C using spectrophotometry with the m-cresol purple indicator, following established procedures described by Clayton and Byrne (1993). In addition, the TChl *a* concentration was determined using a chlorophyll *a* fluorometer (ECO-AFL/FL, Sea-Bird Electronics, WA, USA) attached to a CTD probe. The fluorescence measurements were converted to TChl *a* concentration using a regression method based on the relationship between fluorescence and TChl *a*, which was established using high-performance liquid chromatography (HPLC) as the reference method.

DNA extraction and sequencing

The small organelle-enriched metagenome pioneer version (SoEM-pv) method, as validated by Jin et al. (2023), was used to identify marine plankton via environmental DNA (eDNA). DNA extraction involved homogenizing the pellet sample in a buffer of 250 mM sucrose, 30 mM Tris-HCl, 10 mM EDTA, and pH 7.5, using an IKA-T10 homogenizer (IKA, Staufen, Germany). Small organelles were concentrated from the homogenate through a modified differential centrifugation method (Jo et al., 2019) and the DNA was extracted using the Qiagen DNeasy Blood/Tissue Kit (Qiagen, Hilden, Germany) following the manufacturer's instructions.

For library construction, the TruSeq Nano DNA kit (Illumina, CA, USA) was used, fragmenting approximately 200 ng of DNA to a 550 bp insertion size with a LE220 Focused-ultrasonicator (Covaris, MA, USA). The DNA fragments underwent end repair, the addition of a single "A" base at the 3' end, and ligation of the Illumina adapters. The libraries were purified and template size distribution analysis was performed using the Agilent Technologies 2100 Bioanalyzer and a DNA 1000 Chip (Agilent Technologies, CA, USA). Quantification used qPCR following the protocol guide for Illumina sequencing platforms. Paired-end sequencing (2 × 301 bp) was carried out on the Illumina Miseq platform by Macrogen Inc (Seoul, Korea). The raw sequencing data were deposited in the NCBI SRA database under the accession numbers from SRR24790320 to SRR24790330, and under the NCBI Bioproject accession number PRJNA974865.

Bioinformatics and data processing

We conducted sequence analyses by modifying the bioinformatics analysis pipeline of SoEM-pv (Jo et al., 2019). Raw sequences were preprocessed with Trimmomatic v.0.39 to exclude adapter sequences and low-quality reads below the Phred score average of 33 (Bolger et al., 2014). The paired-end reads were merged using *FLASH* v1.2.11, with a minimum overlap of 20 bp (Magoč and Salzberg, 2011).

Operational taxonomic units (OTUs) were identified from merged sequences using a BLAST search against the non-redundant nucleotide database (accessed November 11, 2021, from https://www.ncbi.nlm.nih.gov/nucleotide/) with an *E*-value under 1e-10 and a query sequence length of at least 400 bp. Confident OTUs were selected based on a minimum of five read counts. The taxonomic identification was obtained by assigning all taxonomic ranks from kingdom to species using the NCBI taxonomy database. Super-kingdoms other than eukaryotes were discarded as part of this process (Jin et al., 2023).

Taxonomic classification and inhabitance (i.e., terrestrial, fresh, brackish, and marine) of each OTU were identified using the scientific name and the World Register of Marine Species (WoRMS) database with the *worrms* package v.0.4.2 (Chamberlain, 2020). To focus on protists, the supergroups of SAR, Excavata, and Amoebozoa were intentionally selected (Adl et al., 2012). Non-marine OTUs that were assigned by WoRMS, were removed. Functional traits of 252 OTUs were assigned to two size groups (nano-size 2–20 μm and micro-size 20–200 μm) and six trophic modes (obligate photoautotroph (OPA), heterotroph (HET), constitutive mixotroph (CM), generalist non-constitutive mixotroph (GNCM), endosymbiotic specialist (eSNCM) and plastidic specialist non-constitutive mixotroph (pSNCM)) (Flynn et al., 2019). The assignments were made using Ramond et al. (2019)'s functional traits database of marine protists. Such functional traits can give insights into the potential roles and ecological functions of the planktonic protist community (PPC) in the JS.

Statistical analysis

We determined that our sampling had sufficient sequence depth based on the rarefaction curves of each sample, but we noted significant variation in sequence depth (Figure S1). To avoid false negative error, we did not rarefy (McMurdie and Holmes, 2014), but instead normalized individual OTU read counts by relative abundance for downstream analysis.

We calculated alpha diversity indices, such as species richness and the Shannon-Wiener index of diversity, using the *vegan* package v.2.6.4 (Oksanen et al., 2022). Faith's phylogenetic diversity (PD) and the net relatedness index (NRI) were computed using the *picante* package v.1.8.2 (Kembel et al., 2010). The phylogenetic tree was created with the *phylostratr* package v.0.2.1 (Arendsee et al., 2019), and all branch lengths were set to "1" using the "compute.brlen" function in the *ape* package v.5.7.1 (Paradis and Schliep, 2019).

To identify statistical differences among seasons and stations, we performed an analysis of variance (ANOVA) or a Kruskal-Wallis H tests, with *post hoc* multiple comparisons based on the Bonferroni test. Non-metric multidimensional scaling (NMDS) and analysis of similarity (ANOSIM) were used to assess differences in PPC using the Jaccard distance to estimate community dissimilarities. Principal component analysis (PCA) and ANOVA were employed to examine variations in environmental conditions across stations and seasons. We utilized several R packages, including *phyloseq*, *dplyr*, *lawstat*, and *ggplot2*, in R v.4.2.2 for data analysis and visualization (McMurdie and Holmes, 2013; Wickham et al., 2023; R Core Team, 2022).

Community assembly processes

The neutral community model (NCM) was employed to evaluate the contribution of stochastic processes to the assembly of PPCs in the JS. The *MicEco* package v.0.9.19 (Russel, 2023) was used to fit the NCM by predicting the relationship between the occurrence frequency and their relative abundance of PPCs. The parameter *Nm* is an estimate of the dispersal between communities, with *N* representing the metacommunity size (i.e., total number of reads), and *m* representing the migration rate. OTUs falling above and below the 95% confidence intervals of NCM were assumed to be non-stochastically distributed.

To assess the assembly processes of three NCM prediction groups, a framework based on phylogenetic and null model analyses was employed, as described by Stegen et al. (2013). We measured variations in the phylogenetic turnover index and taxonomic turnover index using the β-nearest taxon index (βNTI) and Bray-Curtis-based Raup-Crick (RC_{Bray}), respectively. These were calculated using the *picante* package v.1.8.2 (Kembel et al., 2010) and the "raup_crick" function

(Stegen et al., 2013). A value of |βNTI| > 2 indicated the dominance of deterministic processes; a value of βNTI < -2 indicated homogeneous selection with significantly less phylogenetic turnover than expected; βNTI > 2 indicated heterogeneous selection with significantly more phylogenetic turnover than expected. In cases where |βNTI| < 2, RC_{Bray} > 0.95 and RC_{Bray} < -0.95 implied the relative influences of dispersal limitation and homogeneous dispersal, respectively. A value of $|RC_{Bray}|$ < 0.95 implied the influence of an "undominated" fraction (Zhou and Ning, 2017).

Co-occurrence network analysis

To study inter-species relationships, we conducted a network analysis of the PPCs using the SparCC approach, which accurately infers correlation from compositional data, particularly with small sample sizes (Friedman and Alm, 2012; Kurtz et al., 2015). We used the "sparcc" function in the *SpiecEasi* package v.1.1.2 (Kurtz et al., 2015) for network inference, only retaining edges with correlation magnitudes > 0.7 and statistical significance < 0.01, drawn with the *igraph* package v.1.4.1 (Csardi and Nepusz, 2006). We visualized the network and calculated topological properties such as clustering coefficient, average path length, and centrality using Gephi software v.0.10.1 (Bastian et al., 2009). Individual nodes in the plankton network were categorized into a network hub, module hub, connector, and peripheral, based on their topological roles (Guimera and Nunes Amaral, 2005).

To determine module transition patterns along seasonal change, we normalized and averaged the relative abundance of OTUs in each module (Chun et al., 2019). We evaluated the interaction between modules and seven environmental variables using a partial Mantel test, with a significance level estimated by 9999 permutations using the "mantel.partial" function in the *vegan* v.2.6.4 software package (Oksanen et al., 2022). We measured community dissimilarity using the Bray–Curtis distance and regressed it against a pairwise Euclidean distance of environmental variables using Spearman's correlations. In the network, a module is a group of species with similar trait sets that potentially form coevolutionary units.

Results

Variation of environmental conditions

Consistent mixing was observed throughout all seasons at the shallow-water (S) station in the JS. In contrast, strong stratification was observed in September at the thermohaline front (F) and deep-water (D) stations displayed (Figures 1B, C). There were no significant differences in the environmental variables between spatial locations (Table S1). However, in November, distinct environmental conditions were observed near the F station due to a thermohaline front (Figures 1B–D). However, the strait experienced significant changes in environmental conditions over time (Figure S2). Surface water temperature peaked in September (26.33 ± 0.86°C) and dropped to its lowest in March (13.58 ± 1.14°C). Conversely, salinity showed an opposing trend, with values ranging from 30.49 to 34.41 (Figures 1C; S2). DIP and DISi were inversely correlated with temperature and displayed significant correlations (r = -0.705, -0.727, $p < 0.05$); however, DIN did not show a significant correlation (r = -0.589, p = 0.057). In contrast, pH had a significant positive correlation with temperature (r = 0.909, p < 0.001).

Spatiotemporal pattern and phylogenetic structure of PPC

Preprocessing the Illumina sequencing of small organelle-enriched DNA molecules (as per section 2.3.) revealed a total of 252 protistan OTUs from the surface water of three stations in the JS. The taxonomic and phylogenetic diversity of the PPC did not significant vary with spatial locations or temporal changes. However, the indices of phylogenetic structure differed (Figure 2). In November, NRI was higher (p = 0.052) compared with other months, and Faith's PD was somewhat lower, indicating a more clustered phylogenetic structure and less phylogenetic diversity in the PPC. During November, the PPC demonstrated a more clustered phylogenetic structure (NRI > 0, Figure 2D), implying that environmental filtering played a significant role in PPC structuring. This suggests that specific environmental factors selected certain protist species, leading to a less diverse community (see to Table 1 in Skouroliakou et al., 2022). The NRI values showed weaker phylogenetic clustering in June and March, indicating less environmental filtering and a more diverse PPC during these seasons.

NMDS ordination results indicated that PPCs in the JS clustered more strongly by season than by station (Figure 3A). ANOSIM also supported this finding, showing that seasonal variations significantly influenced the PPC structure (R = 0.987, p < 0.001) more than spatial variations (R = -0.133, p = 0.907). Essentially, differences in community composition were driven more by seasonal environmental changes than by variations in water masses or locations.

The number of unique species and species richness varied between seasonal protist communities, while spatial communities demonstrated similar values (Figure 3B). When comparing ten different phyla, the PPCs in November were primarily composed of Ochrophyta (mostly diatoms, at 91%), constituting 95% of the community (Figures 4A, D), while PPCs displayed a more balanced composition in March, with a variety of phyla. Relative abundance of Myzozoa (averaging 49% across three stations), including *Alexandrium catenella* (10%), *A. pacificum* (12%), and *A. tamarense* (16%), was considerably higher in March compared with other periods. Similarly, the relative abundance of Chlorophyta *Bathycoccus prasinos* (7.3%) and Cryptophyta *Teleaulax amphioxeia* (6.8%) was also higher. Although the taxonomic composition was generally similar across size fractions, the relative abundance of micro-sized protists increased by about 50% from June to November, then decreased in March (Figures 4B, E). In the JS, Bacillariophyceae (Ochrophyta), commonly known as diatoms, and Dinophyceae (Myzozoa) were the most abundant and diverse groups within the PPCs. Bacillariophyceae accounted for 59.4% of the sequence abundance and 48.4% of the OTU richness, while Dinophyceae represented 27.4% of the sequence abundance and 35.3% of the OTU richness.

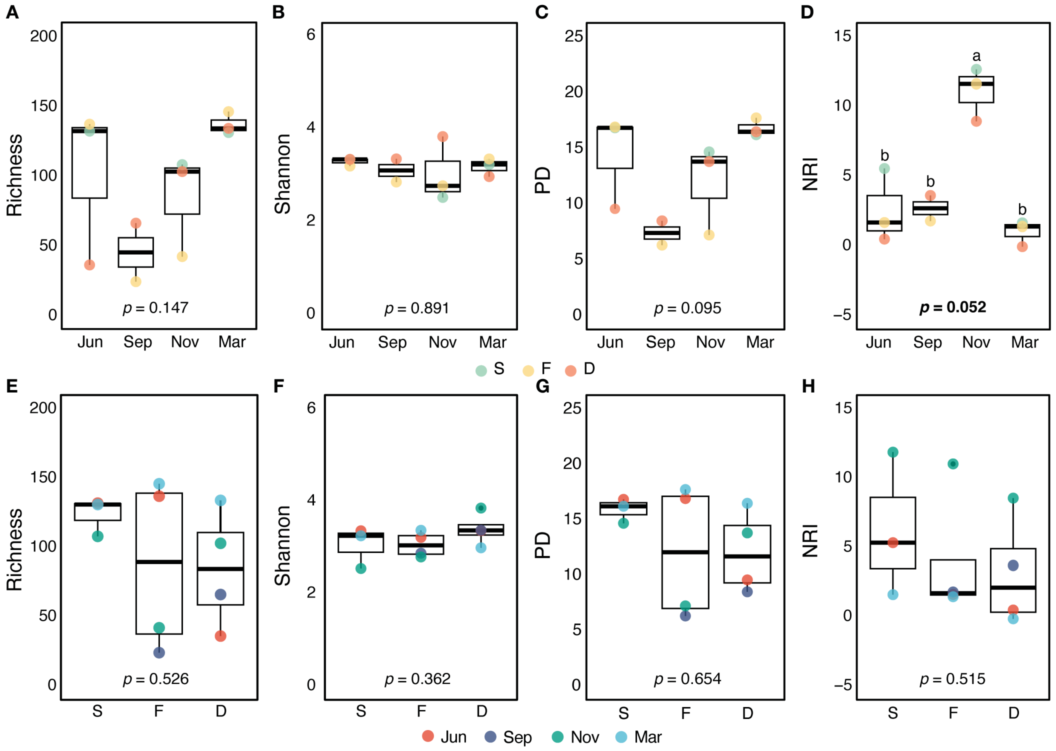

FIGURE 2

Comparison of alpha diversity indices across four seasons **(A–D)** or three stations **(E–H)**. Statistical significance (*p*-value) was determined to assess differences in protistan species richness **(A, E)** and Shannon diversity or Shannon-Wiener index **(B, F)** across seasons and stations using ANOVA. Faith's phylogenetic diversity (PD) **(C, G)** and the net relatedness index (NRI) **(D, H)** were evaluated using the Kruskal-Wallis H test. *Post hoc* multiple comparison results based on the Bonferroni test are indicated by small letters. Each colored dot represents the value of a sample. The solid black lines represent the median, while the black dots represent the mean.

The taxonomic composition of protists, classified by their trophic mode, demonstrated a trend similar to the relative abundance of Myzozoa (Figure 4). Myzozoa, which are dinoflagellates capable of mixotrophy (a combination of phototrophy and phagotrophy), showed a positive correlation with the proportion of nano-sized protists in the community.

Community assembly processes

The NCM was applied to investigate the variability in the occurrence frequency of the entire PPCs in the JS. The model accounted for a large proportion ($R^2 = 0.628$) of this variability (Figure 5A), suggesting that stochastic processes predominantly drove the assembly of the PPC in this strait. The null model analysis results showed that the assembly of PPCs in the JS was greatly influenced by stochastic processes (Figure 5B). Within the neutral group, stochastic processes comprised undominated processes (50.9%), homogenizing dispersal (47.3%), and dispersal limitation (1.8%).

The OTUs were classified into three groups–above, below, and neutral–based on the NCM predictions. Most of the OTUs (87%) fell under the neutral prediction group, while a smaller portion was classified as non-neutral above or non-neutral below (4% and 8%, respectively). OTUs in the non-neutral above prediction group, which exhibited higher frequency and lower relative abundance than the neutral prediction group, comprised two *Pseudo-nitszchia* species, three *Chaetoceros* species, four Ochrophyta, and two Ciliophora (Figure 5C; Table S2). In contrast, OTUs in the non-neutral below prediction group, which demonstrated lower frequency and higher relative abundance, included five *Alexandrium* species, *Protoceratium reticulatum*, *Prorocentrum triestinum*, two other Myzozoa, six Ochrophyta, and four Chlorophyta and Haptophyta.

There were no differences in the size fraction of the OTUs between the neutral and non-neutral prediction groups (Figure 5D). However, trophic mode composition varied between the groups (Figure 5E). The above prediction group included a HET ciliate, *Sterkiella histriomuscorum*, and an eSNCM Ciliophora, in addition to mainly OPA (Table S2). By contrast, the below prediction group was predominantly composed of CM dinoflagellates and a GNCM Cercozoa species, *Ebria tripartita*.

Seasonal dynamics of protists in major modules

The correlation-based network of the PPC in the JS included 149 nodes representing distinct species and 209 edges indicating their interactions (Figure 6A; Table 1). The presence of 61 unique

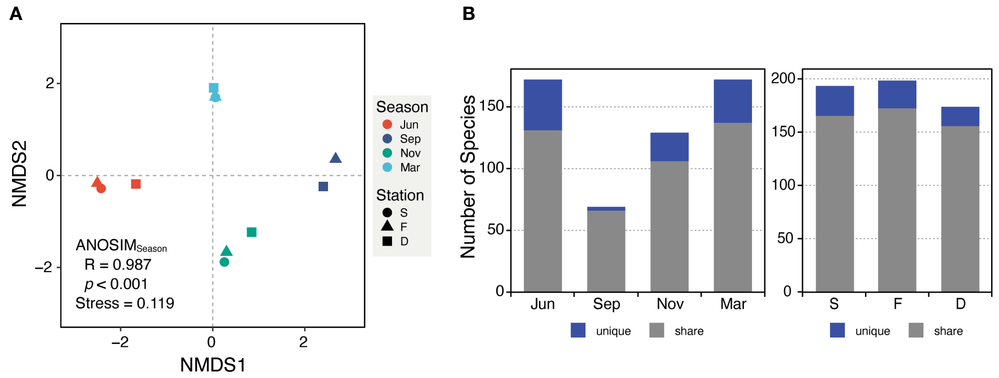

FIGURE 3
The dissimilarity between planktonic protist communities across four seasons and three stations were visualized using different approaches. **(A)** Non-metric multidimensional scaling (NMDS) ordination based on the Jaccard distance and the analysis of similarities (ANOSIM) statistic. Each colored circle, triangle, or square represents a specific sample. **(B)** The number of unique species (blue) and share species (gray) for each season and station.

modules, many of which consisted of a single node, suggests the existence of distinct subgroups within the community with a certain level of functional differentiation. Approximately 72% of the interactions were positive (gray lines in Figure 6A), indicating symbiotic relationships, while 28% were negative (blue lines), indicating the presence of competitive interactions within the community. An average clustering coefficient of 0.39 and a path length of 3.95 suggests a propensity for species to form clusters and establish efficient relationships within the network. A network diameter of 9 indicates a well-connected community. The average betweenness centrality score of 72.5 highlights the existence of specific key species that act as bridges, facilitating interactions between different parts of the network.

Within the primary network, there were 86 nodes and 202 links, primarily arranged into eight major modules, which accounted for 92% of the network. The modules and their proportions were as follows: Module I (12.8%), Module II (9.4%), Module III (10.1%), Module IV (6.0%), Module V (6.0%), Module VI (4.0%), Module

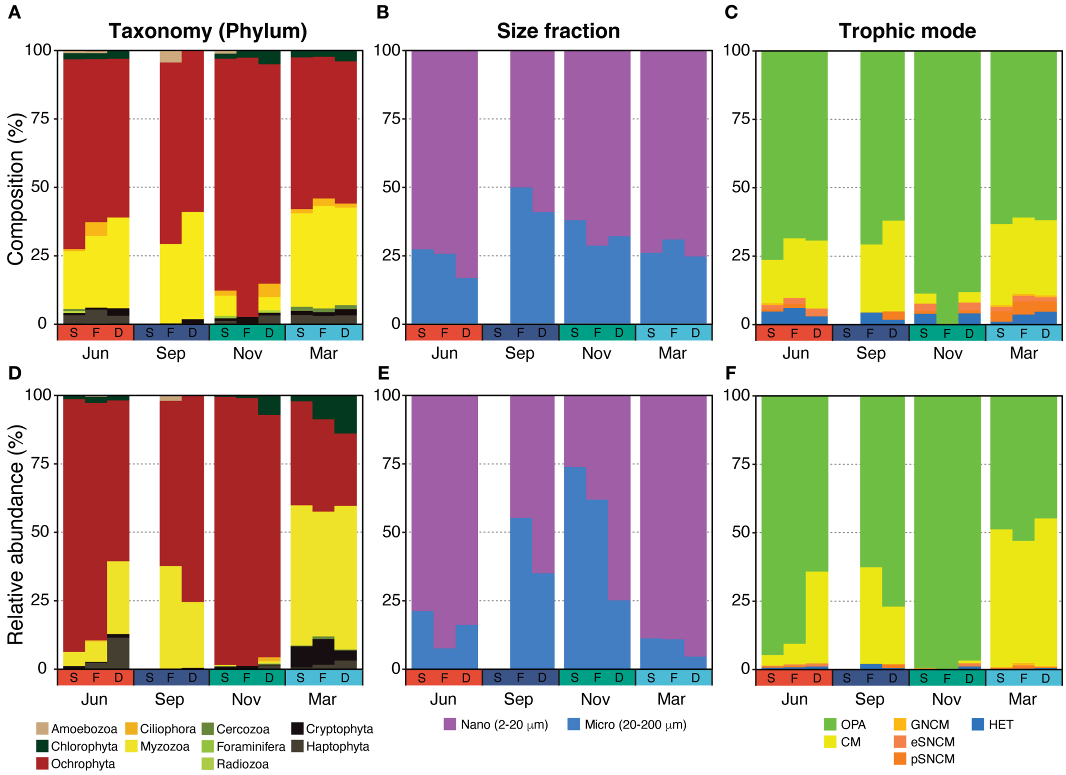

FIGURE 4
Spatiotemporal changes of species composition and relative abundance of the planktonic protist community at the phylum level **(A, D)**, size fraction **(B, E)**, and trophic mode **(C, F)** across the shallow-water (S), thermohaline front (F), and deep-water (D) stations.

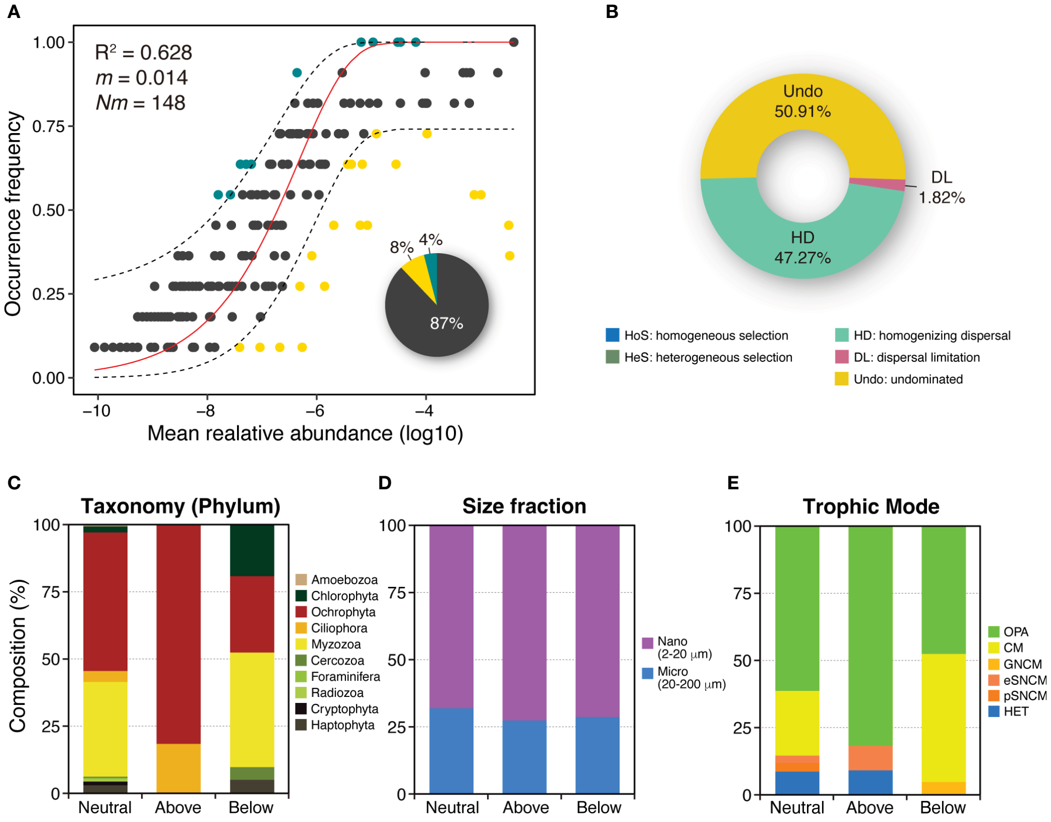

FIGURE 5
Analysis of the relative influences of deterministic and stochastic processes on planktonic protist community assembly. **(A)** Fit of the neutral community model (NCM) for community assembly. The plot shows the predicted occurrence frequencies of planktonic protist communities based on all samples collected in the Jeju Strait. The solid red line represents the best fit to the NCM described by Sloan et al. (2006), while the dashed blue lines indicate the 95% confidence interval around the model prediction. Protistan OTUs occurring more or less frequently than predicted by the NCM are depicted using different colors (dark green and yellow dots). *Nm* represents the metacommunity size multiplied by immigration, and R^2 indicates the fit to the NCM model. The pie chart illustrates the composition of three groups (above, below, and neutral prediction based on the NCM) in the total occurrence species. **(B)** Representation of the proportion of ecological assembly processes as determined by the null model. The community assembly is mainly influenced by deterministic processes, including homogeneous selection (HoS) and heterogeneous selection (HeS), and by stochastic processes like homogenizing dispersal (HD), dispersal limitation (DL), and undominated processes (Undo) that include weak selection, weak dispersal, diversification, and drift. **(C–E)** Species composition of three prediction groups on the basis of phylum, size fraction, and trophic mode in the planktonic protist community. Each bar represents pooled communities, with OTUs divided into separate partitions based on whether they were consistent within the neutral prediction or deviated above or below it.

VII (2.7%), and Module VIII (2.0%) (Table S3). The transition pattern of the major protist community modules was evaluated using normalized relative abundance, and the correlation between modules and environmental variables was studied via a partial Mantel test (Figures 6B, C). The results showed that in the JS, the PPC transitioned in the following sequence: Modules III and IV, Module VIII, Modules I and V, Modules II and VII (Figure 6B). Modules III, IV, and VIII exhibited a positive correlation with temperature (r = 0.360–0.566, $p < 0.05$), while Modules III and VIII demonstrated a strong positive correlation with salinity (r = 0.610–0.646, $p < 0.005$). Module III was primarily composed of nano-sized diatoms such as *Skeletonema*, *Thalassiosira*, and *Chaetoceros*. Module IV, comprising *Pseudonitzschia*, *Alexandrium minutum*, and *Akashiwo sanguinea*, showed a positive correlation with pH (r = 0.482, p = 0.002). Modules I and V displayed the highest normalized relative abundance in November, while Module I, which comprised micro-sized diatoms such as *Coscinodiscus*, *Rhizosolenia*, and *Biddulphia*, was significantly associated with DISi (r = 0.397, p = 0.024). In March, Modules II and VII were abundant and had a high proportion of dinoflagellates in OTU composition. The raphid pennate diatom *Seminavis robusta* played a role as a hub in Module II, and the toxic dinoflagellate *Alexandrium fundyense* was the connector linking the primary network and Module VII (Figure 6C; Table S3). These findings were not related to any environmental variables (Figures 6A; S3).

Discussion

Seasonal dynamics: summer thermoclines and autumn thermohaline fronts in the JS

The JS is characterized by dynamic environmental conditions influenced by different water masses, including the Korea Coastal Current (KCC), the JWC, and Changjiang Dilute Water (CDW). Our study revealed distinct oceanic phenomena occurring during

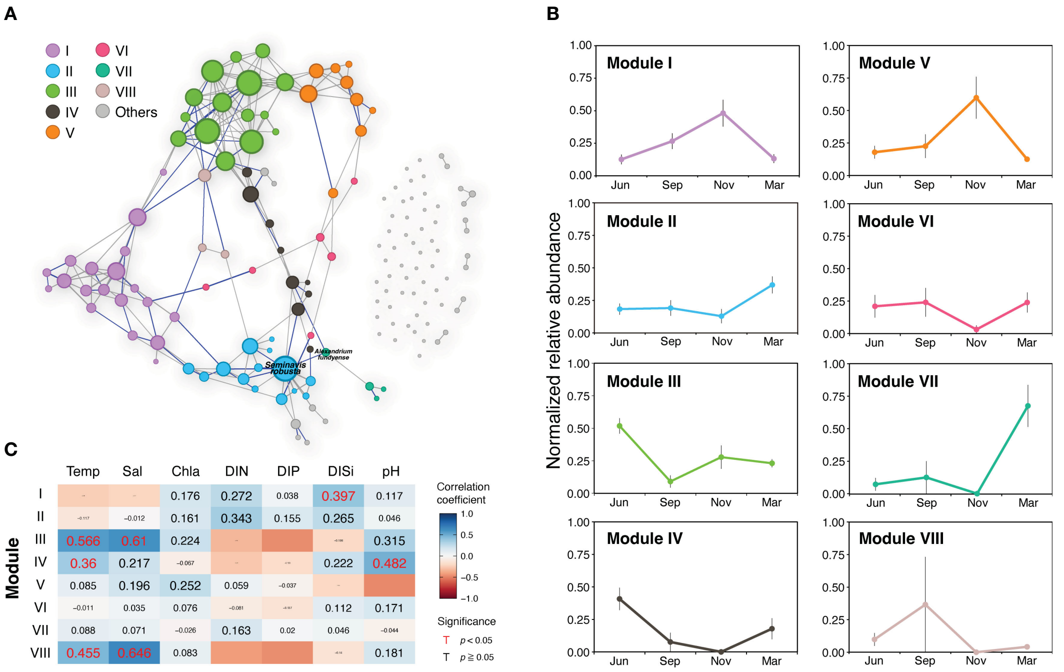

FIGURE 6
(A) Planktonic protist community networks based on all samples collected in the Jeju Strait. The size of nodes is proportional to the number of edges for each node. The gray and blue lines connecting paired nodes represent positive (co-occurrence) and negative (exclusion) interactions, respectively, with strong and significant correlations ($|r| > 0.7$, $p < 0.05$). Nodes are colored based on their modularity class. Two labeled nodes indicate the module hub and connector species (see Figure S3 for more details). **(B)** Transition pattern of major modules represented by changes in normalized relative abundance across seasons (mean ± standard error). **(C)** Spearman correlation between environmental variables and relative abundance of nodes belonging to major modules. The background colors and values indicate Spearman's correlation coefficient (r). The value size reflects the significance level (*p*-value), with red values representing statistically significant correlations.

different seasons, manifested as thermoclines and thermohaline fronts (Figures 1B, C). In June 2017, we observed the development of a seasonal thermocline near Jeju Island in the deep-water areas of the JS. A thermocline represents a layer within the water column where there is a rapid temperature change with increasing depth. Over time, this thermocline became deeper and wider, reaching its peak extent in September. Additionally, we noticed the presence of low salinity water extending above the thermocline throughout the JS. The formation of a thermocline leads to vertical stratification within the water column, resulting in distinct phytoplankton communities with varying nutrient. This vertical stratification has a significant influence on the structure of the PPCs (Mena et al., 2019; Venkataramana et al., 2021).

In November, we observed the occurrence of thermohaline fronts in the JS (Figures 1B, C). Thermohaline fronts serve as boundaries between different water masses based on variations in temperature and salinity. They indicate significant shifts in the temperature and salinity structures of the ocean during seasonal changes, impacting the distribution of marine life and nutrient availability (Franks, 1992). In the JS, the clockwise flow of the warmer and saltier JWC around Jeju Island, combined with the well-mixed coastal water off southwestern Korea, creates a thermohaline front near station F. This front potentially contributes to the observed temperature inversion (Kim et al., 2022). The formation of a thermohaline front along the 15–18°C isotherms in November corresponds to the horizontal distribution of surface temperature (Figure 1B). Thermohaline fronts are globally recognized for promoting ocean mixing through the horizontal intrusion of water masses. They also serve as biodiversity hotspots, fostering phytoplankton growth and attracting higher trophic level organisms, which support important fisheries with abundant zooplankton (Mcginty et al., 2014; Haberlin et al., 2019; Kim et al., 2020a).

Phylogeny and taxonomy PPC diversity

In this study, we analyzed the alpha diversity indices of PPCs in the JS. Our analysis showed that seasonal changes in environmental

TABLE 1 Properties of the protistan community network in the Jeju Strait.

Nodes	Edges	Positive edges (%)	Negative edges	Average clustering coefficient	Average path length	Diameter	Average betweenness	Modularity (the number of modules)
149	209	151 (72.25)	58	0.392	3.948	9	72.47	0.635 (61)

conditions had a significant impact on Faith's PD and NRI. Specifically, the NRI exhibited a substantial increase in November compared to other seasons (Figure 2D), which can be attributed to the presence of thermohaline fronts and the resulting distinctive environmental conditions. This finding suggests that community assembly during November was more deterministic, as indicated by the high NRI. This implies a higher likelihood of co-occurrence among closely related species than would be expected by chance. A positive NRI value signifies a clustered or converged phylogenetic structure within the community (Webb et al., 2002). The observed community assembly pattern may be influenced by environmental filtering or niche-based processes, commonly driven by recruitment and mortality dynamics affected by local environmental conditions. This suggests that environmental filtering plays a significant role in shaping the community structure (Letten et al., 2014; Chai et al., 2016).

Throughout the study period, no significant variations were observed in the alpha diversity indices across different spatial locations (Figure 3). This indicates a relatively homogeneous spatial distribution and composition of PPC in the JS. It also suggests that factors influencing the presence and abundance of planktonic protist, such as nutrient availability, water temperature, salinity, and other ecological conditions, did not exhibit significant spatial variability during the study period. However, it is important to note that other aspects of PPC, such as functional traits or specific species compositions, may still exhibit differences, even in the absence of significant variations in alpha diversity indices (Roselli and Litchman, 2017; Anderson et al., 2021).

Overall, our study highlights the influence of seasonal changes in environmental conditions on the alpha diversity of PPCs in the JS. Furthermore, it emphasizes the role of environmental filtering and deterministic community assembly processes during specific seasons, as indicated by the observed patterns in NRI. These findings will contribute to our understanding of the ecological dynamics and assembly mechanisms governing PPCs in this strait.

Representative groups of planktonic protists in the JS

In the JS, Bacillariophyceae (Ochrophyta) and Dinophyceae (Myzozoa) were found to be the most abundant and diverse groups within PPCs. Several highly abundant OTUs identified in this study were also observed in previous investigations of protistan or microbial eukaryotic communities in the northern East China Sea (Faria et al., 2014; Kim et al., 2020b; Kim et al., 2022; Sun et al., 2022).

The composition of the PPCs varies throughout the year, primarily due to nutrient conditions. For instance, in June, areas characterized by high nutrient conditions, such as shallow-water and front zones, were mainly dominated by nano- and micro-sized diatoms (Figures 4A, D). However, in September, when the JS experiences strong stratification and nutrient depletion, the community was dominated by both diatoms and dinoflagellates. With their swimming ability and mixotrophic capabilities, dinoflagellates exhibit competitive advantages under these conditions, allowing them to persist in the euphotic zone and compensate for low nutrient concentrations (Flynn et al., 2019). In November, when nutrient concentrations were high (DIN: 5–10 μM, DIP: 0.6–0.8 μM), diatoms were found to dominate both in composition and relative abundance in the shallow and frontal waters, suggesting that they are strong competitors in environments with elevated nutrient concentrations (Burson et al., 2018).

The surface waters of the deep-water area (station D) in June and all stations in September, which were characterized by limited nutrient availability, account for a significant proportion of smaller nano-sized (2-20 μm) phytoplankton, referred to as nano-sized obligate photoautotrophs (OPAs) (Figure 4). This preference for the smaller size is likely due to the higher surface area to volume ratio of smaller phytoplankton, which confers advantages in nutrient uptake in nutrient-limited environments (Harrison et al., 2015; Fernández-González et al., 2022). Additionally, interactions between predators and prey have been observed to influence the species composition of PPCs in such environments. It has been suggested that there is a stronger predator-prey coupling for smaller phytoplankton (Behrenfeld et al., 2021). Considering the seasonal changes observed in the species composition and relative abundance of the PPC in the JS, mixotrophic and heterotrophic protists showed contrasting quantitative changes compared with larger micro-sized (20-200 μm) PPC (Figure 4). This dynamic could potentially favor the survival of smaller phytoplankton species over larger ones, as they may be more efficiently consumed by their predators, such as heterotrophs or mixotrophs (Figures 4C, F). The shift toward smaller phytoplankton can also impact the overall functioning of marine ecosystems and biogeochemical cycles, as areas dominated by smaller phytoplankton often exhibit lower biodiversity levels (Henson et al., 2021).

Little dispersal limitation but high importance of neutral process for PPCs

Dispersal limitation significantly influences plankton community assembly (Lear et al., 2014). Organisms tend to colonize habitats closer to their source, with community similarities decreasing as distance increases. Cell size is also an important factor in shaping community structure through dispersal limitation (de Vargas et al., 2015). The beta diversity index, which measures community similarity, reflects the influence of dispersal limitation. A higher index indicates less similarity and a greater influence of dispersal limitation, while a lower index suggests more similarity and less influence (Zhou and Ning, 2017).

The NCM is commonly used to assess the importance of stochastic processes, particularly neutral processes, in microbial community assembly (Chen et al., 2019; Ramond et al., 2021). The NCM has demonstrated that neutral processes play a dominant role in shaping community variations. In this study, the NCM explained a significant portion ($R^2 = 0.62$) of the variability in the occurrence frequency of the entire PPC, highlighting the importance of neutral processes in driving PPC variations. Similar findings regarding the high contribution of neutral processes have been observed in protistan or microbial eukaryotic communities in the rivers and coastal waters of the South China Sea (Chen et al., 2017; Zou et al., 2021; Xu et al., 2020). This is due to factors such as the high and random dispersal rate of microorganisms, which is caused by the absence of distance barriers and the rapid flow rates of rivers and ocean currents, preventing the formation of distance-decay patterns. These findings underscore the importance of neutral processes in shaping the assembly and variations of PPCs, particularly in environments where dispersal rates are high and distance barriers are limited. The prevalence of neutral processes suggests that chance events and random processes, including dispersal and ecological drift, have a stronger impact on community composition in the JS than deterministic factors.

The dispersal rate of plankton can have varying effects on community structure. If the rate is high, it results in homogenization, while limited dispersal results in dispersal limitation (Vellend and Agrawal, 2010; Logares et al., 2018). The rate of immigration for PPCs in the JS was considerably lower (m = 0.014) than in other studies on microbial eukaryotic communities (m = 0.2–0.4) (Chen et al., 2017; Xu et al., 2020; Zhang et al., 2021), indicating that the PPC in the JS was highly limited by dispersal. This suggests that spatial dispersal limitation had minimal influence on the regional structure of PPC in the JS. Neutral processes, including ecological drift and homogenizing dispersal, primarily drive the variation within PPCs, overshadowing deterministic factors such as environmental conditions and species traits, as revealed by the NCM. Despite a low immigration rate, protists display a remarkable drive to disperse, facilitating a uniform distribution of species and diminishing distinct spatial patterns or distance-decay effects. These findings highlight the significant influence of stochastic processes and random events on community dynamics and protist distribution patterns.

Our results suggest that the assembly of PPCs in the JS is primarily driven by stochastic processes, particularly homogenizing dispersal and ecological drift, with minimal influence from dispersal limitation. Homogenizing dispersal, which accounts for 47% of the contribution, indicates that these plankton communities were widely dispersed and are distributed relatively evenly through the strait. This indicates a high level of similarity in community composition among different locations in the JS. In essence, there is a strong “mixing” effect, with organisms frequently moving and redistributing themselves throughout the ecosystem. Ecological drift, accounting for 51% of the contribution, suggests that random changes in species abundance over time also play a significant role in shaping these communities. The presence or absence of certain species in the community is largely influenced by chance events, such as random births and deaths or unpredictable environmental fluctuations. The very low contribution of dispersal limitation (1.82%) indicates that the movement of organisms across the strait is not significantly restricted. This could be attributed to the absence of physical barriers or the organisms’ strong dispersal abilities. Therefore, most species can reach almost all habitats across the strait, and community assemblages are not strongly influenced by the inability of species to disperse. Overall, these findings suggest that the PPCs in the JS are highly dynamic and are primarily shaped by random processes rather than deterministic environmental selection or dispersal constraints. It implies that these communities are highly resilient to changes in environmental conditions, as they are not tightly bound to specific environmental factors or locations. However, the strong influence of random processes also means that predicting the future development of these communities can be challenging.

In addition, a distinct group represented by yellow dots in Figure 5A has been characterized for several species within Chlorophyta and Myzozoa. This group exhibits a lower frequency but higher relative abundance compared to the prediction for neutrally occurring species, as shown by the NCM. Notably, species belonging to the Chloropicophyceae class are commonly found in oceanic waters, indicating their preference for such habitats (Lopes dos Santos et al., 2017). Another noteworthy genus is *Bathycoccus*, a cosmopolitan picophytoplankton genus classified in the Mamiellophyceae. *Bathycoccus prasinos*, the sole species within this genus, is a small non-motile green microalga characterized by intricate scales. It plays a vital role in the marine ecosystem by significantly contributing to primary oceanic production (Belevich et al., 2020). Interestingly, *Bathycoccus prasinos* has been identified as the most abundant species in the East China Sea during the Spring season (Xu et al., 2016). The below group comprises several species within the Myzozoa, specifically belonging to the Dinophyceae class, including notorious species such as *A. catenella, A. pacificum*, *A. tamarense, Protoceratium reticulatum*, and *Prorocentrum triestinum*, which are all known for causing harmful algal blooms (HABs) globally and in Korea specifically (Alves-de-Souza et al., 2014; Anderson et al., 2021; Min and Kim, 2023). HABs are typically episodic, occurring infrequently but in exceptionally high concentrations when they do happen. In the JS, these taxa exhibited a higher relative abundance in March compared with other periods. For example, the bloom of *P. reticulatum* in a Chilean fjord during the summers of 2016 and 2017 exemplified this occurrence pattern, with blooms observed at an average water temperature of 16°C (Alves-de-Souza et al., 2019).

Representative biotic interactions of microbial eukaryotes in the JS

In this study, we investigated the relationship between eight distinct modules and various environmental variables, with a particular focus on monitoring changes in their normalized relative abundance over time. We found that Modules I, III, IV, and VIII had significant associations with specific environmental factors, indicating potential influences on their biological characteristics. However, it is important to note that correlation does not imply causality, and further research is needed to validate and obtain a more comprehensive understanding of these relationships.

The plankton community network analysis of all samples in this study revealed that Module I primarily consisted of diatoms and other silicate-utilizing organisms, including micro-sized diatoms such as *Coscinodiscus*, *Rhizosolenia*, and *Biddulphia* genera (Table S3). The presence of Module I was found to positively correlate with DISi. This suggests that these genera can efficiently utilize dissolved inorganic silica to construct and maintain their cell walls (Martin-Jézéquel et al, 2000).

Module III shows a clear seasonal pattern, with its normalized relative abundance peaking in June and reaching its lowest point in September. The partial Mantel test analysis revealed significant positive correlations between Module III and both temperature (r = 0.566, p = 0.002) and salinity (r = 0.610, p = 0.005). However, there were insignificant negative correlations with DIN, DIP, and DISi. These findings suggest that the species represented in Module III primarily comprised common nano-sized diatoms, including *Skeletonema*, *Thalassiosira*, and *Chaetoceros*, which have successfully adapted to thrive in warmer and saltier conditions. However, their activity and abundance may be curtailed during the summer months due to nutrient constraints in the JS.

Module IV, which displays a seasonal pattern similar to Module III, exhibits a significant positive correlation with both temperature and pH. This suggests that the organisms within this module may thrive under specific temperature conditions and pH levels. They could be adapted to warmer conditions and specific pH ranges that occur at certain times of the year, which explains the observed seasonal peak in June. The major species belonging to Module IV include *Pseudonitzschia* spp., *Alexandrium minutum*, and *Akashiwo sanguinea*, all types of plankton that play significant roles in marine ecosystems. These species are known for their ability to form blooms in coastal Korean waters, which can sometimes be harmful to other marine life because of the toxins they produce, such as domoic acid and neurotoxins, which can cause amnesic and paralytic shellfish poisoning in humans (Min and Kim, 2023).

The traits of Module VIII seem to be significantly affected by both seasonal transitions and certain environmental conditions, particularly temperature and salinity. The abundance of organisms in Module VIII follows a distinct annual pattern, peaking in September and gradually diminishing to zero by November. This pattern suggests a significant seasonal impact on the presence and prevalence of organisms within Module VIII, which may correspond to specific life cycle stages or the availability of resources. The organisms in this module might possess adaptations suited to environments with higher salinity and specific temperature ranges. However, because only four species within this module were identified, providing detailed information about their individual characteristics will be problematic.

Modules II, V, VI, and VII do not show significant correlations with the environmental variables, based on the results of partial Mantel tests, which suggests that these modules may operate independently from the tested variables and their variations. However, it is important to note that this interpretation is specific to the current context, and there may be other factors or complex interactions that could influence these modules.

This study employed SoEM sequencing methodology to investigate the seasonal and spatial dynamics of the PPC in the JS. The identification of 61 modules within the PPC network aligns with the concept of ecological niches, suggesting the presence of distinct subgroups or functional units. This modular structure indicates that different species within the PPC specialize in specific ecological roles or inhabit different habitats, contributing to the stability and resilience of the ecosystem (Forster et al., 2021). The modular organization of cellular networks, as observed in protein-interaction studies in yeast, suggests that specific biological responses may be controlled by such modules (Xue et al., 2018; Liu et al., 2019). Similarly, in the case of protists, clusters derived solely from network structure may define modules that fulfill similar biological roles (Rives and Galitski, 2003; Lewis et al., 2010). Thus, the modular structure observed in the PPC network indicates the presence of distinct ecological niches, which in turn contribute to ecosystem stability and resilience. This analysis enhances our understanding of species co-existence, resource utilization, and environmental adaptability.

Data availability statement

The data presented in the study are deposited in the NCBI Sequence Read Archive (SRA) repository (https://www.ncbi.nlm.nih.gov/bioproject/PRJNA974865).

Author contributions

JM prepared the initial draft, while all authors contributed to the conceptualization, investigation, writing, reviewing, and editing.

Funding

This research was supported by National Research Foundation (NRF) grants (NRF-2016R1A6A1A03012647, NRF-2020R1A2C3005053, NRF-2022M3I6A1085991) to KYK funded by the Korean government (MSIT).

Conflict of interest

The authors declare that the research was conducted in the absence of any commercial or financial relationships that could be construed as a potential conflict of interest.

Publisher's note

Supplementary material

The Supplementary Material for this article can be found online at: https://www.frontiersin.org/articles/10.3389/fmars.2023.1225640/full#supplementary-material

References

Adl, S. M., Simpson, A. G., Lane, C. E., Lukeš, J., Bass, D., Bowser, S. S., et al. (2012). The revised classification of eukaryotes. *J. Eukaryot. Microbiol.* 59 (5), 429–514. doi: 10.1111/j.1550-7408.2012.00644.x

Aguilar, P., and Sommaruga, R. (2020). The balance between deterministic and stochastic processes in structuring lake bacterioplankton community over time. *Mol. Ecol.* 29 (16), 3117–3130. doi: 10.1111/mec.15538

Alves-de-Souza, C., Iriarte, J. L., and Mardones, J. I. (2019). Interannual Variability of *Dinophysis acuminata* and *Protoceratium reticulatum* in a Chilean Fjord: Insights from the Realized Niche Analysis. *Toxins* 11 (1), 19. doi: 10.3390/toxins11010019

Alves-de-Souza, C., Varela, D., Contreras, C., de la Iglesia, P., Fernández, P., Hipp, B., et al. (2014). Seasonal variability of Dinophysis spp. and Protoceratium reticulatum associated to lipophilic shellfish toxins in a strongly stratified Chilean fjord. *Deep Sea Res. Part II: Top. Stud. Oceanogr.* 101, 152–162. doi: 10.1016/j.dsr2.2013.01.014

Anderson, S. I., Barton, A. D., Clayton, S., Dutkiewicz, S., and Rynearson, T. A. (2021). Marine phytoplankton functional types exhibit diverse responses to thermal change. *Nat. Commun.* 12 (1), 6413. doi: 10.1038/s41467-021-26651-8

Arendsee, Z., Li, J., Singh, U., Seetharam, A., Dorman, K., and Wurtele, E. S. (2019). Phylostratr: a framework for phylostratigraphy. *Bioinformatics* 35 (19), 3617–3627. doi: 10.1093/bioinformatics/btz171

Bastian, M., Heymann, S., and Jacomy, M. (2009). Gephi: an open source software for exploring and manipulating networks. *Proc. Int. AAAI Conf. Web Soc. media* 3 (1), 361–362. doi: 10.1609/icwsm.v3i1.13937

Behrenfeld, M. J., Boss, E. S., and Halsey, K. H. (2021). Phytoplankton community structuring and succession in a competition-neutral resource landscape. *ISME Commun.* 1 (1), 12. doi: 10.1038/s43705-021-00011-5

Belevich, T. A., Milyutina, I. A., Abyzova, G. A., and Troitsky, A. V. (2020). The pico-sized Mamiellophyceae and a novel *Bathycoccus* clade from the summer plankton of Russian Arctic Seas and adjacent waters. *FEMS Microbiol. Ecol.* 97 (2), fiaa251. doi: 10.1093/femsec/fiaa251

Bolger, A. M., Lohse, M., and Usadel, B. (2014). Trimmomatic: a flexible trimmer for Illumina sequence data. *Bioinformatics* 30 (15), 2114–2120. doi: 10.1093/bioinformatics/btu170

Burson, A., Stomp, M., Greenwell, E., Grosse, J., and Huisman, J. (2018). Competition for nutrients and light: testing advances in resource competition with a natural phytoplankton community. *Ecology* 99 (5), 1108–1118. doi: 10.1002/ecy.2187

Caron, D. A., Countway, P. D., Jones, A. C., Kim, D. Y., and Schnetzer, A. (2012). Marine protistan diversity. *Ann. Rev. Mar. Sci.* 4 (1), 467–493. doi: 10.1146/annurev-marine-120709-142802

Chai, Y., Yue, M., Liu, X., Guo, Y., Wang, M., Xu, J., et al. (2016). Patterns of taxonomic, phylogenetic diversity during a long-term succession of forest on the Loess Plateau, China: insights into assembly process. *Sci. Rep.* 6 (1), 27087. doi: 10.1038/srep27087

Chamberlain, S. (2020). *worrms: World Register of Marine Species (WoRMS) Client. R package version 0.4.2.* Available at: https://CRAN.R-project.org/package=worrms.

Chang, K. I., Teague, W. J., Lyu, S. J., Perkins, H. T., Lee, D. K., Watts, D. R., et al. (2004). Circulation and currents in the southwestern East/Japan Sea: Overview and review. *Prog. Oceanogr.* 61 (2), 105–156. doi: 10.1016/j.pocean.2004.06.005

Chase, J. M., and Myers, J. A. (2011). Disentangling the importance of ecological niches from stochastic processes across scales. *Philos. Trans. R. Soc B: Biol. Sci.* 366 (1576), 2351–2363. doi: 10.1098/rstb.2011.0063

Chen, W., Pan, Y., Yu, L., Yang, J., and Zhang, W. (2017). Patterns and processes in marine microeukaryotic community biogeography from xiamen coastal waters and intertidal sediments, southeast China. *Front. Microbiol.* 8. doi: 10.3389/fmicb.2017.01912

Chen, W., Ren, K., Isabwe, A., Chen, H., Liu, M., and Yang, J. (2019). Stochastic processes shape microeukaryotic community assembly in a subtropical river across wet and dry seasons. *Microbiome* 7, 1–16. doi: 10.1186/s40168-019-0749-8

Chun, S.-J., Cui, Y., Lee, C. S., Cho, A. R., Baek, K., Choi, A., et al. (2019). Characterization of distinct cyanoHABs-related modules in microbial recurrent association network. *Front. Microbiol.* 10. doi: 10.3389/fmicb.2019.01637

Clayton, T. D., and Byrne, R. H. (1993). Spectrophotometric seawater pH measurements: total hydrogen ion concentration scale calibration of m-cresol purple and at-sea results. *Deep Sea Res. I: Oceanogr. Res. Pap.* 40 (10), 2115–2129. doi: 10.1016/0967-0637(93)90048-8

Csardi, G., and Nepusz, T. (2006). The igraph software package for complex network research. *Int. J. Complex Syst.* 1695 (5), 1–9. doi: 10.5281/zenodo.7682609

de Vargas, C., Audic, S., Henry, N., Decelle, J., Mahé, F., Logares, R., et al. (2015). Eukaryotic plankton diversity in the sunlit ocean. *Science* 348 (6237), 1261605. doi: 10.1126/science.1261605

Eom, S. H., Jeong, H. J., Ok, J. H., Park, S. A., Kang, H. C., You, J. H., et al. (2021). Interactions between common heterotrophic protists and the dinoflagellate *Tripos furca*: implication on the long duration of its red tides in the South Sea of Korea in 2020. *Algae* 36 (1), 25–36. doi: 10.4490/algae.2021.36.2.22

Faria, D. G., Lee, M.-D., Lee, J.-B., Lee, J., Chang, M., Youn, S. H., et al. (2014). Molecular diversity of phytoplankton in the East China Sea around Jeju Island (Korea), unraveled by pyrosequencing. *J. Oceanogr.* 70 (1), 11–23. doi: 10.1007/s10872-013-0208-2

Fernández-González, C., Tarran, G. A., Schuback, N., Woodward, E. M. S., Arístegui, J., and Marañón, E. (2022). Phytoplankton responses to changing temperature and nutrient availability are consistent across the tropical and subtropical Atlantic. *Commun. Biol.* 5 (1), 1035. doi: 10.1038/s42003-022-03971-z

Flynn, K. J., Mitra, A., Anestis, K., Anschütz, A. A., Calbet, A., Ferreira, G. D., et al. (2019). Mixotrophic protists and a new paradigm for marine ecology: where does plankton research go now? *J. Plankton Res.* 41 (4), 375–391. doi: 10.1093/plankt/fbz026

Forster, D., Qu, Z., Pitsch, G., Bruni, E. P., Kammerlander, B., Pröschold, T., et al. (2021). Lake ecosystem robustness and resilience inferred from a climate-stressed protistan plankton network. *Microorganisms* 9 (3), 549. doi: 10.3390/microorganisms9030549

Franks, P. J. S. (1992). Sink or swim: Accumulation of biomass at fronts. *Mar. Ecol. Progr. Ser.* 82, 1–12. doi: 10.3354/meps082001

Friedman, J., and Alm, E. J. (2012). Inferring correlation networks from genomic survey data. *PloS Comput. Biol.* 8 (9), e1002687. doi: 10.1371/journal.pcbi.1002687

Glibert, P. M., and Mitra, A. (2022). From webs, loops, shunts, and pumps to microbial multitasking: Evolving concepts of marine microbial ecology, the mixoplankton paradigm, and implications for a future ocean. *Limnol. Oceanogr.* 67 (3), 585–597. doi: 10.1002/lno.12018

Guimera, R., and Nunes Amaral, L. A. (2005). Functional cartography of complex metabolic networks. *Nature* 433 (7028), 895–900. doi: 10.1038/nature03288

Gutiérrez-Rodríguez, A., Lopes dos Santos, A., Safi, K., Probert, I., Not, F., Fernández, D., et al. (2022). Planktonic protist diversity across contrasting Subtropical and Subantarctic waters of the southwest Pacific. *Prog. Oceanogr.* 206, 102809. doi: 10.1016/j.pocean.2022.102809

Haberlin, D., Raine, R., McAllen, R., and Doyle, T. K. (2019). Distinct gelatinous zooplankton communities across a dynamic shelf sea. *Limnol. Oceanogr.* 64 (4), 1802–1818. doi: 10.1002/lno.11152

Harrison, P. J., Zingone, A., Mickelson, M. J., Lehtinen, S., Ramaiah, N., Kraberg, A. C., et al. (2015). Cell volumes of marine phytoplankton from globally distributed coastal data sets. *Estuar. Coast. Shelf Sci.* 162, 130–142. doi: 10.1016/j.ecss.2015.05.026

Heino, J., Melo, A. S., Siqueira, T., Soininen, J., Valanko, S., and Bini, L. M. (2015). Metacommunity organisation, spatial extent and dispersal in aquatic systems: patterns, processes and prospects. *Freshw. Biol.* 60 (5), 845–869. doi: 10.1111/fwb.12533

Henson, S. A., Cael, B. B., Allen, S. R., and Dutkiewicz, S. (2021). Future phytoplankton diversity in a changing climate. *Nat. Commun.* 12 (1), 5372. doi: 10.1038/s41467-021-25699-w

Hutchinson, G. E. (1957). Concluding remarks. *Cold Spring Harbor Symp. Quant. Biol.* 22 (1), 415–427. doi: 10.1101/SQB.1957.022.01.039

Jin, S., Lee, H.-G., Park, C., and Kim, K. Y. (2023). Small-organelle-enriched metagenomics: An improved method for environmental DNA-based identification of marine plankton. *Limnol. Oceanogr.: Methods* 21 (4), 178–191. doi: 10.1002/lom3.10538

Jo, J., Lee, H.-G., Kim, K. Y., and Park, C. (2019). SoEM: a novel PCR-free biodiversity assessment method based on small-organelles enriched metagenomics. *Algae* 34 (1), 57–70. doi: 10.4490/algae.2019.34.2.26

Kembel, S. W., Cowan, P. D., Helmus, M. R., Cornwell, W. K., Morlon, H., Ackerly, D. D., et al. (2010). Picante: R tools for integrating phylogenies and ecology. *Bioinformatics* 26 (11), 1463–1464. doi: 10.1093/bioinformatics/btq166

Kim, H. K., Chan, B. K. K., Lee, S. K., and Kim, W. (2020). Biogeography of intertidal and subtidal native and invasive barnacles in Korea in relation to oceanographic current ecoregions and global climatic changes. *J. Mar. Biolog. Assoc. U.K.* 100 (7), 1079–1091. doi: 10.1017/S0025315420001009

Kim, J.-K., Choi, B.-J., Kim, J., and Sun, Y.-J. (2022a). Wind-driven retreat of cold water pool and abrupt sea temperature rise off the southwest coast of Korea in summer 2017. *J. Mar. Syst.* 231, 103739. doi: 10.1016/j.jmarsys.2022.103739

Kim, S.-Y., and Lee, T. (2022). Estimation of monthly dissolved inorganic carbon inventory in the outheastern Yellow Sea. *Sea* 27 (4), 194–210. doi: 10.7850/JKSO.2022.27.4.194

Kim, Y., Youn, S.-H., Oh, H. J., Kang, J. J., Lee, J. H., Lee, D., et al. (2020b). Spatiotemporal variation in phytoplankton community driven by environmental factors in the northern East China Sea. *Water* 12 (10), 2695. doi: 10.3390/w12102695

Kurtz, Z. D., Müller, C. L., Miraldi, E. R., Littman, D. R., Blaser, M. J., and Bonneau, R. A. (2015). Sparse and compositionally robust inference of microbial ecological networks. *PloS Comput. Biol.* 11 (5), e1004226. doi: 10.1371/journal.pcbi.1004226

Lear, G., Bellamy, J., Case, B., Lee, J., and Buckley, H. (2014). Fine-scale spatial patterns in bacterial community composition and function within freshwater ponds. *ISME J.* 8, 1715–1726. doi: 10.1038/ismej.2014.21

Lee, S. Y., Jeong, H. J., Kang, H. C., Ok, J. H., You, J. H., Park, S. A., et al. (2021a). Comparison of the spatial-temporal distributions of the heterotrophic dinoflagellates *Gyrodinium dominans*, *G. jinhaense*, and *G. moestrupii* in Korean coastal waters. *Algae* 36, 1, 37–50. doi: 10.4490/algae.2021.36.3.4

Lee, B., Kim, J. K., Kim, M., Choi, B.-J., Kim, K. Y., and Park, M. G. (2023). Northward movement of the tropical dinoflagellate *Ornithocercus* and *Triposolenia* genera in Korean coastal waters is strongly associated with the inflow of the Jeju Warm Current. *Front. Mar. Sci.* 10. doi: 10.3389/fmars.2023.1156121

Lee, H.-G., Kim, H. M., Min, J., Park, C., Jeong, H. J., Lee, K., et al. (2020). Quantification of the paralytic shellfish poisoning dinoflagellate *Alexandrium* species using a digital PCR. *Harmful Algae* 92, 101726. doi: 10.1016/j.hal.2019.101726

Lee, C. H., Min, J., Lee, H. G., and Kim, K. Y. (2021b). Thermal plasticity of growth and chain formation of the dinoflagellates *Alexandrium affine* and *Alexandrium pacificum* with respect to ocean acidification. *Algae* 36 (4), 285–298. doi: 10.4490/algae.2021.36.12.1

Leibold, M. A., Holyoak, M., Mouquet, N., Amarasekare, P., Chase, J. M., Hoopes, M. F., et al. (2004). The metacommunity concept: a framework for multi-scale community ecology. *Ecol. Lett.* 7 (7), 601–613. doi: 10.1111/j.1461-0248.2004.00608.x

Letten, A. D., Keith, D. A., and Tozer, M. G. (2014). Phylogenetic and functional dissimilarity does not increase during temporal heathland succession. *Proc. R. Soc B* 281 (1797), 20142102. doi: 10.1098/rspb.2014.2102

Lewis, A. C. F., Jones, N. S., Porter, M. A., and Deane, C. M. (2010). The function of communities in protein interaction networks at multiple scales. *BMC Syst. Biol.* 4 (1), 100. doi: 10.1186/1752-0509-4-100

Lie, H.-J., and Cho, C.-H. (1997). Surface current fields in the eastern East China Sea. *J. Korean Soc Oceanogr.* 32 (1), 1–7.

Lim, A. S., and Jeong, H. J. (2022). Primary production by phytoplankton in the territorial seas of the Republic of Korea. *Algae* 37 (4), 265–279. doi: 10.4490/algae.2022.37.11.28

Lima-Mendez, G., Faust, K., Henry, N., Decelle, J., Colin, S., Carcillo, F., et al. (2015). Determinants of community structure in the global plankton interactome. *Science* 348 (6237), 1262073. doi: 10.1126/science.1262073

Liu, L., Chen, H., Liu, M., Yang, J. R., Xiao, P., Wilkinson, D. M., et al. (2019). Response of the eukaryotic plankton community to the cyanobacterial biomass cycle over 6 years in two subtropical reservoirs. *ISME J.* 13 (9), 2196–2208. doi: 10.1038/s41396-019-0417-9

Logares, R., Tesson, S. V. M., Canbäck, B., Pontarp, M., Hedlund, K., and Rengefors, K. (2018). Contrasting prevalence of selection and drift in the community structuring of bacteria and microbial eukaryotes. *Environ. Microbiol.* 20, 2231–2240. doi: 10.1111/1462-2920.14265

Lopes dos Santos, A., Pollina, T., Gourvil, P., Corre, E., Marie, D., Garrido, J. L., et al. (2017). Chloropicophyceae, a new class of picophytoplanktonic prasinophytes. *Sci. Rep.* 7 (1), 14019. doi: 10.1038/s41598-017-12412-5

Magoč, T., and Salzberg, S. L. (2011). FLASH: fast length adjustment of short reads to improve genome assemblies. *Bioinformatics* 27 (21), 2957–2963. doi: 10.1093/bioinformatics/btr507

Martin-Jézéquel, V., Hildebrand, M., and Brzezinski, M. A. (2000). Silicon metabolism in diatoms: implications for growth. *J. Phycol.* 36 (5), 821–840. doi: 10.1046/j.1529-8817.2000.00019.x

Mcginty, N., Johnson, M. P., and Power, A. M. (2014). Spatial mismatch between phytoplankton and zooplankton biomass at the Celtic Boundary Front. *J. Plankton Res.* 36 (6), 1446–1460. doi: 10.1093/plankt/fbu058

McMurdie, P. J., and Holmes, S. (2013). phyloseq: an R package for reproducible interactive analysis and graphics of microbiome census data. *PloS One* 8 (4), e61217. doi: 10.1371/journal.pone.0061217

McMurdie, P. J., and Holmes, S. (2014). Waste not, want not: why rarefying microbiome data is inadmissible. *PloS Comput. Biol.* 10 (4), e1003531. doi: 10.1371/journal.pcbi.1003531

Mena, C., Reglero, P., Hidalgo, M., Sintes, E., Santiago, R., Martín, M., et al. (2019). Phytoplankton community structure is driven by stratification in the oligotrophic mediterranean sea. *Front. Microbiol.* 10. doi: 10.3389/fmicb.2019.01698

Min, J., and Kim, K. Y. (2022). Quantification of the ichthyotoxic raphidophyte *Chattonella marina* complex by applying a droplet digital PCR. *Algae* 37 (4), 281–291. doi: 10.4490/algae.2022.37.11.30

Min, J., and Kim, K. Y. (2023). Seasonal change and subniche dynamics of three *Alexandrium* species in the Korea Strait. *Harmful Algae* 125, 102420. doi: 10.1016/j.hal.2023.102420

Ok, J. H., Jeong, H. J., Kang, H. C., and Park, S. A. (2021). Ecophysiology of the kleptoplastidic dinoflagellate *Shimiella gracilenta*: I. spatiotemporal distribution in Korean coastal waters and growth and ingestion rates. *Algae* 36 (4), 263–283. doi: 10.4490/algae.2021.36.11.28

Ok, J. H., Jeong, H. J., Kang, H. C., and Park, S. A. (2022). Ecophysiology of the kleptoplastidic dinoflagellate *Shimiella gracilenta*: II. Effects of temperature and global warming. *Algae* 37 (1), 49–62. doi: 10.4490/algae.2022.37.3.2

Oksanen, J., Simpson, G., Blanchet, F., Kindt, R., Legendre, P., Minchin, P., et al. (2022). *vegan: Community Ecology Package. R package version 2.6-4*. Available at: https://CRAN.R-project.org/package=vegan.

Paradis, E., and Schliep, K. (2019). ape 5.0: an environment for modern phylogenetics and evolutionary analyses in R. *Bioinformatics* 35 (3), 526–528. doi: 10.1093/bioinformatics/bty633

R Core Team (2022). *R: A language and environment for statistical computing. R Foundation for Statistical Computing*, Vienna, Austria. Available at: http://www.R-project.org/.

Ramond, P., Siano, R., Schmitt, S., de Vargas, C., Marié, L., Memery, L., et al. (2021). Phytoplankton taxonomic and functional diversity patterns across a coastal tidal front. *Sci. Rep.* 11 (1), 2682. doi: 10.1038/s41598-021-82071-0

Ramond, P., Sourisseau, M., Simon, N., Romac, S., Schmitt, S., Rigaut-Jalabert, F., et al. (2019). Coupling between taxonomic and functional diversity in protistan coastal communities. *Environ. Microbiol.* 21 (2), 730–749. doi: 10.1111/1462-2920.14537

Rives, A. W., and Galitski, T. (2003). Modular organization of cellular networks. *PNAS* 100 (3), 1128–1133. doi: 10.1073/pnas.0237338100

Roselli, L., and Litchman, E. (2017). Phytoplankton traits, functional groups and community organization. *J. Plankton Res.* 39 (3), 491–493. doi: 10.1093/plankt/fbx019

Russel, J. (2023). *MicEco: Various functions for microbial community data. R package version 0.9.19*. Available at: https://github.com/Russel88/MicEco/.

Seeleuthner, Y., Mondy, S., Lombard, V., Carradec, Q., Pelletier, E., Wessner, M., et al. (2018). Single-cell genomics of multiple uncultured stramenopiles reveals underestimated functional diversity across oceans. *Nat. Commun.* 9 (1), 310. doi: 10.1038/s41467-017-02235-3

Shin, C.-W., Min, H. S., Lee, S., Kang, H.-W., Ku, B., Kim, D. G., et al. (2022). Current structure and volume transport in the jeju strait observed for a year with multiple ADCP moorings. *Ocean Sci. J.* 57 (3), 365–380. doi: 10.1007/s12601-022-00079-7

Skouroliakou, D.-I., Breton, E., Irion, S., Artigas, L. F., and Christaki, U. (2022). Stochastic and deterministic processes regulate phytoplankton assemblages in a temperate coastal ecosystem. *Microbiol. Spectr.* 10 (6), e02427–e02422. doi: 10.1128/spectrum.02427-22

Stegen, J. C., Lin, X., Fredrickson, J. K., Chen, X., Kennedy, D. W., Murray, C. J., et al. (2013). Quantifying community assembly processes and identifying features that impose them. *ISME J.* 7 (11), 2069–2079. doi: 10.1038/ismej.2013.93

Stegen, J. C., Lin, X., Konopka, A. E., and Fredrickson, J. K. (2012). Stochastic and deterministic assembly processes in subsurface microbial communities. *ISME J.* 6 (9), 1653–1664. doi: 10.1038/ismej.2012.22

Sun, Y., Youn, S.-H., Kim, Y., Kang, J. J., Lee, D., Kim, K., et al. (2022). Interannual variation in phytoplankton community driven by environmental factors in the northern East China Sea. *Front. Mar. Sci.* 9. doi: 10.3389/fmars.2022.769497

Vellend, M., and Agrawal, A. (2010). Conceptual synthesis in community ecology. *Q. Rev. Biol.* 85 (2), 183–206. doi: 10.1086/652373

Venkataramana, V., Mishra, R. K., Sabu, P., Anilkumar, N., Sarkar, A., Naik, R. K., et al. (2021). Stratification governs the plankton community structure and trophic interaction in the Southwestern tropical Indian Ocean during boreal summer. *Reg. Stud. Mar. Sci.* 48, 101987. doi: 10.1016/j.rsma.2021.101987

Webb, C. O., Ackerly, D. D., McPeek, M. A., and Donoghue, M. J. (2002). Phylogenies and community ecology. *Ann. Rev. Ecol. Syst.* 33 (1), 475–505. doi: 10.1146/annurev.ecolsys.33.010802.150448

Wickham, H., François, R., Henry, L., Müller, K., and Vaughan, D. (2023). dplyr: A grammar of data manipulation. R package version 1.1.2. Available at: https://CRAN.R-project.org/package=dplyr.

Won, J., Lee, Y., Lee, H., and Noh, J. H. (2021). Effect of marine environment changes on the abundance and community composition of cyanobacteria in the south sea of korea. *Ocean Polar Res.* 43 (4), 279–293. doi: 10.4217/OPR.2021.43.4.279

Xu, Z., Chen, Y., Meng, X., Wang, F., and Zheng, Z. (2016). Phytoplankton community diversity is influenced by environmental factors in the coastal East China Sea. *Eur. J. Phycol.* 51 (1), 107–118. doi: 10.1080/09670262.2015.1107138

Xu, Z., Li, Y., Lu, Y., Li, Y., Yuan, Z., Dai, M., et al. (2020). Impacts of the Zhe-Min Coastal Current on the biogeographic pattern of microbial eukaryotic communities. *Prog. Oceanogr.* 183, 102309. doi: 10.1016/j.pocean.2020.102309

Xue, Y., Chen, H., Yang, J. R., Liu, M., Huang, B., and Yang, J. (2018). Distinct patterns and processes of abundant and rare eukaryotic plankton communities following a reservoir cyanobacterial bloom. *ISME J.* 12, 2263–2277. doi: 10.1038/s41396-018-0159-0

Zhang, J., Hu, A., Sun, Y., Yang, Q., Dong, J., Long, L., et al. (2021).). Dispersal limitation expands the diversity of coral microbiome metacommunity in the south China sea. *Front. Mar. Sci.* 8. doi: 10.3389/fmars.2021.658708

Zhou, J., and Ning, D. (2017). Stochastic community assembly: does it matter in microbial ecology? *Microbiol. Mol. Biol. Rev.* 81 (4), e00002–e00017. doi: 10.1128/MMBR.00002-17

Zou, K., Wang, R., Xu, S., Li, Z., Liu, L., Li, M., et al. (2021). Changes in protist communities in drainages across the Pearl River Delta under anthropogenic influence. *Water Res.* 200, 117294. doi: 10.1016/j.watres.2021.117294

Frontiers in Marine Science

TYPE Original Research
PUBLISHED 06 September 2023
DOI 10.3389/fmars.2023.1244639

Check for updates

OPEN ACCESS

EDITED BY
Yanpei Zhuang,
Jimei University, China

REVIEWED BY
Gustaaf Marinus Hallegraeff,
University of Tasmania, Australia
Sheean Haley,
Columbia University, United States

*CORRESPONDENCE
Jakob Karl Giesler
jakob.giesler@awi.de

RECEIVED 22 June 2023
ACCEPTED 22 August 2023
PUBLISHED 06 September 2023

CITATION
Giesler JK, Lemley DA, Adams JB and Moorthi SD (2023) Interactive effects of salinity, temperature and food web configuration on performance and harmfulness of the raphidophyte *Heterosigma akashiwo*. *Front. Mar. Sci.* 10:1244639. doi: 10.3389/fmars.2023.1244639

Interactive effects of salinity, temperature and food web configuration on performance and harmfulness of the raphidophyte *Heterosigma akashiwo*

Jakob Karl Giesler[1,2*], Daniel Alan Lemley[3,4], Janine Barbara Adams[3,4] and Stefanie Devi Moorthi[1]

[1]ICBM, Institute for Chemistry and Biology of the Marine Environment, Carl von Ossietzky University of Oldenburg, Oldenburg, Germany, [2]AWI, Alfred Wegener Institute, Helmholtz Centre for Polar and Marine Research, Bremerhaven, Germany, [3]DSI-NRF Research Chair in Shallow Water Ecosystems, Department of Botany, Nelson Mandela University, Gqeberha, South Africa, [4]Institute for Coastal and Marine Research, Nelson Mandela University, Gqeberha, South Africa

The cosmopolitan raphidophyte *Heterosigma akashiwo* commonly forms harmful algal blooms (HABs) in diverse estuaries discharging into Algoa Bay, South Africa, potentially leading to hypoxia, fish kills and a decline in key primary consumers. Despite the high environmental variability in these estuaries, little is known about how abiotic factors such as temperature and salinity constrain bloom formation and harmfulness of *H. akashiwo*. The present study therefore investigates growth, competition, and grazing interactions of *H. akashiwo* in laboratory experiments in response to two naturally relevant levels of salinity (15, 30) and temperature (16, 22°C), respectively. Experiments were set up with the naturally co-occurring dinoflagellate competitor *Heterocapsa rotundata* and two estuarine microzooplankton consumers, i.e., nauplii of the copepod *Acartia tonsa* and the rotifer *Brachionus plicatilis*. In monoculture, *H. akashiwo* growth was promoted at high temperature – low salinity conditions, while *H. rotundata* thrived under low temperature – high salinity conditions. In polyculture, *H. akashiwo* dominated at high temperature irrespective of the salinity regime, while at low temperature, it only dominated at low salinity and was suppressed by *H. rotundata* at high salinity. Grazing assays revealed highly negative effects of *H. akashiwo* on copepod nauplii survival and growth as well as mucus-induced immobilization, especially at high temperatures in combination with low salinity, while the estuarine adapted rotifers showed highest mortalities at the higher salinity level. The presence of *H. rotundata* significantly alleviated the harmful effects of *H. akashiwo* on both grazers, and the selectively feeding copepod nauplii actively avoided *H. akashiwo* when non-harmful prey was present. Overall, this study demonstrates that population dynamics and harmful effects of *H. akashiwo* are interactively determined by both abiotic conditions and food web configuration, implying competitor and consumer specific tolerances to the abiotic environment and their susceptibility to the harmful alga *H. akashiwo*.

KEYWORDS

***Heterosigma akashiwo*, harmful algal bloom, estuaries, temperature, salinity, mucus production, selective grazing**

1 Introduction

Heterosigma akashiwo is a harmful raphidophyte, occurring in various coastal and estuarine waters around the world. Numerous bloom events have been reported for temperate regions including Canada (Taylor and Haigh, 1993), the United States (Kempton et al., 2007), Japan (Li and Smayda, 2000) and China (Wang et al., 2007), as well as for subtropical waters of Brazil (Branco et al., 2014) and multiple South African estuaries (Lemley et al., 2018b; Lemley et al., 2021). The cosmopolitan distribution of *H. akashiwo* reflects its broad ecological tolerance to wide ranges of temperature, salinity, and light intensity (Martinez et al., 2010; Strom et al., 2013; Allaf and Trick, 2019). As such, this species is well-adapted to the highly variable and potentially stressful temperature and salinity regimes of estuarine ecosystems, such as the Sundays and Hartenbos estuaries in South Africa. These microtidal estuarine systems are characterized by highly variable abiotic conditions (Lemley et al., 2018b), mouth conditions (Adams et al., 2020), and levels of anthropogenic pressures (e.g., flow modification, nutrient loading) (Dalu et al., 2018; Lemley et al., 2021). Both estuaries experience aggravated nutrient pollution, however, the primary source of anthropogenic nutrients varies between the Sundays (agricultural practices) and Hartenbos (treated wastewater discharges) estuaries. The resulting continuous supply of nutrient rich freshwater makes both systems particularly susceptible to harmful algal blooms (HABs) caused by *H. akashiwo*. This species dominates the phytoplankton community in the Sundays Estuary mainly during spring/summer when elevated water temperatures and stratified mesohaline waters facilitate nearly monospecific bloom events (>550 µg Chl a L^{-1}) (Lemley et al., 2018b). Such HAB events have been shown to severely impact the ecosystem by, for example, inducing bottom-water hypoxia (Lemley et al., 2018b), reduced abundance of key primary consumers (Smit et al., 2021) as well as deleterious effects on mugilid fish gills (Bornman et al., 2022) and embryonic fish cells (Sandoval-Sanhueza et al., 2022). While for most HAB-forming species the predominating mode of harmfulness is well understood, different harmful mechanisms have been proposed for *H. akashiwo*. They include the production of neurotoxins (Khan et al., 1997), cytotoxins (Sandoval-Sanhueza et al., 2022), allelochemicals (Yamasaki et al., 2007; Yamasaki et al., 2009; Qiu et al., 2012), reactive oxygen species (Yang et al., 1995; Oda et al., 1997; Twiner and Trick, 2000), and adhesive mucus, with the latter potentially leading to gill clogging of fish and blocking of the zooplankton filtration apparatus (Nakamura et al., 1998; Lemley et al., 2018b). Yet, there is no scientific consensus about which of these mechanisms is the predominant harmful mode in the raphidophyte.

Another bloom-forming species in the Sundays Estuary is the dinoflagellate *Heterocapsa rotundata*, which represents a dominant competitor of *H. akashiwo* (Adams et al., 2020). Although *H. rotundata* is well documented as red tide-forming species, it is not recognized as causing harmful effects (Iwataki, 2008). Field data indicate that the two species proliferate at contrasting environmental conditions in terms of temperature and, locally, also in terms of salinity, with *H. akashiwo* generally preferring increased water temperatures and *H. rotundata* thriving at lower temperatures (Rothenberger et al., 2009; Lemley et al., 2018b). Therefore, the variability of these abiotic conditions can be considered an important driving force for the bloom dynamics of these two species, consequently also affecting herbivorous grazer populations and higher trophic levels (Burkholder et al., 2018). While Lemley et al. (2018a; 2020) demonstrated the *in-situ* limiting effect of *H. akashiwo* blooms on co-occurring plankton taxa in the Sundays Estuary, Qiu et al. (2012) investigated competitive interactions between *H. akashiwo* and other phytoplankton species in controlled laboratory experiments. The outcome revealed a strong inhibitory effect of a Japanese strain of *H. akashiwo* on the dinoflagellate *Akashiwo sanguinea* caused by allelochemical polysaccharide-protein complexes that even led to cell deformation in the competitor. Other studies focused on the harmful effects of *H. akashiwo* on primary consumers and provided evidence for adverse effects of this HAB species on *in-situ* larval fish and zooplankton densities (Smit et al., 2021), on survival, grazing, and recruitment of the copepod *Schmackeria inopinus* (Yu et al., 2010), as well as on population growth of the rotifer *Brachionus plicatilis* (Xie et al., 2007; Yan et al., 2009). However, neither the competition studies nor the grazing assays conducted so far took into account how competitive outcome and the coupled grazer proliferation could be altered by different abiotic environmental conditions. Yet, interactive effects of abiotic and biotic determinants are crucial to be considered in order to fully understand the mechanisms driving bloom dynamics of harmful species and to enhance our predictive understanding of such blooms (Purz et al., 2021).

The present study therefore investigates the bloom dynamics and associated harmfulness of a South African *H. akashiwo* strain in response to altered temperature and salinity regimes in monoculture, as well as in a food web context including a dinoflagellate competitor and two different herbivorous consumers. In this context, harmfulness is defined by adverse effects on competitors (such as growth inhibition) and consumers (such as mortality and grazing deterrence). A full-factorial competition experiment was conducted at two naturally relevant levels of salinity and temperature, respectively, to identify growth preferences of *H. akashiwo* in monoculture and its competitive ability in polyculture under different environmental conditions. In subsequent grazing assays, two different consumers were added to the system (separately) under the same temperature and salinity regimes to test for consumer mortality, grazing rates, and consumer-specific sensitivity to the harmful algae. For all experiments, only species were used that are known to co-occur with *H. akashiwo* in brackish estuarine waters, i.e., the dinoflagellate *H. rotundata* as competitor, the non-selectively feeding rotifer *Brachionus plicatilis* and nauplii of the selectively feeding copepod *Acartia tonsa* as grazers.

Based on the patterns previously observed in the field and in small-scale laboratory experiments, temperature and salinity variations were expected to differentially select for the dominance of the two phytoplankton species in polyculture. In both monoculture and polyculture experimental setups, *H. akashiwo* was expected to be promoted at high temperature – low salinity conditions and *H. rotundata* at low temperature – high salinity conditions. Furthermore, herbivorous consumers were predicted to experience negative effects in terms of survival, grazing, and developmental stages in the presence of *H. akashiwo*. The strongest harmful effects were expected to be found under optimum growth conditions of the harmful alga (i.e., at high temperature – low salinity conditions). The presence of non-harmful prey was hypothesized to promote consumer growth in monoculture and alleviate the harmful effects of *H. akashiwo* in mixed prey cultures.

2 Materials and methods

2.1 Experimental cultures and culture conditions

The raphidophyte *Heterosigma akashiwo* (strain code UOL_HA1) was isolated from a water sample taken from the Hartenbos Estuary along the warm-temperate south coast of South Africa in 2019 (i.e., less than one year until use in experiments), and the dinoflagellate *Heterocapsa rotundata* was obtained from the Roscoff Culture Collection, France (strain code RCC3042). Both algae were cultivated in f/2 medium (Guillard, 1975) prepared from 0.2 µm filtered and sterilized seawater with a salinity of 30, taken from the Jade Bay in Wilhelmshaven, Germany. By dilution with f/2 medium, the cultures were kept in exponential growth phase and were cultivated under controlled conditions in a climate chamber at 18°C, 70 µmol photons m^{-2} s^{-1} and a 12:12 h light:dark period. Eggs of the copepod *Acartia tonsa* were obtained from the AWI Biological Institute Helgoland (BAH), Germany, and stored at 6°C in total darkness until use. The rotifer *Brachionus plicatilis* was obtained from the aquatic retailer Interaquaristik, Germany, and was grown under the same culture conditions as described for the phytoplankton species. Every two weeks, the *Brachionus* culture was transferred into new medium and was fed with the green algae *Tetraselmis* sp. (also derived from the Roscoff Culture Collection, France).

2.2 Competition experiment

A competition experiment was conducted to investigate the growth and competitive ability of *H. akashiwo* in the presence of the dinoflagellate *H. rotundata* under variable estuarine conditions by establishing two levels of temperature (16 and 22°C) in combination with two levels of salinity (15 and 30) in a full factorial design. Temperature and salinity levels were selected based on the findings of Lemley et al. (2018b) in the Sundays Estuary, South Africa, and thus represent typical ranges for the naturally occurring variability of temperature and salinity in South African estuaries. Both algae were inoculated at equal biovolume proportions to account for the size difference of the two species. For that purpose, the dimensions of 30 cells of each species were measured using a Zeiss Axiovert 10 inverted microscope and the individual cell biovolume of *H. akashiwo* and *H. rotundata* was calculated according to Hillebrand et al. (1999). Both species were inoculated at a total biovolume of 2.43×10^6 µm^3, corresponding to an initial cell density of 5×10^3 cells ml^{-1} for *H. akashiwo* and 21×10^3 cells ml^{-1} for *H. rotundata* (cell volume *H. akashiwo*: 487 µm^3, cell volume *H. rotundata*: 114 µm^3). Both species were set up in monoculture and polyculture, using an additive design, i.e., inoculating each species with the same biovolume in monoculture and polyculture, resulting in twice the total biovolume in the polycultures compared to monocultures. This additive design was chosen in consideration of the subsequent grazing assays, where the consumers were incubated with the same algal monocultures and polycultures. This assured equal amounts of the harmful algae (i.e., equal concentrations of potentially harmful substances) in all treatments. Each treatment was replicated by four, resulting in a total of 48 experimental units (3 species combinations x 2 salinity levels x 2 temperature levels x 4 replicates), containing 200 ml culture in a sterile 250 ml Erlenmeyer flask. To establish the lower salinity level of 15, f/2 medium was diluted with fully desalinated water enriched with f/2 nutrient concentrations and the salinity was checked with a Multi 3630 IDS SET KS2 sensor. The experimental units were incubated, using the empty containers of an indoor mesocosm facility (Planktotrons, (Gall et al., 2017) at their respective experimental temperature (16°C and 22°C) and a light intensity of 100 µmol photons m^{-2} s^{-1} with a light:dark period of 12:12 hours. To ensure equal illumination among the experimental units and avoid cell aggregation the flasks were exposed to slow mechanical rotation and were additionally homogenized by hand every 12 hours. Sampling was conducted every 48 hours and comprised subsamples of 500 µl from each experimental unit. Samples were fixed in a 48-well microplate (83.3923 Sarstedt AG & Co KG ©) with formalin at a final concentration of 2% for quantification conducted with a Leica DMIL inverted bright field microscope at a magnification of 100x. Every fourth day, an additional 10 ml of each experimental unit were sampled for subsequent dissolved macronutrient analysis. Furthermore, at the end of the experiment, 10 ml samples were taken from each experimental unit for particulate macronutrient analysis. The experiment was terminated after 28 days, when the last treatment had reached the stationary growth phase.

2.3 Copepod grazing assay

A grazing assay was conducted to evaluate whether and how the potential harmful effects of *H. akashiwo* on copepod nauplii are altered by different temperature and salinity regimes, as well as by the presence of a non-harmful competitor. Prior to the main experiment, a pilot study was performed in which the effect of a *H. akashiwo* culture (4 x 10^4 cells ml^{-1}) on *A. tonsa* nauplii (1 individual ml^{-1}) survival was compared to a starvation control (sterile filtered seawater without algal food) in a five-day incubation. This was done to test whether the harmful effects of *H. akashiwo* on copepod nauplii exceed a pure starvation effect, i.e., whether the potential mucus production of the harmful algae mainly hinders filter feeding in the consumer, leading to starvation, or whether the harmful effects are stronger, indicating the production of allelochemicals or other harmful substances.

For the subsequent full factorial grazing assay, the same experimental salinity and temperature levels and the same algae species combinations were used as in the competition experiment *(Section 3.2)*, but with the addition of *A. tonsa* nauplii at an initial density of 1 individual ml^{-1}. To provide sufficient prey for the nauplii, *H. akashiwo* was inoculated with an initial cell density of 1.5 × 10^4 cells ml^{-1}, corresponding to 6.4 × 10^4 cells ml^{-1} *H. rotundata*, resulting in equal biovolume proportions of each phytoplankton species in monoculture and polyculture. Phytoplankton were inoculated again using the additive design, resulting in twice the total algal biovolume in polyculture to ensure that the grazers were exposed to the same biovolume of *H. akashiwo* and thus the same amount of potentially harmful substances in all treatments (see above). Due to space constraints, no additional non-grazer control treatments containing only the phytoplankton species were set up; instead, the competition experiment, which was conducted only a few weeks before, was used as non-grazer control.

After hatching, nauplii stock cultures were prepared according to Meunier et al. (2016). Experimental units were set up with growth medium and phytoplankton/consumer stock cultures in a total volume of 200 ml contained in 250 ml Erlenmeyer flasks. The preparation of the experimental units in terms of salinity was identical to the procedure described for the competition experiment. After incubation in the Planktotron containers, phytoplankton sampling was conducted every 24 hours with the identical procedure as described for the competition experiment. For evaluation of zooplankton mortality, additional 10 ml subsamples were taken daily from each experimental unit and transferred into 6-well microplates for quantification with an inverted light microscope. The mortality was then calculated by dividing the number of dead individuals in the live samples by the total number of nauplii counted in each sample after fixation with formalin at 2% final concentration. An individual was considered dead after no physical movement for at least 60 seconds was observed. The experiment was terminated after five days, when the first treatment showed a mortality of 100%. At the end of the experiment, the developmental stages of the nauplii in different treatments were evaluated by micrographs of three individuals within each replicate taken with a Jenoptik Gryphax Kapella camera connected to a Zeiss Axiovert 10 microscope. At the end of the experiment, additional 10 ml subsamples were taken from each experimental unit for dissolved and particulate macronutrient analysis, respectively. For the particulate macronutrient subsamples, grazers were removed by filtration through a 20 µm nylon mesh.

2.4 Rotifer grazing assay

A second grazing assay was conducted with the rotifer *Brachionus plicatilis* to test for potential differences in grazer sensitivity to the harmful algae. Since the results of the prior competition experiment (*Section 3.2*) indicated that salinity effects depended on temperature, the rotifer bioassay was reduced to the two salinity levels (15 and 30) at a fixed experimental temperature of 16°C. This reduced experimental setup allowed for the addition of non-grazer control treatments containing only the phytoplankton species in monoculture and polyculture. All treatments were replicated three times.

Prior to the start of the experiment, the rotifers were starved for 24 hours by careful rinsing with sterile seawater on a 50 µm nylon mesh to remove any prey items, followed by resuspension in 500 ml beakers. After the starvation period, these cultures were used as stocks for the experiment. Next, the experimental units, with a total volume of 150 ml each, were inoculated with the rotifers at a density of 1 individual ml^{-1}. The preparation of the experimental units in terms of salinity, as well as the initial cell densities of the two phytoplankton species, was identical to the copepod nauplii bioassay (*Section 3.3*). After incubation in the Planktotron containers under the same controlled conditions at 16°C, grazer and phytoplankton sampling for microscopy were conducted every third day (including day 0) with identical procedures as previously described in *Section 2.2* and *2.3*, respectively. The experiment was terminated after six days.

2.5 Analysis of particulate and dissolved macronutrients

Samples for dissolved inorganic nutrients (nitrogen, phosphorus, silicate) were prefiltered through 0.2 µm syringe filters (Sarstedt Filtropour S) and stored in PE bottles at -20°C until analysis using a SAN++ Continuous Flow Analyzer (CFA, Skalar Analytical B.V., Netherlands). For particulate intracellular carbon (C), nitrogen (N), and phosphorus (P) analyses, two 10 ml subsamples were filtered on pre-combusted and acid washed

Whatman GF/F filters for CN and P analyses, respectively. The CN elemental composition was measured using a CHN analyzer (Thermo, Flash EA 1112). Particulate phosphate was measured as orthophosphate by molybdate reaction after sulfuric acid digestion according to Grasshoff et al. (2009).

2.6 Data analyses

To test for optimum growth conditions of the two phytoplankton species, as well as for the impact of the competitor in the competition experiment (*Section 3.2*), treatment effects on phytoplankton biovolume were tested for each species separately, using linear mixed models (LMMs) with temperature, salinity, presence of the competitor, and time as fixed factors, as well as the index number of the experimental unit representing the random factor. The LMMs were conducted using the "lmer" function from the "lmerTest" package (Kuznetsova et al., 2017) that includes the Satterthwaite approximation for obtaining p-values. To meet the model assumptions of homoscedasticity, algal biovolumes were square root transformed prior to the analysis. For testing dominance shifts over time in the polycultures, log ratios of the two phytoplankton species biovolumes were calculated for each sampling point which were then analyzed separately for each factorial treatment combination against time using Kruskal-Wallis tests. Subsequently, non-parametric pairwise Wilcoxon rank sum *post hoc* tests were used to compare the log ratios of every sampling day to the log ratio of day 0 at which both species were inoculated at equal biovolume proportions. Moreover, non-linear models were fitted for each experimental unit individually by means of the "nls" base R function using sampling data from the start until the day of the maximum achieved biovolume to obtain the maximum growth rates and carrying capacities of the two phytoplankton species in each treatment. Only significant model fits were used to extract parameters for maximum growth rates and carrying capacities. These were then tested separately for both species using two-way ANOVAs with salinity and temperature as independent variables. To test for differences in phytoplankton particulate molar C:N ratios at the end of the competition experiment and nauplii grazing assay, a three-way ANOVA was performed with species composition, temperature, and salinity as independent variables. Model assumptions of homogeneous variances and normally distributed residuals were tested with Fligner-Killeen tests and Shapiro-Wilk tests, respectively. Due to technical problems with the particulate phosphorous analysis, P-concentrations could not be considered here and no C:P or N:P ratios could be calculated.

In the nauplii and rotifer grazing assays, effects on mortality were analyzed using LMMs with temperature, salinity, prey composition, and time as fixed factors, as well as the index of the experimental unit as random factor for the nauplii grazing assay. The same factors, except for temperature (i.e., experiment was conducted at only one temperature level) were used for rotifers. To calculate grazing rates, phytoplankton growth rates in the absence of consumers (gross growth rate = μ) and with consumers (net growth rate = r) were calculated between day 0 and day 5 by subtracting ln-transformed starting biovolume from ln-transformed final biovolume and dividing this by the respective number of experimental days (five days for *A. tonsa* nauplii, six days for *B. plicatilis*). The net population grazing rate (g) was then calculated as $\mu - r$. For the prey mixture treatments that contained both phytoplankton species, biovolumes were pooled prior to the grazing rate calculations. As previously described, there were no additional non-grazer controls for the copepod grazing assay so that the competition experiment was used as such. Consequently, the resulting grazing rates require cautious interpretation as the two experiments were set up with different initial biovolumes. However, no density-dependent effects on phytoplankton growth could be expected in any of the experiments during the first five days of the experiments (duration of the nauplii grazing assay). Moreover, the experiments were conducted in the same mesocosm containers with only a short time interval in between and represented identical conditions, allowing to compare phytoplankton growth rates in the different setups. To test for differences in relative population grazing rates of the nauplii in different temperature and salinity treatments, generalized least squares (GLS) models were conducted, to compensate for groups with non-homogeneous variances by using weights. Effects on rotifer relative population grazing rates were tested using three-way ANOVAs with temperature, salinity, and prey composition as independent variables. Moreover, to test for selective grazing effects in the mixed prey cultures, separate grazing rates were calculated for both phytoplankton species which were then tested in a three-way ANOVA with temperature, salinity, and phytoplankton species identity for the nauplii bioassay, and a two-way ANOVA with salinity and phytoplankton species identity for the rotifer bioassay. For comparing the sensitivity to harmful effects of *A. tonsa* and *B. plicatilis*, another LMM was performed on grazer mortality as dependent variable and salinity, prey composition, grazer identity, and time as independent variables. However, from the nauplii grazing assay, only data from the lower temperature treatments were considered here, since the rotifer grazing assay was conducted only at 16°C. Differences in population grazing rates between the two grazer species were tested using a three-way ANOVA with the same set of independent variables (except for time).

Post-hoc analyses were conducted with estimated marginal means pairwise comparisons using the "emmeans" function from the "emmeans" package (Lenth, 2021) for GLS models and Tukey *post-hoc* tests for LMMs and ANOVAs, respectively. All statistical analyses and graphs of this study were performed using the R statistical environment 4.0.2. (R Core Team, 2020).

3 Results

3.1 Competition experiment

H. akashiwo and *H. rotundata* biovolumes were both significantly and interactively affected by salinity, temperature, time, and the presence of the competitor, except for *H. rotundata* biovolumes that did not show a significant effect by its competitor (Table 1).

In monoculture, *H. akashiwo* biovolume was significantly higher at the higher experimental temperature and lower salinity level (Figures 1A, D). Low salinity treatments resulted in higher carrying capacities for *H. akashiwo* (Table 2). The positive temperature effect was reflected in higher maximum growth rates for *H. akashiwo* at 22°C compared to 16°C ($p < 0.001$), being highest (0.53 day^{-1}, Table S1) in the low salinity – high temperature treatment, differing from all other treatment combinations ($p < 0.004$). Depending on the respective treatment, *H. akashiwo* reached its maximum biovolume in monoculture between day 18 and 24, with the 16°C treatments generally achieving a time-delayed, but notably higher carrying capacity than at 22°C (Figures 1A, D).

H. rotundata biovolume was promoted by the higher salinity level of 30 in combination with the lower experimental temperature of 16°C compared to the other treatment combinations ($p < 0.001$, Figures 1B, E), which resulted in a maximum growth rate of 0.52 day^{-1} in this treatment and the highest carrying capacity ($p < 0.001$). By contrast, under low salinity – high temperature conditions, *H. rotundata* biovolume production was strongly inhibited, reflected by a lower maximum growth rate compared to the other treatments (Table S1), and a maximum biovolume accounting for only 29% of the maximum biovolume achieved under the optimum high-salinity low-temperature conditions. Compared to *H. akashiwo*, the dinoflagellate generally exhibited lower total carrying capacities that were, however, achieved between day 6 and 14 depending on the treatment, and therefore several days earlier than for *H. akashiwo* in monoculture.

Temperature and salinity effects on *H. akashiwo* biovolume were generally stronger in polycultures compared to monocultures (Figures 1C, F). Within the high temperature treatments, *H. akashiwo* showed slightly higher maximum growth rates at the lower salinity level and a suppressed carrying capacity at the higher salinity level accounting for only 78% of the carrying capacity achieved in the corresponding monoculture treatment. At higher temperature, *H. akashiwo* dominated over *H. rotundata* for most of the experimental duration (Figures 1F, S1) indicated by significant differences of the log ratio from day 0 (Table S2). More precisely,

TABLE 1 **Results of linear mixed models testing the effects of salinity, temperature, competitor and day (fixed effects) on the square rooted biovolumes of *H. akashiwo* and *H. rotundata* (monocultures and polyculture treatments together) with beaker number (id) as random factor.**

		H. akashiwo			*H. rotundata*		
		sqrt(biovolume)			sqrt(biovolume)		
Fixed Effect	Df	*F*	*p*		*F*	*p*	
Salinity	1	355.0	<0.001	*	5715.3	<0.001	*
Temp.	1	347.5	<0.001	*	1807.2	<0.001	*
Competitor	1	470.2	<0.001	*	3.3	0.08	
Day	14	2961.8	<0.001	*	812.6	<0.001	*
Salinity × Temp.	1	21.5	<0.001	*	326.0	<0.001	*
Salinity × Competitor	1	171.0	<0.001	*	26.0	<0.001	*
Temp. × Competitor	1	226.5	<0.001	*	58.4	<0.001	*
Salinity × Day	14	49.7	<0.001	*	342.4	<0.001	*
Temp. × Day	14	34.0	<0.001	*	65.8	<0.001	*
Competitor × Day	14	61.1	<0.001	*	6.1	<0.001	*
Salinity × Temp. × Competitor	1	27.4	<0.001	*	16.3	<0.001	*
Salinity × Temp. × Day	14	31.9	<0.001	*	113.3	<0.001	*
Salinity × Competitor × Day	14	25.7	<0.001	*	18.4	<0.001	*
Temp. × Competitor × Day	14	64.5	<0.001	*	15.2	<0.001	*
Salinity × Temp. × Competitor × Day	14	20.0	<0.001	*	11.2	<0.001	*
Random Effect							
σ^2		209087.9			77523.5		
$\tau_{00\ id}$		58417.7			5474.0		
ICC		0.22			0.07		
N_{id}		32			32		
Observations		480			480		
Marginal R^2/Conditional R^2		0.989/0.991			0.986/0.987		

Degrees of freedom (df), F and p-values are given for each effect. Values marked with an asterisk (*) indicate significant effects ($p < 0.05$).

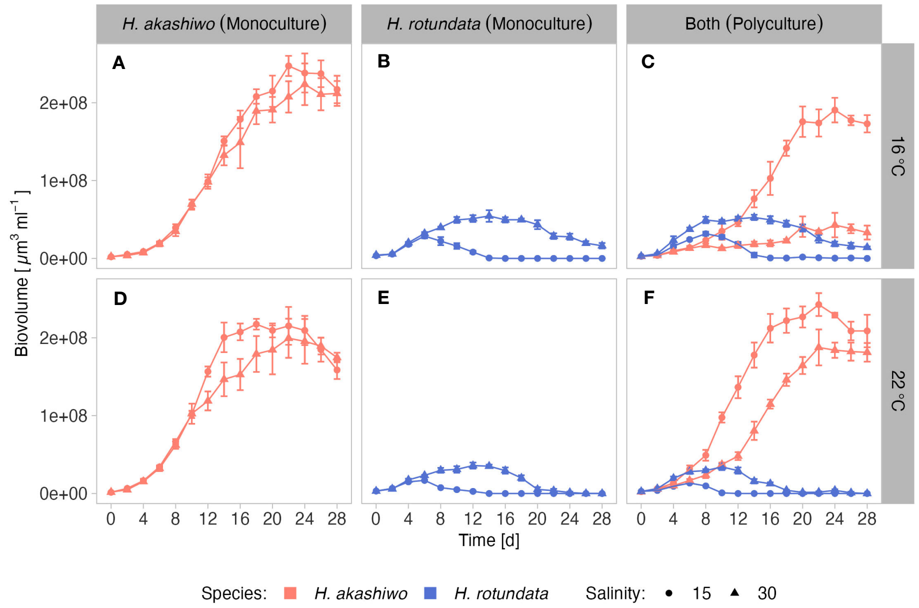

FIGURE 1
Mean biovolume (± SD) of H. akashiwo (red line) and H. rotundata (blue line) over time incubated in monocultures and polycultures (facet columns) at two levels of salinity (15 and 30; represented by shape) and two levels of temperature (16°C and 22°C; represented by facet rows). Labels indicate culture and temperature combinations, i.e., **(A)** = *H. akashiwo* monoculture at 16°C; **(B)** = *H. rotundata* monoculture at 16°C; **(C)** = polyculture at 16°C; **(D)** = *H. akashiwo* monoculture at 22°C; **(E)** = *H. rotundata* monoculture at 22°C; **(F)** = polyculture at 22°C.

within the high temperature treatments, *H. akashiwo* dominated over *H. rotundata* at the lower salinity level from day 2 onwards, whereas at the higher salinity level *H. rotundata* exhibited a temporary dominance from day 4 to 6, after which *H. akashiwo* dominated again from day 12 until the end of the experiment. Within the low temperature treatments, *H. akashiwo* dominated the low salinity treatment from day 12 onwards but was significantly inhibited by its competitor at high salinity until day 18, after which it dominated the community again. As such, competitive interactions strongly depended on salinity, especially within the low temperature treatments (Figure 1C), which was also reflected by the significant interactive effects of temperature, salinity, and competitor presence for *H. akashiwo* biovolume, maximum growth rate, and carrying capacity (Tables 1 and 2). At low temperature – low salinity, *H. akashiwo* performed similar in the presence of *H. rotundata* as under the corresponding monoculture conditions. At the higher salinity level, *H. akashiwo* showed strongly suppressed growth rates and reached only 20% of the maximum biovolume of its corresponding monoculture.

Dissolved nutrient concentrations indicated phosphorous depletion in the *H. akashiwo* monocultures as well as in the polycultures starting from day 12 onwards (Figure S2). Dissolved nitrogen was depleted several days later at day 20 (Figure S3). However, C:N ratios across the different treatment combinations were relatively low and ranged from 5.1 to 9.1, indicating that algal cells were not N limited. C:N ratios were significantly affected by

TABLE 2 ANOVA results testing the effects of temperature, salinity and the presence of a competitor (Comp) on the maximum growth rate (r_{max}) and carrying capacities (CC) of *H. akashiwo* and *H. rotundata* (monocultures and polyculture treatments together).

Effect	Df	*H. akashiwo*						*H. rotundata*					
		r_{max}			CC			r_{max}			Log(CC)		
		F	*P*		*F*	*P*		*F*	*P*		*F*	*P*	
Temp.	1	94.5	<0.001	*	47.5	<0.001	*	2.5	0.124		411.4	<0.001	*
Salinity	1	127.4	<0.001	*	109.9	<0.001	*	20.3	<0.001	*	1062.0	<0.001	*
Competitor	1	33.0	<0.001	*	95.3	<0.001	*	20.6	<0.001	*	25.8	<0.001	*
Salinity × Temp.	1	1.8	0.190		19.8	<0.001	*	12.3	0.002	*	6.1	0.021	*
Salinity × Competitor	1	3.1	0.091		41.1	<0.001	*	11.2	0.003	*	8.2	0.008	*
Temp. × Competitor	1	2.5	0.125		110.7	<0.001	*	0.0	0.877		0.4	0.517	
Temp. × Salinity × Competitor	1	24.0	<0.001	*	20.2	<0.001	*	0.6	0.445		0.4	0.518	

Degrees of freedom (Df), F and p-values are given for each effect. Values marked with an asterisk (*) indicate significant effects ($p < 0.05$).

species composition, with *H. akashiwo* generally having higher C:N ratios than *H. rotundata* ($p < 0.001$), yet showing interactive effects with temperature and salinity (Figure S4; Table S3).

3.2 Nauplii pilot study and grazing assay

In the preliminary pilot study, the mortality of the *A. tonsa* nauplii was higher when incubated with *H. akashiwo* compared to the filtered seawater control ($p = 0.032$). In the filtered seawater treatment, nauplii mortality showed a steady linear increase over time (Figure S5), resulting in a mean mortality of 72% after five days of incubation. In contrast, mean nauplii mortality increased from 3 to 83% between day 1 and day 2 in the *H. akashiwo* treatment.

In the full factorial nauplii grazing assay conducted under the same temperature and salinity levels used in the competition experiment, nauplii mortality was interactively affected by salinity, temperature, prey composition, and time (Table 3; Figure 2). Nauplii mortality at the end of the experiment was higher when incubated with *H. akashiwo* monocultures compared to *H. rotundata* monocultures or the polyculture treatments containing both phytoplankton species ($p < 0.001$, Table S4). In the *H. akashiwo* monocultures, nauplii mortality was higher at 22°C than at 16°C ($p < 0.001$), starting from day 2 onwards. Contrastingly, in the 16°C treatments, mortality was still 0% after two days of incubation and started to increase thereafter. Across both temperatures, nauplii mortality increased earlier at the lower salinity level compared to high salinity but converged in both salinities over the course of the experiment, which is reflected in the significant interaction of salinity and time (Table 3). The highest overall mortality was observed in *H. akashiwo* monocultures under low salinity – high temperature conditions, i.e., the optimal growth conditions of *H. akashiwo*, with the first experimental unit reaching a mortality of 100% on day 3. Treatments containing the non-harmful prey *H. rotundata*, either in monoculture or in polyculture with *H. akashiwo*, were similar to each other and showed low nauplii mortality over time with no notable differences among each other (Table S4). Regarding the developmental stages of the nauplii

TABLE 3 (a) Results of a linear mixed model (LMM) testing the effects of salinity, temperature, prey composition and day (fixed effects) on nauplii mortality with beaker number (id) as random factor. (b) Results of a generalized least squares model (GLS) testing the effects of salinity, temperature and prey composition on relative population grazing rate.

Fixed Effect	Mortality (LMM)				Grazing Rate (GLS)			
	Df	*F*	*p*		Df	*F*	*p*	
Salinity	1	18.1	<0.001	*	1	3.0	0.092	
Temp.	1	75.8	<0.001	*	1	104.2	<0.001	*
Prey	2	172.3	<0.001	*	2	31.1	<0.001	*
Day	5	57.0	<0.001	*	-	-	-	
Salinity × Temp.	1	0.4	0.552		1	6.6	0.014	*
Salinity × Prey	2	6.3	0.005	*	2	5.3	0.009	*
Temp. × Prey Composition	2	57.6	<0.001	*	2	21.5	<0.001	*
Salinity × Day	5	2.7	0.021	*	-	-	-	
Temp. × Day	5	11.6	<0.001	*	-	-	-	
Prey × Day	10	32.9	<0.001	*	-	-	-	
Salinity × Temp. × Prey	2	1.4	0.250		2	1.2	0.315	
Salinity × Temp. × Day	5	1.7	0.147		-	-	-	
Salinity × Prey × Day	10	1.3	0.213		-	-	-	
Temp. × Prey × Day	10	8.0	<0.001	*	-	-	-	
Salinity × Temp. × Prey × Day	10	1.2	0.301		-	-	-	
Random Effect								
σ^2	117.48				-	-	-	
$\tau_{00\ \mathrm{id}}$	6.03				-	-	-	
ICC	0.05				-	-	-	
N_{id}	48				-	-	-	
Observations	288				-	-	-	
Marginal R^2/Conditional R^2	0.836/0.844				-	-	-	

Degrees of freedom (df), F and p-values are given for each effect. Values marked with an asterisk (*) indicate significant effects ($p < 0.05$).

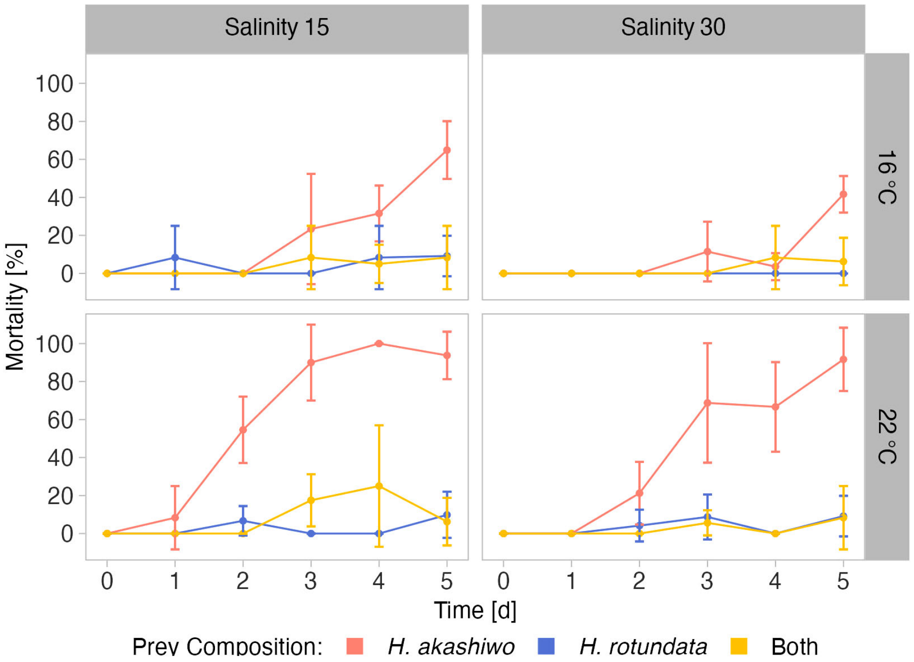

FIGURE 2
Mortality of *A. tonsa* nauplii over time when exposed to *H. akashiwo*, *H. rotundata* or both algae species in combination (indicated by color) across two levels of temperature (16°C and 22°C) and salinity (15 and 30) represented by facet grid rows and columns, respectively.

at the end of the experiment, nauplii exposed to *H. akashiwo* monocultures did not develop beyond the N1 state in any treatment combination of temperature and salinity, while nauplii in the *H. rotundata* monocultures and the polycultures developed to stages N4 and N3, respectively, at 16°C and even reached copepodite stages C2 – C4 in the 22°C treatments (Figure S6).

Population grazing rates of the *A. tonsa* nauplii were significantly and interactively affected by prey composition and temperature, while the salinity effect was not significant, but depended on prey composition and temperature (twofold interactions of salinity with both factors, Table 3). Average nauplii grazing rates were lowest in *H. akashiwo* monoculture treatments irrespective of temperature and salinity levels (Figure 3). In the *H. rotundata* monoculture as well as in the polyculture treatments, however, nauplii grazing rates strongly differed with temperature and salinity. While grazing rates were generally very low at 16°C and did not exceed a mean of 0.1 day^{-1}, grazing rates increased with temperature, especially at low salinity, resulting in significant differences of this treatment compared to most other treatment combinations (Table S5). *H. rotundata* monoculture treatments experienced the highest grazing impact (0.39 day^{-1}). Considering separate grazing rates for both phytoplankton species in the polyculture treatments, grazing rates on *H. rotundata* were higher than on *H. akashiwo* in the higher experimental temperature ($p < 0.001$, Figure 4; Tables 4, S6), regardless of salinity.

Dissolved nutrient concentrations indicated no macronutrient depletion of phosphorous or nitrogen during the experiment (Figures S7, S8). C:N ratios of the phytoplankton ranged between 6.7 and 8.2 (Figure S9).

4.3 Rotifer grazing assay

The second grazing assay was conducted with the rotifer *B. plicatilis* at only one temperature (16°C), but both salinity levels which were also used in the nauplii grazing assay. Here, rotifer mortality was significantly affected by prey composition and time; both factors depending on salinity (two-fold interactive effects of both factors with salinity, Figure 5; Table 5).

As in the nauplii grazing assay, grazer mortality at the last sampling day was higher in *H. akashiwo* monoculture treatments compared to the *H. rotundata* monoculture or polyculture treatments ($p < 0.004$, Table S7). Within the *H. akashiwo* treatments, the highest mortality was found at the high salinity level ($p = 0.023$) with a mean mortality of 65% at the end of the experiment, which was notably higher than the mortality at the low salinity level (20%). Rotifer mortality in treatments containing the non-harmful prey *H. rotundata* in monoculture or in polyculture with *H. akashiwo* did not differ from each other and did not exceed a mean mortality of 10%.

The relative population grazing rates were very low across all treatments and included negative values, indicating that for some treatments phytoplankton growth rates were even higher in the presence of grazers compared to the non-grazed controls (Figure 6). However, the relative population grazing rate of *B. plicatilis* differed with salinity as well as interactively with salinity and prey composition (Table 5). This was reflected in similar grazing rates across different prey compositions at the low salinity level, but significant differences at the higher salinity level (Table S8). However, despite these significant differences, the overall grazing impact of the rotifers and therefore also the effect size was very low.

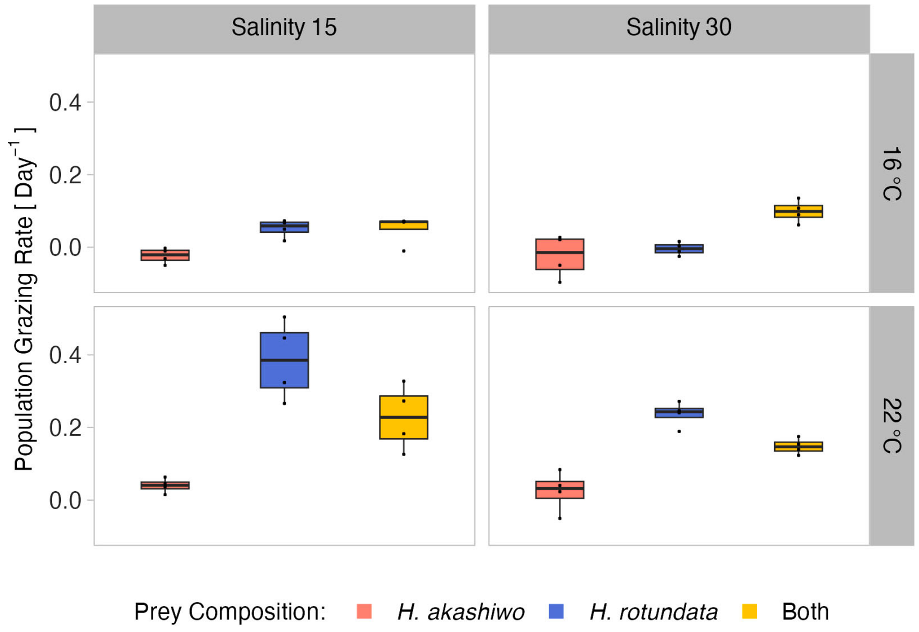

FIGURE 3
A tonsa nauplii relative population grazing rate day^{-1}at the different prey algae compositions *H. akashiwo*, *H. rotundata* and both algae in combination (indicated by color) across two levels of temperature (16°C and 22°C) and salinity (15 and 30) represented by facet grid rows and columns, respectively.

In polycultures, grazing rates on *H. rotundata* were higher than for *H. akashiwo* at the lower salinity level ($p = 0.012$, Tables 4, S9). Yet, differences between the species-specific relative grazing rates were also relatively small (< 0.1) and are likely an artefact of the enhanced growth of *H. akashiwo* in this treatment since *B. plicatilis* is known to have a non-selective feeding behavior (Figure S10).

Comparing the mortality of *B. plicatilis* and *A. tonsa* nauplii in the 16°C treatments, grazer mortality was significantly and interactively affected by prey composition and time (significant main factors and interaction), while salinity effects were only important in relation to time (Table S7). Grazer mortality did not differ notably between the two consumer species, indicating similar

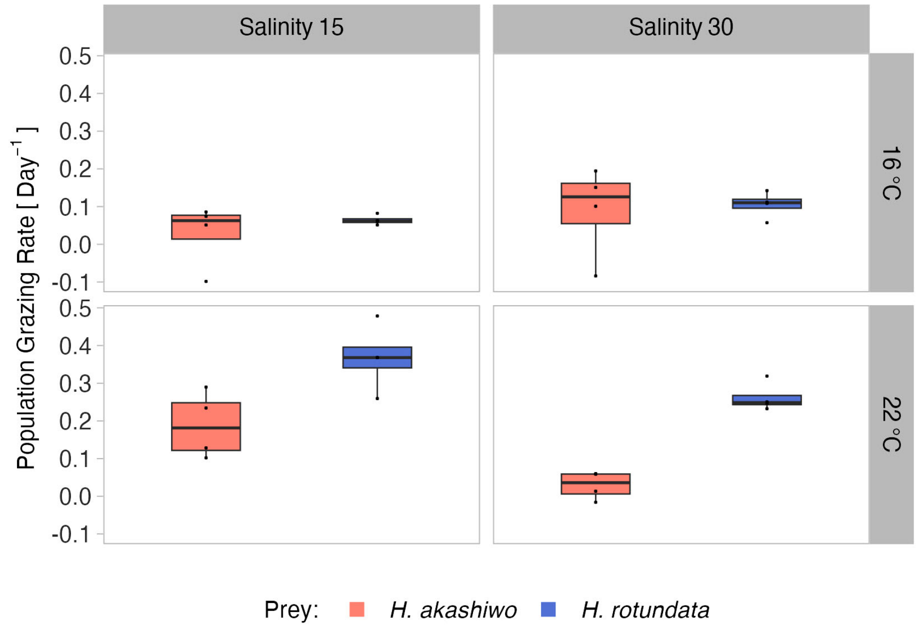

FIGURE 4
Relative population grazing rates of the selective feeding *A. tonsa* nauplii in the polyculture treatments separated by prey algae species (indicated by color) across two levels of temperature (16°C and 22°C) and salinity (15 and 30) represented by facet grid rows and columns, respectively.

TABLE 4 ANOVA results testing differences among grazing rates in the polyculture treatments as a response to algae species identity, temperature and salinity for *A. tonsa* and *B. plicatilis*.

Effect	*A. tonsa* Grazing Rate (polyculture)				*B. plicatilis* Grazing Rate (polyculture)			
	Df	*F*	*p*		Df	*F*	*p*	
Prey	1	20.2	<0.001	*	1	4.1	0.079	
Temp.	1	29.6	<0.001	*	-	-	-	
Salinity	1	2.5	0.128		1	2.4	0.160	
Prey × Temp.	1	12.4	0.002	*	-	-	-	
Prey × Salinity	1	0.1	0.761		1	16.1	0.004	*
Temp. × Salinity	1	12.9	0.001	*	-	-	-	
Prey × Temp. × Salinity	1	0.5	0.475		-	-	-	

Degrees of freedom (df), F and p-values are given for each effect. Values marked with an asterisk (*) indicate significant effects ($p < 0.05$).

sensitivities of both grazers in response to the harmful algae. However, salinity affected grazer mortality in *H. akashiwo* monocultures in contrasting ways, with *B. plicatilis* exhibiting higher mortality at high salinity and nauplii showing higher mortality at the low salinity level (Figures 2, 5; Table S11).

Population grazing rates of the two grazers differed from each other and were interactively affected by salinity and prey composition (significant main effects and two-way interactions, Table S10). The grazing rates of the two consumers did not exceed an average of 0.1 day^{-1} in the lower temperature level. The observed interactive effect of consumer identity and prey composition indicated that the presence of non-harmful prey led to higher grazing rates for the *A. tonsa* nauplii. In contrast, the presence of non-harmful prey did not result in increased grazing for *B. plicatilis* based on its overall minor grazing impact across all factorial combinations (Figures 3, 6; Table S12).

4 Discussion

As expected, based on field observations, *H. akashiwo* was promoted at high temperature – low salinity conditions, while *H. rotundata* proliferated at the contrasting low temperature – high salinity conditions. In competition, *H. akashiwo* dominated the system at the higher temperature regime irrespective of salinity. At low temperature, however, salinity determined the competitive outcome, promoting *H. akashiwo* over *H. rotundata* at low salinity and vice versa at high salinity. Both studied grazers were negatively affected by *H. akashiwo* in monoculture; however, salinity levels altered these effects in different ways, leading to higher mortality at low salinity for *A. tonsa* nauplii and at high salinity for the rotifer *B. plicatilis*. Furthermore, for both grazers, the presence of non-harmful prey significantly alleviated the harmful effects caused by *H. akashiwo*. In contrast to the non-selective filter feeder *B. plicatilis*, the highly selective *A. tonsa* nauplii strongly avoided *H. akashiwo* in the polyculture treatments.

The observed growth preferences of *H. akashiwo* match the findings of Lemley et al. (2018b), who identified optimum growth conditions for *H. akashiwo* at elevated water temperatures of 20 - 26°C and a salinity preference towards brackish conditions (4–24) in the Sundays Estuary. Similar patterns could be observed in the Golden Horn Estuary in the northeast Sea of Marmara, Turkey, where a short-term increase in water temperature from 15.7°C to 20.2°C in combination with a decrease in salinity from 18.7 to 16.4 triggered a *H. akashiwo* HAB with a density of 10^{3} cells ml^{-1} (Dursun et al., 2016). However, despite the identification of its

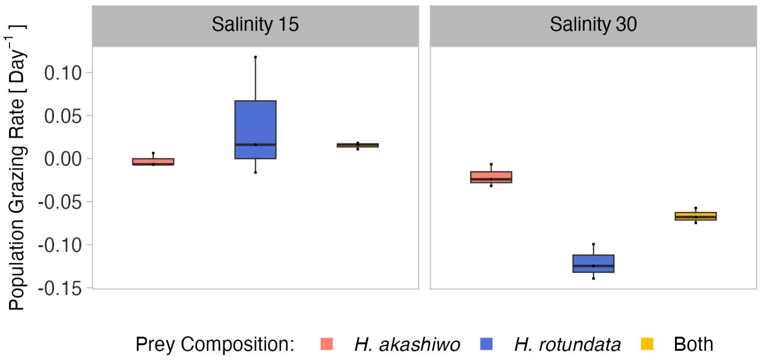

FIGURE 5
Mortality of *B. plicatilis* over time when exposed to *H. akashiwo*, *H. rotundata* or both algae species in combination (indicated by color) across two levels of salinity (15 and 30) represented by facet grid columns.

TABLE 5 ANOVA results testing the effects of salinity and prey composition on *B. plicatilis* mortality and population grazing rate.

Effect	Mortality (AOV)				Grazing Rate (AOV)			
	Df	*F*	*p*		Df	*F*	*p*	
Salinity	1	6.5	0.025	*	1	36.2	<0.001	*
Prey Composition	2	11.6	0.002	*	2	1.4	0.290	
Salinity × Prey Composition	2	4.1	0.043	*	2	8.1	0.006	*

Degrees of freedom (df), F and p-values are given for each effect. Values marked with an asterisk (*) indicate significant effects ($p < 0.05$).

optimum growth conditions in the present study, *H. akashiwo* also exhibited its previously reported high tolerance against broad ranges of temperature and salinity regimes outside of its optimum growth window (Martinez et al., 2010; Strom et al., 2013; Allaf and Trick, 2019). This was evidenced by only minor performance differences across treatments in monoculture as well as by dominating three out of four temperature – salinity combinations in competition.

The performance of the dinoflagellate competitor *H. rotundata* in competition with *H. akashiwo* was similar to its respective monoculture growth controls, although *H. rotundata* was shown to decline in the presence of *H. akashiwo* in the field (2018a). Our laboratory study implies a low suppressive potential of the studied South African *H. akashiwo* strain against its competitor under the selected experimental conditions. Yamasaki et al. (2007) indicated that the harmful substances produced by *H. akashiwo* may be highly species-specific. In their study, *H. akashiwo* substantially suppressed the growth of the harmful diatom species *Chaetoceros muelleri* and *Skeletonema costatum*, while having no harmful effect on cultures of the dinoflagellate *Prorocentrum cordatum.* Another possible explanation for the lack of a negative impact of *H. akashiwo* on *H. rotundata* in our study could be the higher growth rate of *H. rotundata* compared to *H. akashiwo*, resulting in a distinct time lag for the two species to reach their carrying capacity. Consequently, this could have led to *H. rotundata* already being naturally in decline by the time *H. akashiwo* reached cell densities at which allelopathy became relevant. This advantageous high growth rate could represent a protection strategy to avoid elevated concentrations of allelopathic or other harmful substances (Arzula et al., 1999). This idea matches the results of Yamasaki et al. (2007), who demonstrated that substantial inhibitory effects by *H. akashiwo* on its competitors did not come into effect before the end of their exponential growth phase, indicating that the extent of the harmful effect is not only dependent on cell concentration, but also on the specific growth phase of *H. akashiwo*.

Interestingly in this study, however, the negative effect of *H. rotundata* on *H. akashiwo* growth under high salinity – low temperature conditions point towards an inhibitory potential of *H. rotundata*. Although it is generally known that *H. rotundata* can form red tides in terms of large monospecific bloom events, this species has not been associated with direct harmful effects on competitors or consumers so far. Therefore, the suppressed growth of *H. akashiwo* observed in mixed culture with *H. rotundata* in this treatment is more likely based on a competitive advantage of the dinoflagellate under these environmental conditions. Given the fact that the total biovolume in polyculture was twice as high as in the monocultures based on the additive experimental design, it is likely that interspecific competition in polycultures constrained populations dynamics before intraspecific competition did in monocultures. Moreover, it should be noted, that dissolved phosphorous was depleted in most treatments at day 12 resulting in an increasing effect of nutrient limitation over the course of the experiment.

Since *H. akashiwo* is a globally occurring species, experimental evidence for growth preferences of a certain strain from a particular habitat raises the question to which degree these findings can be transferred to other strains in other systems, i.e., what is the extent of intraspecific trait variation for this species. Martinez et al. (2010)

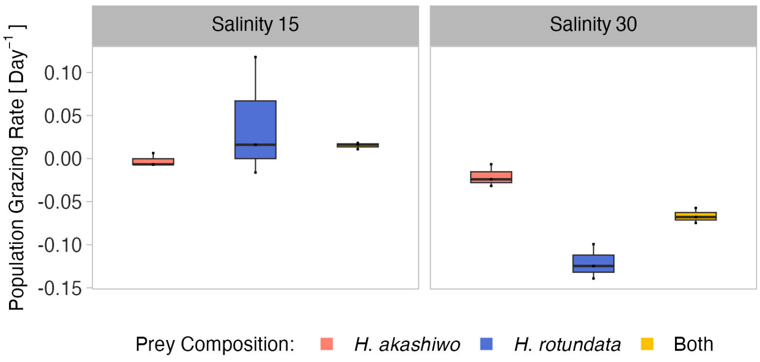

FIGURE 6
B. plicatilis relative population grazing rate day^{-1}at the different prey algae compositions *H. akashiwo*, *H. rotundata* and both algae in combination (indicated by color) across two levels of salinity (15 and 30) represented by facet grid columns.

investigated the growth responses of six different strains of *H. akashiwo* originating from a broad latitudinal range at different levels of temperature, salinity, and light intensity and demonstrated an across-strain preference for the higher experimental temperature of 23°C (vs. 17°C). Salinity preferences depended on strain identity, yet all strains showed a fast adaptive capability to different salinity regimes. The high halotolerance of *H. akashiwo* was intensively studied by Strom et al. (2013), who indicated that this tolerance is likely to be an evolutionary defense strategy developed by this species against marine micrograzers that allows it to escape by inhabiting low salinity surface waters that are unsuitable for marine grazers.

Copepod nauplii exposed to *H. akashiwo* monocultures in this study showed increased mortality as well as inhibited grazing activity, implying a high sensitivity of these grazers to the harmful effects of *H. akashiwo*. This was also confirmed in our pilot grazing assay in which the negative effects of *H. akashiwo* on *A. tonsa* nauplii far exceeded those of pure starvation in the filtered seawater control. Furthermore, the selective feeding behavior indicated that the nauplii were able to recognize the prey as harmful and actively avoid it. Since the C:N ratios of *H. akashiwo* were only marginally higher than the Redfield C:N ratio, this grazer deterrence effect was likely not based on low algal food quality, although unfortunately no particulate organic phosphorous data could be evaluated to further support this finding.

As for the *A. tonsa* nauplii in our study, Colin and Dam (2002) demonstrated suppressed ingestion rates, as well as reduced survival and egg production in adult *A. tonsa* copepods when restricted to *H. akashiwo* monoculture prey. Similar effects were found by Tomas and Deason (1981) who generally showed concentration dependent suppressed filtration rates of *Acartia* spp. in the presence of *H. akashiwo* (formerly *Olistodiscus luteus*). In the present study, nauplii mortality was highest in high temperature – low salinity treatments, thus coinciding with the optimum growth conditions of *H. akashiwo*. These stronger negative effects at high versus low temperature are contrary to the findings of Allaf and Trick (2019) who investigated cell permeability as a proxy for cytotoxicity of H. akashiwo at different levels of temperature, salinity and light. They found the highest cell permeability at 15°C (vs. 20 and 25°C) in a H. akashiwo strain isolated from Clam Bay, USA, thus, indicating an increasing cytotoxicity of H. akashiwo with decreasing temperature. Yet, the study did not test the actual adverse effects on primary consumers at the studied conditions, therefore neglecting how different environmental conditions could alter the susceptibility of grazers towards the harmful substances produced by *H. akashiwo*. Furthermore, the discrepancies to the present study could potentially be explained by strain-specific differences in the predominant mode of harmfulness of this species. For instance, John et al. (2015) demonstrated that within a toxigenic population of the dinoflagellate *Alexandrium fundyense*, single strains were capable of allelopathy to protect the population from grazing, while other strains did not show any allelopathic capabilities, but produced potent saxitoxins. In the present study, neither toxin production nor cell permeability were determined. However, based on observations during the experiments, mucus production by *H. akashiwo* likely played a major role in causing the lethal effects on both grazers in this study, as after 24h, for instance, the majority of nauplii and rotifers were trapped in mucus and were strongly immobilized. Similar observations were made by Xie et al. (2007) who also found an enhanced immobilization of rotifers due to mucus produced by *H. akashiwo*. As harmful effects of *H. akashiwo* on the nauplii exceeded those of pure starvation, it is likely that other harmful substances were involved in the high consumer mortality observed here, which are either excreted together with the mucus or are located on the cell surface of *H. akashiwo*, causing harmful effects upon cell contact (Yamasaki et al., 2009).

The fact that the strongest effects on nauplii mortality in this study were found in the *H. akashiwo* monocultures at high temperature conditions could be based on increased metabolic rates of *H. akashiwo*, resulting in increased net mucus production at higher temperature. Additionally, the immobile nauplii in the *H. akashiwo* monocultures were likely to use up their energy reserves more rapidly at higher temperature due to increased metabolic rates, but also due to their increased physical efforts to detach themselves from the mucus. This also supports the pattern that the temperature effect on mortality in *H. akashiwo* monocultures was much larger than the salinity effect, which was in contrast to that observed for *B. plicatilis*, indicating that salinity affected consumer fitness rather than the harmfulness of *H. akashiwo*.

In contrast, nauplii mortality was much lower in treatments containing *H. rotundata*, either in monoculture or in polyculture with *H. akashiwo*, which indicates that the presence of non-harmful prey can substantially buffer the adverse effects caused by *H. akashiwo*. This further matches the findings of Colin and Dam (2002), who demonstrated that reduced survival, ingestion and egg production rates of adult *A. tonsa* individuals induced by *H. akashiwo* were alleviated when non-harmful prey was present as an alternative food source. In addition to providing an alternative high-quality food source, the adhesive nature of potential allelochemicals (Branco et al., 2014) may cause them to attach to the non-harmful algae and thus reduce the ambient concentration of these substances for primary consumers. Similar suggestions were made by Prince et al. (2008), who found growth inhibitory effects caused by allelopathic compounds exuded by the red-tide-forming dinoflagellate *Karenia brevis* to be reduced in the presence of the diatom species *Skeletonema costatum*.

The observed lethal effects of *H. akashiwo* on *B. plicatilis* match the findings of Xie et al. (2007), who also showed a population decrease of *B. plicatilis* when exposed to *H. akashiwo* monocultures. Moreover, the presence of the dinoflagellate *Alexandrium tamarense* in polyculture with *H. akashiwo* alleviated the population decrease in a similar way as the presence of *H. rotundata* reduced the mortality of the rotifers in this study. Comparing the sensitivity of *A. tonsa* nauplii and *B. plicatilis* to *H. akashiwo* exposure, similar harmful effects were found for both tested metazoan grazers. Interestingly, salinity had opposite effects on the mortality of the two grazers, resulting in the highest mortality of *A. tonsa* nauplii at the low salinity level, while *B. plicatilis* experienced the highest mortality at the higher salinity level. This interactive effect of prey composition, salinity, and consumer identity indicates that although both grazers can be found in estuarine ecosystems (Paffenhöfer and Stearns, 1998), *A. tonsa* generally prefers a higher salinity level, whereas *B. plicatilis* is promoted by a lower salinity level. Consequently, when exposed to non-optimum salinities, the grazers need to spend more energy on osmoregulatory processes (Goolish and Burton, 1989), which consequently might reduce their fitness and lead to higher mortality when exposed to unfavorable prey.

Overall, the present study highlighted the growth dynamics of two dominant bloom-forming phytoplankton species in estuarine ecosystems, and demonstrated their preference for contrary temperature and salinity regimes. The observed growth optima for the two species match field observations and contribute to the explanation of alternating bloom occurrence patterns of *H. akashiwo* and *H. rotundata* in the field (Hilmer and Bate, 1991; Rothenberger et al., 2009; Lemley et al., 2018b). Moreover, *H. akashiwo* could only be outcompeted by *H. rotundata* at high salinity – low temperature conditions but dominated at low salinity – low temperature and at high temperature irrespective of salinity, emphasizing the importance of the interplay of natural abiotic conditions and their variability in estuarine ecosystems for determining the bloom dynamics of this species. Environmental variability in estuaries can be induced by weather changes or openings and closings of the river mouth, representing environmental resetting events which are necessary to constrain monospecific *H. akashiwo* blooms and thus strengthen ecosystem resilience. However, anthropogenic regulating interventions like the construction of barrages and water extraction for agricultural purposes reduce flow velocity and lead to permanently closed river mouth states, which in turn favor optimum bloom conditions of *H. akashiwo* (Dalu et al., 2018; Lemley et al., 2018b). This impeded abiotic variability inducing the formation and persistence of *H. akashiwo* blooms may increase even further in the future, especially under global warming additionally promoting the harmful raphidophyte, and can only be controlled by other measures that have the potential to reduce HAB events, such as the reduction of nutrient input to the ecosystem. In future studies, it is therefore crucial to consider the effects of inorganic and organic nutrient pollution in concert with other environmental factors to derive a comprehensive understanding of the bloom dynamics of *H. akashiwo* and *H. rotundata* in estuarine systems. Furthermore, this study demonstrated negative effects of *H. akashiwo* on copepod nauplii as well as rotifers, which likely have been caused by mucus production and potentially associated harmful substances of *H. akashiwo*. The poorly characterized nature of this mucus opens up an important research perspective to identify its chemical composition and quantify its production under different environmental conditions as well as its immobilizing and lethal effects on different targets. In an ecosystem context, however, not only the direct adverse effects on zooplankton need to be considered, but also the consequences of a potential decline in key estuarine primary consumers for higher trophic levels, as well as interactive effects with the temporally and spatially highly variable environment.

Data availability statement

The datasets presented in this study can be found in online repositories. The names of the repository/repositories and accession number(s) can be found in the article/Supplementary Material.

Author contributions

SM, JA and DL conceived the idea and designed the study. JG conducted the experiments, performed the statistical analyses and drafted the manuscript with input from all co-authors. All authors contributed to the article and approved the submitted version.

Funding

This work was supported by the German Research Foundation grant no. HI848/26-1.

Acknowledgments

We thank Heike Rickels (ICBM Terramare, Wilhelmshaven, Germany) for analysis of dissolved and particulate nutrient samples as well as technical support in the lab. Furthermore, we also thank Jan-Claas Dajka (HIFMB, Oldenburg, Germany) for advice in data analysis and Cedric Meunier (AWI, Helgoland, Germany) for providing the *A. tonsa* eggs.

Conflict of interest

The authors declare that the research was conducted in the absence of any commercial or financial relationships that could be construed as a potential conflict of interest.

Publisher's note

Supplementary material

The Supplementary Material for this article can be found online at: https://www.frontiersin.org/articles/10.3389/fmars.2023.1244639/full#supplementary-material

References

Adams, J. B., Taljaard, S., Van Niekerk, L., and Lemley, D. A. (2020). Nutrient enrichment as a threat to the ecological resilience and health of South African microtidal estuaries. *Afr. J. Aquat. Sci.* 45, 23–40. doi: 10.2989/16085914.2019.1677212

Allaf, M., and Trick, C. G. (2019). Multiple-stressor design-of-experiment (DOE) and one-factor-at-a-time (OFAT) observations defining *Heterosigma akashiwo* growth and cell permeability. *J. Appl. Phycol.* 31, 3515–3526. doi: 10.1007/s10811-019-01833-6

Arzula, G. V., Miriam, S., Guzmanc, L., and Erard-Lea Denn, E. (1999). Comparison of allelopathic properties in three toxic *Alexandrium* species. *J. Exp. Mar. Biol. Ecol.* 232, 285–295. doi: 10.1016/S0022-0981(98)00120-8

Bornman, E., Adams, J. B., and Strydom, N. A. (2022). Algal blooms of *Heterosigma akashiwo* and Mugilidae gill alterations. *Estuaries Coasts* 45, 1674–1687. doi: 10.1007/s12237-021-01038-6

Branco, S., Menezes, M., Alves-De-Souza, C., Domingos, P., Schramm, M. A., and Proenca, L. A. (2014). Recurrent blooms of *Heterosigma akashiwo* (Raphidophyceae) in the PIraque Channel, Rodrigo de Freitas Lagoon, southeast Brazil. *Braz. J. Biol.* 74, 529–537. doi: 10.1590/bjb.2014.0074

Burkholder, J. M., Shumway, S. E., and Glibert, P. M. (2018). "Food web and ecosystem impacts of harmful algae," in *Harmful Algae Blooms*. Eds. S. E. Shumway, J. M. Burkholder and S. L. Morton (Hoboken: Wiley).

Colin, S. P., and Dam, H. G. (2002). Testing for toxic effects of prey on zooplankton using sole versus mixed diets. *Limnol. Oceanogr.* 47, 1430–1437. doi: 10.4319/lo.2002.47.5.1430

Dalu, T., Magoro, M. L., Tonkin, J. D., Human, L. R. D., Perissinotto, R., Deyzel, S. H. P., et al. (2018). Assessing phytoplankton composition and structure within micro-estuaries and micro-outlets: a community analysis approach. *Hydrobiologia* 818, 177–191. doi: 10.1007/s10750-018-3605-0

Dursun, F., Taş, S., and Koray, T. (2016). Spring bloom of the raphidophycean *Heterosigma akashiwo* in the Golden Horn Estuary at the northeast of Sea of Marmara. *Ege J. Fish. Aquat. Sci.* 33, 201–207. doi: 10.12714/egejfas.2016.33.3.03

Gall, A., Uebel, U., Ebensen, U., Hillebrand, H., Meier, S., Singer, G., et al. (2017). Planktotrons: A novel indoor mesocosm facility for aquatic biodiversity and food web research. *Limnol. Oceanogr.: Methods* 15, 663–677. doi: 10.1002/lom3.10196

Goolish, E. M., and Burton, R. S. (1989). Energetics of osmoregulation in an intertidal copepod: effects of anoxia and lipid reserves on the pattern of free amino acid accumulation. *Funct. Ecol.* 3, 81–89. doi: 10.2307/2389678

Grasshoff, K., Kremling, K., and Ehrhardt, M. (2009). *Methods of Seawater Analysis* (New York: Wiley-VHC).

Guillard, R. R. L. (1975). "Culture of phytoplankton for feeding marine invertebrates," in *Culture of Marine Invertebrates Animals*. Eds. M. L. Smith and M. H. Chanley (New York: Plenum Press).

Hillebrand, H., Dürselen, C.-D., Kirschtel, D., Pollingher, U., and Zohary, T. (1999). Biovolume calculation for pelagic and benthic microalgae. *J. Phycol.* 35, 403–424. doi: 10.1046/j.1529-8817.1999.3520403.x

Hilmer, T., and Bate, G. C. (1991). Vertical migration of a flagellate-dominated bloom in a shallow South African estuary. *Botanica Marina* 34, 113–121. doi: 10.1515/botm.1991.34.2.113

Iwataki, M. (2008). Taxonomy and identification of the armored dinoflagellate genus *Heterocapsa* (Peridiniales, Dinophyceae). *Plankton Benthos Res.* 3, 135–142. doi: 10.3800/pbr.3.135

John, U., Tillmann, U., Hulskotter, J., Alpermann, T. J., Wohlrab, S., and van de Waal, D. B. (2015). Intraspecific facilitation by allelochemical mediated grazing protection within a toxigenic dinoflagellate population. *Proc. Biol. Sci.* 282, 20141268. doi: 10.1098/rspb.2014.1268

Kempton, J., Keppler, C., Lewitus, A., Shuler, A., and Wilde, S. (2007). A novel *Heterosigma akashiwo* (Raphidophyceae) bloom extending from a South Carolina bay to offshore waters. *Harmful Algae* 7, 235–240. doi: 10.1016/j.hal.2007.08.003

Khan, S., Arakawa, O., and onoue, Y. (1997). Neurotoxins in a toxic red tide of *Heterosigma akashiwo* Raphidophyceae in Kagoshima. *Aquacult. Res.* 28, 9–14. doi: 10.1111/j.1365-2109.1997.tb01309.x

Kuznetsova, A., Brockhoff, P. B., and Christensen, R. H. B. (2017). lmerTest Package: Tests in Linear Mixed Effects Models. *Journal of Statistical Software* 82, 1–26. doi: 10.18637/jss.v082.i13

Lemley, D. A., Adams, J. B., and Rishworth, G. M. (2018a). Unwinding a tangled web: a fine-scale approach towards understanding the drivers of harmful algal bloom species in a eutrophic South African estuary. *Estuaries Coasts* 41, 1356–1369. doi: 10.1007/s12237-018-0380-0

Lemley, D. A., Adams, J. B., Rishworth, G. M., and Purdie, D. A. (2020). Harmful algal blooms of *Heterosigma akashiwo* and environmental features regulate *Mesodinium cf. rubrum* abundance in eutrophic conditions. *Harmful Algae* 100, 101943. doi: 10.1016/j.hal.2020.101943

Lemley, D. A., Adams, J. B., and Strydom, N. A. (2018b). Triggers of phytoplankton bloom dynamics in permanently eutrophic waters of a South African estuary. *Afr. J. Aquat. Sci.* 43, 229–240. doi: 10.2989/16085914.2018.1478794

Lemley, D. A., Lamberth, S. J., Manuel, W., Nunes, M., Rishworth, G. M., van Niekerk, L., et al. (2021). Effective management of closed hypereutrophic estuaries requires catchment-scale interventions. *Front. Mar. Sci.* 8. doi: 10.3389/fmars.2021.688933

Lenth, R. V. (2021). *emmeans: Estimated Marginal Means, aka Least-Squares Means. R package version 1.6.1. ed.* Available at: https://CRAN.R-project.org/package=emmeans.

Li, Y., and Smayda, T. (2000). *Heterosigma akashiwo* (Raphidophyceae): On prediction of the week of bloom initiation and maximum during the initial pulse of its bimodal bloom cycle in Narragansett Bay. *Plankton Biol. Ecol.* 47, 80–84.

Martinez, R., Orive, E., Laza-Martinez, A., and Seoane, S. (2010). Growth response of six strains of *Heterosigma akashiwo* to varying temperature, salinity and irradiance conditions. *J. Plankton Res.* 32, 529–538. doi: 10.1093/plankt/fbp135

Meunier, C. L., Boersma, M., Wiltshire, K. H., and Malzahn, A. M. (2016). Zooplankton eat what they need: copepod selective feeding and potential consequences for marine systems. *Oikos* 125, 50–58. doi: 10.1111/oik.02072

Nakamura, A., Okamoto, T., Komatsu, N., Ooka, S., Oda, T., Ishimatsu, A., et al. (1998). Fish Mucus Stimurates the Generation of Superoxide Anion by *Chattonella marina* and *Heterosigma akashiwo*. *Fish. Sci.* 64, 866–869. doi: 10.2331/fishsci.64.866

Oda, T., Nakamura, A., Shikayama, M., Kawano, L., Ishimatsu, A., and Muramatsu, T. (1997). Generation of reactive oxygen species by Raphidophycean phytoplankton. *Biosci. Biotech. Biochem.* 61, 1658–1662. doi: 10.1271/bbb.61.1658

Paffenhöfer, G.-A., and Stearns, D. E. (1998). Why is *Acartia tonsa* (Copepoda: Calanoida) restricted to nearshore environments? *Mar. Ecol. Prog. Ser.* 42, 33–38. doi: 10.3354/meps042033

Prince, E. K., Myers, T. L., Naar, J., and Kubanek, J. (2008). Competing phytoplankton undermines allelopathy of a bloom-forming dinoflagellate. *Proc. Biol. Sci.* 275, 2733–2741. doi: 10.1098/rspb.2008.0760

Purz, A. K., Hodapp, D., and Moorthi, S. D. (2021). Dispersal, location of bloom initiation, and nutrient conditions determine the dominance of the harmful dinoflagellate *Alexandrium catenella* : A meta-ecosystem study. *Limnol. Oceanogr.* 66, 3928–3943. doi: 10.1002/lno.11933

Qiu, X., Yamasaki, Y., Shimasaki, Y., Gunjikake, H., Matsubara, T., Nagasoe, S., et al. (2012). Allelopathy of the raphidophyte *Heterosigma akashiwo* against the dinoflagellate *Akashiwo sanguinea* is mediated via allelochemicals and cell contact. *Mar. Ecol. Prog. Ser.* 446, 107–118. doi: 10.3354/meps09476

Rothenberger, M. B., Burkholder, J. M., and Wentworth, T. R. (2009). Use of long-term data and multivariate ordination techniques to identify environmental factors governing estuarine phytoplankton species dynamics. *Limnol. Oceanogr.* 54, 2107–2127. doi: 10.4319/lo.2009.54.6.2107

R Core Team (2020). *A language and environment for statistical computing. 4.0.2. ed* (Austria: Vienna).

Sandoval-Sanhueza, A., Aguilera-Belmonte, A., Basti, L., Figueroa, R. I., Molinet, C., Alvarez, G., et al. (2022). Interactive effects of temperature and salinity on the growth and cytotoxicity of the fish-killing microalgal species *Heterosigma akashiwo* and *Pseudochattonella verruculosa*. *Mar. pollut. Bull.* 174, 113234. doi: 10.1016/j.marpolbul.2021.113234

Smit, T., Lemley, D. A., Adams, J. B., and Strydom, N. A. (2021). Preliminary insights on the fine-scale responses in larval *Gilchristella aestuaria* (Family Clupeidae) and dominant zooplankton to estuarine harmful algal blooms. *Estuarine Coast. Shelf Sci.* 249, 107072. doi: 10.1016/j.ecss.2020.107072

Strom, S. L., Harvey, E. L., Fredrickson, K. A., and Menden-Deuer, S. (2013). Broad salinity tolerance as a refuge from predation in the harmful Raphidophyte alga *Heterosigma akashiwo* (Raphidophyceae). *J. Phycol.* 49, 20–31. doi: 10.1111/jpy.12013

Taylor, F. J. R., and Haigh, R. (1993). "The ecology of fish-killing blooms of the chloromonad flagellate *Heterosigma* in the Strait of Georgia and adjacent waters," in *Toxic Phytoplankton Blooms in the Sea*. Ed. T. J. A. S., Y. Smayda (New York: New York: Elsevier Science Publishers).

Tomas, C., and Deason, E. (1981). The Influence of Grazing by two *Acartia* Species on *Olisthodiscus luteus*. *Mar. Ecol.* 2, 215–223. doi: 10.1111/j.1439-0485.1981.tb00096.x

Twiner, M. J., and Trick, C. G. (2000). Possible physiological mechanisms for production of hydrogen peroxide by the ichthyotoxic flagellate *Heterosigma akashiwo*. *J. Plankton Res.* 22, 1961–1975. doi: 10.1093/plankt/22.10.1961

Wang, S., Tang, D., He, F., Fukuyo, Y., and Azanza, R. V. (2007). Occurrences of harmful algal blooms (HABs) associated with ocean environments in the South China Sea. *Hydrobiologia* 596, 79–93. doi: 10.1007/s10750-007-9059-4

Xie, Z., Xiao, H., Tang, X., Lu, K., and Cai, H. (2007). Interactions between red tide microalgae and herbivorous zooplankton: effects of two bloom-forming species on the rotifer *Brachionus plicatilis* (O.F. Muller). *Hydrobiologia* 600, 237–245. doi: 10.1007/s10750-007-9237-4

Yamasaki, Y., Nagasoe, S., Matsubara, T., Shikata, T., Shimasaki, Y., Oshima, Y., et al. (2007). Allelopathic interactions between the bacillariophyte *Skeletonema costatum* and the raphidophyte *Heterosigma akashiwo*. *Mar. Ecol. Prog. Ser.* 339, 83–92. doi: 10.3354/meps339083

Yamasaki, Y., Shikata, T., Nukata, A., Ichiki, S., Nagasoe, S., Matsubara, T., et al. (2009). Extracellular polysaccharide-protein complexes of a harmful alga mediate the allelopathic control it exerts within the phytoplankton community. *ISME J.* 3, 808–817. doi: 10.1038/ismej.2009.24

Yan, T., Wang, Y., Wang, L., Chen, Y., Han, G., and Zhou, M. (2009). Application of rotifer *Brachionus plicatilis* in detecting the toxicity of harmful algae. *Chin. J. Oceanol. Limnol.* 27, 376–382. doi: 10.1007/s00343-009-9104-4

Yang, C. Z., Albright, L. J., and Yousif, A. N. (1995). Oxygen-radical-mediated effects of the toxic phytoplankter *Heterosigma carterae* on juvenile rainbow trout *Oncorhynchus mykiss*. *Dis. Aquat. Organisms* 23, 101–108. doi: 10.3354/dao023101

Yu, J., Yang, G., and Tian, J. (2010). The effects of the harmful alga *Heterosigma akashiwo* on cultures of *Schmackeria inopinus* (Copepoda, Calanoida). *J. Sea Res.* 64, 287–294. doi: 10.1016/j.seares.2010.04.002

frontiers | Frontiers in Marine Science

TYPE Original Research
PUBLISHED 10 October 2023
DOI 10.3389/fmars.2023.1280612

Phytoplankton spring succession pattern in the Yellow Sea surveyed at Socheongcho Ocean Research Station

Myung Jin Hyun[1,2], Dong Han Choi[1,3], Howon Lee[1], Jongseok Won[1,3], Go-Un Kim[4], Yeonjung Lee[1,3], Jin-Young Jeong[4], Kongtae Ra[2,5], Wonseok Yang[1,3], Jaeik Lee[4], Jongmin Jeong[4], Charity Mijin Lee[6] and Jae Hoon Noh[1]*

[1]Ocean Climate Response & Ecosystem Research Department, Korea Institute of Ocean Science and Technology, Busan, Republic of Korea, [2]Ocean Science, University of Science and Technology, Daejeon, Republic of Korea, [3]Ocean Science and Technology School, Korea Maritime and Ocean University, Busan, Republic of Korea, [4]Coastal Disaster & Safety Research Department, Korea Institute of Ocean Science and Technology, Busan, Republic of Korea, [5]Marine Environment Research Department, Korea Institute of Ocean Science and Technology, Busan, Republic of Korea, [6]Ocean Law Research Department, Korea Institute of Ocean Science and Technology,y, Busan, Republic of Korea

EDITED BY
Zhaohe Luo,
Ministry of Natural Resources, China

REVIEWED BY
Meng Zhou,
Shanghai Jiao Tong University, China
Yoonja Kang,
Chonnam National University,
Republic of Korea

*CORRESPONDENCE
Jae Hoon Noh
jhnoh@kiost.ac.kr

RECEIVED 24 August 2023
ACCEPTED 21 September 2023
PUBLISHED 10 October 2023

CITATION
Hyun MJ, Choi DH, Lee H, Won J, Kim G-U, Lee Y, Jeong J-Y, Ra K, Yang W, Lee J, Jeong J, Lee CM and Noh JH (2023) Phytoplankton spring succession pattern in the Yellow Sea surveyed at Socheongcho Ocean Research Station. *Front. Mar. Sci.* 10:1280612. doi: 10.3389/fmars.2023.1280612

The spring phytoplankton bloom is a critical event in temperate oceans typically associated with the highest productivity levels throughout the year. To investigate the bloom process in the Yellow Sea, daily data on physical, chemical, and phytoplankton taxonomic group biomass, calculated via the chemotaxonomic approach, were collected from late March or early April to late May between 2018 and 2020 at the Socheongcho Ocean Research Station. During early spring (late March to mid-April), phytoplankton biomass increased, accompanied by a decrease in nutrient levels, with Bacillariophyceae and Cryptophyceae being the dominant groups. As water temperature increased, a pycnocline began to develop in late April, leading to a peak of the phytoplankton bloom dominated by chlorophytes and Cryptophyceae. Network analysis suggested that this phytoplankton bloom was caused by the onset of vertical stratification induced by increased sea surface temperature. The chlorophyte peak induced phosphate limitation above the pycnocline, resulting in succession to Prymnesiophyceae and Dinophyceae. Following pycnocline formation, phytoplankton biomass below the pycnocline was dominated by Bacillariophyceae and Cryptophyceae, with decreasing or fluctuating trends depending on phosphate concentration. Apart from these general patterns, 2019 and 2020 both had distinctive traits. The 2019 data revealed lower phosphate concentrations than the other 2 years, leading to a smaller chlorophyte peak at the surface compared to 2018 and extreme phosphate limitation above the pycnocline. This limitation resulted in decreased biomass of late successional groups, including Prymnesiophyceae and Dinophyceae. Pycnocline formation was delayed in year 2020, and stratification was significantly weaker compared to the previous 2 years. Due to the pycnocline delay, the surface chlorophyte peak did not develop and no succession to late successional groups was observed. Instead, high levels of Bacillariophyceae and Cryptophyceae biomass were observed throughout the water column with no surface bloom. Thus, among various environmental factors, increasing surface water temperature and phosphate concentrations play pivotal roles in shaping phytoplankton bloom dynamics. Distinct yearly variation points to the broader impacts of climate shifts, emphasizing the need for continued marine monitoring.

KEYWORDS

phytoplankton, spring bloom, Yellow Sea, chemotaxonomy, Socheongcho Ocean Research Station, dynamic factor analysis

1 Introduction

Phytoplankton play a critical role in the Earth's ecosystem, serving as the base of the marine food web and significantly contributing to the global carbon cycle (Hilligsøe et al., 2011; Harris, 2012; Winder and Sommer, 2012; Worden et al., 2015; Basu and Mackey, 2018). One of the key processes in phytoplankton dynamics is the spring bloom, i.e., a rapid increase in phytoplankton biomass that occurs in temperate and polar regions when conditions become favorable after the winter season. The spring bloom is driven by multiple factors, including increased light availability, rising water temperatures, water column stabilization, and the accumulation of high nutrient concentrations due to low utilization throughout the winter (Sommer et al., 2012; Hashioka et al., 2013; Olita et al., 2014; Rumyantseva et al., 2019).

Among these factors, vertical stabilization of the water column has been identified as the primary factor triggering initiation of the phytoplankton spring bloom. However, there remains controversy regarding whether depth-associated parameters such as the mixed layer depth (MLD) play a critical role or whether the strength of vertical mixing is the key determinant of bloom initiation (Sverdrup, 1953; Huisman et al., 1999; Behrenfeld et al., 2013; Rumyantseva et al., 2019). To elucidate the mechanism underlying phytoplankton spring bloom initiation in the Yellow Sea, time-series data were collected regarding phytoplankton biomass, nutrient concentrations, conductivity–temperature–depth (CTD) sensor readings, and environmental factors that influence vertical mixing (e.g., wind speed, wave height, and surface water temperature).

Considering that the duration of the spring phytoplankton bloom is typically > 1 month, it can be challenging to devise a strategy for sampling and data collection. Traditional research vessel-based approaches have limitations in the acquisition of time-series data from a fixed location. Previous research has utilized fixed ocean stations, such as Station ALOHA (A Long-Term Oligotrophic Habitat Assessment) located north of Hawaii in the Pacific Ocean, to overcome these limitations (Karl et al., 2001; Bidigare et al., 2014; Karl and Church, 2017; Van den Engh et al., 2017; Karl and Church, 2019). In this study, a fixed station, the Socheongcho Ocean Research Station (S-ORS), was utilized for the collection of time-series data in the Yellow Sea.

The Yellow Sea is one of the world's most productive continental shelves and undergoes dynamic changes in water temperature, stratification, nutrients, and ecological traits (Kim et al., 2019). Therefore, utilizing S-ORS, we collected time-series datasets to investigate the spring bloom process in the Yellow Sea. To confirm whether a bloom pattern present in a given year is unique or repetitive, we conducted a 3-year study of this process from 2018 to 2020.

In addition to the investigation of environmental factors driving the spring bloom, we examined changes in phytoplankton groups in response to changes in environmental conditions, which drive shifts in community composition and the dominance of specific taxa during the bloom period. Because phytoplankton groups play diverse roles in biogeochemical cycles, analyses of phytoplankton community composition and function are essential for elucidating Earth's systems (Barton et al., 2013; Eggers et al., 2014; Litchman et al., 2015; Weithoff and Beisner, 2019; Nissen et al., 2021). Therefore, the identification of factors that drive these changes, as well as the ecological and biogeochemical consequences of the spring bloom, is important for efforts to understand the impacts of climate change and other anthropogenic stressors on marine ecosystems.

To analyze the phytoplankton community, we used a chemotaxonomic approach, allocating chlorophyll *a* (Chl-*a*) concentrations to major phytoplankton groups using the CHEMTAX program (Mackey et al., 1996). CHEMTAX is widely used for phytoplankton community structure analysis due to its advantage of directly allocating Chl-*a*, an indicator of phytoplankton biomass, to various phytoplankton groups.

Building upon the CHEMTAX approach, we employed multivariate analysis to interpret the phytoplankton spring bloom process. Dynamic factor analysis (DFA), a type of state-space time-series analysis, was used to examine this time-dependent process in surface waters and to elucidate the mechanism underlying the phytoplankton bloom process. Additionally, redundancy analysis (RDA) was performed for all data points to elucidate the overall pattern of community succession. Through the investigation of time-series data related to the spring phytoplankton bloom process from 2018 to 2020, we aim to provide insights into the spring succession patterns of phytoplankton communities in this important and dynamic marine ecosystem.

2 Materials and methods

2.1 Research site and period

The study was conducted at S-ORS (Figures 1, 2), located in the Yellow Sea (37°25'23.3"N, 124°44'16.9"E), with a water depth of 50m. Yellow Sea is a semi-enclosed sea surrounded by the Korean Peninsula and China. The research was conducted during the spring season, which begins in late March or early April and ends in late May, over a period of 3 years. Further details regarding the sampling and research periods for each year are provided in Table 1.

2.2 Sample collection

Seawater was collected daily using a rosette sampler attached to a CTD recorder (SBE 19plus V2; Sea-Bird Scientific, Bellevue, WA, USA), except when unavoidable issues such as extreme weather conditions prevented sampling. We generally collected water samples at five depths: 0, 10, 20, 30, and 40 m. However, the sampling depths were slightly modified to include the sub-surface chlorophyll maximum (SCM) layer if present. Identification of the SCM was conducted using a fluorescence sensor equipped on the CTD. This process was conducted during daylight hours at low tide to account for the significant tidal ranges found in the Yellow Sea.

After obtaining the water sample, we followed appropriate methods to collect pigment and nutrient samples. First, we filtered 1 L of seawater through GF/F filters (Whatman PLC, Maidstone, UK) and then collected the filter paper for pigment sampling, while the filtrate was collected for dissolved inorganic nutrients. All samples were stored in a deep freezer on site and then transported on dry ice to the laboratory, where they were stored in another deep freezer until analysis.

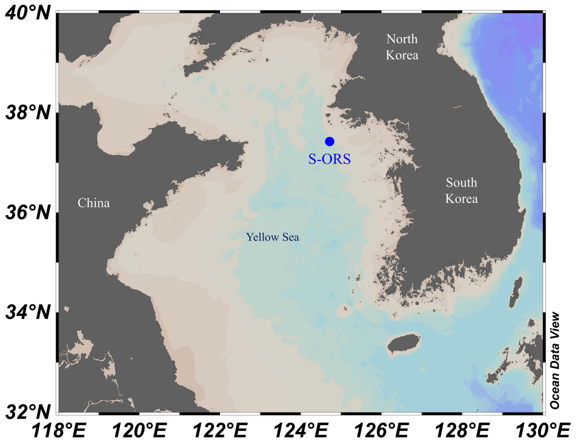

FIGURE 1
Location of the Socheongcho Ocean Research Station (S-ORS; blue dot).

2.3 Determination of pigment concentrations using high-performance liquid chromatography

The process of measuring pigment concentrations was described by Hyun et al. (2022), and we followed their detailed procedure. To maximize extraction efficiency, the filter papers were freeze-dried prior to extraction, soaked in 4 ml of an aqueous acetone solution (5:95 v:v), wrapped with aluminum foil to prevent exposure to light, and stored in a refrigerator at 4°C for 24 hours. The extracts were filtered again using 0.2-μm polytetrafluoroethylene syringe filters (Hyundai Micro, Seoul, Korea) to remove particles that may damage the HPLC system. After filtration, 1 ml of each filtrate was transferred into brown amber vials and 400 μl of HPLC-grade water was added.

The pigments were separated and measured using an HPLC system (LC-2030c 3D; Shimadzu Corporation, Kyoto, Japan) following a modified version of the protocol described by Zapata et al. (2000). Specifically, the separation of pigments was performed through reverse-phase chromatography using a C8 column (150 × 4.6 mm, 3.5 μm particle size, 100 Å pore size; Waters Corporation, Milford, MA, USA). The concentrations of the separated pigments were measured using the 440-nm chromatogram detected with a photodiode-array detector. Additionally, the purity of each peak was confirmed through measurement of wavelengths from 370 to 800 nm.

The factors used to convert peak area to pigment concentrations were determined on an annual basis prior to analysis when the C8 column was replaced for maintenance. This process involved analysis of standard pigments (DHI LAB, Hørsholm, Denmark) and the generation of a calibration curve. Additionally, to facilitate peak identification, a mixture of standard pigments was evaluated (first and last samples daily) during HPLC operation.

2.4 Chemotaxonomic analysis

The processes used to determine the Chl-*a* concentration and composition for each taxonomic group were conducted using CHEMTAX software (version 1.95) and the Bayesian Compositional Estimator (BCE) tool. In chemotaxonomic analysis, the inclusion of either too many or too few taxa can introduce substantial error into the results. To mitigate this possible source of error, taxa included in the calculation were carefully selected based on the examination of corresponding next-generation sequencing (NGS) data. The method used for NGS analysis strictly adhered to the procedures outlined by Choi et al. (2016); Yang et al. (2021), and Hyun et al. (2022).

Although the selection of taxa is an important aspect of chemotaxonomic analysis, the statistical methods used also have inherent limitations. CHEMTAX is underdetermined, which can introduce bias (Latasa, 2007; Van den Meersche et al., 2008),

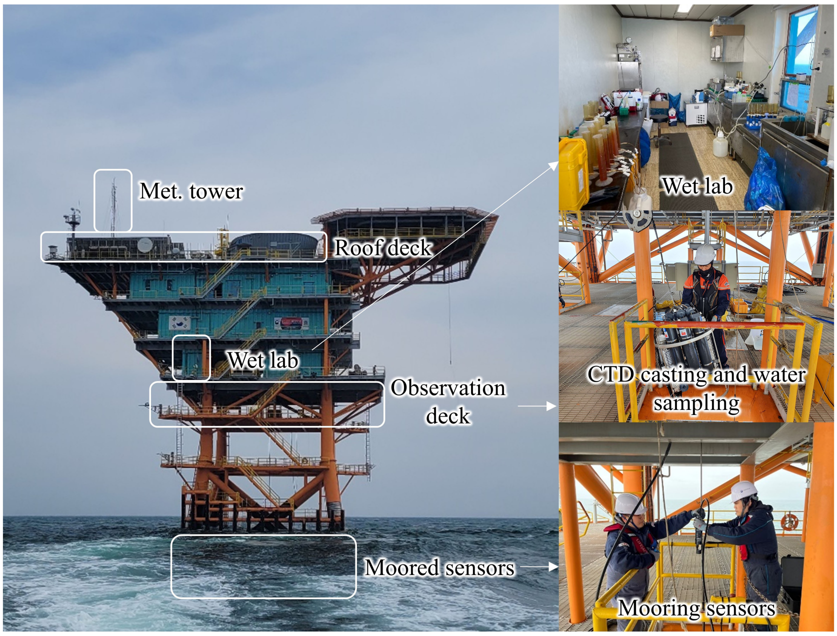

FIGURE 2
Images of S-ORS, including observation facilities used in this research.

whereas BCE has issues with reproducibility (Hyun et al., 2022). Therefore, this study utilizes a combination of these methods to address these issues: the underdetermined bias of CHEMTAX can be dealt with by constraining the pigment ratio variation range (Hyun et al., 2022), while BCE is appropriate for obtaining a range of coefficients rather than exact coefficient values. Therefore, we first determined the pigment variation range using BCE; the initial ratios and ratio limit matrices (RLMs) were obtained based on that range. Finally, CHEMTAX analysis was conducted with the initial ratios and RLMs to assess taxonomic composition.

Prior to the CHEMTAX analysis, the samples were pre-clustered based on sampling date into 14 clusters. This process was used to prevent decreased precision of both CHEMTAX and BCE analyses caused by the inclusion of too many samples in a single run. BCE analysis was conducted using the BCE package (Van den Meersche and Soetaert, 2022) in the R programming language (R Core Team, 2022). The starting pigment ratio was obtained by reconstructing the pigment ratio statistics of Roy et al. (2011), and is presented in Supplementary Table S1.

For each cluster, 100,000 iterations were conducted with a burn-in length of 35,000. An updated covariance value of 100 was applied, and the jump length was finely adjusted separately for each cluster to avoid autocorrelation in the trace plot and achieve an acceptance rate of 30–80%. Detailed information about the pre-clustering, adjusted jump length, and resulting acceptance rate for each cluster is provided in Supplementary Table S2. For settings that are not listed in the Supplementary Material, we used the defaults provided in the BCE package.

TABLE 1 Start and end dates of sample collection during each year.

Year	Start date	End date	Duration
2018	March 25th	May 26th	63 days
2019	April 4th	May 20th	47 days
2020	March 26th	May 18th	54 days

The initial ratios and RLMs used for CHEMTAX analysis were based on the 99% confidence intervals produced by the BCE analysis of pigment ratios. CHEMTAX analysis was conducted with the following settings, which were adapted from Latasa (2007): iteration limit of 5,000, epsilon limit of 0.0001, initial step size of 25, step ratio of 2, cutoff of 30,000, and bounded relative weighting.

To visualize the station location and results, which include Chl-*a* concentrations for each phytoplankton group, CTD, and nutrient data, we used the Ocean Data View software (Schlitzer, 2022).

2.5 Environmental factors associated with vertical mixing

Wind speed, wave height, atmospheric temperature, and sea surface temperature (SST) data were collected by sensors equipped on S-ORS. Specific details of the equipment are presented in Supplementary Table S3. The locations of sensors in S-ORS are depicted in Figure 2.

Wind speed, atmospheric temperature, and SST data were collected on a minute-by-minute basis, then averaged to obtain daily average values. Significant wave height was continuously calculated throughout each day, rather than averaged.

The stratification, MLD, pycnocline depth, and density gradient of the pycnocline were calculated based on the vertical CTD profile for each day. Water column stratification was determined as the sigma-t difference between the bottom (at 40 m) and surface waters.

The MLD was defined as the shallowest depth at which sigma-t exceeds the surface value by more than 0.03 kg/m³ (de Boyer Montégut et al., 2004). Because of CTD instrument instability near the surface, we used the value at 5 m as a proxy for surface density. The density gradient was determined as the density difference relative to the depth 1 m above, and the pycnocline was defined as the depth with the maximum density gradient on a particular day.

Pearson's correlation-based network analysis was conducted between Chl-*a* and the parameters associated with vertical mixing to examine how those factors influence the spring bloom process. For this network analysis, data collected after the Chl-*a* peak were excluded to focus on the bloom formation process, rather than the bloom decrease process.

2.6 Multivariate analysis and time-series analysis

To elucidate the process through which environmental variables affect the biomass of each phytoplankton group, multivariate analysis to explain the patterns is needed. Statistical analysis was conducted using the R programming language (R Core Team, 2022). RDA was performed to identify significant distribution patterns of phytoplankton group biomass in relation to environmental factors. This analysis was conducted using the Vegan package (version 2.6-2) (Simpson et al., 2022).

Time-series analysis was conducted to address time-dependent mechanisms that are difficult to explain with RDA. DFA was performed on surface water samples using the MARSS package (Holmes et al., 2012; Holmes et al., 2021a; Holmes et al., 2021b) and the results were visualized using the ggplot2 package (Wickham, 2016). For the DFA model, we established the observation equation [Equation (1)] and state space equation [Equation (2)]:

$$y_t = \Gamma\alpha_t + \mu + Dx_t + \varepsilon_t \tag{1}$$

$$\alpha_t = \alpha_{t-1} + \eta_t \tag{2}$$

where y_t represents the phytoplankton biomass of each group at time t, formatted as a 6 × n matrix in which rows represent the six phytoplankton groups analyzed with CHEMTAX, while columns represent samples. α represents the state value, which is a latent factor influencing the observed variables; it is a 5 × n matrix because we included five state space variables. Γ represents the factor loadings that link the observed variables to the state space, and is a 6 × 5 matrix. μ indicates the intercept, and x represents the five covariates included in the model: temperature, salinity, nitrate, phosphate, and silicate. D represents factor loadings linking the covariates with the observed variable. ϵ and η are error terms for the observation and state space, respectively. For ϵ, an optimized diagonal and unequal matrix is used, while for η an identity matrix is employed.

The number of state spaces is determined by comparing the corrected Akaike information criterion (AICc) for one to five state spaces and selecting the smallest AICc, which was obtained with five state spaces. To identify covariates to include in the model, we tested multiple physical and chemical environmental variables, including the nitrogen to phosphorus (NP) ratio. Through the comparison of AICc values, we selected five covariates. To prevent the model from being underdetermined, we constrained some elements of the Γ, μ, and D matrices. The designs for these matrices are shown in (3). $\gamma_{i,j}$, a_i, $d_{i,j}$ are the parameters calculated by the model, while the 0 values remain unmodified.

$$\Gamma = \begin{bmatrix} \gamma_{11} & 0 & 0 & 0 & 0 \\ \gamma_{21} & \gamma_{22} & 0 & 0 & 0 \\ \gamma_{31} & \gamma_{32} & \gamma_{33} & 0 & 0 \\ \gamma_{41} & \gamma_{42} & \gamma_{43} & \gamma_{44} & 0 \\ \gamma_{51} & \gamma_{52} & \gamma_{53} & \gamma_{54} & \gamma_{55} \\ \gamma_{61} & \gamma_{62} & \gamma_{63} & \gamma_{64} & \gamma_{65} \end{bmatrix}, \mu = \begin{bmatrix} 0 \\ 0 \\ 0 \\ 0 \\ 0 \\ a_6 \end{bmatrix}, D = \begin{bmatrix} d_{11} & d_{12} & d_{13} & d_{14} & d_{15} \\ d_{21} & d_{22} & d_{23} & d_{24} & d_{25} \\ d_{31} & d_{32} & d_{33} & d_{34} & d_{35} \\ d_{41} & d_{42} & d_{43} & d_{44} & d_{45} \\ d_{51} & d_{52} & d_{53} & d_{54} & d_{55} \\ d_{61} & d_{62} & d_{63} & d_{64} & d_{65} \end{bmatrix} \tag{3}$$

3 Results

3.1 Physical characteristics

The physical characteristics of the water column during the spring research periods of 2018, 2019, and 2020 were investigated in this study (Figure 3). The temperature of the water during the 2018 sampling period ranged from 4.43 to 15.10°C, with a steady increase over time. Initially, no significant temperature differences were observed with depth. However, the surface temperature increased rapidly, resulting in the development of a thermocline in late April that persisted around a depth of 15 m for most of May. The 2019 research period exhibited a similar pattern, with a water temperature ranging from 6.45 to 15.76°C and a thermocline forming at a shallower depth of around 10 m. In contrast, the 2020 season displayed significant differences, with a much narrower temperature range between 6.78 and 11.32°C and a shallow thermocline that developed only toward the end of the research period.

During the 2018 and 2019 research periods, salinity showed decreasing trends, ranging from 31.136 to 32.632 PSU and 31.647 to 32.313 PSU, respectively. However, the 2020 research period exhibited a distinct trend, with salinity remaining relatively constant between 32.086 and 32.405 PSU throughout the study period.

In early spring of 2018 and 2019, when sampling began, no significant density differences were found, indicating a well-mixed environment at the start of sampling.

The pycnocline began to form in late April and persisted until the end of the research period. In contrast, during 2020, the pycnocline was not well developed until the end of the study period, allowing for greater vertical mixing.

The temperature–salinity (T-S) diagram presented in Figure 4 provides a clear representation of the observed trend. Salinity was highest in 2020, followed by 2019 and then by 2018. However, potential temperature, rather than salinity, was the primary driver of the observed vertical density differences. In 2018, potential temperature was lowest during the early spring season and gradually increased over time, thereby contributing to the

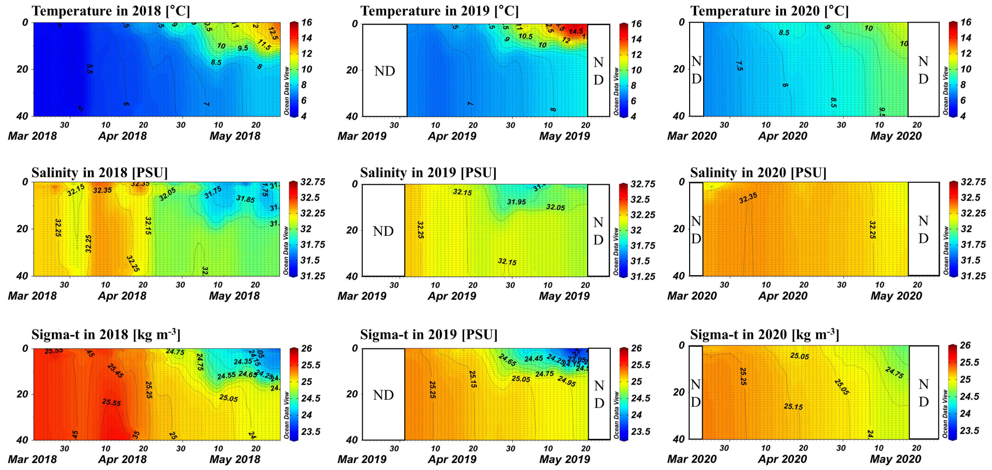

FIGURE 3
Contour plots of temperature, salinity, and density for each year. The x-axis represents time (days), and the y-axis represents water depth (m).

observed vertical density difference. Potential temperature increased more rapidly in 2019, resulting in a vertical density difference similar to that observed in 2018. The trend in 2020 differed significantly, with potential temperature being highest at the start of the research period and surface potential temperature being lowest at the end of the study period among the 3 years, resulting in a relatively small vertical density difference.

3.2 Distributions of inorganic nutrients

The concentrations of nitrate, phosphate, and silicates, which are major inorganic nutrients utilized by marine primary producers, exhibited a common pattern of high levels in early spring followed by steady decreases ~ over time (Figure 5). The rate of decrease in nutrient concentrations was highest above the pycnocline, especially for phosphate, resulting in an increase in the NP ratio of surface water after pycnocline formation and indicating phosphate limitation in the upper water column. In 2020, no significant pycnocline formed, resulting in a more uniform nutrient pattern throughout the water column, which may have impacted the phytoplankton community.

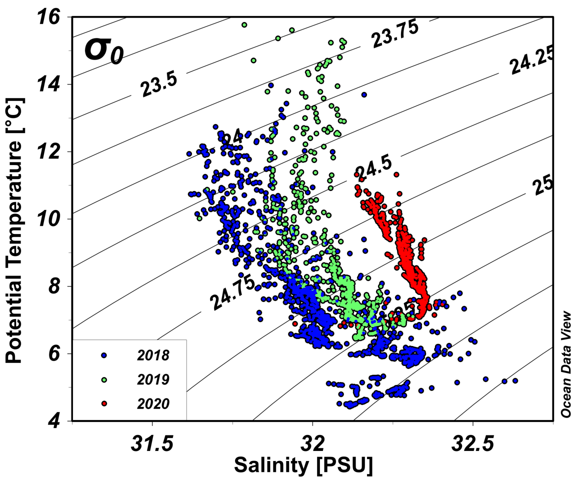

FIGURE 4
Temperature–salinity diagram for 1-m bin-averaged conductivity-temperature-depth (CTD) data for all dates. Blue, green, and red dots represent data from 2018, 2019, and 2020, respectively.

During early spring of 2018, which had the lowest water temperature among the 3 years studied, nutrient concentrations exhibited fluctuations rather than a steady decrease. The concentration of nitrate ranged between 4.85 and 8.30 μM, that of phosphate ranged between 0.44 and 0.93 μM, and that of silicate ranged between 2.64 and 6.39 μM prior to 20 April. Subsequently, nutrient concentrations decreased significantly, particularly in surface waters, with the concentration of nitrate ranging between 0.52 and 10.83 μM, that of phosphate ranging between 0.16 and 1.24 μM, and that of silicate ranging between 0.21 and 4.18 μM until the end of the 2018 study period. Extreme values of the NP ratio (typically > 30 with a maximum value of 55.0) were observed in surface water between 26 April and 16 May as phosphate became limited. These extreme events occurred in surface waters only after the pycnocline formed, and the average NP ratio for the entire 2018 sampling period was 15.02 ± 6.82.

Among the years studied, 2019 had the lowest phosphate concentrations, which showed a tendency to decrease shortly after the research period began. The concentration of nitrate fluctuated between 2.11 and 26.27 μM. The concentration of phosphate ranged between 0.02 and 0.57 μM, and that of silicate ranged between 0.25 and 5.91 μM. These concentrations resulted in high NP ratios, with an average of 26.98 ± 24.15. Extreme values were observed in surface waters, with a maximum of 225.68.

In 2020, a similar decreasing trend in nutrient concentrations was observed, with less significant vertical differences compared to the previous 2 years. The concentration of nitrate ranged between 0.60 and 8.37 μM, that of phosphate ranged between 0.06 and 1.28 μM, and that of silicate ranged between 0.12 and 10.60 μM. The average NP ratio during this season was 18.55 ± 14.85, and no extreme values were observed in surface water.

The NP ratios were generally distributed near the 16:1 line, with only a few outliers (Figure 6). Extremely high NP ratios were typically observed in surface waters after pycnocline formation, but no clear distributional trend of extremely low ratios was observed. Furthermore, most data from 2019 fell above the 16:1 line, indicating an overall pattern of phosphate limitation during that year.

3.3 Distributions of phytoplankton groups revealed through the chemotaxonomic approach

The Chl-*a* concentrations of the phytoplankton groups are shown in Figure 7. Throughout the 3-year study period, several common trends were observed. Bacillariophyceae and Cryptophyceae were the dominant phytoplankton groups throughout the study, with their biomass increasing as concentrations of nutrients, particularly phosphate, decreased throughout the water column in the early period. As the pycnocline developed, large increases in chlorophytes and cryptophytes were observed near the water surface, while the biomass of Bacillariophyceae decreased throughout the water column, as did the that of Cryptophyceae below the pycnocline. Slight increases in Prymnesiophyceae and Dinophyceae occurred above the pycnocline just after the chlorophyte bloom. *Synechococcus* exhibited an overall pattern similar to that of Bacillariophyceae, although it had much lower biomass than the other groups. Table 2 provides the average concentrations and concentration ranges of Chl-*a* for each group and year.

In the early spring period of 2018, Bacillariophyceae was the dominant group; its biomass showed the opposite trend to the nutrient concentrations, particularly phosphate. This finding suggests that during the early spring season, the top-down effect outweighed the bottom-up effect (i.e., phytoplankton uptake controlled nutrient levels). After the pycnocline developed, the biomass of Bacillariophyceae was rapidly replaced with chlorophytes in the surface water. On 7 May, the peak of the bloom, chlorophytes contributed 8,437 ng L^{-1} of the total of 10,101 ng L^{-1} Chl-*a*; Bacillariophyceae accounted for only 700 ng L^{-1} in the same sample. Above the pycnocline, cryptophytes were the second most abundant group during this period. Thereafter, the biomass of Prymnesiophyceae and Dinophyceae increased, while the three major groups decreased simultaneously above the pycnocline. Despite the increase, the biomass of Prymnesiophyceae and Dinophyceae did not exceed that of the three major groups.

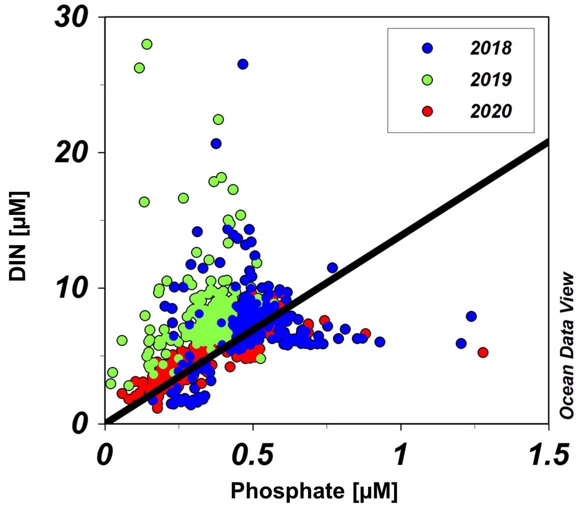

FIGURE 6
Nitrogen to phosphorus (NP) ratios for all samples. Blue, green, and red dots represent data from 2018, 2019, and 2020, respectively. Solid line is a 16:1 line.

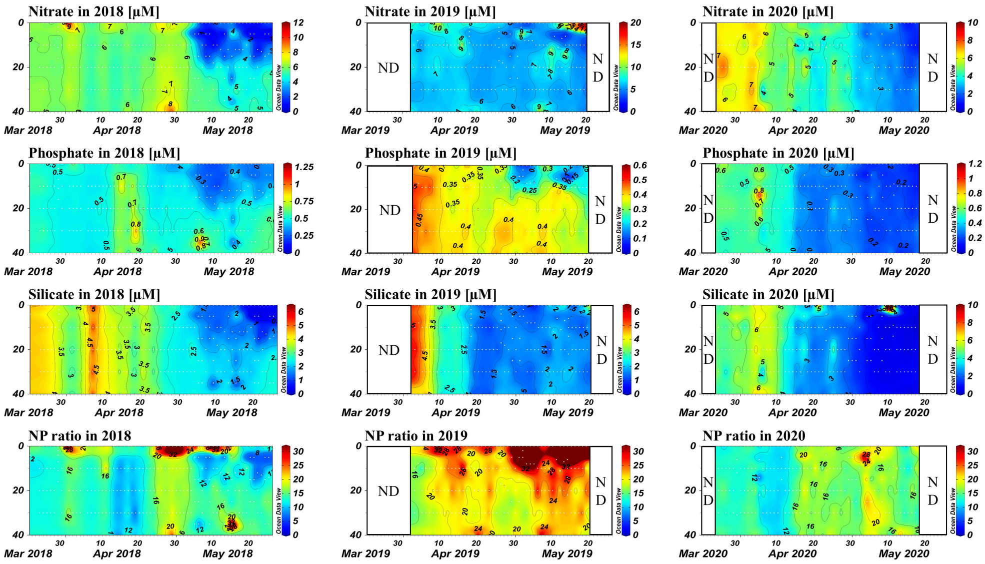

FIGURE 5
Contour plots of nitrate, phosphate, and silicate concentrations, and NP ratios, for each year. The x-axis represents time (days), and the y-axis represents depth.

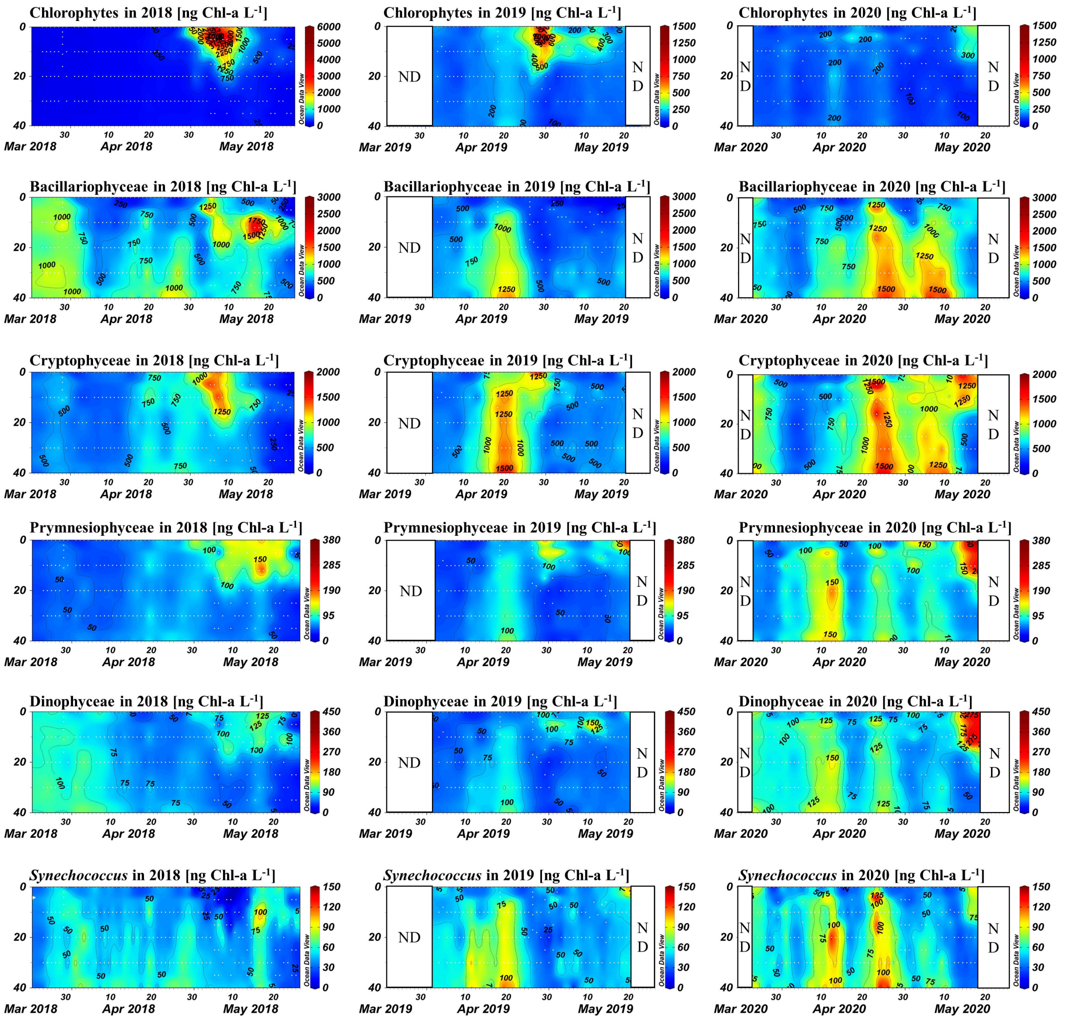

FIGURE 7
Contour plots of Chl-*a* concentrations for each phytoplankton group, for each year, calculated by chemotaxonomic analysis. The x-axis represents time (days), and the y-axis represents water depth (m). Consistent scales are used where possible for ease of comparison; however, the 2018 chlorophyte bloom necessitated a unique scale.

In 2019, at the beginning of the research period, Bacillariophyceae and Cryptophyceae were the two major groups, in accordance with 2018. The biomass of these two taxa increased throughout the water column as levels of phosphate and silicate decreased, and this increase continued until the pycnocline began to develop. One difference in this trend from 2018 is that the biomass of all other groups increased simultaneously. The surface chlorophyte and Cryptophyceae bloom occurred after the pycnocline had developed, but its scale was much smaller than in 2018; 2,095 ng L^{-1} Chl-*a* was derived from chlorophytes, and 1,869 ng L^{-1} from

TABLE 2 Average concentrations and concentration ranges of chlorophyll *a* (Chl-*a*) for each phytoplankton group and year.

Groups	Average concentration (ng L^{-1})			Concentration range (ng L^{-1})		
	2018	2019	2020	2018	2019	2020
Chlorophytes	393±771	227±192	152±61	67-8,437	32-2,095	56-494
Bacillariophyceae	701±353	538±297	768±385	40-2,886	59-1,640	121-2,128
Cryptophyceae	557±259	666±349	810±386	65-1,726	116-1,869	177-2,083
Prymnesiophyceae	70±35	65±33	93±46	0-289	9-239	14-368
Dinophyceae	76±28	65±26	95±47	0-191	10-209	21-441
Synechococcus	47±19	53±22	58±27	0-116	6-122	15-145
Total Chl-*a*	1,844±1,088	1,613±719	1,977±806	286-10,101	290-4,700	441-4,730

Cryptophyceae, out of the total 4,700 ng L^{-1} Chl-*a*. After that period, a slight increase in Prymnesiophyceae and Dinophyceae biomass was observed, as in 2018, but the extent and duration of these increases were smaller.

During 2020, no bloom of chlorophytes and Cryptophyceae in the surface water was observed, as the pycnocline was not present during the 2020 research period. Instead, high levels of Bacillariophyceae and Cryptophyceae biomass persisted longer throughout the water column compared to the other 5 years. Consequently, the maximum Chl-*a* value during 2020 was observed in the bottom water (40 m) on 27 April, whereas in the other two years the maximum value occurred in the surface water during the extreme biomass increase of the chlorophytes; of the 4,730 ng L^{-1} of Chl-*a*, 2,090 ng L^{-1} was from Bacillariophyceae and 1,959 ng L^{-1} was from Cryptophyceae. Around 15 May, a surface Chl-*a* increase was detected as the pycnocline began to form, which was much later than in the other 2 years studied. However, the extent of this increase was smaller (maximum value, 3,590 ng L^{-1} Chl-*a*), as the available nutrients had been consumed by Bacillariophyceae and Cryptophyceae. Instead of chlorophytes and Cryptophyceae accounting for most of the biomass, all groups excluding Bacillariophyceae increased simultaneously.

3.4 Relationships among vertical mixing parameters and resulting nutrients and phytoplankton Chl-*a* concentrations in each taxonomic group

Network analysis was conducted between the parameters associated with vertical mixing and the resulting nutrient and Chl-a concentrations for each phytoplankton group. For this analysis, only surface data prior to the Chl-a peak were included to focus on the bloom formation process. Table 3 presents Pearson's correlation coefficients (r) between Chl-a and each variable. Additional network analysis was conducted to investigate interrelationships among variables (Figure 8). Only correlations with r< −0.45 or r > 0.45 were included in the network analysis plot.

Among the factors influencing mixing, wave height and wind were strongly correlated with each other (r = 0.79), but were rarely linked with other variables, the sole exception being the correlation between pycnocline depth and wave height (r = 0.45). In contrast, atmospheric and sea surface temperatures (SSTs) were related to seven other nodes spanning multiple categories. However, only two edges connected vertical mixing parameters with these two temperatures: one between MLD and atmospheric temperature and another between stratification and SST. Surface density, which had the most connections, was related to three factors affecting mixing, three vertical mixing parameters, two nutrient factors, and Chl-*a* content of one specific taxonomic group.

Total Chl-a was linked with density, stratification, salinity, and the density gradient in the pycnocline. However, when segmented into groups, Chlorophytes correlated solely with stratification, while Cryptophyceae associated with seven factors, excluding the biomass of other taxonomic groups. The Bacillariophyceae, which is one of the main group for the spring S-ORS only shows the correlation between other taxonomic groups but the other environment factors, while Prymnesiophyceae have connected with density, SST, and atmosphere temperature but not with vertical mixing or nutrients. Dinophyceae and *Synechococcus* each correlate with two specific phytoplankton groups but not connected with other environmental factors. Notably, the mixed layer depth does not have any connections with any phytoplankton group.

TABLE 3 Pearson's correlation coefficients between vertical mixing-related environmental factors and surface Chl-*a* concentrations.

	Wind speed	Significant wave height	Atmospheric temperature	Sea surface temperature	Stratification	Mixed layer depth	Pycnocline	Density gradient in pycnocline	Beam attenuation
Significant wave height	0.79								
Atmospheric temperature	-0.15	-0.27							
Sea surface temperature	-0.05	-0.01	0.72						
Stratifictaion	-0.09	-0.13	0.44	0.46					
Mixed layer depth	-0.11	0.03	-0.49	-0.37	-0.58				
Pycnocline	0.37	0.45	-0.18	-0.13	-0.14	0.12			
Density gradient in pycnocline	-0.00	-0.07	0.39	0.36	0.73	-0.67	-0.09		
Beam attenuation	0.11	0.08	0.23	0.35	0.32	-0.05	-0.02	0.31	
Surface Chlorophyll *a*	0.15	0.10	0.39	0.31	0.49	-0.28	0.03	0.53	0.50

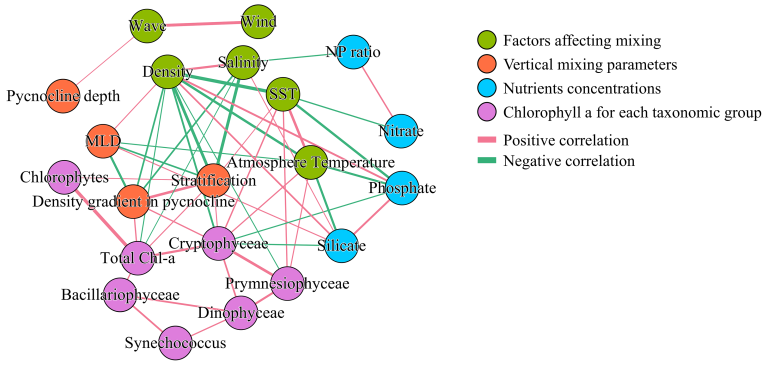

FIGURE 8
Network analysis of surface Chl-a concentrations for each phytoplankton group and variables related to vertical mixing, based on Pearson's correlation analysis, assessed using correlation coefficients (r). Only relationships with r< −0.45 or r > 0.45 are shown. Edge thickness indicates correlation strength.

3.5 Multivariate analysis of phytoplankton Chl-*a* concentrations for each group and related environmental variables

To explore the relationship between phytoplankton community structure and key environmental variables, we performed RDA (Figure 9). Prior to the development of the pycnocline, when physical characteristics such as low temperature, high density, and elevated salinity were consistent, most of the sample data clustered near the center of the RDA1 axis. However, data points with higher temperatures, particularly those collected near the surface after the development of the pycnocline, shifted toward the first quadrant. The density gradient of the pycnocline emerged as a predominant factor explaining the variance in data points away from the surface. The placement of the data points appears to align with the directions of the variables. However, distinctions between years for data collected below the surface were not readily apparent on the triplot.

With respect to phytoplankton groups, chlorophytes tended to be present at high levels when the temperature, pycnocline density gradient and NP ratio were high, and salinity was low. Prymnesiophyceae had high abundance when the temperature was high and nutrient concentrations were low. Bacillariophyceae and Cryptophyceae had high biomass when both the NP ratio and pycnocline density gradient were low. However, Cryptophyceae favored higher temperatures than Bacillariophyceae. Dinophyceae exhibited a preference for low pycnocline density gradient, but to a lesser extent than Bacillariphyceae and Cryptophyceae, and they thrived at intermediate nutrient and temperature levels. *Synechococcus* biomass appeared to increase at high salinity and MLD, along with a low NP ratio and pycnocline density gradient. However, the biomass of *Synechococcus* was too low for accurate determination of the trend in their distribution.

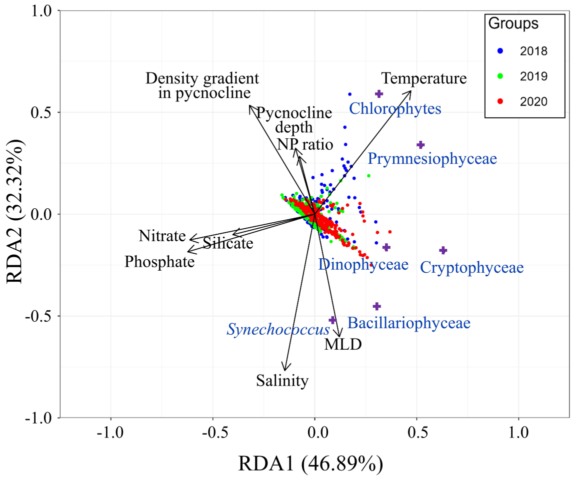

FIGURE 9
Redundancy analysis triplot illustrating relationships between phytoplankton community structure and major environmental variables. Blue, green, and red dots represent data from 2018, 2019, and 2020, respectively; purple crosses indicate phytoplankton groups.

3.6 DFA of surface Chl-*a* for each group

RDA reveals the overall pattern of phytoplankton biomass across environmental gradients, but does not elucidate the mechanisms occurring throughout the study period. Therefore, we conducted time-series analysis to reveal these mechanisms. The DFA model was employed for this analysis. Figure 10 compares the actual and model-expected values. The overall trend accurately predict by model, with only minor discrepancies observed for extreme values.

Plots used for model diagnostics are presented in Supplementary Figure S1. These plots confirm that there was no time-dependent pattern among the residuals and that the assumption of normal distribution was approximately met, although with some degree of tailing, indicating the failure of prediction for extreme values. No significant autocorrelation was detected among the residuals. These diagnostics demonstrate that the DFA model established here is valid, despite its failure to predict extreme values accurately.

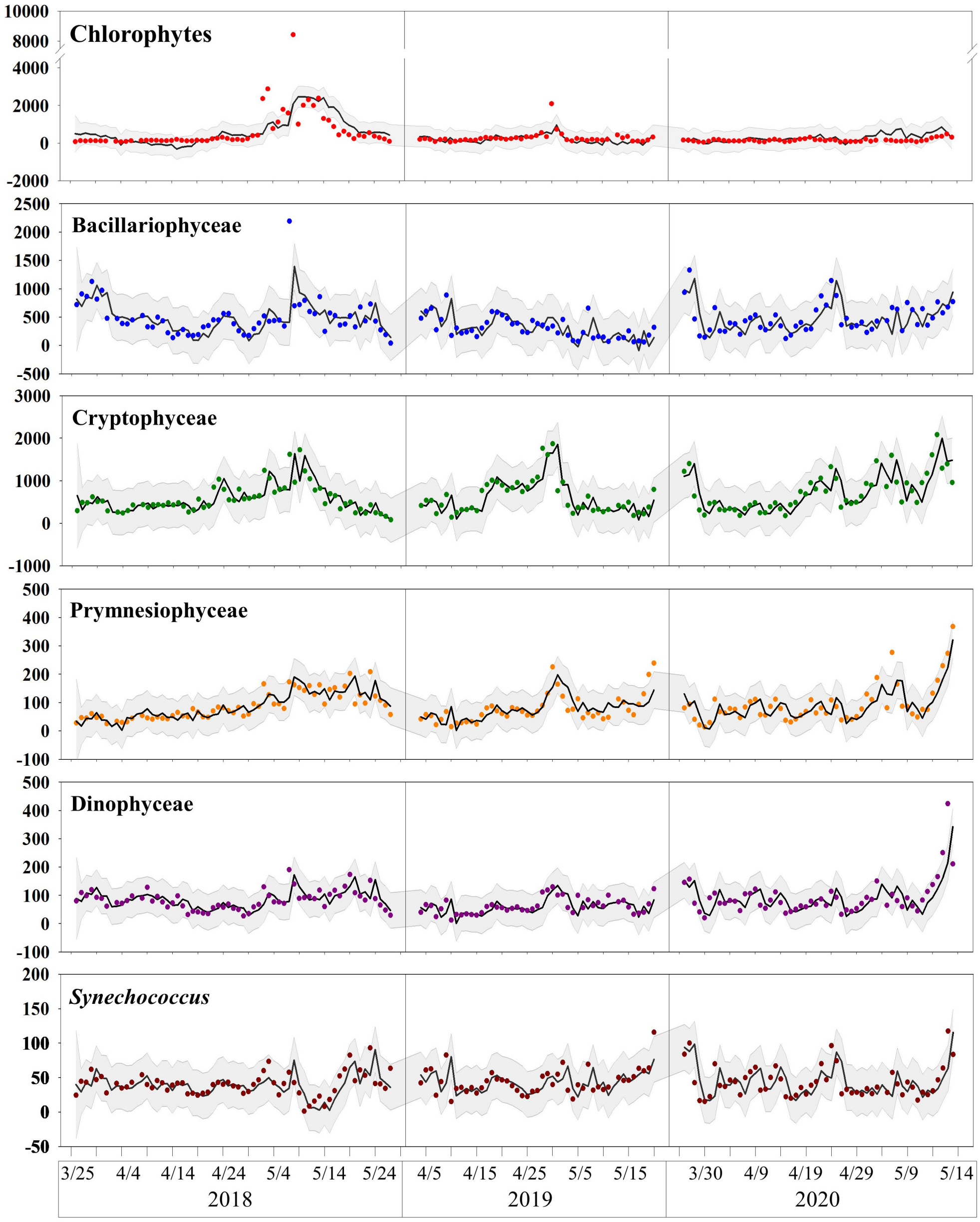

FIGURE 10
Comparison of actual and expected values obtained from the DFA model. Points represent actual values, line represents expected values, and gray shaded area indicates the 95% confidence interval of the model.

Table 4 shows the coefficients obtained by the DFA model. The factor loadings for covariates show how environmental factors affect the biomass of each phytoplankton group. Each loading indicates the correlation between an environmental factor and the biomass of a group. Most phytoplankton groups have negative correlations with phosphate and nitrate concentrations. Overall, two groups appear in this analysis: one with larger negative factor loadings for phosphate and temperature, and one with smaller negative or positive loadings for phosphate and temperature. The first group includes chlorophytes, Bacillariophyceae, and Cryptophyceae, while the second group comprises Prymnesiophyceae, Dinophyceae, and *Synechococcus*.

Silicate had positive factor loadings for all groups. The loadings for Bacillariophyceae, Prymnesiophyceae, Dinophyceae, and *Synechococcus* ranged between 2 and 4, whereas chlorophytes and Cryptophyceae had high loadings of 35 and 24, respectively. Bacillariophyceae and Cryptophyceae have negative loadings for nitrate, similar to phosphate. Chlorophytes exhibit the largest positive loading.

TABLE 4 Dynamic factor analysis (DFA) model results: factor loadings for covariates obtained from the DFA model.

Groups	Factor loadings for covariates				
	Temperature	Salinity	Nitrate	Phosphate	Silicate
Chlorophytes	-11	11	14	-709	35
Bacillariophyceae	-75	28	-10	-237	3
Cryptophyceae	-40	8	-4	-179	24
Prymnesiophyceae	8	-2	1	-90	4
Dinophyceae	-1	1	-1	-45	2
Synechococcus	1	-15	-15	5	2

4 Discussion

4.1 Applicability of time-series analysis based on data from fixed station S-ORS

DFA is a state-space model used for time-series analysis that fuses two multiple linear regressions, a covariate component and a state-space component. The covariate component explains the effects of environmental factors included in the model on phytoplankton biomass, whereas the state-space component captures the impacts of time-dependent environmental fluctuations that are not included as covariates in the model. These elements may be excluded from the model as a result of practical concerns such as ensuring model validity (e.g., to prevent excessive explanatory variables from undermining model robustness) or challenges associated with data collection. Unaccounted factors can range from the influence of zooplankton grazing and the physiological state of cells to atmospheric effects.

The factor loadings for the biomass of various phytoplankton groups, i.e., the covariate component, are shown in Table 4. These loadings are analogous to multiple linear regression slopes, and they provide substantial insights. For example, Bacillariophyceae had the lowest factor loading for temperature but the highest for salinity, which suggests a preference for unstable water columns that explains its dominance in early spring and persistence in waters beneath the pycnocline post-surface bloom. Although Cryptophyceae also had low factor loading for temperature and high factor loading for salinity, its values were less extreme than those of Bacillariophyceae. This difference may allow Cryptophyceae to contribute significantly to surface blooms in conditions where Bacillariophyceae struggles to survive. In contrast, Chlorophytes appear to thrive in relatively stable water columns. Their lowest factor loading for phosphate implies higher phosphate consumption, compared to other groups, and their positive factor loading for nitrate suggests that, although they consume nitrate, they consume it in lower amounts than phosphate. This finding suggests that chlorophyte surface blooms lead to surface phosphate limitation. The remaining three taxonomic groups appeared to favor more stable water columns and demonstrated higher resilience to low-phosphate environments, as inferred from their factor loadings.

A notable trend was observed in the state-space component of the DFA model: the state contribution (State loading × State space; $\Gamma\alpha_t$) was significantly correlated with the group biomass of the previous day (chlorophytes: r = 0.68, Bacillariphyceae: r = 0.36, Cryptophyceae: r = 0.75, Prymnesiophyceae: r = 0.58, Dinophyceae: r = 0.72, *Synechococcus*: r = 0.54). This result indicates that, in addition to environmental impact, the biomass of the previous day contributes significantly to that of the following day.

Those patterns were not elucidated through network analysis. Bacillariophyceae, Dinophyceae, and *Synechococcus* had no edges connected with any environmental factors, which indicates that network analysis failed to explain the trend of the phytoplankton group along the environmental gradient. Thus, the network analysis was unable to reveal the combined effect of multiple variables, as it was based on single-correlation analysis. Network analysis has its strengths, although it failed to clarify the link between the environment and phytoplankton response in this study. Because our network analysis was conducted based on correlations between variables, it identified patterns that are typically difficult to discern through DFA and RDA due to multicollinearity. For example, network analysis revealed that stratification and density gradients in the pycnocline directly impacted the phytoplankton community, whereas the MLD showed no direct correlation. Moreover, our analysis also showed that wind and wave height have a much weaker impact on water stratification than temperature increases.

Although RDA is frequently utilized for analyzing phytoplankton communities, based on a combination of elements from multiple linear regression and PCA, its effectiveness can be compromised by data loss. Specifically, it often captures only overarching trends. In the RDA model employed in this study, the r^2 value was only 0.19, indicating significant data loss during the multiple linear regression phase. The subsequent PCA stage further accentuated this loss, with the RDA1 and RDA2 axes accounting for 46.89% and 32.32% of the variance, respectively, and representing an additional data loss of 20.79%. This oversimplification can be misinterpreted if the results are not carefully reviewed. For example, in the triplot, the pycnocline density gradient appeared to be positively correlated with the pycnocline depth and NP ratio, and to be negatively correlated with MLD; however, none of these inferences are true.

Therefore, it is clear that time-series data analysis can reveal detailed patterns that were not discerned through RDA or network analysis, which are primary analytical methods in community ecology. In this study, the time-series dataset was acquired at the fixed station S-ORS. As demonstrated in our research on the spring phytoplankton bloom pattern, S-ORS is a valuable facility for acquiring time-series datasets, and will contribute significantly to our understanding of oceanic processes.

4.2 Initiation of the surface phytoplankton bloom process

As shown in Table 3 and Figure 8, there were concurrent increases in phytoplankton biomass and parameters associated with weakened vertical mixing. However, in contrast to previous research suggesting that the formation of a shallow MLD above the critical depth initiates phytoplankton bloom in spring (Sverdrup, 1953; Rumyantseva et al., 2019), network analysis revealed that depth-associated parameters such as MLD and pycnocline depth did not directly affect the increase in phytoplankton biomass in early spring. Instead, parameters such as stratification and the density gradient in the pycnocline were more strongly correlated with Chl-*a* concentrations, relative to any other factors related to vertical mixing.

Weakened vertical mixing appears to result from an increase in SST, which is driven by increases in solar radiation and atmospheric temperature. Wind speed and wave height appear to have minimal impact on vertical mixing intensity or MLD, but they show weak correlations with pycnocline depth. Therefore, in the Yellow Sea, we concluded that the increase in biomass in spring results from weakened vertical mixing, which is caused by increased SST.

However, when Chl-*a* was divided into groups, the reactions to vertical mixing appeared to differ among groups. Chlorophytes, the dominant group within the surface bloom, appeared to be have direct interaction only with stratification, and Cryptophyceae, the second most dominant group in the surface bloom, exhibited complex interactions with stratification, atmosphere temperature, SST, density, pycnocline density gradient, and phosphate and silicates contents. As surface phytoplankton are associated with stratification, and most edges linked with Cryptophyceae are associated with vertical mixing, the surface phytoplankton bloom appears to have been initiated by the onset of vertical mixing. This finding is consistent with the concepts underlying the critical turbulence hypothesis (Huisman et al., 1999).

However, the biomass increase that occurred below the surface water before the surface bloom must be interpreted differently. Bacillariophyceae, the dominant group under the pycnocline, had no network edges connected with environmental factors. However, the RDA revealed strong preferences for a weak pycnocline density gradient and low temperature. This result is consistent with the DFA factor loadings on temperature and salinity. Therefore, we conclude that Bacillariophyceae prefers environmental conditions with active vertical mixing.

Although DFA analysis revealed that the increasing biomass of Bacillariophyceae was coupled with rapid nutrient consumption, we were unable to explain the faster consumption rate than that observed in the previous bloom, based on our data. However, the DFA state contribution showed a linear relationship with the biomass of the previous day, and Bacillairophyceae had the weakest correlation ($r = 0.36$). Thus, unlike other phytoplankton groups, the biomass of Bacillariophyceae was more substantially affected by the unknown variable than the biomass of the previous day or vertical mixing.

One strong possible explanation for this discrepancy is the disturbance and recovery hypothesis (Behrenfeld et al., 2013), which argues that in winter, phytoplankton–grazer interactions tend to become unbalanced as the relative water temperature increase alters the division and mortality rates of both phytoplankton and grazer. However, as our study did not collect data on grazers, this hypothesis cannot be tested using our data. However, interactions above and below surface blooms must occur based on different mechanisms, as different groups induce the bloom from each direction.

4.3 Phytoplankton spring bloom succession pattern observed repeatedly across years

The overall pattern of the spring bloom observed at S-ORS is illustrated in Figure 11. During the early spring season, the biomass of all phytoplankton groups is low, consisting mostly of Bacillariophyceae and Cryptophyceae. As temperature increases, the biomass of those taxa begins to increase, coinciding with decreasing concentrations of nutrients, especially phosphate, from the surface to bottom water.

This pattern shifts when the surface temperature increases and the thermocline begins to develop in late April or early May. A rapid increase in chlorophyte biomass occurs during this period. The consistent timing of the chlorophyte bloom, along with the small negative factor loading for temperature, suggests that the stability of the water column may be an important contributor to the increase in chlorophyte biomass. Cryptophyceae also increase in biomass during this period, while Bacillariophyceae do not. The biomass of Bacillariophyceae above the pycnocline decreases during this period, while their biomass below the pycnocline either decreases or fluctuates both during and after this period. This pattern is caused by the preference of the Bacillariophyceae for a turbulent water column over a stable water column, as shown by DFA and RDA. The availability of phosphate appears to be a critical determinant of Bacillariophyceae biomass.

As the DFA model indicates, chlorophytes have the highest consumption rate of phosphate, but not as much nitrate. The chlorophyte bloom above the pycnocline leads to depletion of phosphate, resulting in extremely high N:P ratio values. This stress, stemming from phosphate limitation as evidenced by the extreme N:P ratio, leads to a subsequent decrease in the biomass of nutrient-demanding groups such as chlorophytes, Bacillariophyceae, and Cryptophyceae (Egge, 1998; Lafarga-De la Cruz et al., 2006; Lin et al., 2016; Ramos-Rodriíguez et al., 2017; Tragin and Vaulot, 2018; Andersen et al., 2020). While their preference for phosphate over nitrate might vary based on environmental and physiological states, given the clear phosphate limitation in the surface water, it's reasonable to infer that this limitation restricts their biomass. This trend is coupled with a slight increase in Prymnesiophyceae and *Synechococcus*, which have lower nutrient demand. The Dinophyceae, known to be nutrient-demanding, also increase their biomass in this period. Lin et al. (2016) summarized the factors contributing to the rise of Dinophyceae in nutrient-limited late

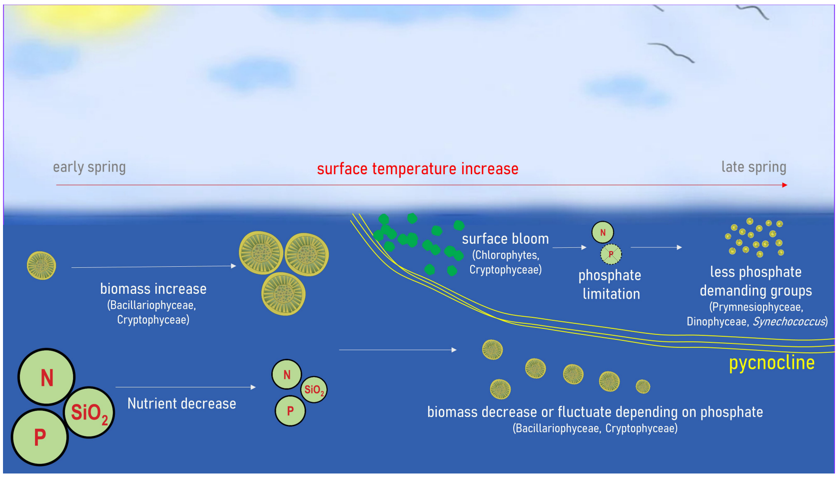

FIGURE 11
Schematic diagram of the spring bloom at S-ORS.

spring: their motility allows them to migrate vertically (Sinclair and Kamykowski, 2008; Hall and Paerl, 2011), accessing deeper nutrient-rich waters; their ability to utilize DOP and DON (Sunda et al., 2006; Burkholder et al., 2008); their capacity for phagotrophy; and their defense mechanisms that deter grazing (Sunda et al., 2006; Hong et al., 2012; Waggett et al., 2012; Hardison et al., 2013).

In 2019, the phosphate concentration was the lowest compared to the other two years. Consequently, the nitrate concentration did not decrease as significantly as it did in the other years. This is likely because phosphate limitation hindered the utilization of nitrate by phytoplankton. As phosphate limitated the surface chlorophyte peak appears to be smaller in 2019 than 2018. Furthermore, the surface increases of Prymnesiophyceae, Dinophyceae, and *Synechococcus* immediately after the chlorophyte peak appears to be less significant and somewhat delayed compared to 2018. These patterns indicate that concentrations of nutrients (e.g., phosphate) and temperature are the major factors that determine phytoplankton community composition, consistent with multiple recent studies (Skákala and Lazzari, 2021; Hyun et al., 2023; Zhang G. et al., 2023).

Overall, the concentration of phosphate appears to be the most significant determinant of the magnitude and timing of the spring bloom. The increase in temperature, which results in the formation of a pycnocline and induces the chlorophyte bloom, is another important factor during this period. However, in 2020, the temperature increase in surface water was further delayed, resulting in a distinct pattern.

4.4 Differences in spring bloom patterns among 3 years and their environmental drivers

While the difference between 2018 and 2019 is generally limited to phosphate concentration, 2020 exhibited significantly different physical characteristics, leading to a different spring bloom pattern. The formation of a pycnocline, which initially induces a chlorophyte bloom above it that later switches to less phosphate-demanding groups, was significantly delayed (until mid- to late May) in 2020. As a result, no chlorophyte bloom occurred, which prevented phosphate limitation. This absence of phosphate limitation allowed for a longer period of high Bacillariophyceae and Cryptophyceae biomass throughout the water column compared to the previous 2 years. As the pycnocline began to develop in mid-May, the biomass of all phytoplankton groups increased simultaneously, but the maximum chlorophyll concentration in surface water was much lower than in the other 2 years.

Overall, a phytoplankton spring bloom anomaly occurred in 2020 due to weakened stratification (Kim et al., 2023a). According to a previous studies, this weakened thermal stratification was primarily induced by latent heat flux release driven by strong northwesterly winds in April 2020, accompanied by anticyclonic and cyclonic circulation patterns over Siberia and the East Sea (Kim et al. 2022; Kim et al., 2023b). The anomaly was also influenced by warm winter temperatures. The prevailing northwesterly winds generated a cold surface anomaly, which increased vertical water column mixing, resulting in a weakened phytoplankton spring bloom. These factors combined to create conditions that were not conducive to a healthy spring bloom in the Yellow Sea.

Climate change may have played a role in the weakened stratification observed in the Yellow Sea in 2020. Climate change can affect ocean temperature, currents, and atmospheric conditions, all of which can impact ocean stratification patterns. Further research is needed to clarify the complex interactions among these factors and their potential impacts on marine ecosystems. In the era of big data in marine science, characterized by an explosion of *in situ* observations, quantitative remote sensing products, techniques for managing uncertainties in marine remote sensing data, and efforts to connect historical and modern datasets are particularly important for accurate monitoring of the spatial and temporal distributions and variabilities of phytoplankton community composition (Mélin, 2019; Brewin et al., 2023; Zhang Y. et al., 2023).

5 Conclusions

This study elucidated the intricate dynamics of the seasonal phytoplankton bloom in the Yellow Sea. We found that the initiation of the phytoplankton spring bloom process is closely associated with weakened vertical mixing, which is driven by increased SST. Our research revealed a consistent pattern of phytoplankton spring bloom succession across years; changes in phosphate concentration and temperature played significant roles. However, the year 2020 exhibited a unique pattern due to delayed pycnocline formation and weakened stratification, highlighting the potential impacts of climate change on this process. These findings underscore the complex interplay between physical and biological factors in terms of shaping phytoplankton dynamics; they suggest that further research is needed to clarify these interactions and potential impacts on marine ecosystems.

Taxonomically, chlorophytes and Cryptophyceae, which dominated the surface bloom, interacted directly with stratification. Bacillariophyceae, which was dominant beneath the pycnocline, appeared to prefer turbulent water conditions. As the surface water became nutrient-limited, there was a shift to late successional groups such as Dinophyceae, Prymnesiophyceae, and *Synechococcus*.

Data availability statement

The raw data supporting the conclusions of this article will be made available by the authors, without undue reservation.

Author contributions

JN and MH conceptualized and designed the study. MH, JN, and KR developed the methodology. MH, DC, HL, JL, and JW conducted data curation. MH managed the software. MH and G-UK performed the formal analysis. MH, KR, HL, JW, WY, JL, and JJ conducted the investigation. JN, J-YJ, and DC provided resources. MH, G-UK, and KR curated the data. MH, WY, HL, JW, and JN wrote the first draft of the manuscript. JN, YL, J-YJ, DC, KR, G-UK, JL, JJ, and CL wrote, reviewed, and edited the manuscript. MH and JN created the visualizations. JN, DC, and YL supervised the project. JN and J-YJ administered the project and acquired the funding. All authors contributed to the article and approved the submitted version.

Funding

The authors declare financial support was received for the research, authorship, and/or publication of this article. This research was supported by Korea Institute of Marine Science & Technology Promotion(KIMST) funded by the Ministry of Oceans and Fisheries (grant nos. 20210607 and 20210696).

Acknowledgments

We thank the Korea Hydrographic and Oceanographic Agency for their assistance with our stay at S-ORS and for providing sensor data acquired at the facility.

Conflict of interest

The authors declare that the research was conducted in the absence of any commercial or financial relationships that could be construed as a potential conflict of interest.

Publisher's note

Supplementary material

The Supplementary Material for this article can be found online at: https://www.frontiersin.org/articles/10.3389/fmars.2023.1280612/full#supplementary-material

References

Andersen, I. M., Williamson, T. J., González, M. J., and Vanni, M. J. (2020). Nitrate, ammonium, and phosphorus drive seasonal nutrient limitation of chlorophytes, cyanobacteria, and diatoms in a hyper-eutrophic reservoir. *Limnology Oceanography* 65 (5), 962–978. doi: 10.1002/lno.11363

Barton, A. D., Pershing, A. J., Litchman, E., Record, N. R., Edwards, K. F., Finkel, Z. V., et al. (2013). The biogeography of marine plankton traits. *Ecol. Lett.* 16 (4), 522–534. doi: 10.1111/ele.12063

Basu, S., and Mackey, K. R. (2018). Phytoplankton as key mediators of the biological carbon pump: Their responses to a changing climate. *Sustainability* 10 (3), 869. doi: 10.3390/su10030869

Behrenfeld, M. J., Doney, S. C., Lima, I., Boss, E. S., and Siegel, D. A. (2013). Annual cycles of ecological disturbance and recovery underlying the subarctic Atlantic spring plankton bloom. *Global biogeochemical cycles* 27 (2), 526–540. doi: 10.1002/gbc.20050

Bidigare, R. R., Buttler, F. R., Christensen, S. J., Barone, B., Karl, D. M., and Wilson, S. T. (2014). Evaluation of the utility of xanthophyll cycle pigment dynamics for assessing upper ocean mixing processes at Station ALOHA. *J. plankton Res.* 36 (6), 1423–1433. doi: 10.1093/plankt/fbu069

Brewin, R. J., Pitarch, J., Dall'Olmo, G., van der Woerd, H. J., Lin, J., Sun, X., et al. (2023). Evaluating historic and modern optical techniques for monitoring phytoplankton biomass in the Atlantic Ocean. *Front. Mar. Sci.* 10, 1111416. doi: 10.3389/fmars.2023.1111416

Burkholder, J. M., Glibert, P. M., and Skelton, H. M. (2008). Mixotrophy, a major mode of nutrition for harmful algal species in eutrophic waters. *Harmful algae* 8 (1), 77–93. doi: 10.1016/j.hal.2008.08.010

Choi, D. H., An, S. M., Chun, S., Yang, E. C., Selph, K. E., Lee, C. M., et al. (2016). Dynamic changes in the composition of photosynthetic picoeukaryotes in the northwestern Pacific Ocean revealed by high-throughput tag sequencing of plastid 16S rRNA genes. *FEMS Microbiol. Ecol.* 92 (2):fiv170. doi: 10.1093/femsec/fiv170

de Boyer Montégut, C., Madec, G., Fischer, A. S., Lazar, A., and Iudicone, D. (2004). Mixed layer depth over the global ocean: An examination of profile data and a profile-based climatology. *J. Geophysical Research: Oceans* 109 (C12003). doi: 10.1029/2004JC002378

Egge, J. (1998). Are diatoms poor competitors at low phosphate concentrations? *J. Mar. Syst.* 16 (3-4), 191–198. doi: 10.1016/S0924-7963(97)00113-9

Eggers, S. L., Lewandowska, A. M., Barcelos e Ramos, J., Blanco-Ameijeiras, S., Gallo, F., and Matthiessen, B. (2014). Community composition has greater impact on the functioning of marine phytoplankton communities than ocean acidification. *Global Change Biol.* 20 (3), 713–723. doi: 10.1111/gcb.12421

Hall, N. S., and Paerl, H. W. (2011). Vertical migration patterns of phytoflagellates in relation to light and nutrient availability in a shallow microtidal estuary. *Mar. Ecol. Prog. Ser.* 425, 1–19. doi: 10.3354/meps09031

Hardison, D. R., Sunda, W. G., Shea, D., and Litaker, R. W. (2013). Increased toxicity of Karenia brevis during phosphate limited growth: ecological and evolutionary implications. *PloS One* 8 (3), e58545. doi: 10.1371/journal.pone.0058545

Harris, G. (2012). *Phytoplankton ecology: structure, function and fluctuation* (Amsterdam, Netherlands: Springer Science & Business Media).

Hashioka, T., Vogt, M., Yamanaka, Y., Le Quéré, C., Buitenhuis, E., Aita, M. N., et al. (2013). Phytoplankton competition during the spring bloom in four plankton functional type models. *Biogeosciences* 10 (11), 6833–6850. doi: 10.5194/bg-10-6833-2013

Hilligsøe, K. M., Richardson, K., Bendtsen, J., Sørensen, L.-L., Nielsen, T. G., and Lyngsgaard, M. M. (2011). Linking phytoplankton community size composition with temperature, plankton food web structure and sea–air CO2 flux. *Deep Sea Res. Part I: Oceanographic Res. Papers* 58 (8), 826–838. doi: 10.1016/j.dsr.2011.06.004

Holmes, E. E., Scheuerell, M. D., and Ward, E. J. (2021a) *Analysis of multivariate time-series using the MARSS package (version 3.11.4) [R package]*. Available at: https://CRAN.R-project.org/package=MARSS/vignettes/UserGuide.pdf.

Holmes, E. E., Ward, E. J., and Kellie, W. (2012). MARSS: multivariate autoregressive state-space models for analyzing time-series data. *R J.* 4 (1), 11. doi: 10.32614/RJ-2012-002

Holmes, E. E., Ward, E. J., Scheuerell, M. D., and Wills, K. (2021b) *MARSS: Multivariate Autoregressive State-Space Modeling. (version 3.11.4) [R package]*. Available at: https://CRAN.R-project.org/package=MARSS.

Hong, J., Talapatra, S., Katz, J., Tester, P. A., Waggett, R. J., and Place, A. R. (2012). Algal toxins alter copepod feeding behavior. *PloS One* 7 (5), e36845. doi: 10.1371/journal.pone.0036845

Huisman, J., van Oostveen, P., and Weissing, F. J. (1999). Critical depth and critical turbulence: two different mechanisms for the development of phytoplankton blooms. *Limnology oceanography* 44 (7), 1781–1787. doi: 10.4319/lo.1999.44.7.1781

Hyun, S., Cape, M. R., Ribalet, F., and Bien, J. (2023). Modeling cell populations measured by flow cytometry with covariates using sparse mixture of regressions. *Ann. Appl. Stat* 17 (1), 357. doi: 10.1214/22-AOAS1631

Hyun, M. J., Won, J., Choi, D. H., Lee, H., Lee, Y., Lee, C. M., et al. (2022). A CHEMTAX study based on picoeukaryotic phytoplankton pigments and next-generation sequencing data from the ulleungdo–dokdo marine system of the east sea (Japan sea): improvement of long-unresolved underdetermined bias. *J. Mar. Sci. Eng.* 10 (12), 1967. doi: 10.3390/jmse10121967

Karl, D. M., Björkman, K. M., Dore, J. E., Fujieki, L., Hebel, D. V., Houlihan, T., et al. (2001). Ecological nitrogen-to-phosphorus stoichiometry at station ALOHA. *Deep Sea Res. Part II: Topical Stud. Oceanography* 48 (8-9), 1529–1566. doi: 10.1016/S0967-0645(00)00152-1

Karl, D. M., and Church, M. J. (2017). Ecosystem structure and dynamics in the North Pacific Subtropical Gyre: new views of an old ocean. *Ecosystems* 20, 433–457. doi: 10.1007/s10021-017-0117-0

Karl, D. M., and Church, M. J. (2019). Station ALOHA: A gathering place for discovery, education, and scientific collaboration: station ALOHA: A gathering place for discovery, education, and scientific collaboration. *Limnology Oceanography Bull.* 28 (1), 10–12. doi: 10.1002/lob.10285

Kim, Y. S., Jang, C. J., Noh, J. H., Kim, K.-T., Kwon, J.-I., Min, Y., et al. (2019). A Yellow Sea monitoring platform and its scientific applications. *Front. Mar. Sci.* 6, 601. doi: 10.3389/fmars.2019.00601

Kim, G.-U., Lee, J., Kim, Y. S., Noh, J. H., Kwon, Y. S., Lee, H., et al. (2023a). Impact of vertical stratification on the 2020 spring bloom in the Yellow Sea. *Sci. Rep* 13 (1), 14320. doi: 10.1038/s41598-023-40503-z

Kim, G.-U., Lee, K., Lee, J., Jeong, J.-Y., Lee, M., Jang, C. J., et al. (2022). Record-breaking slow temperature evolution of spring water during 2020 and its impacts on spring bloom in the Yellow Sea. *Front. Mar. Sci.* 562. doi: 10.3389/fmars.2022.824361

Kim, G.-U., Oh, H., Kim, Y. S., Son, J.-H., and Jeong, J.-Y. (2023b). Causes for an extreme cold condition over Northeast Asia during April 2020. *Sci. Rep.* 13 (1), 3315. doi: 10.1038/s41598-023-29934-w

Lafarga-De la Cruz, F., Valenzuela-Espinoza, E., Millán-Núnez, R., Trees, C. C., Santamaría-del-Ángel, E., and Núnez-Cebrero, F. (2006). Nutrient uptake, chlorophyll a and carbon fixation by Rhodomonas sp.(Cryptophyceae) cultured at different irradiance and nutrient concentrations. *Aquacultural Eng.* 35 (1), 51–60. doi: 10.1016/j.aquaeng.2005.08.004

Latasa, M. (2007). Improving estimations of phytoplankton class abundances using CHEMTAX. *Mar. Ecol. Prog. Ser.* 329, 13–21. doi: 10.3354/meps329013

Lin, S., Litaker, R. W., and Sunda, W. G. (2016). Phosphorus physiological ecology and molecular mechanisms in marine phytoplankton. *J. Phycology* 52 (1), 10–36. doi: 10.1111/jpy.12365

Litchman, E., de Tezanos Pinto, P., Edwards, K. F., Klausmeier, C. A., Kremer, C. T., and Thomas, M. K. (2015). Global biogeochemical impacts of phytoplankton: a trait-based perspective. *J. Ecol.* 103 (6), 1384–1396. doi: 10.1111/1365-2745.12438

Mackey, M., Mackey, D., Higgins, H., and Wright, S. (1996). CHEMTAX-a program for estimating class abundances from chemical markers: application to HPLC measurements of phytoplankton. *Mar. Ecol. Prog. Ser.* 144, 265–283. doi: 10.3354/meps144265

Mélin, F. (2019). *Uncertainties in ocean colour remote sensing*. International Ocean Colour Coordinating Group (IOCCG): Dartmouth, NS, Canada

Nissen, C., Gruber, N., Münnich, M., and Vogt, M. (2021). Southern Ocean phytoplankton community structure as a gatekeeper for global nutrient biogeochemistry. *Global Biogeochemical Cycles* 35 (8), e2021GB006991. doi: 10.1029/2021GB006991

Olita, A., Sparnocchia, S., Cusí, S., Fazioli, L., Sorgente, R., Tintoré, J., et al. (2014). Observations of a phytoplankton spring bloom onset triggered by a density front in NW Mediterranean. *Ocean Sci.* 10 (4), 657–666. doi: 10.5194/os-10-657-2014

Ramos-Rodríguez, E., Perez-Martinez, C., and Conde-Porcuna, J. M. (2017). Strict stoichiometric homeostasis of Cryptomonas pyrenoidifera (Cryptophyceae) in relation to N: P supply ratios. *J. Limnol* 76 (1), 182–189. doi: 10.4081/jlimnol.2016.1487

R Core Team (2022). *"R: A language and environment for statistical computing"* (Vienna, Austria: Foundation for Statistical Computing).

Roy, S., Llewellyn, C. A., Egeland, E. S., and Johnsen, G. (2011). *Phytoplankton pigments: characterization, chemotaxonomy and applications in oceanography.* (Cambridge, UK: Cambridge University Press).

Rumyantseva, A., Henson, S., Martin, A., Thompson, A. F., Damerell, G. M., Kaiser, J., et al. (2019). Phytoplankton spring bloom initiation: The impact of atmospheric forcing and light in the temperate North Atlantic Ocean. *Prog. oceanography* 178, 102202. doi: 10.1016/j.pocean.2019.102202

Schlitzer, R. (2022). *"Ocean data view (software)"*.. Bremerhaven, Germany: Alfred Wegener Institute

Simpson, G. L., Blanchet, F. G., Kindt, R., Legendre, P., Minchin, P. R., O'Hara, R. B., et al. (2022) *vegan: Community Ecology Package (version 2.6-2) [R package]*. Available at: https://CRAN.R-project.org/package=vegan.

Sinclair, G. A., and Kamykowski, D. (2008). Benthic–pelagic coupling in sediment-associated populations of Karenia brevis. *J. plankton Res.* 30 (7), 829–838. doi: 10.1093/plankt/fbn042

Skákala, J., and Lazzari, P. (2021). Low complexity model to study scale dependence of phytoplankton dynamics in the tropical Pacific. *Phys. Rev. E* 103 (1), 012401. doi: 10.1103/PhysRevE.103.012401

Sommer, U., Adrian, R., De Senerpont Domis, L., Elser, J. J., Gaedke, U., Ibelings, B., et al. (2012). Beyond the Plankton Ecology Group (PEG) model: mechanisms driving plankton succession. *Annu. Rev. ecology evolution systematics* 43, 429–448. doi: 10.1146/annurev-ecolsys-110411-160251

Sunda, W. G., Graneli, E., and Gobler, C. J. (2006). Positive feedback and the development and persistence of ecosystem disruptive algal blooms 1. *J. Phycology* 42 (5), 963–974. doi: 10.1111/j.1529-8817.2006.00261.x

Sverdrup, H. (1953). On conditions for the vernal blooming of phytoplankton. *J. Cons. Int. Explor. Mer* 18 (3), 287–295. doi: 10.1093/icesjms/18.3.287

Tragin, M., and Vaulot, D. (2018). Green microalgae in marine coastal waters: The Ocean Sampling Day (OSD) dataset. *Sci. Rep.* 8 (1), 14020. doi: 10.1038/s41598-018-32338-w

Van den Engh, G. J., Doggett, J. K., Thompson, A. W., Doblin, M. A., Gimpel, C. N., and Karl, D. M. (2017). Dynamics of Prochlorococcus and Synechococcus at station ALOHA revealed through flow cytometry and high-resolution vertical sampling. *Front. Mar. Sci.* 4, 359. doi: 10.3389/fmars.2017.00359

Van den Meersche, K., and Soetaert, K. (2022) *Package 'BCE' (version 2.2.0) [R package]*. Available at: https://CRAN.R-project.org/package=BCE.

Van den Meersche, K., Soetaert, K., and Middelburg, J. J. (2008). A Bayesian compositional estimator for microbial taxonomy based on biomarkers. *Limnology Oceanography-Methods* 6, 190–199. doi: 10.4319/lom.2008.6.190

Waggett, R. J., Hardison, D. R., and Tester, P. A. (2012). Toxicity and nutritional inadequacy of Karenia brevis: synergistic mechanisms disrupt top-down grazer control. *Mar. Ecol. Prog. Ser.* 444, 15–30. doi: 10.3354/meps09401

Weithoff, G., and Beisner, B. E. (2019). Measures and approaches in trait-based phytoplankton community ecology–from freshwater to marine ecosystems. *Front. Mar. Sci.* 6, 40. doi: 10.3389/fmars.2019.00040

Wickham, H. (2016). *ggplot2: elegant graphics for data analysis* (Springer-Verlag New York, USA).

Winder, M., and Sommer, U. (2012). Phytoplankton response to a changing climate. *Hydrobiologia* 698, 5–16. doi: 10.1007/s10750-012-1149-2

Worden, A. Z., Follows, M. J., Giovannoni, S. J., Wilken, S., Zimmerman, A. E., and Keeling, P. J. (2015). Rethinking the marine carbon cycle: factoring in the multifarious lifestyles of microbes. *Science* 347 (6223), 1257594. doi: 10.1126/science.1257594

Yang, W., Noh, J. H., Lee, H., Lee, Y., and Choi, D. H. (2021). Weekly variation of prokaryotic growth and diversity in the inner bay of Yeong-do, Busan. *Ocean Polar Res.* 43 (1), 31–43. doi: 10.4217/OPR.2021.43.1.031

Zapata, M., Rodríguez, F., and Garrido, J. L. (2000). Separation of chlorophylls and carotenoids from marine phytoplankton: a new HPLC method using a reversed phase C8 column and pyridine-containing mobile phases. *Mar. Ecol. Prog. Ser.* 195, 29–45. doi: 10.3354/meps195029

Zhang, G., Liu, Z., Zhang, Z., Ding, C., and Sun, J. (2023). The impact of environmental factors on the phytoplankton communities in the Western Pacific Ocean: HPLC-CHEMTAX approach. *Front. Mar. Sci.* 10, 1185939. doi: 10.3389/fmars.2023.1185939

Zhang, Y., Shen, F., Sun, X., and Tan, K. (2023). Marine big data-driven ensemble learning for estimating global phytoplankton group composition over two decades, (1997–2020). *Remote Sens. Environ.* 294, 113596. doi: 10.1016/j.rse.2023.113596

frontiers | Frontiers in Marine Science

TYPE Original Research
PUBLISHED 13 December 2023
DOI 10.3389/fmars.2023.1221639

EDITED BY
Yanpei Zhuang,
Jimei University, China

REVIEWED BY
Kazuhiro Yoshida,
Saga University, Japan
Marius Nils Müller,
Macau University of Science and Technology, Macau SAR, China
Pat Wongpan,
University of Tasmania, Australia

*CORRESPONDENCE
Zoé L. Forgereau
✉ zoe.figaro@orange.fr
Karley Campbell
✉ karley.campbell@uit.no

RECEIVED 12 May 2023
ACCEPTED 26 October 2023
PUBLISHED 13 December 2023

CITATION
Forgereau ZL, Lange BA, Gradinger R, Assmy P, Osanen JE, García LM, Søreide JE, Granskog MA, Leu E and Campbell K (2023) Photophysiological responses of bottom sea-ice algae to fjord dynamics and rapid freshening. *Front. Mar. Sci.* 10:1221639. doi: 10.3389/fmars.2023.1221639

Photophysiological responses of bottom sea-ice algae to fjord dynamics and rapid freshening

Zoé L. Forgereau[1*], Benjamin A. Lange[2,3], Rolf Gradinger[1], Philipp Assmy[3], Janina E. Osanen[1], Laura M. García[1], Janne E. Søreide[4], Mats A. Granskog[3], Eva Leu[5] and Karley Campbell[1,6*]

[1]Department of Arctic and Marine Biology, Faculty of Biosciences, Fisheries and Economics, UiT The Arctic University of Norway, Tromsø, Norway, [2]Remote Sensing, Norwegian Geotechnical Institute, Oslo, Norway, [3]Oceans and Sea Ice, Norwegian Polar Institute, Fram Centre, Tromsø, Norway, [4]Department of Arctic Biology, The University Centre in Svalbard, Longyearbyen, Norway, [5]Akvaplan-niva AS, Oslo, Norway, [6]Department of and Environment and Geography, Centre for Earth Observation Science, University of Manitoba, Winnipeg, MB, Canada

Sea ice algae have a broad salinity tolerance but can experience stress during rapid decreases in salinity that occur with seasonal ice melt and during ice sample melt. This study investigated the impact of salinity on the photophysiological responses of bottom-ice algal communities from two Svalbard fjords (Tempelfjorden and Van Mijenfjorden). To further investigate the impact of salinity alone, and particularly to rapid freshening, the responses of a lab-cultured ice algal community from Van Mijenfjorden were assessed. Photophysiological responses were mainly determined via ^{14}C-based incubations which provided photosynthesis-irradiance curves. Main findings showed that i) the bottom-ice algal community in Tempelfjorden was characterized by lower photosynthetic efficiency and chlorophyll *a* biomass than the Van Mijenfjorden communities, and ii) a lab-cultured ice algal community from Van Mijenfjorden dominated by pennate diatoms had significantly lower photosynthetic efficiency, maximum photosynthesis and photoacclimation index after a decrease in salinity from 33 to 10. The lower photosynthetic efficiency and chlorophyll *a* biomass at Tempelfjorden may be attributed to the almost two-fold lower bulk-ice salinity in Tempelfjorden compared to Van Mijenfjorden, which was likely associated with freshwater inputs from the tidewater glacier Tunabreen during sea ice formation. Other factors such as under-ice light intensities, brine volume fraction and brine nutrient concentrations likely also contributed to variability in ice algal response. Furthermore, experimental results indicated that the cultured Van Mijenfjorden community was negatively impacted by a rapid (within 4 to 24 h) reduction in salinity from 33 to 10. We further documented a significant start of recovery of these algae after 168 h. From this work, we surmise that decreases in surface water salinity, for example arising from the intensifying freshening of fjord waters, may only cause temporary changes in ice algal photoacclimation state and thus in chlorophyll *a* biomass. Further, this study also supports the need for salinity buffered melt of sea ice samples to reduce artificial bias in biological measurements.

KEYWORDS

hypoosmotic stress, photoacclimation, primary productivity, sea ice algae, Svalbard fjords, Arctic coastal waters, freshwater, climate change

1 Introduction

Sea ice algae contribute between 2–26% of the total annual marine primary productivity in seasonally sea ice-covered coastal waters of the Arctic (Legendre et al., 1992a; Arrigo, 2017). These photosynthetic organisms play an important role in the marine carbon cycle through their assimilation of inorganic carbon and generation of organic carbon (Wassmann et al., 2011). The majority of sea ice algal growth within coastal first-year ice (FYI) occurs in the spring (Leu et al., 2015), and communities are typically concentrated in the bottommost skeletal layer of the ice (Meiners et al., 2018; Van Leeuwe et al., 2018). Here, these bottom-ice algae experience growth conditions largely governed by the characteristics of the underlying water column, with salinities usually in the range of 30 – 35 (Arrigo, 2014). In late spring-summer, bottom-ice algae must seasonally cope with large salinity decreases in the sea ice and surface waters, from more than 30 down to as low as zero, with snow and sea ice melt (Holt and Digby, 1985; Gradinger et al., 2010; Arrigo, 2014).

Such decreases in salinity may become especially significant in fjord systems in the future with glacial calving, and release of meltwater intensifies with climate change (Błaszczyk et al., 2019; Halbach et al., 2019). Increases in sea ice melt within coastal areas due to increased precipitation over the Arctic Ocean (Bintanja and Andry, 2017; IPCC, 2019) could additionally contribute to the overall freshening of Arctic coastal surface waters. The resultant freshening of surface waters may lower bulk-ice salinity with reduced permeability of sea ice in the area, and in turn, reduce the amount of habitable space for sea ice algae to grow (e.g., Vonnahme et al., 2021). Bottom-ice algae may be directly exposed to these fresher surface waters due to their concentrated growth at the ice-ocean interface, although the extent of exposure for these algae to the fresher conditions will also depend on the sea ice location [e.g., with latitude, sea ice type (first-year ice versus multi-year ice)] and with the time at which the freshening occurs (e.g., seasonality spring versus summer). Western Svalbard fjords are thought to be especially prone to increases in freshwater with climate change, with drastic declines in winter ice cover (Pavlova et al., 2019; Urbański and Litwicka, 2021), and increased freshwater inputs from glaciers (Calleja et al., 2017; Błaszczyk et al., 2019; Fransson et al., 2020) or rivers (McGovern et al., 2020; Pogojeva et al., 2022) already documented. The fjords adjacent to the West Spitsbergen Shelf are also subject to strong seasonality, including the widespread freshening of surface waters with local precipitation events, snow and sea ice melt, river runoff, as well as the direct discharge that comes from the nearby calving glaciers (Svendsen et al., 2002).

The impact of freshening (i.e., low salinity) has been often observed to change sea ice algal photophysiology (e.g., Bates and Cota, 1986; Campbell et al., 2019), and reduce sea ice algal chlorophyll *a* (Chl *a*) or biomass (e.g., Haecky and Andersson, 1999; Granskog et al., 2003; Campbell et al., 2019), as well as to facilitate a greater proportion of flagellate cells in the algal community (e.g., Piiparinen et al., 2010; Rintala et al., 2014). A number of these assessments focused on the impact of sea ice sample melt. To minimize hypoosmotic stress, some studies have advocated to add three to four parts of filtered seawater (FSW) to one part of ice (e.g., Garrison and Buck, 1986; Mikkelsen and Witkowski, 2010; Campbell et al., 2019), while still others used a direct melting of bulk-ice samples without adding FSW (e.g., Søgaard et al., 2010; Kaartokallio et al., 2013; Fernández-Méndez et al., 2018) since the addition of FSW is suggested to enhance primary productivity via the introduction of nutrients (Rintala et al., 2014). This highlights a lack of consensus in standardizing the methodology for obtaining accurate photophysiological parameters, Chl *a* and community composition from sea ice algae. Furthermore, despite work to date on melt procedure, it remains uncertain what the long-term acclimation response (i.e., more than 48 h) of Arctic bottom-ice algal communities is to decreasing salinity. Acclimation is defined, in this study, as the ability of sea ice algae to become accustomed to new surrounding conditions (e.g., salinity, nutrients, light) through physiological processes. Acclimation and physiological responses to reduced salinities occur on short-term

---

Abbreviations: Chl *a*, Chlorophyll *a;* DIC, Dissolved inorganic carbon; FSW, Filtered seawater; NO_2 + NO_3, Nitrite + nitrate; PO_4, Phosphate; POC/N, Particulate organic carbon and nitrogen; $Si(OH)_4$, Silicate; GPP, Gross primary productivity; PI Curves, Photosynthesis-irradiance curves; α^B, Photosynthetic efficiency; P_s^B, Maximum photosynthetic rate in the absence of photoinhibition; P_m^B, Maximum photosynthetic rate in the presence of photoinhibition; I_k, Photoacclimation index; β^B, Photoinhibition rate; PAR, Photosynthetically active radiation; TF, Tempelfjorden; VM, Van Mijenfjorden; TF1, Tempelfjorden – Site 1; VM1, Van Mijenfjorden – Site 1; VM2, Van Mijenfjorden – Site 2.

(times scale of hours) and/or comparatively long-term (time scales of days). Previous research suggested that sea ice algae may have the capability to recover from hypoosmotic stress after a period of 72 h, but this potential capability for recovery remains uncertain (Campbell et al., 2019).

In this study, we aim to determine the responses of bottom-ice algal communities to differences in salinity, and experimentally, to rapid decreases in salinity (i.e., freshening) on short-term (i.e., 4 h-24 h) and comparatively longer-term (i.e., 168 h) time scales. We tested the hypothesis that low Chl *a*, reduced photosynthetic capability, and greater abundance of flagellates are characteristics of more freshwater influenced sea ice environments by contrasting the natural communities of bottom-ice algae in two seasonally ice-covered western Svalbard fjords of varying freshwater inputs; Tempelfjorden (TF) and Van Mijenfjorden (VM). These two fjords were selected due to the presence of the tidewater glacier Tunabreen in TF that was likely to provide comparatively greater freshwater inputs to TF compared to VM (Hald et al., 2001; Murray et al., 2003; Fransson et al., 2015; Larsen et al., 2018; Fransson et al., 2020; Pogojeva et al., 2022). We further conducted controlled experiments to assess the impacts of a rapid decrease in salinity on a cultured community collected in VM through short and long-term laboratory-based salinity acclimation experiments. Through this work, we provide insight on the potential consequences of the freshening of Arctic coastal waters on sea ice algal communities and their ability to acclimate to changing salinity conditions. We also outline recommendations on the best practice for ice melting procedure.

2 Materials and methods

2.1 Environmental characteristics of Tempelfjorden and Van Mijenfjorden

2.1.1 Description of study areas and sampling sites

Sampling took place in TF and VM in spring 2021. Water at the ice-ocean interface and sea ice samples were collected at one site in TF (TF1) on 12 April, and at two sampling sites in VM that are referred to as Site 1 (VM1) on 17 April and Site 2 (VM2) on 14 April (Figure 1). The TF site is located at the easternmost (inner) part of Isfjorden. This 14-km-long and 5-km-wide fjord (Forwick et al., 2010; Pogojeva et al., 2022) lacks a distinct sill at its opening (Fransson et al., 2020) and is divided into two basins (Fransson et al., 2020; Pogojeva et al., 2022). Van Mijenfjorden is the second largest fjord on the west coast of Spitsbergen, with a length of 50 km and width of 10 km (Larsen et al., 2018). It is located further south than TF and is also divided into two basins (Larsen et al., 2018). At the mouth of VM fjord is the island of Akseløya, which together with an outer sill of 34 m restricts the inflow of comparatively warm and saline Atlantic waters and protects the landfast sea-ice (fast-ice) cover from significant wave action (Skarðhamar and Svendsen, 2010).

The tidewater glacier Tunabreen and the land-terminating glaciers Bogebreen and Von Postbreen are important freshwater sources in TF (Fransson et al., 2015; Fransson et al., 2020; Pogojeva et al., 2022) and were close to our sampling site TF1 (about 8 – 9 km

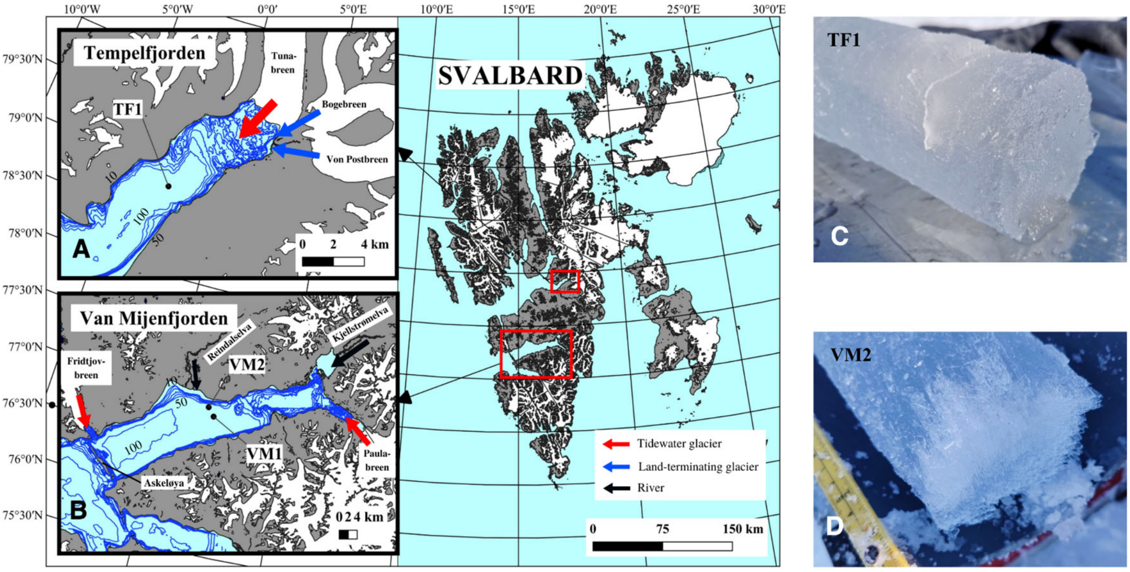

FIGURE 1
Map of the field study sampling sites in two Svalbard fjords at Tempelfjorden **(A)**: TF1, and at Van Mijenfjorden **(B)**: VM1 and VM2 (Definitions Sections 1, 2.1.1). The land, glaciers (e.g., Tunabreen, Bogebreen, Von Postbreen, Paulabreen and Fridtjovbreen) and fjord water are colored in grey, white and light blue, respectively. Black lines represent the two rivers flowing into Van Mijenfjorden (i.e., Reindaselva and Kjellstrømelva). The arrows represent the freshwater inflow either from a tidewater glacier (red), a land-terminating glacier (blue) or a river (black). The size of the arrows indicates the importance of the freshwater inflow for the fjord system in TF (Fransson et al., 2015; Fransson et al., 2020; Pogojeva et al., 2022) and in VM (Hald et al., 2001; Murray et al., 2003; Larsen et al., 2018). Map layer is from the Norwegian Polar Institute Map Data and Services. Blue isobaths represent the bathymetry based on Geonorge (version 13.3.655). Visible skeletal layer was absent at TF1 **(C)** while a more-defined skeletal layer (roughly 2 cm) was observed at VM2 **(D)** which was similarly seen at VM1.

away) (Figure 1). Despite VM receiving freshwater from the tidewater glaciers Fridtjovbreen (Murray et al., 2003), and Paulabreen (Hald et al., 2001), as well as from the Kjellstrømelva river in the Kjellstrømdalen valley (Hjelle, 1993; Larsen et al., 2018), the sampling sites VM2 and VM1 were further away from these freshwater sources (20 km or more) compared to the proximity of TF1 to Tunabreen. Reindalselva was the closest freshwater source from VM2 (about 6 km away) and VM1 (about 9 km away) (Figure 1), but was considered to have a low freshwater influence (i.e., less significant freshwater influence than, for instance, ice melt or glacial meltwater release, and which therefore results in lower exposure of sea ice algae to rapid decreases in salinity) since rivers in Svalbard typically release more freshwater in late spring-summer, after our sampling events (Hjelle, 1993; McGovern et al., 2022). Therefore, the rivers in VM were considered to have a negligible freshwater influence on VM2 and VM1, at the time of sampling, specifically compared to the influence of Tunabreen on TF1.

2.1.2 Environmental characteristics

Prior to the collection of each ice core, average of snow depth, ice thickness and freeboard for individual sampling sites were measured. Ice cores were collected at TF1 (total n = 13), VM1 (n = 7) and VM2 (n = 12) using a 9-cm (inner diameter) ice core barrel (Kovacs Enterprise Mark II). A total of eight, four and five of these ice cores from TF1, VM1 and VM2 were pooled and melted, respectively, with the addition of interface-FSW (0.2 µm) at an approximate ratio of three parts FSW to one part ice ($FSW_{3:1}$) based on the method used by Campbell et al. (2019) for primary productivity and photophysiology assessments, and for further measurements of particulate organic carbon-nitrogen and Chl *a* (Section 2.1.3). The FSW added to the samples was prepared from surface seawater which was sampled within 10 cm of the ice-ocean interface at all sites through an ice core hole using a peristaltic pump (Masterflex® L/S® Portable Sampling Pump) and which was immediately filtered (0.2 µm) following transport to the laboratory. Here, bulk-ice samples were melted in a saltwater solution (0.2 µm FSW) to avoid the decreases in salinity, and are compared to undiluted bulk-ice salinity treatments of about 3 or 10 (Weeks and Ackley, 1982). This would otherwise cause cell damage and reductions in Chl *a*, cell abundance and/or community composition (Garrison and Buck, 1986; Mikkelsen and Witkowski, 2010; Chamberlain et al., 2022), primary productivity, and shifts in algal photophysiology (Ralph et al., 2007; Campbell et al., 2019). All ice samples were melted at room temperature in darkness over a period of 24 h and regularly checked for complete melt. The melting procedure was stopped as soon as the last pieces of sea ice had melted in order to prevent the samples from warming up to room temperature. One ice core was collected at VM1 and VM2 for obtaining Chl *a* profiles of the entire ice column. The bottom 10 cm of each core were sectioned into 0 – 3 and 3 – 10 cm segments (distance from ice – ocean-interface) and then further sectioned at an interval of 10 – 13 cm from 10 cm toward the top (sea ice surface). Each segment was then melted with FSW dilution prior to processing for obtaining Chl *a* measurements. An additional ice core was collected at each sampling site to measure ice temperature and bulk-ice salinity profiles. Each of these cores were sectioned into bottom 2.5 cm and above 5 cm thick sections prior to melting without FSW dilution. Additionally, one ice core was collected and sectioned at each sampling site for measurement of inorganic nutrients and dissolved inorganic carbon. These measurements were only taken in the 3 cm bottom-ice segments after melting without FSW dilution.

Under-ice light measurements were done using an Underwater Hyperspectral Imager (UHI, Model 4, Ecotone AS, Norway). Briefly, during each survey the UHI was mounted on an under-ice arm, lowered under the ice through three overlapping ice core holes (14 cm internal diameter) and subsequently lifted-up by pivoting at a point just below the hole so that the arm could extend the UHI sensor 1.1 m towards the sun to minimize any influence of the hole on the transmitted photosynthetically active radiation (PAR, 400 – 700 nm) measured by the UHI. The UHI surveys covered a bottom-ice area of approximately 1.0 x 0.5 m, consisting of 968 x ~ 2000 pixels. Each pixel collected spectral radiance in 214 wavelength bins. Spectral radiance values were integrated over the PAR wavelength range (W m^{-2} sr^{-1}) and converted to irradiance over the entire survey region (W m^{-2}). Irradiance was then converted to photon fluxes (µmol photons m^{-2} s^{-1}) using 1 µmol photons m^{-2} s^{-1} = 0.217 W m^{-2} (Nicolaus and Katlein, 2013).

Temperature was measured directly at the ice-ocean interface at all sites using a CTD (SonTek Castaway®). Unfortunately, only temperature measurements could be taken from the Castaway due to technical issues of the instrument´s conductivity sensor. Interface salinity was instead measured using a conductivity meter (ProfiLine Cond 3110-WTW) in the laboratory, after surface seawater was sampled within 10 cm of the ice-ocean interface at all sites through an ice core hole, using a peristaltic pump (Masterflex® L/S® Portable Sampling Pump). Physical parameters such as sea ice temperature and bulk-ice salinity were measured for the entire ice core at a vertical resolution of 5 cm. Sea ice temperature was measured along an entire ice core, starting at 2.5 cm distance from the ice-ocean interface and continuing in 5 cm intervals over the entire core length using a thermometer probe (RS PRO RS 1720), which was inserted into ca. 4 cm deep holes drilled into the core at each measurement spot. The same core was then immediately sectioned into bottom 2.5 cm and above 5 cm thick sections and melted back at laboratory facilities. Following a 24 h melt period and complete melt, bulk-ice salinity was measured using a conductivity meter (ProfiLine Cond 3110-WTW). Brine volume fraction was calculated from bulk-ice salinity and sea ice temperature measurements using the equation based on Frankenstein and Garner (1967) for a bulk-ice temperature between −8.2°C – −2.06°C.

2.1.3 Biogeochemical characteristics in Tempelfjorden and Van Mijenfjorden

Additional measurements of chemical-biological parameters were completed on bottom-ice sections (0 – 3 cm) following undiluted sample melt (i.e., individual section melt without FSW additions), including: inorganic nutrients [nitrite + nitrate (NO_2 + NO_3), phosphate (PO_4) and silicic acid ($Si(OH)_4$)], dissolved inorganic carbon (DIC), and particulate organic carbon (POC) and nitrogen (PON), and also following diluted pooled sample melt (i.e., 3 cm pooled core sections melting into cooler jugs filled up with FSW), including DIC, Chl *a*, ice algal community composition (method described further below), and gross primary productivity (GPP; method described Section 2.1.4).

Pseudo-duplicate samples (i.e., two samples which were taken from the same ice core) for analysis of inorganic nutrients were also collected from the ice-ocean interface water at each site, as well as from undiluted melted 3 cm individual ice core sections. Wearing vinyl gloves, seawater or melted ice samples were filtered through an acid washed swinnex filter holder assembled with 25 mm GF/F filter (Whatman) into 15 mL acid washed Falcon tubes. The samples were stored at −20°C until analysis within six months on a nutrient autoanalyzer (QuAAtro 39, SEAL Analytical, Germany), following the method described by Vonnahme et al. (2021). As sea ice algae live within brine channels, the *in situ* brine nutrient concentrations were further calculated by first calculating brine salinity following the equation from Assur (1960) for a bulk-ice temperature above −8.2°C, and then by multiplying the nutrient concentrations with the ratio of brine salinity to bulk-ice salinity. Molar ratios of NO_2 + NO_3 to PO_4 (N:P) and NO_2 + NO_3 to $Si(OH)_4$ (N:Si) were also calculated for the ice-ocean interface, bulk-ice and brine.

Dissolved inorganic carbon (DIC) was measured on sea ice from undiluted melted 3 cm individual ice core sections and also from diluted melted 3 cm pooled ice core sections incubated for measuring GPP (Section 2.1.4), following the method used by Hu et al. (2018). In the field, bottom-ice core sections were sealed in impermeable gas bags (Nylon/Poly bags) using a vacuum sealer (Cabela's brand sealer). Ice samples were then melted in darkness and sub-sampled in duplicate within 24 h of collection. This was done by using a glass syringe to fill 15 mL exetainers before spiking with 20 µL of $HgCl_2$ and storage at 4°C in the dark. Analysis of DIC samples was conducted within six months of collection using an Infrared CO_2 analyzer (Apollo SciTech Inc., United States), and were further verified to be within ± 3 µmol kg^{-1} following a routine analysis of Certified Reference Materials provided by A. G. Dickson, Scripps Institution of Oceanography, San Diego, California.

Samples of particulate organic carbon and nitrogen (POC/N), Chl *a* and community composition were all completed on the diluted meltwater of 3 cm pooled ice core sections described above. For POC/N, volumes of 60 to 400 mL were filtered onto 21 mm GF/F filters (Whatman) previously combusted at 450°C for 6 h. A blank with only FSW was included for each sampling event. All samples were stored at −20°C in the dark and were processed in the laboratory within six months on a CHN Analyzer (Lab-Leeman CEC 440, United Kingdom) following the method described by Reigstad et al. (2008). Pseudo-duplicates of Chl *a* were filtered onto a 25 mm GF/F filter (Whatman) before placement into 20 mL glass vials (Wheaton) and pigment extraction into 10 mL of 90% acetone at 4°C in darkness for 24 h. Following extraction, raw fluorescence measurements were taken using a Turner Designs Trilogy fluorometer (Parsons et al., 1984) before and after addition of 2N HCl. Community composition was assessed by subsampling 100 mL of the pooled ice samples into a Nalgene bottle and fixation with 10 mL of a 20% formalin solution before storage at 4°C, giving a final concentration of 2% in the sample. Cell identification was based on previous research from von Quillfeldt (1996) and Hasle et al. (1994), and it was done under an inverted microscope (Leica DM IL LED, Germany), largely to genus level, and were counted in an Utermöhl chamber (Hydro-Bios, 2.973 mL) over three transects of 20 mm for a total of 400 cells (at minimum). Samples with low cell concentrations from TF1 and VM2 were first settled using a sedimentation column (Hydro-Bios, total sedimentation volume of 10 mL), while the samples from VM1 were directly transferred into the Utermöhl counting chamber (Hydro-Bios, 2.973 mL).

2.1.4 Measurement of gross primary productivity on sea ice samples

Gross primary productivity (GPP) was measured at each site following the method of Campbell et al. (2016). Here, 10 to 12 60 mL polystyrene culture flasks (Corning) were each filled with 50 mL sample of pooled ice meltwater and were incubated for 3 h at −2°C, with the addition of 1 mL of a ^{14}C radioactive solution (4 µCi mL^{-1}) (Strickland and Parsons, 1972). This was done in a light chamber providing an irradiance range of approximately 10 to 300 µmol photons m^{-2} s^{-1} using cool white light emitting diode (LED; Co/tech 15W IP65). The average (n = 3) integrated PAR for each flask position was determined immediately prior to each incubation using a Walz US-SQS/L probe. One or two darkened polystyrene flasks were used as blanks, being incubated with 50 µL of 3-3,4-dichlorophenyl-1,1-dimethylurea (DCMU) at 25 µmol L^{-1} to inhibit photosynthetic activity and thus to only quantify ^{14}C passively entering the algal cells via osmosis (Legendre et al., 1983). This was done to correct ^{14}C active uptake measurements obtained when algal cells carry out photosynthesis. Following incubation, each sample was filtered onto a 25 mm GF/F filter (Whatman) and filters were placed into 20 mL glass scintillation vials before acidification with 0.5 N HCl. After the filters dried over 24 h, 10 mL of Ecolume scintillation cocktail were added to the glass scintillation vials. Radioactivity of these samples were measured using a scintillation counter (Tri-Carb 2900 TR) within one month. Photosynthesis versus irradiance (PI) curves were modelled using the exponential function in the presence of photoinhibition (Platt et al., 1980). The Chl *a*-normalized photophysiological parameters known as maximum photosynthetic rate in the absence P_s^B or presence of photoinhibition P_m^B (µg C µg Chl a^{-1} h^{-1}), respectively, photosynthetic efficiency α^B (µg C µg Chl a^{-1} h^{-1} [µmol photons m^{-2} s^{-1}]$^{-1}$), photoacclimation index I_k (µmol photons m^{-2} s^{-1}), photoinhibition rate β^B (µg C µg Chl a^{-1} h^{-1} [µmol photons m^{-2} s^{-1}]$^{-1}$) were determined with Matlab (R2020b (9.9.0), Mathworks Inc., USA). The exponential equation from Platt et al. (1980) was specified for the fittype function of Curve Fitting Toolbox, Matlab R2020b (9.9.0), Mathworks Inc., USA.

2.2 Laboratory-based experiments on a Van Mijenfjorden cultured ice algal community

2.2.1 Collection and growth of Van Mijenfjorden culture

Algae from VM2 on 14 April were collected for experiments at UiT The Arctic University of Norway. This was done by placing a subsample of the pooled ice meltwater into pre-prepared sterile Guillard F/2 growth media containing silica (Andersen, 2005) before transport for experimentation. The VM2 algae were grown at 4°C (INCU-Line 150R Premium incubator) and 30 µmol photons m^{-2} s^{-1} in artificial seawater (salinity 33) following the American Society for Testing and Materials (ASTM D1141-98) composition and containing the same Guillard F/2 growth media with silica (Andersen, 2005). Cultures were acclimated to these growth conditions for approximately four months prior to experimentation at the same temperature and light conditions. 10% of the algal culture was placed in 50 mL fresh media every two weeks over the four-month period. Algae were placed in new media and mixing occurred each time new media was made. Experiments were done with this culture in a stage of exponential growth phase (Supplementary Figure 1), corresponding to a specific growth rate of 0.36 d^{-1}. The community composition of cultures was assessed at the time of experimentation (see details Section 3.2.1).

2.2.2 Experimental procedure

The experiment consisted of growing VM2 cultures under irradiance of 30 µmol photons m^{-2} s^{-1} for 4, 24 and 168 h in two salinity treatments: one control ocean surface water salinity treatment of 33, to which the VM2 cultured algae were acclimated, and one lowered salinity treatment of 10 (Figure 2). The salinity 33 was selected as the stock culture and control salinity treatment since Arctic surface water salinities typically range from 30 – 35 (Arrigo, 2014), and because the VM2 community had been acclimated to an *in situ* surface water salinity of approximately 30 (Section 3.1.1). Similarly, 10 was chosen as the experimental treatment as the melting of sea ice core sections, without buffering with FSW, may lead to a bulk-ice salinity of 10 (Campbell et al., 2019), but is also similar to what bottom-ice algae can experience during the melt season (Hop et al., 2011; Mundy et al., 2011; Smith et al., 2022). To start a given experimental treatment, 5% of cultured algae were transferred to individual sterile cell culture flasks (Thermo scientific Nunc EasYFlask) containing media at either control or experimental salinities.

To assess acclimation responses of the VM2 cultured ice algal community to decreases in salinity, Chl *a*, relative community composition (%), cell abundance (cells L^{-1}), ^{14}C-based GPP and photophysiology were measured at each defined time point (Figure 2), using the methodologies outlined above (Sections 2.1.3 and 2.1.4). In this study, the new acclimation state (i.e., recovery) of cultured ice algae to low salinity of 10 was mainly determined by significant increases in photophysiological parameters (P_s^B and α^B) towards the values observed in the control salinity of 33, restoring their pre-exposure levels. The Chl *a* concentration was also measured at initial time of the experiment (0 h) to investigate the evolution of algal biomass in the treatments over time. All measurements from culture experiments followed the methodology described previously for field samples, with the exception that samples for community composition and cell abundance were fixed with acidic lugol solution, and theoretical DIC concentrations assuming 100% saturation (Parsons et al., 1984) were used rather than directly measured. This experiment was conducted in triplicate over the course of four months.

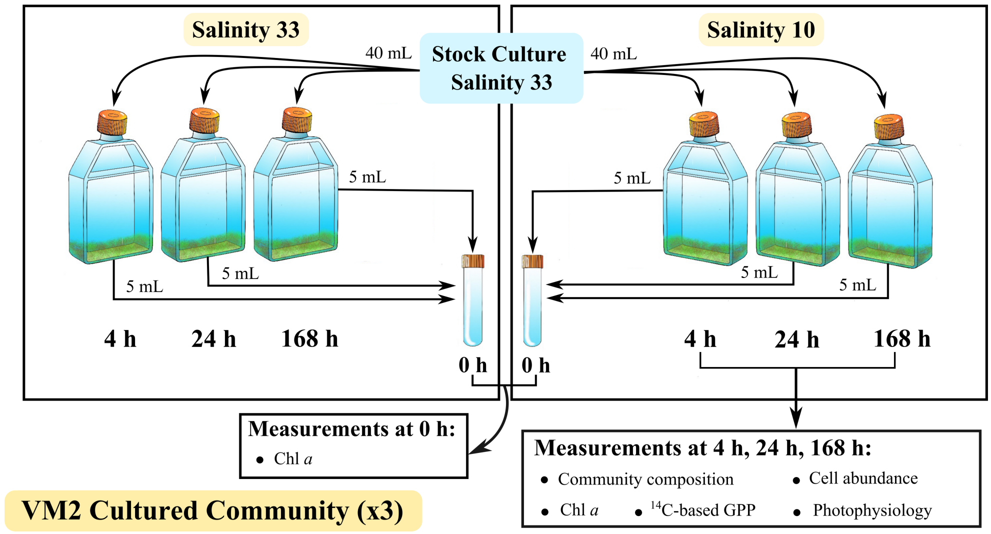

FIGURE 2
Experimental design for two treatments of salinity: Control 33 and low 10, showing measurements at the initial time (0 h) of the experiment and after a 4 h, 24 h and 168 h growth of a VM2 cultured ice algal community (Definitions Sections 1, 2.1.1, 2.2.1), in a given salinity treatment. Definitions of the measurements are given in Sections 1, 2.1.3, 2.2.2.

2.3 Statistical analyses

All statistical analyses were conducted using the statistical software SPSS (IBM version 28.0.0). Prior to running any statistical tests, assumptions of normality and homogeneity of variances were verified conducting a Shapiro-Wilk test and Levene's test, respectively. When comparing culture-based measurements in the two salinity treatments, an independent t-test was conducted if variances were found to be homogenous and an unequal variance Welch t-test was conducted if they were not homogenous. Independent and Welch t-tests are reported with t-statistic t (*df*), where *df* is the degrees of freedom.

When comparing culture-based measurements between the three time points at a given salinity, a one-way ANOVA was conducted. If the assumption of normality or homogeneity of variances was not verified, the data were log transformed prior and the assumptions were verified again. In the case the log transformed data still did not verify one of the previous assumptions, a Kruskal Wallis H test was conducted. The ANOVA tests of significance ($p < 0.05$) were further processed with Fisher´s *post hoc* test of significance. ANOVA results are reported with the F-statistic F (*df1*, *df2*) where *df1* is the degrees of freedom pertaining to time points, and *df2* is the number of observations less the number of time points. Kruskal Wallis H results were reported with the H-statistic, H (*df1*). *Post hoc* tests were not run since the results of the Kruskal Wallis H test were never significant ($p > 0.05$). Respective *p*-values were reported for all statistical tests. Significance for all statistical analyses in this study was determined for *p*-values < 0.05.

3 Results

3.1 Dynamics of Tempelfjorden and Van Mijenfjorden systems

3.1.1 Environmental characteristics of the sampling sites

Snow depth was the thickest at VM1 with an average of 14.9 ± 0.6 cm, followed by TF1 (4.1 ± 0.7 cm) and VM2 (3.0 ± 0.0 cm) (Table 1). Overall, sea ice was 10.8 – 22.3 cm thicker at VM1 (39.8 ± 1.0 cm) and VM2 (51.3 ± 0.3 cm), respectively, than at TF1 (29.0 ± 1.2 cm) (Table 1). Negative ice freeboard was only measured at VM1 (–1.0 ± 0.7 cm) (Table 1). Under-ice PAR was the lowest at VM1 (0.8 µmol photons m^{-2} s^{-1}) and about two-fold higher at TF1 (5.1 µmol photons m^{-2} s^{-1}) than at VM2 (2.1 µmol photons m^{-2} s^{-1}). Temperature of the water collected directly at the ice-ocean interface was distinct between TF1 (–1.2°C) and VM (–1.8°C) (Table 1). Salinity of this interface water was also similar across all sampling sites, ranging from 29.9 – 30.0 (Table 1). Bottom-ice bulk-ice salinity was almost two-fold lower at TF1 (4.1) than at VM1 (7.4) or VM2 (7.6) (Table 1). Moreover, the bulk-ice salinity profile at TF1 differed from those at VM1 and VM2, as bulk-ice salinity was the greatest at the snow-ice surface and lowest in the ice-ocean bottom at TF1 (Figure 3). Brine volume fraction was lower in the 2.5 cm bottom-ice at TF1 (6.5%) than at VM1 (16.2%) and VM2 (14.9%) (Figure 3). A more-defined skeletal layer of roughly 2 cm was documented at the bottom-ice of VM1 and VM2, which is in contrast to the bottom-ice of TF1 where no visible skeletal layer was observed (Figure 1; Supplementary Figure 2).

Nutrient concentrations (NO_2 + NO_3, PO_4 and $Si(OH)_4$) were similar at the ice-ocean interface of the two fjords, which were always greater than in the bulk-ice samples (Table 1). In contrast to the ice-ocean interface, notable differences in the nutrient concentrations were found in the bottom (bulk)-ice of the three sampling sites. Here, the bulk-ice NO_2 + NO_3 concentrations were approximately seven-fold and nearly twenty-eight-fold lower at TF1 (0.28 ± 0.02 µmol L^{-1}) than at VM2 (1.83 ± 0.00 µmol L^{-1}) and at VM1 (7.76 ± 0.12 µmol L^{-1}), respectively (Table 1). Bulk-ice PO_4 of the bottom-ice was also the lowest in TF1 (0.18 ± 0.00 µmol L^{-1}), but similar at the VM sites (VM1: 0.45 ± 0.03 µmol L^{-1}; VM2: 0.41 ± 0.02 µmol L^{-1}) (Table 1). However, bulk-ice $Si(OH)_4$ was the lowest at VM1 (0.50 ± 0.09 µmol L^{-1}) followed by TF1 (0.79 ± 0.42 µmol L^{-1}) and was the highest at VM2 (1.30 ± 0.00 µmol L^{-1}) (Table 1). The bulk-ice molar ratios of dissolved inorganic N:P and N:Si were the lowest at TF1 (N:P: 1.6; N: Si: 0.4) followed by VM2 (N:P: 4.5; N:Si: 1.4) and VM1 (N:P: 17.2; N: Si: 15.5) (Table 1). Similar to the trend in the bulk-ice, NO_2 + NO_3 concentrations were largely lower in the brine at TF1 (3.72 ± 0.25 µmol L^{-1}) than at VM2 (10.50 ± 0.01 µmol L^{-1}) and at VM1 (40.74 ± 0.61 µmol L^{-1}). In contrast to the bulk-ice, PO_4 was similar in the brine of the three sampling sites (TF1: 2.40 ± 0.01 µmol L^{-1}; VM1: 2.39 ± 0.14 µmol L^{-1}; VM2: 2.37 ± 0.11 µmol L^{-1}), and $Si(OH)_4$ was higher at TF1 (10.41 ± 5.48 µmol L^{-1}) than at VM2 (7.45 ± 0.01 µmol L^{-1}) and at VM1 (2.63 ± 0.48 µmol L^{-1}) (Table 1). Nevertheless, molar ratios were identical in the brine and in the bulk-ice (Table 1). The DIC concentrations were about three-fold lower in the bottom-ice of TF1 (230.6 ± 1.4 µmol kg^{-1}) than at VM1 (635.4 ± 5.8 µmol kg^{-1}) and VM2 (675.0 ± 0.5 µmol kg^{-1}) (Table 1).

3.1.2 Biological characteristics of the sampling sites

Concentrations of POC/N were the lowest at TF1 in the bulk-ice (POC: 45.6 mg C m^{-2}; PON: 3.7 mg N m^{-2}) and they were the highest at VM1 in the bulk-ice (POC: 215.8 mg C m^{-2}; PON: 32.3 mg N m^{-2}) (Table 1). Bulk-ice POC : PON molar ratios were found the highest at TF1 (14.4), followed by VM2 (10.5) and VM1 (7.8). Overall, Chl *a* was higher in the bottom-ice (ranging from 3.6 ± 0.0 to 65.3 ± 4.7 µg L^{-1}, also reported as 0.4 ± 0.0 to 7.4 ± 0.5 mg m^{-2}) than in the ice-ocean interface (ranging from 0.1 ± 0.0 to 0.2 ± 0.0 µg L^{-1}) (Table 1). The Chl *a* in the bottom-ice of TF1 was lower (0.4 ± 0.0 mg m^{-2}) than at VM2 (1.3 ± 0.5 mg m^{-2}) and at VM1 (7.4 ± 0.5 mg m^{-2}). The Chl *a* at the snow-ice interface of VM1 was greater than at the bottom-ice at this location, which contrasts with the sea ice Chl *a* profile of VM2 (Figure 3). The community at TF1 was characterized by pennate diatoms being the most abundant group (66%) and also by flagellates (34%) (Figure 4). The bottom-ice algal communities in VM were clearly dominated by pennate diatoms [at VM1 (99%) and VM2 (96%)], especially *Nitzschia* spp. [mainly *N. frigida* (Grunow)] at VM2, but were characterized by a lower

TABLE 1 Environmental characteristics of three sampling sites TF1, VM1 and VM2 (Definitions Sections 1, 2.1.1).

		TF1			VM1			VM2		
General										
	Date	12/04/2021			17/04/2021			14/04/2021		
	Coordinates	78.41 °N, 17.08 °E			77.80 °N, 15.76 °E			77.82 °N, 15.71 °E		
	Snow depth (cm)	4.1 ± 0.7			14.9 ± 0.6			3.0 ± 0.0		
	Ice thickness (cm)	29.0 ± 1.2			39.8 ± 1.0			51.3 ± 0.3		
	Ice Freeboard (cm)	0.4 ± 0.5			−1.0 ± 0.7			4.7 ± 0.7		
	PAR (µmol photons m^{-2} s^{-1})		5.1		0.8			2.1		
	Environment	**IO**[a]	**BI**[b]	**PC**[c]	**IO**	**BI**	**PC**	**IO**	**BI**	**PC**
Physical										
IO[a]	Temperature (°C)	−1.2	—	—	−1.8	—	—	−1.8	—	—
Chemical										
IO/Bulk-ice	Salinity	30.0	4.1	23.5	30.0	7.4	25.9	29.9	7.6	25.7
	$NO_2 + NO_3$ (µmol L^{-1})	7.94 ± 0.00	0.28 ± 0.02	—[d]	7.85 ± 0.54	7.76 ± 0.12	—	7.77 ± 0.22	1.83 ± 0.00	—
	PO_4 (µmol L^{-1})	0.67 ± 0.00	0.18 ± 0.00	—	0.62 ± 0.05	0.45 ± 0.03	—	0.63 ± 0.02	0.41 ± 0.02	—
	$Si(OH)_4$ (µmol L^{-1})	4.42 ± 0.00	0.79 ± 0.42	—	4.06 ± 0.00	0.50 ± 0.09	—	3.91 ± 0.16	1.30 ± 0.00	—
	N:P	11.9	1.6	—	12.7	17.2	—	12.3	4.5	—
	N:Si	1.8	0.4	—	1.9	15.5	—	2.0	1.4	—
	DIC (µmol kg^{-1})	—	230.6 ± 1.4	1743.3 ± 4.7	—	635.4 ± 5.8	1893.3 ± 2.2	—	675.0 ± 0.5	1898.2 ± 14.6
Brine	$NO_2 + NO_3$ (µmol L^{-1})	—	3.72 ± 0.25	—	—	40.74 ± 0.61	—	—	10.50 ± 0.01	—
	PO_4 (µmol L^{-1})	—	2.40 ± 0.01	—	—	2.39 ± 0.14	—	—	2.37 ± 0.11	—
	$Si(OH)_4$ (µmol L^{-1})	—	10.41 ± 5.48	—	—	2.63 ± 0.48	—	—	7.45 ± 0.01	—
	N:P	—	1.6	—	—	17.0	—	—	4.4	—
	N:Si	—	0.4	—	—	15.5	—	—	1.4	—
Biological										
IO/Bulk-ice	POC (mg C m^{-2})	—	45.6	52.3	—	215.8	247.7	—	64.8	74.4
	PON (mg N m^{-2})	—	3.7	4.2	—	32.3	37.1	—	7.2	8.3
	POC : PON	—	14.4	—	—	7.8	—	—	10.5	—
	Chl *a* (µg L^{-1})	0.2 ± 0.0	3.6 ± 0.0	3.7 ± 0.0	0.1 ± 0.0	65.3 ± 4.7	84.8 ± 7.0	0.2 ± 0.0	10.9 ± 0.4	11.4 ± 0.9
	Chl *a* (mg m^{-2})	—	0.4 ± 0.0	0.4 ± 0.0	—	7.4 ± 0.5	10.0 ± 0.8	—	1.3 ± 0.1	1.3 ± 0.1

[a] Ice-ocean interface (10 cm).

[b] Bottom-ice (3 cm).

[c] Pooled cores (3 cm) with added filtered seawater.

[d] Em dashes indicate when data were not collected or measured.

Definitions of the parameters are given in Sections 2.1.2, 2.1.3. Measurements are presented as average values with their respective standard deviation ($n = 8$ at TF1, $n = 4$ at VM1, $n = 5$ at VM2 for snow depth, ice thickness and freeboard; $n = 2$ for nutrients, DIC and Chl *a*) except for the ice-ocean interface temperature and salinity, the bulk-ice salinity, and POC/N ($n = 1$).

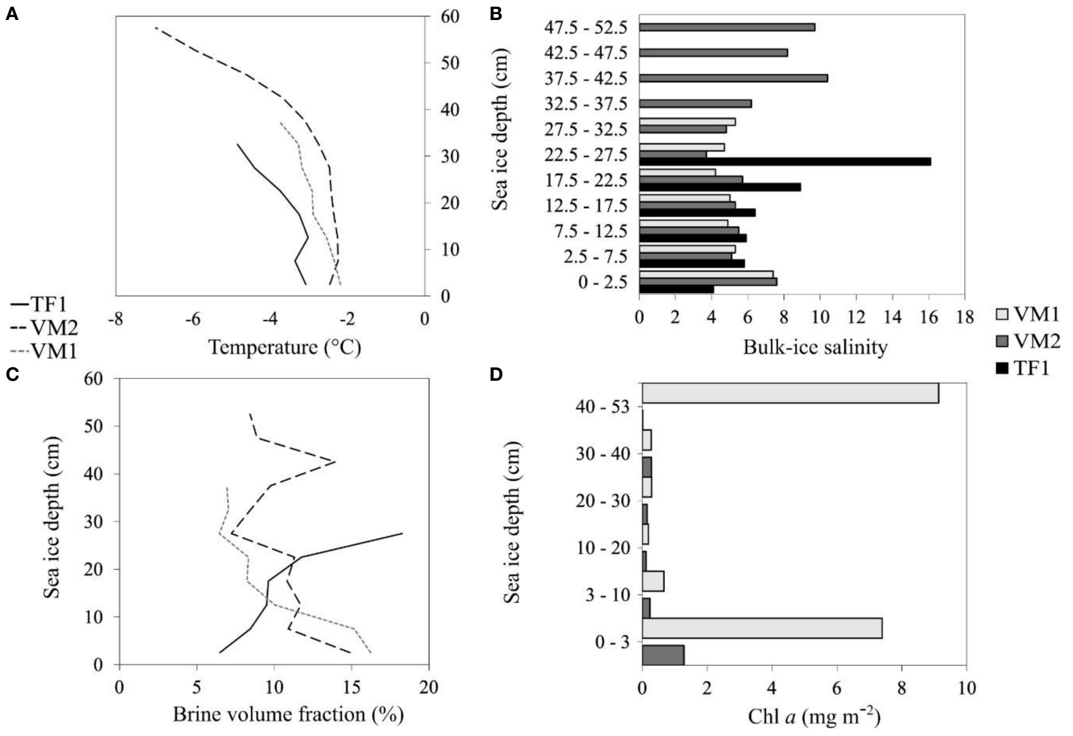

FIGURE 3
Sea ice profiles of temperature **(A)**, bulk-ice salinity **(B)**, brine volume fraction **(C)** and Chl *a* **(D)** from the bottom-ice upwards (zero is at bottom-ice) (Definition Sections 1 and 2.1.2). Black solid lines and black bars; light grey dashed lines and solid light grey bars; black dashed lines and dark grey bars correspond to the sea ice profiles at TF1, VM1 and VM2, respectively (Definitions Sections 1 and 2.1.1). Sea ice profiles of Chl *a* were obtained for VM1 and VM2 but not for TF1 (data not collected).

abundance of flagellates [at VM1 (1%) and VM2 (4%)], by contrast to TF1 (Figure 4).

3.1.3 Photophysiology of natural fjord communities

The shape of the PI curves highlights variability in the photophysiological parameters (Figure 5), specifically the curve for the VM1 community (Figure 5B), which clearly shows the steepest initial slope representative of the highest photosynthetic efficiency α^B (145.3 x 10^{-4} µg C µg Chl a^{-1} h^{-1} [µmol photons m^{-2} $s^{-1}]^{-1}$), and the steepest photoinhibition slope, which is indicative of the highest photoinhibition rate β^B (5.9 x 10^{-4} µg C µg Chl a^{-1} h^{-1} [µmol photons m^{-2} $s^{-1}]^{-1}$). Overall, maximum photosynthetic rates P^B_s, P^B_m were comparable between communities from all sites. However, the TF1 community showed a lower α^B (52.9 x 10^{-4} µg C µg Chl a^{-1} h^{-1} [µmol photons m^{-2} $s^{-1}]^{-1}$) and a greater photoacclimation index I_k (49.0 µmol photons m^{-2} s^{-1}) (Figure 5A) than either of the VM sites (Figures 5B, C). Photoinhibition rates β^B were documented in all samples, with the highest rate for the VM1 community, and similar rates for the TF1 and VM2 communities, respectively.

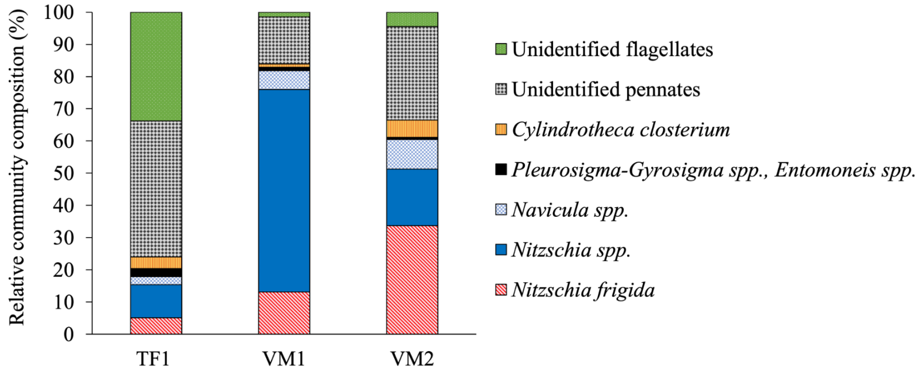

FIGURE 4
Relative algal community composition in the bottom-ice core sections (3 cm) of TF1, VM1 and VM2 (Definitions Sections 1, 2.1.1).

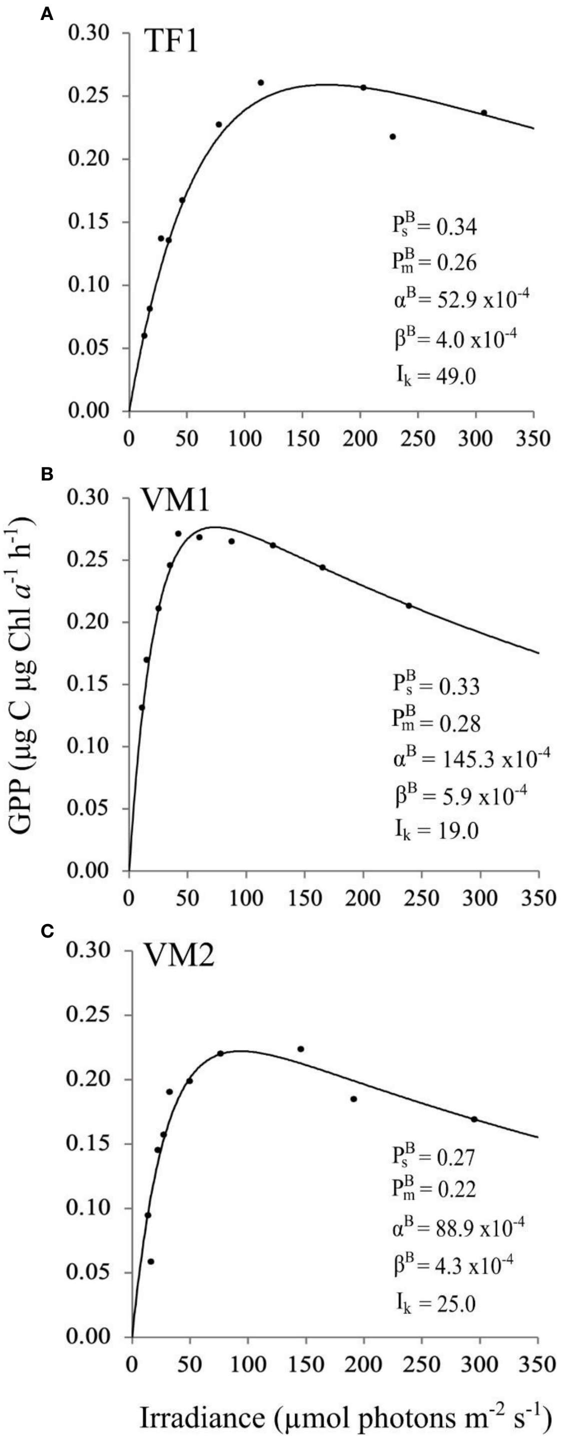

FIGURE 5
PI curves (Definition Section 2.1.4), fitted with the exponential model (Platt et al., 1980) and presented with the respective photophysiological parameters (Definitions Section 2.1.4), of the natural bottom-ice algal communities collected at TF1 **(A)**, VM1 **(B)**, VM2 **(C)** (Definitions Sections 1, 2.1.1). The definition of GPP is given in Section 2.1.3.

3.2 Culture-based experimentation

3.2.1 Temporal changes in chlorophyll *a*, cell abundance and community composition

Over the course of the entire experiment, Chl *a* ranged from an average of 16.6 – 319.4 µg L^{-1} in the control salinity treatment of 33 and from 23.6 – 69.5 µg L^{-1} in the lowered salinity experimental treatment of 10 (Figure 6). The concentration of Chl *a* was significantly lower at salinity 10 than at 33 after 168 h (Figure 6; Table 2). Moreover, a significant increase in Chl *a* was observed after 24 h at salinity 33 compared to the initial Chl *a* at the start of the experiment (Figure 6; Table 2). In contrast, no significant difference from initial Chl *a* was found at salinity 10 after 4 h or 24 h exposure (Figure 6; Table 2). However, significant increases in Chl *a* were observed in both salinity treatments after 168 h compared to the initial Chl *a* concentration (Figure 6; Table 2).

The species composition of the ice algal culture (Figure 7) differed from the community composition in the original sample (Figure 4). Overall, the cultured community was dominated in terms of cell abundance (>70%) by pennate diatoms mainly including *Synedropsis hyperborea* (Grunow) as well as other unidentified pennate diatoms. Unidentified flagellates were also present in the culture (<30%) in much greater relative abundance than in the natural community (4%). Some of these flagellates resembled chlorophytes of the genera *Chlamydomonas* and *Pyramimonas*. No centric diatoms were observed in our cultured samples. Furthermore, there were no noticeable changes in the relative community composition between the two salinity treatments (Figure 7), and the relative abundance of flagellates between the three time points within a given experimental treatment did not appear to vary (Table 2). However, significant differences in the cell abundance between the salinity 33 and 10 treatments were evident after 4 h and 168 h of exposure (Table 2), with notable lower abundance after 4 h at salinity 33 (Figure 7A) and after 168 h at salinity 10 (Figure 7B). In both 33 and 10 salinity treatments, cell abundances were significantly greater after 168 h in comparison to 4 h and 24 h treatments (Figure 7; Table 2). Dead pennate diatoms (i.e., empty frustules) were found in greater relative abundance in the lowered salinity treatment of 10 (from 8 ± 5 to 10 ± 5%) than in the control salinity treatment of 33 (from 1 ± 1 to 3 ± 1%) for each time point (Supplementary Table 1).

3.2.2 Photophysiology of cultured ice algae

The PI curves and photophysiological parameters (i.e., P_s^B, α^B and I_k), were significantly lower at salinity 10 versus 33, at all time points (Figures 8, 9; Table 2). The photophysiological parameters in the lowered salinity treatment of 10 did not appear to change between 4 h and 24 h but did increase after 168 h (Figures 8, 9). This increase was significant for P_s^B and α^B between 4 h and 168 h, and also between 24 h and 168 h (Table 2). These parameters were largely constant over time in the control salinity treatment of 33, with a visual but insignificant decrease in α^B after 168 h (Figures 8, 9; Table 2).

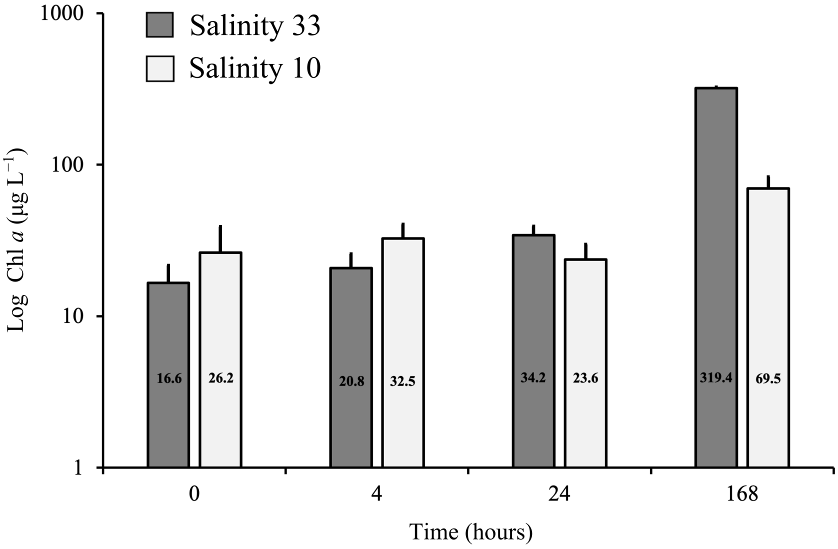

FIGURE 6
Average (*n* = 3) Chl *a* concentrations (Definition Sections 1, 2.1.3), with standard deviation of a VM2 cultured ice algal community (Definitions Sections 1, 2.1.1, 2.2.1), after growing for 4 h to 168 h in two salinity treatments, 33 (control; dark grey) and 10 (lowered salinity; light grey). Average (*n* = 4) Chl *a* is also presented at initial time (0 h), with standard deviation. Chl *a* is here given in log-scale.

4 Discussion

4.1 Variability in sea ice algal abundances between Tempelfjorden and Van Mijenfjorden sampling sites

4.1.1 Distribution of ice algal chlorophyll *a*

A typical Chl *a* distribution for Arctic FYI (Thomas, 2017), with maximum concentrations near-to the ice-ocean interface, was clearly seen at VM2 (Figure 3). However, VM1 showed a more atypical Chl *a* profile, with greatest values at the snow-ice interface. Together with the negative freeboard at VM1 (Table 1), this indicates the presence of surface flooding and of an infiltration community. Surface flooding has not been considered a common feature of the Arctic, but it is increasingly observed with ongoing climate change, particularly in the vicinity of the Barents Sea, where the sea ice has become thinner and is thus more easily pushed below sea level by its snow cover (McMinn and Hegseth, 2004; Provost et al., 2017; Fernández-Méndez et al., 2018).

Snow depth has a large influence on light availability for bottom-ice algae due to its high albedo and attenuation of incoming solar radiation (Grenfell and Maykut, 1977; Nicolaus et al., 2010; Järvinen and Leppäranta, 2011), with higher Chl *a* typically found under thin versus thicker snow covers in early to mid-spring (Campbell et al., 2015; Leu et al., 2015; Lange et al., 2017), and typically during the early phase of bloom development. However, our study shows the opposite trend, with lowest Chl *a* in the bottom-ice of TF1 and VM2, which had thinner snow depths and higher under-ice irradiances than VM1, which had the highest Chl *a* under thickest snow depth and lowest under-ice irradiances (Table 1). This observation may be a result of variable weather conditions between the sites, as milder atmospheric temperatures were reported in TF just three days prior sampling (9 April 2021, −1.3°C on average) (Seklima, 2021a), than in VM (11 April 2021, −7.5°C on average; 14 April 2021, −15°C on average) (Seklima, 2021b). Here, this difference in temperature likely enhanced the melting of fast-ice at TF1. Besides, we surmise that the algal community was more developed at VM1 due to an earlier time of ice formation (MET, 2021), as evidenced by the thicker ice cover in combination with a thicker snow cover at this site (Table 1). This would have reduced sloughing of algae from the ice at VM1 compared to the two other sites.

4.1.2 Fjord freshwater and nutrient regimes

The impact of glacial freshwater runoff on reducing bulk-ice salinity in TF has been documented previously, where bottom-ice bulk salinities of 2.5 – 4 and mid-top bulk-ice salinities of 4.5 – 10 were reported (Alkire et al., 2015; Fransson et al., 2020). The bulk-ice salinity profile from our study at TF1 aligns with these reported values (Figure 3), and supports a similar influence of freshwater. Interannual variability in the amount of glacial-derived freshwater has been shown for TF with data from stable oxygen isotopic ratios (δO^{18}) of sea ice cores (Fransson et al., 2020) demonstrating the possibility of five-fold difference in the volume of glacial meltwater inputs between consecutive April months. The data for our TF site are comparable to April 2012 in Fransson et al. (2020), where the bulk-ice salinity of the bottom-ice was approximately 4, due to documented freshwater inputs from the tidewater glacier Tunabreen. Here, the sea ice that measured 23 cm in thickness was shown to be 54% sourced from glacial meltwater, on average. We could not detect the presence of low salinity melt water below the sea ice in our surface water salinity data nor do we have oxygen isotope data as an alternative indicator (Table 1). However, our snapshot sea ice data are similar in terms of ice thickness and bulk-ice salinity to the Fransson et al. (2020) study suggesting that the TF site could have been influenced by glacial meltwater input.

TABLE 2 Statistical analyses comparing the photophysiological parameters P_s^B, α^B, and I_k (Definitions Section 2.1.4), Chl *a* (Definition Sections 1, 2.1.3), the relative abundance of flagellates to the community composition and the cell abundance of cultured algae (Definitions Section 2.2.2), either between the two salinity treatments without considering time points (33 vs. 10), or between the two salinity treatments at the same time point (e.g., 4 h_{33} vs. 4 h_{10}), or between time points in a given salinity treatment (e.g., 4 h_{33} vs. 24 h_{33} vs. 168 h_{33}).

		P_s^B	α^B	I_k	Chl *a*	Flagellates	Cell abundance
Welch t-test	33 vs. 10	8.331[a] (*8.997*)[c] < **0.001**	5.332 (*8.692*) < **0.001**	3.591 (*11.106*) **0.004**	—	—	—
Independent t-test	4 h_{33} vs. 4 h_{10}	—[d]	—	—	—	—	−5.007[a] (*4*) **0.007**
	24 h_{33} vs. 24 h_{10}	—	—	—	−1.379 (*4*) 0.240	—	0.614 (*4*) 0.572
	168 h_{33} vs 168 h_{10}	—	—	—	4.584 (*4*) **0.010**	—	5.380 (*4*) **0.006**
One-way ANOVA (F), or Kruskal Wallis H test (H)	4 h_{33} vs. 24 h_{33} vs. 168 h_{33}	**(H)** 5.067 (*2*) 0.079	**(F)** 0.693[b] (*2,6*) 0.536	**(H)** 1.156 (*2*) 0.561	**(F)** 46.909 (*3,9*)< **0.001**	**(H)** 1.424 (*2*) 0.491	**(F)** 38.120 (*2,6*) < **0.001**
	4 h_{10} vs. 24 h_{10} vs. 168 h_{10}	**(F)** 17.612 (*2,6*) **0.003**	**(F)** 8.490 (*2,6*) **0.018**	**(F)** 0.694 (*2,6*) 0.536	**(F)** 11.998 (*3,9*) **0.002**	**(F)** 0.695 (*2,6*) 0.535	**(F)** 11.992 (*2,6*) **0.008**
ANOVA - Fisher´s *Post hoc* test of significance	0 h_{33} vs. 4 h_{33}	—	—	—	0.333	—	—
	0 h_{33} vs. 24 h_{33}	—	—	—	**0.023**	—	—
	0 h_{33} vs. 168 h_{33}	—	—	—	< **0.001**	—	—
	4 h_{33} vs. 24 h_{33}	—	—	—	0.142	—	0.781
	168 h_{33} vs 4 h_{33}	—	—	—	< **0.001**	—	< **0.001**
	168 h_{33} vs 24 h_{33}	—	—	—	< **0.001**	—	< **0.001**
	0 h_{10} vs. 4 h_{10}	—	—	—	0.464	—	—
	0 h_{10} vs. 24 h_{10}	—	—	—	0.764	—	—
	0 h_{10} vs. 168 h_{10}	—	—	—	< **0.001**	—	—
	4 h_{10} vs. 24 h_{10}	0.580	0.935	—	0.341	—	0.340
	168 h_{10} vs. 4 h_{10}	**0.002**	**0.011**	—	**0.002**	—	**0.011**
	168 h_{10} vs. 24 h_{10}	**0.003**	**0.012**	—	< **0.001**	—	**0.003**

[a] The t-value is reported for the Welch t-test (unequal variance t-test) and for the independent t-test (equal variance t-test).
[b] The F statistic and H statistic values are reported for the one-way ANOVA test and the Kruskal Wallis H test, respectively.
[c] p values and Degrees of freedom (df) are reported for all tests. Fisher´s post-hoc test p-value is also reported. Significant values ($p < 0.05$) are in bold.
[d] Em dashes indicate that the test was not run for the given treatment.

Furthermore, we noted the absence of a pronounced skeletal layer at TF1 (Figure 1; Supplementary Figure 2). This may result from the above-freezing temperature of the ice-ocean interface at TF1 (Table 1), which could have promoted sea ice melt at the time of sampling and thus potentially led to hypoosmotic stress of ice algal cells. It is also possible that our interface sampling approach via a peristaltic pump missed the freshwater layer immediately beneath the ice, as this can occur in very thin layers directly at the ice water interface. We suggest that freshwater inputs from glacial run-off occurred mainly at the time of ice formation prior to our sampling events as evidenced by the lower bulk-ice salinity. Also, the presence or absence of low salinity surface water at the time of sampling does not necessarily reflect the conditions during ice growths, that determine the bulk-ice salinity. We exclude for example the age of sea ice as a major factor explaining the differences in bulk-ice salinities as suggested for example for multi-year ice versus first-year ice (e.g., Lange et al., 2015) or drainage with increasing ice age (Cox and Weeks, 1988), given the similar age of the ice present. We therefore used the low bulk salinity as strongest indicator for low surface water salinity impact during ice formation as known from other Arctic sites (e.g., Vonnahme et al., 2021) or brackish surface water sea ice systems like the Baltic Sea (e.g., Geilfus et al., 2021). Furthermore, it is plausible that a freshwater layer in TF1 was not detected in our study, due to wave propagated mixing, which has previously been measured in TF (Rabault et al., 2016; Sutherland and Rabault, 2016). The latter insight is supported by wind gust data for TF of 16.4 m s^{-1} on 11 April, 2021 (the day prior to fieldwork), and up to 20.6 m s^{-1} on 07 April, 2021 (five days prior to fieldwork), thus indicating gale or even strong gale prior to sampling (Seklima, 2021c). Wave propagation could also potentially have disrupted the

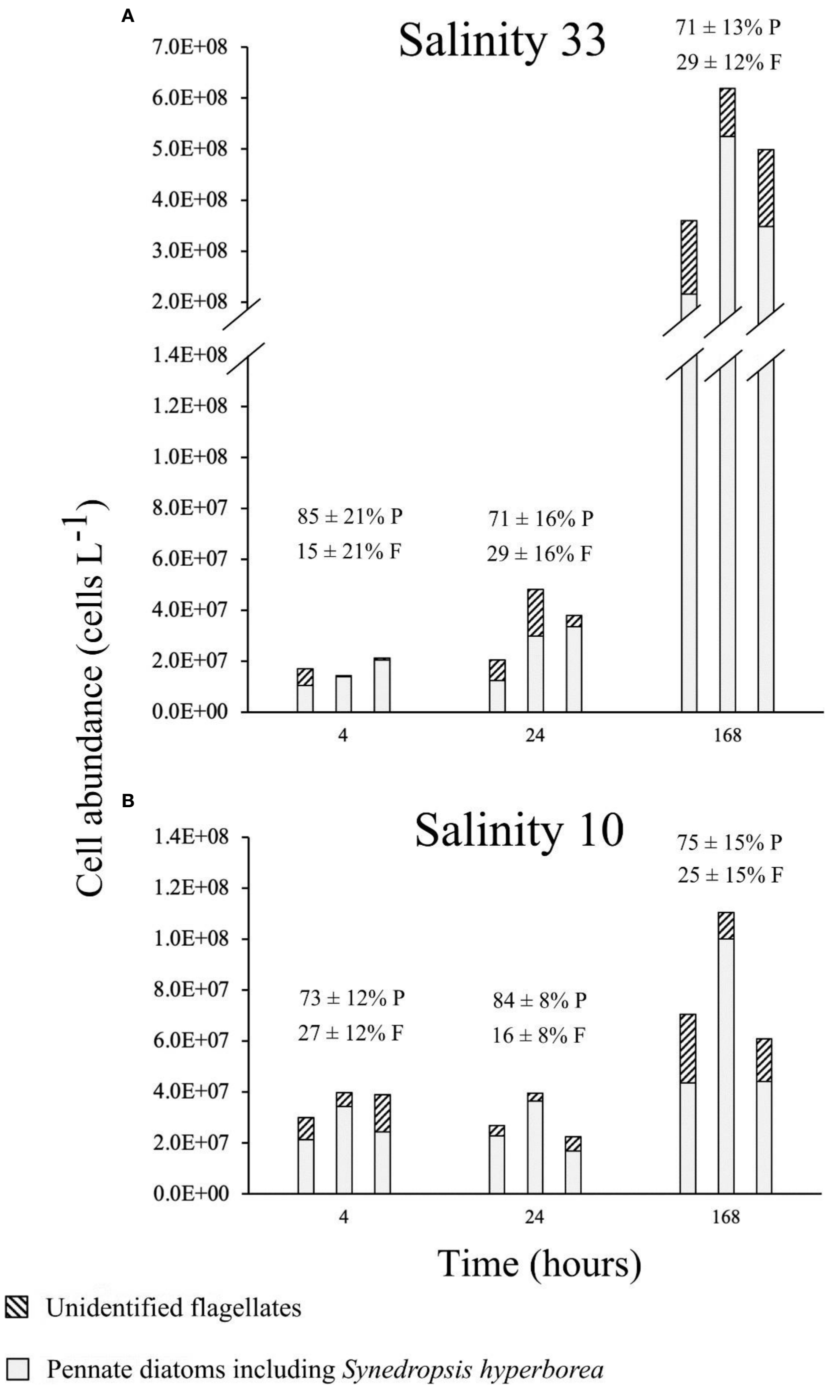

FIGURE 7
Algal abundances (triplicates) of the VM2 cultured ice algal community (Definitions Sections 1, 2.1.1, 2.2.1), after growing for 4 h, 24 h and 168 h in two salinity treatments, 33 [control; ***(A)**] and 10 [lowered salinity; **(B)**]. Relative community composition is also shown with the average (*n* = 3) relative abundance of pennate diatoms (P) and flagellates (F) with standard deviation.

formation of a clearly defined skeletal layer at TF1. In contrast to observations at TF1, the bulk-ice salinity in VM formed typical C-shaped profiles for young growing Arctic FYI (Thomas, 2017), with higher salinities at the bottom and the surface than in the middle of the profile (Figure 3). From this typical profile, we infer no direct indication of freshwater impacts at the VM sites. Sea ice was also saltier at the bottom-ice of VM sites than at TF1, since the average bulk-ice salinity of 7.5 was relatively high compared to 4.1. Thus, we conclude that sea ice algae at TF1 were likely exposed to freshwater inputs than at the VM sites.

The comparatively low Chl *a* in TF versus VM may be at least in-part explained by the differences in sea ice physical properties related to freshwater influence. Here, greater freshwater in TF could have **i)** reduced the colonization and subsequent accumulation of

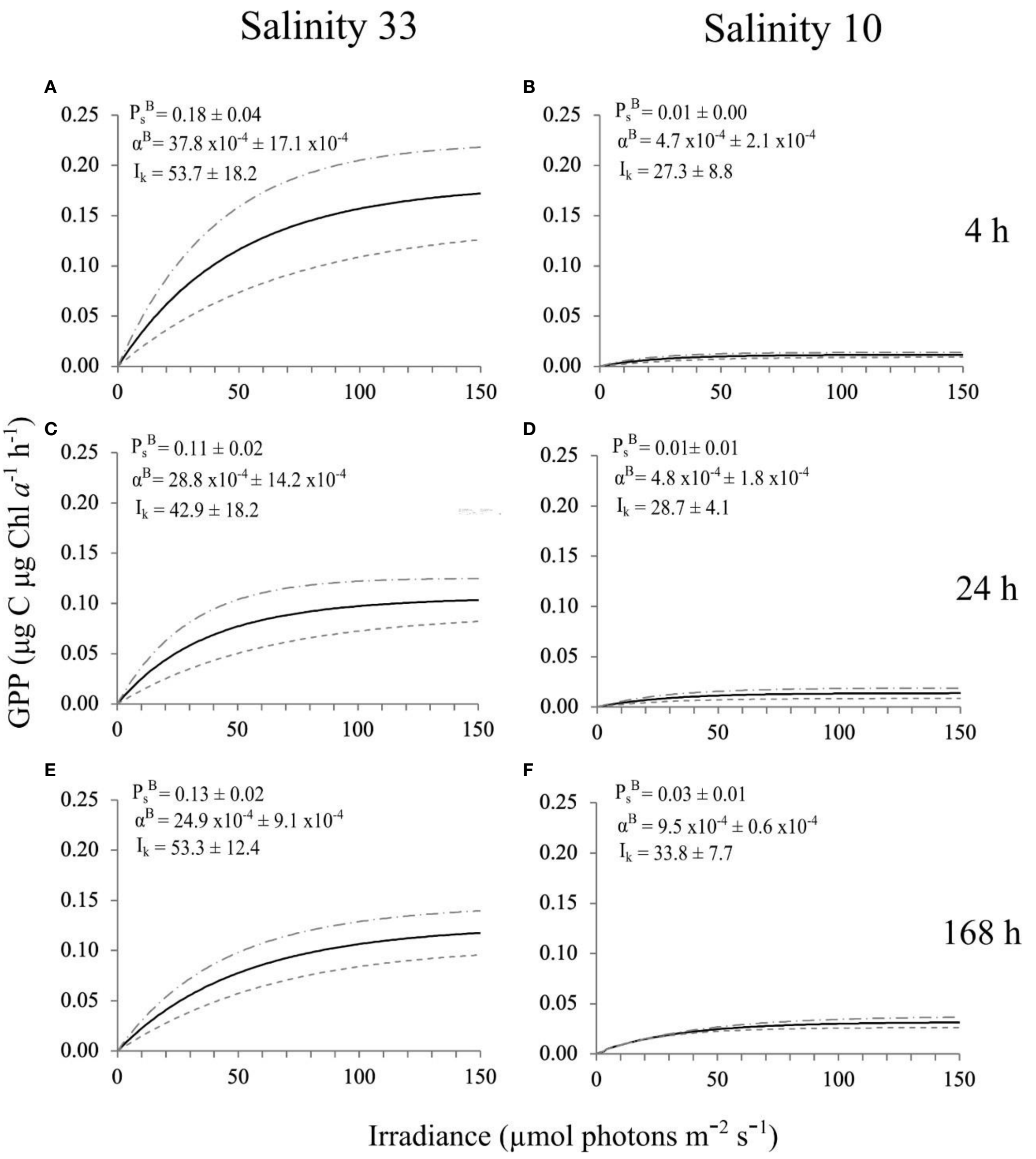

FIGURE 8
PI curves (Definition Section 2.1.4), fitted with the exponential model (Platt et al., 1980), and respective photophysiological parameters (Definitions Section 2.1.4), of a VM2 cultured ice algal community (Definitions Sections 1, 2.1.1, 2.2.1), after growing for 4 h, 24 h and 168 h in two salinity treatments, 33 [control; **(A, C, E)**], and 10 [lowered salinity; **(B, D, F)**]. The black solid line corresponds to the average (*n* = 3) photophysiological responses of the cultures and grey dashed lines represent the ± standard deviation. The definition of GPP is given in Sections 2.1.3, 2.1.4.

Chl *a* by altering the bottom-ice microstructure (i.e., ice porosity, permeability and extent of skeletal layer) (Arrigo, 2014; Arrigo, 2017; Thomas, 2017), and/or ii) reduced algal growth through hypoosmotic stress (Legendre et al., 1992b). An impact of freshwater on habitable space for sea ice algae has been observed previously in the Baltic Sea, where brackish sea ice with low bulk-ice salinity and low brine volume fraction supported low algal biomass on the order of 0.2 to 1.2 mg Chl *a* m^{-2} (Haecky and Andersson, 1999; Granskog et al., 2003). As detailed above, similarities to the Fransson et al. (2020) study and a documented lower bulk-ice salinity, lower brine volume fraction in TF1 compared to VM sites (Table 1; Figure 3) and visual observations of a poorly-defined skeletal layer at TF1 (Figure 1; Supplementary Figure 2) suggest freshwater influence impact on ice algal Chl *a* in our study. We note that indirectly, the lower ice porosity would have also reduced the permeability of the bottom-ice to nutrient-carrying ocean water (Granskog et al., 2006; Vonnahme et al., 2021), inducing nutrient stress on TF1 ice algae. Such a phenomenon of nutrient limitation is supported by the low bulk-ice nutrient concentrations at TF1 (Table 1), which were similar to nutrient concentrations reported elsewhere in Arctic fjords cited as having nutrient limited conditions ($NO_3 + NO_2$:<2.5 µmol L^{-1}, PO_4:<1 µmol L^{-1}, $Si(OH)_4$:<2 µmol L^{-1}), including TF and VM (Mikkelsen et al., 2008; Kaartokallio et al., 2013; Fransson et al., 2020; Kvernvik et al., 2021).

The POC : PON molar ratio (14.4) at TF1 was considerably higher than the average Redfield ratio (6.6) that is typical for marine

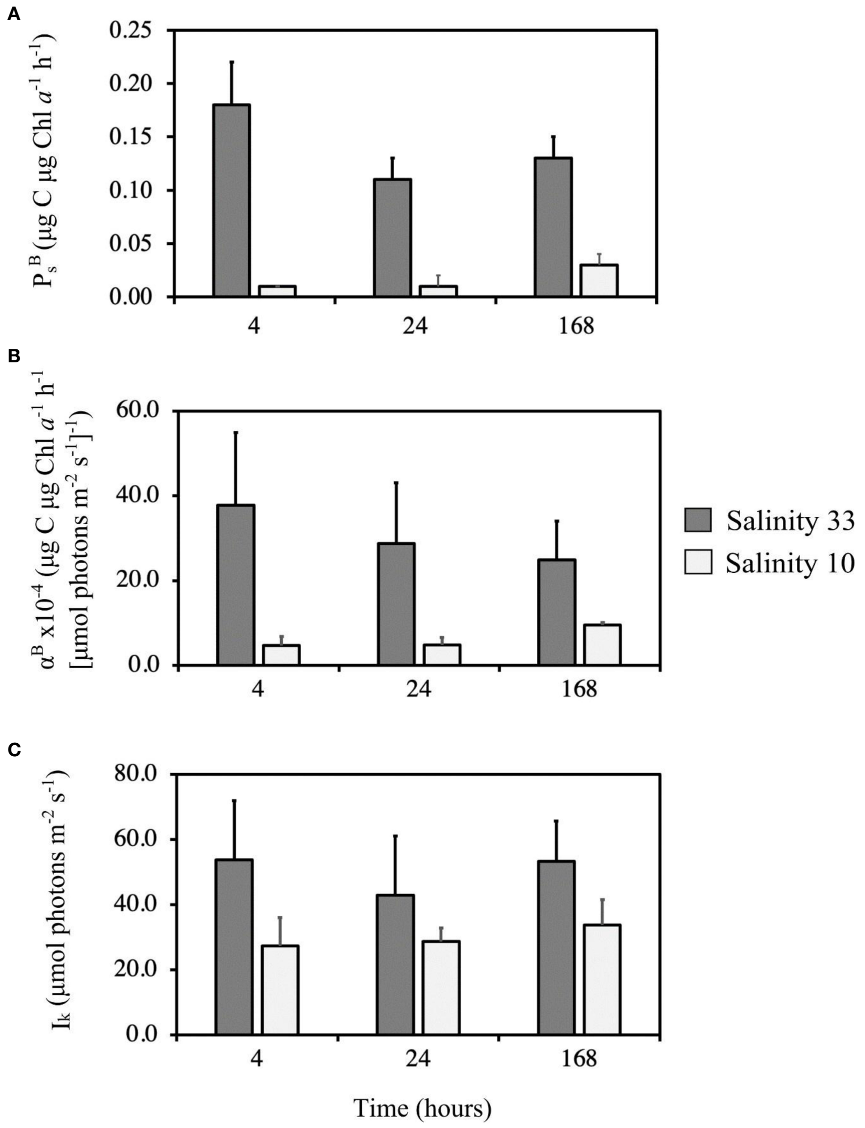

FIGURE 9
Average (n = 3) photophysiological parameters [P_s^B **(A)**, α^B **(B)**, and I_k **(C)**, (Definitions Section 2.1.4)], with respective standard deviation of a VM2 cultured ice algal community (Definitions Sections 1, 2.1.1, 2.2.1), after growing for 4 h, 24 h and 168 h in two salinity treatments, 33 (control; darker grey) and 10 (lowered salinity; light grey).

phytoplankton in deep oceans, but also above the Sterner ratio (8.3), which can be used to compare POC : PON in the Arctic Ocean and shelves (Frigstad et al., 2014). This suggests potential nitrogen limitation (Demers et al., 1989; Gosselin et al., 1990). It is important to mention that POC : PON molar ratios may range from 3 – 24 mol:mol in the sea ice (e.g., Arctic Canadian shelves) (Niemi and Michel, 2015), which means these ratios can be well-above the Redfield and Sterner ratios in sea ice. However, the highest values reported in that review stem from situations where algal material probably did not account for the majority of particulate organic matter (i.e., outside blooms, during winter). It is also worth considering that non-algal particulate organic matter including detritus and extracellular polymeric substances (EPS) can be important carbon sources, specifically outside the sea ice algal bloom period (e.g., Riedel et al., 2008), this can lead to highly variable POC : PON ratios (Niemi and Michel, 2015), thus limiting their use as indicators of algal physiological status. However, since the markedly increased POC : PON molar ratio at TF1 in this study was measured during spring algal bloom succession (Frigstad et al., 2014), we consider it indicative of a physiological state affected by nitrogen shortage. This is further in line with findings from an earlier study of sea ice algal seasonal succession in VM that showed a clear effect of decreasing nitrate concentrations on POC : PON molar ratios, as well as on photosynthetic yield (Leu et al., 2020; Kvernvik et al., 2021). Further evidence pointing towards nitrate as the limiting nutrient at TF1 comes from additional ratios such as N: P (1.6) which was lower than the Redfield (16) and the Sterner (20) molar ratios and N:Si (0.4) which was also lower than the ratio (1.07) for marine diatoms growing under continuous light (Brzezinski, 1985). Additionally, the lower bulk-ice salinity and

Chl *a* at TF1 also suggest a potential greater hypoosmotic stress on ice algal cells. Other drivers which may have contributed to the lower Chl *a* at TF1 include snow depth (Section 4.1.1), ice thickness and age. The sea ice was thinner at TF1 than at VM1 and VM2 (Table 1), which could suggest that it was younger in TF. This suggestion is confirmed by Svalbard ice charts showing that fast-ice only started covering TF1 around 22 March, 2021 while fast-ice already started covering VM1 and VM2 around 15 February, 2021 (MET, 2021). This difference in ice age has likely led to later cell incorporation in TF than in VM sea ice and therefore to less time for the algal biomass to accumulate.

Despite higher Chl *a* at VM2 and VM1 sites, low bulk-ice nutrient concentrations (Table 1) were likely to have also limited algal growth in at least part of this fjord. Similar to TF1, the POC : PON (10.5) and N:P (4.5) ratios at VM2 were greater and lower than the Redfield and Sterner ratios, respectively. By contrast, VM1 had the highest nitrogen (NO_2 + NO_3) concentrations of any site (Table 1), and the bulk-ice POC : PON molar ratio (7.8) as well as molar ratios of N:P (17.2) were similar to Redfield ratios and slightly lower than Sterner ratios. This suggests potential nitrogen replete growth conditions at VM1 which could explain the highest Chl *a* value at VM1.

Our insights on Redfield and Sterner organic matter and nutrient ratios and Chl *a* variability demonstrate that ice algal communities exposed to the same water masses, with separation on the scale of only a few kilometers, could exhibit different states of nutrient limitation (Leu et al., 2010; Leu et al., 2020). This is perhaps unsurprising given that previous studies have shown states of ice algal nutrient limitation to vary over even finer horizontal scales (e.g., meters), although for reasons of snow depth-related differences in nutrient demand (Campbell et al., 2016). Bulk-ice nutrient concentrations represent a proxy for nutrient availability but are themselves often considered to be an underestimate of nutrient availability to sea ice algae living within the brine channels. As a result, we also considered salinity corrected values of nutrients in the brine (Section 3.1.1), while investigating variability in sea ice algal photophysiology and growth. Since previous studies found that decreases in α^B can be caused by a reduction in salinity (e.g., Bates and Cota, 1986; Campbell et al., 2019), or by nutrient-limited growth conditions (e.g., Cota and Horne, 1989; Campbell et al., 2016), we suggest here that the lowest α^B at TF1 (Figure 5), could also be explained by the low bulk-ice salinity and low nutrient concentrations in the brine at that site, specifically of NO_2 + NO_3 (Table 1), while the higher α^B at VM2 and VM1 (Figure 5), could be due to higher bulk-ice salinity and the higher NO_2 + NO_3 concentrations in the brine of these two sites (Table 1). Despite the differences in bulk-ice salinity and nutrient concentrations, P^B_m were similar across sites. P^B_s, P^B_m are influenced by the rate of electron transport within a cell and the size of the photosynthetic unit, which collectively respond to variations in environment like temperature, light and nutrient conditions. It is thus conceivable that sites of different nutrient availability may have similar maximum photosynthetic rates if there are contrasting influences from other environmental factors. For example, we documented that TF1 and VM2 likely had greater nutrient limitation (which could lower P^B_m, P^B_s), but also greater light availability (which could reduce the pigmentation and density of reaction centers within a given cell, and thus reduce P^B_m, P^B_s). Together, these effects may have balanced the net impact on P^B_m, P^B_s at TF1 and VM2 relative to VM1 (which had more nutrients but lower light intensities).

It is also important to mention that sea ice algal biomass indicators like POC/N, Chl *a* and photophysiological responses may vary according to seasons (Leu et al., 2010; Leu et al., 2020; Kvernvik et al., 2021). Nevertheless, it is still worth discussing the differences between sampling sites in POC/N and Chl *a*, especially since the occurrence of lower Chl *a* in sea ice of lower bulk-ice salinity in our study is supported by previous studies (Granskog et al., 2003; Vonnahme et al., 2021). We would have ideally collected several times, but this was made impossible due to logistical setbacks (e.g., high avalanche risk, thin ice cover). Algal succession scenarios and thus are only representative for the time of sampling.

The molar ratios of dissolved inorganic N:Si at VM1 (15.5) and VM2 (1.4) were above the typical ratio of 1.07 while the molar ratio at TF1 (0.4) was well-below it. The higher silicate concentrations relative to nitrate at TF1 compared to VM1 and VM2 is likely the result of greater exposure to land run-off (glacial or riverine inputs) at TF1 as glaciers have been shown to be major sources of silicate to marine systems (Tréguer and Rocha, 2013; Meire et al., 2016; Fransson et al., 2020). This further supports glacial meltwater as a major source of freshwater at TF1. Besides, a surplus of silicate can be observed in sea ice (Fripiat et al., 2017; Yoshida et al., 2020) and dissolved silicate concentration in ice are governed by diatom growth, abundance and frustule dissolution in addition to exchange with the water column below. In our study, the pennate diatom abundance was relatively high at VM1 (99% of the relative abundance) and assuming a low silica dissolution rate (Nelson et al., 1991), this could also explain the high N:Si ratio at that site. Furthermore, marine diatoms can efficiently store nutrients (e.g., NO_3) and release these nutrients in significant concentrations under stress (Lomas and Glibert, 2000). It is here suggested that the direct melting of individual ice cores for nutrient measurements may have led to cell lysis (Garrison and Buck, 1986), and thus to the release of internal nitrogen pools, while $Si(OH)_4$ remained bound to the silica frustule of diatoms. Nevertheless, it is noteworthy that the bulk-ice $Si(OH)_4$ and PO_4 concentrations were generally comparable to bottom-ice values reported for spring sea ice of other Arctic fjords, which similarly reported nutrient limited growth conditions (Mikkelsen et al., 2008; Kaartokallio et al., 2013; Kvernvik et al., 2021).

4.1.3 Community composition and seasonal progression of sea ice algae

The fjords of this study were characterized by different community compositions. The VM communities were dominated by pennate diatoms like *Nitzschia* spp. (including *Nitzschia frigida* (Grunow)), which are typical of Arctic sea ice (Poulin et al., 2011). The community at TF1 was also dominated by pennate diatoms, but displayed a greater relative abundance of flagellates (Figure 4). High relative contributions of flagellates to total community composition are often characteristic of brackish ice-covered waters like the Baltic Sea (Piiparinen et al., 2010; Rintala et al., 2014), at times of low salinity during melt season (Van Leeuwe et al., 2018), or during periods of limited nutrient availability (Gradinger, 1999). Thus, the TF1 community composition provides further evidence to our hypothesis that the TF sea ice algae may have been influenced by freshwater to a greater degree than in VM, and that they experienced the greatest nutrient limitation within this study.

The variability in community composition between the two fjords may also be explained by differences in the seasonal progression of sea ice algae. The phenology of sea ice algae is influenced by both the timing of ice freeze-up, as well as by seasonal changes in the physical-chemical ice environment, for instance in light, nutrient, or salinity conditions (Tedesco et al., 2019). Based on observations from MET (2021) sea ice started to form earlier at the VM sites (around 15 February) than at TF1 (around 22 March). Lower algal Chl *a* and greater abundance of flagellates in the bottom-ice of TF1 may thus be in-part a result of an earlier stage in the seasonal progression of sea ice algae, where the typically high spring accumulation of diatoms had not yet begun, due to later formation of sea ice in the spring. In comparison, higher Chl *a* and the greater abundance of diatoms in the bottom-ice of VM suggests that the seasonal progression of sea ice algae was at a more advanced stage, and that the algae were in their accumulation phase of growth (Leu et al., 2015), especially at VM1 where Chl *a* was the highest and where pennate diatoms represented more than 98% of the algal community (Figure 4). This is also in accordance with spring algal successional patterns in newly formed Arctic sea ice which transitioned from a community resembling the composition of its source water towards a more matured, typical ice algal community (Kauko et al., 2018). Another factor which potentially led to differences in flagellate abundance between the two fjords is the seeding assemblage in the surface water, at the time of ice formation and in each site location. It is possible that there was greater abundance of flagellates at TF1 than at the VM sites when sea ice formed, although we do not have any data to support this assumption.

4.1.4 Dependence of photophysiology on under-ice characteristics and research methodology

Photophysiological parameters reported in this study are within the previously reported range of values summarised by Van Leeuwe et al. (2018). In comparison to our study, the maximum photosynthetic rate P_{max}, the photosynthetic efficiency α, and the photoacclimation index I_k documented in early May, 2017, for VM sea ice algae by Kvernvik et al. (2021), were different compared to our reported values. We attribute these differences to the use of different methodological approaches, sampling time and environmental conditions between the studies. For example, we measured GPP by incubating bottom-ice algae with ^{14}C for 3 h *in vivo* after melting bulk-ice samples with FSW (salinity of about 30 from the ice-ocean interface water) at room temperature for 24 h, while Kvernvik et al. (2021) measured net primary productivity (NPP) by incubating algal samples with ^{14}C for 24 h underneath the sea ice, immediately after scraping the algae off from the lowermost layer of the ice core. Furthermore, our study took place approximately two weeks earlier, had a dominance of pennate diatoms (versus a mixed community of unidentified coccoidal cells and diatoms), and was covered by less snow.

In addition to the potential influence of salinity and nutrients as described above (Section 4.1.2), further differences in the photophysiological parameters α^B and I_k may be a result of differences in the under-ice light regimes. Indeed, α^B was seen to decrease with increasing irradiance as a result of snow depth and the transition from early to late spring melt (Cota, 1985). A clear negative correlation between irradiance and α was also found in the seasonal study from VM in 2017 (Kvernvik et al., 2021). Thus, our lower α^B at TF1 and VM2 with snow depths thinner by approximately a factor of four and five, respectively, compared to VM1 that had the greatest α^B, supports this photophysiological response of ice algal communities. In contrast to α^B, the I_k in our study was greater at TF1 by a factor of approximately two to three compared to the VM communities (Figure 5). This suggests that the TF1 community had photoacclimated to higher irradiance, which is in agreement with the higher PAR value at this site under thin snow depth (Table 1). This is perhaps unsurprising in the context of similar P^B_s , P^B_m responses documented, as α^B is understood to be inversely proportional to I_k (Platt et al., 1980; Cota and Horne, 1989). Besides, the highest β^B at VM1 (Figure 5B), indicates a greater sensitivity to high irradiance levels compared to the TF1 and VM2 (Platt et al., 1980; Geider and Osborne, 1992). A heightened sensitivity is likely explained by the thickest snow depth at VM1 and thus the lowest light availability at that same site (Table 1), consistent with algae being more shade-acclimated as a result. Nevertheless, it is difficult to conclude about the influence of under-ice light regimes on the photophysiology of TF1, VM1 and VM2 sea ice algal communities due to daily and seasonal variations. Ideally, light transmission data and photoprotective pigments to Chl *a* ratios would have been required to better understand the potential of light as a main driver of the photophysiological responses of these sea ice algal communities, but these measurements are not available.

In addition to the under-ice light regimes, it is important to consider ice-ocean interface salinity and ice-ocean interface nutrients to which sea ice algae are acclimated (Arrigo, 2014). These were similar across sites based on measurements of our study (Table 1). Nevertheless, we cannot exclude that we did not capture the true ice-ocean interface salinity, for instance due to methodological challenges (Section 4.2.1). The definite cause of variability in Chl *a* and photophysiology is impossible to determine only based on the fieldwork results since the influence of salinity, light intensities and nutrient availability often overlaps when assessing photophysiological responses under variable co-factors. Lower Chl *a* and α^B could still indicate the occurrence of environmental stressors such as lower salinity and nutrient availability (Section 4.1.2), and may represent acclimation responses to higher light intensities due to photoprotective mechanisms (e.g., decreasing Chl *a* under increased light intensity conditions) (e.g., Campbell et al., 2015). Unfortunately, the logistical constraints of our study reduced the number of sampling events and thus limit the application of robust statistics.

Given the strong differences between sites, combined with evidence from previous studies, we suggest that salinity could have been one of the drivers of variable Chl *a* and photophysiology between the two fjords.

4.2 Impact of salinity on the photophysiological responses of a Van Mijenfjorden cultured ice algal community

The field data did not provide evidence of significant and independent effects of low salinity on the VM communities, neither directly (i.e., hypoosmotic stress) nor indirectly (i.e., reduced ice porosity) (Table 1; Figure 3). However, experimental results on cultures from VM2 showed that a rapid decrease in salinity (i.e., within 24 h) had the capability to negatively affect cell Chl *a* and photophysiology (Figures 6, 8, 9). The impact of low salinity on Chl *a* was especially significant after 168 h of exposure (Figure 6; Table 2), while the photophysiolgical response was more sensitive with a significant impact documented at all time points (4 h to 168 h) (Figures 8, 9; Table 2). Sea ice algal growth and photophysiology are often considered optimal at salinities ranging from 30 – 50 (Arrigo and Sullivan, 1992; Søgaard et al., 2011), although they may survive salinities below 10 and above 60 (Grant and Horner, 1976; Kottmeier and Sullivan, 1988; Kirst, 1990). Deviations from these ranges of optimal salinity can have a detrimental effect on ice algal cells to the point of causing cell death (Ralph et al., 2007).

Previous studies have shown that Chl *a* may be reduced under conditions of low salinity stress (e.g., Campbell et al., 2019; Yan et al., 2020; Chamberlain et al., 2022), and other studies have found that growth rates of Arctic sea ice diatoms were lower at salinities less than 12 in comparison to higher salinities ranging from 15 – 50 (Grant and Horner, 1976; Zhang et al., 1999). This supports the observed slower algal growth (i.e., lower Chl *a*) in our lowered salinity treatment of 10 after 168 h. Previous studies have also found lower P^B_m or P^B_s and α^B for Arctic sea ice algae exposed to salinities less than 20 following acclimation to a salinity of 30 (Bates and Cota, 1986; Campbell et al., 2019), which is in further agreement with our significantly lower P^B_s and α^B in the lowered salinity treatment of 10. Based on these results, we suggest that *in situ* melting of sea ice, glacial and riverine run-off, rain and snow events, as well as the lab-based ice melting procedure are likely to negatively impact the photophysiology of sea ice algae on the short-term (4 – 24 h) and Chl *a* on the longer-term (168 h). This would be a result of freshwater sources having the potential to rapidly dilute the salinity of the surface water to 10 under the sea ice (Hop et al., 2011; Mundy et al., 2011; Smith et al., 2022) or to lower salinity during lab-based experiments (Weeks and Ackley, 1982; Campbell et al., 2019).

Shifts in community composition and cell abundance due to changes in salinity have been suggested by a number of previous studies. For instance, with centric diatoms and flagellates outcompeting pennate diatoms under comparatively low *in situ* salinity conditions (e.g., Campbell et al., 2018), and the documented abundance of flagellates in sea ice of brackish waters in the Baltic Sea (Piiparinen et al., 2010; Rintala et al., 2014) or in surface melt ponds in the high Arctic (Lee et al., 2011; Mundy et al., 2011). Additionally, previous studies have reported a dominance of centric diatoms or flagellates over pennate diatoms in ice algal communities exposed to a decrease in salinity from about 32 to 29 (Yan et al., 2020) and 12 (Zhang et al., 1999). However, in this experimental study we found no evidence of salinity affecting community composition (Figure 7; Table 2), and thus no preference for flagellates over diatoms to grow under comparatively low salinity conditions. An undocumented change in community composition could be a result of unsufficient exposure time of 168 h (i.e., one week) to low salinity conditions in our experiment (e.g., Kauko et al., 2018). Future studies should further investigate shifts in community composition to low salinity stress over longer-term acclimation time (e.g., a month). Although no notable changes were found in the relative community composition, significant changes in the cell abundance of cultured algae were found between the control salinity treatment of 33 and the lowered salinity treatment of 10, after 4 h and 168 h (Figure 7; Table 2). The significant difference at 4 h could have been a result of variable start Chl *a* concentrations for experimental work (Figure 6), although both treatments were initiated during the period of exponential growth. Similar to discussion on differences in Chl *a* during experimentation (Section 4.2), the lower cell abundance after 168 h at salinity 10 supports slower algal growth with comparatively long-term exposure to low salinity. The greater relative abundance of dead pennate diatoms at salinity 10 than at 33 (Supplementary Table 1), also indicates that the algae could have been more stressed in the low salinity treatment, leading even to cell mortality.

Despite the lack of change in the relative community composition with low salinity stress exposure, we note that changes in community composition of the VM2 cultured ice algal community (Figure 7) occurred relative to the *in situ* fjord community (Figure 4). For example, a loss of *Nitzschia frigida* and a shift towards dominance of *Synedropsis hyperborea* was seen in the cultures. These changes in community composition have occurred during the four-month period cultures were grown in the laboratory prior to experimentation. In turn, this would have introduced variability into the specific photophysiological parameters measured during experiments. Changes in community composition of our culture from VM during this could have been due to temperature stress [growth at 4 °C in the laboratory versus at −1.8 °C *in situ*), alternations to growth nutrients of media (enriched Guillard F/2 growth media in the laboratory versus low nutrient concentrations in field (Table 1)] and acclimation to culturing light intensities of 30 µmol photons m^{-2} s^{-1} versus acclimation to 2.1 µmol photons m^{-2} s^{-1} in the field). Additionally, the VM2 cultured community had a fast growth rate (Supplementary Figure 1), which could have led to nutrient shortage and therefore enhanced competition for nutrients between species, where *Synedropsis hyperborea* may have better acclimated to the limited nutrient availability than other species, explaining its observed dominance. Another factor which could explain the dominance of this *Synedropsis hyperborea* is that this species attaches well to surfaces (e.g., walls of culture bottles) as it is an epiphytic species growing on other diatoms (von Quillfeldt et al., 2009). The loss of *Nitzschia frigida* in the cultured community is unfortunate as this pennate diatom species often dominates the Arctic bottom-ice (Poulin et al., 2011; Van Leeuwe et al., 2018) and is therefore highly representative of Arctic bottom-ice algal communities. Nevertheless, *Synedropsis hyperborea* has also been reported as a dominating pennate diatom in the Arctic sea ice (Tamelander et al., 2009; von Quillfeldt et al., 2009), specifically under summer melting conditions where only the frustules of other diatoms remained (Hegseth and von Quillfeldt, 2022), and it is also a common epiphyte of the Arctic centric diatom *Melosira arctica* (Hasle et al., 1994; Poulin et al., 2014). Thus, the magnitude of the responses of the VM2 cultured community dominated by *Synedropsis hyperborea* in our results supports the strong impact of low salinity stress that likely apply to sea ice pennate diatom-dominated communities in general. This outcome is also supported by previous studies showing that the growth and photophysiological performance of the characteristic Arctic pennate diatom *Nitzschia frigida* was negatively impacted by low salinity stress (e.g., Zhang et al., 1999; Campbell et al., 2019). Nevertheless, we suggest that future culture experiments should be run closer to the sampling time to avoid changes in community composition, and thus to obtain responses as representative as possible of natural bottom-ice algal communities.

It could however be worth mentioning observed differences between *Synedropsis hyperborea* and *Nitzschia frigida*, especially since photophysiological parameters may increase with increasing cell size (e.g., Taguchi, 1976). In our taxonomic analysis, we distinguished *Synedropsis hyperborea* and *Nitzschia frigida* primarily by colony structure, with *Synedropsis hyperborea* typically exhibiting non-branched colonies, and individual cell morphology and size. Notably, previous studies reported a size range of 13 – 96 µm for *Synedropsis hyperborea* and 45 – 75 µm for *Nitzschia frigida* (Grøntved, 1950; Medlin and Hasle, 1990; Hasle et al., 1994). In our study, cultured *Synedropsis hyperborea* cells measured 40 – 45 µm in apical length, while *in situ Nitzschia frigida* cells averaged approximately 60 µm. This suggests that the photophysiological responses we studied in the lab might not have been as intense as they could have if *Nitzschia frigida* had been dominating the culture. Unfortunately, we could not confirm this hypothesis since the species did not grow in the laboratory.

4.2.1 Impacts of salinity on temporal changes in the photophysiological responses of culture experiments

To avoid death, sea ice algae must acclimate by releasing osmolytes and salts (ions) or by altering the ion permeability via changes in the protein structure of cell membranes to cope with intracellular influx of water. This can take days to weeks before full recovery is achieved (Grant and Horner, 1976; Vargo et al., 1986; Kirst, 1990). Based on the significantly greater values of P_s^B and α^B in the control versus lowered salinity treatment of 10 after 168 h (in comparison to 4 h or 24 h) (Figures 8, 9, Table 2), we suggest that the VM2 cultured algae faced hypoosmotic stress after short-term exposure (after 4 h and 24 h) but were capable of recovering, to some extent, on a longer-term basis. However, the photophysiological parameters P_s^B, α^B and I_k remained significantly lower at salinity 10 than at 33 at all time points of our experiment, indicating that within a 168 h time period, full recovery from the hypoosmotic stress was not possible. In contrast to this recovery response documented at low salinity 10, photophysiological parameters were largely consistent across time points in the control salinity of 33 (Figures 8, 9). This is with the exception of a decrease in α^B that could highlight nutrient limitation and cell self-shading effect (Borowitzka and Vonshak, 2017), especially provided that the VM2 cultured community was relatively fast-growing (Supplementary Figure 1), and reached high Chl *a* (319.4 µg L^{-1}) after a 168 h growth at salinity 33 (Figure 6).

It is worth mentioning that the photophysiological responses measured in our study are likely to be representative of the most salinity tolerant species, to the control salinity of 33 and to the low salinity of 10. We surmise that our measurements are mainly representative of *Synedropsis hyperborea*′s responses since it was the predominant species in our cultured community and also because it has previously been observed in meltwater environments (e.g., Hegseth and von Quillfeldt, 2022). In addition, some microalgae potentially recovered better to the rapid decrease in salinity than others, but this assumption, unfortunately, cannot be supported from our dataset. We believe that future studies could isolate sea ice algal species from a cultured community and grow them separately in axenic cultures to further investigate and predict their specific photophysiological and acclimation responses to rapid decreases in salinity likely to occur in the Arctic coastal waters.

Our observations of limited recovery in photophysiological responses of the VM2 cultured community (i.e., only after 168 h) suggest a longer acclimation time than previously documented for a bottom-ice algal community from the Sea of Okhotsk. There, ice algae subject to smaller decreases in salinity from about 32 to 29 showed full recovery of the photosynthetic activity within 80 h (Yan et al., 2020). However, the slight recovery of photophysiological responses in our study was greater than the Southern Ocean bottom-ice algal community studied by Ryan et al. (2004), where cells were unable to recover even after 5 days of growth at a reduced salinity of 10 (Ryan et al., 2004). Such differences in the time required for acclimation could be explained by the extent of salinity change/existing acclimation status, where the difference of 23 in our study was far greater than the change of 3.4 in Yan et al. (2020) However, the differences in salinity between our study and Ryan et al. (2004) were comparable. Contrasting community composition could also be a factor in the differing responses between these reported studies, since the Sea of Okhotsk community of Yan et al. (2020) was dominated by centric diatoms (*Thalassiosira*), which may have better acclimation capability than pennate diatoms (Yan et al., 2020). By contrast, the Antarctic pack-ice community in Ryan et al. (2004) and our VM2 cultured community were dominated by pennate diatoms (*Fragilariopsis curta* versus *Synedropsis hyperborea*, respectively) and had limited ability to recover to the low salinity of 10. Another environmental factor that could explain the difference in the time required for photosynthetic recovery is nutrient availability. Indeed, the sea-ice algae studied by Yan et al. (2020) were sampled close to the land under high macro- and micro-nutrient concentrations (Kanna et al., 2014; Kanna et al., 2020), while the bottom-ice algae collected by Ryan et al. (2004) low Fe concentrations in Southern Ocean surface waters (Boyd et al., 2007) and sea ice (Pankowski and McMinn, 2008), which might delay photosynthetic recovery. In contrast, nutrient concentrations in our study were rather low but typical for Svalbard fjords. Despite differences in acclimation responses, all three studies showed that bottom-ice algal communities were stressed by short-term exposure to rapid decreases in salinity. The ability of Arctic sea ice diatoms to recover from salinity stress is less clear, but we assume that it is feasible given the likelihood this was required for their evolution in coping with seasonal variations in salinity that are typical for the ice-ocean interface of the Arctic Ocean.

It is also worth mentioning that our study only investigated the effects of a decrease in salinity from 33 to 10 (difference of 23), representing a rapid drop in salinity as observed in nature during rain events on sea ice or during unbuffered melting of ice core sections (e.g., Galindo et al., 2014; Campbell et al., 2019). Ideally, we would have also assessed the acclimation responses of sea ice algae to decreases in salinity of less intensity (e.g., from 33 to 25, or to 20), which was unfortunately limited due to time constraints. Future studies could assess the physiological acclimation responses of sea ice algae to increases and decreases in salinity as observed in nature, which are known to strongly impact ice algal growth and diversity (e.g., Grant and Horner, 1976; Zhang et al., 1999).

4.3 Potential implications of freshening of the Arctic coastal waters and ongoing climate warming

The potential negative effects of freshening on the ice algal biomass/photophysiological in natural sea ice and the significant experimental evidence of negative short-term salinity reductions on ice algal growth and photophysiology, suggest that increased amounts of freshwater accumulating in Arctic coastal waters through glacial meltwater run-off, increased riverine input and precipitation, have the potential to negatively impact ice algal Chl *a* and primary productivity. A similar suggestion was made regarding freshwater impacts on phytoplankton in Arctic coastal waters (e.g., Chucki sea), during the summer season, with negative impact on the primary productivity and biomass of coastal phytoplankton (Yun et al., 2014; Yun et al., 2016). Our results also indicate the potential of sea ice algae to slowly acclimate to a decreased salinity in terms of primary productivity and photosynthetic efficiency. Nevertheless, predicting the potential effects of less-saline conditions are difficult since different sea ice algal communities may respond differently on long-term exposure (e.g., see section 4.2.1), although based on our study, lower algal Chl *a* and cell abundance could be expected after a week of growth in a decreased salinity. Despite the lack of changes in community composition in our results, we consider it is still important to assess this variable while predicting future changes in sea ice algal photophysiological responses, especially since other studies have observed shifts in taxa and species after a decrease in salinity (e.g., Zhang et al., 1999; Yan et al., 2020), and because it may have an impact on higher trophic levels (Thomas, 2017). However, all predicted consequences based on our results and mentioned above may vary, for instance with: i) the specific ability of different bottom-ice algal species and communities to acclimate to lower salinity, ii) sea ice regionality and seasonality (e.g., differences in regional and seasonal sea ice characteristics), iii) alterations in other environmental factors than salinity (e.g., light and nutrient availability) arising from Arctic freshening (e.g., Brown et al., 2020).

4.4 Recommendations for best practice

Rapid versus gradual melting of bulk-ice samples leads to sharp decreases in salinity that are likely to be harmful for ice algae, as seen in their photophysiological responses (Garrison and Buck, 1986; Mikkelsen and Witkowski, 2010). In contrast to previous studies that recommend rapid direct melt of bulk-ice samples (at room temperature for about 12 h) (Rintala et al., 2014), or a slow melt without the addition of FSW to buffer changes in salinity (at 4 °C for 4.5 days) (Mikkelsen and Witkowski, 2010), we advocate against directly melting bulk-ice samples due to the significant impact of a salinity reduction from 33 to 10 on Chl *a* (Figure 6), cell abundance (Figure 7), and photophysiological parameters of experimental cultures (Figures 8, 9). Instead, we support recommendations to buffer bulk-ice samples by adding FSW, thus yielding a final bulk-ice salinity on the order of 20 – 30 (Campbell et al., 2019). Alternatively, samples can be buffered such that the final salinity of melted ice is representative of *in situ* salinities of ice-ocean interface or brine environments (Campbell et al., 2019). We also recommend to gradually melt the bulk-ice samples to avoid rapid decreases in salinity and intense hypoosmotic stress, for instance, for 24 h. However, melting ice samples for days prior to measurements should be avoided as decreases in salinity may lead to the underestimation of Chl *a* and cell abundance on long-term exposure, and it is likely to alter the algal photophysiology from normal *in situ* states of acclimation.

5 Conclusion

The sea ice in two Arctic fjords (Tempelfjorden and Van Mijenfjorden) had different bulk-ice salinities at the time of sampling, which alongside differences in brine nutrient concentrations, under-ice light availability, and other factors (e.g., community composition/seasonal progression of sea ice algae, ice permeability and age), may help explain observed variability in ice algal Chl *a* and photophysiology. A direct effect of freshening (i.e., low salinity) on the photophysiological responses of Svalbard bottom-ice algal communities could not be determined from the field data however we suggest that the low bulk-ice salinity and associated factors (brine volume fraction, nutrient availability) caused regional differences between the two studies fjords. The results from laboratory-based experiments demonstrated that a rapid drop in salinity, representative of influx of meltwater/freshwater run-off in fjord systems, has the potential to negatively affect Chl *a* biomass and algal photophysiology.

Our results suggest that the freshening of Arctic fjord waters due to climate warming, and proximity to freshwater sources (e.g., tidewater glaciers), specifically in late spring, and could result in lower sea ice algal primary productivity and photosynthetic efficiency on short-term growth (i.e., 4 – 24 h) under decreased salinity conditions as well as to lower Chl *a* and cell abundance on comparatively longer-term growth (i.e., 168 h). Nevertheless, this remains uncertain as sea ice algal community composition may change in response to freshening, highlighting the need for further species-specific studies on salinity stress responses. We note that since sea ice algal photophysiological responses are not only dependent on salinity, but also on other environmental factors that are likely to vary with the freshening of Arctic coastal waters and ongoing climate warming, we advocate sea ice scientists to investigate the combined effects of decreased salinity and other predicted environmental stressors on the long-term acclimation responses of bottom-ice algal communities growing in Arctic coastal regions. Areas of specific interests are regions where freshening is likely to increase or develop earlier in the season due to enhanced meltwater run-off from land (riverine inputs, glacial meltwater input, ice sheet melting) and sea ice melt.

Data availability statement

The datasets analyzed for this study can be found in the Norwegian Polar Institute (NPI) database on the following link: https://data.npolar.no/dataset/9c525398-0b05-4781-a236-15de282d34b0.

Author contributions

This work was conducted by ZLF and KC, and was based on the scientific experimental design of KC. All figures and tables were prepared by ZLF. Co-authors KC, BAL, RG, PA, LMG, JEO, MAG, JES and EL provided input either during the field season or/and during the laboratory experiments, as well as during the writing and editing of the article that was led by ZLF.

Funding

The author(s) declare financial support was received for the research, authorship, and/or publication of this article. This research was supported by PHOTA (Physical drivers of ice algal HOTspots in a changing Arctic Ocean) funded by the Fram Centre Arctic Ocean Flagship Program (Tromsø, Norway, #66014), Diatom-ARCTIC (Diatom Autoecological Responses with Changes To Ice Cover) project funded by the NERC Science of the Environment (NE/R012849/1; 03F0810A) and OASYS (Ocean-Air synoptic operations using coordinated autonomous robotic SYStems and micro underwater gliders) funded by the Research Council of Norway (project # 284477). Parts of this work were supported by the Norwegian Polar Institute's Arctic Ocean and Svalbard programs, and the Research Council of Norway through projects CAATEX (grant no 280531), HAVOC (grant no 280292) and the Arctic Field Grant (AFG # 322575 to ZLF). It was also funded by ACCES (project funding UNIS sea ice work): JES was funded through the 2017-2018 Belmont Forum and BiodivERsA joint call for research proposals, under the BiodivScen ERA-Net COFUND programme with Norwegian Research Council (grant no 296836) being the funding organization. This work also represents a contribution to the Scientific Coalition of Oceanographic Research (SCOR) working group ECV-Ice (Essential Climate Variables). The work by KC is also supported by the RCN BREATHE (Bottom sea ice Respiration and nutrient Exchanges Assessed for THE Arctic, grant # 325405) project.

Acknowledgments

ZLF would like to specifically acknowledge Paul Dubourg and Ulrike Dietrich for their support in the laboratory; Cecilie von Quillfeldt for sharing her diatom taxonomy expertise, thus allowing more accurate identification of main taxa and species of sea ice algae; Eirik Hellerud and Geir Ove Aspnes from NPI logistics in Longyearbyen for keeping us safe and warm during the fieldwork.

Conflict of interest

The authors declare that the research was conducted in the absence of any commercial or financial relationships that could be construed as a potential conflict of interest.

Publisher's note

Supplementary material

The Supplementary Material for this article can be found online at: https://www.frontiersin.org/articles/10.3389/fmars.2023.1221639/full#supplementary-material

References

Alkire, M. B., Nilsen, F., Falck, E., Søreide, J., and Gabrielsen, T. M. (2015). Tracing sources of freshwater contributions to first-year sea ice in Svalbard fjords. *Cont. Shelf Res.* 101, 85–97. doi: 10.1016/j.csr.2015.04.003

Andersen, R. A. (2005). *Algal culturing techniques. 1st ed.* (Burlington, MA: Elsevier Academic Press), 589.

Arrigo, K. R. (2014). Sea ice ecosystems. *Annu. Rev. Mar. Sci.* 6, 439–467. doi: 10.1146/annurev-marine-010213-135103

Arrigo, K. R. (2017). "Sea ice as a habitat for primary producers," in *Sea ice*, *3rd ed.* Ed. D. N.Thomas (Hoboken, NJ: Wiley-Blackwell), 352–369.

Arrigo, K. R., and Sullivan, C. W. (1992). The influence of salinity and temperature covariation on the photophysiological characteristics of Antarctic sea ice microalgae. *J. Phycol.* 28, 746–756. doi: 10.1111/j.0022-3646.1992.00746.x

Assur, A. (1960). *Composition of sea ice and its tensile strength. 1st ed.* (University of California: US Army Snow, Ice and Permafrost Research Establishment), 58.

Bates, S. S., and Cota, G. F. (1986). Fluorescence induction and photosynthetic responses of Arctic ice algae to sample treatment and salinity. *J. Phycol.* 22, 421–429. doi: 10.1111/j.1529-8817.1986.tb02484.x

Bintanja, R., and Andry, O. (2017). Towards a rain-dominated arctic. *Nat. Clim. Change* 7, 263–267. doi: 10.1038/nclimate3240

Błaszczyk, M., Ignatiuk, D., Uszczyk, A., Cielecka-Nowak, K., Grabiec, M., Jania, J., et al. (2019). Freshwater input to the Arctic fjord Hornsund (Svalbard). *Polar Res.* 38, 1–18. doi: 10.33265/polar.v38.3506

Borowitzka, M. A., and Vonshak, A. (2017). Scaling up microalgal cultures to commercial scale. *Eur. J. Phycol.* 52, 407–418. doi: 10.1080/09670262.2017.1365177

Boyd, P. W., Jickells, T., Law, C. S., Blain, S., Boyle, E. A., Buesseler, K. O., et al. (2007). Mesoscale iron enrichment experiments 1993-2005: synthesis and future directions. *Science* 315, 612–617. doi: 10.1126/science.1131669

Brown, K. A., Holding, J. M., and Carmack, E. C. (2020). Understanding regional and seasonal variability is key to gaining a pan-Arctic perspective on Arctic Ocean freshening. *Front. Mar. Sci.* 7. doi: 10.3389/fmars.2020.00606

Brzezinski, M. A. (1985). The Si: C: N ratio of marine diatoms: interspecific variability and the effect of some environmental variables. *J. Phycol.* 21, 347–357. doi: 10.1111/j.0022-3646.1985.00347.x

Calleja, M. L., Kerhervé, P., Bourgeois, S., Kędra, M., Leynaert, A., Devred, E., et al. (2017). Effects of increase glacier discharge on phytoplankton bloom dynamics and pelagic geochemistry in a high Arctic fjord. *Prog. Oceanogr.* 159, 195–210. doi: 10.1016/j.pocean.2017.07.005

Campbell, K., Mundy, C., Barber, D., and Gosselin, M. (2015). Characterizing the sea ice algae chlorophyll *a*–snow depth relationship over Arctic spring melt using transmitted irradiance. *J. Mar. Syst.* 147, 76–84. doi: 10.1016/j.jmarsys.2014.01.008

Campbell, K., Mundy, C., Belzile, C., Delaforge, A., and Rysgaard, S. (2018). Seasonal dynamics of algal and bacterial communities in Arctic sea ice under variable snow cover. *Polar Biol.* 41, 41–58. doi: 10.1007/s00300-017-2168-2

Campbell, K., Mundy, C., Juhl, A. R., Dalman, L. A., Michel, C., Galley, R. J., et al. (2019). Melt procedure affects the photosynthetic response of sea ice algae. *Front. Earth Sci.* 7. doi: 10.3389/feart.2019.00021

Campbell, K., Mundy, C., Landy, J., Delaforge, A., Michel, C., and Rysgaard, S. (2016). Community dynamics of bottom-ice algae in Dease Strait of the Canadian Arctic. *Prog. Oceanogr.* 149, 27–39. doi: 10.1016/j.pocean.2016.10.005

Chamberlain, E., Balmonte, J., Torstensson, A., Fong, A., Snoeijs-Leijonmalm, P., and Bowman, J. (2022). Impacts of sea ice melting procedures on measurements of microbial community structure. *Elem. Sci. Anth.* 10, 1–17. doi: 10.1525/elementa.2022.00017

Cota, G. F. (1985). Photoadaptation of high Arctic ice algae. *Nature* 315, 219–222. doi: 10.1038/315219a0

Cota, G. F., and Horne, E. P. (1989). Physical control of Arctic ice algal production. *Mar. Ecol. Prog. Ser.* 52, 111–121.

Cox, G., and Weeks, W. (1988). Numerical simulations of the profile properties of undeformed first-year sea ice during the growth season. *J. Geophys. Res.: Oceans* 93, 12449–12460. doi: 10.1029/JC093iC10p12449

Demers, S., Legendre, L., Maestrini, S. Y., Rochet, M., and Ingram, R. G. (1989). Nitrogenous nutrition of sea-ice microalgae. *Polar Biol.* 9, 377–383. doi: 10.1007/BF00442528

Fernández-Méndez, M., Olsen, L. M., Kauko, H. M., Meyer, A., Rösel, A., Merkouriadi, I., et al. (2018). Algal hot spots in a changing Arctic Ocean: Sea-ice ridges and the snow-ice interface. *Front. Mar. Sci.* 5. doi: 10.3389/fmars.2018.00075

Forwick, M., Vorren, T. O., Hald, M., Korsun, S., Roh, Y., Vogt, C., et al. (2010). Spatial and temporal influence of glaciers and rivers on the sedimentary environment in Sassenfjorden and Tempelfjorden, Spitsbergen. *Geol. Soc London Spec. Publ.* 344, 163–193. doi: 10.1144/SP344.13

Frankenstein, G., and Garner, R. (1967). Equations for determining the brine volume of sea ice from −0.5° to −22.9°C. *J. Glaciol.* 6, 943–944. doi: 10.3189/S0022143000020244

Fransson, A., Chierici, M., Nomura, D., Granskog, M. A., Kristiansen, S., Martma, T., et al. (2015). Effect of glacial drainage water on the CO2 system and ocean acidification state in an Arctic tidewater-glacier fjord during two contrasting years. *J. Geophys. Res.: Oceans* 120, 2413–2429. doi: 10.1002/2014JC010320

Fransson, A., Chierici, M., Nomura, D., Granskog, M. A., Kristiansen, S., Martma, T., et al. (2020). Influence of glacial water and carbonate minerals on wintertime sea-ice biogeochemistry and the CO2 system in an Arctic fjord in Svalbard. *Ann. Glaciol.* 61, 320–340. doi: 10.1017/aog.2020.52

Frigstad, H., Andersen, T., Bellerby, R. G., Silyakova, A., and Hessen, D. O. (2014). Variation in the seston C: N ratio of the Arctic Ocean and pan-Arctic shelves. *J. Mar. Syst.* 129, 214–223. doi: 10.1016/j.jmarsys.2013.06.004

Fripiat, F., Meiners, K. M., Vancoppenolle, M., Papadimitriou, S., Thomas, D. N., Ackley, S. F., et al. (2017). Macro-nutrient concentrations in Antarctic pack ice: Overall patterns and overlooked processes. *Elem Sci. Anth* 5, 1–13. doi: 10.1525/elementa.217

Galindo, V., Levasseur, M., Mundy, C. J., Gosselin, M., Tremblay, J.É., Scarratt, M., et al. (2014). Biological and physical processes influencing sea ice, under-ice algae, and dimethylsulfoniopropionate during spring in the Canadian Arctic Archipelago. *J. Geophys. Res.: Oceans* 119, 3746–3766. doi: 10.1002/2013JC009497

Garrison, D. L., and Buck, K. R. (1986). Organism losses during ice melting: A serious bias in sea ice community studies. *Polar Biol.* 6, 237–239. doi: 10.1007/BF00443401

Geider, R. J., and Osborne, B. A. (1992). "The photosynthesis-light response curve," in *Algal photosynthesis*, *1st ed.* (New York, NY: Springer Science), 156–191. doi: 10.1007/978-1-4757-2153-9_7

Geilfus, N.-X., Munson, K., Eronen-Rasimus, E., Kaartokallio, H., Lemes, M., Wang, F., et al. (2021). Landfast sea ice in the Bothnian Bay (Baltic Sea) as a temporary storage compartment for greenhouse gases. *Elem Sci. Anth* 9, 28. doi: 10.1525/elementa.2021.00028

Gosselin, M., Legendre, L., Therriault, J. C., and Demers, S. (1990). Light and nutrient limitation of sea-ice microalgae (Hudson Bay, Canadian Arctic). *J. Phycol.* 26, 220–232. doi: 10.1111/j.0022-3646.1990.00220.x

Gradinger, R. (1999). Vertical fine structure of the biomass and composition of algal communities in Arctic pack ice. *Mar. Biol.* 133, 745–754. doi: 10.1007/s002270050516

Gradinger, R., Bluhm, B., and Iken, K. (2010). Arctic sea-ice ridges—Safe heavens for sea-ice fauna during periods of extreme ice melt? *Deep Sea Res. Part II Top. Stud. Oceanogr.* 57, 86–95. doi: 10.1016/j.dsr2.2009.08.008

Granskog, M., Kaartokallio, H., Kuosa, H., Thomas, D. N., and Vainio, J. (2006). Sea ice in the Baltic Sea–a review. *Estuar. Coast. Shelf Sci.* 70, 145–160. doi: 10.1016/j.ecss.2006.06.001

Granskog, M., Kaartokallio, H., and Shirasawa, K. (2003). Nutrient status of Baltic Sea ice: Evidence for control by snow-ice formation, ice permeability, and ice algae. *J. Geophys. Res.: Oceans* 108, 1–9. doi: 10.1029/2002JC001386

Grant, W., and Horner, R. A. (1976). Growth responses to salinity variation in four Arctic ice diatoms. *J. Phycol.* 12, 180–185. doi: 10.1111/j.1529-8817.1976.tb00498.x

Grenfell, T. C., and Maykut, G. A. (1977). The optical properties of ice and snow in the Arctic Basin. *J. Glaciol.* 18, 445–463. doi: 10.3189/S0022143000021122

Grøntved, J. (1950). *Phytoplankton studies. First* ed (Copenhaguen: I kommission hos Munksgaard), 1–27.

Haecky, P., and Andersson, A. (1999). Primary and bacterial production in sea ice in the northern Baltic Sea. *Aquat. Microb. Ecol.* 20, 107–118. doi: 10.3354/ame020107

Halbach, L., Vihtakari, M., Duarte, P., Everett, A., Granskog, M. A., Hop, H., et al. (2019). Tidewater glaciers and bedrock characteristics control the phytoplankton growth environment in a fjord in the Arctic. *Front. Mar. Sci.* 6. doi: 10.3389/fmars.2019.00254

Hald, M., Dahlgren, T., Olsen, T.-E., and Lebesbye, E. (2001). Late holocene palaeoceanography in van mijenfjorden, svalbard. *Polar Res.* 20, 23–35. doi: 10.3402/polar.v20i1.6497

Hasle, G. R., Medlin, L. K., and Syvertsen, E. E. (1994). *Synedropsis* gen. nov., a genus of araphid diatoms associated with sea ice. *Phycologia* 33, 248–270. doi: 10.2216/i0031-8884-33-4-248.1

Hegseth, E. N., and von Quillfeldt, C. (2022). The sub-ice algal communities of the Barents sea pack ice: temporal and spatial distribution of biomass and species. *J. Mar. Sci. Eng.* 10, 1–29. doi: 10.3390/jmse10020164

Hjelle, A. (1993). *Geology of svalbard* (First ed (Oslo: Norsk Polarinstitutt), 162).

Holt, B., and Digby, S. A. (1985). Processes and imagery of first-year fast sea ice during the melt season. *J. Geophys. Res.: Oceans* 90, 5045–5062. doi: 10.1029/JC090iC03p05045

Hop, H., Mundy, C. J., Gosselin, M., Rossnagel, A. L., and Barber, D. G. (2011). Zooplankton boom and ice amphipod bust below melting sea ice in the Amundsen Gulf, Arctic Canada. *Polar Biol.* 34, 1947–1958. doi: 10.1007/s00300-011-0991-4

Hu, Y. B., Wang, F., Boone, W., Barber, D., and Rysgaard, S. (2018). Assessment and improvement of the sea ice processing for dissolved inorganic carbon analysis. *Limnol. Oceanogr.: Methods* 16, 83–91. doi: 10.1002/lom3.10229

IPCC (2019). *IPCC special report on the ocean and cryosphere in a changing climate.* H.-O. Pörtner, D. C. Roberts, V. Masson-Delmotte, P. Zhai, M. Tignor, E. Poloczanska, et al (eds.). (Cambridge, UK and New York, NY, USA: Cambridge University Press), 755 pp. doi: 10.1017/9781009157964

Järvinen, O., and Leppäranta, M. (2011). Transmission of solar radiation through the snow cover on floating ice. *J. Glaciol.* 57, 861–870. doi: 10.3189/002214311798043843

Kaartokallio, H., Søgaard, D., Norman, L., Rysgaard, S., Tison, J.-L., Delille, B., et al. (2013). Short-term variability in bacterial abundance, cell properties, and incorporation of leucine and thymidine in subarctic sea ice. *Aquat. Microb. Ecol.* 71, 57–73. doi: 10.3354/ame01667

Kanna, N., Lannuzel, D., van der Merwe, P., and Nishioka, J. (2020). Size fractionation and bioavailability of iron released from melting sea ice in a subpolar marginal sea. *Mar. Chem.* 221, 1–8. doi: 10.1016/j.marchem.2020.103774

Kanna, N., Toyota, T., and Nishioka, J. (2014). Iron and macro-nutrient concentrations in sea ice and their impact on the nutritional status of surface waters in the southern Okhotsk Sea. *Prog. Oceanogr.* 126, 44–57. doi: 10.1016/j.pocean.2014.04.012

Kauko, H. M., Olsen, L. M., Duarte, P., Peeken, I., Granskog, M. A., Johnsen, G., et al. (2018). Algal colonization of young Arctic sea ice in spring. *Front. Mar. Sci.* 5. doi: 10.3389/fmars.2018.00199

Kirst, G. (1990). Salinity tolerance of eukaryotic marine algae. *Annu. Rev. Plant Biol.* 41, 21–53. doi: 10.1146/annurev.pp.41.060190.000321

Kottmeier, S. T., and Sullivan, C. W. (1988). Sea ice microbial communities (SIMCO). *Polar Biol.* 8, 293–304. doi: 10.1007/BF00263178

Kvernvik, A. C., Hoppe, C. J. M., Greenacre, M., Verbiest, S., Wiktor, J. M., Gabrielsen, T. M., et al. (2021). Arctic sea ice algae differ markedly from phytoplankton in their ecophysiological characteristics. *Mar. Ecol. Prog. Ser.* 666, 31–55. doi: 10.3354/meps13675

Lange, B. A., Flores, H., Michel, C., Beckers, J. F., Bublitz, A., Casey, J. A., et al. (2017). Pan-Arctic sea ice-algal chl *a* biomass and suitable habitat are largely underestimated for multiyear ice. *Glob. Change Biol.* 23, 4581–4597. doi: 10.1111/gcb.13742

Lange, B. A., Michel, C., Beckers, J. F., Casey, J. A., Flores, H., Hatam, I., et al. (2015). Comparing springtime ice-algal chlorophyll *a* and physical properties of multi-year and first-year sea ice from the Lincoln Sea. *PloS One* 10, e0122418. doi: 10.1371/journal.pone.0122418

Larsen, E., Lyså, A., Rubensdotter, L., Farnsworth, W. R., Jensen, M., Nadeau, M. J., et al. (2018). Lateglacial and Holocene glacier activity in the Van Mijenfjorden area, western Svalbard. *Arktos* 4, 1–21. doi: 10.1007/s41063-018-0042-2

Lee, S. H., McRoy, C. P., Joo, H. M., Gradinger, R., Cui, X., Yun, M. S., et al. (2011). Holes in progressively thinning Arctic sea ice lead to new ice algae habitat. *Oceanography* 24, 302–308. doi: 10.5670/oceanog.2011.81

Legendre, L., Ackley, S., Dieckmann, G., and Gulliksen, B. (1992a). Ecology of sea ice biota. part 2. Global Significance. *Polar Biol.* 12, 429–444. doi: 10.1007/BF00243114

Legendre, L., Demers, S., Yentsch, C. M., and Yentsch, C. S. (1983). The 14C method: Patterns of dark CO2 fixation and DCMU correction to replace the dark bottle. *Limnol. Oceanogr.* 28, 996–1003. doi: 10.4319/lo.1983.28.5.0996

Legendre, L., Martineau, M.-J., Therriault, J.-C., and Demers, S. (1992b). Chlorophyll *a* biomass and growth of sea-ice microalgae along a salinity gradient (southeastern Hudson Bay, Canadian Arctic). *Polar Biol.* 12, 445–453. doi: 10.1007/BF00243115

Leu, E., Brown, T. A., Graeve, M., Wiktor, J., Hoppe, C. J., Chierici, M., et al. (2020). Spatial and temporal variability of ice algal trophic markers—with recommendations about their application. *J. Mar. Sci. Eng.* 8, 676. doi: 10.3390/jmse8090676

Leu, E., Mundy, C., Assmy, P., Campbell, K., Gabrielsen, T., Gosselin, M., et al. (2015). Arctic spring awakening–Steering principles behind the phenology of vernal ice algal blooms. *Prog. Oceanogr.* 139, 151–170. doi: 10.1016/j.pocean.2015.07.012

Leu, E., Wiktor, J., Søreide, J., Berge, J., and Falk-Petersen, S. (2010). Increased irradiance reduces food quality of sea ice algae. *Mar. Ecol. Prog. Ser.* 411, 49–60. doi: 10.3354/meps08647

Lomas, M. W., and Glibert, P. M. (2000). Comparisons of nitrate uptake, storage, and reduction in marine diatoms and flagellates. *J. Phycol.* 36, 903–913. doi: 10.1046/j.1529-8817.2000.99029.x

McGovern, M., Borgå, K., Heimstad, E., Ruus, A., Christensen, G., and Evenset, A. (2022). Small Arctic rivers transport legacy contaminants from thawing catchments to coastal areas in Kongsfjorden, Svalbard. *Environ. Pollut.* 304, 1–7. doi: 10.1016/j.envpol.2022.119191

McGovern, M., Pavlov, A. K., Deininger, A., Granskog, M. A., Leu, E., Søreide, J. E., et al. (2020). Terrestrial inputs drive seasonality in organic matter and nutrient biogeochemistry in a high Arctic fjord system (Isfjorden, Svalbard). *Front. Mar. Sci.* 7. doi: 10.3389/fmars.2020.542563

McMinn, A., and Hegseth, E. (2004). Quantum yield and photosynthetic parameters of marine microalgae from the southern Arctic Ocean, Svalbard. *J. Mar. Biol. Assoc. United Kingdom* 84, 865–871. doi: 10.1017/S0025315404010112h

Medlin, L. K., and Hasle, G. R. (1990). Some Nitzschia and related diatom species from fast ice samples in the Arctic and Antarctic. *Polar Biol.* 10, 451–479. doi: 10.1007/BF00233693

Meiners, K. M., Vancoppenolle, M., Carnat, G., Castellani, G., Delille, B., Delille, D., et al. (2018). Chlorophyll-*a* in Antarctic landfast sea ice: A first synthesis of historical ice core data. *J. Geophys. Res.: Oceans* 123, 8444–8459. doi: 10.1029/2018JC014245

Meire, L., Meire, P., Struyf, E., Krawczyk, D., Arendt, K., Yde, J., et al. (2016). High export of dissolved silica from the Greenland Ice Sheet. *Geophys. Res. Lett.* 43, 9173–9182. doi: 10.1002/2016GL070191

MET. (2021). *Norway*. Available at: https://cryo.met.no/archive/ice-service/icecharts/quicklooks/ (Accessed 19 April 2022).

Mikkelsen, D. M., Rysgaard, S., and Glud, R. N. (2008). Microalgal composition and primary production in Arctic sea ice: a seasonal study from Kobbefjord (Kangerluarsunnguaq), West Greenland. *Mar. Ecol. Prog. Ser.* 368, 65–74. doi: 10.3354/meps07627

Mikkelsen, D. M., and Witkowski, A. (2010). Melting sea ice for taxonomic analysis: a comparison of four melting procedures. *Polar Res.* 29, 451–454. doi: 10.3402/polar.v29i3.6088

Mundy, C. J., Gosselin, M., Ehn, J. K., Belzile, C., Poulin, M., Alou, E., et al. (2011). Characteristics of two distinct high-light acclimated algal communities during advanced stages of sea ice melt. *Polar Biol.* 34, 1869–1886. doi: 10.1007/s00300-011-0998-x

Murray, T., Luckman, A., Strozzi, T., and Nuttall, A.-M. (2003). The initiation of glacier surging at Fridtjovbreen, Svalbard. *Ann. Glaciol.* 36, 110–116. doi: 10.3189/172756403781816275

Nelson, D. M., Ahern, J. A., and Herlihy, L. J. (1991). Cycling of biogenic silica within the upper water column of the Ross Sea. *Mar. Chem.* 35, 461–476. doi: 10.1016/S0304-4203(09)90037-8

Nicolaus, M., Gerland, S., Hudson, S. R., Hanson, S., Haapala, J., and Perovich, D. K. (2010). Seasonality of spectral albedo and transmittance as observed in the Arctic Transpolar Drift in 2007. *J. Geophys. Res.: Oceans* 115, 1–21. doi: 10.1029/2009JC006074

Nicolaus, M., and Katlein, C. (2013). Mapping radiation transfer through sea ice using a remotely operated vehicle (ROV). *Cryosphere* 7, 763–777. doi: 10.5194/tc-7-763-2013

Niemi, A., and Michel, C. (2015). Temporal and spatial variability in sea-ice carbon: nitrogen ratios on Canadian Arctic shelves. *Elem. Sci. Anth.* 3, 1–12. doi: 10.12952/journal.elementa.000078

Pankowski, A., and McMinn, A. (2008). Ferredoxin and flavodoxin in eastern Antarctica pack ice. *Polar Biol.* 31, 1153–1165. doi: 10.1007/s00300-008-0451-y

Parsons, T. R., Maita, Y., and Lalli, C. M. (1984) *A manual of chemical & biological methods for seawater analysis* (New York, NY: Pergamon Press, Elsevier) (Accessed First ed).

Pavlova, O., Gerland, S., and Hop, H. (2019). "Changes in sea-ice extent and thickness in Kongsfjorden, Svalbard, (2003–2016)," in *The ecosystem of kongsfjorden, svalbard* (Cham: Springer Nature), 105–136. doi: 10.1007/978-3-319-46425-1_4

Piiparinen, J., Kuosa, H., and Rintala, J.-M. (2010). Winter-time ecology in the Bothnian Bay, Baltic Sea: nutrients and algae in fast ice. *Polar Biol.* 33, 1445–1461. doi: 10.1007/s00300-010-0771-6

Platt, T., Gallegos, C., and Harrison, W. G. (1980). Photoinhibition of photosynthesis in natural assemblages of marine phytoplankton. *J. Mar. Res.* 38, 687–701.

Pogojeva, M., Polukhin, A., Makkaveev, P., Staalstrøm, A., Berezina, A., and Yakushev, E. (2022). Arctic inshore biogeochemical regime influenced by coastal runoff and glacial melting (case study for the Templefjord, Spitsbergen). *Geosciences* 12, 1–29. doi: 10.3390/geosciences12010044

Poulin, M., Daugbjerg, N., Gradinger, R., Ilyash, L., Ratkova, T., and von Quillfeldt, C. (2011). The pan-Arctic biodiversity of marine pelagic and sea-ice unicellular eukaryotes: a first-attempt assessment. *Mar. Biodivers.* 41, 13–28. doi: 10.1007/s12526-010-0058-8

Poulin, M., Underwood, G. J., and Michel, C. (2014). Sub-ice colonial *Melosira arctica* in Arctic first-year ice. *Diatom Res.* 29, 213–221. doi: 10.1080/0269249X.2013.877085

Provost, C., Sennéchael, N., Miguet, J., Itkin, P., Rösel, A., Koenig, Z., et al. (2017). Observations of flooding and snow-ice formation in a thinner Arctic sea-ice regime during the N-ICE2015 campaign: Influence of basal ice melt and storms. *J. Geophys. Res.: Oceans* 122, 7115–7134. doi: 10.1002/2016JC012011

Rabault, J., Sutherland, G., Ward, B., Christensen, K. H., Halsne, T., and Jensen, A. (2016). Measurements of waves in landfast ice using inertial motion units. *IEEE Trans. Geosci* 54, 6399–6408. doi: 10.1109/TGRS.2016.2584182

Ralph, P. J., Ryan, K. G., Martin, A., and Fenton, G. (2007). Melting out of sea ice causes greater photosynthetic stress in algae than freezing in. *J. Phycol.* 43, 948–956. doi: 10.1111/j.1529-8817.2007.00382.x

Reigstad, M., Wexels Riser, C., Wassmann, P., and Ratkova, T. (2008). Vertical export of particulate organic carbon: Attenuation, composition and loss rates in the northern Barents Sea. *Deep Sea Res. Part II Top. Stud. Oceanogr.* 55, 2308–2319. doi: 10.1016/j.dsr2.2008.05.007

Riedel, A., Michel, C., Gosselin, M., and LeBlanc, B. (2008). Winter–spring dynamics in sea-ice carbon cycling in the coastal Arctic Ocean. *J. Mar. Syst.* 74, 918–932. doi: 10.1016/j.jmarsys.2008.01.003

Rintala, J.-M., Piiparinen, J., Blomster, J., Majaneva, M., Müller, S., Uusikivi, J., et al. (2014). Fast direct melting of brackish sea-ice samples results in biologically more accurate results than slow buffered melting. *Polar Biol.* 37, 1811–1822. doi: 10.1007/s00300-014-1563-1

Ryan, K., Ralph, P., and McMinn, A. (2004). Acclimation of Antarctic bottom-ice algal communities to lowered salinities during melting. *Polar Biol.* 27, 679–686. doi: 10.1007/s00300-004-0636-y

Seklima. (2021a). *Svalbard lufthavn* (Norway: The Norwegian Meteorological Institute). Available at: https://seklima.met.no (Accessed 8 May 2022).

Seklima. (2021b). *Sveagruva* (Norway: The Norwegian Meteorological Institute). Available at: https://seklima.met.no (Accessed 8 May 2022).

Seklima. (2021c). *Svalbard lufthavn* (Norway: The Norwegian Meteorological Institute). Available at: https://seklima.met.no (Accessed 23 August 2023).

Skarðhamar, J., and Svendsen, H. (2010). Short-term hydrographic variability in a stratified Arctic fjord. *Geol. Soc London Spec. Publ.* 344, 51–60. doi: 10.1144/SP344.5

Smith, M. M., von Albedyll, L., Raphael, I. A., Lange, B. A., Matero, I., Salganik, E., et al. (2022). Quantifying false bottoms and under-ice meltwater layers beneath Arctic summer sea ice with fine-scale observations. *Elem. Sci. Anth.* 10, 1–19. doi: 10.1525/elementa.2021.000116

Søgaard, D. H., Hansen, P. J., Rysgaard, S., and Glud, R. N. (2011). Growth limitation of three Arctic sea ice algal species: effects of salinity, pH, and inorganic carbon availability. *Polar Biol.* 34, 1157–1165. doi: 10.1007/s00300-011-0976-3

Søgaard, D. H., Kristensen, M., Rysgaard, S., Glud, R. N., Hansen, P. J., and Hilligsøe, K. M. (2010). Autotrophic and heterotrophic activity in Arctic first-year sea ice: seasonal study from Malene Bight, SW Greenland. *Mar. Ecol. Prog. Ser.* 419, 31–45. doi: 10.3354/meps08845

Strickland, J. D. H., and Parsons, T. R. (1972). *A practical handbook of seawater analysis. 2nd ed.* (Ottawa, ON: Fisheries Research Board of Canada), 310.

Sutherland, G., and Rabault, J. (2016). Observations of wave dispersion and attenuation in landfast ice. *J. Geophys. Res.: Oceans* 121, 1984–1997. doi: 10.1002/2015JC011446

Svendsen, H., Beszczynska-Møller, A., Hagen, J. O., Lefauconnier, B., Tverberg, V., Gerland, S., et al. (2002). The physical environment of Kongsfjorden–Krossfjorden, an Arctic fjord system in Svalbard. *Polar Res.* 21, 133–166. doi: 10.3402/polar.v21i1.6479

Taguchi, S. (1976). Relationship between photosynthesis and cell size of marine diatoms. *J. Phycol.* 12, 185–189. doi: 10.1111/j.1529-8817.1976.tb00499.x

Tamelander, T., Reigstad, M., Hop, H., and Ratkova, T. (2009). Ice algal assemblages and vertical export of organic matter from sea ice in the Barents Sea and Nansen Basin (Arctic Ocean). *Polar Biol.* 32, 1261–1273. doi: 10.1007/s00300-009-0622-5

Tedesco, L., Vichi, M., and Scoccimarro, E. (2019). Sea-ice algal phenology in a warmer Arctic. *Sci. Adv.* 5, 1–12. doi: 10.1126/sciadv.aav4830

Thomas, D. N. (2017). *Sea ice. 3rd ed.* (Hoboken NJ: Wiley-Blackwell), 664. doi: 10.1002/9781118778371

Tréguer, P. J., and Rocha, C. L. D. L. (2013). The world ocean silica cycle. *Annu. Rev. Mar. Sci.* 5, 477–501. doi: 10.1146/annurev-marine-121211-172346

Urbański, J. A., and Litwicka, D. (2021). Accelerated decline of Svalbard coasts fast ice as a result of climate change. *Cryosphere.* 2021, 1–15. doi: 10.5194/tc-2021-21

Van Leeuwe, M. A., Tedesco, L., Arrigo, K. R., Assmy, P., Campbell, K., Meiners, K. M., et al. (2018). Microalgal community structure and primary production in Arctic and Antarctic sea ice: A synthesis. *Elem. Sci. Anth.* 6, 1–25. doi: 10.1525/elementa.267

Vargo, G., Fanning, K., Heil, C., and Bell, L. (1986). Growth rates and the salinity response of an Antarctic ice microflora community. *Polar Biol.* 5, 241–247. doi: 10.1007/BF00446092

Vonnahme, T. R., Persson, E., Dietrich, U., Hejdukova, E., Dybwad, C., Elster, J., et al. (2021). Early spring subglacial discharge plumes fuel under-ice primary production at a Svalbard tidewater glacier. *Cryosphere* 15, 2083–2107. doi: 10.5194/tc-15-2083-2021

von Quillfeldt, C. H. (1996). Ice algae and phytoplankton in north Norwegian and Arctic waters: species composition, succession, and distribution. PhD thesis (Tromsø: University of Tromsø).

von Quillfeldt, C. H., Hegseth, E. N., Sakshaug, E., Johnsen, G., and Syvertsen, E. E. (2009). "Ice algae," in *Ecosystem barents sea*. Eds. E. Sakshaug and G.J. &K. M. Kovacs (Trondheim: Tapir Academic Press), 285–302.

Wassmann, P., Duarte, C. M., Agusti, S., and Sejr, M. K. (2011). Footprints of climate change in the Arctic marine ecosystem. *Glob. Change Biol.* 17, 1235–1249. doi: 10.1111/j.1365-2486.2010.02311.x

Weeks, W. F., and Ackley, S. F. (1982). "The growth, structure, and properties of sea ice," in *The geophysics of sea ice* (Boston, MA: Springer), 9–164. doi: 10.1007/978-1-4899-5352-0_2

Yan, D., Yoshida, K., Nishioka, J., Ito, M., Toyota, T., and Suzuki, K. (2020). Response to sea ice melt indicates high seeding potential of the ice diatom *Thalassiosira* to spring phytoplankton blooms: a laboratory study on an ice algal community from the Sea of Okhotsk. *Front. Mar. Sci.* 7. doi: 10.3389/fmars.2020.00613

Yoshida, K., Hattori, H., Toyota, T., McMinn, A., and Suzuki, K. (2020). Differences in diversity and photoprotection capability between ice algae and under-ice phytoplankton in Saroma-Ko Lagoon, Japan: a comparative taxonomic diatom analysis with microscopy and DNA barcoding. *Polar Biol.* 43, 1873–1885. doi: 10.1007/s00300-020-02751-x

Yun, M. S., Whitledge, T. E., Kong, M., and Lee, S. H. (2014). Low primary production in the Chukchi Sea shelf 2009. *Cont. Shelf Res.* 76, 1–11. doi: 10.1016/j.csr.2014.01.001

Yun, M., Whitledge, T., Stockwell, D., Son, S., Lee, J., Park, J., et al. (2016). Primary production in the Chukchi Sea with potential effects of freshwater content. *Biogeosciences* 13, 737–749. doi: 10.5194/bg-13-737-2016

Zhang, Q., Gradinger, R., and Spindler, M. (1999). Experimental study on the effect of salinity on growth rates of Arctic-sea-ice algae from the Greenland Sea. *Boreal Environ. Res.* 4, 1–8.

frontiers | Frontiers in Marine Science

TYPE Original Research
PUBLISHED 05 January 2024
DOI 10.3389/fmars.2023.1283265

OPEN ACCESS

EDITED BY
Yanpei Zhuang,
Jimei University, China

REVIEWED BY
Jianping Li,
Chinese Academy of Sciences (CAS), China
Marco Baity-Jesi,
Swiss Federal Institute of Aquatic Science and Technology, Switzerland

*CORRESPONDENCE
Vito Paolo Pastore
✉ vito.paolo.pastore@unige.it

RECEIVED 25 August 2023
ACCEPTED 06 December 2023
PUBLISHED 05 January 2024

CITATION
Ciranni M, Odone F and Pastore VP (2024) Anomaly detection in feature space for detecting changes in phytoplankton populations.
Front. Mar. Sci. 10:1283265.
doi: 10.3389/fmars.2023.1283265

Anomaly detection in feature space for detecting changes in phytoplankton populations

Massimiliano Ciranni, Francesca Odone and Vito Paolo Pastore*

MaLGa-DIBRIS, Università degli studi di Genova, Genoa, Italy

Plankton organisms are fundamental components of the earth's ecosystem. Zooplankton feeds on phytoplankton and is predated by fish and other aquatic animals, being at the core of the aquatic food chain. On the other hand, Phytoplankton has a crucial role in climate regulation, has produced almost 50% of the total oxygen in the atmosphere and it's responsible for fixing around a quarter of the total earth's carbon dioxide. Importantly, plankton can be regarded as a good indicator of environmental perturbations, as it can react to even slight environmental changes with corresponding modifications in morphology and behavior. At a population level, the biodiversity and the concentration of individuals of specific species may shift dramatically due to environmental changes. Thus, in this paper, we propose an anomaly detection-based framework to recognize heavy morphological changes in phytoplankton at a population level, starting from images acquired in situ. Given that an initial annotated dataset is available, we propose to build a parallel architecture training one anomaly detection algorithm for each available class on top of deep features extracted by a pre-trained Vision Transformer, further reduced in dimensionality with PCA. We later define global anomalies, corresponding to samples rejected by all the trained detectors, proposing to empirically identify a threshold based on global anomaly count over time as an indicator that can be used by field experts and institutions to investigate potential environmental perturbations. We use two publicly available datasets (WHOI22 and WHOI40) of grayscale microscopic images of phytoplankton collected with the Imaging FlowCytobot acquisition system to test the proposed approach, obtaining high performances in detecting both in-class and out-of-class samples. Finally, we build a dataset of 15 classes acquired by the WHOI across four years, showing that the proposed approach's ability to identify anomalies is preserved when tested on images of the same classes acquired across a timespan of years.

KEYWORDS

anomaly detection, deep features extraction, plankton image analysis, deep learning, one-class SVM

1 Introduction

The term plankton refers to drifter microorganisms that flow passively in the water. It includes unicellular plants that contain chlorophyll and perform photosynthesis (Winder and Sommer, 2012), named Phytoplankton, and generally millimetric or smaller animals, called Zooplankton (Brierley, 2017). Phytoplankton significantly impacts global climate regulation and has produced around 50% of the total oxygen in the atmosphere (Benfield et al., 2007). Moreover, it is responsible for approximately 45% of global earth primary production (Uitz et al., 2010), with plankton diatoms being responsible for fixing at least a quarter of the inorganic carbon in the ocean on an annual basis (Brierley, 2017). Zooplankton pastures on Phytoplankton, and is predated by fish and other aquatic animals, collocating these fundamental organisms at the core of the aquatic food chain. Importantly, Plankton organisms can be regarded as a good indicator of climate change and modifications (Hays et al., 2005) with high sensitivity, as subtle environmental perturbations can be magnified by the responses of biological communities (Taylor et al., 2002). Plankton microorganisms, in fact, may exhibit distinct physiological modifications as a response to even slight perturbations in the aquatic environment, resulting in changes at an individual and population level. At an individual level, such physiological alterations may correspond to morphological and behavioral changes. To provide an example, when encountering chemicals released by predators, numerous zooplankton physiologically exhibit morphological and behavioral responses (Ohman, 1988). On a population level, environmental changes may affect biodiversity and species abundance, possibly reverting species dominance (Hanazato, 2001). Recently, it has been proposed to employ plankton as biosensors exploiting acquired images and machine learning tools (Pastore et al., 2019; Pastore et al., 2022). This involves establishing a baseline for the *average* plankton morphology of known classes, included in an initial training set, and using it to identify deviations, which could serve as indicators of environmental changes, whether of human origin or natural.

In the last years, a massive amount of plankton images has been gathered, thanks to technologically advanced automatic acquisition systems (Benfield et al., 2007; Lombard et al., 2019). The availability of such an increasingly large number of images makes manual species identification and image analysis impractical (Alfano et al,. 2022), paving the way to machine learning-based solutions. The majority of available works on automatic plankton image classification involve supervised learning methods relying on annotations. Hand-crafted descriptors based on shape, texture, or multiscale visual features can be used alongside a trainable classifier: for example in Sosik and Olson (2007), multiple hand-crafted features are computed from raw images and then fed to an SVM classifier, while in Zheng et al. (2017) feature selection is employed on several sets of hand-crafted features to maximize features importance, and multiple kernel learning (Gönen and Alpaydın, 2011) is adopted by the authors and provides improved classification performances on different plankton image datasets, with respect to comparable approaches. With the development and diffusion of deep neural networks for vision tasks, deep learning-driven solutions have increasingly been adopted for plankton image classification: in the last few years, the best-performing techniques have been based on ensembles composed of many deep networks, capable of yielding quasi-optimal classification performance on annotated datasets of varying size (Lumini and Nanni, 2019; Kyathanahally et al., 2021; Maracani et al., 2023). Recent works related to plankton image analysis and classification experimented with hybrid approaches, such as Semi-Supervised Learning applied to population counting in Orenstein et al. (2020a), or classification through *Content-Based Image Retrieval* (Yang et al., 2022). We can also find two works employing anomaly detection and *outlier-exposure* techniques to aid classifiers in taxonomic classification: in Pu et al. (2021) the authors build a dataset of anomalies and a custom loss to both improve classification performances and to detect anomalous images; Walker and Orenstein (2021) employ *Hard-Negative-Mining* and *Background Resampling* to improve the detection rate of rare classes. Additionally, for the purpose of this work, it is worth pointing out that in Orenstein and Beijbom (2017) it is shown that pre-training deep neural networks on large-scale general-purpose image datasets gives a better transfer-learning baseline for plankton image classification over the one that could be obtained by pre-training on in-domain planktonic image datasets, even if of comparable size (Maracani et al., 2023). An image-based machine learning framework for the usage of plankton as a biosensor has been proposed in Pastore et al, 2019; Pastore et al, 2022). In Pastore et al. (2019) the authors extract a set of 128 descriptors from a subset of plankton images with 100 images for 10 classes, extracted from the WHOI dataset. The engineered descriptors incorporate both shape-based features, including geometric descriptors and image moments, and texture-based features, such as Haralick and local binary patterns. The authors employ a one-class SVM anomaly detection algorithm, proposing to detect deviation from the average appearance for each of the training classes, as an indicator of potential environmental perturbations. In Pastore et al. (2022), a custom anomaly detection algorithm, TailDeTect (TDT) is exploited to perform novel class detection, starting from an available annotated set of plankton images. The authors exploit a set of 131 hand-crafted features, reaching a high accuracy in the novel class detection task, for an in-house plankton dataset, acquired using a lensless microscope and released in Pastore et al. (2020). An important limitation of these works is the coarse granularity of the investigated plankton dataset. A fundamental prerequisite for a machine learning framework to be actually used in the task of suggesting potential environmental changes using plankton images is represented by the possibility of correctly separating morphologically fine-grained classes, where the intra-class morphological features are in the same order of magnitude as the inter-class ones. Moreover, recent works on unsupervised learning of plankton images (Alfano et al,. 2022), have shown that features extracted by means of ImageNet pre-trained deep neural networks provide an embedding leading to higher accuracy than hand-crafted features.

In this context, we propose a semi-automatic approach where a machine learning framework is designed to automatically detect anomalies in the feature space extracted from acquired phytoplankton images, while an engineering pipeline is sketched to exploit plankton's feedback for revealing potential environmental changes. Our machine learning framework consists in anomaly detection algorithms coupled to features extracted from acquired images by means of ImageNet pre-trained Vision Transformers, relying on the possibility of detecting samples belonging to classes with shape or morphology significantly different with respect to the training ones. Such anomalies can be related to different main sources, including (i) Morphological modifications potentially linked to environmental changes human-made or natural; (ii) novel classes (i.e., classes not included in the training set); (iii) image artifacts (caused by different factors, including the acquisition system and water condition). Besides, it is known that distribution shifts for the same species across time are likely to happen (González et al., 2017). Thus, we may expect a certain number of anomalies to be detected on a regular basis at the site of acquisition. We envision determining critical situations corresponding to a significant increase in the detected anomalies with respect to the average number of anomalies per time. At this stage, we propose to have a human in the loop, so that a selection of such anomalies may be provided to experts in the field to actually discriminate between the different sources of anomalies, potentially recognizing environmental threats. To summarize, the main contributions of this paper can be regarded as follows: (i) We introduce an anomaly detection-based approach for detecting significant variations in acquired phytoplankton images, potentially linked to environmental changes. Differently from the state-of-the-art, we exploit a set of features extracted by an ImageNet22K pre-trained vision transformer, coupled to a dimensionality reduction algorithm based on PCA. Assuming the availability of an initial annotated dataset, we propose to train one anomaly detector for each of the available classes, further arranging them in a parallel architecture, capable of detecting in-class samples and global anomalies, that is, a sample that is simultaneously rejected by all the trained anomaly detectors. The designed approach is modular, allowing to add new classes by training a new corresponding anomaly detector, without the need to re-train the other detectors. We test the proposed approach on two fine-grained publicly available plankton datasets (WHOI22 (Sosik and Olson, 2007) and WHOI40 (Pastore et al., 2020), containing grayscale microscopic images of phytoplankton collected with the Imaging FlowCytobot (IFCB) system typically used as benchmarks for plankton image classification (Zheng et al., (2017); Lumini et al., 2020; Kyathanahally et al., 2021). (ii) We build a phytoplankton image dataset that we name WHOI15, considering 15 classes including detritus among 4 different years of acquisition (from 2007 to 2010), proving that our anomaly detection algorithms can generalize well in recognizing anomalies or a novel class in different years of acquisition with respect to the training one. Exploiting the concept of global anomalies, we sketch an engineering pipeline capable of providing alerts representing phytoplankton changes potentially related to environmental perturbations.

The remainder of the paper is organized as follows: in Sec. 2, we describe the proposed approach and its main components. In Sec. 3, we describe the datasets used in this work, providing experiment details and results, later discussed in Sec. 4.

2 Methods

In this study, we introduce a novel approach for automatically determining anomalies in phytoplankton images, that can be further related to environmental changes. The designed method, as depicted in Figure 1, consists of three key stages: (i) Feature extraction and compression, (ii) Anomaly detection, and (iii) Anomaly storage and analysis. Initially, we assume the availability of a plankton image dataset with expert-provided labels. These images are then processed using an ImageNet pre-trained Vision Transformer to extract relevant features. The resulting high-dimensionality descriptors are then compressed through Principal Component Analysis (PCA) and further used to train an anomaly

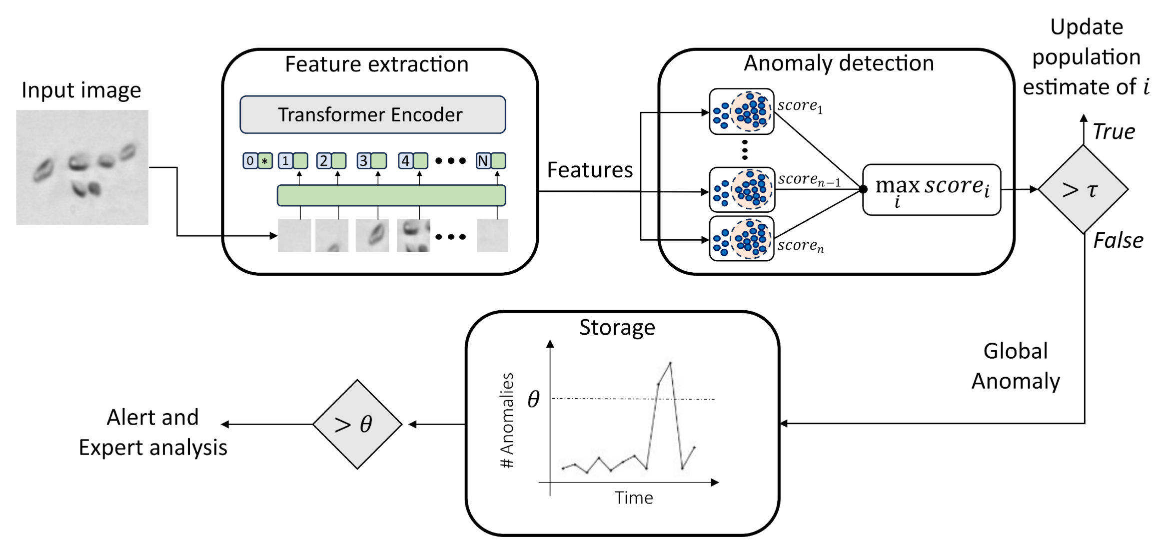

FIGURE 1
Schematic representation of the pipeline proposed to perform environmental monitoring with plankton.

detection algorithm for each of the classes available in the initial training set. In the test phase, the same set of compressed descriptors is extracted from previously unseen plankton images. At this stage, the descriptors are fed to each of the trained anomaly detectors. More details on the investigated anomaly detection algorithms can be found in Sec. 3.3.1. For the anomaly detector i, corresponding to the training classes i, the response is a score of membership $score_i$, which may assume positive or negative values. Intuitively, the lower the score, the more the anomaly detector is confident in rejecting that sample and vice-versa. The entire set of anomaly detectors is placed in a parallel architecture, and the one providing the maximum score is selected, as shown in Figure 1. If the maximum score is higher than a threshold τ, then the sample is recognized as belonging to the corresponding class, and thus, the population count for the corresponding class is increased. Otherwise, we treat the sample as a global anomaly, and we propose to store it for further analysis. This implementation strategy allows us to efficiently handle co-activations, which are likely to happen, either for an abundance of detritus, fibers, and noisy samples or just because of the fine-grained features typically shown by plankton species.

In the following paragraph, we provide more details about each of the three components of the proposed method.

2.1 Feature extraction and compression

Our main idea is to detect and quantify plankton response to environmental threats as significant deviations from the average appearance of plankton microorganisms, inferred from acquired images. To support this objective, the first phase of the proposed approach consists in the extraction of highly discriminative features for plankton images, capable of detecting changes in the visual characteristics of planktonic images with the highest possible resolution.

Inspired by recent works (Salvesen et al., 2022; Alfano et al., 2022; Maracani et al., 2023; Pastore et al., 2023), we exploit a transfer learning framework to extract our set of phytoplankton descriptors. In such an approach, a large-scale dataset (source) is used to learn knowledge that is later transferred to the dataset of interest (target). We adopt a Vision Transformer (ViT-L16) pre-trained on ImageNet22K as a feature extractor, resulting in 1024 deep features per image. Additionally, we reduce the dimensionality of the obtained descriptors with PCA, in an attempt to temper the *curse of dimensionality* (Bellman, 1966; Verleysen and Francois, 2005).

2.2 Anomaly detection

The deep features extracted by means of the pre-trained Vision Transformer are used for training a set of anomaly detection algorithms. We train a separate detector for each class available in the training set. The trained detectors are later organized into a parallel architecture, and during testing, each test image is fed to every individual anomaly detector. Each anomaly detector provides a membership score corresponding to the fed image. At this stage, we have two possible outcomes: (i) the maximum score is higher than or equal to a threshold τ. In this case, the image is classified as belonging to the class corresponding to the detector, and the population counts for that class are updated (ii) the maximum score is lower than a threshold τ. The test image is rejected, labeled as a global anomaly, and stored for further analysis. See Sec. 3.3.1 for more details on the investigated anomaly detection algorithms. The threshold τ is an important hyperparameter, that we tune with an automatic procedure. See section 3.2.3 for more details.

2.3 Anomaly storage and alert

The detected global anomalies are stored and anomaly counting is updated. The number of anomalies as well as the evolution of population counts in time can be regarded as measurable feedback for the environmental monitoring task objective of our work. Describing the engineering framework for measuring the designed feedback is out of the scope of this work. However, we envision the possibility of setting an automatic alert when the anomaly frequency is higher than a threshold, that may be set by field experts through preliminary *in situ* tests. Images triggering anomalies are stored as well, allowing offline expert analyses to get better insights from the generated alerts.

2.4 Evaluation metrics

Our approach is based on the concept of anomaly detection, where one anomaly detector is trained for each distinct class available in the training set. Therefore the performances of our method can be measured through binary evaluation metrics. Specifically, given a sample belonging to training class k, we identify two possible outcomes: (i) the sample is recognized by the detector A_k (it brings the maximum membership score in the anomaly detector k, and such score is higher than the threshold τ, see Sec. 2.2). In this case, the sample is regarded as a True Positive (TP); (ii) the sample is rejected by all the trained detectors and it is treated as a False Negative (FN).

At this stage, we employ a leave-one-out approach, removing the detector A_k from our parallel architecture for each training class k, with two additional outcomes: (iii) the sample is recognized as in class by any of the remaining anomaly detectors. We refer to this sample as a False Positive (FP); (iv) the sample is correctly rejected by all the detectors. In this case, the sample is labeled as a True Negative (TN).

Therefore, exploiting the TP, FP, FN and TN definitions provided above, we select the Sensitivity (True Positive Rate or TPR), the Specificity (True Negative Rate or TNR) and the False Negative Rate (FNR) as reference metrics for our method, computed as described in Equations 1-3:

$$\text{Sensitivity (TPR)} := \frac{\text{True Positives}}{\text{Total Number of Positive Samples}} = \frac{TP}{TP + FN} \quad (1)$$

$$\text{Specificity (TNR)} := \frac{\text{True Negatives}}{\text{Total Number of Negative Samples}} = \frac{TN}{TN + FP} \quad (2)$$

$$FNR := \frac{\text{False Negatives}}{\text{False Negatives} + \text{True Positives}} = \frac{FN}{FN + TP} \quad (3)$$

It is worth noticing that a last important source of errors is represented by misclassified samples, that is, samples recognized by the incorrect anomaly detector. The rate of such misclassifed samples can be obtained from the described metrics, as 1 - (Sensitivity + FNR). In the computation of sensitivity, the FN include both the misclassified and the uncorrectly rejected samples.

3 Experiments

3.1 Datasets description

In this section, we describe the datasets we employed in this work for training the components of our pipeline, testing overall performance, and assessing the effectiveness of the proposed approach.

The images we used for our experiments come from the WHOI-Plankton Dataset (Sosik and Brownlee, 2015), a large-scale dataset containing grayscale microscopic plankton images from 103 different classes, acquired with IFCB by the Woods Hole Oceanographic Institute. We exploit two publicly available subsets commonly used as benchmarks in the plankton image analysis community: WHOI22 and WHOI40 (Sosik and Olson, 2007; Orenstein and Beijbom, 2017; Lumini and Nanni, 2019; Pastore et al., 2020; Pastore et al., 2023).

The two subsets (Sections 3.1.1 and 3.1.2) are used to tune and evaluate the performance of the different anomaly detection algorithms we consider in our analyses and to select the most appropriate number of principal components to retain for the dimensionality reduction of the deep pre-trained features.

Additionally, we manually extract a selection of phytoplankton images from the full WHOI dataset belonging to different years of acquisitions, with the aim of analyzing the evolution in time of a microorganism reference population. A detailed description of the obtained set can be found in Section 3.1.3. Sample images for the three datasets used in our work are depicted in Figure 2.

3.1.1 WHOI22

WHOI22 constitutes a set of planktonic images gathered between 2005 and 2006 at the Woods Hole Oceanographic Institute, subsequently published in 2007 (Sosik and Olson, 2007). This collection encompasses 22 distinct categories of phytoplankton, containing 300 instances per category. The images are presented in grayscale and vary in dimensions. The dataset is partitioned into two sets: a training set and a test set, each comprising 3,300 samples (150 images for each category), summing up to a total of 6,600 data points. It is worth noting that this dataset is characterized by a fine granularity between different classes, coupled with its exceptional image quality owing to the high-quality acquisitions, which capture intricate morphological particulars.

3.1.2 WHOI40

WHOI40 refers to a specific subset introduced in Pastore et al. (2020), composed of phytoplankton image acquisitions primarily spanning the period from 2011 to 2014. This set provides 40 distinct categories (some of which align with those found in the WHOI22 dataset) for a total of 4,086 samples. Similar to WHOI22, the images are in grayscale and come with varying dimensions, but a predefined test set is not available. This dataset is not as fine-grained as WHOI22, but provides many more classes and therefore it brings different challenges to overcome.

3.1.3 WHOI15 (2007-2010)

In this work, we build a phytoplankton image dataset from the available WHOI large-scale collection, considering samples acquired across four years, from 2007 to 2010. Among the 22 classes available in the WHOI22 dataset, we observe that 15 of them appear with a sufficient number of samples for each of the acquisition years between 2007 and 2010. Specifically, this is observed for the classes labeled as *Asterionellopsis*, *Chaetoceros*,

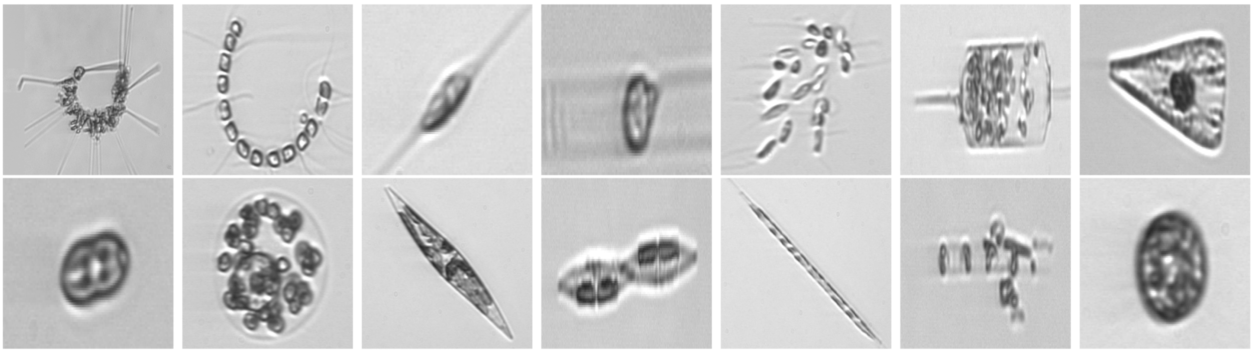

FIGURE 2
Images from WHOI15 (2007-2011), in their appearance once square-resized to become compatible input for deep neural networks. One example for each distinct class is depicted. From upper left to bottom right: *Asterionellopsis, Chaetoceros, Cylindrotheca, Dactyliosolen, Dinobryon, Ditylum, Licmophora, pennate, Phaecystis, Pleurosigma, Pseudonitzschia, Rhizosolenia, Skeletonema, Thalassiosira*. Images from WHOI22 and WHOI40 come from the same superset, the WHOI-Plankton dataset, and exhibit a similar appearance.

Cylindrotheca, *Dactyliosolen*, *Detritus*, *Dinobryon*, *Ditylum*, *Licmophora*, *Pennate*, *Phaeocystis*, *Pleurosigma*, *Pseudonitzschia*, *Rhizosolenia*, *Skeletonema*, *Thalassiosira*. From the 15 classes, we randomly pick a maximum of 500 images, for each class and for each year in that specific time span. With this procedure, we obtain a single dataset that is the union of four different sets, one for each year in the period 2007-2010.

The final dataset has a total of 24,666 images, with an uneven distribution across classes and years. Regarding the number of samples per year, 5841 samples come from 2007, 6323 from 2008, 6696 from 2009, 5,806 from 2010. The exact number of images per class and year are represented as histograms in the Supplementary Material.

3.2 Experiment details

The software implementation of the experiments supporting the proposed methodology is realized using the Python programming language (Python Software Foundation, 2023), with the aid of dedicated machine-learning and deep-learning libraries and frameworks.

Specifically, the deep neural networks adopted in this work are implemented in PyTorch (Paszke et al., 2019), while the weights learned through pre-training the networks on ImageNet come from both Torchvision and TIMM models repositories (Maintainers and Contributors, 2016; Wightman, 2019).

Regarding the anomaly detectors and PCA routines, we rely on the *scikit-learn* library (Pedregosa et al., 2011), which provides efficient and reliable implementations of many state-of-the-art machine learning algorithms. Generic numerical computing operations and data manipulation are implemented with the aid of NumPy (Harris et al., 2020) and Pandas (Pandas Development Team, 2023).

The following dedicated subsections discuss the experimental setup regarding feature extraction and the training and testing of our pipeline's components.

3.2.1 Feature extraction

Images belonging to the dataset of interest are first resized to a 224x224 pixel resolution and normalized to obtain input RGB values between 0 and 1, in order to render them compatible with the input requirements of the available pre-trained deep neural networks. Additionally, they are also *standardized* with respect to the RGB color distribution of ImageNet, as in transfer-learning scenarios we desire to shift input image distribution closer to the one learned by the deep neural network during its pre-training. This is obtained by subtracting ImageNet's RGB color mean from input images and further dividing their values by ImageNet's standard deviation. At this stage, images are ready to be fed to the deep feature extractor, which is obtained by removing the fully-connected *classification-head* from the original model. Given a set of N input images, the deep feature extractor produces a feature vector $\phi \in \mathbb{R}^D$ for each of them (with D usually in the order of 10^3), resulting in a final set of deep pre-trained features $\Phi \in \mathbb{R}^{N\times D}$. Before actually performing feature extraction, we gather three separate sets of images X_{tr}, X_{val} and X_{te}: in the case of WHOI22, the test set corresponds to the already pre-defined test set, while for WHOI40 and WHOI15 (2007-2010), we *hold-out* (Yadav and Shukla, 2016) 20% of samples as a test set, performing an additional *hold-out* with an 80/20 ratio, to separate a proper validation set from the remaining images. We then obtain three sets of deep pre-trained features by feeding the three disjointed sets X_{tr}, X_{val} and X_{te} to the deep feature extractor, Φ_{tr}, Φ_{val} and Φ_{te}. As a final step before applying dimensionality reduction to these sets of features, we first proceed to apply *min-max normalization* and *standardization*, extracting the normalization values from Φ_{tr}.

3.2.2 Dimensionality reduction

The three sets of deep pre-trained features Φ_{tr}, Φ_{val} and Φ_{te} undergo dimensionality reduction through PCA, for which we retain the first 50 principal components. The associated linear projection is computed from the training data by fitting PCA on Φ_{tr} and then we apply it to Φ_{tr}, Φ_{val} and Φ_{te}. By doing so, we obtain the final features that are used for training and evaluating the anomaly detectors. We indicate such features as $Z_{tr} \in \mathbb{R}^{N\times 50}$, $Z_{val} \in \mathbb{R}^{N\times 50}$ and $Z_{te} \in \mathbb{R}^{N\times 50}$. In order to test the importance of this specific step and to search for the best possible number of components, we run our analyses also with the plain deep pre-trained features coming from the employed neural network without any kind of compression, and we test several alternatives for the number of components to retain as well. Details on this particular step are outlined in Section 3.3.3.

3.2.3 Training and evaluation

As we are dealing with datasets equipped with labels provided by field experts, our data includes also an associated vector Y containing integer values associated with the class to which each sample belongs. In our case, the pre-trained deep features with reduced dimensionality Z_{tr} belonging to the extracted training set, are used alongside their associated label vectors Y_{tr} to train one anomaly detector per each available class. If the dataset has K classes we instantiate K anomaly detectors, denoted as $\{A_k \mid k \in [1,K]\}$, and each detector A_k is trained only on the $z_i \in Z_{tr}$ such that $Y_{tr_i} = k$. In our approach, a test image is fed to the set of trained anomaly detectors A. From each anomaly detector, we extract the membership score, exploiting the decision function method in the scikit-learn implementation (e.g., the signed distance to the separating hyperplane, in the case of the one-Class SVM). The maximum anomaly score is selected, and if it is higher than or equal to a threshold τ, the sample is assigned to the corresponding class, otherwise it is identified as a global anomaly and stored for further analyses or computations. The threshold τ is tuned with the following automatic procedure, exploiting the extracted validation set Φ_{val}. Ideally, the higher the threshold, the higher the Specificity, and vice-versa. Thus, we perform a grid search to identify the best trade-off between Sensitivity and Specificity. We evaluate candidate thresholds in the interval $[-1,1]$ with a step of 0.05. The negative samples to measure the Specificity are obtained with a leave-one-out approach. Thus, for each of the available classes k and for each of the candidate thresholds, we measure the Sensitivity, as the number of samples belonging to class k correctly detected by the anomaly detector A_k as in class, and the Specificity, corresponding to the number of samples belonging to k rejected when only the remaining anomaly detectors $\{A_j | j \neq k\}$ are considered. The threshold τ is then selected as the one minimizing the absolute difference between the average Sensitivity and the average Specificity.

3.3 Results

In this section, we highlight and comment on the results obtained throughout our experiments. This includes also the intermediate results regarding the tuning of the hyperparameters, as well as the final measured performances on all the considered datasets, including the proposed test ranging through different years of acquisition.

3.3.1 Performance evaluation across different anomaly detection algorithms

The anomaly detection algorithm is a core element of the proposed approach. We consider four different algorithms, LocalOutlierFactor (LoF) (Breunig et al., 2000), Isolation Forest (IFO) (Liu et al., 2008), Robust Covariance estimator (RC) (Rousseeuw and Driessen, 1999), and One-Class SVM (Scholkopf et al., 1999) (with a Radial Basis Function kernel Vert et al., 2004), comparing them in terms of performances on the WHOI22 and the WHOI40 datasets, in the experimental setting previously described. A crucial parameter shared by the evaluated methods is the contamination factor, which controls the prior knowledge regarding the proportion of out-of-distribution samples among training data. The contamination amount is selected among five possible different values, namely: 1%, 5%, 7.5%, 10%, and 15%, choosing the value that maximizes the performances on the validation set. Table 1 shows the obtained results on the WHOI22, while Table 2 reports the results corresponding to the WHOI40 dataset.

The one-class SVM algorithm with a contamination parameter equal to 0.075 overall brings the best average performances (with respect to the training classes) for both validation splits of the two datasets (see Tables 1, 2). For this reason, we use the one-class SVM with a contamination parameter of 0.075, while τ is set to $\tau = -0.05$ for WHOI22 and to $\tau = -0.10$ for WHOI40. This configuration brings the test performances reported in Table 3, corresponding to a Sensitivity of 0.839 for WHOI22 and 0.870 for WHOI40. We also report a score of 0.094 for WHOI22 and 0.085 for WHOI40 in terms of FNR, while Specificity reaches 0.782 and 0.840 for the two datasets respectively.

3.3.2 Impact of the deep feature extractor on the performance

We perform a comparative study on the deep feature extractor used to obtain the set of descriptors fed to the anomaly detectors. Our objective is to empirically prove that the pre-trained ViTL-16 used in this study as a feature extractor leads to the best performances, in terms of highest anomaly detection accuracy when used as input, compared to other deep neural networks. In detail, we compare Sensitivity, FNR, and Specificity on our target datasets, when using different pre-trained deep neural networks to extract features representing the input to the one-class SVM anomaly detectors. We compare four ImageNet-1K pre-trained CNNs, namely MNASNet 1.3 (Tan et al., 2019), ResNet101 (He et al., 2015), EfficientNetB1 (Tan and Le, 2019), DenseNet201 (Huang et al., 2016), three ImageNet-1K pre-trained Vision transformers (SwinV2-T (Liu et al., 2021), DeiT-B (Touvron et al., 2021), and ConViTB (d'Ascoli et al., 2021)), and a vision transformer pre-trained on ImageNet-22k (ViT-L16 (Dosovitskiy et al., 2020), our selected model), with Tables 4, 5 reporting the obtained results. The ViTL-16 pre-trained transformer provides the best representation. In the case of WHOI22, it brings an improvement in Sensitivity of 1.7% over the DenseNet-201, and of 6% in Specificity over ConViT-B, which are the second best-performing models in terms of the two individual metrics. Considering the performances on WHOI40, DenseNet-201 is the second best-performing model in terms of both Sensitivity and Specificity but the ImageNet-22k pre-trained ViTL-16 achieves a 1% higher Sensitivity, and a sensible improvement in Specificity of 13% over the best-performing alternative.

3.3.3 Ablation study on dimensionality reduction

In our experiments, we involve the usage of a PCA dimensionality reduction algorithm with 50 components. In this section, we provide an ablation study to empirically experiment with the impact of dimensionality reduction on performance. We test the usage of the original deep pre-trained features, as well as different numbers of principal components used for projecting features in the associated lower-dimensional space, on our target datasets. Specifically, we compare Sensitivity, FNR, and Specificity when using the plain features extracted from the ViTL-16 encoder, with dimensionality equal to 1024, and the features obtained through PCA reduction with a number of principal components varying between 10 and 200, as input for the one-class SVM anomaly detectors. The performances measured in our experiments are outlined in Table 6 for the WHOI22 dataset and (Table 7) for the WHOI40 one. A PCA with 50 components is confirmed to lead to the best performances for both datasets.

3.3.4 Comparison with state-of-the-art multi-class classification methods

WHOI22 is a popular benchmark dataset exploited in several works focusing on plankton image classification (Lumini and Nanni, 2019; Kyathanahally et al., 2021; Maracani et al., 2023). Even if the general framework of classification is different from the one faced in this work, in this paragraph we provide a comparison in an attempt to frame our results with respect to the existing state-of-the-art. To do so, it is possible to focus only on the Sensitivity, which measures the correct predictions per class, ignoring the results of the leave-one-out approach that is instead used to evaluate the Specificity (i.e., to measure the number of correctly predicted anomalies). Exploiting different ensembles of CNNs or transformers, in Maracani et al. (2023) the authors report a test accuracy of 0.966 on the WHOI22, while in Kyathanahally et al.

TABLE 1 Performance across different anomaly detection algorithms and contamination parameters on a hold-out validation set from the training set of the WHOI22 dataset.

WHOI22	Cont. (%)	Best τ	Sensitivity	FNR	Specificity
LOF	1.0	0.200	0.724 ± 0.188	0.176 ± 0.147	0.759 ± 0.239
	5.0	0.100	0.742 ± 0.137	0.168 ± 0.115	0.759 ± 0.246
	7.5	0.050	0.803 ± 0.100	0.111 ± 0.073	0.733 ± 0.267
	10.0	0.050	0.748 ± 0.110	0.173 ± 0.098	0.764 ± 0.245
	15.0	-0.000	0.795 ± 0.106	0.114 ± 0.081	0.727 ± 0.266
SVM	1.0	-0.000	0.778 ± 0.102	0.166 ± 0.067	0.826 ± 0.197
	5.0	-0.000	0.778 ± 0.100	0.165 ± 0.064	0.825 ± 0.200
	7.5	**-0.050**	**0.827 ± 0.098**	**0.110 ± 0.054**	**0.789 ± 0.190**
	10.0	-0.050	0.814 ± 0.092	0.127 ± 0.049	0.803 ± 0.215
	15.0	-0.100	0.798 ± 0.089	0.142 ± 0.059	0.817 ± 0.176
IFO	1.0	0.050	0.756 ± 0.144	0.105 ± 0.084	0.424 ± 0.256
	5.0	0.050	0.548 ± 0.142	0.380 ± 0.138	0.836 ± 0.169
	7.5	0.050	0.414 ± 0.129	0.539 ± 0.146	0.905 ± 0.112
	10.0	-0.000	0.756 ± 0.140	0.062 ± 0.056	0.276 ± 0.208
	15.0	-0.000	0.730 ± 0.088	0.111 ± 0.076	0.406 ± 0.245
COV	1.0	-0.250	0.688 ± 0.302	0.002 ± 0.007	0.188 ± 0.230
	5.0	-0.250	0.830 ± 0.144	0.039 ± 0.031	0.545 ± 0.322
	7.5	-0.250	0.782 ± 0.159	0.082 ± 0.052	0.652 ± 0.294
	10.0	-0.050	0.773 ± 0.145	0.124 ± 0.094	0.718 ± 0.295
	15.0	-0.250	0.691 ± 0.122	0.255 ± 0.109	0.858 ± 0.224

With this procedure, we selected the best algorithm, contamination, and threshold (τ) to be later employed on the test set, which for WHOI22 is natively available. The best overall result is highlighted in bold.

TABLE 2 Performance across different anomaly detection algorithms and contamination parameters on a hold-out validation set from the WHOI40 dataset.

WHOI40	Cont. (%)	Best τ	Sensitivity	FNR	Specificity
LOF	1.0	0.150	0.710 ± 0.293	0.150 ± 0.177	0.722 ± 0.306
	5.0	0.050	0.804 ± 0.165	0.095 ± 0.080	0.720 ± 0.290
	7.5	0.050	0.772 ± 0.175	0.138 ± 0.120	0.801 ± 0.237
	10.0	0.050	0.756 ± 0.164	0.167 ± 0.132	0.833 ± 0.221
	15.0	-0.000	0.800 ± 0.124	0.121 ± 0.078	0.777 ± 0.259
SVM	1.0	-0.000	0.794 ± 0.143	0.182 ± 0.122	0.948 ± 0.079
	5.0	-0.050	0.863 ± 0.114	0.103 ± 0.083	0.871 ± 0.162
	7.5	**-0.100**	**0.882 ± 0.106**	**0.083 ± 0.069**	**0.840 ± 0.196**
	10.0	-0.100	0.860 ± 0.111	0.108 ± 0.082	0.872 ± 0.163
	15.0	-0.200	0.865 ± 0.103	0.103 ± 0.074	0.849 ± 0.191
IFO	1.0	0.050	0.690 ± 0.208	0.100 ± 0.100	0.416 ± 0.292
	5.0	0.050	0.583 ± 0.220	0.396 ± 0.215	0.964 ± 0.063
	7.5	-0.000	0.853 ± 0.100	0.040 ± 0.048	0.406 ± 0.258

(Continued)

TABLE 2 Continued

WHOI40	Cont. (%)	Best τ	Sensitivity	FNR	Specificity
	10.0	-0.000	0.823 ± 0.118	0.048 ± 0.056	0.442 ± 0.303
	15.0	-0.000	0.791 ± 0.137	0.119 ± 0.095	0.675 ± 0.255
COV	1.0	-0.250	0.475 ± 0.335	0.022 ± 0.040	0.250 ± 0.299
	5.0	-0.250	0.444 ± 0.235	0.480 ± 0.214	0.886 ± 0.156
	7.5	-0.250	0.027 ± 0.133	0.973 ± 0.133	1.000 ± 0.000
	10.0	-0.250	0.025 ± 0.125	0.975 ± 0.125	1.000 ± 0.000
	15.0	-0.250	0.021 ± 0.099	0.979 ± 0.099	1.000 ± 0.000

With this procedure, we selected the best algorithm, contamination, and threshold (τ) to be later employed on the test set, which for WHOI40 is a disjointed hold-out subset of the full dataset. The best overall result is highlighted in bold.

(2021) a value of 0.961 is obtained, and (Lumini and Nanni, 2019) reports a test accuracy of 0.958. With a sensitivity of 0.839, our method shows a drop of ~ 12% with respect to state-of-the-art classification accuracy. This is somehow expected, bearing in mind that in our experiments we tune our algorithm's components to balance the trade-off between Sensitivity and Specificity. The aim of our work is in fact not to maximize the multi-class classification performance, but rather to design a method capable of detecting anomalies in a feature space of reference, starting from phytoplankton images, while maintaining a reasonable classification performance. Additionally, it is worth underlining that in Lumini and Nanni (2019); Kyathanahally et al. (2021); Maracani et al. (2023), the authors use ensembles of at least four deep neural networks, that need to be trained on the target plankton image dataset. In our work, instead, we use a single pre-trained transformer as a feature extractor (with no further training), and we only train one anomaly detector per class, significantly reducing the computational burden of the proposed method.

3.3.5 Temporal analysis through anomaly detection in feature space

Our best-performing pipeline involves the usage of one-class SVM anomaly detectors, with input represented by the 50 principal components computed on ImageNet-22K pre-trained ViTL-16 features extracted from plankton images. At this stage, we exploit the WHOI15 dataset to test the ability of the proposed approach to generalize over time. In this dataset, we select 15 classes that are acquired for 4 consecutive years in the large-scale WHOI dataset (see Sec. 3.1.3). Thus, we can test the performance of our pipeline across time in a realistic scenario, where the same classes are acquired across different years. This experiment is helpful to have insights into the natural in-time variability of a group of interesting classes, and we expect our anomaly detection algorithms to be able to recognize with reasonable accuracy samples of their respective class, even if they are acquired in different years with respect to the ones used for training. We train a single one-class SVM algorithm for each of the 15 available classes for each one of the 4 years of the acquisition included in the dataset we built, and we perform the automatic extraction of a dedicated threshold τ for each year on the respective validation sets. Later, we test the trained algorithms on the test set extracted from the year corresponding to the training samples, and for each one of the available subsequent years. For instance, for images acquired in 2008, we train the detectors on the 2008 training set, we derive τ from 2008's validation set, and evaluate the performance on the test data acquired in the same and the following years (2008, 2009, and 2010). Table 8 shows the obtained results.

TABLE 3 Results of the best configurations for the test sets of the two datasets, WHOI22 and WHOI40.

Dataset	Sensitivity	FNR	Specificity
WHOI22	0.839 ± 0.083	0.094 ± 0.029	0.782 ± 0.228
WHOI40	0.870 ± 0.107	0.085 ± 0.076	0.840 ± 0.211

In experiments in which the training year and the testing year coincide, we can see that the performances are comparable with those obtained on WHOI22 and WHOI40. This is indicated on the diagonal of (Table 8), where Sensitivity has a minimum of 0.82 in 2010 and a maximum of 0.859 in 2009. Regarding Specificity, we can observe a minimum of 0.773 in 2007 and a maximum of 0.856 in 2009, while FNR is close to 0.10, with a minimum of 0.075 in 2007. A drop in Sensitivity is observed when the test year differs from the training one. This is somewhat to be expected due to the distribution shift in the images across time. Among the multiple possible reasons,

TABLE 4 Ablation on WHOI22 regarding the best pre-trained model for deep feature extraction.

Pre-Trained Model	Sensitivity	FNR	Specificity
MNASNet 1.3	0.767 ± 0.158	0.080 ± 0.037	0.528 ± 0.256
ResNet-101	0.768 ± 0.105	0.091 ± 0.037	0.514 ± 0.249
EfficientNet-B1	0.803 ± 0.117	0.078 ± 0.031	0.568 ± 0.262
DenseNet-201	0.822 ± 0.084	0.082 ± 0.026	0.631 ± 0.252
SwinV2-T	0.804 ± 0.094	0.085 ± 0.035	0.659 ± 0.251
ConViT-B	0.805 ± 0.088	0.110 ± 0.035	0.722 ± 0.212
DEiT-B	0.802 ± 0.112	0.088 ± 0.026	0.614 ± 0.263
ViTL-16 (22k)	**0.839 ± 0.083**	**0.094 ± 0.029**	**0.782 ± 0.228**

Best results are highlighted in bold.

TABLE 5 Ablation on WHOI40 regarding the best pre-trained model for deep feature extraction.

Pre-Trained Model	Sensitivity	FNR	Specificity
MNASNet 1.3	0.814 ± 0.155	0.076 ± 0.073	0.551 ± 0.306
ResNet-101	0.811 ± 0.125	0.089 ± 0.054	0.631 ± 0.292
EfficientNet-B1	0.831 ± 0.130	0.063 ± 0.062	0.580 ± 0.290
DenseNet-201	0.860 ± 0.124	0.068 ± 0.062	0.715 ± 0.283
SwinV2-T	0.816 ± 0.133	0.084 ± 0.072	0.579 ± 0.301
ConViT-B	0.833 ± 0.138	0.073 ± 0.063	0.676 ± 0.255
DEiT-B	0.840 ± 0.144	0.075 ± 0.060	0.659 ± 0.254
ViTL-16 (22k)	**0.870 ± 0.107**	**0.085 ± 0.076**	**0.840 ± 0.211**

Best results are highlighted in bold.

we can include per-class populations, which are not the same for all classes across years, naturally occurring fluctuations that may be hard to infer from a single year of training, as well as potential factors related to the acquisition system.

The highest drop involves the experiment in which the detectors are trained on images from 2007 and tested on 2010 corresponding to a decrease of 0.21 in Sensitivity. For the other training years, the drops in Sensitivity are around 0.18, with an average Sensitivity always above 0.65. The decrease in Sensitivity is associated with an increase in the FNR, generally ranging between 0.20 and 0.25 in tests run on subsequent years. Specificity, instead, shows little differences over time or even improves in some cases, suggesting that the pipeline is able to correctly recognize the presence of completely novel objects and instances with respect to the training set.

To give more insights into the individual classes and distribution shifts across years, we perform an experiment where we train our anomaly detection algorithm on a joint dataset including years 2007, 2008, and 2009, while testing on the samples from 2010. In this experiment, we obtain an average Sensitivity of 0.768, 0.135 in FNR, and an average Specificity of 0.725, improving significantly the overall performances on the unseen year with respect to the previous experiments. The lowest Sensitivity is measured for the class *Ditylum*, confirming the behavior observed in the results reported in Figure 3. Regarding the Specificity, the most problematic classes are *Skeletonema* and *Thalassiosira*, similarly to what obtained with the individual years experiments. Nonetheless, the increase in Sensitivity suggests that a more diverse set of examples and periodic retraining with more recent acquisitions may be helpful to keep the system up to date with respect to the naturally occurring modifications in the observed populations.

4 Discussion

Plankton organisms can play an important role in assessing environmental perturbations, as they react to even slight changes in the environment with physiological modifications in morphology and behavior. In this work, we propose a machine learning framework to perform anomaly detection in phytoplankton images, with the aim to support the detection of perturbations in the environment by monitoring changes in the microorganisms' morphology. We propose a method based on anomaly detection algorithms, trained on top of deep pre-trained features, extracted by means of a vision transformer pre-trained on ImageNet22K.

TABLE 6 Ablation on Feature Compression algorithm and impact of dimensionality reduction on performances for the WHOI22 dataset.

WHOI22	Z	Sensitivity	FNR	Specificity
Original Features	–	0.737 ± 0.098	0.172 ± 0.041	0.680 ± 0.277
PCA	10	0.776 ± 0.148	0.050 ± 0.028	0.514 ± 0.298
	20	0.832 ± 0.108	0.071 ± 0.031	0.688 ± 0.290
	50	**0.839 ± 0.083**	**0.094 ± 0.029**	**0.782 ± 0.228**
	200	0.827 ± 0.103	0.096 ± 0.032	0.717 ± 0.259

Z indicates the number of principal components selected for the compression.
Best results are highlighted in bold.

TABLE 7 Ablation on Feature Compression algorithm and impact of dimensionality reduction on performances for the WHOI40 dataset.

WHOI40	Z	Sensitivity	FNR	Specificity
Original Features	0	0.776 ± 0.116	0.165 ± 0.094	0.755 ± 0.275
PCA	10	0.823 ± 0.147	0.041 ± 0.047	0.561 ± 0.324
	20	0.844 ± 0.136	0.069 ± 0.053	0.726 ± 0.291
	50	**0.870 ± 0.107**	**0.085 ± 0.076**	**0.840 ± 0.211**
	200	0.858 ± 0.115	0.098 ± 0.077	0.788 ± 0.253

Z indicates the number of principal components selected for the compression.
Best results are highlighted in bold.

TABLE 8 Average Sensitivity, FNR, and Specificity of the parallel OneClass-SVMs trained on the reduced deep pre-trained features coming from WHOI10 from different years and tested on the same type of features extracted from images coming from subsequent years of WHOI's acquisitions, starting from 2007 up to 2010.

Test Year Train Year		2007	2008	2009	2010
2007	Sensitivity	0.841 ± 0.176	0.662 ± 0.110	0.669 ± 0.151	0.634 ± 0.179
	FNR	0.075± 0.083	0.225 ± 0.117	0.247 ± 0.110	0.258 ± 0.115
	Specificity	0.773 ± 0.108	0.788 ± 0.134	0.861 ± 0.095	0.795 ± 0.148
2008	Sensitivity	–	0.835 ± 0.112	0.656 ± 0.178	0.657 ± 0.186
	FNR	–	0.103 ± 0.070	0.265 ± 0.150	0.208 ± 0.091
	Specificity	–	0.820 ± 0.172	0.842 ± 0.126	0.732 ± 0.108
2009	Sensitivity	–	–	0.859 ± 0.067	0.683 ± 0.173
	FNR	–	–	0.093 ± 0.048	0.206 ± 0.102
	Specificity	–	–	0.856 ± 0.126	0.777 ± 0.168
2010	Sensitivity	–	–	–	0.823 ± 0.192
	FNR	–	–	–	0.095 ± 0.060
	Specificity	–	–	–	0.791 ± 0.190

The first row reports results from training on the train features from 2007 and testing on the test set of each available following year. The upper-triangular form of this table derives from the fact that we do not test on past years but only on the test sets of the same and following years of acquisition.

Assuming an initial training set is available, we first design a parallel architecture composed of one anomaly detection algorithm per available class. When a test image is fed to each of the detectors, we select the detector providing the maximum membership score. If such score is above an automatically determined threshold, we consider the sample as in class, and update the population count for the corresponding class. Otherwise, we treat the sample as a global anomaly, storing it for further analysis and updating the anomaly count. At this stage, we propose to exploit our approach to suggest potential critical situations, which may be related to environmental perturbations, by using a threshold on the number of global anomalies per time. This threshold is likely to depend on the specific site of sample acquisition, and needs to be tuned by experts in the field. We perform comparative studies on the deep feature extractor and different anomaly detectors in terms of performances on two publicly available benchmark datasets, the WHOI22 (Sosik and Olson, 2007), and the WHOI40 (Pastore et al., 2020). Our experiments show that the best performances correspond to the adoption of a one-class SVM algorithm trained on top of the first 50 principal components computed on features extracted with a ViTL-16 pre-trained on ImageNet22K. The usage of a pre-trained neural network for feature extraction makes our approach very efficient, as the only training process regards the anomaly detectors. To provide a reference on the time needed for the computation, we consider the experiments on the WHOI22 dataset. The feature extraction with ViTL-16 requires an average of 0.032 ± 0.003 seconds per image, while the detectors average training time per class, is 6.26 ± 2.62 milliseconds. The computational times are averaged among 10 different runs, on a laptop with AMD Ryzen 9 6900 HS, with 16 GB of RAM and a GPU NVIDIA RTX 3080, with 8 GB of VRAM. Feature extraction is performed on the GPU.

We then build a dataset containing 15 classes acquired from 2007 to 2010 in the WHOI large-scale dataset (Sosik and Brownlee, 2015), which we refer to as WHOI15. Our aim is to exploit the WHOI15 to evaluate the generality of our solution across samples acquired in different years. Thus, we train our pipeline on the images acquired in one year, evaluating the performances on the test set of the same year and the data acquired in the following years. A drop in Sensitivity is observed, in general, when testing on classes acquired across different years, with no impact on the Specificity, evaluated with a leave-one-out approach. The performances are similar to the benchmark datasets (WHOI22 and WHOI40) when our method is trained on the training set of one year, and tested on the test set corresponding to the same year. We hypothesize that the drop in Sensitivity across different years may be related to natural fluctuations, difficult to infer from a single year of training, as well as potential changes related to the water conditions and the acquisition system. Nonetheless, the average Sensitivity has a minimum value of 0.63, with a high deviation with respect to individual classes (see Table 8). A limitation of the dataset used in this work is the relatively low number of available images per class, with a severe imbalance in some years of acquisition. The highest number of images for training is 400 per class (with a minimum of 36, see Supplementary Material for more details), which is likely not enough for actually covering intra-class variance in appearance, which may be high for specific classes. To further investigate in this direction, we perform an experiment where the 2010 samples are used for testing, and the remaining years' images are used for training. We select the 2010 dataset as a test because it shows the highest drop in Sensitivity in our previous experiment. We obtain a significant improvement in average Sensitivity, and a general trend more similar to the single-year experiment, where

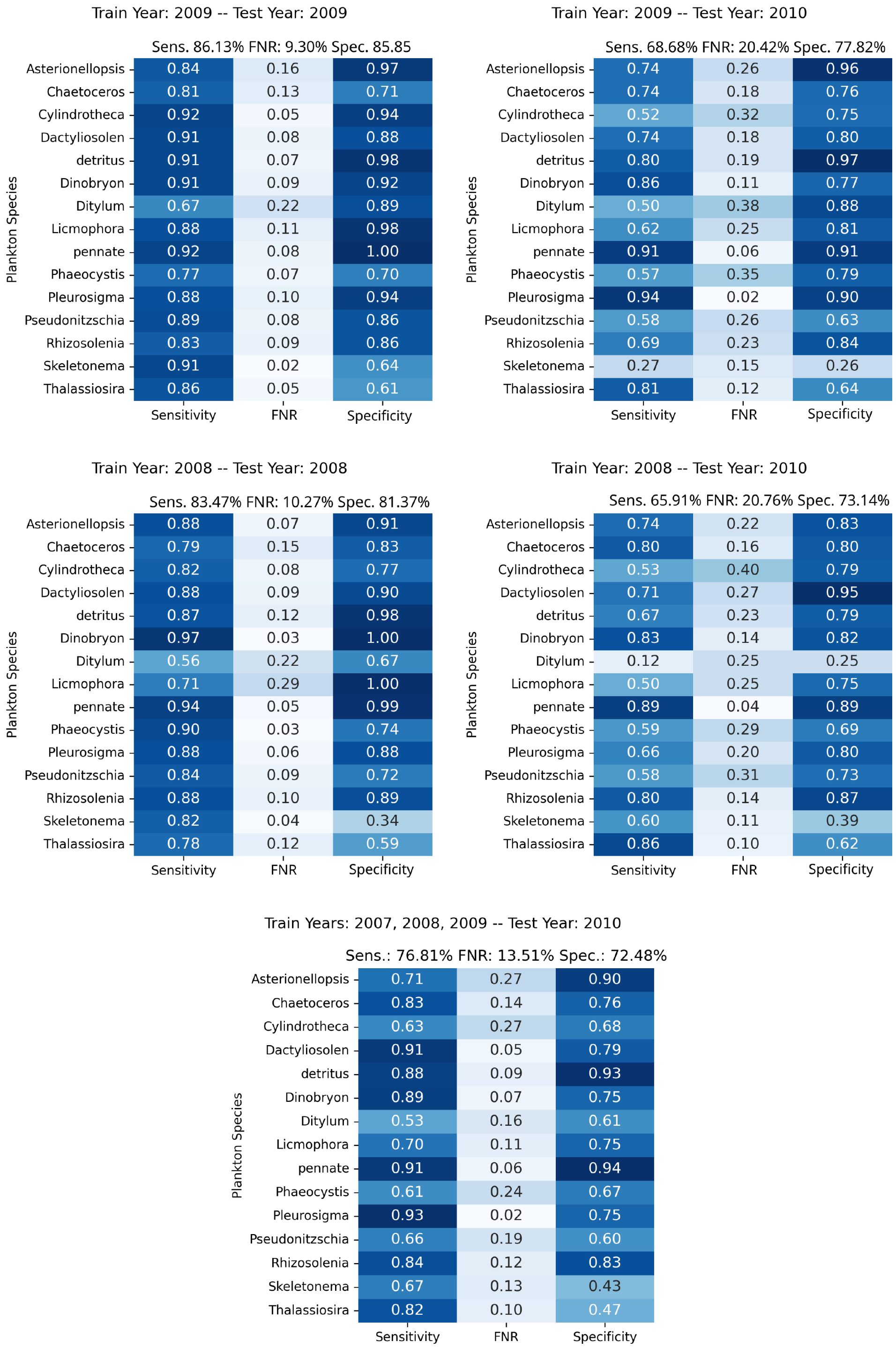

Train Year: 2009 -- Test Year: 2009

Sens. 86.13% FNR: 9.30% Spec. 85.85

	Sensitivity	FNR	Specificity
Asterionellopsis	0.84	0.16	0.97
Chaetoceros	0.81	0.13	0.71
Cylindrotheca	0.92	0.05	0.94
Dactyliosolen	0.91	0.08	0.88
detritus	0.91	0.07	0.98
Dinobryon	0.91	0.09	0.92
Ditylum	0.67	0.22	0.89
Licmophora	0.88	0.11	0.98
pennate	0.92	0.08	1.00
Phaeocystis	0.77	0.07	0.70
Pleurosigma	0.88	0.10	0.94
Pseudonitzschia	0.89	0.08	0.86
Rhizosolenia	0.83	0.09	0.86
Skeletonema	0.91	0.02	0.64
Thalassiosira	0.86	0.05	0.61

Train Year: 2009 -- Test Year: 2010

Sens. 68.68% FNR: 20.42% Spec. 77.82%

	Sensitivity	FNR	Specificity
Asterionellopsis	0.74	0.26	0.96
Chaetoceros	0.74	0.18	0.76
Cylindrotheca	0.52	0.32	0.75
Dactyliosolen	0.74	0.18	0.80
detritus	0.80	0.19	0.97
Dinobryon	0.86	0.11	0.77
Ditylum	0.50	0.38	0.88
Licmophora	0.62	0.25	0.81
pennate	0.91	0.06	0.91
Phaeocystis	0.57	0.35	0.79
Pleurosigma	0.94	0.02	0.90
Pseudonitzschia	0.58	0.26	0.63
Rhizosolenia	0.69	0.23	0.84
Skeletonema	0.27	0.15	0.26
Thalassiosira	0.81	0.12	0.64

Train Year: 2008 -- Test Year: 2008

Sens. 83.47% FNR: 10.27% Spec. 81.37%

	Sensitivity	FNR	Specificity
Asterionellopsis	0.88	0.07	0.91
Chaetoceros	0.79	0.15	0.83
Cylindrotheca	0.82	0.08	0.77
Dactyliosolen	0.88	0.09	0.90
detritus	0.87	0.12	0.98
Dinobryon	0.97	0.03	1.00
Ditylum	0.56	0.22	0.67
Licmophora	0.71	0.29	1.00
pennate	0.94	0.05	0.99
Phaeocystis	0.90	0.03	0.74
Pleurosigma	0.88	0.06	0.88
Pseudonitzschia	0.84	0.09	0.72
Rhizosolenia	0.88	0.10	0.89
Skeletonema	0.82	0.04	0.34
Thalassiosira	0.78	0.12	0.59

Train Year: 2008 -- Test Year: 2010

Sens. 65.91% FNR: 20.76% Spec. 73.14%

	Sensitivity	FNR	Specificity
Asterionellopsis	0.74	0.22	0.83
Chaetoceros	0.80	0.16	0.80
Cylindrotheca	0.53	0.40	0.79
Dactyliosolen	0.71	0.27	0.95
detritus	0.67	0.23	0.79
Dinobryon	0.83	0.14	0.82
Ditylum	0.12	0.25	0.25
Licmophora	0.50	0.25	0.75
pennate	0.89	0.04	0.89
Phaeocystis	0.59	0.29	0.69
Pleurosigma	0.66	0.20	0.80
Pseudonitzschia	0.58	0.31	0.73
Rhizosolenia	0.80	0.14	0.87
Skeletonema	0.60	0.11	0.39
Thalassiosira	0.86	0.10	0.62

Train Years: 2007, 2008, 2009 -- Test Year: 2010

Sens.: 76.81% FNR: 13.51% Spec.: 72.48%

	Sensitivity	FNR	Specificity
Asterionellopsis	0.71	0.27	0.90
Chaetoceros	0.83	0.14	0.76
Cylindrotheca	0.63	0.27	0.68
Dactyliosolen	0.91	0.05	0.79
detritus	0.88	0.09	0.93
Dinobryon	0.89	0.07	0.75
Ditylum	0.53	0.16	0.61
Licmophora	0.70	0.11	0.75
pennate	0.91	0.06	0.94
Phaeocystis	0.61	0.24	0.67
Pleurosigma	0.93	0.02	0.75
Pseudonitzschia	0.66	0.19	0.60
Rhizosolenia	0.84	0.12	0.83
Skeletonema	0.67	0.13	0.43
Thalassiosira	0.82	0.10	0.47

FIGURE 3

Per-class performances of the proposed approach in the experiments involving the WHOI15 dataset, simulating different years of acquisition and testing. Top Left, Top Right, Middle Left, and Middle Right depict experiments in which training and test procedures involve single years; the specific years are outlined in the upper part of each figure. Bottom: Results from training on the years 2007, 2008, and 2009, while testing on features extracted from 2010 acquisitions, simulating the accumulation of samples through time in order to test on newly acquired data.

training and evaluation are performed on the same year. These results suggest that periodic re-training and cumulating training samples across time could help maintain high performances in the designed method. Nonetheless, some classes still show a drop in Sensitivity (e.g., *Ditylum*) or Specificity (e.g., *Skeletonema* and *Thalassiosira*) with respect to the average. Exploring the images of these classes, we realized that they are more blurred and less detailed in the 2010 dataset than in the other years of acquisition.

Regarding the aim of the designed method, it is worth stressing that our anomaly detection approach intends to detect significant variations of phytoplankton images in a feature space of reference. However, such deviations can be related to different sources, including novel classes (not included in the initial training set), plankton morphological modifications due to environmental changes, and a possible source of errors caused by image distortions or noise. Yet, an automatic disentanglement of the different sources of anomalies is not possible with our proposed approach. However, we sketch a possible pipeline to handle the different sources of anomalies. First, we propose to measure the average number of anomalies in a certain period of time and situ of acquisition. We can indeed expect a systematic amount of errors related to image distortions or noise, or simply related to intrinsic algorithm mistakes, in such a period of time. For this reason, we propose to set a threshold on the number of detected anomalies with respect to the average number of anomalies per time. Only if the number of anomalies is higher than this threshold, an alert should be emitted. At this point, we envision a human in the loop that can manually identify signaled anomalies. As further support for the human expert, a possibility could be to group the features corresponding to the anomalies using clustering algorithms, as the one described in Pastore et al. (2023), where plankton images are shown to be clustered with high accuracy. Sample images belonging to each of the detected clusters could be reviewed by the expert, providing a label, that can be used to train new anomaly detectors, in the case of novel classes. Finally, in this work we focus on phytoplankton microscopic images acquired with IFCB. However, it's worth underlining that plankton image analysis may include several subdomains and imaging devices over phytoplankton and IFCB, for instance, zooplankton images acquired with diverse acquisition systems and modalities, such as silhouette grayscale images acquired with the *In Situ* Ichthyoplankton Imaging System (ISIIS) (Cowen et al., 2015), grayscale scan images collected with ZooScan (Elineau et al., 2018), and color dark field images obtained with devices as the Scripps Plankton Camera (SPC) (Orenstein et al., 2020b), and the Imaging Plankton Probe (IPP) (Li et al., 2021), just to name a few. We expect our method and designed pipeline to be in general applicable to such different sources and types of images, nonetheless, further experiments and tests are required to assess the generality and the specific performances of the proposed anomaly detection approach with respect to the identified domains.

Even if further research is necessary to prove the accuracy of the proposed approach in actually detecting plankton responses related to changes in the environment, we believe that this work may be a stepping stone towards the fundamental aim of using plankton as a biosensor, supporting the detection of potentially critical situations and environmental perturbations.

Data availability statement

Publicly available datasets were analyzed in this study. This data can be found here: https://hdl.handle.net/10.1575/1912/7341. The WHOI15 dataset, as well as the code needed for reproducing our results are available at: https://github.com/Malga-Vision/Anomaly-detection-in-feature-space-for-detecting-changes-in-phytoplankton-populations.

Author contributions

MC: Data curation, Investigation, Methodology, Software, Validation, Visualization, Writing – original draft. FO: Funding acquisition, Investigation, Methodology, Supervision, Validation, Visualization, Writing – original draft. VP: Conceptualization, Funding acquisition, Investigation, Methodology, Project administration, Supervision, Validation, Visualization, Writing – original draft.

Funding

The author(s) declare that no financial support was received for the research, authorship, and/or publication of this article.

Acknowledgments

VP was supported by FSE REACT-EU-PON 2014–2020, DM 1062/2021, COD. 11-G-14987-1.

Conflict of interest

The authors declare that the research was conducted in the absence of any commercial or financial relationships that could be construed as a potential conflict of interest.

Publisher's note

Supplementary material

The Supplementary Material for this article can be found online at: https://www.frontiersin.org/articles/10.3389/fmars.2023.1283265/full#supplementary-material

References

Alfano, P. D., Rando, M., Letizia, M., Odone, F., Rosasco, L., and Pastore, V. P. (2022). "Efficient unsupervised learning for plankton images," in *2022 26th international conference on pattern recognition (ICPR) (IEEE)*, 1314–1321.

Bellman, R. (1966). Dynamic programming. *Science* 153, 34–37. doi: 10.1126/science.153.3731.34

Benfield, M. C., Grosjean, P., Culverhouse, P. F., Irigoien, X., Sieracki, M. E., Lopez-Urrutia, A., et al. (2007). Rapid: research on automated plankton identification. *Oceanography* 20, 172–187. doi: 10.5670/oceanog.2007.63

Breunig, M. M., Kriegel, H.-P., Ng, R. T., and Sander, J. (2000). Lof: Identifying density-based local outliers. *SIGMOD Rec.* 29, 93–104. doi: 10.1145/335191.335388

Brierley, A. S. (2017). Plankton. *Curr. Biol.* 27, R478–R483. doi: 10.1016/j.cub.2017.02.045

Cowen, R. K., Sponaugle, S., Robinson, K. L., Luo, J.Oregon State University, et al. (2015). *Planktonset 1.0: Plankton imagery data collected from f.g. walton smith in straits of florida from 2014-06-03 to 2014-06-06 and used in the 2015 national data science bowl (ncei accession 0127422)*. doi: 10.7289/V5D21VJD

d'Ascoli, S., Touvron, H., Leavitt, M. L., Morcos, A. S., Biroli, G., and Sagun, L. (2021). Convit: improving vision transformers with soft convolutional inductive biases. *J. Stat. Mechanics: Theory Experiment* 2022, 2286–2296. doi: 10.1088/1742-5468/ac9830

Dosovitskiy, A., Beyer, L., Kolesnikov, A., Weissenborn, D., Zhai, X., Unterthiner, T., et al. (2020). *An image is worth 16x16 words: Transformers for image recognition at scale*

Elineau, A., Desnos, C., Jalabert, L., Olivier, M., Romagnan, J.-B., et al. (2018). Zooscannet: plankton images captured with the zooscan. doi: 10.17882/55741

Gönen, M., and Alpaydın, E. (2011). Multiple kernel learning algorithms. *J. Mach. Learn. Res.* 12, 2211–2268.

González, P., Álvarez, E., Díez, J., and López-Urrutia, Á. (2017). and del coz, J Validation methods for plankton image classification systems. *J.Limnology Oceanography: Methods* 15, 221–237.

Hanazato, T. (2001). Pesticide effects on freshwater zooplankton: an ecological perspective. *Environ. pollut.* 112, 1–10. doi: 10.1016/S0269-7491(00)00110-X

Harris, C. R., Millman, K. J., van der Walt, S. J., Gommers, R., Virtanen, P., Cournapeau, D., et al. (2020). Array programming with numpy. *Nature* 585, 357–362. doi: 10.1038/s41586-020-2649-2

Hays, G. C., Richardson, A. J., and Robinson, C. (2005). Climate change and marine plankton. *Trends Ecol. Evol.* 20, 337–344. doi: 10.1016/j.tree.2005.03.004

He, K., Zhang, X., Ren, S., and Sun, J. (2015). "Deep residual learning for image recognition," in *2016 IEEE conference on computer vision and pattern recognition (CVPR)*, 770–778.

Huang, G., Liu, Z., and Weinberger, K. Q. (2016). "Densely connected convolutional networks," in *2017 IEEE conference on computer vision and pattern recognition (CVPR)*, 2261–2269.

Kyathanahally, S. P., Hardeman, T., Merz, E., Bulas, T., Reyes, M., Isles, P., et al. (2021). Deep learning classification of lake zooplankton. *Front. Microbiol.* 12, 3226. doi: 10.3389/fmicb.2021.746297

Li, J., Chen, T., Yang, Z., Chen, L., Liu, P., Zhang, Y., et al. (2021). Development of a buoy-borne underwater imaging system for in *situ* mesoplankton monitoring of coastal waters. *IEEE J. Oceanic Eng.* 47(1), 88–110. doi: 10.1109/JOE.2021.3106122

Liu, Z., Lin, Y., Cao, Y., Hu, H., Wei, Y., Zhang, Z., et al. (2021). Swin transformer: Hierarchical vision transformer using shifted windows. *2021 IEEE/CVF Int. Conf. Comput. Vision (ICCV)*, 9992–10002. doi: 10.1109/ICCV48922.2021.00986

Liu, F. T., Ting, K. M., and Zhou, Z.-H. (2008). "Isolation forest," in *Proceedings of the 2008 eighth IEEE international conference on data mining* (USA: IEEE Computer Society), 413–422. doi: 10.1109/ICDM.2008.17

Lombard, F., Boss, E., Waite, A. M., Vogt, M., Uitz, J., Stemmann, L., et al. (2019). Globally consistent quantitative observations of planktonic ecosystems. *Front. Mar. Sci.* 6. doi: 10.3389/fmars.2019.00196

Lumini, A., and Nanni, L. (2019). Deep learning and transfer learning features for plankton classification. *Ecol. Inf.* 51, 33–43. doi: 10.1016/j.ecoinf.2019.02.007

Lumini, A., Nanni, L., and Maguolo, G. (2020). Deep learning for plankton and coral classification. *Appl. Computing Inf* 19, 265–283. doi: 10.1016/j.aci.2019.11.004

Maintainers and Contributors (2016) *Torchvision: Pytorch's computer vision library*. Available at: https://github.com/pytorch/vision.

Maracani, A., Pastore, V. P., Natale, L., Rosasco, L., and Odone, F. (2023). In-domain versus out-of-domain transfer learning in plankton image classification. *Sci. Rep.* 13, 10443. doi: 10.1038/s41598-023-37627-7

Ohman, M. (1988). Behavioral responses of zooplankton to predation. *Bull. Mar. Sci.* 43, 530–550.

Orenstein, E. C., and Beijbom, O. (2017). "Transfer learning and deep feature extraction for planktonic image data sets," in *2017 IEEE winter conference on applications of computer vision (WACV) (IEEE)*, 1082–1088.

Orenstein, E. C., Kenitz, K. M., Roberts, P. L., Franks, P. J., and Jaffe, J. S. (2020a). Semi-and fully supervised quantification techniques to improve population estimates from machine classifiers. *Limnology Oceanography: Methods* 18, 739–753. doi: 10.1002/lom3.10399

Orenstein, E. C., Ratelle, D., Briseño-Avena, C., Carter, M. L., Franks, P. J. S., Jaffe, J. S., et al. (2020b). The scripps plankton camera system: A framework and platform for in *situ* microscopy. *Limnology Oceanography: Methods* 18, 681–695. doi: 10.1002/lom3.10394

Pandas Development Team (2023). *pandas-dev/pandas: pandas*. doi: 10.5281/zenodo.8092754

Pastore, V. P., Ciranni, M., Bianco, S., Fung, J. C., Murino, V., and Odone, F. (2023). Efficient unsupervised learning of biological images with compressed deep features. *Image Vision Computing* 104764. doi: 10.1016/j.imavis.2023.104764

Pastore, V. P., Megiddo, N., and Bianco, S. (2022). "An anomaly detection approach for plankton species discovery," in *Image Analysis and Processing–ICIAP 2022: 21st International Conference*, Lecce, Italy, May 23–27, 2022. 599–609.

Pastore, V. P., Zimmerman, T., Biswas, S. K., and Bianco, S. (2019). "Establishing the baseline for using plankton as biosensor," in *Imaging, manipulation, and analysis of biomolecules, cells, and tissues XVII (SPIE)*, vol. 10881. , 44–49.

Pastore, V. P., Zimmerman, T. G., Biswas, S. K., and Bianco, S. (2020). Annotation-free learning of plankton for classification and anomaly detection. *Sci. Rep.* 10, 12142. doi: 10.1038/s41598-020-68662-3

Paszke, A., Gross, S., Massa, F., Lerer, A., Bradbury, J., Chanan, G., et al. (2019). "Pytorch: An imperative style, high-performance deep learning library," in *Advances in neural information processing systems*, vol. vol. 32 . Eds. H. Wallach, H. Larochelle, A. Beygelzimer, F. d'Alché-Buc, E. Fox and R. Garnett (Curran Associates, Inc).

Pedregosa, F., Varoquaux, G., Gramfort, A., Michel, V., Thirion, B., Grisel, O., et al. (2011). Scikit-learn: machine learning in python. *J. Mach. Learn. Res.* 12, 2825–2830.

Pu, Y., Feng, Z., Wang, Z., Yang, Z., and Li, J. (2021). "Anomaly detection for in *situ* marine plankton images," in *Proceedings of the IEEE/CVF international conference on computer vision*, 3661–3671.

Python Software Foundation (2023) *Python programming language*. Available at: https://www.python.org.Version3.9.

Rousseeuw, P., and Driessen, K. (1999). A fast algorithm for the minimum covariance determinant estimator. *Technometrics* 41, 212–223. doi: 10.1080/00401706.1999.10485670

Salvesen, E., Saad, A., and Stahl, A. (2022). "Robust deep unsupervised learning framework to discover unseen plankton species," in *In fourteenth international conference on machine vision (ICMV 2021) (SPIE)*, vol. vol. 12084. , 241–250.

Scholkopf, B., Williamson, R., Smola, A., Shawe-Taylor, J., and Platt, J. (1999). "Support vector method for novelty detection," in *Proceedings of the 12th international conference on neural information processing systems* (Cambridge, MA, USA: MIT Press), 582–588.

Sosik, P. E. E.H.M, and Brownlee, ,. E. F. (2015) *WHOI-Plankton, annotated plankton images - data set for developing and evaluating classification methods*. Available at: http://hdl.handle.net/10.1575/1912/7341.

Sosik, H. M., and Olson, R. J. (2007). Automated taxonomic classification of phytoplankton sampled with imaging-in-flow cytometry. *Limnology Oceanography: Methods* 5, 204–216. doi: 10.4319/lom.2007.5.204

Tan, M., Chen, B., Pang, R., Vasudevan, V., Sandler, M., Howard, A., et al. (2019). "Mnasnet: Platformaware neural architecture search for mobile," in *Proceedings of the IEEE/CVF conference on computer vision and pattern recognition*, 2820–2828.

Tan, M., and Le, Q. (2019). "Efficientnet: Rethinking model scaling for convolutional neural networks," in *International conference on machine learning*.

Taylor, A. H., Allen, J. I., and Clark, P. A. (2002). Extraction of a weak climatic signal by an ecosystem. *Nature* 416, 629–632. doi: 10.1038/416629a

Touvron, H., Cord, M., Douze, M., Massa, F., Sablayrolles, A., and Jégou, H. (2021). "Training dataefficient image transformers & distillation through attention," in *International conference on machine learning (PMLR)*, 10347–10357.

Uitz, J., Claustre, H., Gentili, B., and Stramski, D. (2010). Phytoplankton class-specific primary production in the world's oceans: Seasonal and interannual variability from satellite observations. *Global Biogeochemical Cycles* 24. doi: 10.1029/2009GB003680

Verleysen, M., and Francois, D. (2005). “The curse of dimensionality in data mining and time series prediction,” in *International work-conference on artificial neural networks* (Springer), 758–770.

Vert, J.-P., Tsuda, K., and Scholkopf, B. (2004). A primer on kernel methods. *Kernel Methods Comput. Biol.* 47, 35–70. doi: 10.7551/mitpress/4057.003.0004

Walker, J. L., and Orenstein, E. C. (2021). “Improving rare-class recognition of marine plankton with hard negative mining,” in *Proceedings of the IEEE/CVF international conference on computer vision*, 3672–3682.

Wightman, R. (2019) *Pytorch image models*. Available at: https://github.com/rwightman/pytorch-image-models.

Winder, M., and Sommer, U. (2012). Phytoplankton response to a changing climate. *Hydrobiologia* 698, 5–16. doi: 10.1007/s10750-012-1149-2

Yadav, S., and Shukla, S. (2016). “Analysis of k-fold cross-validation over hold-out validation on colossal datasets for quality classification,” in *2016 IEEE 6th International conference on advanced computing (IACC)* (IEEE), 78–83.

Yang, Z., Li, J., Chen, T., Pu, Y., and Feng, Z. (2022). Contrastive learning-based image retrieval for automatic recognition of in *situ* marine plankton images. *ICES J. Mar. Sci.* 79, 2643–2655. doi: 10.1093/icesjms/fsac198

Zheng, H., Wang, R., Yu, Z., Wang, N., Gu, Z., and Zheng, B. (2017). Automatic plankton image classification combining multiple view features via multiple kernel learning. *BMC Bioinf.* 18, 570. doi: 10.1186/s12859-017-1954-8

Frontiers in
Marine Science

Explores ocean-based solutions for emerging global challenges

The third most-cited marine and freshwater biology journal, advancing our understanding of marine systems and addressing global challenges including overfishing, pollution, and climate change.

Discover the latest Research Topics

See more →

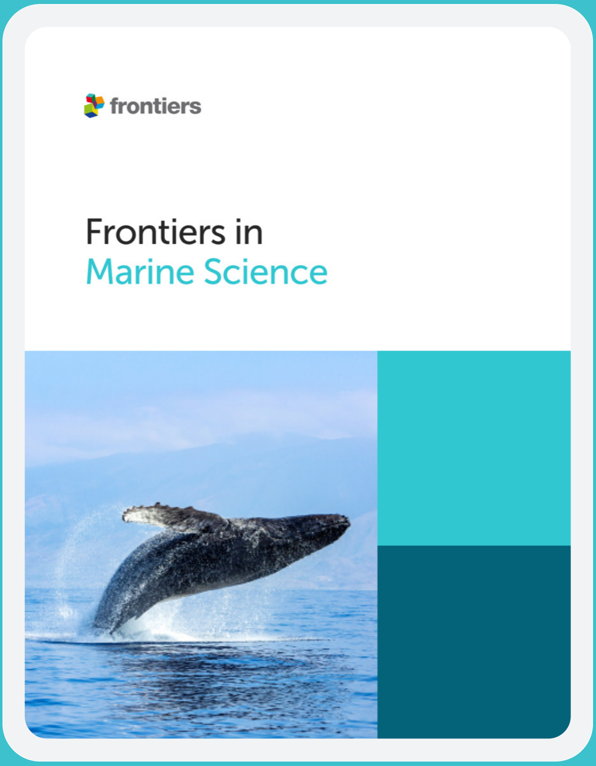

frontiers

Frontiers in
Marine Science

Frontiers

Avenue du Tribunal-Fédéral 34
1005 Lausanne, Switzerland
frontiersin.org

Contact us

+41 (0)21 510 17 00
frontiersin.org/about/contact